

JAERI - M
93-057

REVIEW OF JT-60U EXPERIMENTAL RESULTS
FROM JANUARY TO OCTOBER, 1992

March 1993

JT-60 Team

JAERI-M レポートは、日本原子力研究所が不定期に公刊している研究報告書です。

入手の問い合わせは、日本原子力研究所技術情報部情報資料課（〒319-11茨城県那珂郡東海村）あて、お申しこしください。なお、このほかに財団法人原子力弘済会資料センター（〒319-11 茨城県那珂郡東海村日本原子力研究所内）で複写による実費頒布をおこなっております。

JAERI-M reports are issued irregularly.

Inquiries about availability of the reports should be addressed to Information Division
Department of Technical Information, Japan Atomic Energy Research Institute, Tokai-
mura, Naka-gun, Ibaraki-ken 319-11, Japan.

©Japan Atomic Energy Research Institute, 1993

編集兼発行 日本原子力研究所
印刷 いばらき印刷(株)

Review of JT-60U Experimental Results
from January to October, 1992

JT-60 Team*

Department of Fusion Plasma Research
and
Department of Fusion Facility
Naka Fusion Research Establishment
Japan Atomic Energy Research Institute
Naka-machi, Naka-gun, Ibaraki-ken

(Received February 16, 1993)

Heating experiments have been carried out in JT-60U with plasma current up to 4 MA, toroidal field up to 4.2 T and neutral beam heating power of 30 MW. Carbon-fiber-composite divertor plates with good alignment and beveled edges provide excellent power handling capability; no carbon burst has been observed during 5 s heating pulses at ~20 MW. H-mode was observed at high toroidal field of 4.2 T. Confinement improvement factor of up to 1.6 over the L-mode scaling has been obtained during continuous ELMy phase at 4.2 T, 2.7 MA and an injection power of 25 MW. Confinement enhancement of 2.2 has been obtained transiently. At plasma current of 3.5 MA, diamagnetic stored energy of 7.7 MJ and energy confinement time of 0.36 s have been obtained. Discharges with high poloidal beta exhibit an enhancement in energy confinement of a factor of 3 relative to L-mode and high bootstrap current (58% of plasma current). In this regime, high ion temperatures of 38 keV, electron temperatures of 12 keV, maximum diamagnetic stored energy of 6.1 MJ and neutron yield of $2.8 \times 10^{16} \text{ s}^{-1}$ were obtained. Effects of current profile and sawtooth on mhd and confinement have been systematically demonstrated, suggesting importance of current profile and sawtooth for improving plasma performance. Schemes to avoid locked modes and disruptions have been checked experimentally. Divertor measurement indicates that high q, high density

operation is favorable for divertor heat handling; remote radiative cooling becomes significant and divertor heat load is less peaked in this operation mode. Quantitative analysis of divertor spectroscopy data indicates that the carbon production rate at the divertor plate is explained by deuterium, oxygen and carbon sputtering. Toroidal ripple loss power of NB-injected fast ions to the first wall was investigated by using an infrared TV camera. Absolute values of the ripple loss power and dependence on plasma parameters were consistent with values calculated by an orbit following Monte-Carlo code. In the LHCD area, the linear dispersion relation and accessibility condition for LH wave were experimentally validated. Furthermore, the power directly lost via high energy electron was shown to scale as the slowing down time, implying that direct loss power will be negligible in ITER. Current drive of 400kA (25% of the total plasma current) was realized with tangential NB. ICRF experiments using two new antennas started. The maximum coupled power to plasmas so far reached 3.6 MW for 1.4 s. Sawtooth stabilization at a high \bar{n}_e/P_{tot} value ($\sim 0.9 \times 10^{19} \text{m}^{-3} \text{MW}^{-1}$) was achieved.

Keywords: Tokamak, H-Mode, L-Mode, High Poloidal Beta, Divertor, MHD, Transport Process, Disruption, Current Drive, Progress Report

JT-60 Team*

T. Abe, H. Akasaka, K. Akiba¹⁾, M. Akiba, N. Akino, T. Ando, K. Annoh, I. Aoki, T. Aoyagi, T. Arai, K. Arakawa, M. Araki, N. Asakura, M. Azumi, P. Bertoldi⁴⁾, A.A.E. van Blokland³⁾, T. Bonicelli⁴⁾, D. Campbell⁴⁾, S. Chiba, D. Chiron⁴⁾, M. Dairaku, N. Ebisawa, T. Fujii, H. Fujita, T. Fujita, H. Fukuda¹⁾, T. Fukuda, A. Funahashi, H. Gunji¹⁾, J.C.M. de Haas⁵⁾, H. Haginoya¹⁾, K. Hamamatsu, M. Hanada, T. Hatae, K. Hill⁶⁾, H. Hiratsuka, T. Hirayama, S. Hiroki, K. Hiruta, K. Hisada¹⁾, M. Honda, H. Horiike, S. Hoshi¹⁾, R. Hosoda, N. Hosogane, D. Humphreys⁷⁾, H. Hsuan⁶⁾, H. Ichige, S. Ide, K. Igarashi¹⁾, T. Iguchi⁸⁾, K. Iida, Yu. Ikeda, Yo. Ikeda, T. Imai, T. Inoue, M. Isaka, N. Isei, S. Ishida, K. Itami, M. Ito¹⁾, T. Iwahashi¹⁾, N. Iwama¹⁶⁾, G.L. Jackson⁹⁾, R. Jinbo¹⁾, T.T.C. Jones⁴⁾, S. Kakizaki¹⁾, Y. Kamada, A. Kaminaga, T. Kashimura¹⁾, M. Kawai, Y. Kawamata, Y. Kawano, M. Kazawa, M. Kikuchi, H. Kimura, K. Kimura¹¹⁾, T. Kimura, H. Kishimoto, S. Kitamura, A. Kitsunezaki, S. Kiuchi¹⁾, K. Kiyono, T. K. Kodama, T. Koike, Y. Koide, M. Komata, I. Kondo, T. Kondoh, S. Konoshima, H. Kubo, S. Kunieda, K. Kurihara, M. Kuriyama, M. Kusaka¹⁾, Y. Kusama, S. Maebara, K. Maeno, T. Matoba, M. Matsukawa, M. Matsuoka, Y. Matsuzaki, S. Miura¹⁾, N. Miya, K. Miyachi, K. Miyake¹⁾, Y. Miyo, M. Mizuno, K. Mogaki, A. Morioka¹²⁾, S. Moriyama, Y. Murakami, M. Nagami, A. Nagashima, K. Nagashima, To. Nagashima¹⁾, Ta. Nagashima, S. Nagaya, K. Nagayama¹⁾, O. Naito, H. Nakamura, T. Nakafuji¹⁾, N. Nakayamada⁸⁾, M. Nemoto, Y. Neyatani, H. Ninomiya, T. Nishimura¹³⁾, Y. Nishino¹⁾, T. Nishitani, H. Nobusaka¹⁾, S. Numazawa¹⁾, K. Obara, K. Odajima, N. Ogiwara, Y. Ohara, T. Ohga, T. Ohshima, M. Ohta, S. Ohuchi¹⁾, Y. Ohuchi, A. Oikawa, Y. Okumura, K. Omori, S. Omori, Y. Omori, H. Oohara, M. Oozeki¹⁾, T. Ozeki, M. Saidoh, M. Saigusa, N. Saito, K. Sakamoto, A. Sakasai, S. Sakata, T. Sakuma¹⁾, T. Sasajima, N. Sasaki¹⁾, Mi. Sato, Ma. Sato, M. Sawahata, M. Seimiya, M. Seki, S. Seki, K. Shibamura, G. Schilling⁶⁾, M. Shimada, Kaz. Shimizu, Kat. Shimizu¹⁾, M. Shimizu, Y. Shimomura, M. Shimono, S. Shinozaki, H. Shirai, M. Shitomi, D. Stork⁴⁾, H. Sugai¹⁴⁾, K. Sukanuma, T. Sugie, M. Sugihara, H. Sunaoshi, N. Suzuki, N. Suzuki, Y. Suzuki¹⁾, T. Suzuki, H. Takagi¹⁵⁾, M. Takahashi, S. Takahashi, T. Takahashi¹⁾, A. Takasa¹⁾, M. Takasaki¹⁾, H. Takatsu, T. Takayasu¹⁾, H. Takeuchi, A. Takeshita¹⁾, T. Takizuka, S. Tamura, S. Tanaka, T. Tanaka, Yuj. Tanaka, Yut. Tanaka¹⁰⁾, A. Tanga⁴⁾, K. Tani, T. Tani, T. Taylor⁹⁾, M. Terakado, T. Terakado, ? Teranishi¹⁶⁾, K. Tobita, T. Totsuka, N. Toyoshima, T. Tsuchiya¹⁾, T. Tuda, T. Tsugita, S. Tsuji, Y. Tsukahara, M. Tsuneoka, A. Tsurumi¹⁾, K. Uehara, S. Uno, Y. Uramoto, H. Usami¹⁾, K. Ushigusa, K. Usui, M. Yagi, J. Yagyu, M. Yamage¹⁴⁾, K. Yamagishi, M. Yamagiwa, M. Yamamoto, S. Yamamoto, T. Yamamoto, O. Yamashita, T. Yasuda¹⁾, K. Yokokura, K. Yokoyama, H. Yoshida, M. Yoshida, R. Yoshino, Y. Yoshioka¹⁾, I. Yonekawa, J.P. Wang²⁾, K. Watanabe, S.W. Wolfe³⁾.

- 1) Staff on loan
- 2) JAERI fellowship; Present address: University of Wisconsin, Madison, Wisconsin, USA
- 3) STA Fellowship
- 4) JET Joint Undertaking, Abingdon, Oxfordshire, UK
- 5) JAERI fellowship; Present address: Centre d'etudes nucleaires de Cadarache, Saint-Paul-lez-Durance, France
- 6) Princeton Plasma Physics Laboratory, Princeton, New Jersey, USA
- 7) JAERI fellowship; Present address: General Atomics, San Diego, California, USA
- 8) University of Tokyo, Bunkyo-ku, Tokyo, Japan
- 9) General Atomics, San Diego, California, USA
- 10) Kyushu University, Fukuoka, Fukuoka, Japan
- 11) Keio University, Yokohama, Kanagawa, Japan
- 12) Tokai University, Hiratuka, Kanagawa, Japan
- 13) Osaka University, Suita, Osaka, Japan
- 14) Nagoya University, Nagoya, Aichi, Japan
- 15) Kobe University of Mercantile Marine, Kobe, Hyogo, Japan
- 16) Toyama Prefectural University, Japan

JT-60U 1992年1月-10月期実験結果のレビュー

日本原子力研究所那珂研究所炉心プラズマ研究部・核融合装置試験部

JT-60 チーム*

(1993年2月16日受理)

JT-60Uにおいて最大プラズマ電流4MA, 最大トロイダル磁場4.2T, 最大中性粒子入射パワー30MWの条件で加熱実験を行った。ダイバータ板には炭素繊維複合材料を材料として用いており、高精度に設置を行ったうえ、さらに端部をテーパ加工した。そのためダイバータ板は熱処理能力が優れており、約20MWの加熱パルスでも炭素の急激な増加は観測されなかった。Hモードを4.2Tの強磁場条件で観測した。トロイダル磁場4.2T, プラズマ電流2.7MA, 入射パワー25MWで連続したELMが発生する条件において、閉じ込めをLモード比例則から1.6倍改善した。過渡的ではあるが、Lモード閉じ込め比例則の2.2倍の閉じ込め改善を達成した。プラズマ電流が3.5MAの条件で、反磁性ループで測定したプラズマ蓄積エネルギーは7.7MJ, エネルギー閉じ込め時間は0.36秒に達した。高トロイダルベータ放電は、Lモード閉じ込め比例則の3倍にも達する閉じ込め特性と、高いブートストラップ電流(プラズマ電流の58%)を有している。この放電領域では、イオン温度38keV, 電子温度12keV, 反磁性ループで測定したプラズマ蓄積エネルギー6.1MJ, 中性粒子発生率 2.8×10^{18} 個/sを達成した。電流分布と鋸歯状振動がMHDと閉じ込めに与える影響を系統的に示した。プラズマ性能の向上には、電流分布と鋸歯状振動の制御が有効であることがこの結果から示唆される。またロックモードとディスラプションの回避法の実験的検証を行った。ダイバータ研究では高q高密度運転がダイバータの熱制御特性において優れていることが明らかになった。この放電領域では、遠隔放射冷却が顕著になり、ダイバータの熱負荷の分布が広がるためである。ダイバータ分光の定量的解析によって、ダイバータ板上の炭素不純物発生量は重水素と酸素、炭素のスパッタリングで説明できることを示した。NBで入射した高速イオンの第一壁へのトロイダル・リップル損失を赤外TVカメラで測定した。リップル損失の絶対値及びプラズマ・パラメータへの依存性はモンテ・カルロの手法を用いた粒子軌道計算と良く一致する。LHCDの分野では、LH波の線形分散関係と近接条件を実験的に実証した。さらに高速電子の直接損失を測定し、直接損失のパワーが、減衰時間に比例することを示した。この成果は、ITERにおける直接損失が無視できることを示唆している。また接線NBを用いた電流駆動では、全プラズマ電流の

25%に相当する400kA のビーム電流を駆動出来た。ICRFは、2本のアンテナを用いた実験を開始した。プラズマにカップルしたパワーは最大で3.6MWであり、1.4秒間持続した。また高い \bar{n}_e/P_{ICRF} 値 ($\sim 0.9 \times 10^{19} \text{ m}^{-3} \text{ MW}^{-1}$) で鋸歯状振動を抑制することができた。

JT-60 チーム*

阿部 哲也	・赤坂 博美	・秋葉 賢一 ¹	・秋場 真人	・秋野 昇
安東 俊郎	・安納 勝人	・青木 功	・青柳 哲雄	・新井 貴
荒川喜代次	・荒木 正則	・朝倉 伸幸	・安積 正史	・市毛 尚志
井手 俊介	・五十嵐浩一 ¹⁾	・井口 哲夫 ⁸⁾	・飯田 一広	・池田 幸治
池田裕二朗	・池田 佳隆	・今井 剛	・井上多加志	・井坂 正義
伊世井宣明	・石田 真一	・伊丹 潔	・伊藤 優 ¹⁾	・岩橋 孝明 ¹⁾
岩間 尚文 ¹⁶⁾	・上原 和也	・宇野 定則	・浦本 保幸	・宇佐美広次 ¹⁾
牛草 健吉	・薄井 勝富	・海老沢 昇	・小原健次郎	・小田島和男
荻原 徳男	・小原 祥裕	・大賀 徳道	・大島 貴幸	・太田 充
大内 豊	・大内 章寿 ¹⁾	・及川 晃	・奥村 義和	・大森 俊造
大森憲一郎	・大森 栄和	・大原比呂志	・大関 正弘 ¹⁾	・小関 隆久
柿崎 禎之 ¹⁾	・鎌田 裕	・神永 敦嗣	・桵村 隆則 ¹⁾	・河合規己人
川俣 陽一	・河野 康則	・桃澤 稔	・菊池 満	・木村 晴行
木村 衡 ¹¹⁾	・木村 豊秋	・岸本 浩	・北村 繁	・狐崎 晶雄
木内 重巳 ¹⁾	・清野 公広	・久保 博孝	・国枝 俊介	・栗原 研一
栗山 正明	・日下 誠 ¹⁾	・草間 義紀	・軍司 秀穂 ¹⁾	・児玉 幸三
小池 常之	・小出 芳彦	・小又 将夫	・近藤 育朗	・近藤 貴
木島 滋	・西堂 雅博	・三枝 幹雄	・斎藤 直之	・坂本 慶司
逆井 章	・坂田 信也	・佐久間 猛 ¹⁾	・笹島 唯之	・佐々木 昇 ¹⁾
佐藤 正泰	・佐藤 稔	・沢畠 正之	・柴沼 清	・嶋田 道也
清水 勝宏	・清水 正亜	・清水 和彦 ¹⁾	・下村 安夫	・下野 貢
篠崎 信一	・白井 浩	・都 守正	・神保龍太郎 ¹⁾	・菅井 秀郎 ¹⁴⁾
菅沼 和明	・杉江 達夫	・杉原 正芳	・砂押 秀則	・鈴木 紀男
鈴木 紀男	・鈴木 靖生 ¹⁾	・鈴木 哲	・清宮 宗孝	・関 正美
関 省吾	・高木 一 ¹⁵⁾	・高橋 春次	・高橋虎之助 ¹⁾	・高橋 実
高佐 明 ¹⁾	・高崎 學 ¹⁾	・高津 英幸	・高安 利男 ¹⁾	・竹内 浩
竹下 明 ¹⁾	・滝塚 知典	・田村 早苗	・田中 茂	・田中竹次郎
田中 裕二	・田中 豊 ¹⁰⁾	・谷 啓二	・谷 孝	・大楽 正幸
千葉 真一	・土屋 哲 ¹⁾	・次田 友宣	・津田 孝	・辻 俊二
塚原 美光	・恒岡まさき	・鶴見 聰	・寺門 恒久	・寺門 正之
寺西 大 ¹⁶⁾	・飛田 健次	・戸塚 俊之	・豊島 昇	・永見 正幸
長島 章	・永島 圭介	・永嶋 俊行 ¹⁾	・永島 孝	・永谷 進
長山 清 ¹⁾	・内藤 磨	・中村 博雄	・中藤 隆志 ¹⁾	・信坂 裕通 ¹⁾
中山田憲明	・二宮 博正	・西村泰太郎 ¹³⁾	・西谷 健夫	・西野 好彦 ¹⁾
沼澤 呈 ¹⁾	・根本 正博	・関谷 讓	・濱松 清隆	・花田磨砂也
波多江仰紀	・平塚 一	・平山 俊雄	・廣木 成治	・蛭田 和治
久田 憲央 ¹⁾	・萩野谷裕文 ¹⁾	・藤井 常幸	・藤田 秀男	・藤田 隆明
福田 裕実 ¹⁾	・福田 武司	・船橋 昭昌	・本田 正男	・堀池 寛
星 静男 ¹⁾	・細田隆二郎	・細金 延幸	・前原 直	・前野 勝樹
の場 徹	・松川 誠	・松岡 守	・松崎 誼	・三浦 早苗 ¹⁾

宮 直之 ・ 宮地 謙吉 ・ 三宅 一幸¹⁾ ・ 三代 康彦 ・ 水野 誠
 村上 義男 ・ 藻垣 和彦 ・ 森岡 篤彦¹²⁾ ・ 森山 伸一 ・ 矢木 雅敏
 柳生 純一 ・ 山華 雅司¹⁴⁾ ・ 山岸耕二郎 ・ 山極 満 ・ 山本 正弘
 山本 巧 ・ 山本 新 ・ 山下 修 ・ 安田 泰三¹⁾ ・ 横倉 賢治
 横山 堅二 ・ 吉田 英俊 ・ 吉田 通治 ・ 芳野 隆治 ・ 吉岡 祐二¹⁾ .
 米川 出 ・ 渡部 和弘
 P. Bertoldi⁴⁾ ・ A.A.E. van Blokland³⁾ ・ T. Bonicelli⁴⁾ ・ D.Campbell⁴⁾
 D. Chiron⁴⁾ ・ J. C. M. de Haas⁵⁾ ・ K. Hill⁶⁾ ・ D. Humphreys⁷⁾ ・ H. Hsuan⁶⁾
 G. L. Jackson⁹⁾ ・ T. T. C. Jones⁴⁾ ・ G. Schilling⁶⁾ ・ D. Stork⁴⁾ ・ A. Tanga⁴⁾
 T. Taylor⁹⁾ ・ S. W. Wolfe³⁾ ・ J.P. Wang²⁾

1) 業務協力員

2) 原研フェローシップ、現在、米国、ウイスコンシン大学

3) S T A フェローシップ

4) J E T

5) 原研フェローシップ、現在、フランス、カダラッシュ原子力研究所

6) 米国プリンストン大学プラズマ物理研究所

7) 原研フェローシップ、現在、米国、ゼネラルアトミック社

8) 東京大学

9) 米国、ゼネラルアトミック社

10) 九州大学

11) 慶応大学

12) 東海大学

13) 大阪大学

14) 名古屋大学

15) 神戸商船大学

16) 富山県立大学

Contents

1. H-mode and L-mode Confinements	1
1.1 Fusion Performance in Different Confinement Regimes	1
M. Kikuchi, et al.	
1.2 Operation Procedures and Basic Characteristics of the H-mode .	5
H. Ninomiya, et al.	
1.3 Overview of High Ti H-mode	9
M. Kikuchi, et al.	
1.4 H-mode Regime and ELMS	13
Y. Kamada, et al.	
1.5 Temperature and Current Profile Evolution in Hot Ion H-mode ..	17
M. Sato, et al.	
1.6 Edge Transport Barrier in H- and L-modes	21
M. Kikuchi, et al.	
1.7 Effective Ion Collisionality Regime Across the H-mode Transition	25
T. Fukuda, et al.	
1.8 H-mode Characteristics with Outboard Configuration for Combined IC and NB Heating	29
H. Kimura, et al.	
1.9 Effects of Safety Factor and Internal Inductance on Energy Confinement in L-mode and H-mode	33
Y. Kamada, et al.	
1.10 Effects of Sawtooth Activity on Confinement	37
Y. Kamada, et al.	
1.11 Effects of ELM Activity on Energy Confinement	41
Y. Kamada, et al.	
1.12 Relation between Fast-ion Loss and H-mode Performance	45
A.A.E. van Blokland, et al.	
1.13 Comparison of H-mode Confinement with Tangential and Perpendicular NBI	49
T.T.C. Jones	
1.14 Nondimensional Scaling for JT-60U L-mode Plasmas	53
T. Takizuka, et al.	
1.15 Scaling of Thermal Energy in Tokamaks	57
T. Takizuka, et al.	

1.16	Test of the Theoretical L-mode Scaling with Experimental Data .	61
	M. Yagi, et al.	
1.17	Sawtooth Characteristics and Electron Temperature Profiles from Electron Cyclotron Emission Measurements	64
	N. Isei, et al.	
1.18	Energy Confinement in Ohmically Heated Plasma	68
	N. Isei, et al.	
2.	High Poloidal Beta Confinement	72
2.1	Fusion Performance of High Poloidal Beta Plasmas	72
	S. Ishida, et al.	
2.2	Enhanced Confinement of High Poloidal Beta Plasmas	76
	S. Ishida, et al.	
2.3	Fusion Reactivity	80
	T. Nishitani, et al.	
2.4	Equilibrium Analysis and Pressure Anisotropy of High Poloidal Beta Plasmas	84
	T. Fujita, et al.	
2.5	Beta Limits and β_p Collapses for High β_p Plasmas	88
	S. Ishida, et al.	
2.6	High Normalized β Experiments	92
	Y. Kamada, et al.	
2.7	Estimation of the Bulk Ion-temperature from the Measured Carbon-temperature Using a Simple Model for the 38keV Plasma ..	96
	Y. Koide, et al.	
2.8	The Phenomena Associating the Crush of Central Ion Temperature of 38keV	100
	Y. Koide, et al.	
2.9	Nonlinear Fokker-Planck Analysis of High Ion Temperature Plasma	104
	M. Azumi, et al.	
2.10	Summary of the Compression Experiments	108
	A. Tanga, et al.	
3.	Transport Studies	112
3.1	On and Off-axis NBI Heating Experiments	112
	K. Nagashima, et al.	
3.2	Toroidal Momentum Transport Experiment Using Tangential NBI ..	116
	K. Nagashima, et al.	

3.3	Particle Transport Induced by Temperature Gradient on ICRF Experiments	119
	K. Nagashima, et al.	
3.4	Anti-parallel Toroidal Rotation to Plasma Current during Near-perpendicular NBI	123
	Y. Koide, et al.	
3.5	Co-parallel Toroidal Rotation to Plasma Current during LHCD ..	127
	Y. Koide, et al.	
3.6	Transport Analysis of Ohmically Heated Plasmas by CXRS Measurement	131
	H. Shirai, et al.	
3.7	Transport Analysis of Low Power NBI Heated Plasmas	135
	H. Shirai, et al.	
3.8	High Energy Electron Transport induced by Pellet Injection in Lower Hybrid Current Drive Discharge	138
	K. Nagashima et al.	
4.	Impurity and Divertor	142
4.1	Decaborane-based Boronization System and its Operation Experience	142
	M. Saidoh, et al.	
4.2	Effects of Boronization and Wall Conditioning on H-mode	146
	M. Shimada, et al.	
4.3	Impurity Concentration and Radiation Loss in the Main Plasma ..	150
	T. Sugie, et al.	
4.4	Distributions of Divertor Radiation Loss in Ohmic Discharges ..	154
	N. Hosogane, et al.	
4.5	Heat Flux in Divertor Plasmas	158
	K. Itami, et al.	
4.6	Heat Flux in ELMy Discharges and High Beta Poloidal Discharges	162
	K. Itami, et al.	
4.7	Carbon Generation Mechanism	166
	A. Sakasai, et al.	
4.8	Ion Temperature Characteristics and Impurity Behavior in Divertor Region	170
	A. Sakasai, et al.	

4.9	Study of Impurity and Radiative Loss in Divertor Plasmas with Absolutely Calibrated VUV Spectrometers	174
	H. Kubo, et al.	
4.10	Recycling Study in High Density Discharges	178
	N. Asakura, et al.	
4.11	Recycling in H-mode and High β_p Discharges	182
	N. Asakura, et al.	
4.12	Modelling of Impurity Transport	186
	K. Shimizu, et al.	
4.13	Divertor Analysis with the UEDA Code	190
	S. Tsuji, et al.	
4.14	Helium Ash Experiment with He Beam Fuelling in Divertor Discharges	194
	H. Nakamura, et al.	
4.15	Investigation of First Wall Damage	197
	T. Ando, et al.	
5.	Current Drive	201
5.1	Progress in LHCD Experiments	201
	K. Ushigusa, et al.	
5.2	Behavior of High Energy Electrons during LHCD	205
	T. Kondoh, et al.	
5.3	Verification of LH Wave Dispersion Relation	209
	M. Nemoto, et al.	
5.4	Detection of Non-accessible Wave	213
	Y. Ikeda, et al.	
5.5	Effects of Accessibility on ECE Signal in LHCD Experiments ...	217
	M. Sato, et al.	
5.6	Identification of the Direct Loss of Energetic Electrons during LHCD	221
	K. Ushigusa, et al.	
5.7	Measurement of Pressure Anisotropy in LHCD Discharges	225
	S.W. Wolfe, et al.	
5.8	Combined Fast Wave and Lower Hybrid Wave Experiment	229
	T. Fujii, et al.	
5.9	Hard X-ray Measurement in Combined Fast Wave and Lower Hybrid Wave Experiment	233
	T. Kondoh, et al.	

5.10 Progress in Bootstrap Current Study	236
M. Matsuoka, et al.	
5.11 Current Drive by Using Tangential Neutral Beams	240
M. Matsuoka et al.	
6. Fast Ion Study	243
6.1 Sawtooth Stabilization Experiments by Second Harmonic Minority Ion ICRF Heating	243
H. Kimura, et al.	
6.2 Sawtooth Stabilization Experiments by ICRF Heating in Combination with NBI or LHCD	247
H. Kimura, et al.	
6.3 Electron Temperature Profiles in Sawtooth Stabilization Experiment	251
M. Sato, et al.	
6.4 D - ^3He Experiments by ICRF Heating	255
T. Fujii, et al.	
6.5 CX Measurement of High Energy Ions in D - ^3He Experiments	259
M. Nemoto, et al.	
6.6 Ripple-induced Fast Ion Losses	263
K. Tobita, et al.	
6.7 Triton Burnup	267
T. Nishitani, et al.	
6.8 Neutron Spectrometry with a ^3He Gas Ionization Chamber	271
T. Iguchi, et al.	
6.9 Activation Analysis with 1-D Code in D-D Discharges	275
N. Miya, et al.	
7. Disruption and Plasma Control	279
7.1 Review of Disruptions	279
R. Yoshino, et al.	
7.2 Identification of a Low Density Locked Mode	283
S.W. Wolfe, et al.	
7.3 Error Field Analysis of Magnetic Coils	287
S. Miura, et al.	
7.4 DCW Effect on Density Limit	291
Y. Neyatani, et al.	
7.5 Effects of DCW on Disruptions	295
R. Yoshino, et al.	

7.6	MARFE Limit of Ohmic Divertor Discharges	299
	N. Hosogane, et al.	
7.7	The Current Quench in the Disruptive Termination	303
	R. Yoshino, et al.	
7.8	Softening of the Current Quench in the Disruptive Termination .	307
	R. Yoshino	
7.9	Suppression of Runaway Electrons	311
	R. Yoshino	
7.10	Stable Fast Plasma Shutdown	314
	R. Yoshino	
7.11	Statistical Analysis of Disruptions	317
	Y. Neyatani, et al.	
7.12	A Possibility Study of High Triangularity Operation	321
	M. Matsukawa, et al.	
7.13	Plasma Behavior during the Plasma Termination and Initiation Procedure Observed by the Density Measurement	323
	T. Fukuda, et al.	
8.	MHD	327
8.1	Overview of the Study on MHD Activities	327
	Y. Kamada, et al.	
8.2	Magnetic Fluctuation in High Troyon Factor Discharges	331
	Y. Neyatani, et al.	
8.3	MHD Stability Analyses for β_p Collapse	335
	T. Ozeki, et al.	
8.4	Magnetic Fluctuation in High β_p Plasma	339
	Y. Neyatani, et al.	
8.5	Characteristics of Sawteeth	343
	Y. Kamada	
9.	Diagnostics	347
9.1	Absolute Sensitivity Calibration of VUV Spectrometers	347
	T. Sugie, et al.	
9.2	First Operation Result of CO ₂ Laser Interferometer	351
	Y. Kawano, et al.	
9.3	Motional Stark Effect Polarimeter	355
	H. Kubo, et al.	
9.4	Development of Fourier Transform Spectrometer System	359
	M. Sato, et al.	

9.5	Low-noise Preamplifier System for the 20-channel Grating Polychromator and Application to ECE Image Reconstruction 363
	S. Ishida, et al.	
10.	Heating and Current Drive Machine Status 367
10.1	Port Aging and Capability of High Energy and Power in NB System 367
	M. Kuriyama	
10.2	Power Injection Capability and Impedance Matching of ICRF Antennas 371
	S. Moriyama	
10.3	Antenna Coupling and Radiation Loss during ICRF Power Injection 375
	M. Saigusa	
	Acknowledgements 379

目 次

1. HモードおよびLモード閉じ込め	1
1.1 種々の閉じ込め領域の核融合性能	1
菊池 満, 他	
1.2 Hモードの運転経過と基本特性	5
二宮博正, 他	
1.3 高イオンHモードの概要	9
菊池 満, 他	
1.4 Hモード領域とELM	13
鎌田 裕, 他	
1.5 高イオンHモードの温度と電流分布の時間変化	17
佐藤正泰, 他	
1.6 Hモード, Lモードにおける周辺部輸送バリアー	21
菊池 満, 他	
1.7 Hモード遷移時の実効イオン衝突時	25
福田武司, 他	
1.8 ICとNB複合加熱時の外寄せ配位Hモードの特性	29
木村晴行, 他	
1.9 Lモード, Hモードにおける安全係数と内部インダクタンスの エネルギー閉じ込めに対する影響	33
鎌田 裕, 他	
1.10 閉じ込めに対する鋸歯状振動の影響	37
鎌田 裕, 他	
1.11 ELM振動のエネルギー閉じ込めに対する影響	41
鎌田 裕, 他	
1.12 高速イオン損失とHモード性能の関係	45
A. A. E. van Blokland, 他	
1.13 接線と垂直NBのHモード閉じ込めの比較	49
T. T. C. Jones	
1.14 Lモード実験に対する無次元比例則	53
滝塚知典, 他	
1.15 トカマクの熱エネルギー比例則	57
滝塚知典, 他	

1.16	理論Lモード則の実験データの比較	61
	矢木雅敏, 他	
1.17	電子サイクロトロン放射測定による鋸歯状振動特性と電子温度分布	64
	伊世井宣明, 他	
1.18	ジュール加熱プラズマのエネルギー閉じ込め	68
	伊世井宣明, 他	
2.	高ポロイダルベータの閉じ込め	72
2.1	高ポロイダルベータプラズマの核融合特性	72
	石田真一, 他	
2.2	高ポロイダルベータプラズマの閉じ込め改善	76
	石田真一, 他	
2.3	核融合反応率	80
	西谷健夫, 他	
2.4	高ポロイダルベータプラズマの平衡解析と圧力非等方性	84
	藤田隆明, 他	
2.5	高ポロイダルベータプラズマのベータ限界とポロイダルベータ 崩壊	88
	石田真一, 他	
2.6	高規格化ベータ実験	92
	鎌田 裕, 他	
2.7	38keV プラズマに対する単純モデルを用いたカーボン温度からの バルク温度の評価	96
	小出芳彦, 他	
2.8	38keV におけるイオン温度低下に関する現象	100
	小出芳彦, 他	
2.9	高イオン温度プラズマの非線型フォッカープランク解析	104
	安積正史, 他	
2.10	プラズマ圧縮実験のまとめ	108
	A. Tanga, 他	
3.	輸送研究	112
3.1	NBI 中心加熱と周辺加熱実験	112
	永島圭介, 他	
3.2	接線NBI によるトロイダル角運動量輸送実験	116
	永島圭介, 他	

3.3	ICRF加熱実験での温度勾配によって励起される粒子輸送	119
	永島圭介, 他	
3.4	準垂直NBIによるプラズマ電流と反対方向のトロイダル回転	123
	小出芳彦, 他	
3.5	LHCD時のプラズマ電流方向のトロイダル回転	127
	小出芳彦, 他	
3.6	CXRS測定によるジュール加熱プラズマの輸送解析	131
	白井 浩, 他	
3.7	低パワーNBI加熱プラズマの輸送解析	135
	白井 浩, 他	
3.8	低域混成波電流駆動放電へのペレット入射による高エネルギー	138
	電子輸送	
	永島圭介, 他	
4.	不純物及びダイバータ	142
4.1	デカボランを用いたボロン化システムとその運転経験	142
	西堂雅博, 他	
4.2	Hモードにおけるボロン化の壁調整と効果	146
	嶋田道也, 他	
4.3	主プラズマにおける不純物量と放射損失	150
	杉江達夫, 他	
4.4	オーミック放電におけるダイバータ領域の放射損失の分布	154
	細金延幸, 他	
4.5	ダイバータプラズマにおける熱流束	158
	伊丹 潔, 他	
4.6	ELM放電と高ボロイダルベータ放電における熱流束	162
	伊丹 潔, 他	
4.7	炭素不純物発生機構	166
	逆井 章, 他	
4.8	ダイバータ領域におけるイオン温度特性と不純物の振舞い	170
	逆井 章, 他	
4.9	絶対校正した斜入射分光器によるダイバータ領域における不純物と	174
	放射損失の測定	
	久保博孝, 他	
4.10	高密度放電における粒子リサイクリング	178
	朝倉伸幸, 他	

4.11	Hモードと高 β p放電における粒子リサイクリング	182
	朝倉伸幸, 他	
4.12	不純物輸送のモデリング	186
	清水勝宏, 他	
4.13	UEDAコードによるダイバータ解析	190
	辻 俊二, 他	
4.14	ヘリウム灰輸送と排気	194
	中村博雄, 他	
4.15	第1壁損傷の観察	197
	安東俊郎, 他	
5.	電流駆動	201
5.1	LHCD実験の進展	201
	牛草健吉, 他	
5.2	LHCDにおける高エネルギー電子の振舞	205
	近藤 貴, 他	
5.3	LHCD波の分散式の検証	209
	根本正博, 他	
5.4	非近接波のパワー検出	213
	池田佳隆, 他	
5.5	LHCDにおけるECE信号への近接性条件の影響	217
	佐藤正泰, 他	
5.6	LHCDにおける高速電子の直接損失の同定	221
	牛草健吉, 他	
5.7	LHCDにおける圧力非等方性の測定	225
	S. W. Wolfe, 他	
5.8	速波とLH波との複合電流駆動実験	229
	藤井常幸, 他	
5.9	速波とLH波との複合電流駆動実験における硬X線測定	233
	近藤 貴, 他	
5.10	ブートストラップ電流駆動研究における進展	236
	松岡 守, 他	
5.11	接線NBIビームを用いた電流駆動	240
	松岡 守, 他	
6.	高速イオン研究	243

6.1	小数イオン第2高調波ICRF加熱による鋸歯状振動安定化実験	243
	木村晴行, 他	
6.2	ICRFとNBI又はLHCDとの複合加熱による鋸歯状振動安定化実験	247
	木村晴行, 他	
6.3	鋸歯状振動安定化実験における電子温度分布	251
	佐藤正泰, 他	
6.4	D- ³ He実験	255
	藤井常幸, 他	
6.5	D- ³ He実験における高エネルギーイオンテイルのCX測定	259
	根本正博, 他	
6.6	トロイダル磁場リップルによる高速イオンの損失	263
	飛田健次, 他	
6.7	トリトン燃焼	267
	西谷健夫, 他	
6.8	³ He電離箱による中性子スペクトロスコピー	271
	井口哲夫, 他	
6.9	1次元コードを用いたDD放電における放射化解析	275
	宮 直之, 他	
7.	ディスラプションとプラズマ制御	279
7.1	ディスラプションの概要	279
	芳野隆治, 他	
7.2	低密度ロックドモードの同定	283
	S. W. Wolfe, 他	
7.3	コイルのエラー磁場解析	287
	三浦早苗, 他	
7.4	密度限界に対するDCW効果	291
	関谷 譲, 他	
7.5	ディスラプションに対するDCW効果	295
	芳野隆治, 他	
7.6	OHダイバートプラズマにおけるMARFE限界	299
	細金延幸, 他	
7.7	ディスラプティブな放電停止における電流クウェンチ	303
	芳野隆治, 他	
7.8	ディスラプティブな放電停止における電流クウェンチのソフト化	307

芳野隆治, 他	
7.9 逃走電子の抑制	311
芳野隆治	
7.10 安定な高速プラズマ停止	314
芳野隆治	
7.11 ディスラプションの統計的解析	317
関谷 譲, 他	
7.12 高三角形度運転の可能性	321
松川 誠, 他	
7.13 密度測定によるプラズマ停止と立ちあげ時のプラズマ挙動の評価	323
福田武司, 他	
8. MHD	327
8.1 MHD挙動研究の概要	327
鎌田 裕, 他	
8.2 高トロロン係数放電における磁場揺動	331
関谷 譲, 他	
8.3 βp 崩壊におけるMHD安定性解析	335
小関隆久, 他	
8.4 高 βp プラズマにおける磁場揺動	339
関谷 譲, 他	
8.5 鋸歯状振動の特性	343
鎌田 裕, 他	
9. 計測装置	347
9.1 VUV分光器の絶対感度校正	347
杉江達夫, 他	
9.2 CO ₂ レーザ干渉計の初期測定結果	351
河野康則, 他	
9.3 モーショナルシュタルク偏光計	355
久保博孝, 他	
9.4 フーリエ分光システムの開発	359
佐藤正泰, 他	
9.5 20ch回析格子型ポリクロメータ用低雑音前置増幅器とECE	363
イメージの再構成へのその応用	
石田真一, 他	

10. 加熱及び電流駆動装置	367
10.1 NBシステムにおけるポートエージングと高エネルギー, 高出力	367
運転性能	
栗山正明, 他	
10.2 ICRFアンテナのパワー入力性能とインピーダンスマッチング	371
特性	
森山信一, 他	
10.3 ICRFパワー注入中のアンテナカップリングと放射損失	375
三枝幹雄, 他	
謝 辞	379

1. H-mode and L-mode Confinements

1.1 Fusion Performance in Different Confinement Regimes

M. Kikuchi, S. Ishida, Y. Kamada, T. Nishitani, Y. Koide
H. Ninomiya, M. Shimada, R. Yoshino, H. Takeuchi

1. Introduction

Progress of plasma performances was made in 1992. The maximum fusion triple product $n_i(0)T_i(0)\tau_E$ was doubled ($2 \rightarrow 4.4$) $\times 10^{20} \text{keVsec/m}^3$. A world record ion temperature $T_i(0)=38 \text{keV}$ (high β_p) was observed. Maximum plasma stored energy was increased from 4.3MJ to 7.7MJ (H-mode). The average fusion product $\langle nT \rangle \tau_E^G$ was also significantly improved from $4.3 \times 10^{19} \text{keVsecm}^{-3}$ (1991) to $(0.93-1.2) \times 10^{20} \text{keVsecm}^{-3}$ (high β_p & H-mode, respectively). As one of important feature of JT-60U, high pressure could be attainable since $\langle nT \rangle_t = (2/3)W_{\text{dia}}/V_p \sim gI_p B_t / a_p$. The maximum $\langle nT \rangle_t$ of $\sim 0.08 \text{MPa}$ was obtained in both hot ion H-mode and high β_p regime.

2. Characteristics of Different Confinement Regime.

Two different confinement regimes were explored in 1992. One is H-mode regime obtained with reduced recycling with Boronization. L-H transition power was up to 16MW in 4.2T low density hot ion H-mode without clear D_α drop (see sections 1.3 and 1.4). This mode was characterized with flat n_e and high edge temperature T_{i95} and T_{e95} up to 7keV and 2keV, respectively. This mode was insensitive to the existence of sawteeth if the sawtooth time is sufficiently long. On the other hand, the enhanced confinement in high β_p regime was obtained when the sawteeth were suppressed. Improvement was associated with peaked n_e profile which resulted in the β_p collapse in the central region. The enhanced confinement was seen at the net heating power well below the H-mode threshold. Table 1 shows a list of the plasma parameters obtained in H-mode and high β_p regime.

Table 1 Parameter list of H-mode and high β_p regime

Shot	16168	16128	16023	16045	Shot	16168	16128	16023	16045
Bt(T)	4.2	4.2	4.4	4.4	$W_{\text{dia}}(\text{MJ})$	7.7	6.9	5.7	4.9
$I_p(\text{MA})$	3.5	3.0	1.66	1.85	$\tau_E(\text{s})$	0.36	0.45	0.28	0.4
q_{eff}	3.3	3.8	6.3	5.4	H-factor	1.43	1.8	2.2	2.4
$n_e(\text{E19})$	3.3	3.0	3.4	2.2	$T_i(0)(\text{keV})$	20	22	35	38
$P_{\text{abs}}(\text{MW})$	24	23	23	19	$T_e(0)(\text{keV})$	5.5	7.2	12	8.8
$P_{\text{net}}(\text{MW})$	21	15	20	13	$S_n(10^{16}/\text{s})$	1.9	2.0	2.8	1.8
$P_{\text{rad}}(\text{MW})$	7	9	8	5	Mode	H	H	H- β_p	H- β_p

3. Plasma Stored Energy and Energy Confinement Time

Plasma stored energy W_{dia} and the energy confinement time τ_E^G are shown for L- and H-modes and high β_p regime in Fig. 1. The confinement was significantly improved from L-mode level (1991) to H-mode and high β_p level ($\sim 0.5\text{s}$). Maximum τ_E and stored energy in JT-60U were 0.9sec in an ohmic discharge and 7.7MJ in H-mode, respectively while longest τ_E and largest stored energy were 1.4sec and 13MJ in JET H-modes[1,2].

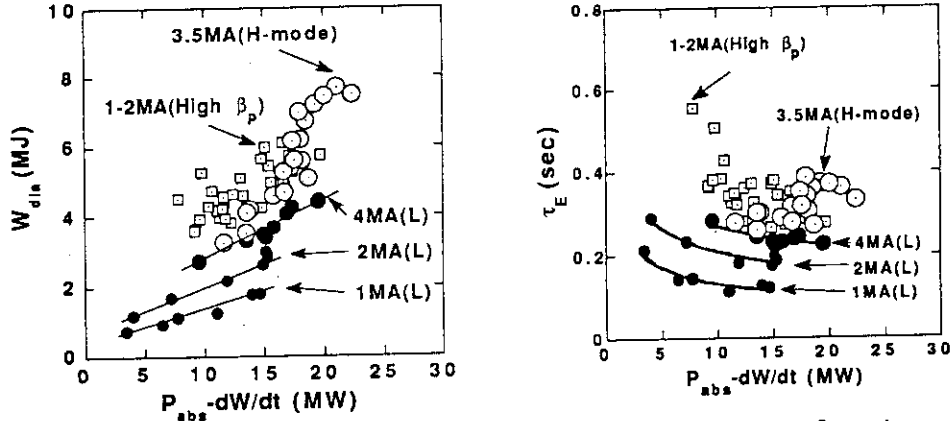


Fig. 1 Total plasma stored energy and energy confinement time for L and H and high β_p regime.

4. High Temperatures

World records of ion temperature $T_i(0)=38\text{keV}$ in high β_p regime (2-nd is 35keV in TFTR[3]) and $T_i(0)=32\text{keV}$ in high T_i H-mode (2-nd is 26keV in JET[2]) were achieved in 1992. The electron temperature up to 12keV in high β_p regime and 10keV in high T_i H-mode regime were obtained while world record is 13keV from JET ICRF plasma[4]. Figure 2 shows central electron and ion temperatures as functions of P_{net} .

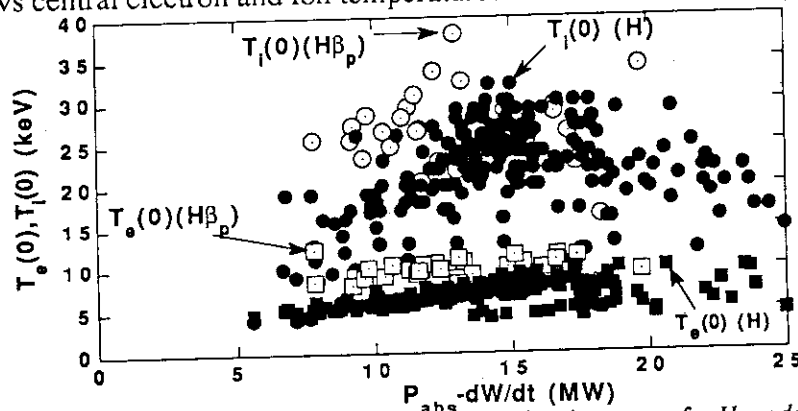


Fig. 2 Central electron and ion temperatures as functions of net heating power for H-mode and high β_p .

5. Fusion Triple Product

Fig. 3 shows the $(n_i(0)\tau_E T_i(0), T_i(0))$ diagram for H mode and high β_p regime with JET/TFTR published data. Maximum JT-60U fusion triple product are now comparable to those of JET and TFTR. A better fusion product for high β_p regime than the H-mode in JT-60U was attributed to its peaked density profile.

These high performance plasmas are characterized by selective ion heating with $T_i(0)/T_e(0) \sim 3-4$. These high performances were obtained transiently and terminated quickly through MHD events such as β_p collapse and ELM.

6. Average Fusion Product

Since high T_i H-mode and high β_p regime were characterized by selective ion heating with NBI, the experimental fusion triple product $n_i(0)\tau_E T_i(0)$ was enhanced from that expected in the α heating scenario. The volume averaged fusion product $\langle nT \rangle \tau_E^G$ [5] may be better as a measure of confinement performance. Figure 4 shows $\langle nT \rangle \tau_E^G$ as a function of I_p together with those from other major tokamaks. The value of $\langle nT \rangle \tau_E^G$ was significantly improved compared with those in 1991. Interestingly, the upper bound is relatively insensitive to I_p while lower bound increases with I_p . This might be caused partly by the operational difficulty at high I_p .

Improvement factor of $\langle nT \rangle \tau_E$ over the low aspect ratio JET/DIHD L mode reaches up to 100. The maximum $\langle nT \rangle \tau_E^G$ in high β_p regime and H-mode were $1.2 \times 10^{20} \text{keVsecm}^{-3}$ and $0.93 \times 10^{20} \text{keVsecm}^{-3}$, respectively.

7. High Pressure Operation

Since high total pressure $\langle nT \rangle_t$ of $\sim 0.9 \text{MPa}$ is required for the power reactor (ex. SSTR), attainment of the high plasma pressure and study of related phenomena are important. JT-60U is characterized by its high pressure capability with high $I_p B_t/a_p$ up to 30MA/T/m at 6MA (practical limit $q_{\text{eff}} \sim 3$ sets $I_p < 4 \text{MA}$). From Troyon relation $\langle \beta_t \rangle = g I_p / a_p B_t$, we obtain $\langle nT \rangle_t (\text{MPa}) = 4 \times 10^{-3} g I_p (\text{MA}) B_t (\text{T}) / a_p (\text{m})$. Figure 5 shows experimental average pressure as a function of $I_p B_t/a_p$ for JT-60U high β_p regime (4.4T)

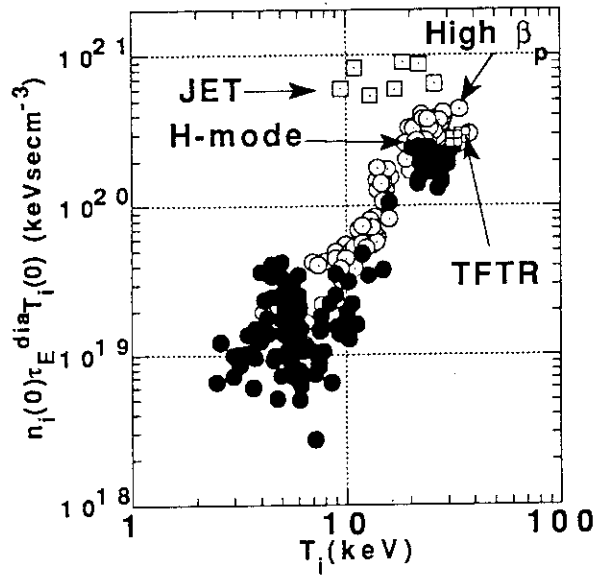


Fig. 3 Fusion triple product v.s. central ion temperature

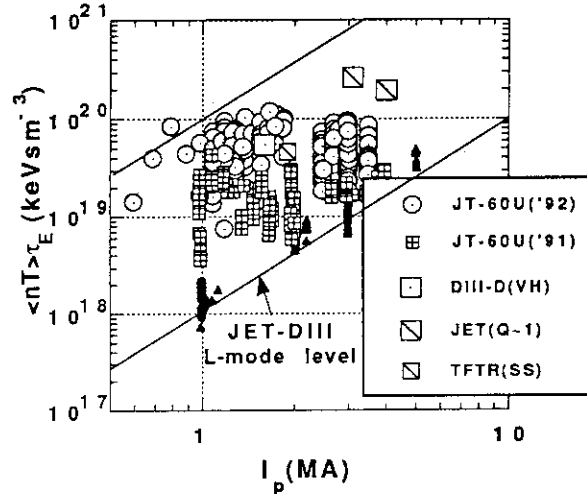


Fig. 4 Average fusion product v.s. plasma current.

and H-mode (4.2T) with DIII-D VH mode and JET($Q_{DT}=1.14$) shots, for comparison. The best DIII-D and JET data are obtained in relatively low $I_p B_t / a_p$ (5-9 MAT/m) regime. And JT-60U high β_p regime produced similar level of plasma pressure up to 0.83MPa. This pressure is limited by so-called β_p collapses occurred in the central region. On the other hand, the hot ion H-mode regime pressure is limited by the appearance of the ELM with high edge ion temperature up to 7keV.

8. High Fusion Neutron Yields

Attainment of the high temperature high pressure plasmas naturally led to the high D-D neutron production rate S_n up to $2.8 \times 10^{16}/s$. Figure 6 shows S_n as a function of total pressure $\langle nT \rangle_t$. Both data from two different confinement regimes lie on similar lines since peaked density profile in high β_p regime compensates smaller plasma volume. An average total pressure of ~ 0.1 - 0.12 MPa is required to reach next target of $S_n=4$ - $5 \times 10^{16}/s$.

9. Summary

The high power D^0 beam injection into JT-60U plasma produces a plasma with fusion triple product of $4.4 \times 10^{20} \text{keVsecm}^{-3}$. Other plasma parameters such as temperature, stored energy, plasma pressure and neutron rate approach to a level of highest values. Further impurity and recycling reductions and improved MHD stability will improve plasma performances significantly in the next year.

Reference

- [1] JONES, T.T.C. et al., 19-th EPS Conf. on Contr. Fus. & P.P. (1992,Innsbruck)I-3.
- [2] JET Team, Proc. 13th IAEA Conf. on P.P. and Contr. Nucl. Fus. Res. (1990, Washington) IAEA-CN-53/A-1-2.
- [3] MEADE,D.M., et al., ibid IAEA-CN-53/A-1-1.
- [4] JACQUINOT,J. et al., Plasma Physics and Controlled Fusion **33**,13(1991)1657.
- [5] KIKUCHI,M. et al., JAERI-M92-073, Paper 3.1.

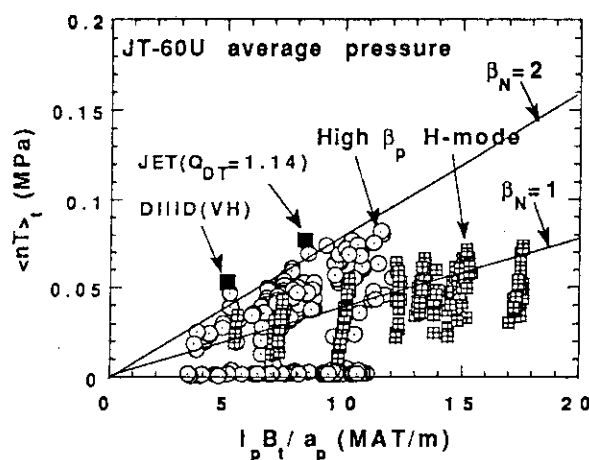


Fig. 5 Total average pressure v.s. $I_p B_t / a_p$.

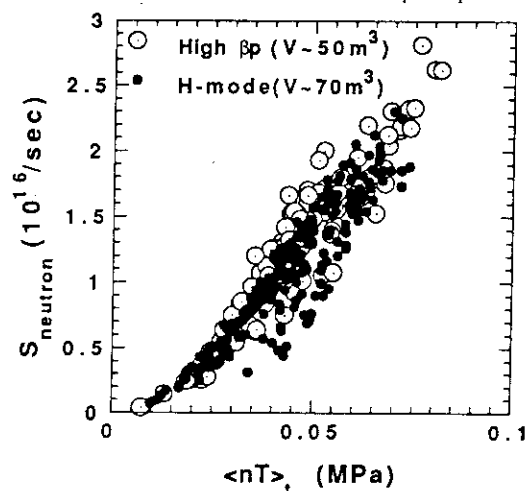


Fig. 6 DD neutron rate v.s. total average pressure.

1.2 Operation Procedures and Basic Characteristics of the H-mode

H. Ninomiya, R. Yoshino, M. Kikuchi, Y. Kamada, M. Shimada, K. Ushigusa,
T. Kondoh, A. Sakasai, K. Tobita, H. Nakamura, T. Fujita, Y. Koide, T. Sugie, H. Kubo,
N. Hosogane, T. Taylor, G. L. Jackson, D.J. Campbell, D. Stork and A. Tanga

1. Introduction

H-mode experiments in 1991 were mainly performed in the region of $I_p = 1.2\text{--}2.0$ MA and $B_t = 1.7\text{--}2.5$ T. The maximum enhancement factor of energy confinement over the ITER-89P law was 1.5 for the non-steady state case and 1.3 for the quasi-steady state case. Therefore, main effort of experiments in 1992 was first made to improve the H-mode characteristics. Another important issue of the H-mode is to study H-mode characteristics at high magnetic field and high power since future experimental and power reactors will operate at high field and high power. JT-60U is capable of studying the H-mode at high field (4.2 T at 3.32 m) and high power (30-40 MW). Therefore, the later phase of H-mode experiments is focused on extending operation regions of H-mode to high field and high power. A clear H-mode was obtained at $B_t = 4$ T. In this section, the operation procedures to obtain these results and basic characteristics of the H-mode are described.

2. Operation Procedures and Basic Characteristics

Figure 1 shows the typical configurations used for the H-mode studies. The configurations were selected to reduce fast ion ripple loss [1] and effect of the D-coil error field [2]. A wide scan of configurations was not made this year.

One explanation of the poor H-mode characteristics in 1991 was insufficient reductions of recycling and impurity. The effective particle confinement time τ_p^* was ~ 1 sec. Therefore,

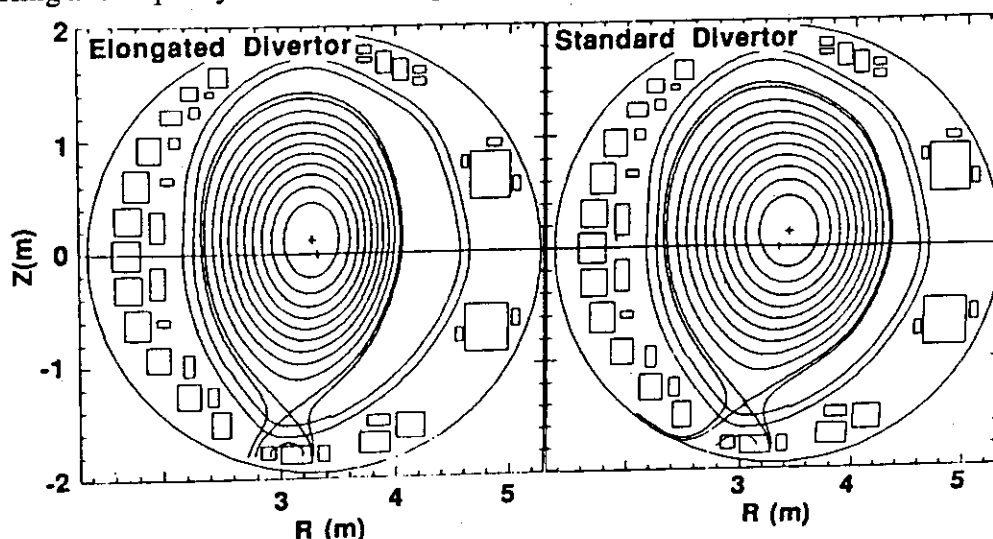


Fig. 1 Typical configurations for the H-mode studies.

main effort of experiments in 1992 was first made to reduce recycling and impurity, for which 4 methods of wall conditioning were used: He TDC, He GDC, boronization and temperature control of the vacuum vessel [3]. The first boronization was made at the end of July. Figure 2 shows the operation region in the I_p - B_t space. In the initial H-mode experiments, standard configuration with the low toroidal field ($B_t=2$ -3T) was used, because the threshold power for the H-transition is low in the low toroidal field case [4] and the content of impurity may be reduced in such low power heating. After obtaining good H-mode at the low toroidal field, the toroidal field and plasma current were increased and elongated configuration was used.

Figure 3 shows the typical time evolution of the H-mode in the case of low toroidal field. After a weak drop of D_α emission (H(I), $t=8.3$ sec), a steeper drop of D_α emission occurs (H(II), $t=8.7$ sec). Duration of this phase is short because edge localized modes (ELM) appear. In JT-60U, ELM occurs at relatively low density ($n_e=2\text{-}3\times 10^{19}\text{m}^{-3}$) as shown in Fig. 4 (detail is discussed in section 1.4). This low threshold density of ELM onset restricts the improvement of plasma performance in JT-60U H-mode. The

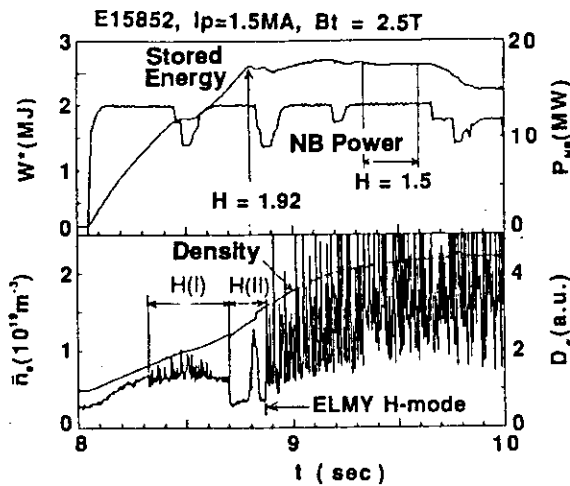


Fig. 3 Typical time evolution of low B_t H-mode.

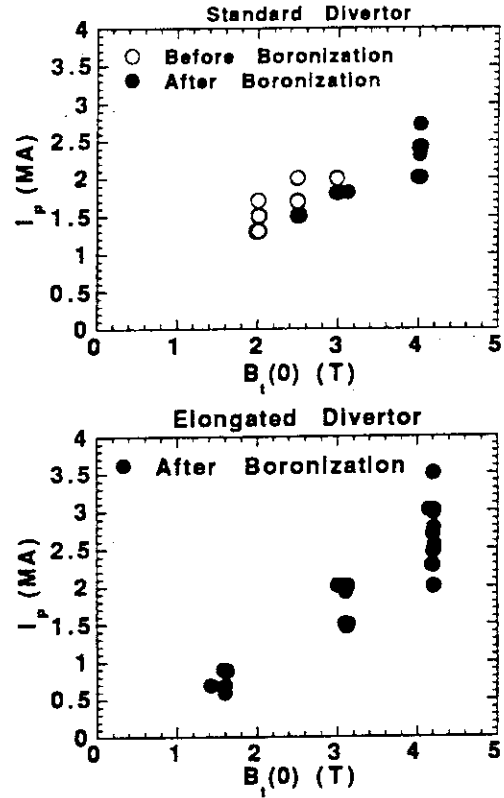


Fig. 2 Operation region in the I_p - B_t space.

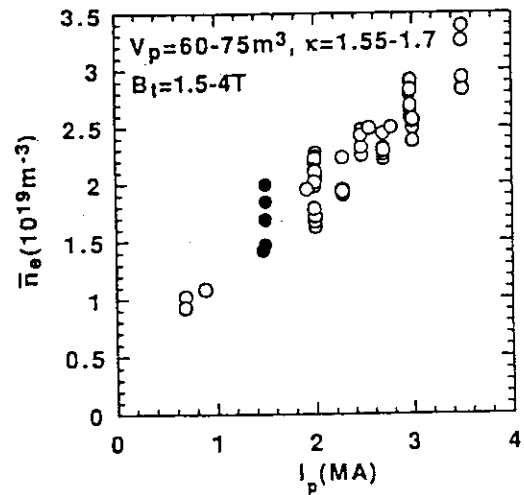


Fig. 4 ELM onset density as a function of plasma current.

carbon bloom has not been observed even at the high heating power of 28 MW.

In the H-mode experiments at the low toroidal field ($B_t=2-3T$), the enhancement factor increases with decrease of the sum of D_α emission in divertor region as shown in Fig. 5. This decrease of D_α emission corresponds to the decrease of recycling. τ_p^* is less than 1 sec in the low D_α emission region. The maximum enhancement factor of 4.9 was obtained. Thus the toroidal field and plasma current were increased. The first boronization was made at the same time, so that there are no data of high toroidal field region before boronization. Reduction in recycling is also the key item in improving the plasma performance in the high toroidal field case. Figure 6 shows the relation between the enhancement factor and D_α emission in 1991 and 1992. The improvement of the enhancement factor in 1992 can be understood by the decrease of recycling. The relation between the enhancement factor and the content of impurity is not clear so far. Figure 7 shows the improvement of plasma performance according to the extension of operation regions. The plasma stored energy, confinement time,

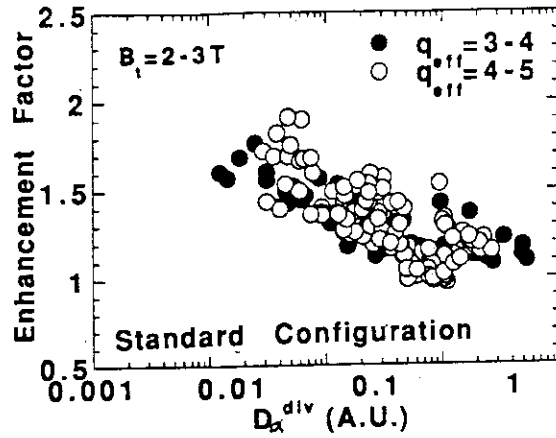


Fig. 5 Enhancement factor as a function of the sum of D_α in divertor region.

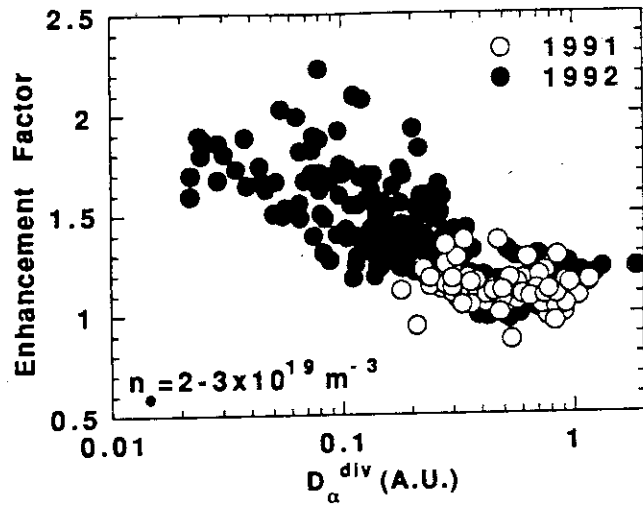


Fig. 6 Enhancement factor as a function of the sum of D_α in divertor region

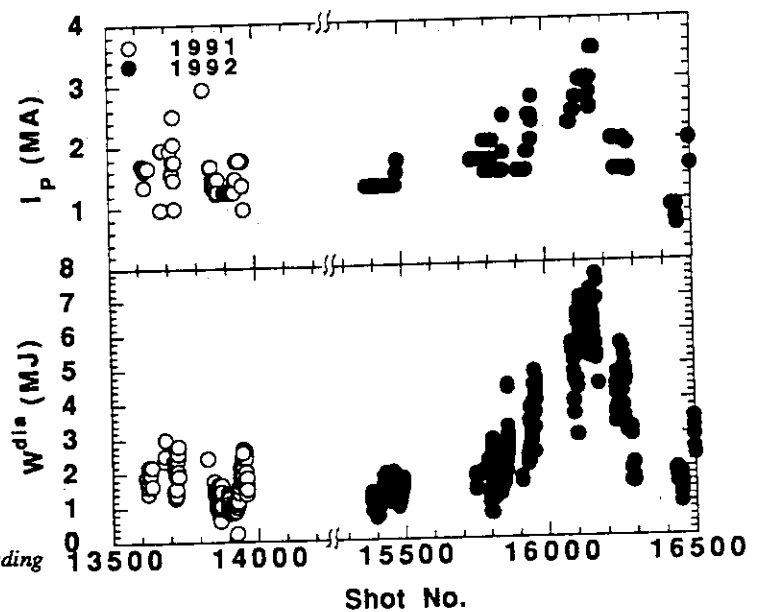


Fig. 7 Improvement of plasma performance according to the extension of operation region.

and central ion and electron temperatures increase with plasma current. Table 1 shows the comparison of main results of the H-mode obtained in 1991 and 1992. The detailed results of these H-mode characteristics are described in section 1.3 and 1.6.

Neutral beams are injected through 10 upper and lower slant ports (near perpendicular, <28 MW) and 2 tangential ports (<12 MW). The difference between these two types of beam was examined in the low toroidal field case. Figure 8 shows the relation between the enhancement factor and the ratio of tangential beam power to the total beam power $P_{NB}^{tan}/P_{NB}^{abs}$. No clear difference between the tangential and near perpendicular injections is observed when we don't consider the effect of ripple loss. The slight increase of enhancement factor with decreasing $P_{NB}^{tan}/P_{NB}^{abs}$ is due to the increase of absorbed power. If we consider the effect of ripple loss, confinement characteristics become better in the perpendicular injection case compared to the tangential case [5]. On the other hand, a ripple loss seems to affect on confinement as described in section 1.12. Therefore, more detailed study is need to understand the effect of ripple loss on confinement.

References

- [1] TOBITA K. et al., this issue 6.6.
- [2] YOSHINO R. et al., Section 2.11 in JAERI-M 92-073 (1992).
- [3] SHIMADA M. et al., this issue 4.2.
- [4] KAMADA Y. et al., this issue 1.4.
- [5] JONES T.T.C., this issue 1.13

Table 1 Comparison of main results of H-mode in 1991 and 1992
(not simultaneous, 1991 results include Lmode)

Items	1991	1992
Plasma Stored Energy	2.8 MJ	7.7 MJ
Confinement Time ($P_{net} \sim 15$ MW)	0.16 s	0.45 s
Enhancement Factor		
Steady State Case	1.3	1.6
Non-Steady State Case	1.5	2.2
Neutron Emission Rate	$3.6 \times 10^{15}/s$	$2.3 \times 10^{16}/s$
Maximum Ion Temp.	15 keV	32 keV
Maximum Electron Temp.		9 keV

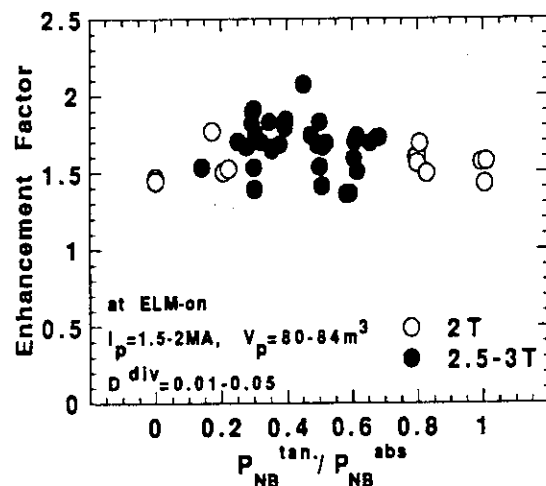


Fig.8 Enhancement factor as a function of the ratio of tangential beam power to the total beam power.

1.3 Overview of High Ti H-mode

M. Kikuchi, H. Ninomiya, M. Shimada, Y. Kamada, Y. Koide, N. Asakura

1. Introduction

Hot ion H-mode regime was studied to obtain high fusion triple product ($n_i(0)T_i(0)\tau_E < 2.5 \times 10^{21} \text{keVsm}^{-3}$). This mode of operation was characterized by low density ($n_e = 1\text{--}3 \times 10^{19} \text{m}^{-3}$) and high ion and electron temperatures ($T_i(0) < 32 \text{keV}$, $T_e(0) < 10 \text{keV}$) with flat density profile. The target density was kept low ($n_e = 0.4\text{--}1.5 \times 10^{19} \text{m}^{-3}$) to attain hot ion regime. High D-D neutron rate S_n up to $2.3 \times 10^{16}/\text{s}$ was obtained in 3MA hot ion H-mode. This regime was obtained even under the existence of sawteeth, in contrast to the high β_p enhanced confinement regime. And no clear D_α drop was seen in many cases during confinement improvement similar to the VH-mode. Power threshold for H-mode was $\sim 16 \text{MW}$ at high field ($B_t(R_p) = 4.2 \text{T}$). Another important aspect of H-mode in JT-60U was the ripple loss. Maximum B_t ripple was kept below 1% to minimize fast ion ripple loss in which power lost from ripple loss was calculated to be $\sim 15\%$ of the total heating power[1]. Experiments were done after 2-nd boronization associated with a reduction of particle recycling[2].

2. Typical Hot Ion H-mode Discharges

Figure 1 shows typical single null divertor configuration used for the H-mode study. Optimization of the configuration was made to reduce fast ion ripple loss. High power neutral beams were injected through 10 upper and lower slant ports (near perpendicular) and 2 tangential ports. Figure 2 shows time evolution of a typical H-mode discharge. The target density was kept at $\sim 1.5 \times 10^{19} \text{m}^{-3}$ to avoid locked modes in this low-q regime. A L- to H-mode transition occurred at $t = 8.5 \text{s}$ accompanied by an increase in dW/dt . The electron and ion collisionalities near the edge ($0.95a$) were roughly ~ 1 and ~ 0.1 at transition, respectively. But this transition is rather weak and no clear flattening of the density

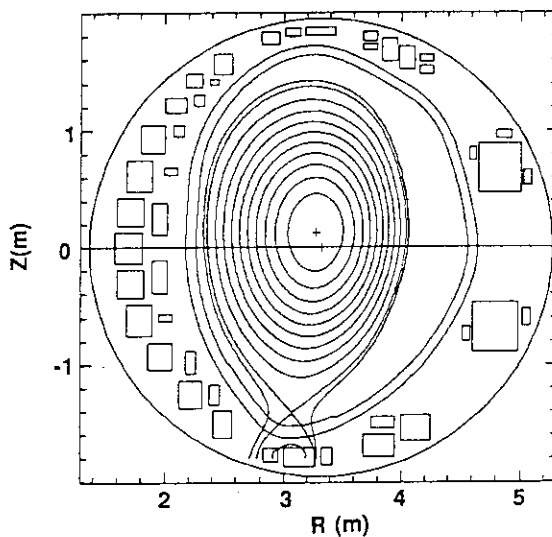


Fig. 1 Typical equilibrium configuration of hot ion H-mode. Maximum B_t ripple of 1%. Typical inboard clearance and X-point height are 10cm and 9cm, respectively.

profile was observed. This discharge attained a maximum plasma stored energy of 7.7MJ with the H-factor of 1.5 over ITER-89P. Central ion temperature reached up to 22keV with sawteeth. Edge temperatures reached up to $T_i(0.95a) = 5\text{keV}$ and $T_e(0.95a) = 2\text{keV}$, respectively. For higher $q_{\text{eff}} (>4)$, lower target density was possible. In such a case, the discharge tends to lose clear D_α drop. Figure 3 shows such an example. But the confinement improvement was obtained with increasing edge temperature irrespective of D_α drop and T_i/T_e ratio. These phenomena will be discussed further in the following section.

3. Current and Power Scans

Hot ion H-mode regime are explored for different plasma currents at $B_t(R_p)=4.2\text{T}$, $I_p = 2\text{MA}$, 2.5MA , 2.7MA , 3MA and 3.5MA . Figure 4 shows a comparison of the diamagnetic stored energy with those of ITER-89P scaling as functions of the net heating power ($P_{\text{abs}}=dW/dt$, $P_{\text{abs}}=P_{\text{NB}}+P_{\text{OH}}$) and edge ion temperature. The confinement enhancement factor (H-factor) varies from 1-2.2, depending on plasma current, heating power and recycling.

The confinement properties were improved with net heating power P_{net} above 14-16MW, independent of the existence of D_α drop. This threshold power changes with toroidal field. An example of 3T / 2MA power scan was also shown in Fig. 4. In this case, confinement improvement started at $P_{\text{net}}\sim 10\text{MW}$. In the usual H-mode, the enhanced confinement is closely related to a formation of the edge transport barrier / high edge temperature. As is clear from Fig. 4, the enhanced confinement was associated with high edge ion temperature. Although the D_α drop is weak, transition can be seen from the change of the dW/dt (Fig.2). Figure 5 shows H-factor as a function of $T_i(0)/T_e(0)$ which is a measure of hot ion effect. Poor correlation of H-factor with $T_i(0)/T_e(0)$ was seen.

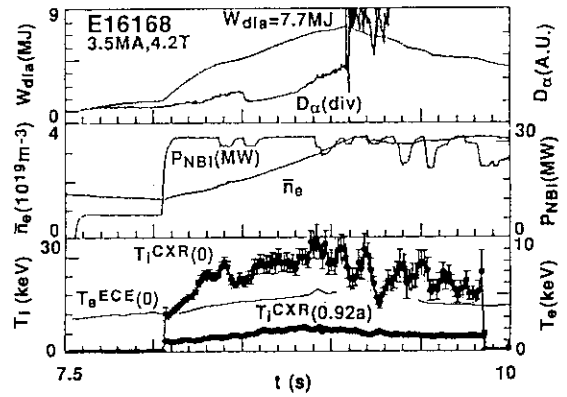


Fig. 2 Discharge waveform of 3.5MA, 4.2T Hot ion H-mode. Higher target density to avoid locked mode resulted in the appearance of D_α drop.

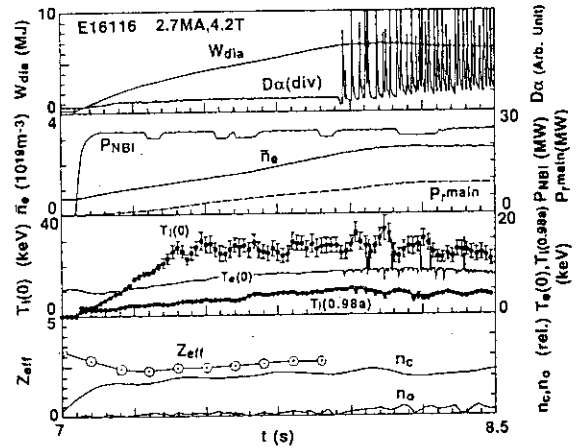


Fig. 3 Typical D_α transition-less H-mode at 2.7MA, 4.2T. High performance was terminated by strong ELM activity.

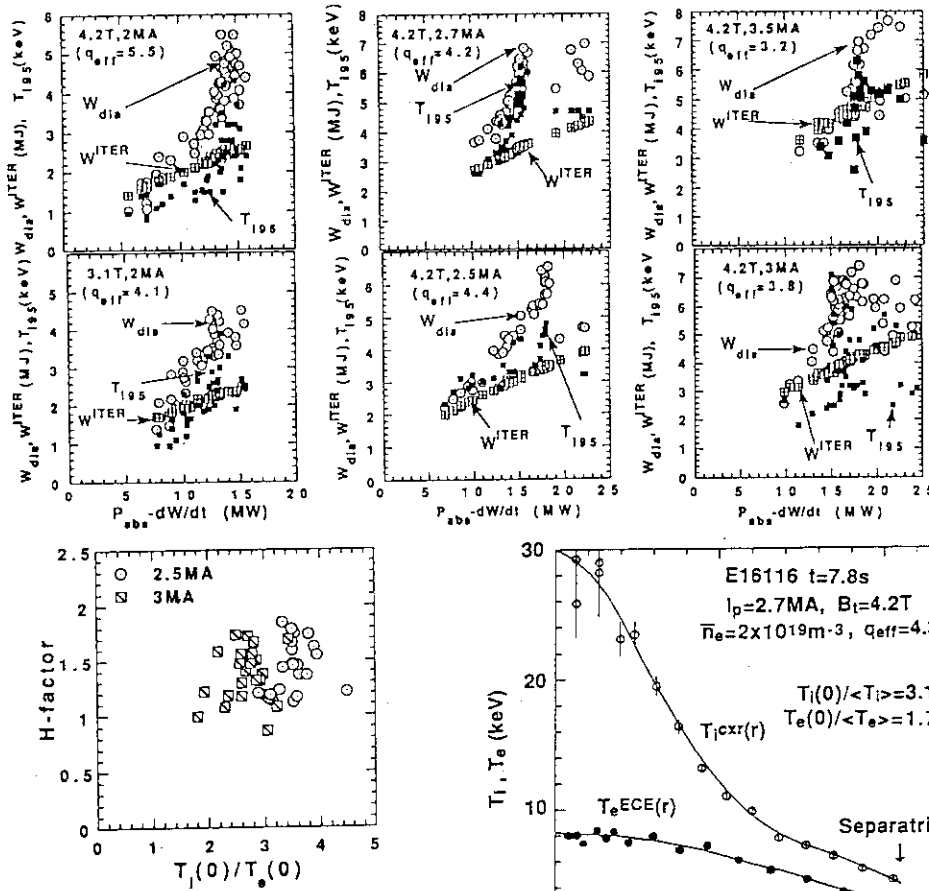


Fig. 5 H-factor as a function of $T_i(0)/T_e(0)$ for $I_p=2.5$ MA and 3 MA discharges.

4. Achievement of Reactor Grade Ion Temperature

In this mode of operation, high central ion and electron temperatures up to 32 keV and 10 keV respectively were obtained. Figure 6 shows typical temperature profiles. The edge electron and ion temperatures reached values of up to 2 keV and 5 keV, respectively. Figure 7 shows central and edge ion temperatures as functions of heating power. For H-modes, the maximum DD neutron rate of $2.3 \times 10^{16}/s$ and maximum fusion triple product of $2.5 \times 10^{20} \text{ keVsm}^{-3}$ were recorded in hot ion H-mode regime.

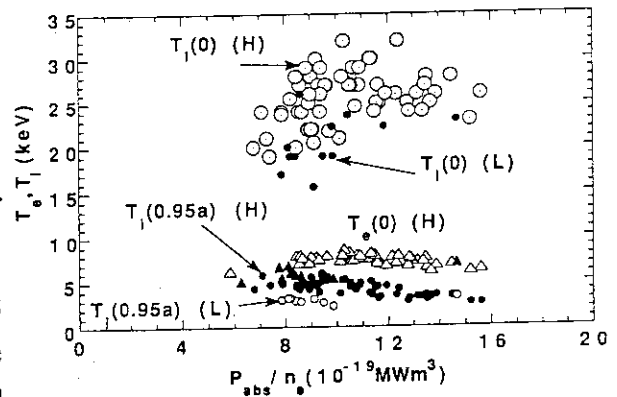


Fig. 6 Typical temperature profiles in hot ion H-mode. Highly peaked ion $T_i(0)/T_i>=3.1$ and broad electron temperature $T_e(0)/T_e>=1.7$ with high edge ion temperature up to 7 keV are observed.

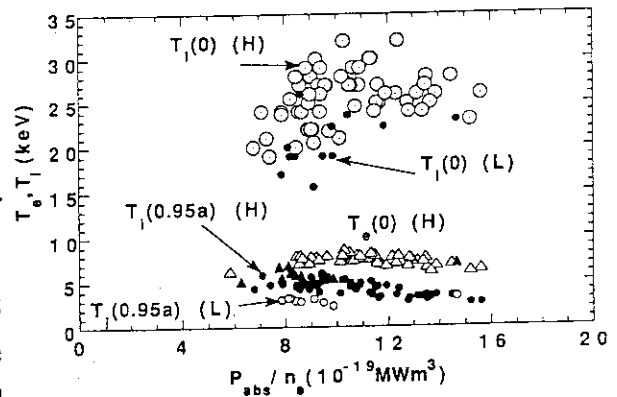


Fig. 7 Central and edge ion and electron temperatures as a function of P_{net}/n_e for L- and H-modes.

Fig. 4 Diamagnetic plasma stored energy (W_{dia}), ITER-89P L-mode prediction (W_{ITER}) and edge ion temperature at 95% minor radius (T_{i95}) as a function of net heating power for I_p (2 MA, 2.5 MA, 2.7 MA, 3 MA, 3.5 MA) and power (5-25 MW) scans. All scan were done with $B_t=4.2$ T except 2 MA, 3.1 T case shown in left low.

5. Relation between Energy and Particle Confinements

The global particle confinement time, τ_p^G , including particle fluxes in the divertor region, were measured with a 15 ch. D_α photodiodes. Figure 8 shows a comparison of τ_p^G and τ_E^{dia} between H- and L-modes. The improvement in the particle confinement was not so significant as in other devices. Since large part of the particle flux comes from the divertor region, the particle confinement time inside the separatrix (τ_p^x) might be significantly longer than τ_p^G .

6. Termination of High Performance

Extension of the plasma performance was not limited by the occurrence of a carbon bloom but by the appearance of frequent ELM's (Fig.3). The cause of the ELM activity at low density has not yet been identified since the main plasma radiation was only 20-30% of the heating power. Figure 9 shows plasma current dependence of the ELM-onset density. As I_p increases, the threshold density (for ELM) increases which could be originated from MHD limit [3].

7. Conclusion

The hot ion H-mode confinement regime was studied in low density discharges. The maximum plasma stored energy of 7.7MJ, maximum ion and electron temperatures of 32keV and 10keV, maximum DD neutron emission rate of $2.3 \times 10^{16}/\text{sec}$ were obtained. Confinement was improved sharply above 14-16MW. The confinement improvement was associated with rapid increase of the edge ion temperature (T_{i95} up to 7keV) with power, in spite of no sharp D_α drop. This suggests that different type of H-mode transition is possible in high temperature plasma without D_α drop.

References

- [1] VAN BLOKLAND, et al., this issue 1.12.
- [2] SHIMADA, M. et al., this issue 4.2
- [3] KAMADA, Y. et al., this issue 1.4

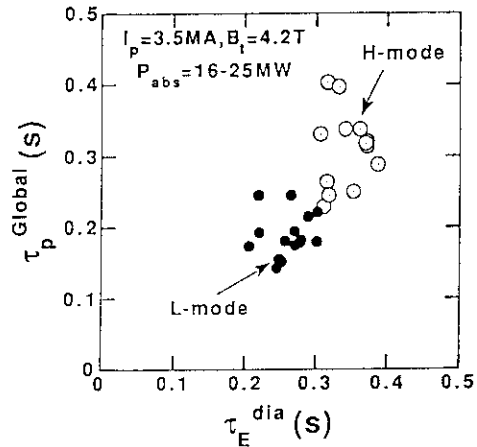


Fig.8 A comparison of global particle confinement time τ_p^G and energy confinement time τ_E^{dia} for L- and H-mode.

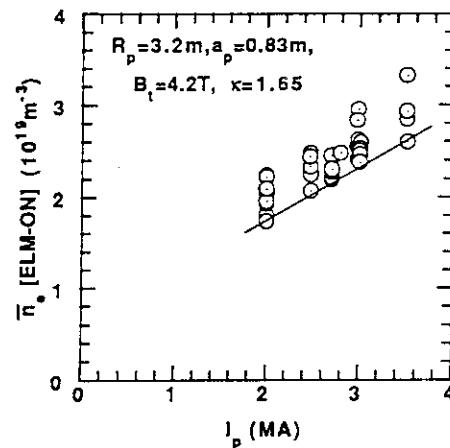


Fig. 9 ELM onset density as a function of plasma current.

1.4 H-mode Regime and ELMs

Y.Kamada, H.Ninomiya and M.Kikuchi

1. Introduction

This section treats the following subjects; i) the threshold heating power P_{abs}^{th} for the L-H transition, ii) conditions of onset of ELMs and iii) the parameter dependence of ELM-frequency. Study on these subjects is important for the control of H-mode status aiming at the realistic steady state operation. This section also contribute to analyze the relationship between MHD activities and confinement. One of the main objectives of confinement and MHD research in JT-60U is to clarify the relationships among l_i , q_{eff} and τ_E including MHD instabilities (see Sec.1.9). The subjects ii) and iii) corresponds to the relationship (5) in Fig.1 in Sec.1.9 (relationship between q_{eff} & l_i and ELMs).

2. Threshold Heating Power for L-H Transition

According to the experimental results in 1991 [1], i) P_{abs}^{th} is proportional to B_t or $B_t^{1.5}$, ii) P_{abs}^{th}/B_t or $P_{abs}^{th}/B_t^{1.5}$ seems to be proportional to a^2/κ by including results of many tokamaks and iii) P_{abs}^{th} is independent of q_{eff} at a fixed B_t . The experiments in 1992 offered data of P_{abs}^{th} over wide ranges of plasma parameters. Figure 1 shows the relationship between P_{abs} and $B_t(0)$ for the three regions s of plasma volume V_p where $B_t(0)$ is the value at the plasma center. The

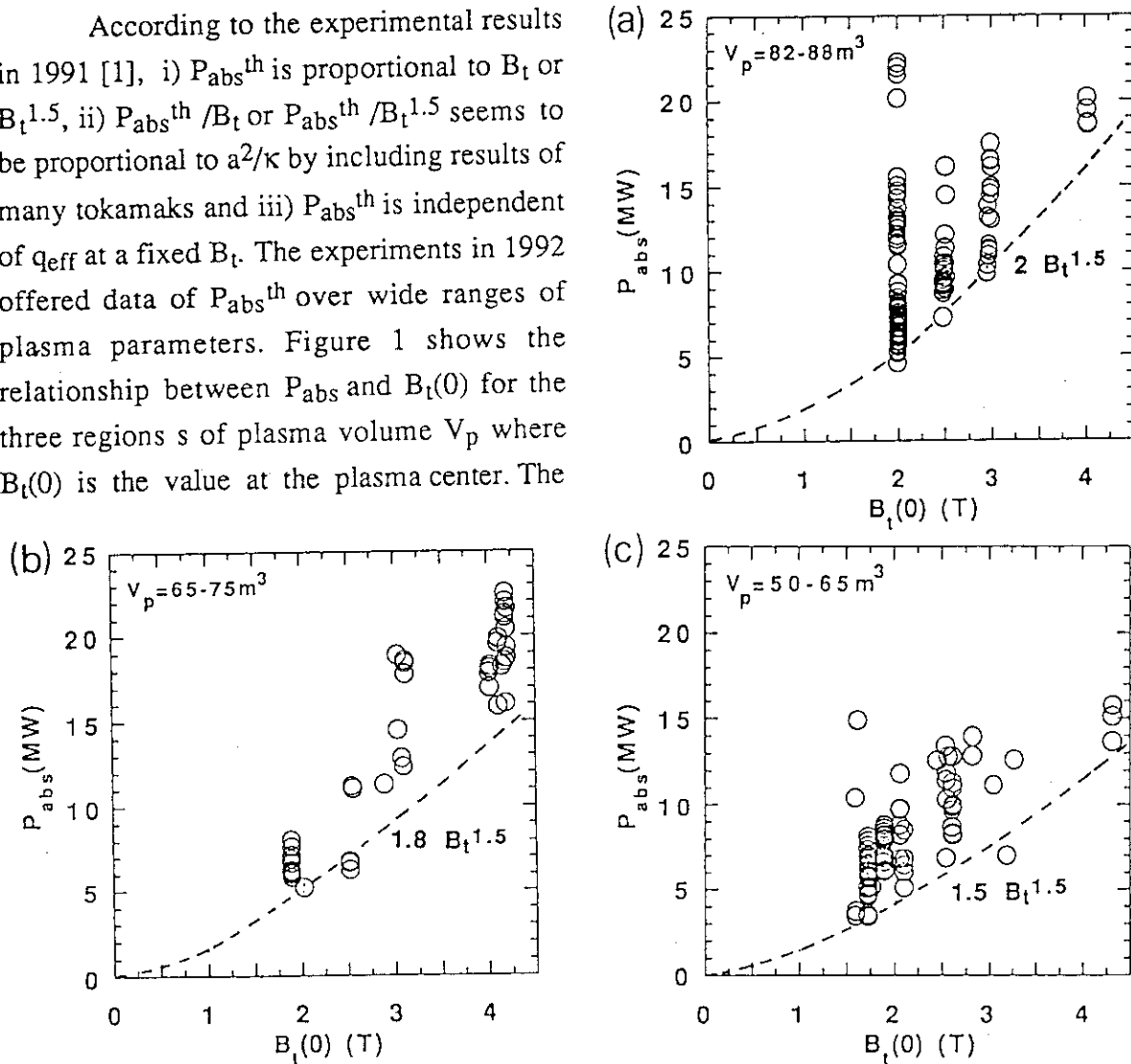


Fig.1: Relationship between P_{abs} and $B_t(0)$ for the three regions s of plasma volume.

direction of the ion gradB drift is toward the x-point. For each region of V_p , the lower envelope of P_{abs} ($=P_{abs}^{th}$) seems to be written as $cB_t^{1.5}$ and the coefficient c increases with increasing V_p (or a). Figure 2, which includes all data, shows that P_{abs}^{th} is proportional to $(a^2/\kappa)B_t^{1.5}$. The solid line corresponds to the scaling obtained in ref.[1] using data of JT-60U, JET, DIII, ASDEX, DIII, PDX and JFT-2M ($P_{abs}^{th}(MW)=3.2(a(m)^2/\kappa)B_t(T)^{1.5}$). In this analyses, the effects of ripple loss is not included. Since the ripple loss increases with increasing V_p in JT-60U, the dependence on a^2/κ may be weaker in the ideal cases without ripple loss.

Another important parameter to be considered is n_e . Figure 3 uses $B_t\bar{n}_e$ instead of $B_t^{1.5}$ for the data with $V_p=82-88m^3$ (corresponding to Fig.1(a)) and P_{abs}^{th} seems to be proportional to $B_t\bar{n}_e$. Experimentally, \bar{n}_e correlates with B_t , because both I_p and P_{abs} tend to be higher at higher B_t and \bar{n}_e increases with B_t . Therefore it is still an open question whether P_{abs}^{th} depends on $B_t^{1.5}$ or $B_t\bar{n}_e$. However it should be noticed that no H-transition have been observed at low \bar{n}_e of $\bar{n}_e < 0.8 \times 10^{19}m^{-3}$ in JT-60U and P_{abs}^{th} cannot be written as a function of $B_t\bar{n}_e$ in this low density region. The analyses of edge density and temperature for the transition is given in Sec.1.3.

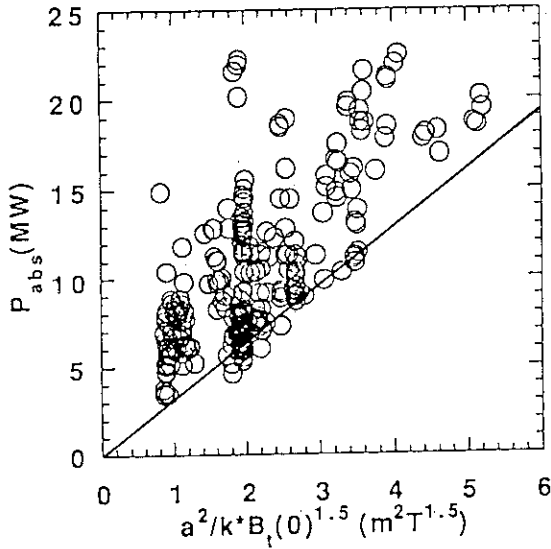


Fig.2: P_{abs}^{th} vs. $(a^2/\kappa)B_t^{1.5}$ for all data used in Fig.1. The solid line corresponds to the scaling ($P_{abs}^{th}(MW)=3.2(a(m)^2/\kappa)B_t(T)^{1.5}$) [1].

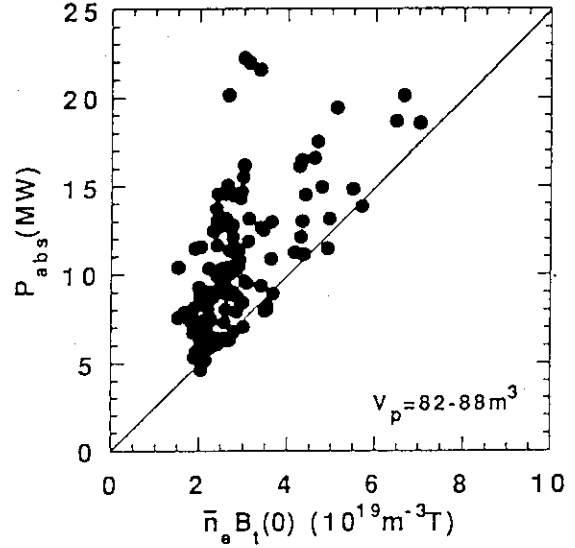


Fig.3: P_{abs}^{th} vs. $B_t\bar{n}_e$ with $V_p=82-88m^3$.

3. Conditions of Onset of ELMs

In the following study, we use the data after bolonization to exclude the effects of the drastic change in particle recycling condition (see Sec.1.2). In JT-60U, the ELM-free phase is observed only when \bar{n}_e is lower than the threshold value \bar{n}_e^{th} . Figure 4 uses the data with $I_p=0.7-3.5MA$, $B_t=1.5-4T$, $V_p=60-75m^3$ and $\kappa=1.55-1.7$. Figure 4(a) shows \bar{n}_e^{th} increases clearly with I_p . To understand this dependence, we use the parameter $B_t^2/(Rq_{eff}^2)\times l_i$ which is a measure parameter for pressure driven instabilities and proportional to $I_p^2 l_i$ for a fixed plasma configuration. This section uses l_i as a measure of the magnetic shear (for a more accurate expression, the shear parameter should be used). We can also observe a clear relationship

between \bar{n}_e^{th} and $B_t^2/(Rq_{eff}^2) \times l_i$. In Fig.4(c), \bar{n}_e^{th} is almost proportional to $(B_t^2/(Rq_{eff}^2) \times l_i)^{1/2}$. In Figs. 4(a)-(c), closed circles corresponds to the data for a fixed $B_t^2/(Rq_{eff}^2)$ ($=0.08-0.11$; 1.5MA, 3T). The behavior of the closed circles indicates \bar{n}_e^{th} increases with l_i even if B_t and I_p are fixed (see Fig.4(a)). Figure 5 includes data of $T_i(95\%)$ which is the ion temperature at 95% of the outermost flux surface. With increasing $B_t^2/(Rq_{eff}^2) \times l_i$, $T_i(95\%)$ also increases and a measure of the threshold edge pressure $T_i(95\%) \bar{n}_e^{th}$ is proportional to $B_t^2/(Rq_{eff}^2) \times l_i$, which may be interpreted that the edge pressure gradient is a function of $B_t^2/(Rq_{eff}^2) \times l_i$. These results suggests that the edge pressure gradient at the appearance of ELM is related to some types of pressure driven instability.

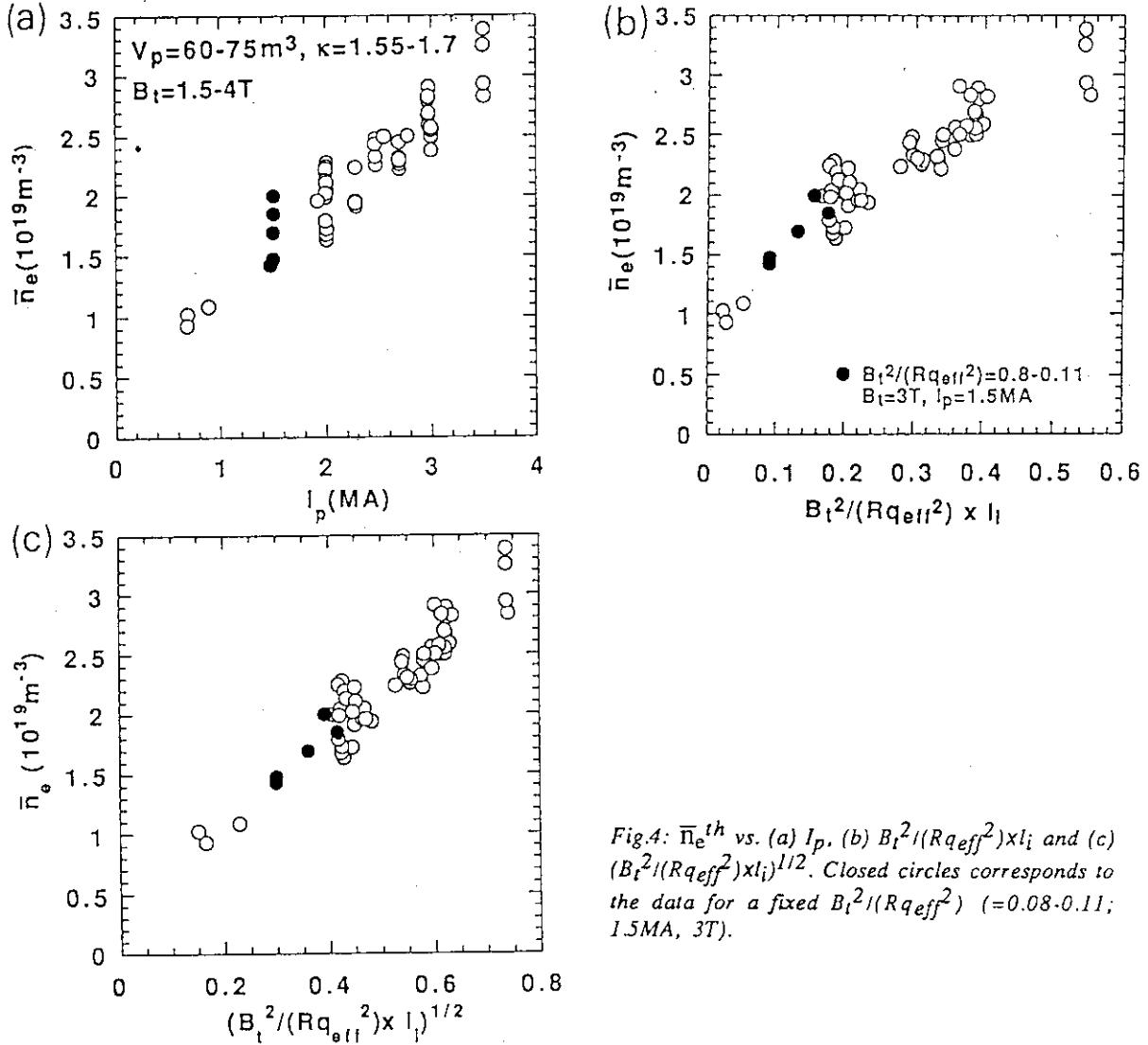


Fig.4: \bar{n}_e^{th} vs. (a) I_p , (b) $B_t^2/(Rq_{eff}^2) \times l_i$ and (c) $(B_t^2/(Rq_{eff}^2) \times l_i)^{1/2}$. Closed circles corresponds to the data for a fixed $B_t^2/(Rq_{eff}^2)$ ($=0.08-0.11$; 1.5MA, 3T).

4. Dependence of ELM Frequency on Plasma Parameters

Figure 6(a) plots the ELM frequency f_{ELM} against P_{NB}^{abs} for $B_t=2T$ (closed circles) and $B_t=3T$ (open circles) with $V_p=82-88m^3$. Values of $B_t^2/(Rq_{eff}^2) \times l_i$ are 0.06-0.09 for the 2T-data and 0.12-0.16 for the 3T-data. The threshold power P_{abs}^{th} for the L-H transition is indicated by dashed lines. Both open and closed circles increases almost linearly with P_{NB}^{abs} if P_{NB}^{abs} is

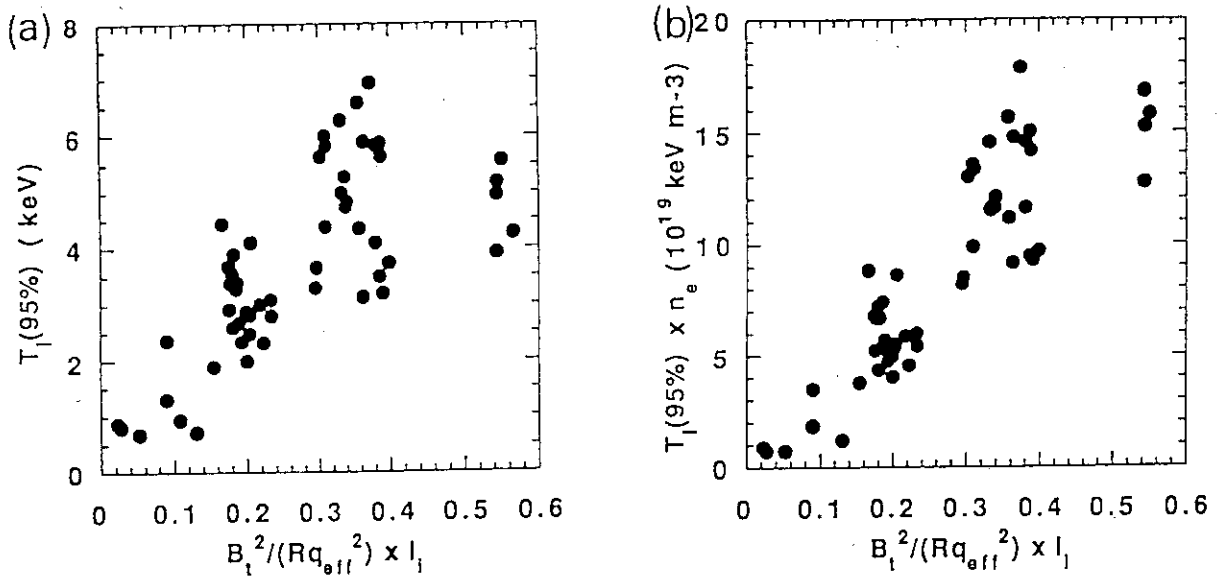


Fig.5: (a) $T_i(95\%)$ and (b) $T_i(95\%)n_e^{th}$ vs. $B_t^2/(Rq_{eff}^2) \times I_i$ for the data used in Fig.4.

high enough compared with P_{abs}^{th} and f_{ELM} for the 3T-case is systematically lower than that for the 2T-case. If P_{NB}^{abs} is close to P_{abs}^{th} , we observe another group with high f_{ELM} (see closed circles). In Fig.6(b), f_{ELM} is plotted against $(P_{NB}^{abs})/(B_t^2/(Rq_{eff}^2) \times I_i)$ for the data with $I_p=1.3-2.4\text{MA}$, $B_t=2-4\text{T}$, $B_t^2/(Rq_{eff}^2) \times I_i=0.07-0.23$. In this figure we also observe two groups of data. In the first group, f_{ELM} increases linearly with $(P_{NB}^{abs})/(B_t^2/(Rq_{eff}^2) \times I_i)$. In the second group, f_{ELM} can be high even at low P_{NB}^{abs} . This separation of data may suggest that the origin of the ELM activity can be categorized into two types.

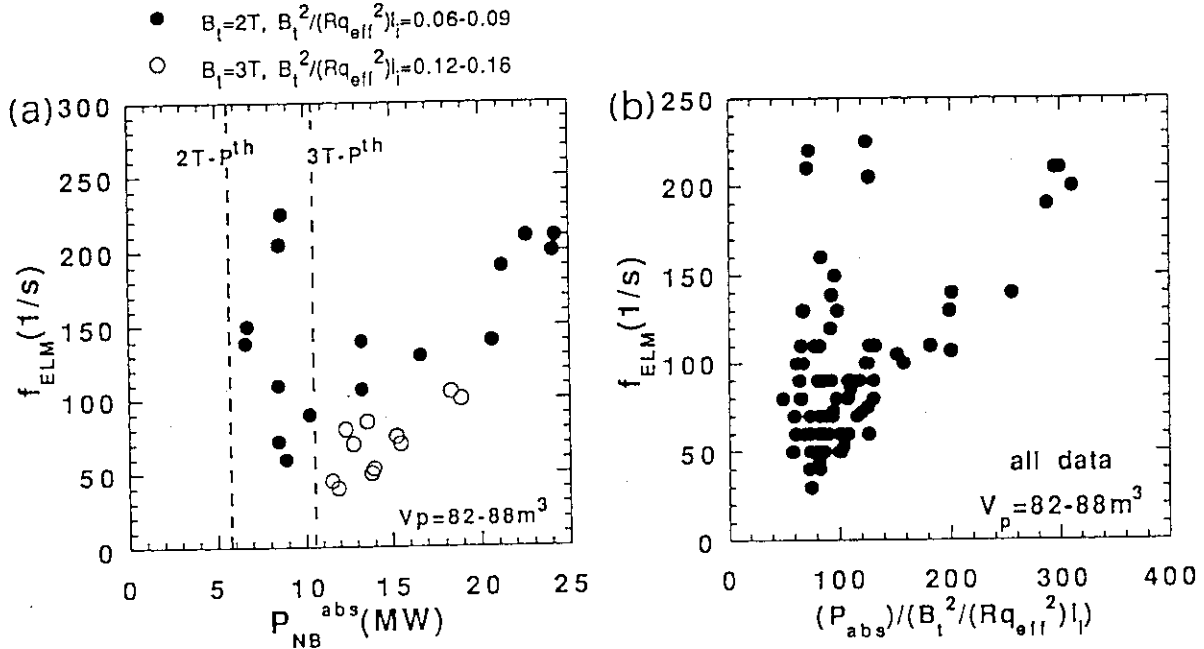


Fig.6: (a) f_{ELM} vs. P_{NB}^{abs} for $B_t=2\text{T}$ and 3T with $V_p=82-88\text{m}^3$. (b) f_{ELM} vs. $(P_{NB}^{abs})/(B_t^2/(Rq_{eff}^2) \times I_i)$ for the data with $V_p=82-88\text{m}^3$, $I_p=1.3-2.4\text{MA}$, $B_t=2-4\text{T}$, $B_t^2/(Rq_{eff}^2) \times I_i=0.07-0.23$.

REFERENCE

- [1] KAMADA, Y., et al., Sec.3.6 in 'Review of JT-60U Experimental Results from March to October, 1991' JAERI-M 92-073, Japan Atomic energy Research Institute (1992)

1.5 Temperature and Current Profiles Evolution in Hot Ion H-mode

M. Sato, M. Kikuchi, M. Azumi and Y. Koide

1. Introduction

The maximum energy confinement of 7.7MJ, ion temperature of 32keV and electron temperature of 10keV has been obtained in a hot ion H-mode of JT-60U [1,2]. The characteristics of the mode are low density and flat profiles of the ion and electron temperatures with high central and peripheral values. Since the plasma pressure at the edge is high, bootstrap current is expected to flow. The bootstrap current is caused by the interaction between the diamagnetic current and trapped particles [3]. Here the time evolution of the electron and ion temperature profiles and current profile in the hot ion H-mode are studied. The bootstrap current is estimated by using a 1.5 dimensional transport code (1.5D code). Preliminary computational results are presented.

2. Temperature Profiles Evolution

A typical equilibrium state and the time evolution of plasma parameters are shown in Fig.1. Electron temperature profiles are determined from the observed electron cyclotron emission (ECE) with a correction for the internal magnetic fields [4]. The ECE is measured by an absolute-calibrated Fourier transform spectrometer (FTS) [5]. After ELMs start at 7.97sec, ECE bursts which are emitted from supra-thermal electrons are observed, and the electron temperature profile may not be determined from the FTS data in the ELM phase. The ion temperature profiles are determined by charge exchange recombination spectrometry (CXRS) [6] during neutral beam injection. Typical time evolution of the electron and ion temperature profiles is shown in Fig.2. The time evolution of the central values and peaking factors of electron and ion temperatures is shown in Fig.3. Just after the neutral beam is injected, the electron temperature is drastically changed: The electron peaking factor decreases from 1.7 to 1.45 and the central electron temperature increases from 5keV to 8keV. On the other hand, during neutral beam heating, the central ion temperature slowly increases from 4keV to 27keV and the ion peaking factor increases from 2.0 up to 3.6 and then decreases to 2.9. Just after the neutral beams are injected into the plasma, the electron temperature profile becomes flat, while the ion temperature profile becomes first peaked and then flat.

3. Current Profile Evolution

The current profile is estimated by using the 1.5D code. The conductivity of the plasma is calculated using the formula is obtained by Hirshmann et al [7]. The bootstrap current is taken into account in the calculation [8]. The input data to the 1.5D code are determined from

the experimental data in the following way. The electron and ion temperature profiles are determined by FTS and CXRS data shown in Fig.2. The electron density profile is determined by FIR interferometers. Z_{eff} is assumed to be uniform in the plasma column and is determined from the observed visible bremsstrahlung, and the profiles of electron density and temperature.

Here the preliminary results are presented. The time evolution of bootstrap current is shown in Fig.4. The total bootstrap current increases during the neutral beam heating. The time evolution of the total and bootstrap plasma current profiles is shown in Fig.5. The bootstrap current flows in the peripheral region, and in total amounts to 20% of the total plasma current.

4. Summary

Just after neutral beams are injected into the plasma to produce the hot ion H-mode, the electron temperature profile becomes flat, while ion temperature profile slowly becomes peaked and then finally flattens. Bootstrap current accounts for over 20% of the total plasma current.

References

- [1] KIKUCHI, M., et al, Proc. 14th Int. Conf. Plasma Phys. and Contr. Nucl. Fus. Res., (1992, Wurtburg, Germany) IAEA-CN-56/A-3-3
- [2] KIKUCHI, M., NINOMIYA, H., et al, Section 1.3, in this review.
- [3] BICKERTON, R. J., et al, Nat. Phys. Sci. 229 (1971) 110
- [4] SATO, M., ISEI, N., ISHIDA, S., AOYAGI, T., and HIRAYAMA, T., JAERI-M 92-073, p342
- [5] SATO, M., ISEI, N. and ISHIDA, S., Section 12.2, in this review.
- [6] KOIDE, Y., SAKASAI, A. and ASAKURA, N., JAERI-M 92-073, p338
- [7] HIRSHMAN, S. P., et al: Nucl. Fusion 17 (1977) 611
- [8] HIRSHMAN, S. P., et al: Nucl. Fusion 21 (1981) 1079

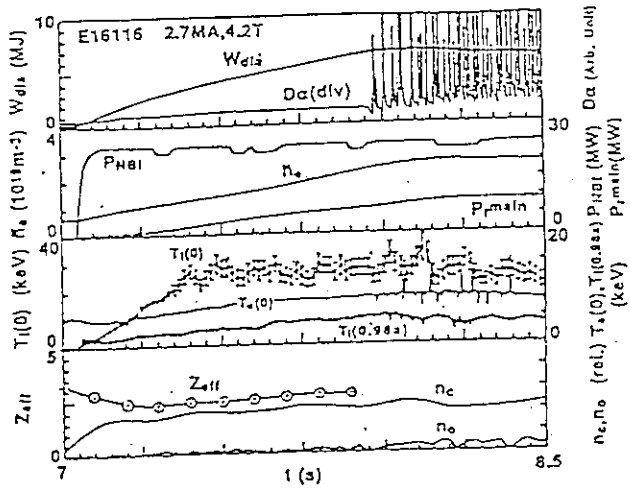


Fig.1. Typical time evolutions of the plasma parameters

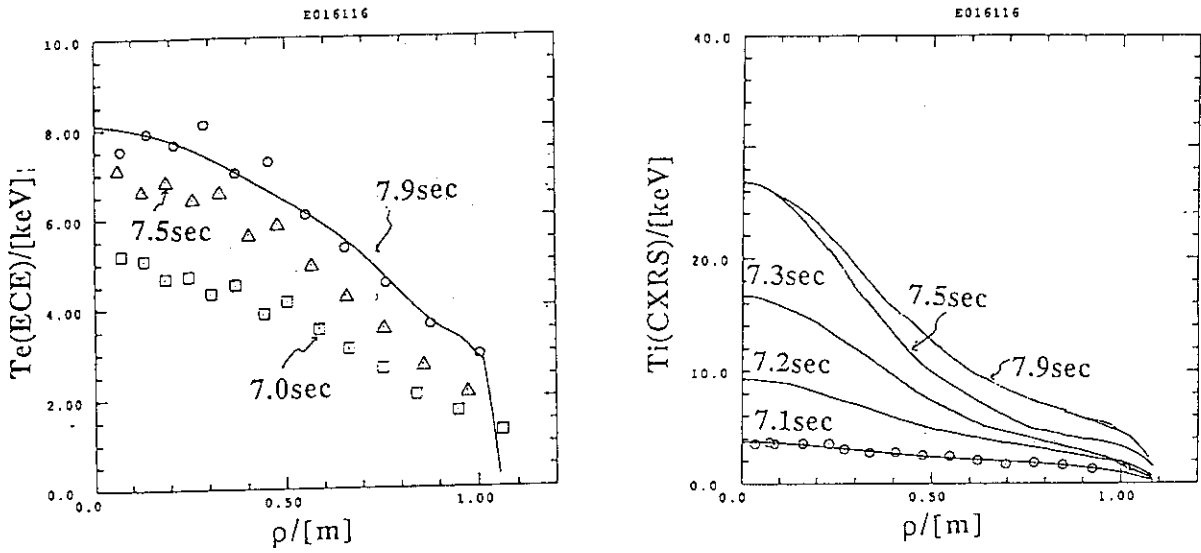


Fig.2. Typical time evolutions of the electron and ion temperature profiles.

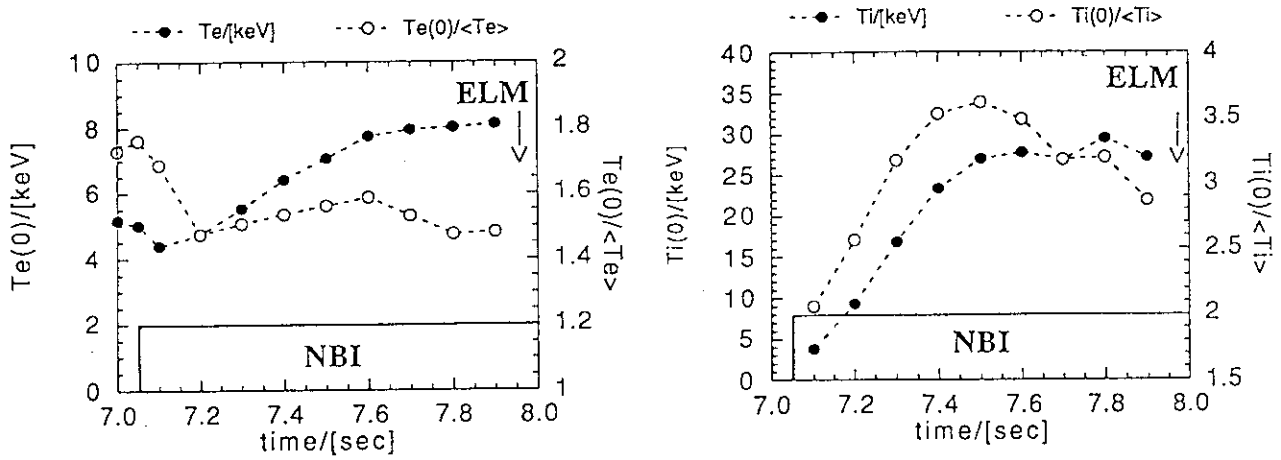


Fig.3 Time evolution of the electron and ion peaking factors and peak value.

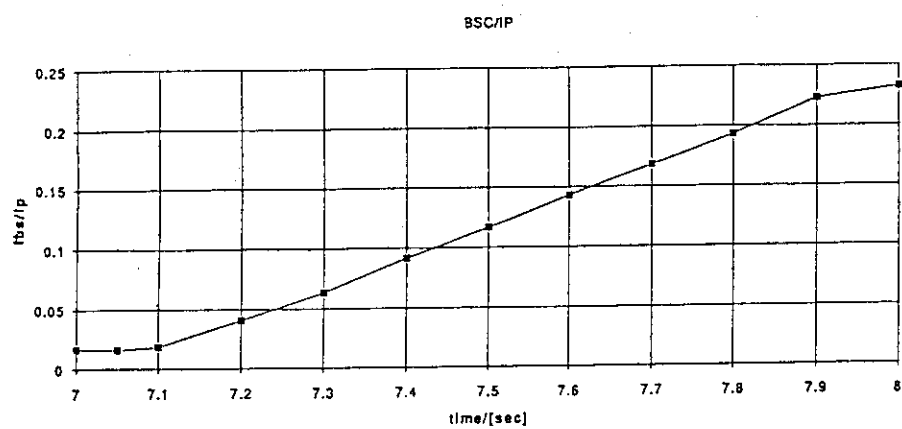


Fig.4. Time evolutions of the calculated bootstrap current and total plasma current.

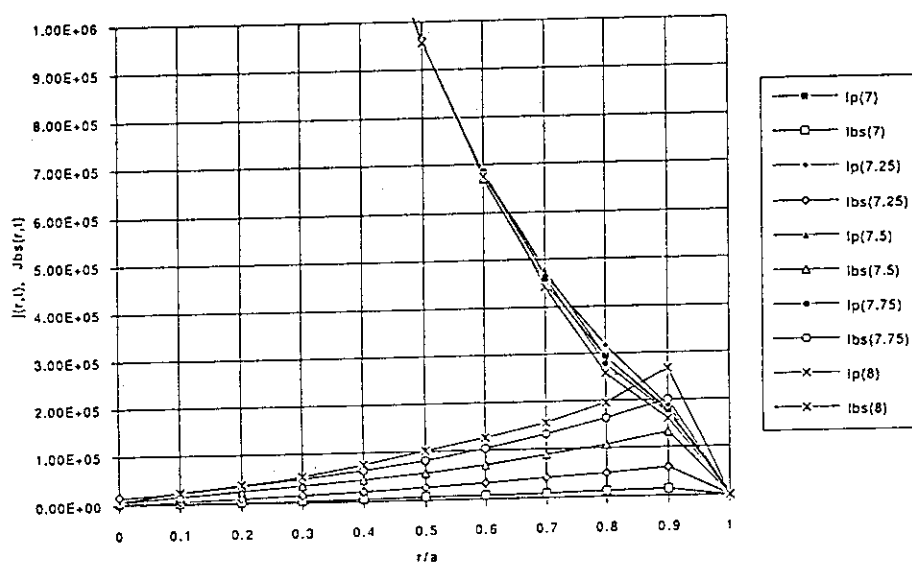


Fig.5. Time evolutions of the total and bootstrap plasma current profiles.

1.6 Edge Transport Barrier in H- and L-modes

M. Kikuchi, H. Yoshida, O. Naito, Y. Koide, T. Fukuda

1. Introduction

Formation of the edge transport barrier at the L- to H-mode transition is an important characteristic of the H-mode. It is widely recognized that the density profile becomes flat and edge temperature pedestal is formed during L- to H-mode transition. However, a formation of the edge transport barrier was seen even in L-mode discharges in JT-60U[1]. The edge T_i up to 7keV was obtained in hot ion H-mode. In this paper, edge T_e and T_i in L- and H-modes are discussed. Measurements are compared with Shaing's theories of H-mode transition and transport barrier [2,3].

2. Width of the Edge Transport Barrier

The edge Thomson scattering system and charge exchange recombination spectroscopy have spatial resolutions of 0.8cm, 1.3cm respectively. Figure 1 shows typical edge T_e profile measurements for $I_p=4\text{MA}$, 3MA and 1.8MA. Formation of the edge temperature pedestal was clearly seen for L and H modes. The measured pedestal width δ was 2.4-5.6cm which becomes narrower with poloidal field ($\delta \sim 1/B_p$).

Shaing[2] has proposed a theory of the H-mode based on the non-ambipolar ion orbit loss near the plasma edge and has proposed a formula for the edge transport barrier width δ considering orbit squeezing effect due to radial electric field E_r , $\delta = \sqrt{\epsilon \rho_{pi}} / \sqrt{S}$ where ϵ , ρ_{pi} and S are inverse aspect ratio, poloidal gyroradius and the orbit squeezing factor, $S = 1 - dE_r/dr / B_p \Omega_p$, respectively.

Since JT-60U is a high poloidal field tokamak ($B_p \sim 0.9\text{T}$ at $I_p=4\text{MA}$), orbit squeezing effect ($\sim dE_r/dr / B_p^2$) is less important ($S \sim 1$) unless $\Delta\Phi \sim 30\text{kV}$ ($dE_r/dr \sim 33\text{MV/m}^2$) in the edge. Shaing's H-mode theory predicts for typical JT-60 data $\delta \sim \sqrt{\epsilon \rho_{pi}} / \sqrt{S} \sim \sqrt{\epsilon \rho_{pi(th)}} \sim \sqrt{0.26} \times 0.74\text{cm} = 0.38\text{cm}$ while the measured width is $\sim 2.4\text{cm}$ (4T, 4MA discharge). However, the basic idea of Shaing's theory indicates the importance of the orbit loss of the energetic ions (Maxwellian tail or fast ions). Since there is a population of fast ions produced by neutral beam injection, the transport barrier

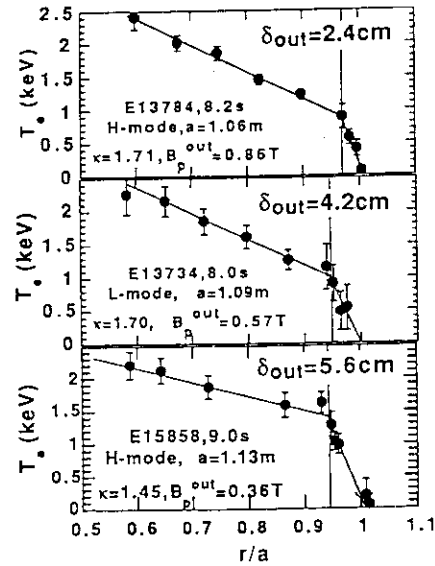


Fig.1 Edge T_e profile measurements for L- and H-modes. Measured edge transport barrier varies with $1/B_p$.

width may be explained by the corresponding theoretical width for a fast ion ($\delta_{\text{fast}} \sim 3.6\text{cm}$), which is close to the measured transport barrier width. A narrower width with B_p ($\delta \sim 1/B_p$) is also consistent with poloidal gyroradius picture. Although experimental width δ is much wider than theoretical width, it should be noted that the electron pressure gradient at this transport barrier ($dP_e/dr = 1.4 \times 10^{21} \text{keV/m}^4 = 0.22 \text{MN/m}^2$ for E13784, Fig.2) is ten times larger than that in the inner plasma region. Such pressure profile shape may not be suitable to get high normalized beta $\beta_N (= \langle \beta_t \rangle / (I_p/aB_t))$ since beta limit will be reached at the edge with lower bulk pressure gradient.

3. Edge T_i at L-H Transition

Sudden L-H transition is one of interesting phenomena in the tokamak edge. Figure 3 shows waveforms of typical two discharges at L-H transition (same B_t , I_p , configuration). Increases in plasma stored energy W_{dia} , edge ion temperature T_{i99} and line average density n_e was seen at transition associated with sharp D_α drop. Shaing proposed a condition of L-H transition, as $v_{*i} = v_{ii} q R / (v_e l^{1.5}) (\sim n_{ii} q R / T_i^2) = 1$.

This theory indicates that the edge ion temperature is key parameter for L-H transition and it increases with plasma density and safety factor ($T_i \sim (q n_i)^{0.5}$). However, as is clearly seen in the figure, L-H transition occurs at lower edge ion temperature for high n_e discharges compared with lower n_e case. The transition is well correlated with the edge ion temperature independent of heating power which is a function of plasma density. Figure 4 shows the $T_{i(0.95a)}$ at L-H transition as a function of line average electron density for various heating power (8-15MW). Open circle shows T_{i95} at 1-st L-H transition after neutral beam injection ($q_{\text{eff}} = 4.4$). Closed circle shows T_{i95} at 2-nd or later L-H transition after neutral beam injection. Later L-H transition occurs at higher

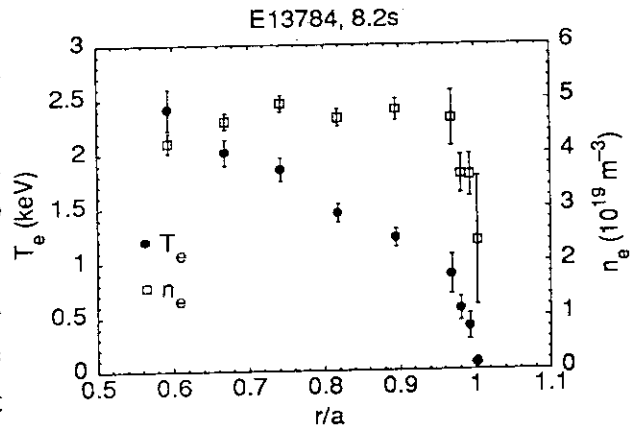


Fig. 2 Edge T_e and n_e profile for a 4MA discharge.

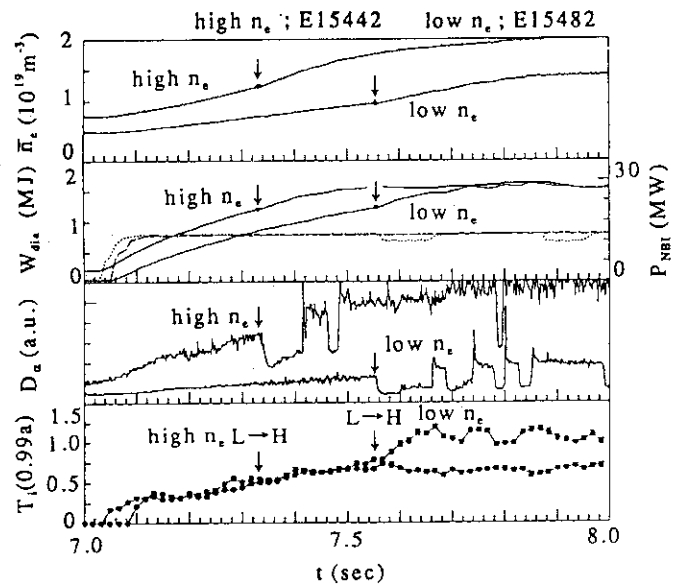


Fig. 3 Time evolutions of low and high density neutral beam heated plasma with L-H transition. $I_p = 1.3\text{MA}$, $B_t = 2\text{T}$.

edge T_i for the same density. Although theory predicts higher edge T_i for higher n_e and q_{eff} ($T_i(\text{edge}) \sim (n_i q_{eff})^{0.5}$), experimental edge T_i is higher at low q_{eff} and low n_e as shown by open squares ($q_{eff}=3.2$) in the figure. Since density profile becomes more broad with increasing plasma density and Z_{eff} generally reduces with density, the edge ion temperature must increase more strongly with average electron density if $v_{*i} = 1$ is the L-H transition condition.

This suggests that simple $v_{*i} = 1$ criterion may not be sufficient for L-H transition condition although the edge ion temperature can be an important parameter to get into the H-mode. The edge ion temperatures corresponding to $v_{*i} = 1$ and $v_{*i}(\text{eff})=1$ defined below are also shown in the figure.

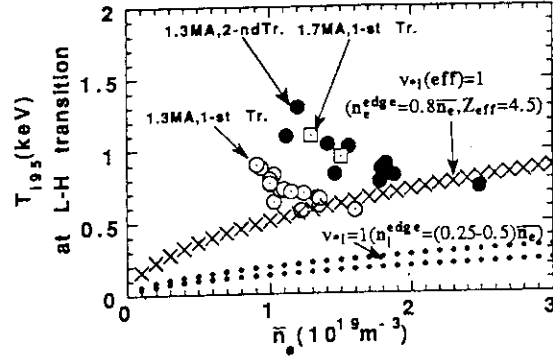


Fig. 4 Edge ion temperature at L-H transition as a function of n_e . Open and closed circles (1.3MA/2T, 1-st transition and 2-nd transition), open square (1.7MA/2T, 1-st transition). T_{i95} corresponding to ion collisionality of 1.0 is also shown.

4. Impurity Effect on L-H Transition

For further understanding, we investigate here the effect of impurity on L-H transition. Since Shaing considered the balance between the poloidal torque by faster ion orbit loss and viscous damping by low energy ion viscosity, effect of impurity on H-mode transition should be important. The normalized viscosity coefficient K_{11}^i may be written by[4],

$$K_{11}^i = \frac{8n_i m_i f_i}{3\sqrt{\pi} f_c} \int_0^\infty dx e^{-x^2} x^4 \frac{v_D^i(x v_{ti})}{1 + 2.48 v_{*i} \frac{v_D^i(x v_{ti}) \tau_{ii}}{x}} \int_{-1}^1 d\left(\frac{v_{||}}{v}\right) (1 - 3\left(\frac{v_{||}}{v}\right)^2)^2 \frac{\frac{v_T^i(x) R q}{v_{ti} x}}{\left(\frac{v_{||}}{v} + \frac{U_{pm}}{x}\right)^2 + \left(\frac{v_T^i(x) R q}{v_{ti} x}\right)^2}$$

Key impurity effect comes from the change of the deflection (v_D^i) and anisotropy relaxation (v_T^i) frequencies by the impurity. Both frequencies have same asymptotic form for $x > 1$, $v_D^i \sim v_T^i \sim 3\sqrt{\pi} Z_{eff} n_e / (4x^3 n_i z_i^2 \tau_{ii})$ and it conserve the structure by replacing $v_i^i \rightarrow v_i^i (Z_{eff} n_e / z_i^2 n_i)$. We may also expect such an effect on fast ion orbit loss. This might change the L-H transition condition to $v_{*i} \sim n_i Z_i^2 / Z_{eff} n_e$ and right hand side ranges from 1 - 1/25 ($Z_{eff}=1-5$).

5. Edge Electron and Ion Temperatures for Hot Ion H-mode

High performance plasmas with $T_i(0)=32\text{keV}$ and $W_{dia}=7.7\text{MJ}$ were obtained in hot ion H-modes at $B_t=4.2\text{T}$ [5]. This mode was reached by intense NB heating to low target density ($<1 \times 10^{19} \text{m}^{-3}$) plasmas by which high edge ion temperature was obtained just after NB injection. In this mode of operation, there was no clear D_α drop as a sign of L-H transition.

The edge ion temperature for similar q_{eff} ($=4.3$ at $I_p=2.7\text{MA}$) was plotted as a function of average electron density in Fig.5 together with those in Fig.4. The edge ion temperature in this mode of operation is much larger than those required for L-H transition. In such a case, we may expect that energy confinement can be improved continuously from L-mode to H-mode without any sharp transition. Here, we call it as "D $_{\alpha}$ Transition-less H-mode".

Although sharp D $_{\alpha}$ drop was not seen, the edge ion temperature up to 7keV were obtained during hot ion H-mode. Figure 6 shows H-factor over ITER-89P as a function of edge ion temperature T_{i95} . Good correlation between H-factor and edge T_i were seen. Required edge ion temperature to obtain some H-factor was rather insensitive to B_t and varies with I_p .

6. Conclusion

Characteristics of edge transport barrier is studied for NB heated plasma in JT-60U. Formation of the edge transport barrier was seen for both L- and H-modes whose width increases inversely with poloidal field B_p and much larger than the theoretical width. Density and q_{eff} dependences of the edge ion temperature at L-H transition were studied. Dependences are different from those expected from collisionality dependences ($T_i \sim (n_i q_{\text{eff}})^{0.5}$). To reconcile this discrepancy, effect of impurity on L-H transition was considered which was shown to be very important. The disappearance of the sudden D $_{\alpha}$ drop in hot ion H-mode regime was discussed by its high edge ion temperature with which Shaing's theory predicts loss of L-H transition.

References

- [1] KIKUCHI, M. et al., JAERI-M 92-073, sec 3.3
- [2] SHAING K.C., CRUME E.C.Jr, P.R.L. 63(1989)2369.
- [3] SHAING K.C., Physics Fluids B 4(1992)290.
- [4] SHAING K.C., in 3rd Workshop on H-mode Physics, JET, June 10(1991)513.
- [5] KIKUCHI, M. et al., this issue sec. 1.3.

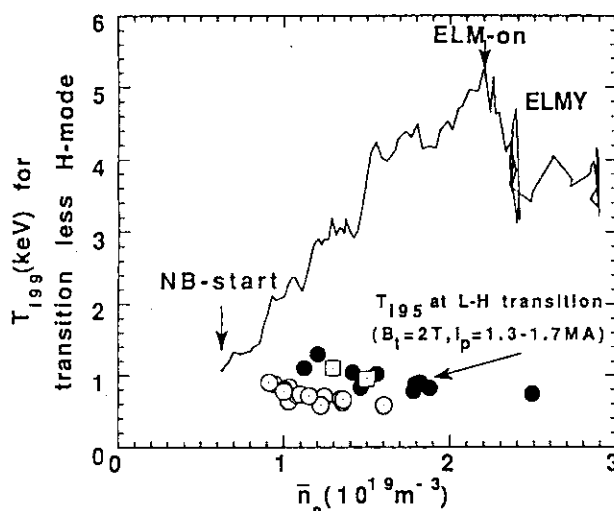


Fig. 5 Edge ion temperature as a function of n_e for D $_{\alpha}$ transition less H-mode. T_{i95} from NB-start to ELM occurrence are shown

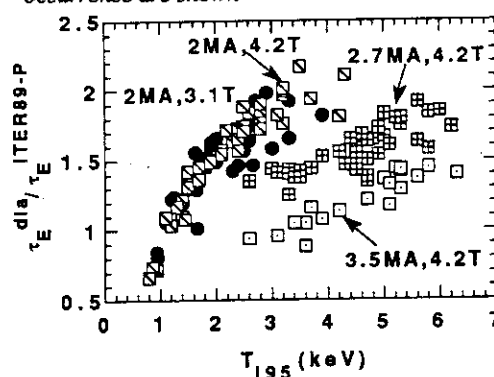


Fig. 6 H-factor as a function of edge ion temperature for $I_p=2\text{MA}$ (3.1T and 4.2T), 2.7MA and 3.5MA.

1.7 Effective Ion Collisionality Regime across the H-mode Transition

T. Fukuda, M. Kikuchi and Y. Koide

1. Introduction

Among the various experimental documentations in JFT-2M [1], ASDEX [2] and JET [3], the significance of the edge plasma temperature has been disputed as one of the key issues to induce the H-mode transition.

Theoretical considerations also take this quantity in terms of the effective ion collisionality ν_i^* . As Shaing predicts [4, 5] from the poloidal momentum balance equation, high-energy collisionless particles contribute to the ion orbit loss and drive a poloidal torque, while low-energy collisional particles contribute to the poloidal viscosity and resist poloidal rotation. The critical ν_i^* at which the poloidal flow velocity makes a sudden change to a more positive value is anticipated to be around unity. The sample calculation in Ref. 4 shows ν_i^* to be 1.85. However, quantitative agreement with the theory has never been previously shown, except for a single discharge in DIII-D [6]. This paper revisits this issue pursuing the parametric investigations in various JT-60 U plasmas including the Hot-ion mode plasma to understand whether the threshold of the ion effective collisionality ever exists and to find the quantitative agreement with the theory.

2. Definitions and the Description of the Data Set

One of the major problems in matching the theoretical bifurcation $\nu_i^* \approx 1$ with the experimental measurements is the lack of a proper definition for ν_i^* for a finite aspect ratio divertor plasma with one ion species. The standard definition $\nu_i^* = \nu_{ii} Rq / \epsilon^{2/3} v_{th}$ is for a large aspect ratio limiter plasma with one ion species. This definition is unfortunately singular on the separatrix of a divertor plasma. The JFT-2M work [7] utilizes this definition but evaluates it 7 mm inside the separatrix to obtain the value of ν_i^* around 50 in both the L- and H-mode, whereas in ASDEX it was larger than three. The DIII-D work also does not include the impurity effect.

In this work, the standard definition of ν_i^* has been employed. For the numerical estimate of ν_i^* , the factors which appears in the Braginskii's definition of the collision frequency and the edge ion temperature at $\rho = 0.94$ obtained from the SLICE code were

used. SLICE code expands the measured quantities on the magnetic flux surfaces separately obtained by an equilibrium solver [9]. Local electron density was evaluated by this code, which evaluates the whole density profile with two interferometer chords. The most recent correction which deals with the wavelength-dependant optical transmissivity of the vacuum window was included.

However, the transition condition is naturally influenced by the impurities. One of the mechanism is the enhancement of the average ionic charge Z_{eff} . When Z_{eff} increases, pitch angle scattering of the bulk ions becomes more frequent and the threshold value increases. The other mechanism is the non-ambipolar loss of impurities. The toroidal rotation ejects impurities from the plasma because the toroidal rotation velocity of the impurity ions, which is close to the bulk rotation velocity due to ion-ion collisions, can be supersonic for heavy impurity species. It does not seem feasible in JT-60 U of which impurity content is considerably high compared to the other machines mentioned above to exclude the impurity effect in evaluating the effective ion collisionality.

For further understanding, we first investigate the effect of ion-impurity collision theoretically in terms of the normalized viscosity coefficient [10, 11]. Key impurity effect comes from the change of the deflection and the anisotropy relaxation frequencies by the impurity. We have applied the replacement of v_i^* with $v_i^* (Z_{\text{eff}} n_e / z_i^2 n_i)$. This treatment is included hereafter for the estimate of the ion collisionality at the transition.

The definition of the H-mode transition can also be an issue of controversy, since the simple reduction in the D_α signal can occur at any occasion. For the data base compiled in this work, reduction in the edge density fluctuation and the changes in the poloidal rotation velocity were also referred to confirm the transition [12].

2. Results from the Data Analysis

Over 50 pulses in the 1992 campaign were analyzed. The temporal evolution of the value of v_i^* is depicted in Fig. 1, together with the D_α signals at two different positions, NB power, average density at two different locations, stored energy and the poloidal rotation velocity. As the NB heating is commenced at 8.0 s, v_i^* starts to decrease according to the increase in the temperature to finally reach the value of 2.6×10^{-2} at 8.68 s when the transition occurs. The required time for the transition to take place is directly relevant to the characteristic time of v_i^* to decrease. The poloidal rotation velocity data taken from two neighboring channels, one of which is situated on separatrix and the other 1.5 cm inside, also documents the creation of the edge poloidal flow velocity shear. Time delay in the poloidal rotation data is due to the integration time constant of milliseconds. When the ELM starts, the value of v_i^* swings back to larger

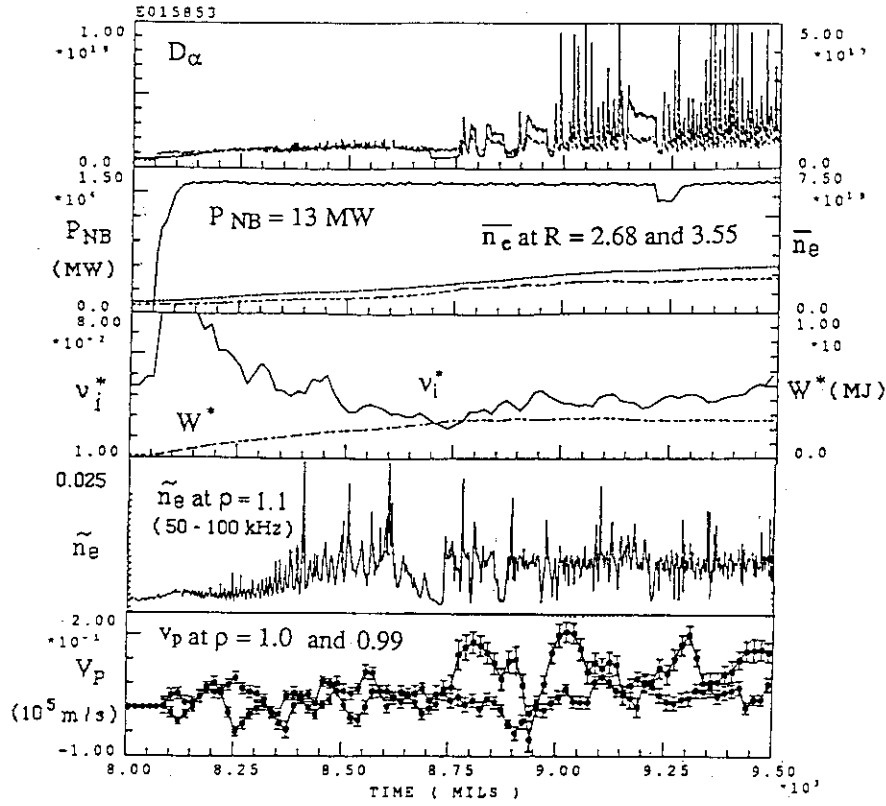


Fig. 1 The temporal evolution of the value of ion effective collisionality depicted together with the $D\alpha$ signals at two different positions, NB power, average density at two different locations, stored energy and the poloidal rotation velocity.

number. This documents the intimate relationship between v_i^* and the plasma mode state. After the procedure described in the previous section, which takes the impurity effect into account, the value of v_i^* , which we denote v_i^{eff} hereafter, at the transition is converted to be 1.1. This is astonishingly close to the theoretical estimate.

In Fig. 2 and 3, the value of v_i^{eff} is shown against other plasma parameters including the difference in the configuration. The threshold of v_i^{eff} does not show clear dependence either on B_r or I_p . All the data points scatter around $v_i^{\text{eff}} = 1$. For the hot-ion mode plasmas, since no clear transition was observable, the lowest value of v_i^{eff} right before the ELM was plotted. Their values are remarkably below one, which can support the transitionless H-mode phenomena. Also as pointed out in Ref. 5, when v_i^{eff} decreases further, only the more positive H-root exists. As to the high β_p discharges published in Ref. 13, the value of v_i^{eff} scatters in the range of 3 to 8, which indicates that the improvement of confinement is purely ascribed to non-H-mode properties.

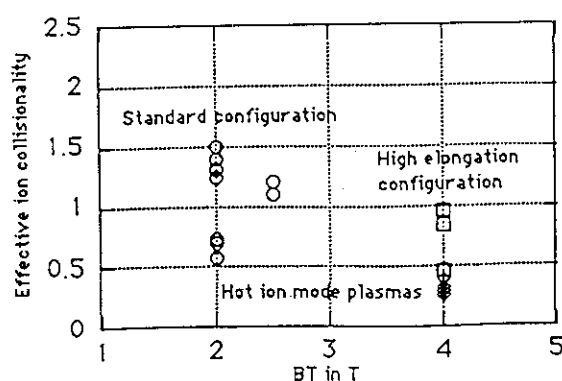


Fig. 2 Magnetic field dependence of the effective collision frequency. Open circles, squares and diamonds respectively correspond to the standard configuration, High-elongation configuration and the hot-ion mode data.

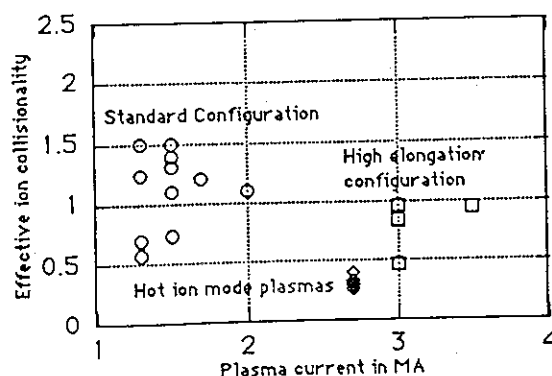


Fig. 3 Plasma current dependence of the effective collision frequency. Open circles, squares and diamonds respectively correspond to the standard configuration, High-elongation configuration and the hot-ion mode data.

References

- [1] ITOH, S. -I, ITO, K. , Comments Plasma Phys. Controlled Fusion 13 (1990)141.
- [2] ITOH. S. -I, FUKUYAMA, A. , TAKIZUKA, T. , ITOH, K. , Fusion Technology 16 (1989) 346.
- [3] BARTLETT, D. , private communication.
- [4] SHAIN, K. C. , CRUME, E. C. , Jr. , HOULBERG, W. A. , Phys. Fluids B2 (1990) 1492.
- [5] SHAIN, K. C. , CRUME, E. C. , Jr. , Phys. Rev. Lett. 63 (1989) 2369.
- [6] BURRELL, K. H. , CARLSTROM, T. N. DOYLE, E. J. , FINKENTHAL, D. , GOHIL, P. et al. , GA-A20993 (1992).
- [7] IDA, K. , HIDEKUMA, S. , MIURA, Y. et al. , Phys. Rev. Lett. , 65 (1990) 1364.
- [8] OHKAWA, T. , ITOH, K. , ITOH, S. -I. , Kakuyugo Kenkyu 59 (1988) 488.
- [9] HIRAYAMA, T. , TANI, K. , SHIRAI, H. , JAERI- M 88-043.
- [10] SHAIN, K. C. , in 3 rd Workshop on H-mode Physics at JET in June 10 (1991) 513.
- [11] KIKUCHI, M. , YOSHIDA, H. , NAITO, O. , KOIDE, Y. , FUKUDA, T. , this report.
- [12] FUKUDA T. , NAGASHIMA, K. , KONOSHIMA, S., HARAGUCHI, K. , TAKAHASHI, T. , NAGASHIMA, A. , MATOBA, T. , Rev. Sci. Instrum. 61 (1990) 3524.
- [13] ISHIDA, S. , MATSUOKA, M. , KIKUCHI, M. et al. , Proc. 14 th IAEA Conference, Würzburg, Germany CN-56/A-3-5 (1992).

1.8 H-mode Characteristics with Outboard Configuration for Combined IC and NB Heating

H. Kimura, N. Asakura, M. Kikuchi, Y. Koide, M. Nemoto and T. Fujii

1. Introduction

Combined ICRF and NBI heating in H-mode will be useful for producing reactor regime plasmas in JT-60U (say, $T_e \sim T_i \sim 10\text{keV}$ at high electron density), since ICRF heating acts mainly as a bulk electron heating through collisional power transfer from energetic minority ions produced by ICRF waves to electrons, while NBI heating provides its power mainly to bulk ions. Divertor configuration with relatively narrow gap between the separatrix and the outboard wall (hereafter we call this an outboard configuration) should be necessary for combined ICRF and NBI heating because of ICRF antenna-plasma coupling. Plasma operation with such configuration is also interesting from a point of view of effects of plasma configuration on H-mode quality, since H-mode experiments on JT-60U [1] have been carried out exclusively with a large gap between the separatrix and the outboard wall (i.e., standard configuration and high elongated configuration) to lessen ripple-induced fast ion loss. In view of these matters, preliminary H-mode experiments with combined ICRF and NBI heating with outboard configuration have been conducted for the first time on JT-60U. H-mode characteristics with outboard configuration will be discussed in comparison with those of standard configuration as well as effects of ICRF heating on H-mode plasmas.

2. Operation Conditions

The toroidal field was set to be 2.5T at the plasma center, which satisfies third harmonic cyclotron resonance of proton ($3\omega_{cH}$) on-axis or sixth harmonic cyclotron resonance of deuteron ($6\omega_{cD}$) on-axis. Wave absorption by the latter damping mechanism can be enhanced by the presence of deuterium beam ions. The plasma current was 1.7MA and the safety factor (q_{eff}) was about 4. The gap between the separatrix and the outboard wall in the equatorial plane (δ_0) was set in the range of 14cm ~ 9cm in order to secure sufficient antenna-plasma coupling (the antenna coupling resistance $R_C \sim 5\Omega$ [2]), while the value of δ_0 is around 27cm for the standard configuration. A sum of the ripple trapped ion loss and the banana drift ion loss for the perpendicular NBI amounts to 35-40% for the outboard configuration and about 25% for the standard configuration. The wall temperature in the present experiment ranged from 135° down to 110°. The NBI heating power was 7 ~ 16 MW including 3 ~ 7 MW of tangential beam, while the ICRF heating power was 2 ~ 3 MW. The ICRF antenna phasing was ($\pi, 0$) mode.

3. Results

Figure 1 (a)-(c) show time evolution of typical H-mode shots of (a) standard configuration (std. config.), (b) outboard configuration (outbd. config.) with NBI only and (c) outbd.

config. with NBI+ICRF. Clear L→H transition appeared in both outbd. config. cases as well as the std. config. case. Threshold power for L→H transition with outbd. config. with NBI+ICRF is about 10 MW, which is slightly higher than the one for std. config. with NBI only. ELMs appear at $\bar{n}_e = 1.6 \times 10^{19} \text{ m}^{-3}$ for the outbd. config. cases, whose value seems common with those of other configurations in JT-60U [3]. Deuterium beam ion acceleration by $6\omega_{cD}$ heating was observed by an active charge exchange (CX) analyzer whose line of sight is about 40 degree to the magnetic axis, although high energy tail of protons by $3\omega_{cH}$ heating was not observed clearly by the simultaneous measurement with the same analyzer. However, the $6\omega_{cD}$ heating has not yet been well optimized in the present experiment, because the power deposition profile of NBI is off-axis for the outbd. config..

Total Radiation Loss

If conditions of the ICRF heating are not optimal like in the present experiment, increase in the total radiation loss tends to be large ($\Delta P_{\text{rad}}^{\text{main}}/P_{\text{IC}} \sim 30\%$ [2]). However, as mentioned above, application of the ICRF heating gives no adverse effects on L→H transition. Figure 2 shows total radiation loss power just before L→H transition versus absorbed power, P_{abs} . IC+NB data are on the line of $P_{\text{rad}}^{\text{tot}}/P_{\text{abs}} = 0.25$, similar to NB only data with std. config.. The data of NB only with outbd. config. is much smaller. The fact suggests that the total radiation loss itself does not critically affect the L→H transition. The radiation loss increases rapidly after L→H transition. It is important to compare the rate of increase in the total radiated power ($dP_{\text{rad}}^{\text{tot}}/dt \times 1/P_{\text{abs}}$) just after L→H transition between IC+NB case and NB alone case. Figure 3 indicates the radiation increase rate as a function of dW_{dia}/dt just after L→H transition. We found that $dP_{\text{rad}}^{\text{tot}}/dt \times 1/P_{\text{abs}}$ is in proportion to dW_{dia}/dt and that impurity release just after L→H transition by ICRF heating, which was problematic in early stage of JET ICRF H-mode experiments [4], was moderate, i.e., similar to the data of NBI alone with std. config..

Neutral Particle Influx

Figure 4 shows the divertor D_α intensity and the main chamber D_α intensity, normalized by P_{abs} , as a function of δ_0 . Both D_α signals are found to be significantly reduced with decreasing value of δ_0 . Moreover, a ratio of the divertor D_α intensity to the main chamber D_α intensity decreases with decreasing value of δ_0 . The result may be related with possible reduction of back flow of the neutral gas from the divertor due to reduction of the conductance of the space between the plasma and the outboard wall with the outbd. config..

Global Energy Confinement

Figure 5 indicates the diamagnetic stored energy versus the loss power, from which ripple-induced loss power is not subtracted, for the outbd. config. (open circle) and the std. config. (open square), comparing them with ITER-89 power-law scaling. Data of the outbd. config. show good results, considering larger ripple-induced ion loss and off-axis NBI heating. The maximum H-factor is about 1.7. Somewhat worse data with outbd. config. are of IC+NB

heating. The reason is possibly due to imperfect optimization of the ICRF heating based on $6\omega_{cD}$ beam ion acceleration.

4. Discussion and Conclusions

It is well known that reducing the edge neutral density is crucial for getting good H-mode. We found that particle influx from the divertor and the first wall could be significantly reduced with decreasing outboard gap. Back flow of neutrals from the divertor may be limited by narrow outboard gap. Thereby H-mode characteristics with the outboard configuration do not degrade in spite of larger ripple-induced ion loss. Moreover, ripple-induced ion loss brings about negative electric potential in the plasma edge, which may facilitate L→H transition [5]. Further detailed studies on these matters including plasma rotation measurements in the edge are needed. We have got following conclusions from the present experiments:

- (1) H-mode can be produced for the outboard configuration with combined IC and NB heating in spite of significant ripple loss and unoptimized ICRF heating.
- (2) H-factor achieved is about 1.7.
- (3) Particle influx in the divertor is significantly reduced with decreasing outboard gap.
- (4) Deuterium beam acceleration by $6\omega_{cD}$ heating was observed. High energy tail of protons due to $3\omega_{cH}$ heating was not observed clearly.

Combination of ICRF heating (5MW) and tangential NBI heating (10MW) with additional perpendicular NBI (< 10MW) at $B_T=4T$ will be the best choice to get much better H-mode with the outboard configuration in the next campaign.

References

- [1] KIKUCHI, M., et al., IAEA-CN-56/A-3-3, (1992, Würzburg).
- [2] SAIGUSA, M., et al., Sec. 10.3 in this Review.
- [3] KAMADA, Y., et al., Sec. 1.4 in this Review.
- [4] JACQUINOT, J., et al., Fusion Engineering and Design **12** (1990) 245.
- [5] SHAIN, K.C., et al., Phys. Fluids B **2** (1990) 1492.

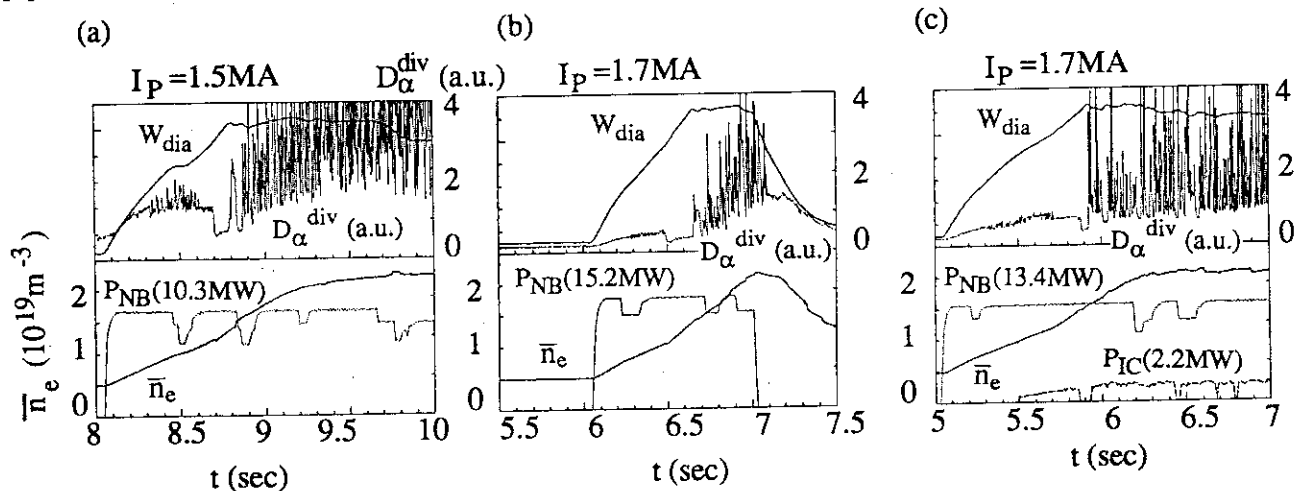


Fig.1 Time evolution of typical H-mode shots. (a) standard configuration (shot E15852; triangularity $\delta=0.18$,

ellipticity $\kappa=1.44$, X-point position $R_X=3.04m$, plasma center position $R_P=3.32m$, tangential beam power $P_{NB||}=3.1MW$, (b) outboard configuration with NBI only (shot E16379; $\delta=0.19$, $\kappa=1.41$, $R_X=3.1m$, $R_P=3.44m$, $P_{NB||}=6.9MW$) and (c) outboard configuration with NBI+ICRF (shot E16389; $\delta=0.22$, $\kappa=1.41$, $R_X=3.1m$, $R_P=3.45m$, $P_{NB||}=5.8MW$).

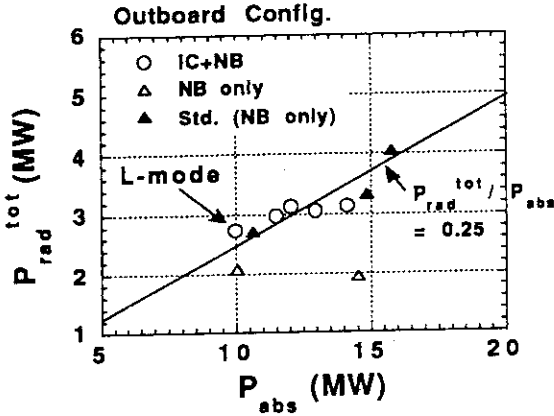


Fig.2 Total radiation loss power just before L→H transition versus absorbed power.

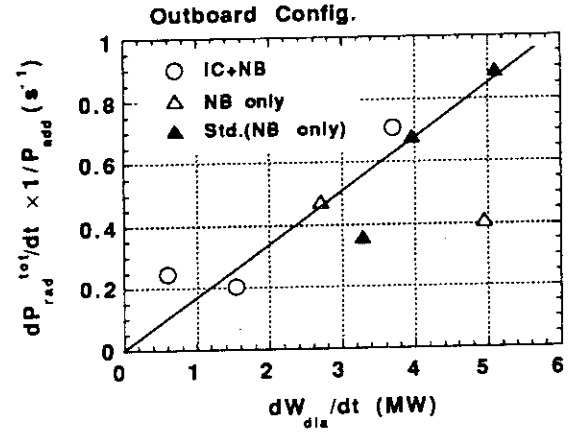


Fig.3 Total radiation increase rate as a function of dW_{dia}/dt just after L→H transition.

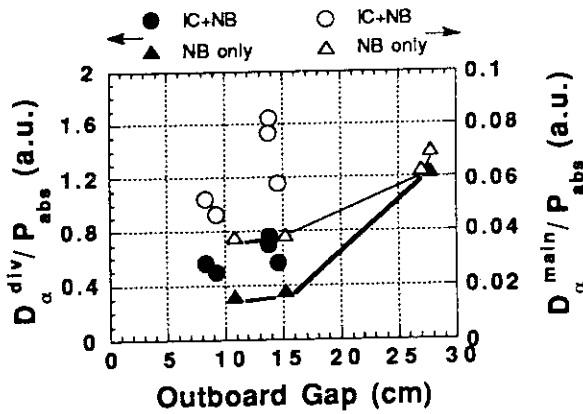


Fig.4 Divertor D_α intensity and main chamber D_α intensity, normalized by P_{abs} , as a function of outboard gap.

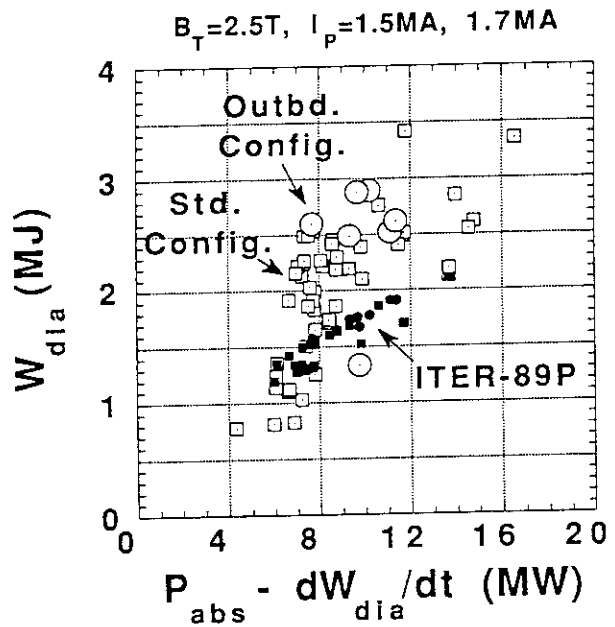


Fig.5 Diamagnetic stored energy versus loss power for the outbd. config. (open circle) and the std. config. (open square), comparing them with ITER-89 power-law scaling.

1.9 Effects of Safety Factor and internal Inductance on Energy Confinement in L-mode and H-mode

Y.Kamada, T.Takizuka, M.Kikuchi and H.Ninomiya

1. Introduction

The purpose of the series of studies in Secs. 1.4, 1.9, 1.10, 1.11, 2.6, 8.1 and 8.5 is to obtain systematic understandings of effects of safety factor q and current profile on MHD activities and τ_E . Concerning τ_E for L-mode, I_p has a strong effect [1]. Although the role of the current profile $j(r)$ is important to understand the origin of the I_p -dependence, the effect of $j(r)$ on τ_E has not been clarified in spite of its strong effect on MHD. Some effects of I_i on τ_E were reported firstly in ref.[2] by current ramp experiments. This paper expands the discussion to generalize the understandings. Another important value is q . In particular, the reason for the degradation in τ_E at low- q is still an open question. For identification of these effects of I_i and q_{eff} , macroscopic instability and micro-turbulence should be separated. Based on this objective, we treat relationships among I_i , q_{eff} and τ_E including MHD instabilities in NB-heated plasmas. Figure 1 gives the scenario for analyzing these relationships ((0)-(5)). The tokamak MHD regions are identified on the I_i - q_{eff} plane ((0); Sec.8.1). Relationships (1), (2) and (3) are given in Secs.8.5, 1.9 (this section) and 1.10, respectively. Section 1.10 also summarizes the relationships (1)-(3) for L-mode. Section 1.11 analyses the H-mode confinement where the relationship (5) is presented. The relationship (4) is given in Sec.1.4. These sections treat low β ($\beta_p < 1$, $\beta_N < 1.5$) plasmas to achieve a basic understanding. The effects of I_i at high- β is presented in Sec.2.6. The summary of these studies were presented in refs.[3] and [4].

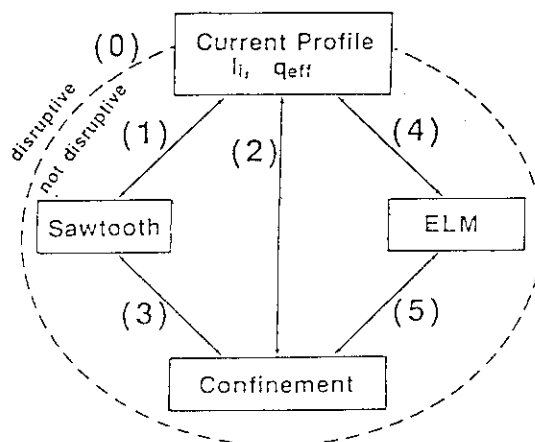


Fig.1: Scenario for analyzing relationships among q_{eff} , I_i , confinement, sawteeth and ELMS.

2. q_{eff} and Confinement in L-mode and H-mode

As shown in Sec.8.1, discharges can be clearly categorized by q_{eff} ($q_{95} \sim 0.8q_{eff}$ in JT-60U) and I_i in the low β region (Fig.2). In Fig.2, we can observe the boundary corresponding to the quasi-stationary current distribution (dashed line). Usually, if I_p is kept constant stably, I_i increases asymptotically toward this boundary. The important behavior of I_i along the dashed line is that I_i is almost constant in the high- q region ($q_{eff} > 5$) and decreases rapidly with decreasing q_{eff} at $q_{eff} < 5$. The dotted line indicates the boundary for appearance of sawteeth.

Figure 3 shows the confinement performance ($H\text{-factor} = \tau_E / \tau_E^{ITER89P}$ [3]) in L-mode

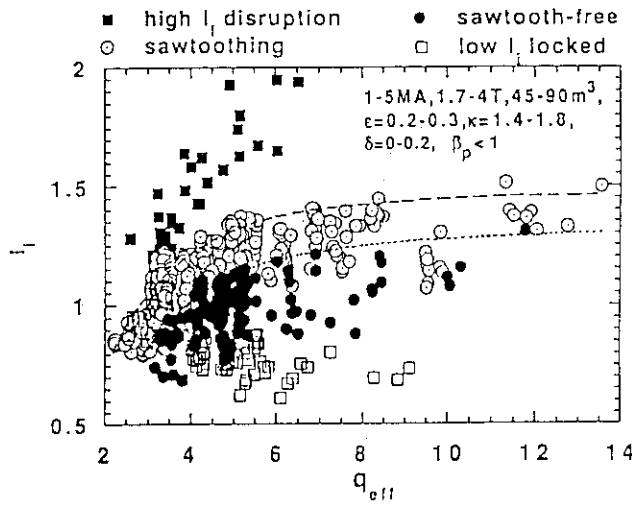


Fig.2: Discharge regions on the q_{eff} - I_i plane.

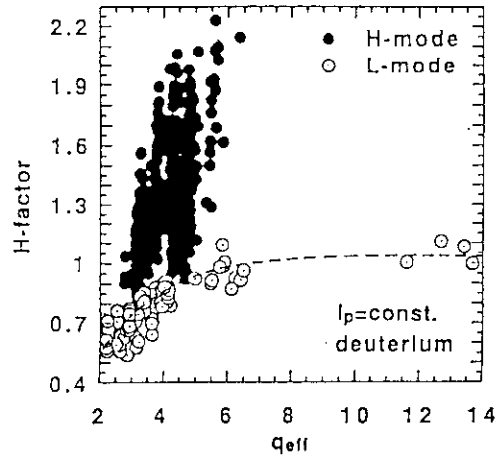


Fig.3: H-factor vs. q_{eff} for NB heated deuterium L-mode and H-mode (ELM-free and ELM) where I_p was kept constant.

and H-mode (ELMy and ELM-free) with $I_p=1-4\text{MA}$, $B_t=1.7-4\text{T}$, $P_{net}=4-25\text{MW}$, $R=3.1-3.3\text{m}$, $a=0.8-0.9\text{m}$ and $\kappa=1.5-1.7$. The net heating power P_{net} consists of absorbed NB power P_{NB} (reionization loss and shine through are subtracted), OH power and dW_{dia}/dt . The ripple loss [5] of beam ions was not included. The dashed line in Fig.3 gives the tendency of the H-factor for L-mode deuterium discharges. The H-factor decreases rapidly with decreasing q_{eff} at low- q ($q_{eff}<5$) and stays nearly constant at high- q ($q_{eff}>5$). Since the dependence of H-factor on q_{eff} is similar to that of I_i on q_{eff} (dashed line in Fig.2), Fig.3 suggests a strong correlation between I_i and the H-factor. In H-mode, the H-factor also degrades with decreasing q_{eff} .

3. I_i and Confinement in L-mode

Figure 4 shows the relationship between the H-factor and I_i for L-mode obtained in deuterium and hydrogen discharges. In Fig.4, data were taken when I_p was kept constant (not I_p -ramp) and the time scales of change in plasma parameters except τ_{sw} were much longer than τ_E . The H-factor increases clearly with I_i over a wide range of q_{eff} : $q_{eff}=2-14$. However, about 50% of scatter is still observed at $I_i \sim 0.8-1.2$ which is caused mainly by the effects of sawteeth (Sec.1.10). In Fig.5, where data with $\tau_{sw}>2\tau_E$ (including sawtooth-free) were used to exclude the effects of sawteeth, it is found that the H-factor in L-mode is almost proportional to $I_i^{0.8}$.

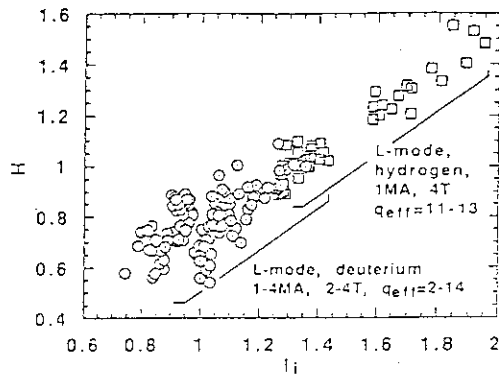


Fig.4: H-factor vs. I_i for L-mode and H-mode discharges.

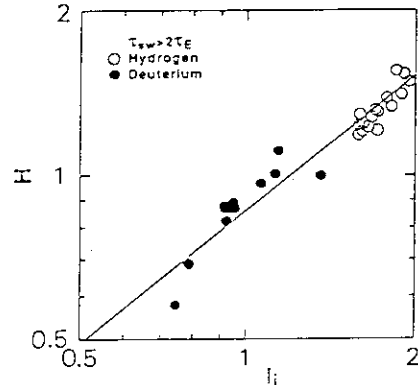


Fig.5: Dependence of H-factor on I_i for L-mode with $\tau_{sw}>2\tau_E$. The solid line indicates $H \sim I_i^{0.8}$.

The high l_i values ($1.5 < l_i < 1.9$) of hydrogen data were obtained when a strong minor disruption occurred in the very early phase of the discharge. However the effects of the minor disruption on τ_E was negligible because $Z_{\text{eff}} < 2.8$, $P_{\text{rad}}^{\text{main}}/P_{\text{net}} < 30\%$ and no evidence of metal impurity accumulation was observed (the first wall is fully covered by carbon). The effective mass number A_i for the hydrogen data was about 1.2. This section is based on the ITER-89P law [1] where $\tau_E \sim A_i^{0.5}$. Clarification of the A_i -dependence was reported in Ref. [6].

4. l_i and Confinement in H-mode

Figure 6 shows the relationship between H-factor and l_i for H-mode where the L-mode data are plotted as a reference. In H-mode, the H-factor also increases with l_i , however the scatter is much larger than that of L-mode which is caused mainly by the effects of sawteeth, ELMs (Sec.1.11) and the complicated l_i -dependence shown below. In Fig.6, some transient data from the I_p ramp down experiments are included, in which I_p was ramped down from 2MA to 1.5MA in 0.5sec during the H-phase. The H-factor reaches to 2.6 which is the maximum H-factor obtained in JT-60U H-mode so far.

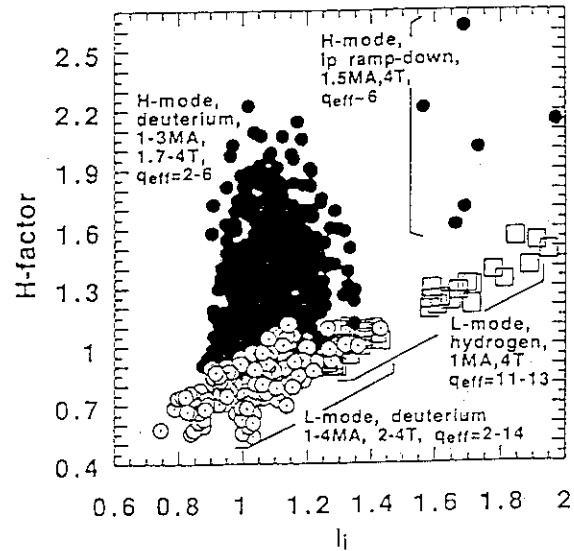


Fig.6: H-factor vs. l_i for H-mode and L-mode.

To analyze the effect of l_i on H-mode confinement, Figs.7(a) and (b) use the data of discharges free from both ELMs and sawteeth at medium q_{eff} , $q_{\text{eff}}=4-5$. Data were taken at the end of the ELM free period (typically 0.3-1s after the start of NBI). The H-factor increases with l_i of the target ohmic plasma rather than l_i at the time when H-factor is calculated. Therefore, in H-mode, the dependence of confinement on l_i is complicated. Our observations are as follows:

i) In H-mode, l_i usually tends to decrease with increasing H-factor due to the edge pedestal of temperature and pressure. Therefore, the H-factor increases with decreasing l_i . ii) In turn, the

H-factor increases with l_i of the target ohmic plasma, which suggests that the peaked $j(r)$ in the inner region causes improved confinement. iii) However, if l_i is increased significantly by I_p ramp down (Fig.6) during the H-phase, the H-factor can be improved, which may be related to increase in magnetic shear in the edge region or poloidal field in the inner region. These observations

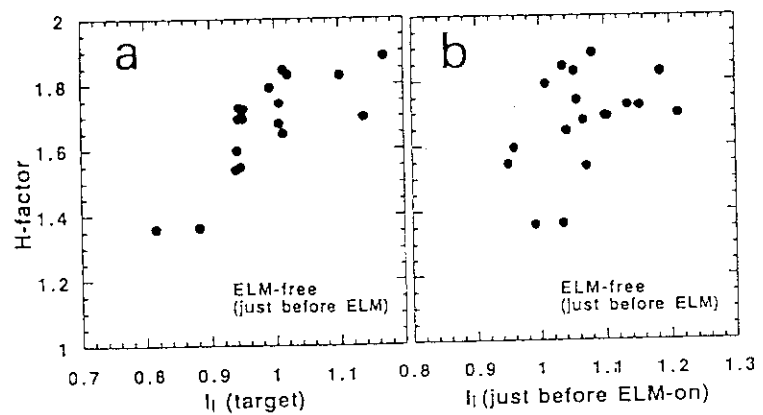


Fig.7: H-factor for H-mode free from both ELMs and sawteeth plotted against l_i of target OH plasma and l_i at the time when H-factor is calculated.

mean that the dependence of τ_E on I_i in H-mode should be discussed by separating the current profile in the central region and the edge region.

5. Discussions

Concerning the relationship between I_i and τ_E in L-mode, this paper reported the results of experiments where I_p was kept constant. By comparison with the I_p -ramp experiment [5, 9, 10], the reason for the I_i -dependence may be related to the strength of poloidal field at the relatively inner region or magnetic shear at the relatively outer region. The effect of sawteeth is independent of this I_i -dependence because the sawtooth region expands with I_i , which should lead to the opposite dependence of the H-factor on I_i (see Secs.8.5 and 1.10). MHD modes with medium (m,n) have not been observed to correlate with the dependence. Therefore, the I_i -dependence may be caused by high (m,n) MHD activities or micro-turbulence. We treated the total energy confinement including thermal and high energy components (W_{th} and W_f). For more detailed analyses, effects of I_i on W_{th} and W_f should be separated. Finally, Fig.8 compares the I_i -dependence of H-factor obtained in many tokamaks (JT-60U [4], TFTR[7], DIII-D [8] and TORESUPRA [9]). From this figure, the I_i -dependence of H-factor seems to be weaker than the linear dependence and $H \sim I_i^{0.8}$ seems to be a good fit for the L-mode.

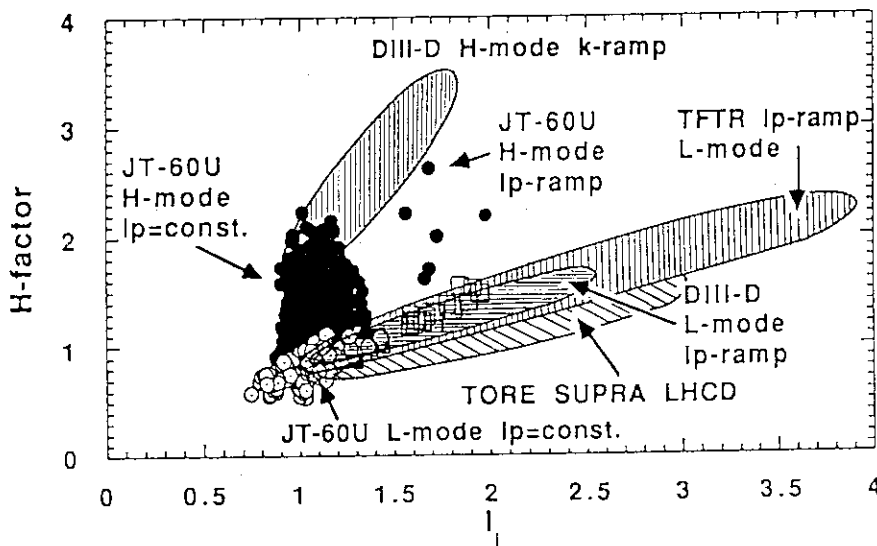


Fig.8: The I_i -dependence of H-factor in many tokamaks (JT-60U [4], TFTR[7], DIII-D [8] and TORESUPRA [9]).

REFERENCES

- [1] UCKAN, N.A., et al., in Plasma Physics and Controlled Nuclear Fusion Research (Proc.13th Int. Conf., Washington, 1990) Vol. III, p307.
- [2] ZARNSTROFF, M.C., et al., *ibid.* Vol.I, p109.
- [3] KAMADA Y., et al., 'Effects of the safety factor and the internal inductance on MHD activities and energy confinement in JT-60U' to appear in Nucl. Fusion.
- [4] KAMADA Y., et al., in Plasma Phys. Cont. Nucl. Fusion Research (Proc.14th Int. Conf., Wurzburg, 1992) IAEA-CN-56/A-7-13.
- [5] NISHITANI, T., et al., *ibid.* IAEA-CN-56/A-6-2.
- [6] KIKUCHI, M., et al., *ibid.* IAEA-CN-56/A-3-3.
- [7] ZARNSTROFF, M.C., et al., *ibid.* IAEA-CN-56/A-2-2.
- [8] Lao, L.L., et al., *ibid.* IAEA-CN-56/A-7-19.
- [9] Equipe TORE SUPRA, *ibid.* IAEA-CN-56/A-1-4.

1.10 Effects of Sawtooth Activity on Confinement

Y.Kamada, T.Takizuka, M.Kikuchi and H.Ninomiya

1. Introduction

One of the main objectives of confinement and MHD research in JT-60U is to clarify the relationships among l_i , q_{eff} and τ_E including MHD instabilities (Sec.1.9). The scenario of our analyses was given in Fig.1 in Sec.1.9, for which this section studies the relationship (3) and then summarizes the relationships (1) (Sec.8.5), (2) (Sec.1.9) and (3) for L-mode using a new scaling of the H-factor. The results quantitatively explains the degradation in confinement at low- q where the effects of sawteeth on confinement becomes stronger at lower q_{eff} . The L-mode confinement cannot be scaled without including the effects of l_i and sawteeth. The summary of the sawtooth effects on confinement was also reported in refs.[1,2].

2. Effects of l_i , q and Sawtooth Activity in Low- q L-mode

This section treats the confinement degradation in the low q region ($q_{eff} < 5$ or $q_{95} < 4$), where H-factor decreases rapidly with decreasing q_{eff} (Fig.3 in Sec.1.9), for which one of the main reasons can be explained by the effect of l_i on confinement. As shown in Sec.1.9, H-factor is proportional to $l_i^{0.8}$, and l_i decreases rapidly with decreasing q_{eff} in the low q region. Therefore with decreasing q_{eff} confinement becomes poor. To clarify this point, Fig.1 shows dependence of $H/l_i^{0.8}$ (H-factor normalized by $l_i^{0.8}$) on q_{eff} for L-mode discharges shown in Figs.3 and 4 in Sec.1.9. The maxima of $H/l_i^{0.8}$ are almost constant over the whole range of q_{eff} . This conclusion is important to understand the confinement degradation in the low q region. In Fig.1, however, large number of data with poor confinement are still observed in the low- q region. To understand the further confinement degradation, effects of sawtooth is examined below for which the key parameters are τ_{sw} and r_{inv} (or r_{mix}). Figure 2 shows the dependence of $H/l_i^{0.8}$ on τ_{sw} and on $(r_{inv}/a)_{sx}$ for

four regions of l_i at $q_{eff}=3.9-4.2$ ($I_p=3\text{MA}$, $B_t=4\text{T}$, $V_p=73-78\text{m}^3$), where the data plotted at $\tau_{sw}=1\text{s}$ and $(r_{inv}/a)_{sx}=0$ are those for sawtooth free discharges with low l_i -values. For these data, $\tau_E = 0.2-0.3\text{s}$. In Fig.2(a), $H/l_i^{0.8}$ increases almost linearly with τ_{sw} at $\tau_{sw} < 1-2\tau_E$, then seems to saturate at $H/l_i^{0.8} \sim 0.92$. The saturated value is comparable to $H/l_i^{0.8}$ for sawtooth free discharges. In Fig.2(b), $H/l_i^{0.8}$ decreases with increasing $(r_{inv}/a)_{sx}$. From (a) and (b), if l_i is kept constant, r_{inv}/a is also nearly constant and $H/l_i^{0.8}$ increases with τ_{sw} (see open

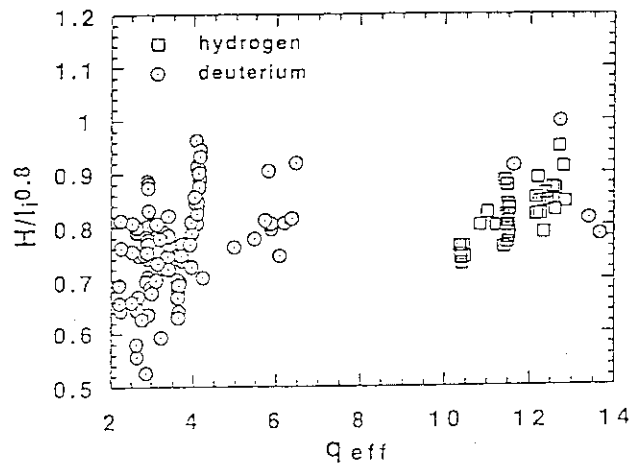


Fig.1: $H/l_i^{0.8}$ vs. q_{eff} for L-mode.

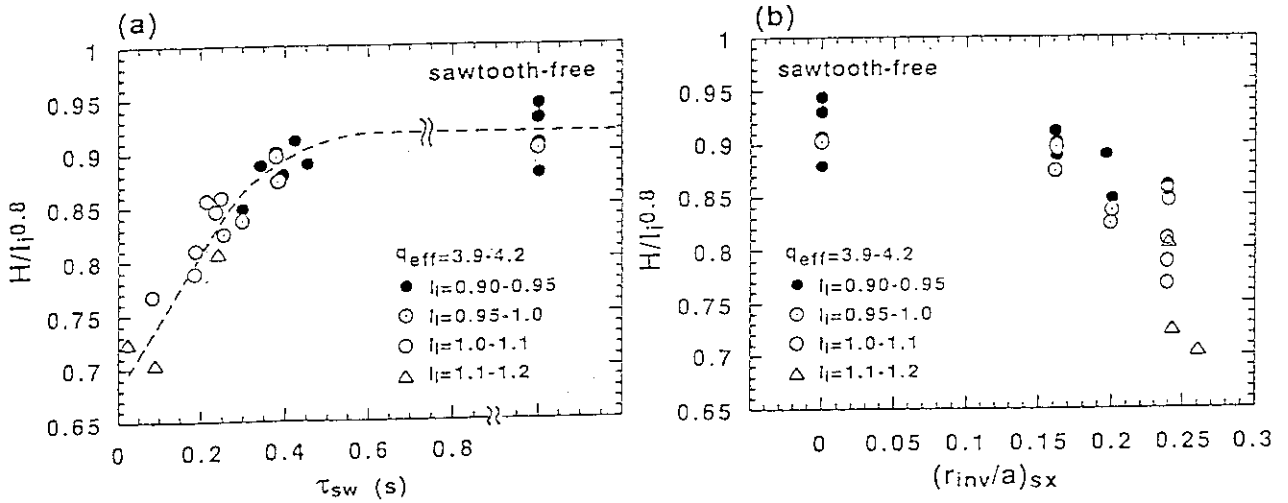


Fig.2: $H/I_i^{0.8}$ vs. (a) τ_{sw} and (b) r_{inv}/a for four regions of I_i at $q_{eff}=3.9-4.2$. Sawtooth-free data are plotted at $\tau_{sw}=1s$ and $(r_{inv}/a)_{sx}=0$.

circles). In case of closed circles, r_{inv} changes widely at nearly the same I_i . This is because r_{inv} changes rapidly around the I_i -threshold for the appearance of sawteeth (see Fig.2 in Sec.8.5) and the spread of the threshold I_i values in our data set is about 0.1. However, once the plasma starts sawtooth regularly, change in r_{inv} is well related to I_i . (in case of closed circles in Fig.2(b), change in $(r_{inv}/a)_{sx}$ is about 0.04.)

The interesting feature of effects of sawtooth on confinement is observed when the dependence of $H/I_i^{0.8}$ on τ_{sw} is examined as a function of q_{eff} . Figure 3 shows the dependence in four regions of q_{eff} : (a) $q_{eff}=2.6-2.7$, (b) $q_{eff}=3.35-3.45$, (c) $q_{eff}=3.9-4.2$ and (d) $q_{eff}=5.0-6.0$, where values of I_i is restricted in a narrow range to keep r_{inv}/a almost constant in each data set. Since the selected value of I_i is around unity, $H/I_i^{0.8}$ is nearly equal to H-factor itself in Fig.3. In each sub set, $H/I_i^{0.8}$ increases linearly with τ_{sw} , however the tendency is different. The slope $f=\Delta(H/I_i^{0.8})/\Delta\tau_{sw}$ decreases and the limit of $H/I_i^{0.8}$ for $\tau_{sw} \rightarrow 0$ ($Y=\lim_{\tau_{sw} \rightarrow 0} (H/I_i^{0.8})$) increases with increasing q_{eff} . For example, in case of (d), even if τ_{sw} increases by a factor of 4, change in $H/I_i^{0.8}$ is only ~10%. On the other hand, in (a), $H/I_i^{0.8}$ increases rapidly with τ_{sw} . We made 10 subsets of data with different

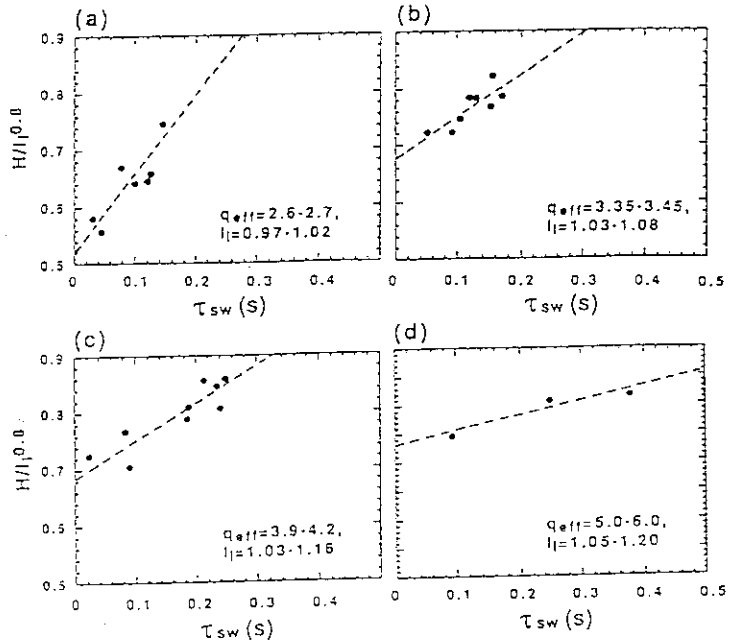


Fig.3: $H/I_i^{0.8}$ vs. τ_{sw} for four regions of q_{eff} : (a) $q_{eff}=2.6-2.7$, (b) $q_{eff}=3.35-3.45$, (c) $q_{eff}=3.9-4.2$ and (d) $q_{eff}=5.0-6.0$.

values of (q_{eff}, l_i) then examined the dependence of f and Y on q_{eff} . In Fig.4, f increases with $1/q_{eff}$ as $f \sim (1/q_{eff})^2$. Since $(r_{inv}/a)_{sc}$ is proportional to $1/q_{eff}$ in the steady state (Sec.8.5), Fig.4 suggests that f is proportional to the area of the sawtooth inversion (or mixing). In Fig.5 where Y is plotted against $(r_{inv}/a)_{sc}$ (eq.(3) in Sec.8.5), Y decreases with increasing $(r_{inv}/a)_{sc}$. The value of Y at $(r_{inv}/a)_{sc}=0$ is assumed to be the same as $H/l_i^{0.8}$ for sawtooth free discharges. The interpretation of the parameter Y is that the confinement performance when the transport coefficients are infinity within r_{mix} . From Figs.2-5, it is concluded that energy confinement in the low q region is a function of τ_{sw} and the dependence is stronger at lower q_{eff} .

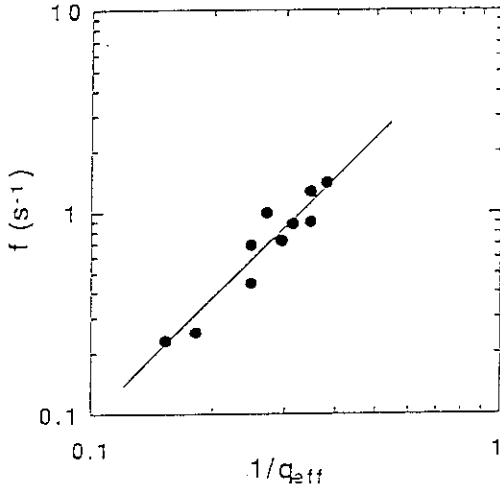


Fig.4: The slope $f = \Delta(H/l_i^{0.8})/\Delta\tau_{sw}$ vs. $1/q_{eff}$.

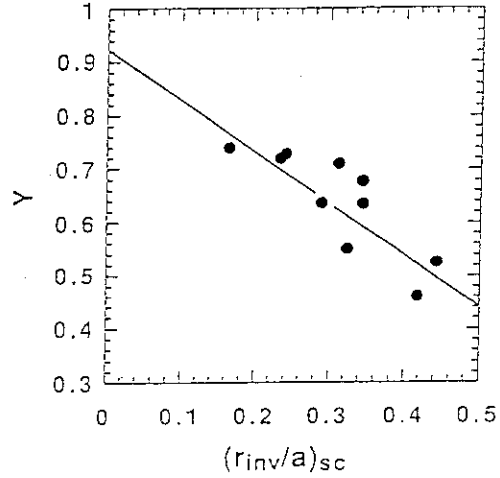


Fig.5: Y (Limit of $H/l_i^{0.8}$ for $\tau_{sw} \rightarrow 0$) vs. $(r_{inv}/a)_{sc}$ given by eq.(3) in Sec.8.5.

Finally, from Figs.5 in Sec.1.9 and Figs.2-5 in this section, we can make a scaling of H -factor given by

$$H_{sc} = (Y + f\tau_{sw})l_i^{0.8} \quad ; \tau_{sw} < (c-Y)/f$$

$$H_{sc} = cl_i^{0.8} \quad ; \tau_{sw} > (c-Y)/f$$

$$f = 10.0/q_{eff}^2, Y = c - 0.96(r_{inv}/a)_{sc}, c = 0.92, (1)$$

where $(r_{inv}/a)_{sc}$ is given by eq.(3) in Sec.8.5. Then H_{sc} can be calculated only with q_{eff} , l_i and τ_{sw} . Figure 6 shows good agreement between experimentally obtained H -factor and H_{sc} . Therefore, the scatter of data around ITER89P law (Fig.3 in Sec.1.9) is understood by introducing the effects of l_i , q_{eff} and τ_{sw} which are not used explicitly in $\tau_E^{ITER89P}$.

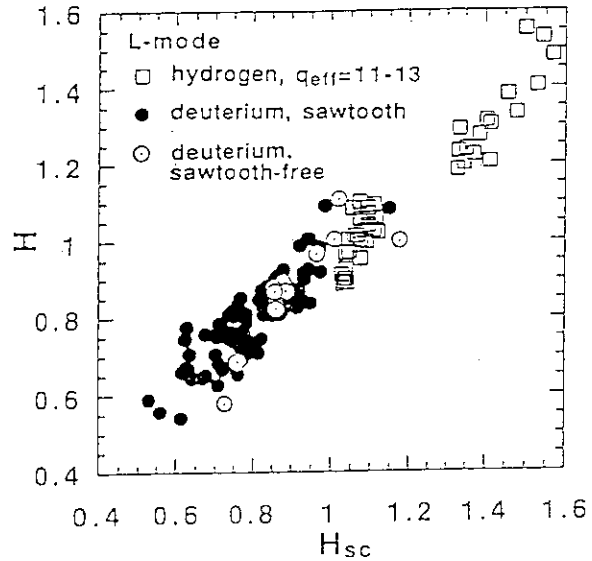


Fig.6: Experimentally obtained H -factor and H_{sc} given by eq.(1) for L-mode discharges shown in Fig.1.

3. Discussions

For the sawtooth effect, the dependence of τ_{sw} on plasma parameters should be discussed. In JT-60U, τ_{sw} increases with volume averaged electron temperature as

$\tau_{sw} \sim \langle T_e \rangle^{3/2} \sim$ resistive diffusion time (see Sec.8.5). Therefore it is reasonable to conclude a kind of positive feedback relation between τ_{sw} and τ_E : Increase in τ_{sw} improves τ_E , then the improved τ_E can cause further increase in τ_{sw} by raising T_e . Therefore, the causality of correlation between $H/l_i^{0.8}$ and τ_{sw} is not clear only from Fig.2. To clarify the causality, the q -dependence of the sawtooth effect was examined in Figs.3-5 which showed that the sawtooth effect becomes strong with decreasing q_{eff} . In turn, the relationship between τ_{sw} and $\langle T_e \rangle$ is almost unchanged over a wide range of q_{eff} (See Sec.8.5). Therefore the cause of change in confinement can be concluded to be the effects of τ_{sw} . Based simply on the full-reconnecting structure of sawteeth [3], the sawtooth activity flattens the central pressure profile inside r_{mix} . Then, the stored energy released from the central region ($q < 1$) should be a function of τ_{sw} and r_{inv} (or r_{mix}). When τ_{sw} is much shorter than the transport time scale in the central region, the central energy confinement τ_E^{center} is a strong function of τ_{sw} . As τ_{sw} becomes longer than the transport time scale, τ_E^{center} is governed by the transport properties and the effects of τ_{sw} becomes weak. This tendency was shown in Fig.2(a). This discussion is supported by the results of JT-60 pellet experiments [4] where τ_E was improved with increase in τ_{sw} similar to Figs.2 and 4. In that case, T_e at the center was decreased compared to gas fuelled discharges and the increase in τ_{sw} was not caused by increase in T_e . In order to clarify the causality further, the relationship between τ_E and τ_{sw} should be examined by active τ_{sw} control to decouple τ_{sw} from T_e with ICRF heating [5] or the combination of co- and counter-injection of NB [6]. To evaluate the role of sawteeth on confinement, ref.[7] reported that the effects of the heating profile is the key factor and the effects of sawtooth becomes smaller for broader heating profiles. The experiment treating the effects of heating profile will be performed in future.

Finally, the high l_i operation with active control of current density profile may be useful in future reactors to improve confinement as reported in this paper and to increase β -limit [8]. However it is important to clarify whether the high- l_i operation is consistent with significant fraction of bootstrap current in the steady state operation.

REFERENCES

- [1] KAMADA Y., et al., 'Effects of the safety factor and the internal inductance on MHD activities and energy confinement in JT-60U' to appear in Nucl. Fusion.
- [2] KAMADA, Y., et al., in Plasma Phys. Cont. Nucl. Fusion Research (Proc.14th Int. Conf., Wurzburg, 1992) IAEA-CN-56/A-7-13.
- [3] KADOMTSEV, B.B., Sov. J. Plasma Phys. **1** (1975) 389.
- [4] KAMADA, Y., et al., in Plasma Phys. Con. Nucl. Fusion Research (Proc.13th Int. Conf., Washington, 1990) Vol.I, IAEA, Vienna, (1991) p291; KAMADA, Y., et al., Nucl. Fusion **31** (1991) 23.
- [5] BHATNAGAR, et al., Plasma Phys. Controll. Fusion **31** (1989) 333.
- [6] FUSSMANN, G., et al., in Plasma Phys. Cont. Nucl. Fusion Research (Proc.12th Int. Conf., Nice, 1992) Vol.I, IAEA, Vienna, (1989) p145.
- [7] CHENG, Z., CALLEN, J.D., Nucl. Fusion **30** (1990) 219.
- [8] TAYLOR, T.S., et al., in Plasma Phys. Cont. Nucl. Fusion Research (Proc.13th Int. Conf., Washington, 1990) Vol. I, IAEA, Vienna, (1991) p.177.

1.11 Effects of ELM Activity on Energy Confinement

Y.Kamada, T.Takizuka, H.Ninomiya and M.Kikuchi

1. Introduction

As discussed in Sec.1.9, one of the main objectives of confinement and MHD research in JT-60U is to clarify the relationships among I_i , q_{eff} and τ_E including MHD instabilities. This section expands the study toward the H-mode in which the effects of ELMs on confinement is the main interest (the relationship (5) in Fig.1 in Sec.1.9). In particular, the effects of sawteeth and ELMs are important at low- q , because about 70% of the plasma volume is governed by these activities (r_{mix} for sawtooth reaches $\sim a/2$ at $q_{\text{eff}}=4$ (Sec.8.5) and the mixing of ELMs is observed at $r>0.8a$). The relationship between q_{eff} & I_i and ELMs was discussed in Sec.1.4. The brief summary of the ELM effects on confinement was reported in ref.[1].

2. The H-factor in H-mode and H_{sc}

In Fig.1, the H-factor for H-mode is plotted against H_{sc} , where H_{sc} is the H-factor of L-mode given by the new scaling law including the effects of I_i and sawteeth (see Sec.1.10). Open and closed circles correspond to the ELMy H-mode and the ELM-free H-mode, respectively. The data of ELM-free H-mode were taken at the end of the ELM-free period (just before the onset of ELMs). The H-factor for both ELM-free and ELMy discharges increases with H_{sc} and the maximum improvement from the L-mode level is about 2.1-2.2 for the ELM-free cases. In case of L-mode (Sec.1.10), the degradation in τ_E at low- q is explained by effects of I_i and sawteeth and a good agreement between the experimentally obtained H-factor and H_{sc} is observed. To clarify that the H_{sc} is also a good measure of confinement in H-mode, the following paragraphs discuss the dependences of H-factor in H-mode on q_{eff} , I_i and sawtooth period τ_{sw} .

Figure 2 shows the dependences of the H-factor and H/H_{sc} (H-factor/ H_{sc}) on q_{eff} for H-mode. For this figure the data were taken when I_p was kept constant (not the I_p -ramp experiment). In Fig.2(a) where the H-factor is plotted against q_{eff} , we can observe the strong degradation in the H-factor with decreasing q_{eff} at the low- q regime of $q_{\text{eff}}<4\sim 5$. This tendency

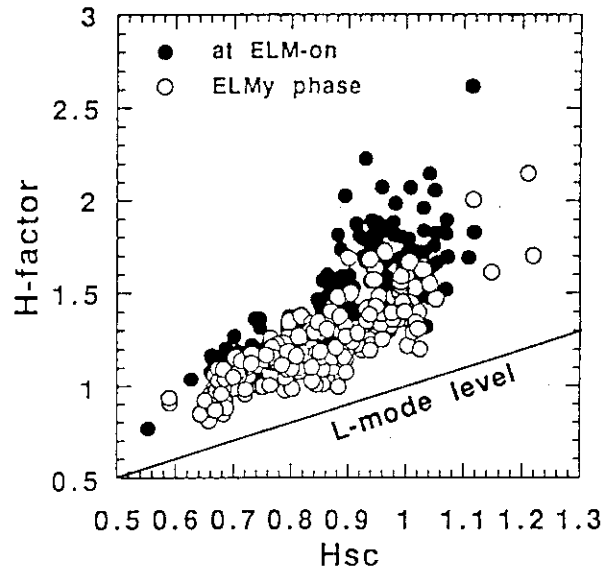


Fig.1: H-factor vs. H_{sc} for H-mode. Open and closed circles correspond to the ELMy H-mode and ELM-free H-mode, respectively.

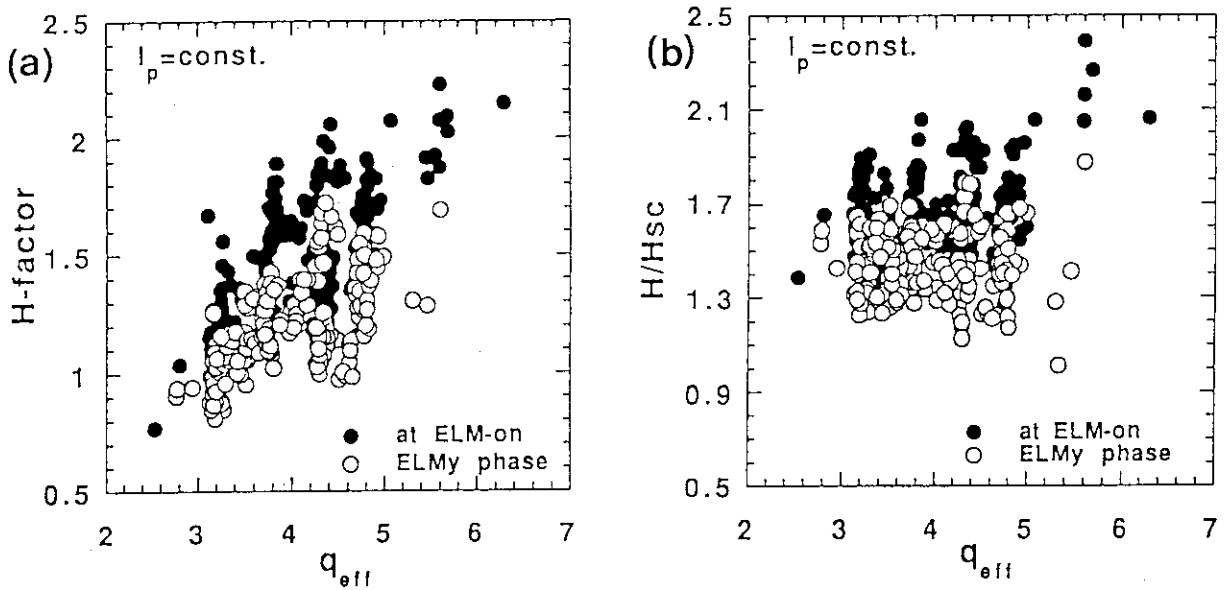


Fig.2: Dependences of the (a) H-factor and (b) H/H_{sc} (H-factor/ H_{sc}) on q_{eff} for H-mode.

is almost the same as that for L-mode shown in Sec.1.9. In Fig.2(b), the maxima of H/H_{sc} is nearly constant over a wide range of q_{eff} for both ELM-free and ELMy data. This result suggests that the degradation in the H-factor at low- q in H-mode is also explained by the effects of I_i and sawteeth.

Concerning the effects of I_i , the H-factor in H-mode tends to increase with I_i as shown in Fig.6 in Sec.1.9. In this section, we use I_i at the time when H-factor is calculated for the calculation of H_{sc} . However, we also discussed that the dependence is complicated in H-mode (Sec.1.9): i) In H-mode, I_i usually tends to decrease with increasing H-factor due to the edge pedestal of temperature and pressure. Therefore, the H-factor increases with decreasing I_i . ii) In turn, the H-factor increases with I_i of the target ohmic plasma, which suggests that the peaked $j(r)$ in the inner region causes improved confinement. iii) However, if I_i is increased significantly by I_p ramp down during the H-phase, the H-factor can be improved, which may be related to increase in magnetic shear in the edge region or poloidal field in the inner region. These observations mean that the dependence of τ_E on I_i in H-mode should be discussed by separating the current profile in the central region and the edge region. Therefore the effects of I_i is not so simple as observed in L-mode.

Concerning the effects of sawteeth on the H-factor, Fig.3 indicates the dependences of the H-factor and H/H_{sc} on τ_{sw} , where values of q_{eff} and I_i are restricted in a narrow range ($q_{eff}=3.5-4$, $I_i=1.0-1.2$) to keep the sawtooth inversion radius nearly constant (see Sec.8.5). Regions of plasma volume is $V_p=68-84m^3$. Closed circles correspond to the ELM-free data and open circles indicate the ELMy data with a fixed ELM frequency f_{ELM} ($1/f_{ELM}=0.011-0.013s$). (The dependence of confinement on f_{ELM} is discussed later.) In Fig.3(a), the H-factor increases with τ_{sw} at $\tau_{sw} < 1 \sim 2\tau_E$ and saturates at H-factor=1.7~1.8 for the ELM-free data and H-factor~1.4 for the ELMy data. In this figure, τ_E for the ELM-free and ELMy data are

0.2-0.5s and 0.15-0.3s, respectively. This tendency is almost similar to that observed in L-mode (Sec.1.1.10). In Fig.3(b), the dependence of H/H_{sc} on τ_{sw} is very weak compared to the dependence of the H-factor on τ_{sw} (Fig.3(a)). In particular H/H_{sc} for the ELMy data is nearly constant (~ 1.5). In case of ELM-free data, $H/H_{sc} = 1.5 \sim 2$. This remaining scatter does not depend on the plasma volume nor the l_i value of the target OH plasma. The possible dependence is that on the particle recycling. Fig.3(c) shows the relationship between H/H_{sc} and the intensity of $D\alpha^{div}/\bar{n}_e$ for the data used in Figs.3(a) and (b). In this plot, H/H_{sc} for the ELM-free data tends to increase with decreasing $D\alpha^{div}/\bar{n}_e$.

3. ELM Frequency and Confinement

As shown in Sec.1.4, the ELM-free phase is observed only when \bar{n}_e is lower than the threshold value \bar{n}_e^{th} , and \bar{n}_e^{th} increases with $B_t^2/(Rq_{eff}^2) \times l_i$ which is a measure parameter for pressure driven instabilities. The ELMy phase is observed when \bar{n}_e exceeds \bar{n}_e^{th} and f_{ELM} seems to increase with increasing P_{NB} and with decreasing $B_t^2/(Rq_{eff}^2) \times l_i$. Based on this knowledge, this section studies the effect of ELMs on confinement.

Figure 4(a) shows the dependence of H/H_{sc} on $1/f_{ELM}$ for ELMy H-mode. With decreasing f_{ELM} , H/H_{sc} increases and reaches the level of ELM-free plasmas ($H/H_{sc} \sim 1.4-2.4$). On the other hand, if H-factor itself is plotted against $1/f_{ELM}$ (Fig.4(b)), the effect of f_{ELM} becomes unclear. Therefore, H/H_{sc} is better for the measure of confinement status than the H-factor.

Figure 5 indicates the relationship between H/H_{sc} and \bar{n}_e for the data used in Fig.4 where no clear dependence of H/H_{sc} on \bar{n}_e is observed. The remaining scatter of the data cannot be explained by the effects of ELMs, sawteeth and l_i .

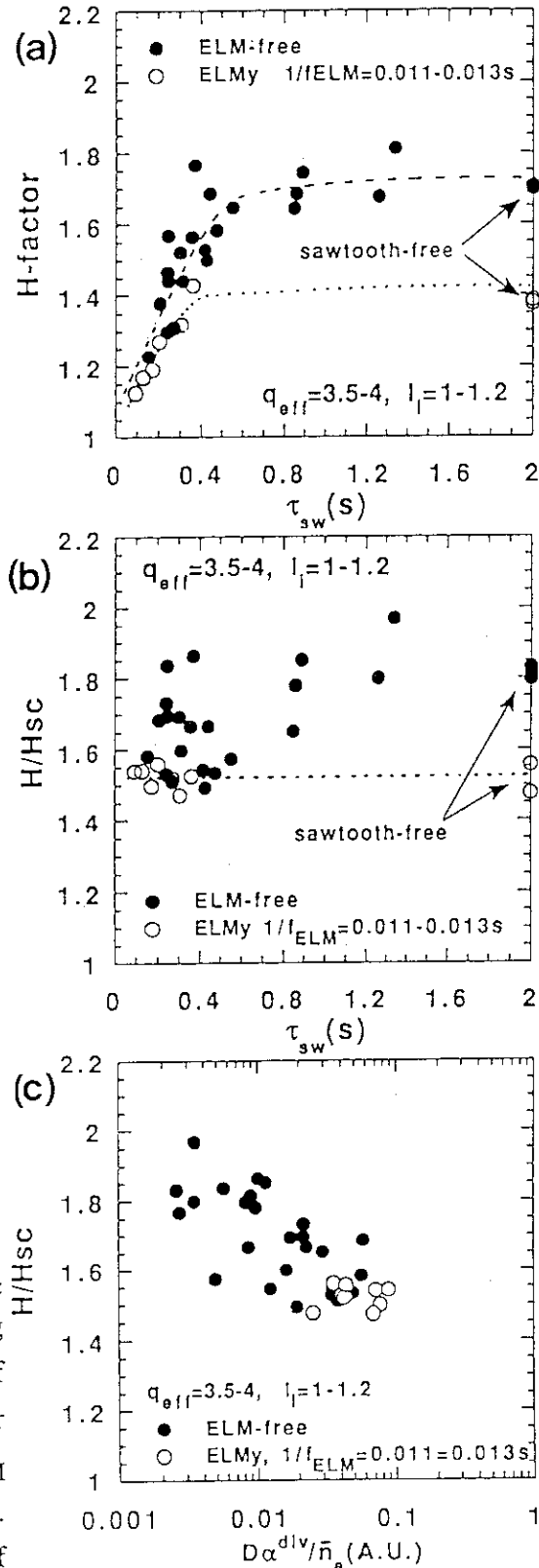


Fig.3: (a) H-factor vs. τ_{sw} , (b) H/H_{sc} vs. τ_{sw} , (c) H/H_{sc} vs. $D\alpha^{div}/\bar{n}_e$. ($q_{eff}=3.5-4$, $l_i=1.0-1.2$, $V_p=68-84m^3$).

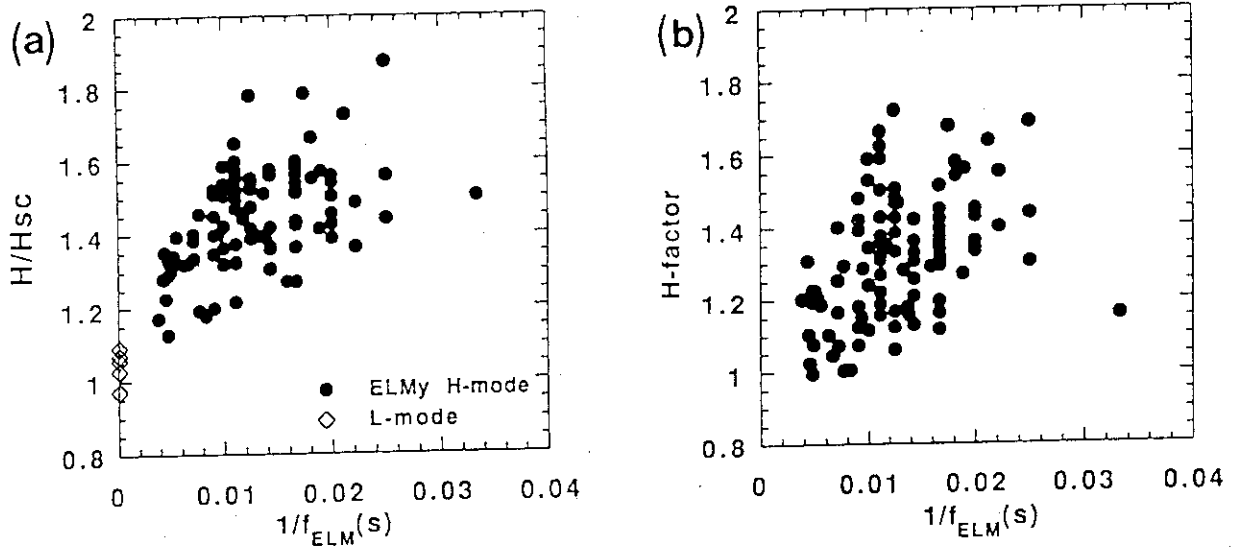


Fig.4: (a) Dependence of H/H_{sc} on the ELM period ($1/f_{ELM}$) for ELMy H-mode. (b) H-factor vs. $1/f_{ELM}$.

Experimentally, as shown in Fig.6, H/H_{sc} increases with decreasing $D_{\alpha}^{div}/\bar{n}_e$ for a fixed $1/f_{ELM}$ ($=0.01-0.013s$).

We found that confinement in H-mode is well described by H/H_{sc} and $1/f_{ELM}$. However, there remain the following problems: i) The complicated dependence of H-factor on I_i was observed (Sec.1.9). ii) The role of recycling is not clear. iii) Effects of density, temperature and pressure profiles has not been analyzed. iv) Thermal confinement has not been analyzed. v) Effects of ripple loss has not been included. In particular, the depth of ELMy region (the transport barrier) from the separatrix should be systematically treated. In JT-60U, we observe two stages of H-mode: The first type is the so-called weak H-mode with small drop in D_{α} signal and the second type is accompanied by a clear large D_{α} -drop. It is important to clarify the relationships among the depth of the transport barrier, particle recycling and the type of H-transition.

REFERENCES

- [1] KAMADA, Y., et al., in Plasma Phys. Cont. Nucl. Fusion Research (Proc.14th Int. Conf., Wurzburg, 1992) IAEA-CN-56/A-7-13.

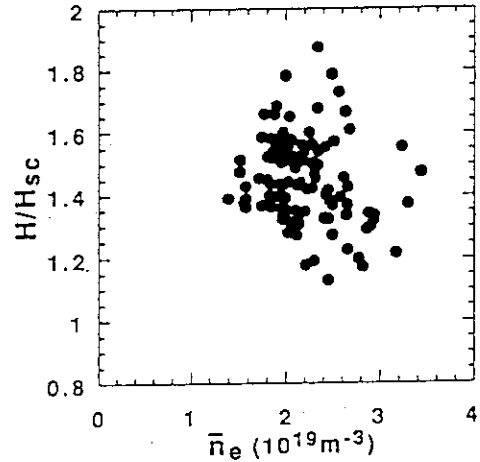


Fig.5: indicates the relationship between H/H_{sc} vs. \bar{n}_e for the data set used in Fig.4.

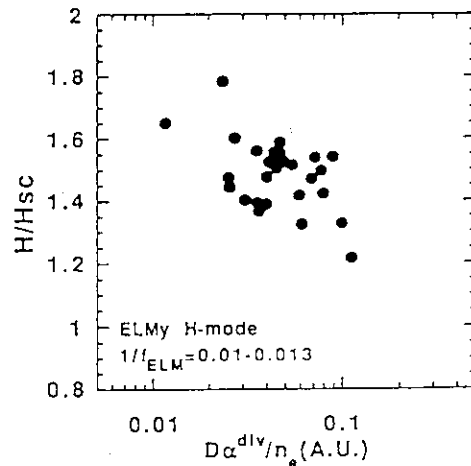


Fig.6: H/H_{sc} vs. $D_{\alpha}^{div}/\bar{n}_e$ for ELMy H-mode with $1/f_{ELM}=0.01-0.013s$.

1.12 Relation between Fast-Ion Loss and H-Mode Performance

A.A.E. van Blokland and M. Kikuchi

1. Introduction

The large toroidal magnetic field ripple and the large power of nearly perpendicular injected neutral particles in JT-60U enable the investigation of the impact of fast-ion loss on the H-mode characteristics. Two plasma configurations with a volume of 70 and 80 m³, respectively, and thus different field ripple are compared with respect to their global confinement characteristics and fast-ion loss due to the magnetic field ripple.

2. Plasma Configurations and Analysis

Figure 1 shows both plasma configurations which were operated at a plasma current of 3 MA. The smaller plasma (see Fig. 1(a)) had a volume $V_p=70$ m³, $B_t=4.2$ T and a $q_{eff}=3.7$; the larger plasma (see Fig. 1(b)) was operated at a volume $V_p=80$ m³, $B_t=4.1$ T and a $q_{eff}=4.2$. For both plasma configurations, the density range was $\langle n_e \rangle = 1.4-2.6 \times 10^{19}$ m⁻³. The maximum ripple for the smaller plasma was about 1%, while it was 2% for the larger plasma. Both parallel and perpendicular neutral beams were operated with injection powers up to 7 and 22 MW, respectively. The shine-through values of the beams were measured by thermocouples and IRTVs.

The fast-ion loss was calculated by the Orbit Following Monte-Carlo simulation code (OFMC) which has been shown to be in good agreement with experimental ripple-loss data [1]. It should, however, be noted that the results from the OFMC code only simulate the power deposition on the first wall and that they do not predict the physical origin of the power loss, since particles that are banana-trapped can be lost in the lower ripple and thus increasing the calculated value for the ripple-trapped loss. The electron temperature and density profiles were measured by an ECE polychromator and a two-channel interferometer, respectively. Ion temperature profiles were obtained from Charge-Exchange Recombination Spectroscopy. Temperature profiles for both configurations are shown in Fig. 2.

3. Experimental and OFMC Results

In Fig. 3, the experimental diamagnetic stored energy is compared with the ITER L-mode scaling as function of the absorbed power. Here, the absorbed power is not only corrected for the shine-through but also for the fast-ion loss from ripple-trapped and banana-drift particles as calculated by the OFMC code. This additional correction will increase the H-factor since the net absorbed power will become lower. A clear difference in global

confinement characteristics can be seen for both configurations. An H-mode was obtained for the smaller plasma, whereas only L-mode behavior was observed for the larger plasma. Only elmy-free plasmas were evaluated in the smaller plasma case. No dependence was observed of the H-factor on the target-density of the plasma.

Figure 4 shows the loss of fast particles expressed in fraction of the injected neutral beam power as a function of the line averaged electron density. The total loss is about 10% higher for the larger plasma in comparison with the smaller case for the density range considered. This difference can be ascribed to the fast-ion loss due to the field ripple. The fast-ion loss is slightly increasing with the density. Although one should be careful to interpret the OFMC results in terms of physical origin of the ripple-loss, it is clear that the banana-drift-loss is dominant in the larger plasma case. The relation between the H-factor and the total fast-ion loss is shown in Fig. 5. For lower values of the fast-ion loss (the smaller plasma), higher H-factors are obtained, whereas for losses higher than 20% (the larger plasma) H-factors were found to be below 1.6.

4. Conclusions

There seems to be a relation between the fast-ion loss and the H-mode performance at JT-60U. It is, however, not clear whether the loss of fast particles is directly responsible for the quality of the global confinement characteristics by generating radial electric fields or that other loss processes, like orbit loss of thermalised ions, are dominant. H-mode experiments with a maximum ripple smaller than 1% can give more evidence for the possible direct impact of fast-ion loss on the H-mode behavior in JT-60U.

The analysis can be improved by separating the total stored energy into thermalised and fast ion- components, since the measured diamagnetic stored energy can be affected by fast ions in the plasma [2]. Furthermore, including additional neoclassical particle transport induced by the toroidal field ripple [3] can give a more complete understanding of the H-mode behavior in JT-60U.

References

- [1] K. TOBITA, K. TANI, Y. NEYATANI, et al., 19th Conf. on Contrl. Fusion and Plasma Phys., Vol. I, pp.171 (1992).
- [2] T.T.C. JONES, paper 1.13 of this Experimental Review.
- [3] K.C. SHAIN, S.P. HIRSCHMANN, and J.D. CALLEN, Phys. Fluids **29**, 521 (1986).

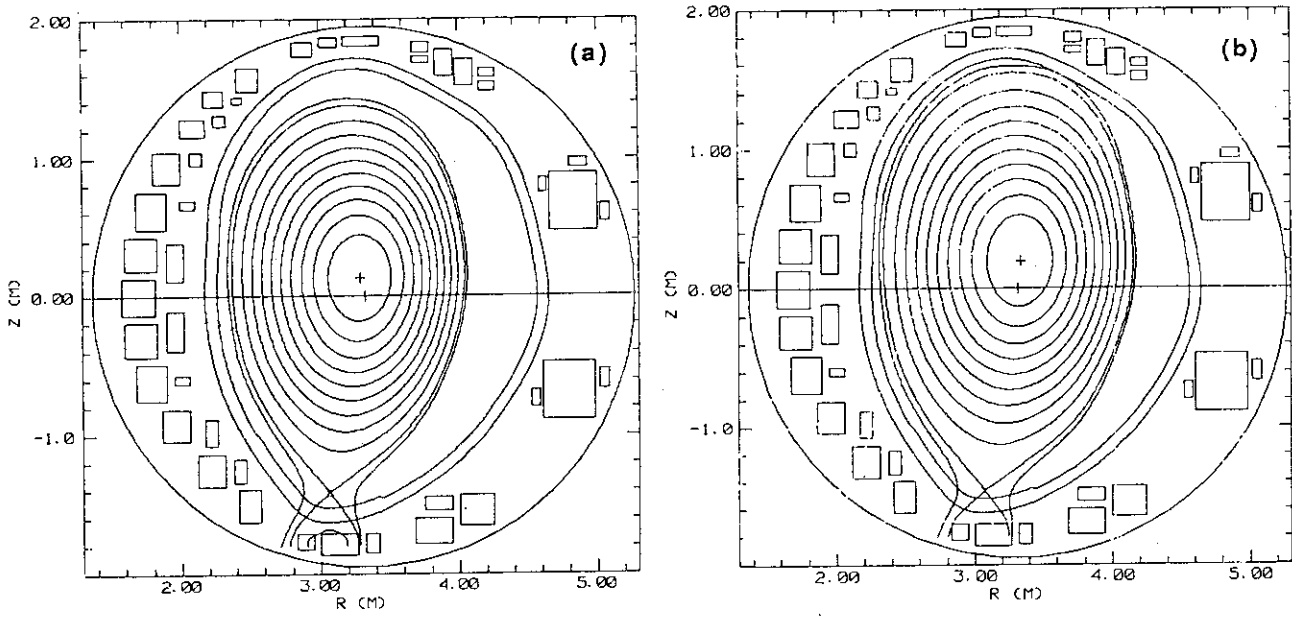


Fig. 1 Examples of the two plasma configurations used for the experiments:

- a) Shot E16149, $t=6.92$ s, $I_p=3$ MA, $B_t=4.2$ T, $q_{eff}=3.7$, $\langle n_e \rangle = 2.3 \times 10^{19}$, $V_p=70$ m³,
 $P_{nbi}=25.0$ MW, $P_{perp}=19.3$ MW, $P_{par}=5.7$ MW;
 b) Shot E16147, $t=7.50$ s, $I_p=3$ MA, $B_t=4.1$ T, $q_{eff}=4.2$, $\langle n_e \rangle = 2.4 \times 10^{19}$, $V_p=80$ m³,
 $P_{nbi}=24.7$ MW, $P_{perp}=19.1$ MW, $P_{par}=5.6$ MW.

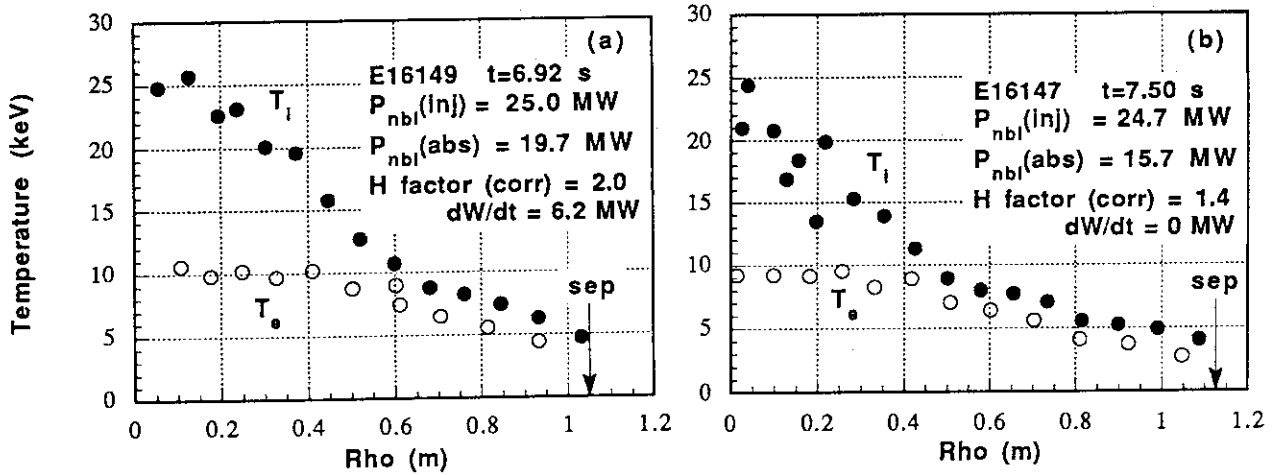


Fig. 2 Experimental plasma profiles for the two configurations shown in Figs 1a and 1b.

$P_{nbi(inj)}$ = NBI power injected into the plasma, $P_{nbi(abs)}$ = NBI power injected with shinethrough, ripple-trapped and banana-drift losses subtracted, sep = position of the separatrix.

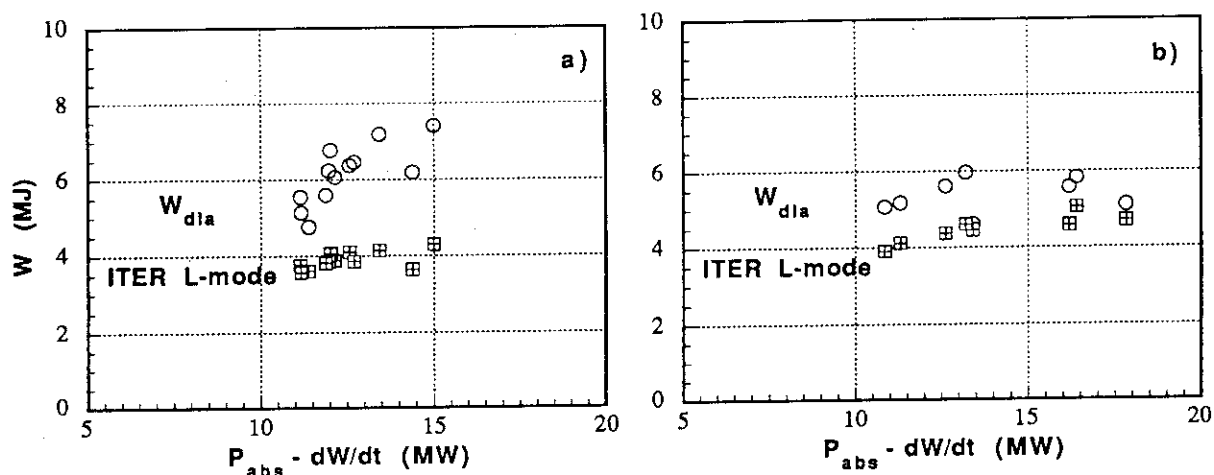


Fig. 3 Comparison between the experimental diamagnetic stored energy and the ITER L-mode scaling for both plasma configurations; a) $V_p = 70 \text{ m}^3$, and b) $V_p = 80 \text{ m}^3$.

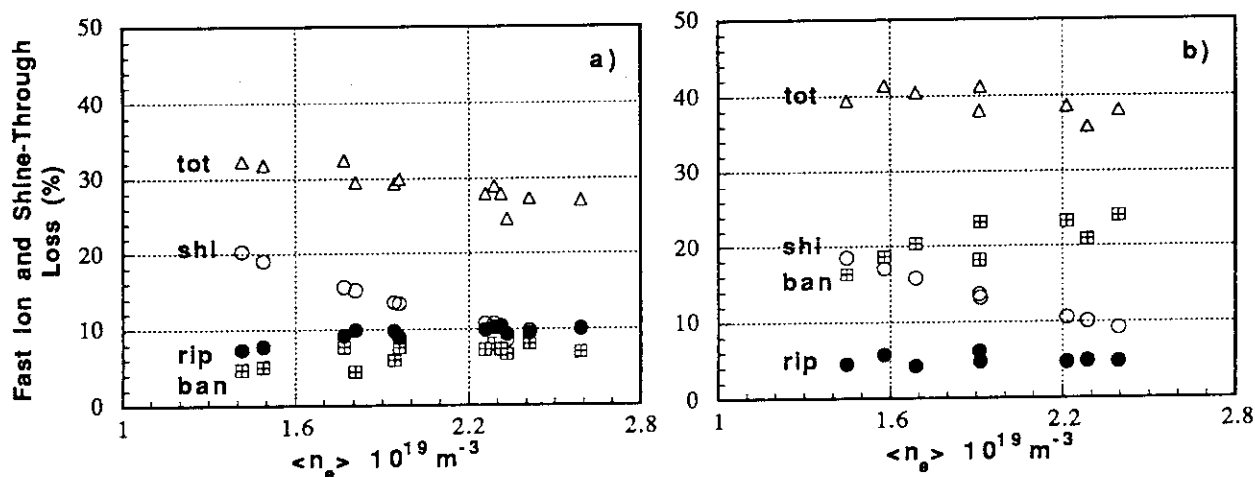


Fig. 4 Fast ion- and shine-through-loss in percentage of the injected neutral beam power; shi = shine-through, rip = ripple-trapped loss, ban = banana-drift loss, tot = shi+rip+ban; a) $V_p = 70 \text{ m}^3$, and b) $V_p = 80 \text{ m}^3$.

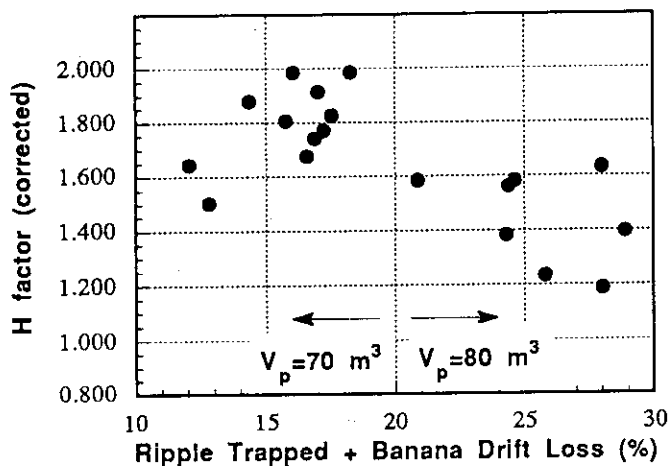


Fig. 5 Corrected H-factor as a function of the total fast-ion loss due to the magnetic field ripple for both plasma configurations.

1.13 Comparison of H-mode confinement with Tangential and Perpendicular NBI

T T C Jones

In this report it is attempted to identify any deleterious effect on H-mode global confinement due to significant ($\approx 25\%$) ripple+first orbit losses which may occur for near perpendicular NBI in the standard divertor plasma configuration shown in Fig.1, e.g. under the effect of the radial electric field which is set up.

1. Method of Tangential versus Perpendicular NBI Assessment in H-mode

JT60-U H-mode is usually characterised by its H-factor, defined as the ratio of the diamagnetic global energy confinement time compared to the ITER89-P power law L-mode scaling. In this report nominal corrections for shinethrough and ripple + first-orbit losses are applied, and the H-factors are recalculated in terms of the absorbed power. The ripple+first orbit losses are taken from an Orbit Following Monte Carlo (OFMC) simulation of a particular discharge (E15489, Table I) similar to those of the present experiments [1] and the shinethrough is estimated from the line averaged density using an empirical formula. Ripple + first-orbit losses are also density dependent as shown by OFMC calculations [2] performed for a series of 3MA discharges with approximately similar configuration and q value as the present experiments. The same density dependence of ripple + first-orbit loss is assumed herein, which largely offsets the $1/n_e$ dependence of the shinethrough fraction. Only a weak density dependence of the combined loss fraction η_{loss} remains, giving $48\% > \eta_{\text{loss}} > 42\%$ for the present density range. The corrected H-factor data are examined for any **residual dependence** on the proportion of perpendicular NBI, and also on other parameters.

Table 1 OFMC calculation of ripple-well trapping and banana first-orbit+stochastic drift loss fractions for discharge E15489 ($I_p=1.7\text{MA}$, $B_T=2.5\text{T}$, $n_{e1}=1.6 \cdot 10^{19}\text{m}^{-3}$)

Case	Rip.Trap	Banana	Total
Perp.Balance	7.8%	19.1%	26.9%
Perp.Co.	6.6%	17.8%	24.4%
Tan.Balance	1.8%	8.6%	10.4%
Tan.Co.	1.9%	2.6%	4.5%

Reliable operation of the NBI system was limited to $\approx 85\text{-}90\text{kV}$, giving $P_{\text{max}}(\text{tan}) \approx 8\text{MW}$ and $P_{\text{max}}(\text{perp}) \approx 20\text{MW}$. The direct comparison of perpendicular versus tangential NBI **above the H-mode power threshold** was therefore restricted to low toroidal field and plasma current. At $1.5\text{MA}/2\text{T}$ the direct comparison was just possible. A few series of higher power discharges with different proportions of perpendicular NBI at constant total power are also analysed. Time-traces of key plasma parameters for a typical H-mode in the

configuration of Fig.1 are shown in Fig.2(a) (shot E015852, 1.5MA/2.5T). Fig.2(b) gives the T_i radial profiles which show the pedestal characteristic of an edge transport barrier.

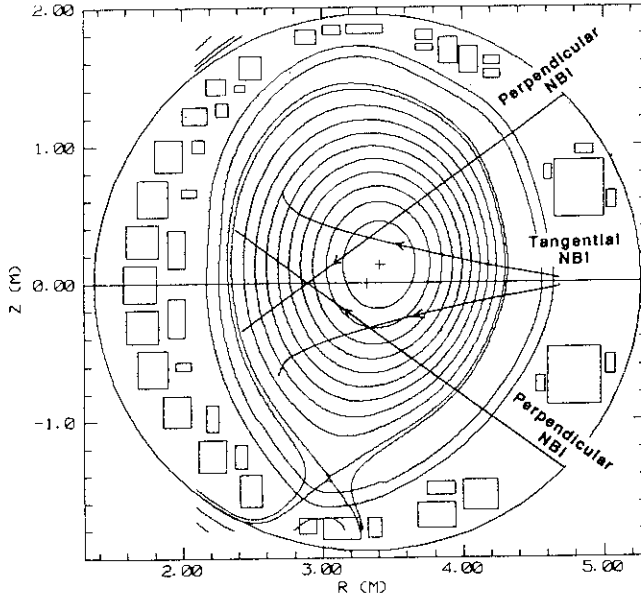


Fig.1 Standard equilibrium configuration for divertor discharges showing projected NBI beam axes.

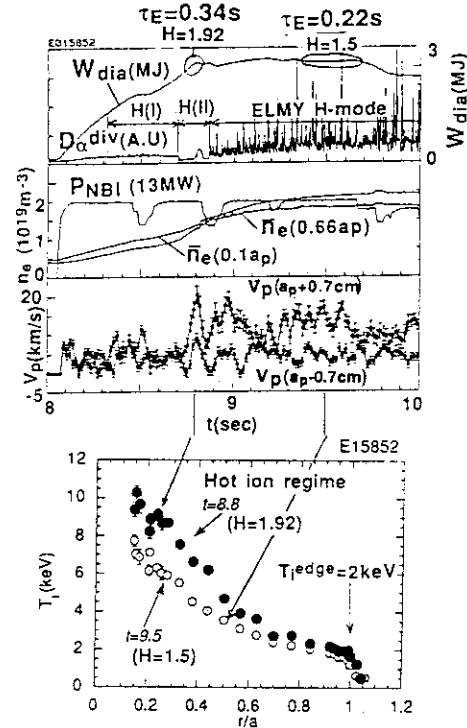


Fig.2 (a) Time-traces for typical H-mode discharge in the configuration of Fig.1 (shot E015852, $I_p=1.5$ MA, $B_t=2.5$ T). (b) Ion temperature radial profiles.

2. Direct Comparison of H-modes with Perpendicular or Tangential NBI only

Fig.3a gives the plot of H-factor versus total NBI power, for 1.5MA/2T discharges with perpendicular NBI fraction $P_{\text{perp}}/P_{\text{nbi}} = 0$ or 1 (data corrected for shinethrough only). There is considerable variation in the H-factors, suggestive of marginal absorbed power for exceeding the H-mode threshold. However, when the estimated ripple + first-orbit corrections are additionally applied (Fig.3b), a clear threshold-like feature in the data is not recovered and, subject to the uncertainty of the beam loss corrections, the H-factor enhancement for perpendicular NBI even exceeds the tangential data. This result indicates that, even if there is a deleterious indirect influence on H-mode confinement by beam-ion losses with perpendicular NBI, there must be an additional effect responsible for increasing the measured diamagnetic stored energy compared with purely tangential NBI. Such an additional effect would have to dominate at least at moderate perpendicular NBI power. A candidate effect consistent with this observation is the sensitivity of the diamagnetic measurement to the perpendicular fast ion energy component, which is larger in the case of near-perpendicular NBI. A further observation, consistent with this explanation, is that the variation of perpendicular NBI H-factors correlates well with the absorbed power per unit plasma density, while the correlation for tangential NBI is not established (Fig.3c). The

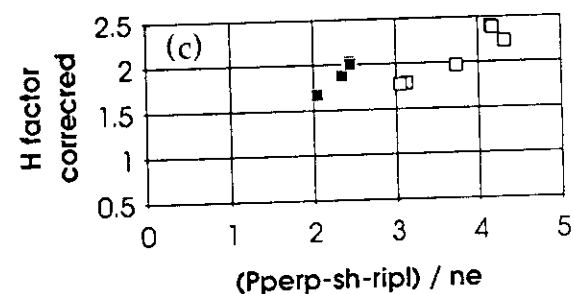
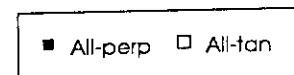
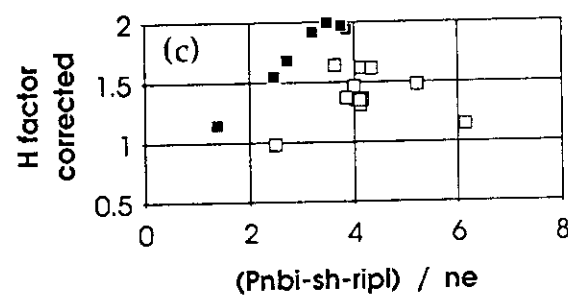
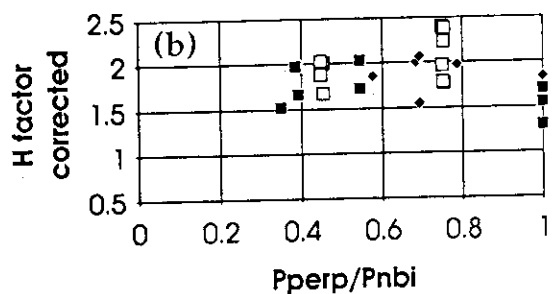
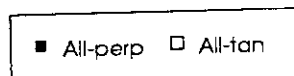
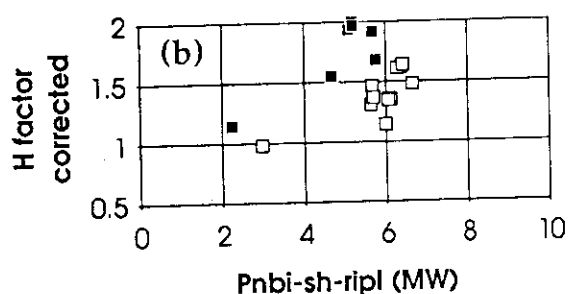
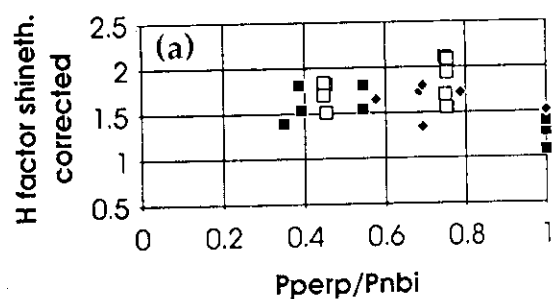
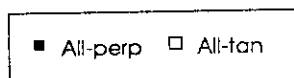
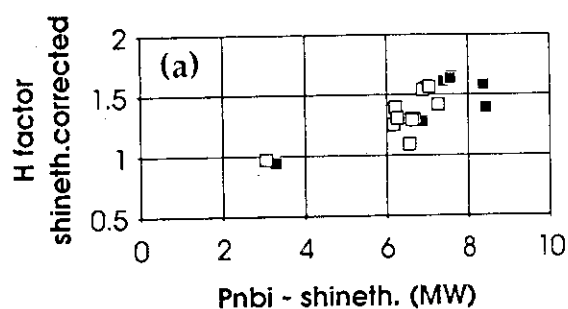


Fig.3 Residual H-factor dependences. H-factor (corrected for shinethrough only) versus total NBI power minus shinethrough (a). H-factor (corrected for shinethrough+ripple and first-orbit losses) versus absorbed NBI power (b) and versus absorbed NBI power per unit plasma density (10^{-19}MWm^3) (c). Data are from 1.5MA/2T discharges with purely perpendicular or tangential NBI.

Fig.4 Dependence of (a) H-factor (corrected for shinethrough only), (b) H-factor (corrected for shinethrough+ripple and first-orbit losses) on $P_{\text{perp}}/P_{\text{nbi}}$ for sets of discharges at constant total NBI power P_{nbi} . The legends give the plasma current and toroidal field values and also P_{nbi} in MW. (c) residual dependence of corrected H-factor on absorbed perpendicular NBI power per unit plasma density (10^{-19}MWm^3) for the {1.5MA/2.5T, $P_{\text{nbi}}=13 \text{MW}$ } dataset.

correlation for perpendicular NBI in Fig.3c is not an artefact of the weak $1/n_e$ dependence of the combined beam loss corrections because the same trend is also observed (to a slightly lesser degree) if the uncorrected data are plotted.

3. Effect of Varying Mix of Perp./Tangential NBI at Constant Total Power

Three groups of data are identified, with total NBI power well above the H-mode power threshold. The discharge parameters are defined in Figs.4. For NBI powers and H-factors corrected only for shinethrough loss, Fig.4a shows that there is no clear dependence upon the perpendicular NBI fraction $P_{\text{perp}}/P_{\text{nbi}}$ for values up to ≈ 0.75 , although the performance with 100% perpendicular NBI is substantially worse. When the ripple + first-orbit corrections are applied there is some indication of a weakly increasing trend up to $P_{\text{perp}}/P_{\text{nbi}} \approx 0.75$, mainly apparent in the $\{1.5\text{MA}/2.5\text{T}, P_{\text{nbi}}=13\text{MW}\}$ dataset, while the 100% perpendicular NBI H-factors are still low. A more obvious feature in Figs.4a and b is the variation within the $\{1.5\text{MA}/2.5\text{T}, P_{\text{nbi}}=13\text{MW}\}$ dataset at each value of P_{perp} . This variation is again associated with P_{perp}/n_e (Fig.4c), consistent with the role of fast perpendicular ions. Conversely, a measure of relative thermal plasma confinement enhancement given by $n_e(0)T_i(0)/W_{\text{ITER89-P}}$ does not exhibit a positive correlation with P_{perp}/n_e . Fig.4c also indicates that the dependence on $1/n_e$ is stronger than the dependence of P_{perp} , consistent with a competing deleterious effect at high P_{perp} which eventually dominates for 100% perpendicular NBI (Fig.4b).

4. Conclusions

For similar total injected power levels, discharges with a large proportion of perpendicular NBI are adversely affected by substantial shinethrough and ripple+first-orbit losses. When corrections for these power losses are taken into account, there are still residual dependences in the H-factors which suggest the existence of additional effects. An enhancement to the corrected H-factor at moderate values of P_{perp} is attributable to the fast-ion contribution to the diamagnetic energy measurement, whilst there is an indication of an overall degradation in H-factor at high values of P_{perp} . These tentative conclusions, based only on global data, will have to be confirmed by further systematic tangential/perpendicular NBI comparison experiments together with detailed transport analysis including separation of the total stored energy into thermalised plasma and perpendicular and parallel fast-ion components.

References

- [1] STORK,D.,TANI,K. and KIKUCHI,M.,private communication.
- [2] VAN BLOKLAND,A.,KIKUCHI,M., section 1.12 in this review.

1.14 Nondimensional Scaling for JT-60U L-mode Plasmas

T. Takizuka, H. Shirai, M. Sato, Y. Koide, Y. Kamada, M. Kikuchi

1. Introduction

Recently in JET [1] and TFTR [2], it has been found that the thermal energy transport of L-mode plasmas is Bohm-like one; the heat diffusivity χ is approximately given by $\chi = (T/eB) \rho_*^\alpha F(\beta, \nu_*, q, \epsilon, \dots)$ with $\alpha \approx 0$, where normalized Larmor radius ρ_* , plasma beta β , collision frequency normalized by bounce frequency ν_* , safety factor q , inverse aspect ratio ϵ , etc. are nondimensional variables. Such finding can make the confinement scaling accurate for the design of future reactors. However, uncertainties of profile parameters etc. make it difficult to exclude gyroBohm-like transport. In order to clarify the dependence of χ on ρ_* as well as on β and ν_* , B_t scan experiment was carried out in JT-60U L-mode plasmas.

2. Experimental Condition and Analysis Method

Experimental parameters are as follows. The major radius R was about 3.2m, minor radius $a \approx 0.85$ m, elongation $\kappa \approx 1.65$, and plasma volume $V \approx 70$ m³. Deuterium beam was injected nearly perpendicularly into deuterium plasma. Beam input power was 5-17 MW, which was much larger than the joule heating power. Ripple loss fraction of beam energy was assumed 10-20% and total loss fraction with shinethrough loss became about 30% [3]. Toroidal magnetic field was changed as $B_t = 4.2$ T, 3.2T and 2.5T. Two series of operations of $q_{\text{eff}} \approx 4.5$ ($B_t/I_p = 4.2$ T/2.5MA) and $q_{\text{eff}} \approx 6.5$ ($B_t/I_p = 4.2$ T/1.8MA) were performed. We could not keep the q profile constant. The internal inductance l_i decreased with the increase of the absorption power P_{abs} as shown in Fig.1, where l_i^5 is roughly proportional to P_{abs}^{-1} . We could not control the value of line averaged electron density n_{e1} . The range of n_{e1} was not wide (1.6 - 3.1×10^{19} m⁻³) and the range of $n_{e1}q_{\text{eff}}$ was much narrow (10 - 14×10^{19} m⁻³). As a result, there existed a strong relation between ρ_p and $q_{\text{eff}}\beta_p$ as shown in Fig.2, where the normalized poloidal Larmor radius is defined as $\rho_p \propto T_*^{0.5} / l_i I_p$ and the normalized poloidal beta $\beta_p \propto n_{e1} T_* / (l_i I_p)^2$. These correlations, $l_i^5 \propto P_{\text{abs}}^{-1}$ and $\rho_p^2 \propto q_{\text{eff}}\beta_p$, causes the uncertainty of the confinement scaling as described later.

In the present paper, the thermal component of the stored energy W_{th} is calculated by the following simple scheme. We assume that the total stored energy is measured diamagnetically with small error, i.e., $W_{\text{dia}} = W_{\text{th}} + W_f$. Effective averaged temperature T_* is defined as $W_{\text{th}} = 3C n_{e1} T_* V$, where an artificial constant C is set 1.4 for the present database. The stored energy of fast ions W_f is determined by the simple classical formula $W_f = W_f(T_*)$. These nonlinear equations are solved iteratively. Calculated fast ion component becomes 20-70% of the total. Electron temperature was diagnosed by ECE measurement. The effective averaged temperature T_* is compared with the ECE measured temperature near $r=2a/3$ T_e^{ECE} .

They agree well with each other as shown in Fig.3, although there is systematic discrepancy between for $q_{\text{eff}} \approx 4.5$ and for $q_{\text{eff}} \approx 6.5$.

3. Nondimensional Scaling

We find that the effective averaged temperature T_* coincides with the measured electron temperature around the important region for L-mode confinement $r \approx 2a/3$. We then assume that the thermal energy confinement time $\tau_{\text{th}} = W_{\text{th}}/P_{\text{abs}}$ is inversely proportional to $\chi(T_*)$. The poloidal Bohm diffusion coefficient $\chi_{\text{Bp}} = T_*/eB_p$ is chosen for the base of the thermal energy transport, where poloidal magnetic field B_p is considered to be proportional to $I_i I_p$. We are standing at a viewpoint that confinement improvement by larger I_i is due to larger B_p in the confinement region.

The nondimensional product $\tau_{\text{th}} \chi_{\text{Bp}}$ is found a weak function of $\rho_{p*} (\propto T_*^{0.5}/I_i I_p)$ or of $q_{\text{eff}} \beta_p (\propto q_{\text{eff}} n_{\text{el}} T_*/I_i^2 I_p^2)$. The dependence of $\tau_{\text{th}} \chi_{\text{Bp}}$ on v_* cannot be observed. Dependences on q_{eff} and I_i are also negligibly weak. Therefore, we describe followings

$$\tau_{\text{th}} \chi_{\text{Bp}} \rho_{p*}^{(1-h)\alpha_p} (q_{\text{eff}} \beta_p)^{h\alpha_p/2} = C_0, \quad 0 \leq h \leq 1, \quad (1a)$$

$$\tau_{\text{th}}^{\text{fit}} = C (I_i I_p)^{\alpha_1} (n_{\text{el}}/P_{\text{abs}})^{\alpha_2} (1/n_{\text{el}} q_{\text{eff}})^{\alpha_3} \quad (1b)$$

with $\alpha_1 = 2(1+\alpha_p)/(4+\alpha_p)$, $\alpha_2 = (2+\alpha_p)/(4+\alpha_p)$ and $\alpha_3 = h\alpha_p/(4+\alpha_p)$. Figure 4 shows the ratio $F = \tau_{\text{th}}^{\text{exp}} / \tau_{\text{th}}^{\text{fit}}$ as a function of ρ_p for $\alpha_p = 0$ (black circle), 0.5 (open circle) and 1 (black square). One can clearly see the ρ_p dependence of F for $\alpha_p = 0$ and 1. The standard deviation σ of F defined by $\sigma^2 = \sum (F-1)^2 / N$ (N is the total number of data points; $N=17$) is shown in Fig.5 as a function of α_p . The value of σ becomes minimum near $\alpha_p = 0.5$, which is extremely small, $\sigma = 1.7\%$. From Figs.4 and 5, we can set α_p equal to 0.5 for the best fitting of experimental data, and estimate the allowable limit of $0.25 < \alpha_p < 0.65$. A nondimensional scaling for the thermal energy confinement in the present JT-60U L-mode plasmas is given by

$$\tau_{\text{th}}^{\text{fit}} = C (I_i I_p)^{6/9} (n_{\text{el}}/P_{\text{abs}})^{5/9} (1/n_{\text{el}} q_{\text{eff}})^{h/9}, \quad 0 \leq h \leq 1. \quad (2)$$

This scaling reproduces experimental data very well as shown in Fig.6.

As was mentioned in section 2, there is another strong correlation of $I_i^5 \propto P_{\text{abs}}^{-1}$. We also take this correlation into consideration and express the nondimensional scaling as follows;

$$\tau_{\text{th}} \chi_{\text{Bohm}} \rho_{p*}^{\alpha_p} \beta^{\alpha_\beta} v_*^{\alpha_v} = C_0, \quad (3a)$$

$$\tau_{\text{th}}^{\text{fit}} = C (I_i I_p)^{6/9} (n_{\text{el}}/P_{\text{abs}})^{5/9} (1/n_{\text{el}} q_{\text{eff}})^x (1/I_i^5 P_{\text{abs}})^y, \quad (3b)$$

where the relations between $(\alpha_p, \alpha_\beta, \alpha_v)$ and (x, y) are $6\alpha_p = 3 - 27x - (16 + 36x)g(y)$ and $\alpha_p/2 + \alpha_\beta - 1/4 = \alpha_v = g(y) = 27y / (16 - 36y)$. The limits of x and y are studied by checking the variation of σ of $F = \tau_{\text{th}}^{\text{exp}} / \tau_{\text{th}}^{\text{fit}}$ against values of x and y as shown in Figs.7

(a) and (b). If we assume that the value of σ below $1.4 \sigma_{\min}$ is allowed for the fitting, then we estimate $x = 0.07 \pm 0.19$ and $y = -0.01 \pm 0.08$. We find from the limit of y , that the effect of collisions on the heat diffusivity is not strong; $-0.19 < \alpha_v < 0.14$. We cannot conclude whether the energy transport is Bohm-like ($\alpha_p = 0$) or gyroBohm-like ($\alpha_p = 1$), but we surmise plausibly α_p taking the value between 0 and 0.6.

4. Conclusion and Discussion

We analyze the data of B_t scan experiment in JT-60U L-mode plasmas. We obtain nondimensional scaling, eq.(2), which reproduces experimental data very well ($\sigma=1.7\%$). The heat diffusivity is supposed of the form $\chi_{Bp} \rho_p^{(1-h)/2} (q_{eff}\beta_p)^{h/4}$. The effect of Larmor radius is rather weak compared with gyroBohm type, and collisional effect is very weak.

The result of the present analysis has to be compared with the transport analysis of the profile data. There existed the correlations among plasma parameters, which cause the uncertainty of the scaling. Analysis of other data set is the future work.

References

- [1] The JET Team (presented by J.G. Cordey), 14th Int. Conf. on Plasma Physics and Controlled Nuclear Fusion Research, Wurzburg, 1992, IAEA-CN-56/D-3-4.
- [2] SCOTT, S.D., et al., 14th Int. Conf. on Plasma Physics and Controlled Nuclear Fusion Research, Wurzburg, 1992, IAEA-CN-56/G-3-3.
- [3] VAN BLOKLAND, A.A.E., KIKUCHI, M., in this review, 1.12.

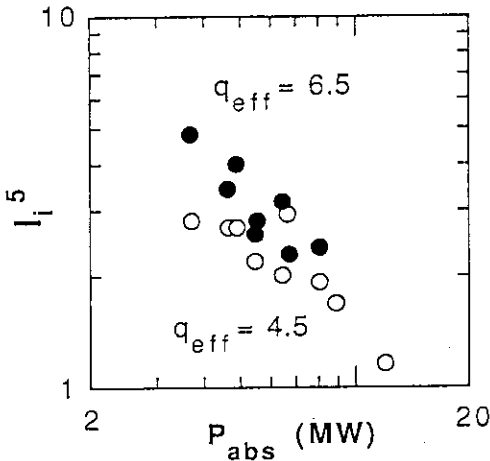


Fig.1 Relation between internal inductance l_i and absorption power P_{abs} for $q_{eff} = 4.5$ (open circle) and $= 6.5$ (black circle). l_i^5 is roughly proportional to P_{abs}^{-1} .

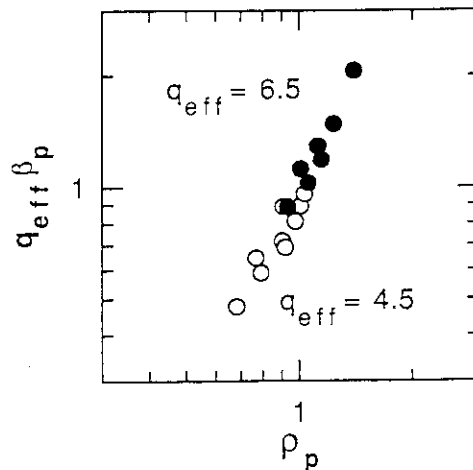


Fig.2 Relation between ρ_p and $q_{eff}\beta_p$. Normalized poloidal Larmor radius is defined as $\rho_p \propto T_*^{0.5} / l_i I_p$ and normalized poloidal beta $\beta_p \propto n_e T_* / (l_i I_p)^2$.

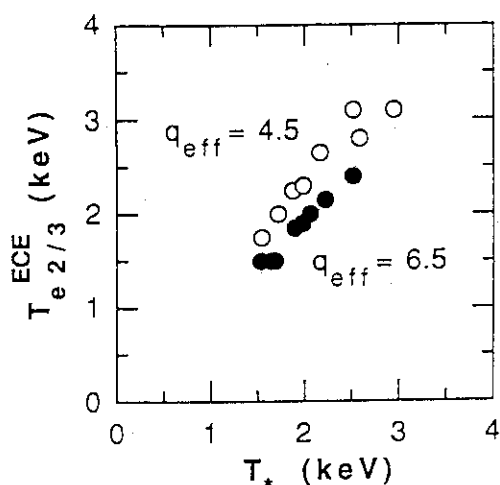


Fig.3 ECE measured temperature T_e^{ECE} near $r=2a/3$ vs effective averaged temperature T_* ($= W_{th}/3C_{ne}V$).

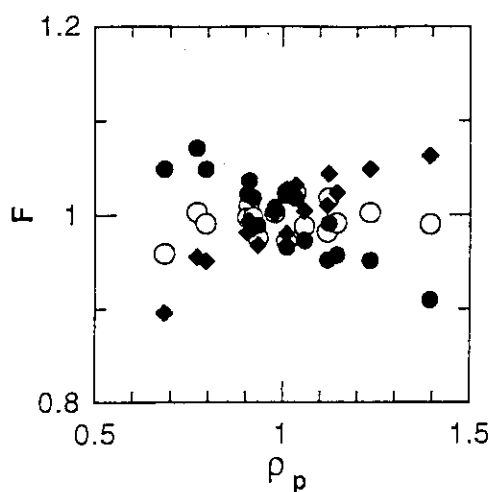


Fig.4 Dependence of ratio $F = \tau_{th}^{exp} / \tau_{th}^{fit}$ on ρ_p for $\alpha_p = 0$ (black circle), 0.5 (open circle) and 1 (black square).

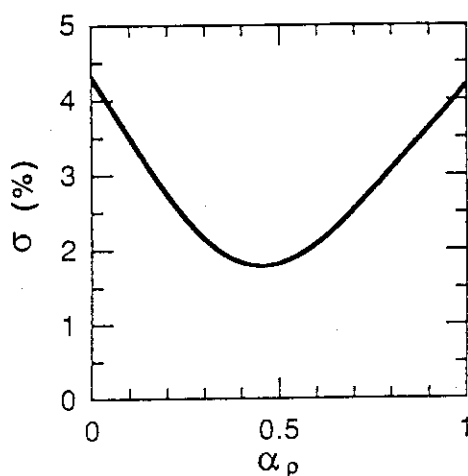


Fig.5 Standard deviation σ of F vs α_p . Minimum of σ is 1.7% around $\alpha_p = 0.5$.

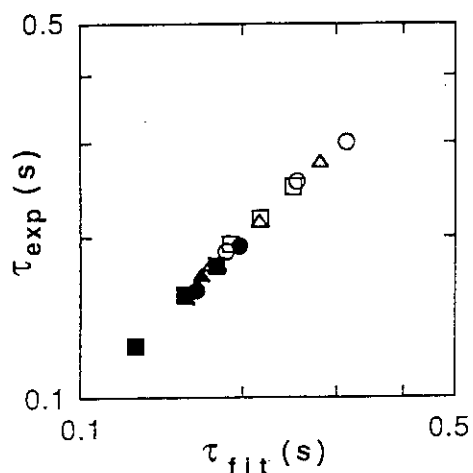


Fig.6 τ_{th}^{fit} vs τ_{th}^{exp} . Scaling of eq.(2) reproduces experimental data very well.

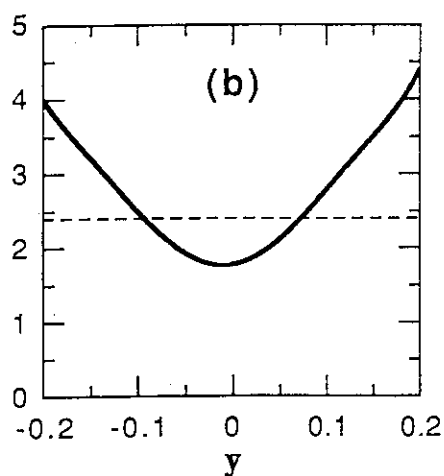
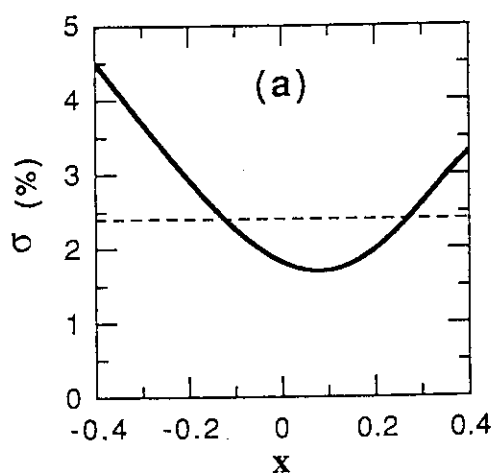


Fig.7 Standard deviation σ of F (a) vs x and (b) vs y . Dashed line corresponds to $1.4\sigma_{min}$.

1.15 Scaling of Thermal Energy in Tokamaks

T. Takizuka, T. Hirayama, M. Kikuchi

1. Introduction

Study of the confinement scaling for thermal energy is very important to clarify the heat transport mechanism in tokamak plasmas as well as to predict the performance of the energy confinement in future tokamak reactors. One of the authors (T. T.) proposed a scaling of thermal energy W_{th} in JT-60 L-mode plasmas [1],

$$W_{th}^{fit} = C (I_p B_t n_{el})^{1/2} P_{abs}^{1/3}, \quad (1)$$

where I_p is the plasma current, B_t the toroidal magnetic field, n_{el} the line averaged electron density and P_{abs} is the absorption power. This scaling is also applicable to the ohmic confinement. The B_t dependence was not accurately determined because of narrow range of B_t value in the database [2]. If one assumes $W_{th} \propto B_t^{1/2}$ as eq.(1) and the heat diffusivity $\chi \propto \beta^{1/2} (\rho/a) (T/eB)$, one obtains the size scaling for eq.(1) and replaces the constant C by $C_0 L^{5/2}$, where β is the plasma beta, ρ the Larmor radius, T the plasma temperature and L is the length representing the plasma size [1].

In the former chapter, Takizuka et al. have shown a new nondimensional scaling of thermal energy based on the data of B_t scan experiment in JT-60U L-mode plasmas [3],

$$W_{th}^{fit} = C (l_i I_p)^{6/9} n_{el}^{5/9} P_{abs}^{4/9} (1/n_{el} q_{eff})^{h/9}, \quad (2)$$

where l_i is the internal inductance, q_{eff} the effective safety factor at plasma surface and h takes the value between 0 and 1. The heat diffusivity has been presumed as $\chi \propto \beta^{h/4} (\rho/a)^{(1-h)/2} (T/eB)$. The size scaling for eq.(2) is given by replacing the constant C with $C_0 L^{(19-2h)/9}$. It should be noted that the values of l_i in the database of JT-60 [2] were not accurately evaluated and the l_i dependence of W_{th} in JT-60 was not found.

The present paper aims to examine the above results by the use of data from JT-60 with lower x-point configuration (we call this configuration JT-60/LX for simplicity) and JT-60U. The data from ASDEX are also used in the present analysis, which were offered by F. Wagner of Max-Planck Institute for Plasma Physics. In this paper, for the convenience, we call the scaling based on eq.(1) as the "gyroBohm type" scaling, and the scaling based on eq.(2) as the "weak-gyroBohm type" one. Hereafter the units of plasma parameters are W_{th} MJ, L m, I_p MA, B_t T, n_{el} $10^{19} m^{-3}$ and P_{abs} MW.

2. GyroBohm Type Scaling

At first we compare the experimental data of JT-60 with the scaling of eq.(1) as shown in Fig.1. The value of constant C is 0.09 and the standard deviation σ of $F = W_{th}^{exp}/W_{th}^{fit}$ is

11.5% [1]. Typical values of plasma parameters are listed in Table I, where R is the major radius, a the minor radius, and κ is the elongation. Next we compare the data of JT-60/LX with the same scaling as used for JT-60. The average of F is about 0.82 for both cases of $I_p = 1\text{MA}$ (open circle) and 2MA (black circle) as shown in Fig.2. Above two experiments are of pure hydrogen discharges. If we assume the square root dependence of W_{th} on ion mass number M_i and on κ , we can separate R and a dependences from $L^{2.5}$ dependence of W_{th} :

$$W_{th}^{GB} = 0.015 (M_i \kappa)^{0.5} R^{1.75} a^{0.75} (I_p B_t n_{el})^{1/2} P_{abs}^{1/3}. \quad (3)$$

Though we have showed a size scaling of $W_{th}^{fit} \propto 0.027 (R a)^{1.25}$ in reference [4], we here correct it as eq.(3). Figure 3 shows the comparison between W_{th}^{GB} and W_{th}^{exp} for the JT-60U database ($M_i = 2$) used in ref.[4], and Fig.4 shows W_{th}^{GB} vs W_{th}^{exp} for the database of ohmically heated plasma in ASDEX ($M_i = 2$). Both figures show the scaling of eq.(3) fitting well the experimental data, though the parameter dependences of the scaling are not fully suitable for the fitting of the data. The average $\langle F \rangle$ and σ (%) for $F_{GB} = W_{th}^{exp}/W_{th}^{GB}$ are summarized in Table II.

3. Weak-GyroBohm Type Scaling

In this section, we derive a weak-gyroBohm scaling based on eq.(2). Here the value of h is chosen to be 0. The square root dependence of W_{th} on M_i and κ is also assumed. The resultant scaling does not include the dependence on a ;

$$W_{th}^{WGB} = 0.0105 (M_i \kappa)^{0.5} R^{19/9} (I_i I_p)^{6/9} n_{el}^{5/9} P_{abs}^{4/9}. \quad (4)$$

Figure 5 shows W_{th}^{WGB} vs W_{th}^{exp} for JT-60, JT-60/LX, JT-60U and ASDEX. The scaling fits well all experimental data. It is noted in this figure that the data of $q_{eff} < 3$ or $n_{el} < 2 \times 10^{19} \text{m}^{-3}$ in JT-60 are omitted, and that the data of $I_p = 1.5\text{MA}$ ($q_{eff} \approx 3.5$) in JT-60/LX are omitted. The effect of sawtooth [5] is supposed to be one of the causes of systematic deviation of these data from the above scaling, while the gyro-Bohm type scaling of eq.(1) derived from JT-60 data may include not only the effects of χ but also the MHD effects. We cannot conclude at present which scaling is better to describe the transport process in tokamak plasmas.

4. Summary and Discussion

We have proposed two scalings of thermal energy in L-mode and ohmically heated plasmas, "gyroBohm type" scaling and "weak-gyroBohm type" scaling, which are based on the database of JT-60, JT-60/LX and JT-60U. Both scalings fit well the experimental data of three devices as well as those of ASDEX.

We apply these scalings for predicting the confinement performance of two reactors, ITER, ($M_i, \kappa, R, a, I_p, I_i, B_t, n_{el}, P_{abs}$) = (2.5, 2.2, 6m, 2.15m, 22MA, 0.8, 4.9T, $13 \times 10^{19} \text{m}^{-3}$, 150MW) and SSTR[6], (2.5, 1.8, 7, 1.75, 12, 0.8, 9, 14, 600). GyroBohm type

scaling and weak-gyroBohm type scaling give the same value of $\tau_{th} = W_{th} / P_{abs} = 1.9$ s for ITER, which is consistent with the global energy confinement time $\tau_E = 2$ s predicted by ITER89 law [7]. On the other hand, for SSTR, $\tau_{th}^{GB} = 0.80$ s and $\tau_{th}^{WGB} = 0.76$ s are a little larger than $\tau_E^{ITER89-P} = 0.67$ s and a little smaller than $\tau_E^{ITER89-OL} = 0.97$ s

The square root dependence of W_{th} on M_i and κ assumed here has to be checked carefully. In order to unify a scaling, data analysis should be continued with the use of data base of other tokamak devices.

References

- [1] TAKIZUKA, T., proc. 1992 Int. Conf. on Plasma Physics (combined with 19th EPS), Innsbruck, 1992, Vol.16C, Part I, 51.
- [2] KIKUCHI, M., KIKUCHI, K., AOYAGI, T., TANI, K., JAERI-M 91-057 (1991).
- [3] TAKIZUKA, T., et al., in this review, 1.14.
- [4] KIKUCHI, M., et al., 14th Int. Conf. on Plasma Physics and Controlled Nuclear Fusion Research, Wurzburg, 1992, IAEA-CN-56/A-3-3.
- [5] KAMADA, Y., et al., in this review, 1.10.
- [6] SEKI, Y., et al., Plasma Physics and Controlled Nuclear Fusion Research 1990 (Proc. 13th Int. Conf. Washington, D.C., 1990) Vol. 3, IAEA, Vienna (1991) 473.
- [7] YUSHMANOV, P.N., et al., Nuclear Fusion 30 (1990) 1999.

Table I Typical values of plasma parameters

	R	a	κ	I_p	Bt
JT-60	3.0	0.88	1.0	1.0 - 3.0	4.0 - 4.5
JT-60/LX	2.9	0.62	1.35	1.0 - 1.5	4.2
JT-60U	3.2	0.85	1.65	1.0 - 2.5	2.5 - 4.2
ASDEX	1.6	0.40	1.0	0.15 - 0.4	1.9 - 2.5

Table II Comparison with scalings

	$\langle F \rangle_{GB}$	σ_{GB}	$\langle F \rangle_{WGB}$	σ_{WGB}
JT-60	0.94	10.7	0.93 *	11.7 *
JT-60/LX	0.96	9.1	1.03 †	6.7 †
JT-60U	1.05	8.6	0.97	1.8
ASDEX	1.01	15.0	0.95	13.2

*; $q_{eff} > 3$ and $n_{el} > \times 10^{19} m^{-3}$. †; $I_p = 1MA$.

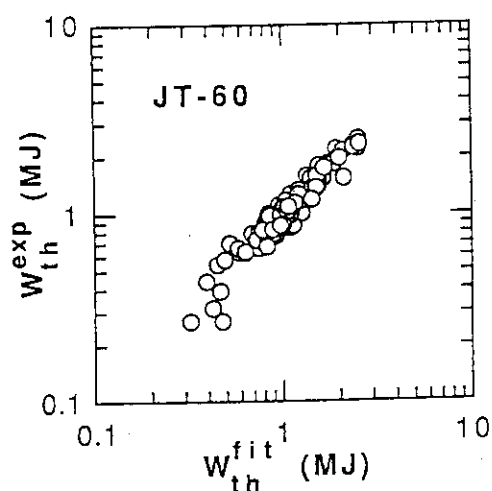


Fig.1 W_{th}^{fit} of eq.(1) vs W_{th}^{exp} for JT-60 L-mode plasmas.

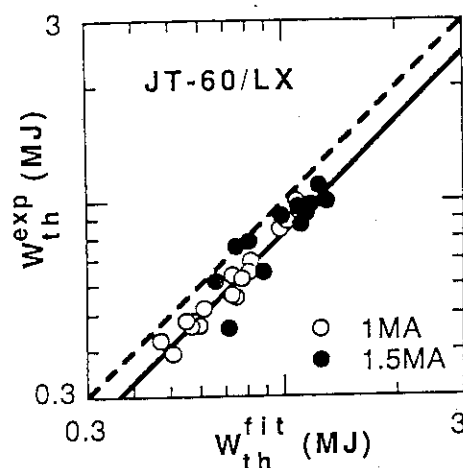


Fig.2 W_{th}^{fit} vs W_{th}^{exp} for JT-60/LX. $F = W_{th}^{exp} / W_{th}^{fit}$ is about 0.82 (dashed line). Open circles correspond to $I_p=1MA$ and black ones to 1.5MA.

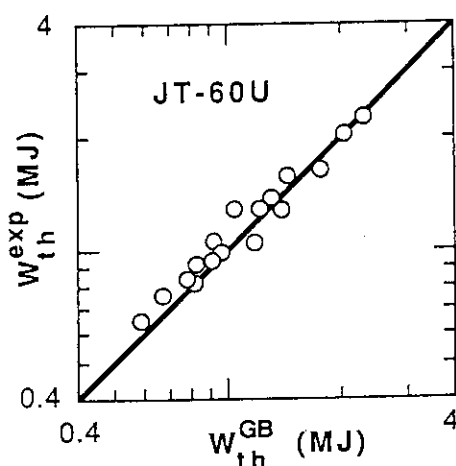


Fig.3 W_{th}^{GB} of eq.(3) vs W_{th}^{exp} for JT-60U.

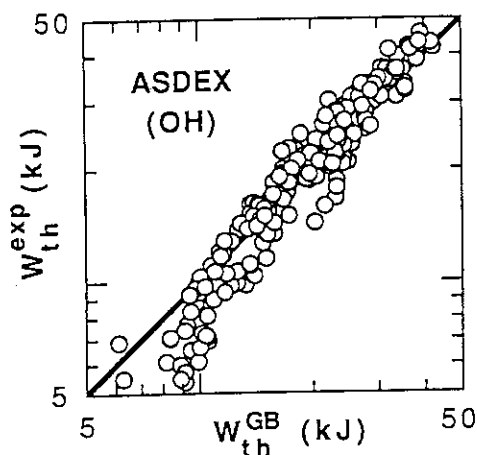


Fig.4 W_{th}^{GB} vs W_{th}^{exp} for ASDEX.

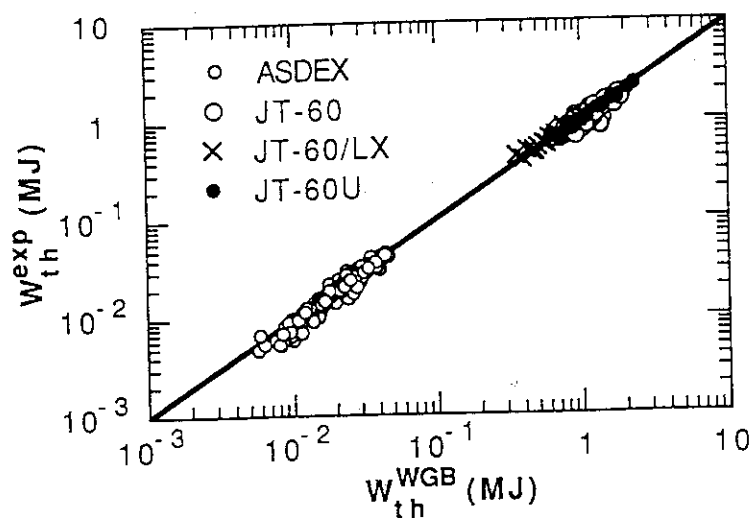


Fig.5 W_{th}^{WGB} of eq.(4) vs W_{th}^{exp} for JT-60, JT-60/LX, JT-60U and ASDEX.

1.16 Test of the Theoretical L-mode Scaling with Experimental Data

M. Yagi, and M. Azumi

1. Introduction

Recently, we have proposed a new instability (λ mode) driven by stochastic diffusion of the current and derived the thermal diffusivity due to this mode[1]. This formula is relevant nature to explain for L-mode plasmas since this belongs to Ohkawa relatives[2] and favorable I_p dependence which has not been explained by the conventional drift wave theory. In the present paper, we compare the thermal diffusivity due to the λ mode with empirically deduced one[3], and also discuss profile resilience predicted by the λ mode model and compare the experimental results.

2. Comparison with Theoretical Model and Experimental Data

Firstly, we compare the thermal diffusivity with empirically deduced one. The thermal diffusivity due to the λ mode is given by $\chi = Cq^2/s^2(R/L_p)^{3/2}A^{1/2}T^{3/2}/(RB^2)$ [1], where C is the numerical constant, q the safety factor, s the shear parameter, R the major radius, L_p the characteristic scale length of the pressure gradient, A the mass number, T the temperature, and B is the toroidal magnetic field. On the other hand Takizuka[3] has presumed that the thermal energy confinement in tokamak L-mode plasma is described by a collisionless or weakly collisional high- β transport model[4] and derived the form $\chi \propto q^{3/2}\beta^{1/2}(\rho/a)(T/eB)$ where ρ is the Larmor radius and other notations are the same as the above. To compare his formula with the present result, temperature dependence is somewhat weaker than his result but it is compensated with local pressure gradient. In our case $\beta^{1/2}$ is replaced with $\beta'^{1.5}$. q dependence is somewhat stronger than his result but favorable dependence. Both formulas are increasing function of r at peripheral region.

Secondary, we discuss the global scaling laws. Using a point-model argument, we obtain $\tau_E \propto a^{0.4}R^{1.2}I_p^{0.8}P_t^{-0.6}A^{-0.2}s^{0.8}L_p^{0.6}n^{0.6}$, where I_p is the total current, P_t the total power, n the density. To compare our result with empirical scaling law[3] $\tau_E \propto (\bar{n}_e I_p B_t)^{0.5} P_t^{-2/3}$, we found that the density and power dependence is fairly good, on the otherhand I_p dependence is somewhat stronger than empirical one. We also comment

the internal inductance effect on the confinement time. In our model equation, internal inductance is directly related with the local value of q and shear parameter. When the current profile becomes peaking, and the internal inductance is increasing, the decrease of the q value and the increase of the shear in the peripheral region lead to the increase of the confinement time ($\tau_E \propto (s/q)^{0.8}$).

3. Temperature Profile

In this section, we discuss the profile resilience. If we assume a localized deposition profile as $P(r) \sim \exp(-(r - r_{heat})^2/\Delta^2)$ and a flat density profile, then we can write $dT/dr \propto -\{s^2/(q^2r) \int_0^r P(x)xdx\}^{2/5}$ based on λ mode model. Figure 1 shows $T(r_1)/\langle T \rangle$ versus r_{heat} where r_1 is the radius of $q = 1$. We choose the parameters as $q_a = 3.0$, $r_1 = 1/q_a$, and $q(r) = q_0 + (q_a - q_0)r^2$. The peaking factor $T(r_1)/\langle T \rangle$ depends weakly on the location of heat-deposition maximum (r_{heat}). We also check the half width of the deposition profile ($\Delta = 0.2 - 0.5$). It seems that the half width of the deposition profile is not so effective for the peaking factor for $r_{heat} < 0.5$. Figure 2 shows $T(r_1)/\langle T \rangle$ versus q_a . The parameters are $\Delta = 0.3$, $r_{heat} = 0.0$ and $r_{heat} = 0.4$, respectively. The experimental data are also plotted where we use $q_{0.95}$ for q_a . There is a tendency that the temperature profile becomes peaked with higher q_a ($T(r_1)/\langle T \rangle \propto q_a^{0.4}$ for $r_{heat} = 0.0$ and $\propto q_a^{0.3}$ for $r_{heat} = 0.4$). This tendency is also observed in experimental data although the absolute value is lower than that in the model. Extension of this model to the two-fluids situation is future work.

References

- [1] ITOH, K., YAGI, M., ITOH, S.-I., FUKUYAMA, A., AZUMI, M., IAEA, Würzburg, 1992, paper CN-56/H-2-2.
- [2] ROSS, D. W., et al., Report of IPSG Working Group on Thermal and Particle Transport in Tokamaks 1987.
- [3] TAKIZUKA, T., EPS, Innsbruck, 1992, paper I-51.
- [4] CONNOR, J. W., TAYLOR, J. B., Nucl. Fusion **17**, 1047(1977).

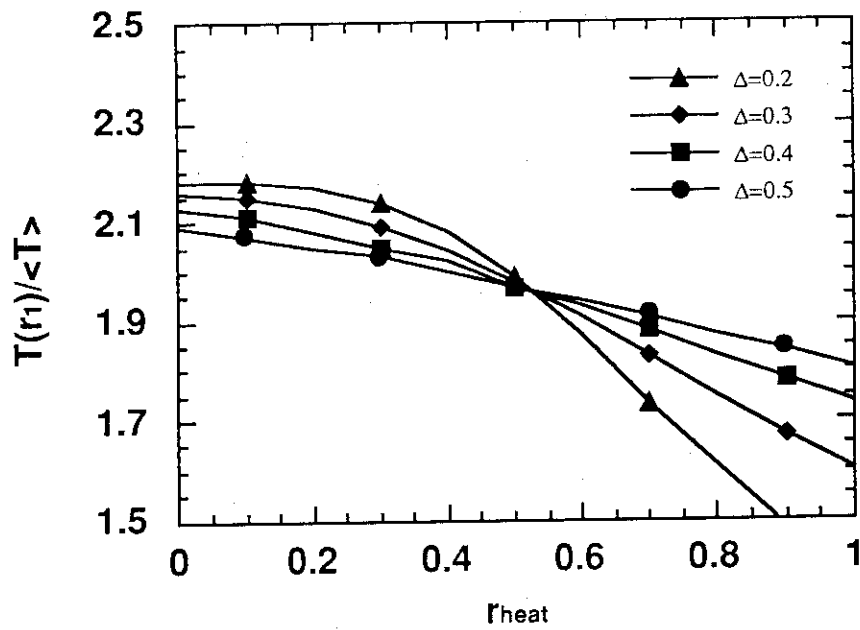


Fig.1 $T(r_1)/\langle T \rangle$ versus Γ_{heat}

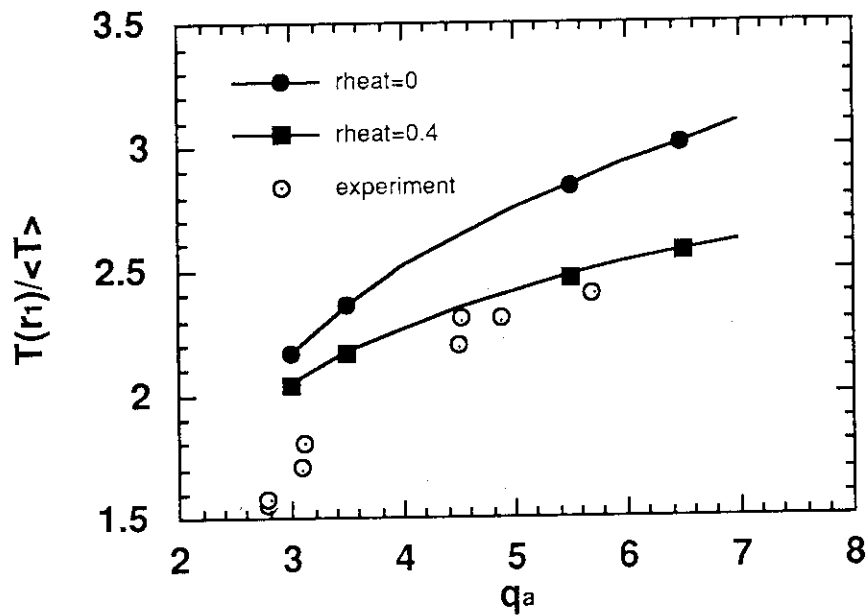


Fig.2 $T(r_1)/\langle T \rangle$ versus q_a

1.17 Sawtooth Characteristics and Electron Temperature Profiles from Electron Cyclotron Emission Measurements

N.Isei, Y.Kamada, S.Ishida, M.Sato, M.Kikuchi, H.Kimura, T.Hirayama

1. Introduction

For steady state tokamaks such as SSTR[1] and SSAT[2], control of the temperature profile becomes one of the most crucial issues for MHD stability since the current and pressure profiles are strongly coupled through the bootstrap current formation. Thus, the importance of study on the temperature profile and its controllability significantly increases for optimization of such a reactor scenario. But according to the principle of profile consistency[3], electron temperature profiles are very stiff and cannot be controlled. Therefore we investigated whether T_e profile is independent of heating profiles, and what dominates the temperature profile.

2. ECE Measurements

Sawtooth inversion radius is obtained from Grating polychromator diagnostic system[4]. T_e profile is obtained from Fourier transform spectrometer diagnostic system [5]. In those measurements the original location of the ECE in the plasma is determined by the total magnetic field strength including poloidal fields, toroidal diamagnetic fields and toroidal paramagnetic fields since the electron cyclotron resonant frequency is dependent on it. The total field is obtained from equilibrium analysis. In order to examine the accuracy of the determined location, the magnetic axis from equilibrium analysis (R_{ax}) is compared with the center of the $q=1$ surface (R_c) which is the averaged value between inside and outside sawtooth inversion positions from the ECE as seen in Fig.1. The ECE location from vacuum fields and that from total fields are expressed by different symbols in this figure. The difference between R_c and R_{ax} is large in the lower q_{eff} region for the case of vacuum field. But the difference is very much reduced by including the internal field effects. However small systematical error is seen for the case of total field. The cause of this error must be made clear in future.

3. Sawtooth Inversion Radius

The relation between sawtooth inversion radius (r_s/a) and safety factor (q_{eff}) is shown in Fig.2, where the ramp up phase, ramp down phase and flat top phase of the plasma current are symbolized differently. In steady state, r_s/a has the value of about $1.43/q_{eff}$ which corresponds to the line in Fig.3. The I_i dependence of the r_s/a for a fixed q_{eff} is shown in Fig.3. At the flat top phase of I_p , inversion radius increases with I_i and the rate is almost constant for a q_{eff} value. Therefore r_s/a can be estimated from I_i and q_{eff} . But at ramp down phase, r_s/a can not be estimated from I_i and q_{eff} , because the increasing rate of r_s/a with I_i is

small in comparison with the case of flat top phase and the rate is thought to depend on the I_p ramp down rate.

4. Electron Temperature Profiles

The q_{eff} dependence of the peaking parameter of T_e profile ($T_e(0)/\langle T_e \rangle$) is shown in Fig.4, where the top of error bar corresponds to the peaking parameter just before sawtooth crash ($T_e(0)/\langle T_e \rangle^{TOP}$), and the bottom to the peaking parameter just after sawtooth crash ($T_e(0)/\langle T_e \rangle^{BOTTOM}$). The $T_e(0)/\langle T_e \rangle$ increases with q_{eff} roughly, although the scatter of the data is large. The relation between $T_e(0)/\langle T_e \rangle$ and sawtooth inversion radius r_s/a for the case of neutral beam (NB) heating and ion cyclotron (IC) heating are shown in Fig.5 and Fig.6, respectively, with the data which have almost the same q_{eff} value of 5, and longer sawtooth period than 0.1sec. In the figures top and bottom of the peaking parameter are symbolized differently. In both cases of NB and IC heating with long sawtooth period, $T_e(0)/\langle T_e \rangle$ at top is nearly constant against r_s/a , although $T_e(0)/\langle T_e \rangle$ at bottom decreases with r_s/a . The $T_e(0)/\langle T_e \rangle$ at top is clearly higher in IC heating than in NB heating from the figures. This is because the difference of heating profiles, which is more peaked in center of the plasma in IC heating than NB heating, affects the T_e profiles. On the other hand $T_e(0)/\langle T_e \rangle$ at bottom is affected by sawtooth much and the heating profile effect is not clearly seen. The l_i dependence of $T_e(0)/\langle T_e \rangle$ at top in NB and IC heating are shown in Fig.7 with the same condition of data as fig.5 and 6. For a fixed l_i , $T_e(0)/\langle T_e \rangle$ at top is clearly higher in IC heating than NB heating. This is because the difference of heating profiles affects the profiles. As observed in NB heating, the l_i dependence of the $T_e(0)/\langle T_e \rangle$ is not clear. This is because the heating profiles in NB heating are independent of l_i . On the contrary in the case of ohmic heating, the different relation between $T_e(0)/\langle T_e \rangle$ and l_i from the case of NB heating can be seen. Figure 8 shows the $T_e(0)/\langle T_e \rangle$ (averaged value at top and bottom) against l_i . In the figure closed symbols stand for the sawtooth-free data and open symbols for the data with sawtooth, and the different symbols are used for each region of the q_{eff} values. The data with sawtooth-free or small inversion radius are situated near the line in Fig.8 because of the relation between r_s/a and l_i as seen in Fig.3. Therefore $T_e(0)/\langle T_e \rangle$ is found to depend on l_i for the plasma affected by sawtooth weakly in ohmic heating. Since the heating profile in ohmic discharges is directly coupled with the current profile, this l_i dependence on $T_e(0)/\langle T_e \rangle$ may represent the heating profile effect on $T_e(0)/\langle T_e \rangle$ in ohmic discharges.

5. Conclusion

Sawtooth activity strongly affects the formation on the T_e profile with decreasing q_{eff} , so that the T_e profile appears to be dependent on the q_{eff} . The heating profile effects might be masked in the sawtooth activity. In case that such a profile flattening effect by sawteeth is small, the T_e profile can be changed by heating profiles as shown for NB and IC heating. In ohmic heating, the l_i dependence of the T_e profile for sawtooth-free or small inversion radius

discharges is suggested to result from ohmic heating profiles. Carefully by eliminating the sawtooth effects on the T_e profile, the heating profile effects on the T_e profile is emerged, which would increase the possibility of temperature profile control for future tokamak reactors.

REFERENCES

- [1] KIKUCHI, M., Nuclear Fusion 30 (1990) 265.
- [2] NEVINS, W.M., et al., IAEA-CN-56/F-1-5 (1992)
- [3] ARUNASALAM, V., et al., Nuclear Fusion 30 (1990) 2111.
- [4] ISHIDA, S., et al., in this review, 9.5
- [5] SATO, M., et al., in this review, 9.4

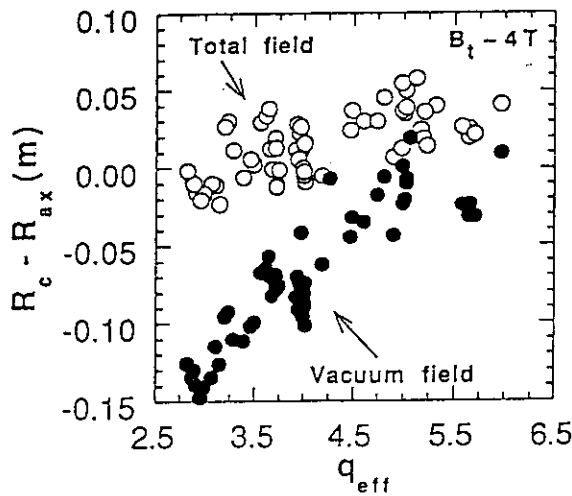


Fig.1 Comparison between magnetic axis from the equilibrium analysis (R_{ax}) and center of the $q=1$ surface (R_c) which is the averaged value between inside and outside inversion positions from the ECE.

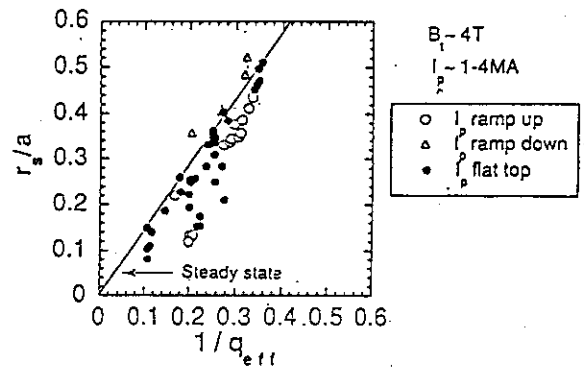


Fig.2 Relation between sawtooth inversion radius (r_s/a) and safety factor (q_{eff}).

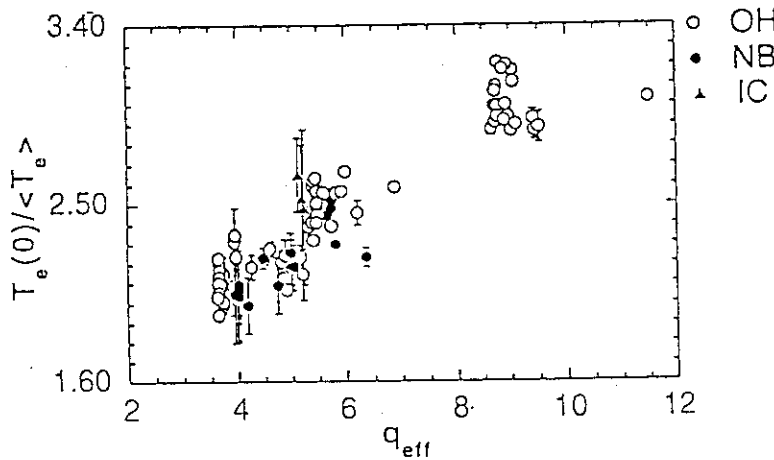


Fig.4 The q_{eff} dependence of the $T_e(0)/\langle T_e \rangle$

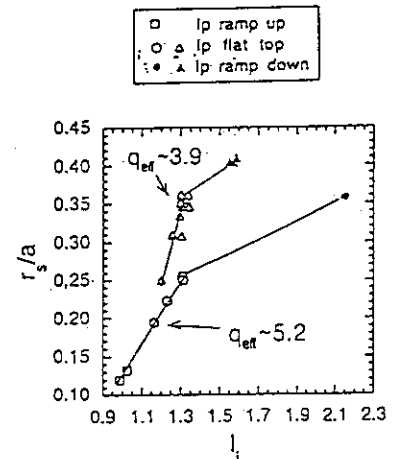


Fig.3 The I_i dependence of inversion radius r_s/a for a fixed q_{eff} .

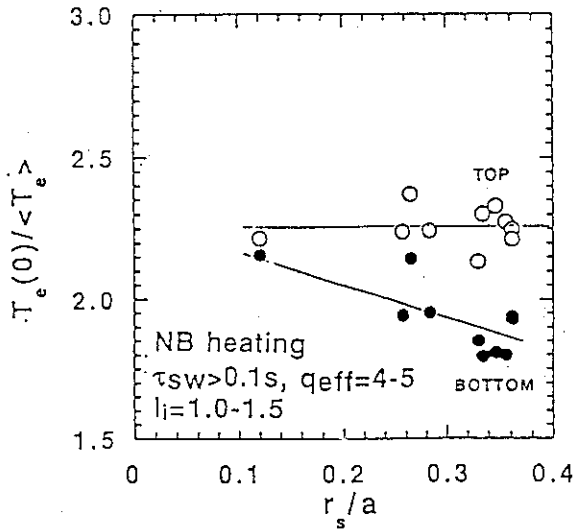


Fig. 5 Relation between the $T_e(0)/\langle T_e \rangle$ and sawtooth inversion radius r_s/a (NB heating).

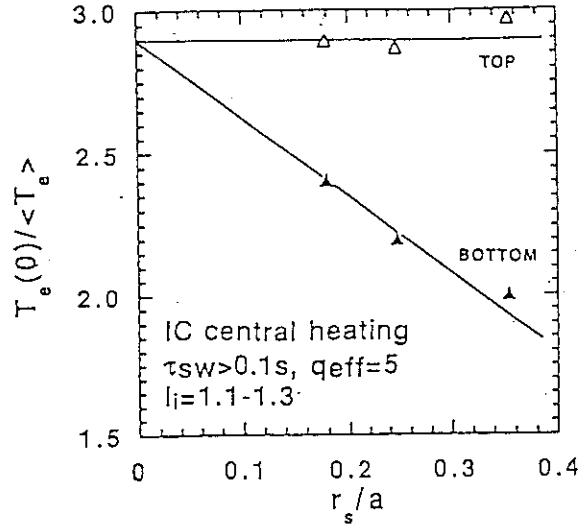


Fig. 6 Relation between the $T_e(0)/\langle T_e \rangle$ and sawtooth inversion radius r_s/a (IC heating).

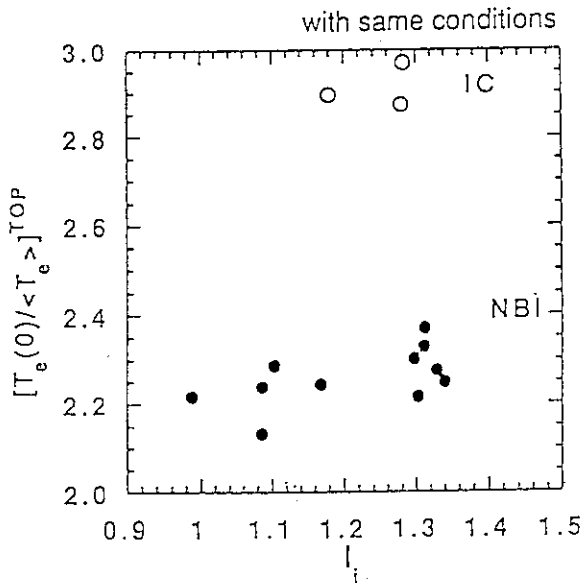


Fig. 7 The l_i dependence of the $T_e(0)/\langle T_e \rangle$ at top in NB and IC heating.

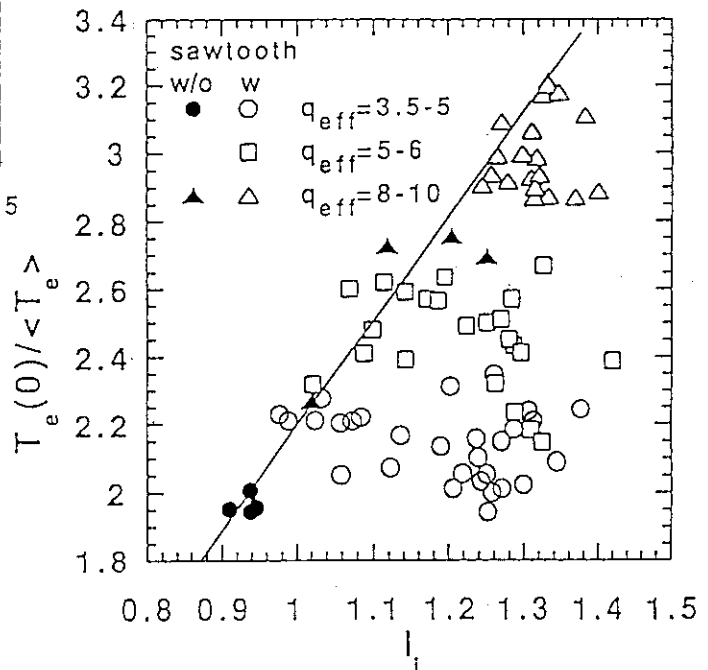


Fig. 8 The l_i dependence of the $T_e(0)/\langle T_e \rangle$ in ohmic heating.

1.18 Energy Confinement in Ohmically Heated Plasma

N.Isei, T.Takizuka, M.Kikuchi, H.Shirai

1. Introduction

Energy confinement in ohmically heated plasma is investigated using T_e from ECE by Fourier transform spectroscopy[1], Z_{eff} from visible bremsstrahlung, two-channel FIR interferometer, neutron emission rate, and magnetics. Toroidal field strength of the data is 4T and the plasma current values are 1.2, 2.0, 2.5 and 3.0MA.

2. Electron Temperature and Ion Temperature

For the purpose of checking the accuracy of measured T_e , the resistive loop voltage is calculated using neoclassical resistivity with T_e and Z_{eff} including bootstrap current correction. The calculation is compared with the measurement as seen in Fig.1. The calculation agrees with measurement within $\sim 10\%$ although it is somewhat less than measurement. In order to explain this small discrepancy, we probably need Z_{eff} up ($\sim 10\%$) or T_e down ($\sim 5\%$).

Ion temperature is calculated from the neutron yield with uniform ion energy confinement time (τ_{Ei})[2]. One of the calculated T_i is compared with the CXRS measurement with short pulse diagnostics neutral beam injection[3]. The measured T_i profiles at $t=7.04s$ are shown in Fig.2 together with that calculated at $t=8.5s$ where both n_e and T_e are almost same. The central ion temperature is agree with calculation. But the temperature seems to be somewhat overestimated. But it is not clear whether this is true. So far, this difference will make up to 30% error on the τ_{Ei} .

3. Comparison of The Stored Energy

Comparison of the kinetic total stored energy (W_{kin}) with the diamagnetically measured energy content (W_{dia}) is shown in Fig.3. The agreement between the two evaluations of the total energy contents is good, but W_{dia} is larger than W_{kin} and the difference seems to increase with current of the plasma.

4. Energy Confinement Time

Density dependence of the energy confinement time (τ_{kin}), which is obtained from the kinetic stored energy and τ_{Ei} , central ion temperature (T_{i0}), central electron temperature (T_{e0}), Z_{eff} , electron total stored energy (W_e) and kinetic total stored energy ($W_e + W_i$) are shown in Fig.4~7. The τ_{Ei} values of about 200msec to 500msec are obtained, and τ_{Ei} decreases with n_e . This tendency is also observed in JT-60[4]. The maximum τ_{kin} value of about 850msec is obtained, although the saturation density of τ_{kin} is not clear.

5. Scaling of The Confinement

The energy confinement time τ_{kin} is compared in Fig.8 with the predicted value τ_{NA} from the neo-ALCATOR scaling defined by

$$\tau_{NA} = 0.007 \times \kappa^{0.5} R^2 a q_a n_e, \quad (1)$$

where κ is the ellipticity, R is the major radius, a is the minor radius, $q_a = 5(1+\kappa^2)a^2 B_t / 2RI_p$ denotes the cylindrical safety factor at the plasma surface. Fig.8 shows the systematical difference between τ_{NA} and τ_{kin} and the large scatter. The main reason of the scatter is thought to be the lack of the term indicating input power (P_{oh}) in eq.(1), because the P_{oh} can not be expressed simply by I_p and n_e as seen in Fig.9.

By considering the term of P_{oh} as

$$\tau_S = 0.34 \times I_p^{0.6} \times n_e^{0.7} / P_{oh}, \quad (2)$$

energy confinement time is reproduced very well. The comparison between τ_{kin} and τ_S defined by eq.(2) is shown in Fig.10. The standard deviation of the scatter is 3.5%.

The thermal energy W^{GB} which is obtained from GyroBohm type scaling[5] and W^{WGB} from Weak-gyroBohm type scaling[5] are compared with kinetic total stored energy W_{kin} in Fig.11 and 12, respectively. The agreement between W^{GB} and W_{kin} is good from Fig.11. By considering the term of (T_e/T_i) and l_i as

$$W^{GB\#} = W^{GB} \times (T_e/T_i)^{0.6} \times l_i^{0.5}, \quad (3)$$

agreement is improved further as seen in Fig.13 and the standard deviation is reduced from 7.1% to 3.8%. The agreement between W^{WGB} and W_{kin} is not so good from Fig.12, but the scatter is very small and the standard deviation is 3.5%. By considering the term of (T_e/T_i) as

$$W^{WGB*} = W^{WGB} \times (T_e/T_i)^{1.5}, \quad (4)$$

agreement is improved as seen in Fig.14, but the standard deviation increases to 7.2%.

REFERENCES

- [1] SATO, M., et al., in this review, 9.4
- [2] ISEI, N., et al., JAERI-M 92-073 (1992) 96.
- [3] SHIRAI, H., et al., in this review, 3.6
- [4] KIKUCHI, M., et al., Kakuyugo Kenkyu Vol.65 Supplement (1991) 51.
- [5] TAKIZUKA, T., et al., in this review, 1.14, 1.15

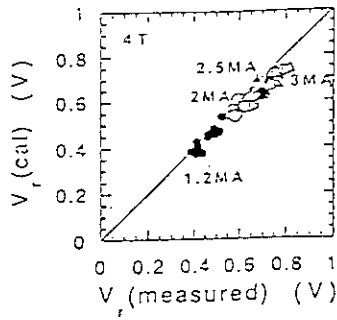


Fig.1 Comparison of measured resistive loop voltages ($V_r(\text{cal})$) and calculated ones ($V_r(\text{measured})$) from the neoclassical theory.

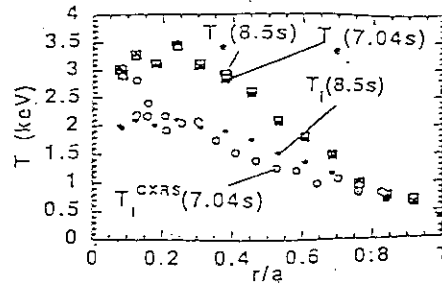


Fig.2 T_i profile by the evaluation from neutron yield with uniform τ_{Ei} (T_i) and by CXRS measurement (T_i^{CXRS}), and T_e profile by ECE measurement.

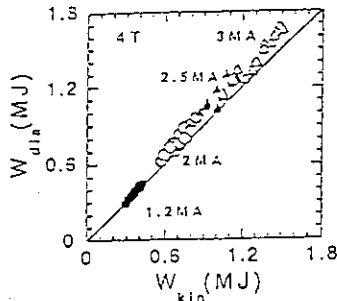


Fig.3 Comparison between the kinetic total stored energy (W_{kin}) and the diamagnetically measured energy content (W_{dia}).

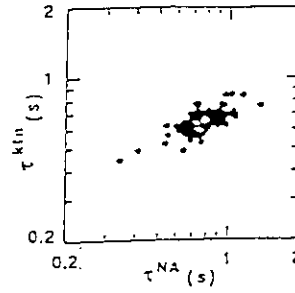


Fig.8 Comparison of the energy confinement time (τ_{kin}) with that from the neo-ALCATOR scaling (τ_{NA}).

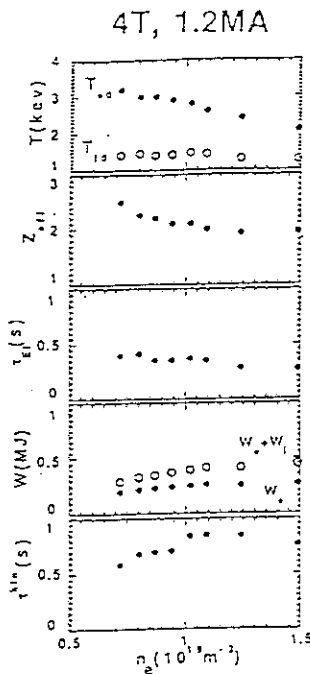


Fig.4 Density dependence ($I_p=1.2\text{MA}$)

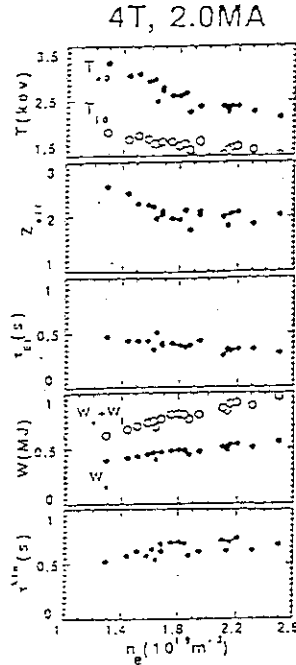


Fig.5 Density dependence ($I_p=2.0\text{MA}$)

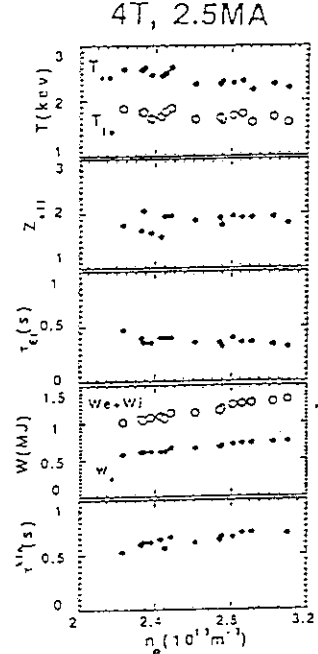
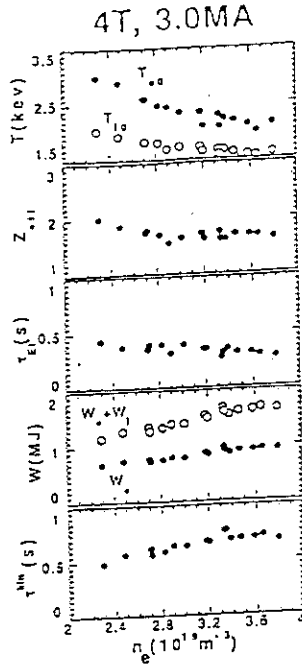
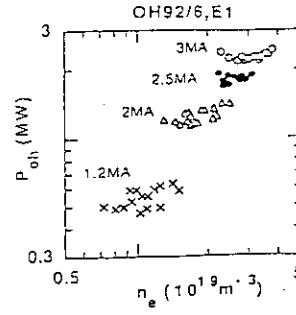
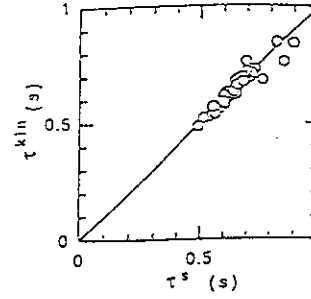
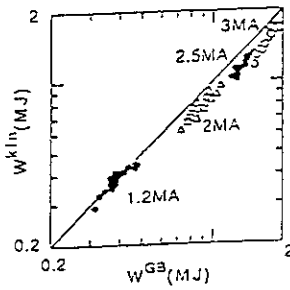
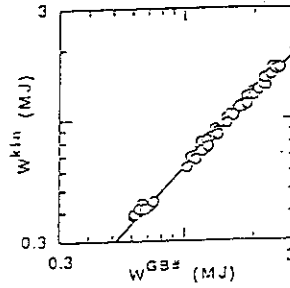
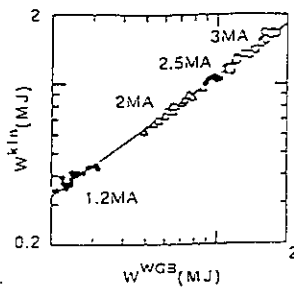
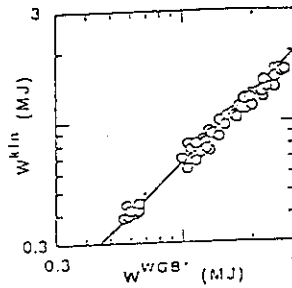


Fig.6 Density dependence ($I_p=2.5\text{MA}$)

Fig.7 Density dependence ($I_p=3.0MA$)Fig.9 Density dependence of the input power (P_{oh})Fig.10 Comparison of the energy confinement time (τ^{kin}) with that from the scaling including the term of input power (τ^S).Fig.11 Comparison of the kinetic total stored energy (W^{kin}) with that from GyroBohm type scaling (W^{GB}).Fig.13 Comparison of the kinetic total stored energy (W^{kin}) with that from GyroBohm type scaling including the term of ($T_e T_i$) and l_i ($W^{GB\#}$)Fig.12 Comparison of the kinetic total stored energy (W^{kin}) with that from Weak-gyroBohm type scaling (W^{WGB}).Fig.14 Comparison of the kinetic total stored energy (W^{kin}) with that from Weak-gyroBohm type scaling including the term of ($T_e T_i$) (W^{WGB*}).

2 High Poloidal Beta Confinement

2.1 Fusion Performance of High Poloidal Beta Plasmas

S. Ishida, T. Nishitani, Y. Koide, M. Kikuchi, R. Yoshino and JT-60 Team

1. Introduction

A goal of high β_p study in JT-60U is to show the feasibility of high β_p operation for a steady state tokamak reactor such as SSTR [1] particularly under the reactor-relevant conditions. The β_p value is defined as $\beta_p = 2\mu_0 \langle p \rangle / \bar{B}_p^2$, where $\langle p \rangle$ is the volume-averaged plasma pressure and \bar{B}_p is the averaged poloidal field at the plasma circumference calculated as $\bar{B}_p = \mu_0 J_p / (\int dl)$. The JT-60U tokamak can operate for a high field non-circular divertor configuration with a high aspect ratio similar to the SSTR concept, which may be beneficial to such a reactor-oriented study. Following the high β_p experiments for hydrogen plasmas in JT-60 [2], high β_p experiments for deuterium plasmas were extensively performed in JT-60U [3], in which a highly enhanced regime of plasma confinement was achieved in excess of the requirement of the reactor design. For the high β_p plasmas, the bootstrap current was a dominant fraction in the plasma current under negligible beam driven currents. The present paper describes the fusion performance of the discharges in the high β_p enhanced confinement (HPEC) regime obtained in the April and August run of JT-60U in 1992.

2. Operation

An extreme plasma configuration was chosen to be located inward in the vacuum vessel in order to satisfy the central beam deposition according to the vertically inclined perpendicular neutral beam lines. The resulting small bore plasma ($\sim 50 \text{ m}^3$) with an aspect ratio of ~ 4.3 was immune from fast ion losses due to the significant toroidal field ripple; the maximum ripple rate was at most $\sim 0.3 \%$ at the plasma surface. This divertor configuration was almost fixed throughout the experiments, with, typically, a major radius of $R_p \sim 3.05 \text{ m}$, a minor radius of $a \sim 0.71 \text{ m}$, an ellipticity of $\kappa \sim 1.7$ and a toroidal field of $B_t \sim 4.4 \text{ T}$ at the plasma center. The plasma current, I_p , was varied in the range of 0.6–1.9 MA ($q_{eff} = 5.5\text{--}17$ or $q^* = 4\text{--}11$); q_{eff} is the effective MHD safety factor and q^* is the cylindrical equivalent safety factor defined as $q^* = \pi a^2 B_t (1 + \kappa^2) / (\mu_0 R_p J_p)$. The central heating and fueling into a low density target plasma was by perpendicular neutral beam injection up to 22 MW with a beam energy of $\sim 90 \text{ keV}$. The off-axis tangential beam injection was additionally used for increasing the total injection power up to 28 MW.

The first wall of the JT-60U was almost fully covered with carbon/carbon composite graphite tiles for divertor plates and isotropic graphite tiles for other wall surfaces, and the wall temperature was kept at $\sim 290^\circ \text{C}$ during the experiments. To obtain a low density degassing discharge, helium glow discharge cleaning was carried out every night and helium Taylor discharge cleaning was carried out between shots. In addition to the low recycling condition, the suppression of resistive internal modes such as sawteeth and $m = 1$ modes plays an essential role in obtaining the large enhancement of confinement. So, the sawtooth free target plasma

was produced by controlling the target internal inductance. No carbon bloom was observed within the present power level.

3. High Performance Discharge

Figure 1 shows the waveforms for a typical high performance discharge at $q_{eff}=6.3$ or $q^*=4.4$ with $I_p=1.7$ MA and $B_t=4.4$ T in the HPEC regime. The W_{da} reaches 5.7 MJ, at which the line-averaged electron density \bar{n}_e is $\sim 3.4 \times 10^{19} \text{ m}^{-3}$, the absorbed heating power is $P_{abs}=22.6$ MW and the global energy confinement time τ_E is 0.28 s. The deuterium-deuterium (DD) fusion neutron rate, S_n , increases up to $2.8 \times 10^{16} \text{ n/s}$. The enhanced confinement phase is sustained for ~ 0.8 s and terminated by the occurrence of a β_p collapse at $\epsilon\beta_p=0.37$. Thereafter, a significant increase in D_α emission (D_α^{div}) from the divertor plasma and radiation losses from the main and divertor plasmas (P_{rad}^{main} and P_{rad}^{div} , respectively) occurs with enhanced recycling. The radiation losses from the divertor plasma tend to be suppressed so that the radiation losses from the main plasma can be dominant in the total radiation losses. For this discharge, the total fast ion losses including the ripple trapped and the banana-drift diffusion losses due to the toroidal field ripple were calculated to be $\sim 2.5\%$ of the injection power, which were remarkably smaller than those for other configurations in JT-60U. The enhancement factor of the energy confinement time against the ITER89-P L-mode scaling defined as $H = \tau_E / \tau_E^{L-mode}$ was 2.2 and the Troyon factor defined as $g = \beta_p [\%] / (I_p [\text{MA}] / a [\text{m}] B_t [\text{T}])$ was $g = 1.8$ just before the β_p collapse. In the above discharge, the central ion temperature $T_i(0)$ and electron temperature $T_e(0)$ reaches ~ 35 keV and ~ 12 keV, respectively. As shown here, high temperature plasmas relevant to a future fusion reactor were routinely obtained in the HPEC regime, where the ion temperature T_i reached ~ 38 keV, which is the record value of ion temperature in all the tokamaks, and electron temperature T_e up to ~ 12 keV. The fluctuation of the central ion temperature indicated in Fig.1 appears to be substantial as it has some correlations with the other diagnostic data such as D_α , soft X-ray and line density signals. However, it should be noted that relative increase in the background light in the central region would result in an enhanced error of the charge-exchange recombination spectroscopic measurements.

4. Fusion Amplification Factor

In this regime, the neutron rate S_n was significantly increased approximately in proportion to the square of the diamagnetic stored energy as shown in Fig.2, which is similar to the feature of TFTR supershots [4]. The maximum fusion power reached 34 kW corresponding to the maximum neutron rate of $2.8 \times 10^{16} \text{ n/s}$ obtained for the above high performance discharge.

The S_n and the DD fusion amplification factor Q_{DD} are plotted for different current regimes as a function of $\epsilon\beta_p$ in Fig.3, where the Q_{DD} is simply defined as (fusion power)/(absorption power). The achievable S_n reached $2.8 \times 10^{16} \text{ n/s}$ with $Q_{DD}=1.5 \times 10^{-3}$ at $q_{eff}=6.3$ ($q^*=4.4$) and $\epsilon\beta_p=0.37$. This neutron rate was calculated to be composed of 53 % thermal-thermal, 36 % beam-thermal and 11 % beam-beam contributions. The tendency of S_n increasing roughly in proportion to $(\epsilon\beta_p)^2$ for a given plasma current is shown here. Since the $\epsilon\beta_p$ limit by the β_p collapse tends to decrease with increasing the I_p , the S_n appears to become peak at lower $\epsilon\beta_p$ with increasing the I_p . As shown in the bottom figure, the Q_{DD} appears to be

well correlated with $\varepsilon\beta_p$. The maximum attainable Q_{DD} of $\sim 1.9 \times 10^{-3}$ was achieved for both low and high current regimes with $I_p = 1.2$ MA ($q_{eff} = 8.0$ or $q^* = 5.6$) and $I_p = 1.9$ MA ($q_{eff} = 5.5$ or $q^* = 4.0$), respectively. Provided that deuterium beams were injected into a 50 % deuterium and 50 % tritium plasma current, the equivalent DT fusion amplification factor, Q_{DT} , calculated would be ~ 0.29 without dW/dt correction for the maximum Q_{DD} shot with $S_\alpha = 2.6 \times 10^{16}$ n/s at $I_p = 1.9$ MA, in which the contribution from the thermonuclear reaction is ~ 38 % of the total DT neutron rate. If the dW/dt correction is included, the equivalent Q_{DT} value would be ~ 0.31 .

5. Fusion Triple Product

For the present plasma configuration, the $n_e(0)$ and Z_{eff} values could not be directly measured, while line-density measurements with two off-axis chords were available. Here, these values are inferred from a kinetic analysis by scanning the n_e profile with Z_{eff} to be consistent with the measured values such as line-density, neutron rate and stored energy. Some of the inferred n_e profiles are validated using the data from a CO2 laser interferometer with a tangential chord through the axis. A diagram of the evaluated fusion triple product of $n_i(0)\tau_E T_i(0)$ as a function of $T_i(0)$ is presented in Fig.4, in which the attainable $n_i(0)\tau_E T_i(0)$ value is shown to reach $\sim 4.4 \times 10^{20} \text{ m}^{-3} \cdot \text{s} \cdot \text{keV}$ with $Z_{eff} \sim 3$ for the above maximum S_α shot with $I_p = 1.7$ MA. The evaluated $nn_i(0)\tau_E T_i(0)$ values have a reasonable linear correlation with the Q_{DD} values for the high β_p discharges as shown in Fig.5.

6. Conclusion

A highly enhanced confinement regime with the H factor up to ~ 3 was achieved for the high β_p operation, for which operational methods such as the adjustment of plasma configuration to the beam lines, wall conditioning and current profile control (or consequent MHD control) were established. The operational plasma current was extended up to 1.9 MA with increasing beam injection power up to 28 MW. The discharges represented: high confinement performance characterized by $T_i \sim 38$ keV, $T_e \sim 12$ keV and $H \sim 3$; high fusion performance by $S_\alpha \sim 2.8 \times 10^{16}$ n/s, $Q_{DD} \sim 1.9 \times 10^{-3}$, equivalent $Q_{DT} \sim 0.31$ and $n_i(0)\tau_E T_i(0) \sim 4.4 \times 10^{20} \text{ m}^{-3} \cdot \text{s} \cdot \text{keV}$. The $T_i(0)$ of 38 keV was the highest value obtained in tokamak plasmas. The attainable $n_i(0)\tau_E T_i(0)$ value reached about a half of the highest value obtained in JET [5], exceeding the TFTR results [6]. These results are not only promising for future high β_p tokamak reactor, but also represent that the JT-60U has the potential of leading the high β_p operation in existing tokamaks.

References

- [1] KIKUCHI, M., Nucl. Fusion 30(1990)265.
- [2] ISHIDA, S., et al., in Plasma Physics and Controlled Fusion Research 1990 (Proc.13th Int. Conf. Washington D.C., 1990), Vol. , IAEA, Vienna (1991)195.
- [3] ISHIDA, S., et al., in Proc.14th. Int. Conf. Washington D.C., 1992, IAEA-CN-56/A-3-5.
- [4] STRACHEN, D., et al., Phys. Rev. Lett. 58(1987)1004.
- [5] JET TEAM, Nucl. Fusion 32(1992)187.
- [6] MEADE, D., et al., in Plasma Physics and Controlled Fusion Research 1990 (Proc.13th Int. Conf. Washington D.C., 1990), Vol. , IAEA, Vienna (1991)9.

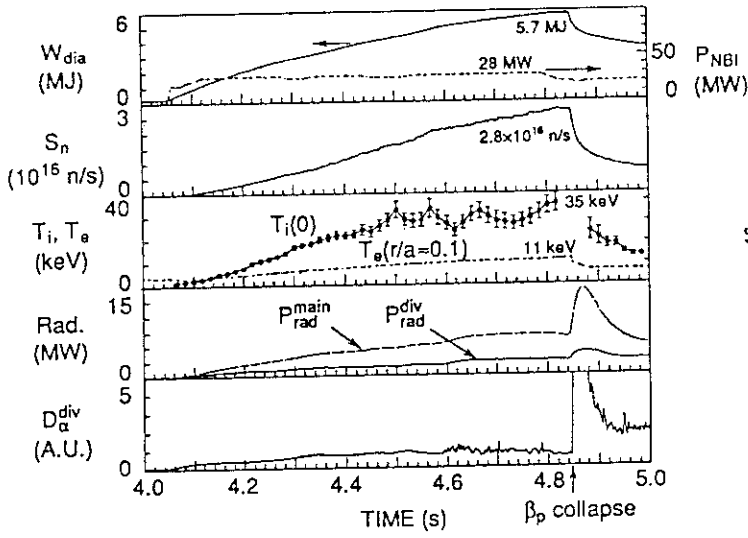


Fig.1 Waveforms of a typical high performance discharge with $I_p=1.7$ MA and $B_t=4.4$ T

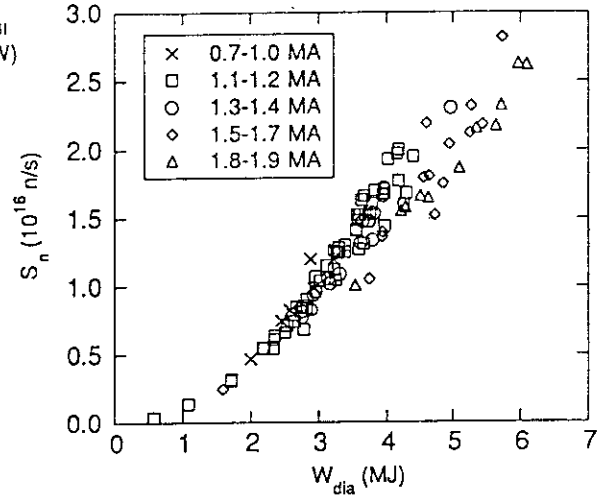


Fig.2 Fusion neutron rate, S_n , as a function of W_{dia}

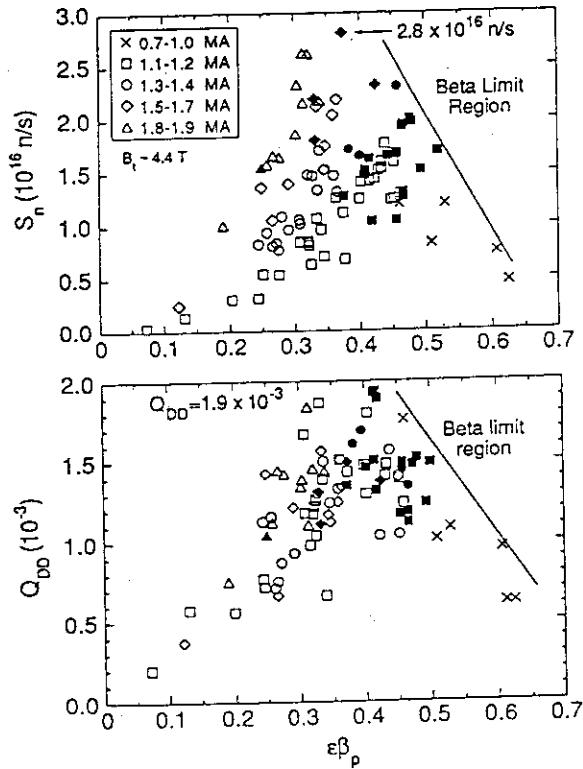


Fig.3 S_n and Q_{DD} as a function of $\epsilon\beta_p$

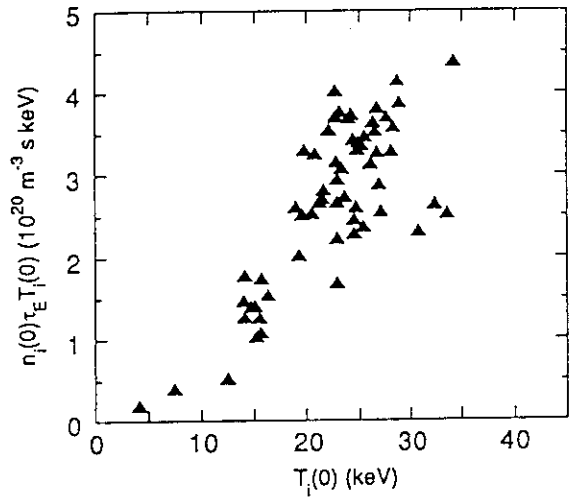


Fig.4 $n_i(0)\tau_E T_i(0)$ as a function of $T_i(0)$

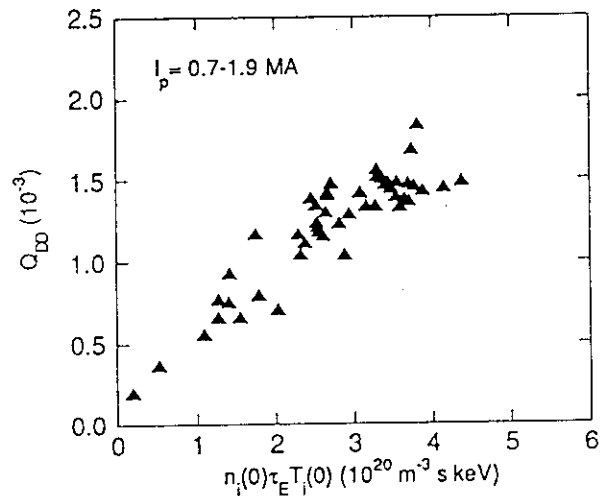


Fig.5 Q_{DD} as a function of $n_i(0)\tau_E T_i(0)$

2.2 Enhanced Confinement of High Poloidal Beta Plasmas

S. Ishida, Y. Koide, T. Fujita, N. Isei and M. Kikuchi.

1. Introduction

In the high β_p operation of JT-60U, a highly enhanced regime of plasma confinement was achieved with reactor-relevant high temperature up to ~ 38 keV and energy confinement times up to a factor of ~ 3 above the ITER89-P L-mode scaling in excess of the requirement of the reactor design for SSTR. To extrapolate the future reactor plasma in such a high β_p regime, confinement characteristics of the high β_p enhanced confinement regime (HPEC) obtained in JT-60U have been extensively investigated by scanning the plasma current, beam power and current profile (or internal plasma inductance, l_i).

In the high β_p regime, a favorable relation for future prospects of high β_p operation was obtained between the L-mode enhancement factor and the $\epsilon\beta_p$ value. Some mutual dependence of scaling parameters such as plasma current and heating power for the enhanced confinement are observed while not seen for the L-mode plasma. To see the relation between confinement and current profile, the l_i dependence of the confinement was investigated. All the results discussed here suggest that the HPEC plasmas are underlined to be distinctive to the L-mode plasma.

2. Confinement Evaluation Basis

The β_p value from magnetic measurements is defined as $\beta_p = 2\mu_0 \langle p \rangle / \bar{B}_p^2$, where $\langle p \rangle$ is the volume-averaged plasma pressure and \bar{B}_p is the averaged poloidal field at the plasma circumference calculated as $\bar{B}_p = \mu_0 J_p / (\int dl)$. Here, the total β_p value defined as $\beta_p = (\beta_p^{dia} + 2\beta_p^{eq})/3$ is obtained from an approximate expression of $\beta_p \approx (2\Lambda - l_i + \beta_p^{dia})/3$ assuming the l_i value is constant during beam injection, where β_p^{dia} and β_p^{eq} are the diamagnetic and equilibrium poloidal beta values, respectively, $\Lambda = \beta_p^{eq} + l_i/2$ and l_i is the value for the target Ohmic plasma just before beam injection. The total β_p values calculated from the above approximation are in good agreement with equilibrium calculations based on full magnetic fitting [1]. This total magnetic pressure is used for evaluation of global confinement properties throughout the present paper unless otherwise noted. The total magnetic stored energy, W , is ~ 2 -10 % smaller than the diamagnetic stored energy, W_{dia} , due to pressure anisotropy.

2. High Temperature Plasmas

High temperature plasmas relevant to a future fusion reactor were routinely obtained in the HPEC regime with ion temperature T_i up to ~ 38 keV and electron temperature T_e up to ~ 12 keV. The T_i was measured by charge exchange recombination spectrometers using a carbon VI emission line (5292 Å). The T_e was obtained from electron cyclotron emission (ECE) measurements for second harmonic extraordinary mode using a fast scanning Michelson interferometer absolutely calibrated.

In Fig.1, typical ion and electron temperature profiles of a high β_p plasma with $a=0.71$,

$R_p=3.04$ m, $\kappa=1.7$, $I_p=1.7$ MA, $B_t=4.2$ T, $\bar{n}_e\sim 3.4\times 10^{19}$ m $^{-3}$, $P_{NB}=22.6$ MW and $\epsilon\beta_p=0.37$ are compared with an L-mode plasma with the similar parameters of $I_p=1.7$ MA, $B_t=4.2$ T, $\bar{n}_e\sim 4\times 10^{19}$ m $^{-3}$ and $P_{NB}\sim 24$ MW but a larger configuration of $a=0.83$ m, $R_p=3.2$ m and $\kappa=1.6$. As shown here, the high temperature plasmas were characterized by a highly peaked T_i profile and a broad T_e profile in comparison with the L-mode plasma; the central values of T_i and T_e are ~ 5 and ~ 2 times, respectively, higher than those of the L-mode plasma.

3. Poloidal Beta Dependence

A highly enhanced confinement regime with energy confinement times up to a factor of ~ 3 above the ITER89-P L-mode scaling was identified in the high β_p operation up to $\epsilon\beta_p\sim 0.5$ in JT-60U. The H factor is shown in Fig.2 as a function of $\epsilon\beta_p$ for different current regimes in the range of $I_p=1.1$ -1.9 MA ($q_{eff}\sim 5.5$ -8.4 or $q^*\sim 4.0$ -6.2) at $B_t\sim 4.4$ T; q_{eff} is the effective MHD safety factor and q^* is the cylindrical equivalent safety factor defined as $q^*=\pi a^2 B_t(1+\kappa^2)/(\mu_0 R_p I_p)$. As shown in this figure, the H factor linearly increases with $\epsilon\beta_p$ up to a factor of ~ 3 above the L-mode scaling; or up to a factor of ~ 1.7 above the JET/DIII-D H-mode thermal confinement scaling [2]. It also seems to be mostly independent of I_p . As indicated by the closed symbols, the β_p collapses occurred for the high H factor discharges above $H\sim 2.0$. Such the strong dependence of the H factor on $\epsilon\beta_p$ would increase the prospects of the high β_p tokamak reactor with a large bootstrap current fraction and a high enhancement factor.

4. Power and Current Dependence

Supershot studies in TFTR have shown the weak or rather negative dependence of energy confinement times on plasma current and total heating power as $\tau_E=W_{tot}/P_{tot}\propto P_{tot}^{-0.06}I_p^{-0.24}$ [3], which seems to be favorable for the future reactor. In JT-60U, independent scans of the scaling parameter have been widely performed to identify the underlying mutual dependence of the scaling parameters in the confinement features.

The dependence of the enhanced confinement on net power and plasma current has been investigated in the wide ranges of $I_p=1.1$ -1.9 MA and $P_{NB}=5$ -28 MW at $B_t\sim 4.4$ T, in which power scan experiments were carried out for $I_p=1.1$ MA and 1.2 MA within the range of $P_{NB}=5$ -22 MW. The variation of the energy confinement time τ_E and the H factor as a function of the net power P_{net} is shown in Fig.3 for the same subset of discharges shown in Fig.2. Here, the P_{net} is defined as $P_{net}=(P_{obs}-dW/dt)\approx(P_{obs}-dW_{dia}/dt)$ and the global energy confinement time from magnetic measurements as $\tau_E=W/P_{net}$. The attainable stored energy reached $W=5.9$ MJ at $P_{net}=16.6$ MW for $I_p=1.9$ MA.

As typically shown for $I_p=1.1$ -1.2 MA ($q_{eff}=8.1$ -8.4 or $q^*=5.6$ -6.2), the attainable τ_E for a given current tends to increase with the P_{net} and reach a maximum value, above it rapidly decreases. As compared to the regime of 1.8-1.9 MA ($q_{eff}=5.6$ -5.8 or $q^*=4.0$ -4.2), an optimum power to maximize the τ_E or H factor at a given current appears to increase with the I_p . This power dependence closely coupled with the I_p is essentially different from that for L-mode or H-mode type discharges; which can be also obtained even if the absorption power was used instead of the net power, in contrast to the report of TFTR supershots [4]. Note that the contribution of the dW/dt correction in the net power ($(dW/dt)/P_{obs}\lesssim 0.3$ for most cases)

might be more significant in JT-60U than in TFTR. Thus, it can be concluded that an appropriate choice of the operating current according to the power level would result in the apparent weak dependence of the enhanced confinement on the power. It should be a future work to see whether a slight decrease in the attainable τ_E and H factor with increasing I_p , as shown in Fig.3, represents the substantial safety factor dependence.

5. Current Profile Dependence

The current profile of the discharges may affect the enhanced confinement as well as MHD stability as recently discussed for L-mode plasmas. The target internal inductance, l_i^{target} , was controlled by changing the beam injection timing without current ramp to investigate whether the confinement and stability in the HPEC regime can be affected by the current profile. In Fig.4, the obtained $\epsilon\beta_p$ and H factor are plotted as a function of the l_i^{target} just before beam injection for a high q region ($7.0 \leq q_{eff} \leq 11$ or $5.0 \leq q^* \leq 7.4$) with $I_p = 0.9 - 1.4$ MA at $B_t \sim 4.4$ T where the coupling of q and l_i would be weaker than in low q regime. As the target l_i is not so changed during the beam injection, the l_i during beam injection can approximate the target l_i . Sawtooth and $m=1$ mode activities were observed in the range of the l_i above ~ 1.2 , resulting in significant confinement degradation. In the lower l_i region below ~ 1.2 , the highly enhanced confinement was obtained without these activities and other significant modes.

As seen in Fig.4, the attainable $\epsilon\beta_p$ values are decreased with decreasing the l_i below an attainable limit line of $\epsilon\beta_p \sim 0.4 \times l_i^2$, suggesting that the broadened current profile reduces the stability limit. On the other hand, the attainable H factor on the l_i appears to be almost constant for the $l_i \lesssim 1.2$, or insensitive to the l_i . This may imply that the current profile does not significantly affect the formation of the enhanced confinement at a given safety factor region if the plasma is MHD-stable. A high target l_i discharge without sawteeth was required to increase a stability margin rather than to improve the confinement by increasing the l_i .

6. Conclusions

A highly enhanced confinement regime with the H factor up to ~ 3 was achieved for the high β_p operation in JT-60U. The power dependence of the enhanced confinement is closely coupled with the plasma current, resulting in the apparent weak power dependence by changing the current according to the power level. It suggests that an optimum combination of the power and the current exists to maximize the confinement enhancement for a given toroidal field. The confinement enhancement appears to be insensitive to the current profile, but the stability limit is rapidly reduced by decreasing l_i .

References

- [1] FUJITA, T, et al., Section 2.4 in this report.
- [2] SCHISSEL, D.P., et al., Nucl. Fusion 31(1991)73.
- [3] BELL, M, et al., in Report of the Workshop of Three Large Tokamak Cooperation on Energy Confinement Scaling under Intensive Auxiliary Heating.
- [4] STRACHAN, D., et al., Phys. Rev. Lett. 58(1987)1004.

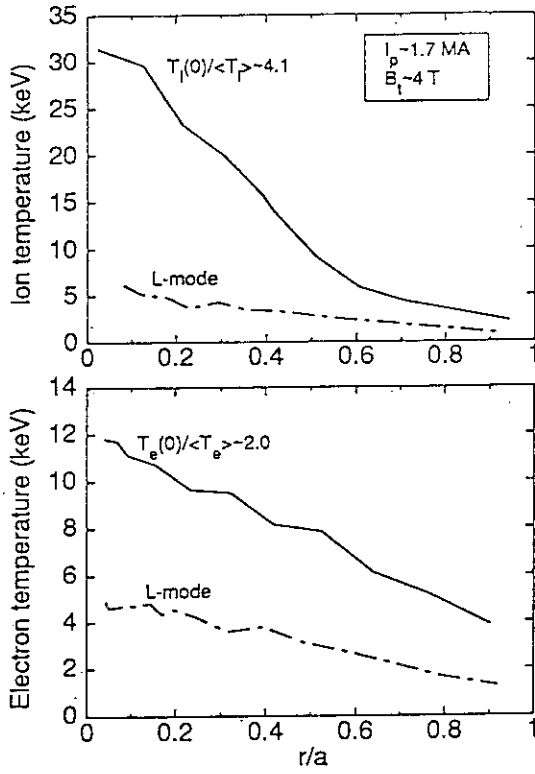


Fig.1 T_i and T_e profiles for a high β_p plasma and an L-mode plasma

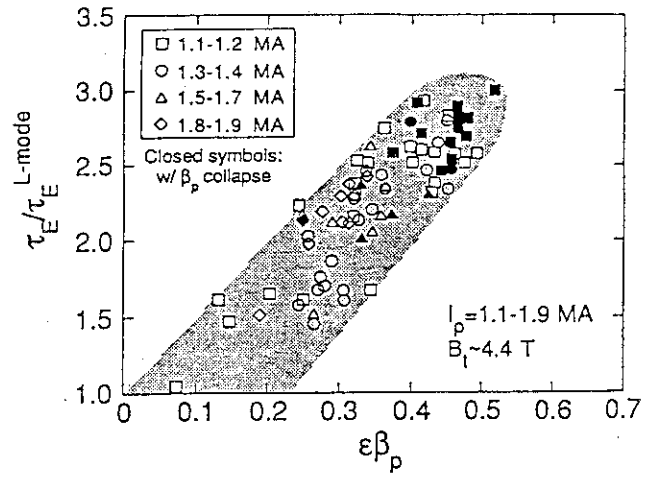


Fig.2 H factor against ITER-89P L-mode scaling as a function of $\epsilon\beta_p$

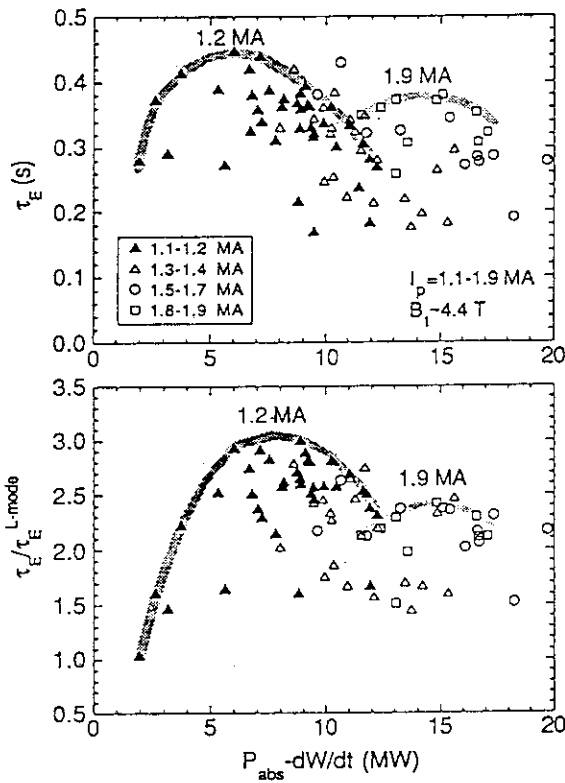


Fig.3 τ_E and H factor as a function of P_{net} with different current regimes

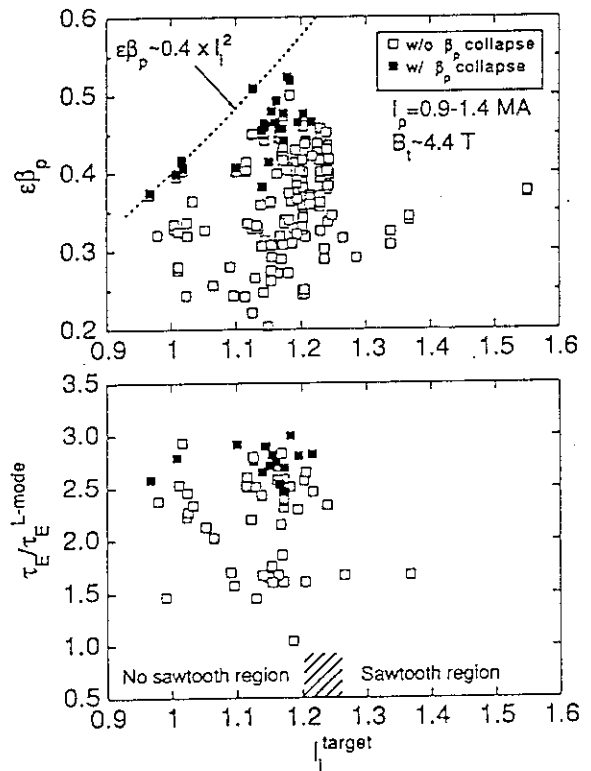


Fig.4 $\epsilon\beta_p$ and H factor as a function of the target i_t

2.3 Fusion Reactivity

T. Nishitani, S. Ishida and Y. Kamada

1. Introduction

The high β_P plasma of JT-60U is characterized by the high ion temperature and the high fusion reactivity. The highest ion temperature of 38 keV and the highest neutron emission rate of 2.8×10^{16} n/s were obtained in 1992. The fusion reactivity is a suitable parameter rather than the stored energy to evaluate the plasma performance, because that represents the fusion power itself. This paper describes the plasma parameter dependences of the fusion reactivity for the high β_P plasmas. The fusion reactivity analysis and the Q_{DT} evaluation of the typical high β_P plasmas were analyzed using the 1.5 D tokamak code.

2. Plasma Parameter dependences of Fusion Reactivity.

Figure 1 shows the heating power dependence of the neutron source intensity in the high β_P plasmas. The neutron source intensity increases with the heating power as $S_n = 1 \times 10^{15} P_{abs}(\text{MW})$ n/s, where S_n is the neutron source intensity, and P_{abs} is the absorbed heating power. The dependence is weaker than that of the TFTR super shot, $S_n \sim P_{abs}^{1.8}$. As reported previously [1], the neutron source intensity is proportional to W^2 , where W is the stored energy. The dependences on the heating power and the stored energy require the power degradation of the energy confinement time as $\tau_E = W/P_{abs} \propto P_{abs}^{-1/2}$. The linear dependence on the heating power indicates that the fusion gain Q_{DD} is constant for the heating power.

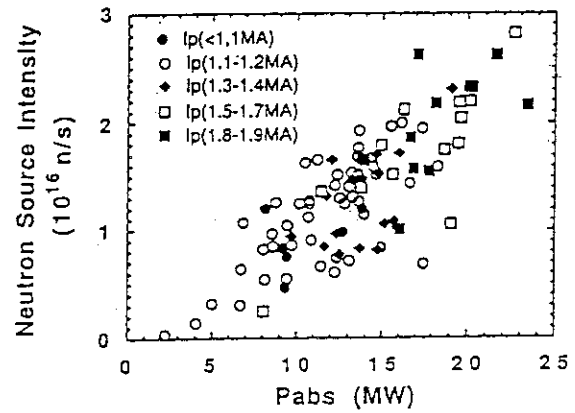


Fig.1 Heating power dependence of the neutron source intensity.

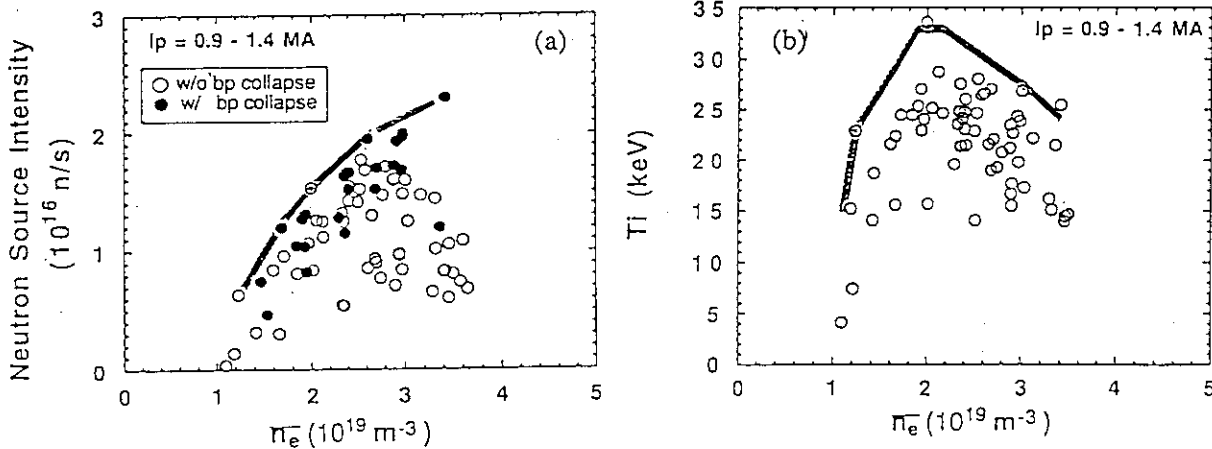


Fig. 2 Density dependences of the neutron source intensity and the central ion temperature.

Density dependences of the neutron source intensity and the central ion temperature are shown in Figs. 2(a) and 2(b), respectively, where the ion temperature was measured with the CXRS. The maximum neutron yield was obtained in the electron density around $3.4 \times 10^{19} \text{ m}^{-3}$, whereas, the maximum ion temperature was obtained around $2.0 \times 10^{19} \text{ m}^{-3}$, which indicates that the optimum density for the neutron yield is higher than that for the ion temperature. The neutron yield was limited by the β_p collapse for the \bar{n}_e lower than $3.4 \times 10^{19} \text{ m}^{-3}$. It decreased beyond the density, which is provably due to the off-axis beam deposition in higher electron density, where the β_p collapse has no longer occurred.

The plasma current dependence of the Q_{DD} is shown in Fig. 3. The upper envelope of the Q_{DD} increase with I_p in the range 0.7-1.2 MA, which confirms that the poloidal β limit increases with the I_p . However, the Q_{DD} is saturated to be 1.9×10^{-3} or little bit decreases with I_p larger than 1.2 MA, which is provably due to the increase in the density with the I_p . Most of the highest Q_{DD} was obtained around 1.2 MA. However, we have possibility to improve the Q_{DD} in the high density regime by increasing the beam energy, which provides the center deposition of the beam.

We investigated the effects of the current profile on the neutron yield by varying the injection timing of the NB in the tokamak discharge. Figure 4 shows the l_i dependence of the neutron source intensity. In a given I_p , the upper envelope of the Q_{DD} increase with the l_i until the threshold for sawteeth due to the increase of the poloidal β limit. The neutron yield degrades significantly in the sawtooth regime, which suggests that the beam fast ions are pushed out from the core by sawteeth. The sawtooth threshold of the l_i decreases with the I_p as reported by Kamada[2]. Therefore we have to inject the NB in the early phase of the discharge for the high I_p . If the sawtooth stabilization in the high β_p plasma using the ICRF or something like that, the neutron yield would be improved in high l_i regime.

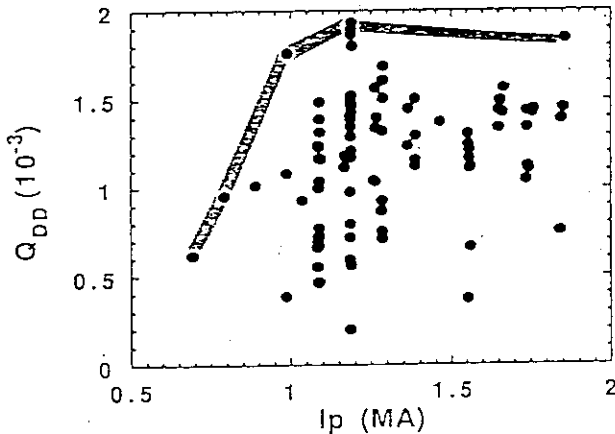


Fig. 3. Plasma current dependence of Q_{DD}

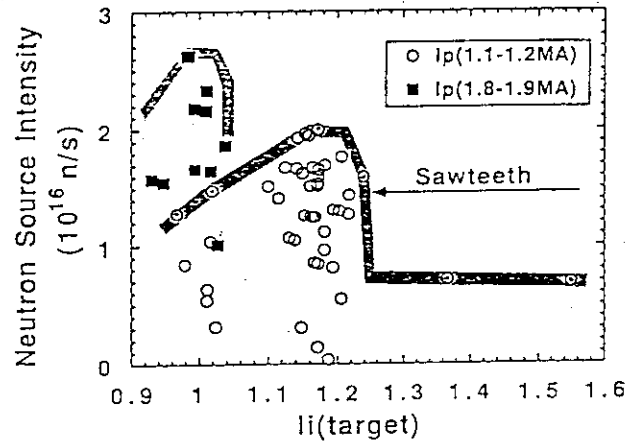


Fig. 4. l_i dependence of the neutron source intensity.

3. Fusion Reactivity Analysis

The fusion reactivity of the NB heated plasma has three contributions: the thermal-thermal, beam-thermal and beam-beam reactions. The profiles of those fusion reactivity components have been analyzed for the typical high β_p plasmas using a steady-state 1.5 D tokamak code TOPICS.

The D-T plasma performance have been projected from the obtained fusion reactivity in the D-D plasma. The analyzed discharges are listed in Table 1. The highest neutron yield, Q_{DD} , the ion temperature and the stored energy were obtained in shots E016023, E016039, E016045, and E016040, respectively. The shot E016160 of the hot ion H-mode was analyzed as a reference.

Table 1. Analyzed shot list.

Shot No.	I_p (MA)	P_{abs} (MW)	S_n ($10^{16}s^{-1}$)	W_{dia} (MJ)	$Ti0$ (keV)	Mode
E016023	1.67	23	2.8	5.7	35	β_p
E016039	1.86	17	2.6	6.0	30	β_p
E016045	1.85	19	1.8	4.9	38	β_p
E016023	1.85	21	2.6	6.1	30	β_p
E016168	3.5	24	1.9	7.7	20	H

Figures 5(a), 5(b), and 5(c) show the profiles of the electron density, the ion temperature, and the electron temperature of those discharges, respectively. A couple of sight line of the FIR interferometer have almost same tangent radii for the high β_p configuration so that the electron density profile is assumed to be parabolic as $n_{e0} [1 - (r/a)^2]^m$, and the power m is determined to reproduce the stored energy and the neutron emission rate within their measurement uncertainties. In E016024, the electron density profile was derived from the FIR interferometer and the CO_2 interferometer with tangential beam line. The peaked electron density profile was performed in the high neutron yield discharges. The hot ion H mode and the highest ion temperature shot have flat electron density profiles. The ion temperature profile is peaked in the high β_p plasmas. The electron temperature profile is also peaked in the high β_p plasmas more than in the hot ion H mode plasma.

The fusion reactivity profiles for E016023 and E016045 are shown in Figs 6(a) and (b), respectively. The thermal-thermal reactions are dominant in E016023. On the other hand, the

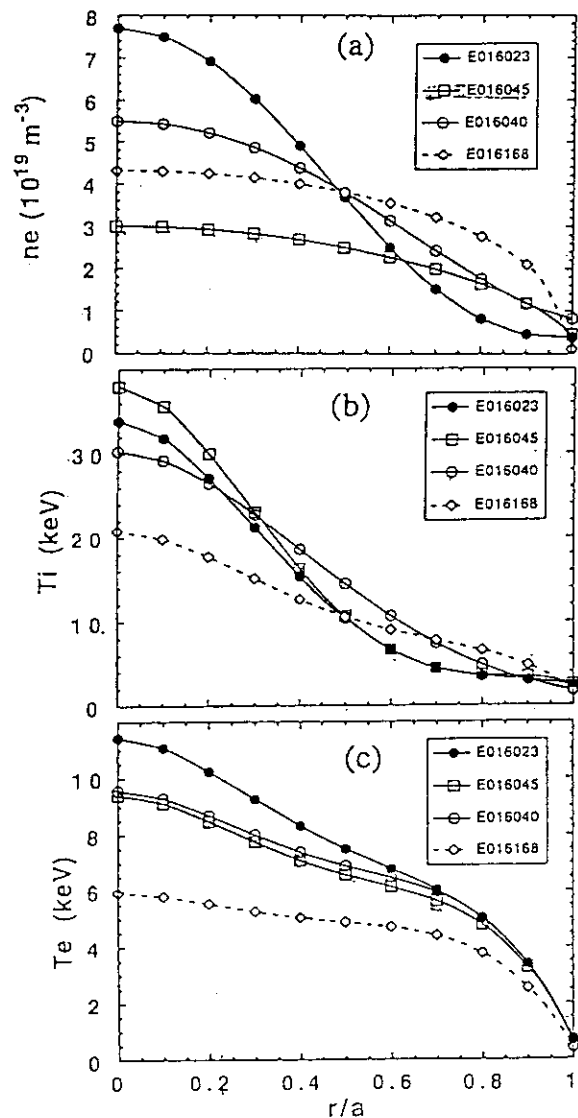


Fig. 5 Profiles of the electron density, the ion temperature, and the electron temperature of analyzed shots.

beam fusion reactions, which are beam-thermal and beam-beam reactions, are contributed more than 90% of the total reactivity.

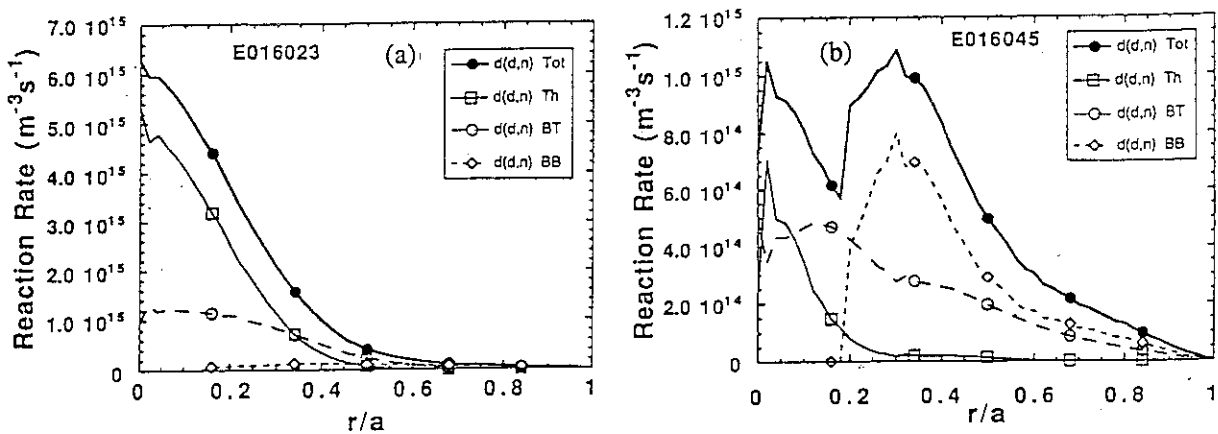


Fig. 6 Fusion reactivity profiles for E016023 and E016045.

The performance of equivalent D-T discharge was simulated by assuming D^0 beam injecting and 50/50 D/T target plasma using same temperatures and electron density profile, Z_{eff} , beam power, and other parameters as a comparable D-D discharge. The analysis results are summarized in Table 2. The ratio of $Q_{\text{DT}}/Q_{\text{DD}}$ is 170-200 except E016045, which is consistent with the result of TFTR supershots, 180 - 200.

Tables 2 Extrapolation to the equivalent D-T plasma

Shot No.	D-D plasma				Extrapolated D-T plasma			
	T-T	B-T	B-B	Q_{DD}	R_{DT}	T-T	B-T	Q_{DT}
E016023	53%	36%	11%	1.5×10^{-3}	2.0×10^{18}	55%	45%	0.25
E016039	36%	51%	13%	1.8×10^{-3}	1.8×10^{18}	38%	62%	0.29
E016045	5%	37%	58%	1.1×10^{-3}	6.7×10^{17}	9%	91%	0.10
E016040	30%	50%	20%	1.5×10^{-3}	1.6×10^{18}	33%	67%	0.21
E016168	38%	52%	10%	1.0×10^{-3}	1.7×10^{18}	38%	62%	0.20

T-T, B-T, and B-B represent thermal-thermal, beam-thermal and beam-beam reactions, respectively.

Conclusion

The neutron source intensity increases linearly with the heating power. The optimum density for the neutron yield is higher than that for the ion temperature. In a given I_p , the Q_{DD} increase with the I_i until the threshold for sawteeth. The neutron yield degrades significantly in the sawtooth regime. The peaked electron density profile was performed in the high neutron yield discharges. The thermal-thermal reactions are dominant in the high neutron yield discharges. On the other hand, the beam fusion reactions are dominant in the highest ion temperature discharge.

References

- [1] ISHIDA, S., et al., in Plasma Physics and Controlled Nuclear Fusion Research, IAEA-CN-56/A-3-5, Würzburg, 1992.
- [2] KAMADA, Y., et al., *ibid.*, IAEA-CN-56/A-7-13, Würzburg, 1992.

2.4 Equilibrium Analysis and Pressure Anisotropy of High Poloidal Beta Plasmas

T. Fujita, S. Tsuji and S. Ishida

1. Introduction

The equilibrium poloidal beta β_p^{eq} and the internal inductance l_i are obtained by the equilibrium analysis based on magnetic data outside the plasma when the plasma shape is an elongated one [1]. When the plasma pressure is not isotropic, we can define β_p^{\parallel} and β_p^{\perp} as $\beta_p^{\parallel} = 2\mu_0 \langle p^{\parallel} \rangle / \overline{B_p}^2$ and $\beta_p^{\perp} = 2\mu_0 \langle p^{\perp} \rangle / \overline{B_p}^2$, respectively. Here p^{\parallel} (p^{\perp}) is the plasma pressure parallel (perpendicular) to the magnetic field and $\overline{B_p} = \mu_0 I_p / (\int dl)$. Since $\beta_p^{\text{eq}} = (\beta_p^{\parallel} + \beta_p^{\perp})/2$ [2] while $\beta_p^{\text{dia}} = \beta_p^{\perp}$, the pressure anisotropy can be investigated by comparing β_p^{eq} and β_p^{dia} , where β_p^{dia} is the poloidal beta obtained by the diamagnetic measurement.

Usually, NB-heated plasmas in JT-60U have larger perpendicular pressure than the parallel one since 10 units of NB are injected nearly perpendicularly while 4 units are injected nearly tangentially. The equilibrium analysis was done and the pressure anisotropy was studied for high poloidal beta (β_p) plasmas in JT-60U [3]. The high β_p plasmas are suitable for the anisotropy study because its poloidal beta can be obtained with good accuracy due to the large value of β_p . The dependence of anisotropy on the plasma density and the tangential beam power fraction was investigated.

2. Analysis Method

We search an equilibrium which minimizes the deviation from the measured magnetic data. The current density profile is assumed as $j(\psi, R) = j_0(\beta_{c0}R/R_p + (1-\beta_{c0})R_p/R) \times (1 + \alpha\psi + \gamma\psi^2 - (1+\alpha+\gamma)\psi^3)$, where ψ is the normalized poloidal flux function ($\psi=0$ at the axis and $\psi=1$ at the surface). The above function has four parameters; j_0 , β_{c0} , α and γ . We scan β_{c0} and α to change β_p and l_i while j_0 and γ are determined so that I_p and $q(0)$ become specified values.

The currents of the poloidal field coils are fixed to the measured values except for the passive horizontal field coils, and four types of imaginary poloidal fields (uniform vertical field, uniform horizontal field and two kinds of quadrupole fields with different phases) are applied to keep the plasma position. The values of passive coil current and the imaginary fields are determined so as to minimize the deviation of calculated poloidal flux at flux loops from the measured one.

We scan β_{c0} and α to search those which minimize

$$\chi^2 = \chi_f^2 + \chi_b^2 + \chi_v^2$$

$$= \sum w_{fi}(\psi_i^{cal} - \psi_i^{exp})^2 + \sum w_{bi}(B_{pi}^{cal} - B_{pi}^{exp})^2 + w_v(B_v^{cal})^2$$

where w_{fi} , w_{bi} and w_v are coefficients to adjust the weight for each signal and B_v^{cal} is the magnitude of the imaginary uniform vertical field. Ideally, we must get the same solution if we use χ_f^2 or χ_b^2 instead of $\chi_f^2 + \chi_b^2 + \chi_v^2$. We found, however, that we get invalid solutions which have a very large value of $\Lambda = \beta_p^{eq} + l_i/2$ when we use χ_f^2 while we get relatively good solutions when we use χ_b^2 only. Therefore, in the analysis here, we omit χ_f^2 and use $\chi^2 = \chi_b^2 + \chi_v^2$ as the function to be minimized.

The value of $q(0)$ is unknown and we must specify its value. For typical cases, $q(0)$ was scanned between 0.75 and 2.75, but the values of χ^2 , β_p and l_i do not vary much; the change of χ^2 is less than $\pm 9\%$ of its mean value and the changes of β_p^{eq} and l_i are less than ± 0.03 and ± 0.05 , respectively. In the analysis here ($B_t = 4.4T$), we use $q(0) = 1.75$ for $0.9MA < I_p < 1.5MA$ and $q(0) = 1.5$ for $1.5MA < I_p < 2MA$.

3. Results

First we analyze the OH phase of high β_p experiments to check the accuracy of the code. Since the pressure is considered to be isotropic for OH plasmas except for runaway discharges, we have $\beta_p^{eq} = \beta_p^{dia}$ and we can get l_i as $l_i = l_i^{FBI} = 2(\Lambda^{FBI} - \beta_p^{dia})$. Here Λ^{FBI} is the value of Λ obtained by FBI (Fast Boundary Identification) code which determines the plasma position, the plasma shape, I_p and Λ by the filament method [4]. In Fig.1, β_p^{eq} , l_i and Λ obtained by the equilibrium analysis are compared with β_p^{dia} , l_i^{FBI} and Λ^{FBI} , respectively. Closed circles denote the data for OH plasmas just before NB injection, while squares about 1 second after the termination of NB. For the case before NB injection, β_p^{eq} is lower than β_p^{dia} by ≈ 0.04 and l_i is

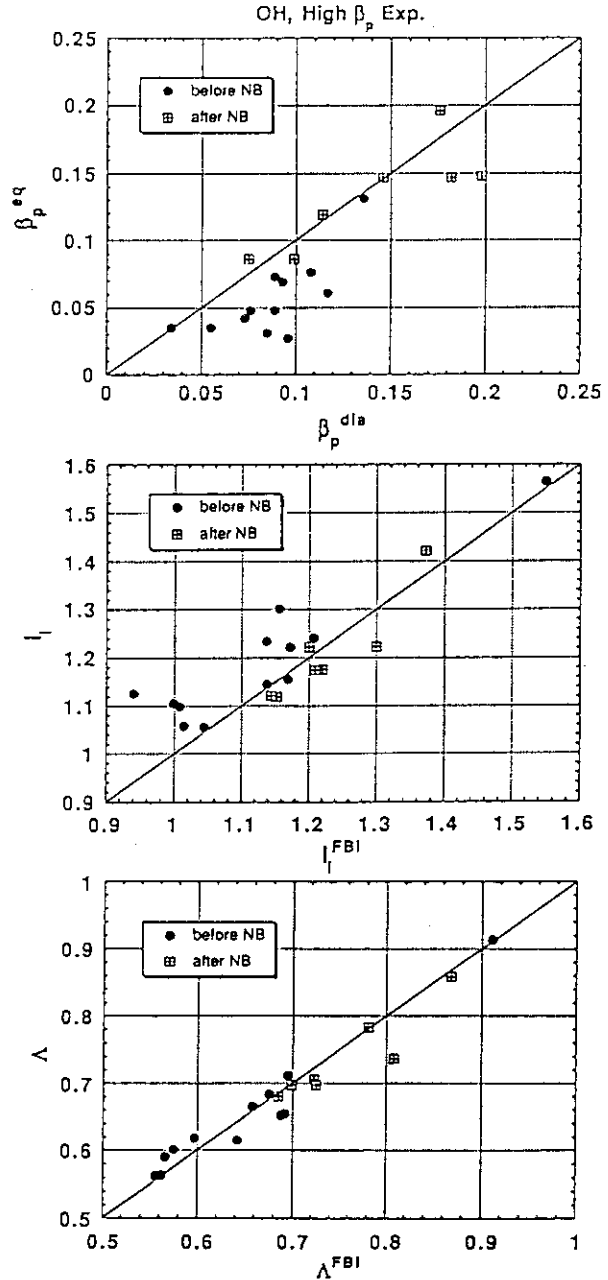


Fig.1. Results of equilibrium analysis on OH plasmas in high β_p experiments.

higher than l_i^{FBI} by ≈ 0.08 . For the case after the termination of NB, however, we find good agreement for both β_p and l_i . Therefore we use the obtained value of β_p^{eq} without correction, though we might underestimate it, and regard it as having a statistical error of 0.04, which corresponds to the error of $\beta_p^{\text{eq}}/\beta_p^{\text{dia}}$ of 0.02 at $\beta_p^{\text{dia}}=2$.

As for NB phase, the analysis has been done for almost all shots of high β_p experiments in 1992. The time was chosen when W^{dia} reaches its maximum. Obtained beta values are compared with β_p^{dia} in Fig.2. For high β_p experiments in April, we find $\beta_p^{\text{eq}}=0.85\beta_p^{\text{dia}}$, which means that $\beta_p^{\text{tot}}=0.90\beta_p^{\text{dia}}$ or that W^{dia} is about 10% overestimation of the true total stored energy. The pressure anisotropy is smaller for high β_p experiments in August; $\beta_p^{\text{eq}}=0.93\beta_p^{\text{dia}}$. This is because the tangential NB was injected in August in addition to the perpendicular NB while only the perpendicular NB was used in April. Dependence of $\beta_p^{\text{eq}}/\beta_p^{\text{dia}}$ on the tangential beam power fraction, $P_{\text{NB}}(\text{tang})/P_{\text{NB}}(\text{total})$, is plotted in Fig.3 for the data in August. The value of $\beta_p^{\text{eq}}/\beta_p^{\text{dia}}$ becomes larger with the increase of $P_{\text{NB}}(\text{tang})/P_{\text{NB}}(\text{total})$. We get $\beta_p^{\text{eq}}>\beta_p^{\text{dia}}$ for the case that only the tangential NB is injected, though such cases are not included in the high β_p experiments.

The total stored energy W^{tot} is obtained as $W^{\text{tot}}=(W^{\text{dia}}+2W^{\text{eq}})/3$, where W^{eq} is the stored energy by the equilibrium analysis. In Fig.4, W^{tot} is compared with W^{app} which is the approximate total stored energy obtained from Λ^{FBI} assuming that l_i does not change during beam injection [5] for the data in August. We find good agreement between W^{tot} and W^{app} , which reflects the fact that the change of l_i is small during

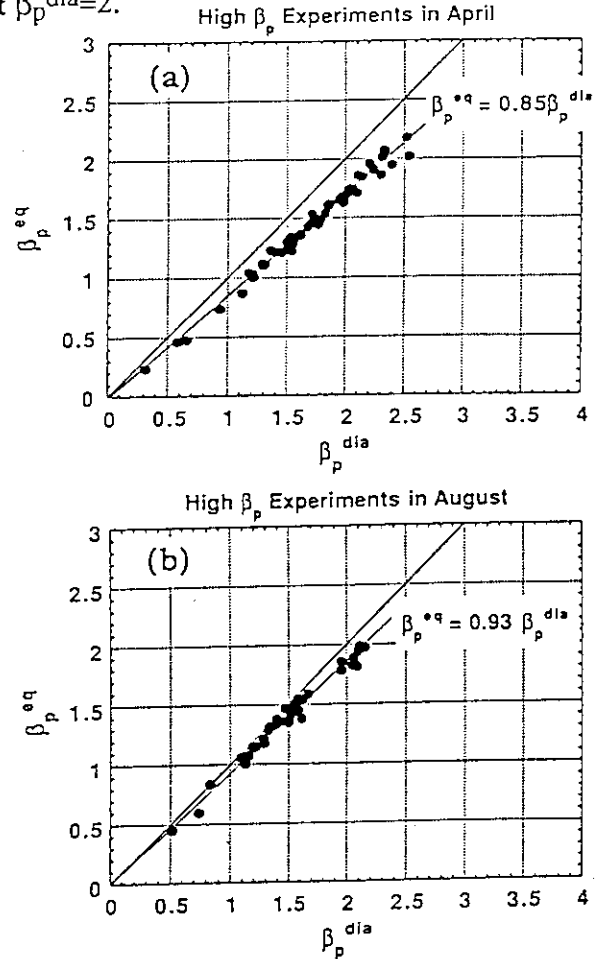


Fig.2. β_p^{eq} as a function of β_p^{dia} for high β_p experiments (a) in April and (b) in August.

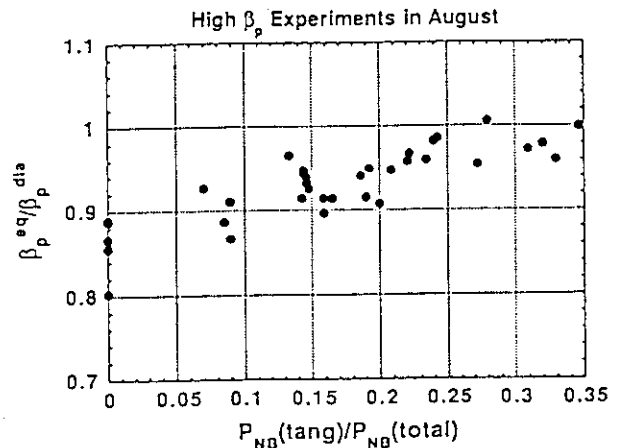


Fig.3. Dependence of pressure anisotropy on the tangential beam power fraction for high β_p experiments in August.

beam injection. Note that the time analyzed in Fig.4 is almost less than 1 second after the start of beam injection. When we treat the case of longer NB pulse operation, the change of l_i cannot be neglected and W^{app} will be inaccurate.

When only the perpendicular beam is injected, the magnitude of the pressure anisotropy reflects the beam component fraction in the total stored energy. This fraction will be larger when the beam slowing-down time gets longer if the bulk energy confinement time is same. Figure 5 shows the dependence of the pressure anisotropy on the plasma density for the data in April. We find that the pressure anisotropy decreases with the increase of density, which is considered to correspond to the decrease of the fraction of beam stored energy due to shortening of the beam slowing-down time.

4. Summary

The equilibrium analysis was done for high β_p plasmas to obtain β_p^{eq} and l_i . By comparing β_p^{eq} with β_p^{dia} , the pressure anisotropy was investigated. The error of β_p^{eq} is estimated to be about 0.04 by the results of analysis of OH plasmas. For high β_p plasmas in April, $\beta_p^{eq}/\beta_p^{dia}$ is about 0.85 and this ratio approaches to unity with the increase of the plasma density. For high β_p plasmas in August where the tangential beam was injected, $\beta_p^{eq}/\beta_p^{dia}$ increases with the tangential beam power fraction in the total beam power.

References

- [1] LAO, L.L., St.JOHN, H., STAMBAUGH, R.D., et al., Nucl. Fusion **25** (1985) 1611.
- [2] COOPER, W.A., WOOTTON, A.J., Plasma Phys. **24** (1982) 1183.
- [3] ISHIDA, S., NISHITANI, T., KOIDE, Y., et al., Section 2.1 in this report.
- [4] SWAIN, D.W., NEILSON, G.H., Nucl. Fusion **22** (1982) 1015.
- [5] ISHIDA, S., KOIDE, Y., FUJITA, T., et al., Section 2.2 in this report.

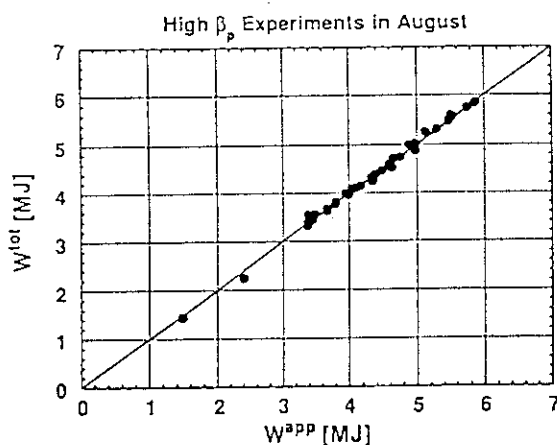


Fig.4. Comparison of W^{tot} with W^{app} for high β_p experiments in August.

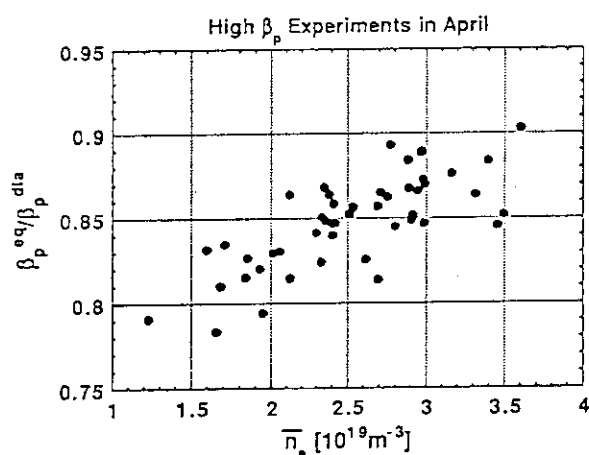


Fig.5. Dependence of pressure anisotropy on the plasma density for high β_p experiments in April.

2.5 Beta Limits and β_p Collapses for High β_p Plasmas

S. Ishida, Y. Neyatani, Y. Kamada and T. Ozeki

1. Introduction

The stability of the high pressure plasmas under a large bootstrap current fraction is crucially important to determine whether the reactor scenario operating for high β_p regime is workable. Although the empirical Troyon limit with a Troyon factor of 2.8-3.5 [1] is widely adopted in conceptual designs of a tokamak reactor, its credibility is questionable for the high β_p plasmas because of the view that the broadened or hollowed current profile due to a large bootstrap current fraction leads to lower limits of the Troyon factor; noted that the Troyon factor is defined as $g = \beta_t[\%]/(I_p[\text{MA}]/a[\text{m}]B_t[\text{T}])$.

In JT-60, high β_p plasmas have revealed a fast β collapse dubbed as a β_p collapse leading to lower limits of the Troyon factor at $\beta_p \sim 3$ with a large bootstrap current fraction up to $\sim 80\%$ of the plasma current, which can be explained by kink-ballooning limit [2]. In JT-60U, the enhanced confinement phase of the high β_p discharges was in most cases terminated by the β_p collapses, while the high pressure plasmas stayed near the boundary of the first regime of MHD stability. With increasing the plasma current, some of the β_p collapses were found to be followed by major disruptions. In this paper, the operational beta regime and the ballooning-like precursor oscillations before the β_p collapses in JT-60U are described.

2. Operational Beta Regime

Operational region on the g versus $\epsilon\beta_p$ diagram for the HPEC regime in JT-60U is shown in Fig.1 in comparison with the JT-60 high β_p regime, where the B_t was in the ranges of ~ 2.7 -4.4 T for JT-60U and ~ 4.7 T for JT-60. High β_p discharges in JT-60U and JT-60 have confirmed an operational β limit existing substantially below the Troyon limit, at which the discharges encountered the β_p collapse. This β limit appears to depend on both the Troyon factor and $\epsilon\beta_p$, as the attainable Troyon factor decreases with $\epsilon\beta_p$ below an approximate limit line of $g \cdot \epsilon\beta_p \sim 1.1$. The attainable $\epsilon\beta_p$ values were clearly decreased with the I_i as discussed in Ref. of [3]. This may provide a possible reason for scattering of the data including β_p collapses. It can be said that the achievable plasma performance has been determined by the MHD stability limit, not by transport or by plasma-wall interaction such as a carbon bloom.

A maximum Troyon factor reached $g=2.3$ for a lower B_t discharge with $I_p=1.1$ MA, $B_t=3.2$ T and $q_{eff}=6.3$ ($q^*=4.3$), in which a high enhancement factor of $H=\tau_E/\tau_E^{L-mode}=2.5$ was also obtained; q_{eff} is the effective MHD safety factor and q^* is the cylindrical equivalent safety factor defined as $q^* = \pi a^2 B_t (1+\kappa^2)/(\mu_0 R_p I_p)$. Further reduction of the toroidal field to 1.5 T lead to significant increase in the Troyon factor reaching the Troyon limit region as shown in Fig.1. Attainment of these discharges near the operational beta region of SSTR would increase the prospects for the high g operation at high β_p . Details of the high g regime are discussed in Ref. of [4].

3. Non Disruptive β_p Collapse

The β_p collapse characterized by a large amplitude partial or incomplete collapse with a fast collapse time was first discovered in JT-60 [2], and turned out to occur in the similar beta region in JT-60U. So far, the β_p collapses were not followed by a major disruption (*i.e.* non disruptive β_p collapse) for the high q operation with $q_{eff} > 6.1$ ($q^* > 4.5$). Figure 2 shows time evolution of the local T_e fluctuation profile prior to a β_p collapse measured by the 20-channel ECE grating polychromator with a digitizing time, Δt , of 20 μs ; the plasma parameters were $I_p = 1.2$ MA, $B_t = 4.4$ T, $q_{eff} = 8.1$ ($q^* = 5.6$), $T_i(0) \sim 24$ keV, $T_e(0) \sim 6.5$ keV, $\bar{n}_e \sim 3 \times 10^{19} \text{ m}^{-3}$, $\epsilon\beta_p = 0.48$, $g = 1.8$ and $H = 2.7$. Here, the T_e fluctuation level is defined as $\Delta T_e / T_e = (\text{fluctuation amplitude}) / (\text{signal average})$. The fluctuation profiles near the midplane in Fig.2 shows that; 1) the precursor oscillations are localized near the inversion location at the β_p collapse, 2) significant inside-outside asymmetry is observed, exhibiting a ballooning feature at the bad-curvature side. The frequency of the fluctuations was ~ 7 kHz. Here, it should be noted that the fluctuations are localized near a half of the minor radius in the low field side, but the peripheral region looks stable in contrast to the following disruptive β_p collapse.

While the Mirnov coil data were not taken, the toroidal and poloidal mode numbers, n and m , respectively, were inferred around the region with the peak fluctuation level from the phase relation between the fluctuation signals of the vertical FIR interferometer with $\Delta t = 5 \mu s$ and the grating polychromator; the toroidal separation of the interferometer at $R = 3.551$ m and the grating polychromator (Ch.16) at $R = 3.548$ m and the poloidal separation of the grating polychromator and the midplane of the plasma are 37° and $\sim 17^\circ$, respectively. The identified mode number was $(m, n) = (4, 3)$. In the other discharge with $I_p = 1.3$ MA, the (3,2) mode was identified with the similar inside-outside asymmetry. It is noted that strong ECE bursts due to emission from nonthermal electrons normally occur during the β_p collapse to conceal the picture during the β_p collapse.

Stability analyses using the ERATO-J code for the above plasma just before the β_p collapse indicate that low- n ideal kink-ballooning modes can be unstable, assuming an flat q profile with the q_0 above unity [5]. Using the BETA code, stability analyses for high- n ballooning modes were also carried out. The experimental pressure gradient was found to be marginal over a region of $r/a \lesssim 0.4$ against the boundary of high- n ballooning limits.

4. Disruptive β_p Collapse

With increasing the plasma current up to 1.9 MA, major disruptions have for the first time occurred following some of the β_p collapses in the August run of 1992. The major disruptions were observed for discharges at $q_{eff} \sim 6.1$ ($q^* \sim 4.5$) of $I_p = 1.6$ MA with a fast T_e decay time of the order of 100 μs . So, it is emphasized that the β_p collapse can induce a major disruption (*i.e.*, disruptive β_p collapse) in the lower q operation.

Figure 3 shows typical waveforms and the T_e fluctuation profiles for precursor oscillations before the major disruption; the plasma parameters just before the disruption are $I_p = 1.6$ MA, $q_{eff} = 6.1$ ($q^* = 4.5$), $T_i(0) \sim 32$ keV, $T_e(0) \sim 11$ keV, $\bar{n}_e \sim 2 \times 10^{19} \text{ m}^{-3}$, $\epsilon\beta_p = 0.33$, $g = 1.6$ and $H = 2.4$. The ballooning-like internal mode is seen to be localized around $r/a \sim 0.6$, similar to the above non-disruptive β_p collapse. In addition, the peripheral mode is also seen to be largely

excited, whose amplitude increases with the minor radius in the peripheral region of the plasma. The disruptive β_p collapse is characterized by the simultaneous excitation of the peripheral mode as well as the ballooning-like mode. This may suggest that the suppression of the peripheral mode can be effective for avoidance of the disruption followed by the β_p collapse.

The mode number is identified to be $(m,n)=(4,2)$ from the interferometer and the polychromator; the m is clearly even. However, the Mirnov coil data with $\Delta t=40 \mu s$ suggest a different toroidal mode number of $n=1$ with the same frequency as the ECE data. As the inconsistency between the ECE and Mirnov coil data is an open question at present, so further analyses and detailed measurements is required for the mode identification.

5. Conclusion

The operational beta regime is bounded by the β_p collapses, in which the achievable limits depend on both g and $\epsilon\beta_p$ ($g \cdot \epsilon\beta_p \lesssim 1.1$). Thus it leads to lower limits of the Troyon factor for high β_p operation. The termination of the enhanced confinement phase is elucidated to be caused by β_p collapses occurring at a stability limit for ideal low- n kink-ballooning modes. The precursor oscillations show the ballooning-like inside-outside asymmetry, the growth rate of which appears to be slow, or of a resistive time scale, rather than that of ideal MHD.

Disruptive β_p collapses have been first observed at $q_{eff}=6.1$ ($q^* \sim 4.5$) in JT-60U, for which the T_e decay time was as fast as the order of $100 \mu s$. Profile measurements of the T_e fluctuations exhibited that the additional peripheral modes were significantly excited before the disruptive β_p collapse, contrary to the case of non-disruptive β_p collapse. In high β_p operation, the suppression of the peripheral modes could be effective for avoidance of the major disruption following the β_p collapse in a lower q region.

References

- [1] STRAIT, E.J., et al., Phys. Rev. Lett. 62(1989)1282.
- [2] ISHIDA, S., et al., Phys. Rev. Lett. 68(1992)1531.
- [3] ISHIDA, S., et al., Section 2.2 in this report.
- [4] KAMADA, Y, et al., Section 2.6 in this report.
- [5] OZEKI, T., et al., Section 8.3 in this report.

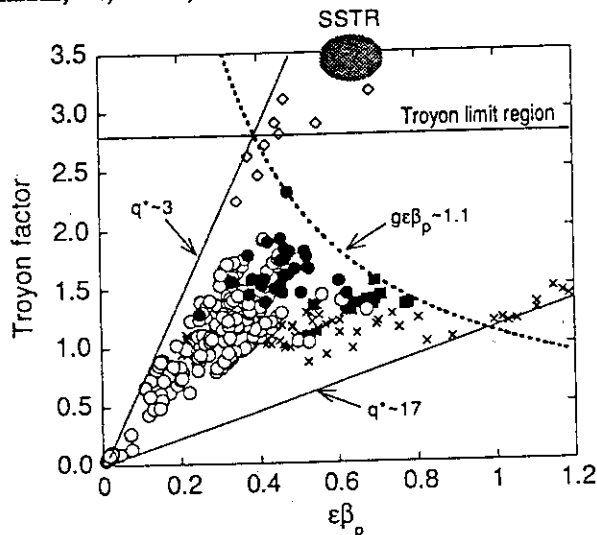
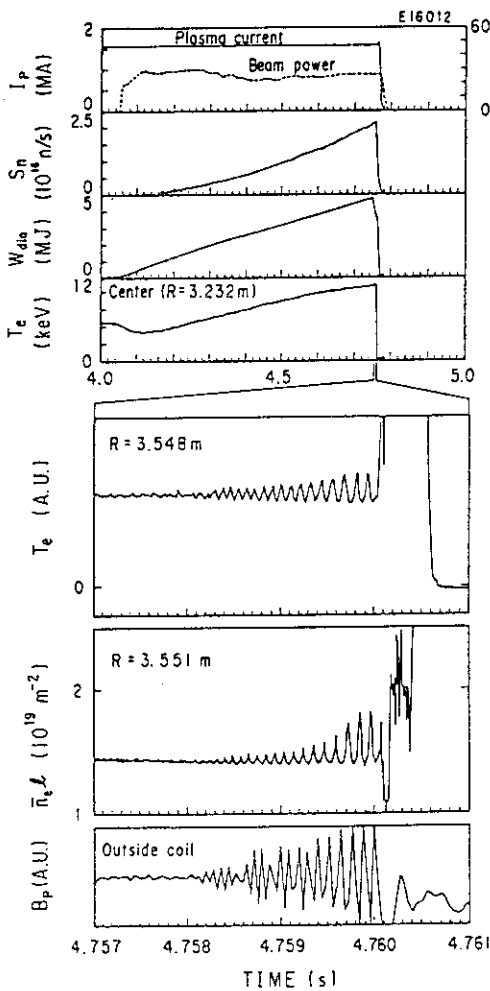
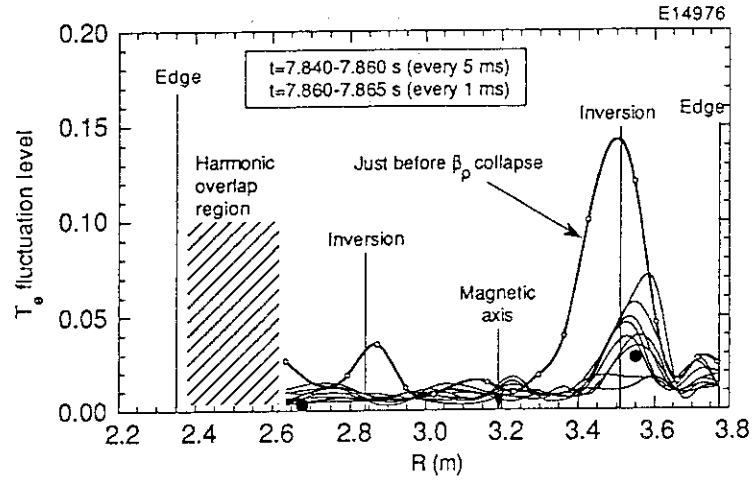
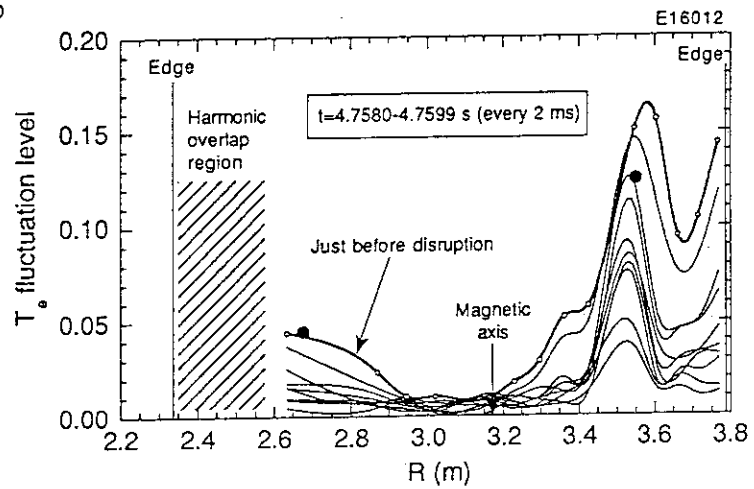


Fig.1 Troyon factor as a function of $\epsilon\beta_p$ for high β_p experiments in JT-60U (open and closed circles) and JT-60 (crosses and closed squares); the discharges suffered by β_p collapses are distinguished by the closed circles and square from others. Open diamonds show the data with $B_t \sim 1.5$ T. The regions of SSTR operation and the Troyon limit ($g=2.8-3.5$) are also indicated.

Fig.2 T_e fluctuation profiles for precursor oscillations of a non-disruptive β_p collapse. The data plotted every 5 ms for $t=7.840-7.860$ s and every 1 ms for $t=7.860-7.865$ s. Each fluctuation level is estimated in average for 200 μ s. The closed circles indicate the fluctuation level of the line density at $t=7.8648$ s.



(a)



(b)

Fig.3 Precursor oscillations of a disruptive β_p collapse: (a) Waveforms of the I_p , S_n , W_{dia} and central T_e with expanded waveforms of the ECE signal at $R=3.548$ m (Polychromator Ch.16), the FIR laser interferometer at $R=3.551$ m and the Mirnov signal; (b) T_e fluctuation profiles for the precursor oscillations. The data are plotted every 2 ms for 4.7580-4.7599 s. Each fluctuation level is estimated in average for 100 μ s. The closed circles indicate the fluctuation level of the line density at $t=4.7598$ s.

2.6 High Normalized β Experiments

Y.Kamada, M.Kikuchi, Y.Neyatani, S.Ishida and H.Ninomiya

1. Introduction

The purpose of this study is to contribute to the concept of steady state tokamak reactors by expanding our operation region toward a high $\beta_N (= \beta_t(\%) / (I_p(\text{MA})/a(\text{m})B_t(\text{T}))$ regime. This study is also a part of the systematic study of 'MHD and confinement' (Sec.1.9). To establish the consistent scenario of the steady state reactor with a high fraction of bootstrap current [1], it is necessary to prove experimentally that the favorable core plasma performance (having high $\beta_N \sim 3.5$, high $\beta_p \sim 2-3$ and high H-factor ~ 2 at the same time) can be sustained steadily with a realistic divertor condition. In turn, from the MHD point of view, it is important to study the β -limit for a relatively high aspect ratio of 4. In particular, the suppression of β_p -collapses (Sec.2.3) and sustainment of the steady high- β_p plasma are the key issues. As the first step, we report the results of high- β_N experiments. The condition of $\beta_N=3.5$, $\beta_p=3$ and H-factor=2 was obtained in a 0.6MA ELMy H-mode discharge. The ELM activity is important to control impurity accumulation and particle and heat flux into the divertor region. The sudden β_p -collapse was suppressed by relatively broad pressure profiles $p(r)$ and peaked current profiles $j(r)$. However, the steady state has not been obtained because of appearance of $m/n=2/1$ mode. Definitions of β_p , β_N , β_t and W^{dia} are the same as those used in Sec.2.2.

2. Discharge Conditions

To describe the strategy of the high- β_N experiment, we start from the review of the two typical modes with good confinement in JT-60U, namely high- β_p mode and high- T_i H-mode.

*high- β_p mode (see Secs.2.1-2.5):

The H-factor and β_p -value reached to ~ 3 and ~ 3 , respectively. The key operational points are i) small volume of $V_p \sim 50\text{m}^3$, ii) strong central heating with perpendicular NB and iii) relatively high- q_{eff} with low- I_i to avoid sawteeth. The key plasma properties are i) a highly peaked $p(r)$ ii) a broad $j(r)$. iii) And, to avoid sawteeth, the maximum target- I_i should be smaller than the I_i -threshold for the appearance of sawtooth ($I_i=1.1-1.2$ for $q_{\text{eff}}=4-8$; see Sec.8.5).

*high- T_i H-mode (see Sec.1):

The H-factor is ~ 2 for ELM-free and ~ 1.6 for ELMy H-modes. The key operational points are i) relatively large volume of $V_p \sim 70-80\text{m}^3$, ii) relatively high I_p (low- q_{eff}) with high- I_i to increase H-factor. The key plasma properties are i) broad peaked $p(r)$. ii) Even the plasma is sawtoothing, good confinement can be achieved when the sawtooth period is long enough.

To increase the attainable values of β_N , theories and experimental results suggest that a broad $p(r)$ with a peaked $j(r)$ is favorable [2]. In practice, for the 'high- β_p mode' in JT-60U reported in Sec.2.2, the limit of β_p was increased by increasing I_i . Based on the above background knowledge, we adopted the operation condition for the high- β_N discharges as follows:

i) The basic philosophy is the combination of high- β_p mode and H-mode to keep good confinement and high values of β .

ii) To achieve a broad $p(r)$, the heating profile was broadened, for which $V_p = 50-60 \text{ m}^3$ (larger than V_p for high- β_p mode) was selected to make the trajectory of perpendicular NB off-axis and also tangential off-axis NB were injected (up to 7MW).

iii) To achieve a peaked $j(r)$, the target- l_i was increased up to 1.5. Since high l_i -values inevitably introduce sawteeth, good confinement cannot be expected in the high- β_p mode.

On the other hand, in H-mode, good confinement can be achieved when the sawtooth period is long enough.

The plasma configuration is given in Fig.1 and the comparison of the discharge regions for high- β_p , H-mode and high- β_N is listed in Table I.

Table I Comparison of Typical Parameters for high- β_p mode, H-mode and high- β_N

	high- β_p	H-mode	high- β_N
B_t (T)	4-4.4	1.7-4	1.5-1.6
I_p (MA)	1-2	1.5-4	0.6-0.9
q_{eff}	4-12	2.5-6	4-8
l_i	0.8-1.2	0.9-1.3	1.3-1.5
$p(r)$	~ peaked	~ broad	~ medium
V_p (m^3)	~ 50	70-80	50-60
NB	perp. central	perp.+para.	perp.+para.
H-factor	<3	<2.2 (ELM-free)	<2.3 (ELMy)

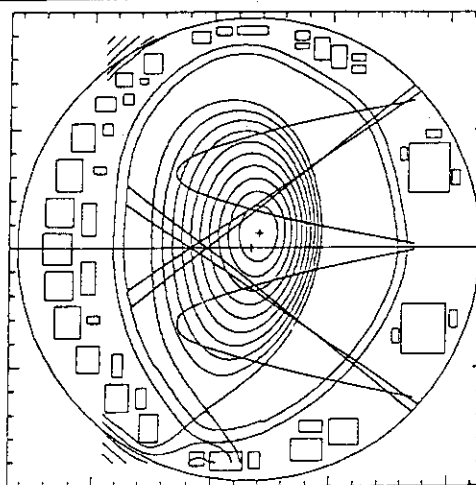


Fig.1: Typical plasma configuration for the high- β_N experiments. Trajectories of NBI are shown by solid lines.

3. Characteristics of High- β_N discharges

Fig.2 shows two cases of high- β_N discharges with (a) medium q_{eff} and (b) high q_{eff} . In Fig.2(a) ($I_p=0.9\text{MA}$, $B_t=1.6\text{T}$, $q_{\text{eff}}=4.5$, $\beta_p=1.8$ and $\beta_N=2.5$ at 8.25s), NB power was increased gradually. H-transition is observed at $t=6.15\text{s}$ and HLMy H-phase continues till the end of the NB pulse. Figure 2(b) shows the discharge with the highest β_N of 3.5 with $\beta_p=3$ and H-factor=2.3 ($t=5.5\text{s}$) ($I_p=0.6\text{MA}$, $B_t=1.6\text{T}$, $q_{\text{eff}}=7.8$). The ELMy H-phase starts from $t=5.08\text{s}$ and the highest stored energy W_{dia} is limited by an MHD activity at $t=5.6\text{s}$ which seems to have a mode number $m/n=2/1$ (see Sec.8.2). Before the MHD activity, W_{dia} seems to be saturating which suggests a possibility to sustain the high- β_N with high- β_p steadily by the control of NB power. The T_i profile at $t=5.5\text{s}$ is given in Fig.3 where highly peaked $T_i(r)$ is observed. Figure 4 shows the soft X ray emission profile $SX(r)$ (line integrated) for the discharge shown in Figs.2(b) and 3. For a reference, $SX(r)$ for a high- β_p discharge with the same q_{eff} is plotted, the reference profile corresponds to that just before the β_p -collapse at $\beta_p=2$. This comparison suggests that $p(r)$ for the high- β_N discharge is broader than that for the high- β_p discharge as expected.

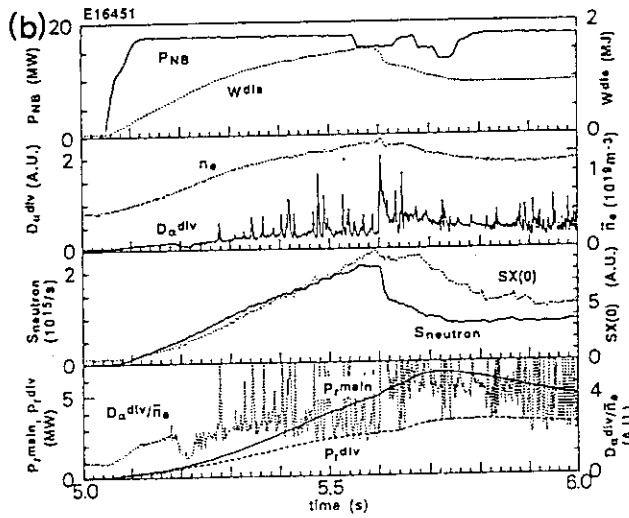
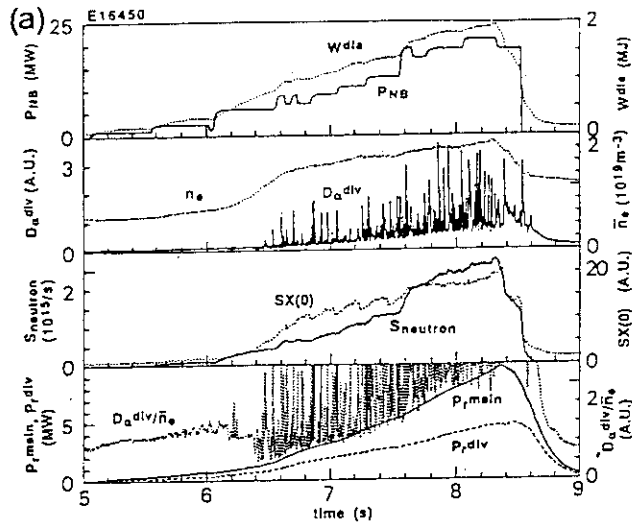


Fig.2 : Two cases of high- β_N discharges with medium q_{eff} (E16450) and (b) high q_{eff} (E16451).

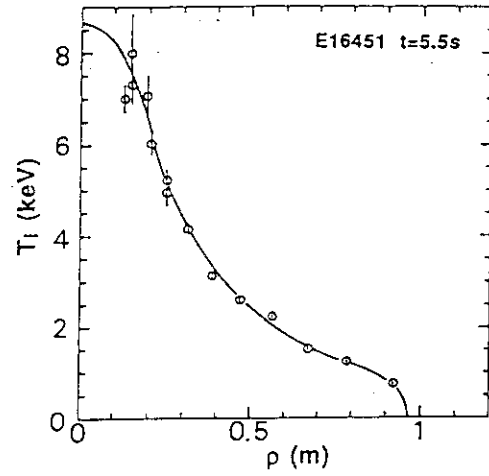


Fig.3: T_i profile at $t=5.5s$ for E16451

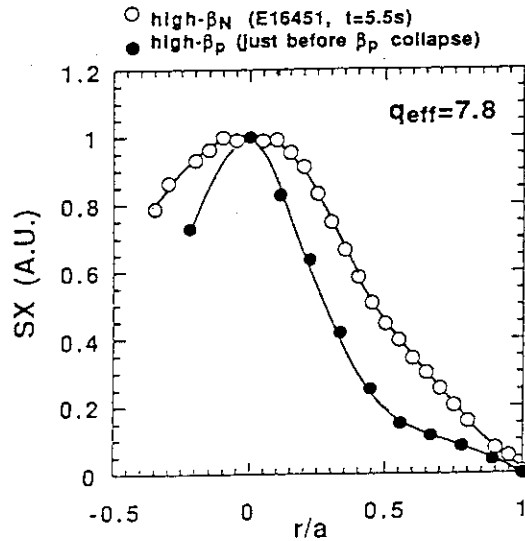


Fig.4: Comparison of $SX(r)$ between E16451 at $t=5.5s$ and a high- β_p discharge just before the β_p -collapse with the same q_{eff} of 7.8.

3. Achieved β_N , β_p and H-factor

Figure 5 shows the achieved β_N , $\epsilon\beta_p$ and H-factor for H-mode, high- β_p mode and high- β_N discharges. The closed circles correspond to the β_p -collapse in the high- β_p mode. By the broadening of $p(r)$ and peaking of $j(r)$ (see Fig.6), attainable β_N and $\epsilon\beta_p$ were increased for a given q_{eff} compared to the high- β_p mode. The important results is that H-factor of ~ 2 is obtained with the ELMy high- β_N H-mode which is favorable to the control of impurity and divertor plasma conditions. To discuss the effects of $j(r)$, Fig.6 plots the dependence on l_i . Here the l_i -values of the target OH plasma is used for high- β_p and high- β_N discharges because the precise evaluation of l_i at high- β_p has not been completed. Because of high electron temperature, the l_i value may be almost unchanged during the short time scale (for high- β_N (high- β_p) data were taken at less than 0.8s (1.2s) after the start of NB injection). In Fig.6(a), higher values of β_N is achieved at higher l_i which is much higher than the threshold l_i value for the appearance of sawteeth (Sec.8.5). The MHD modes responsible for limiting β_N is different

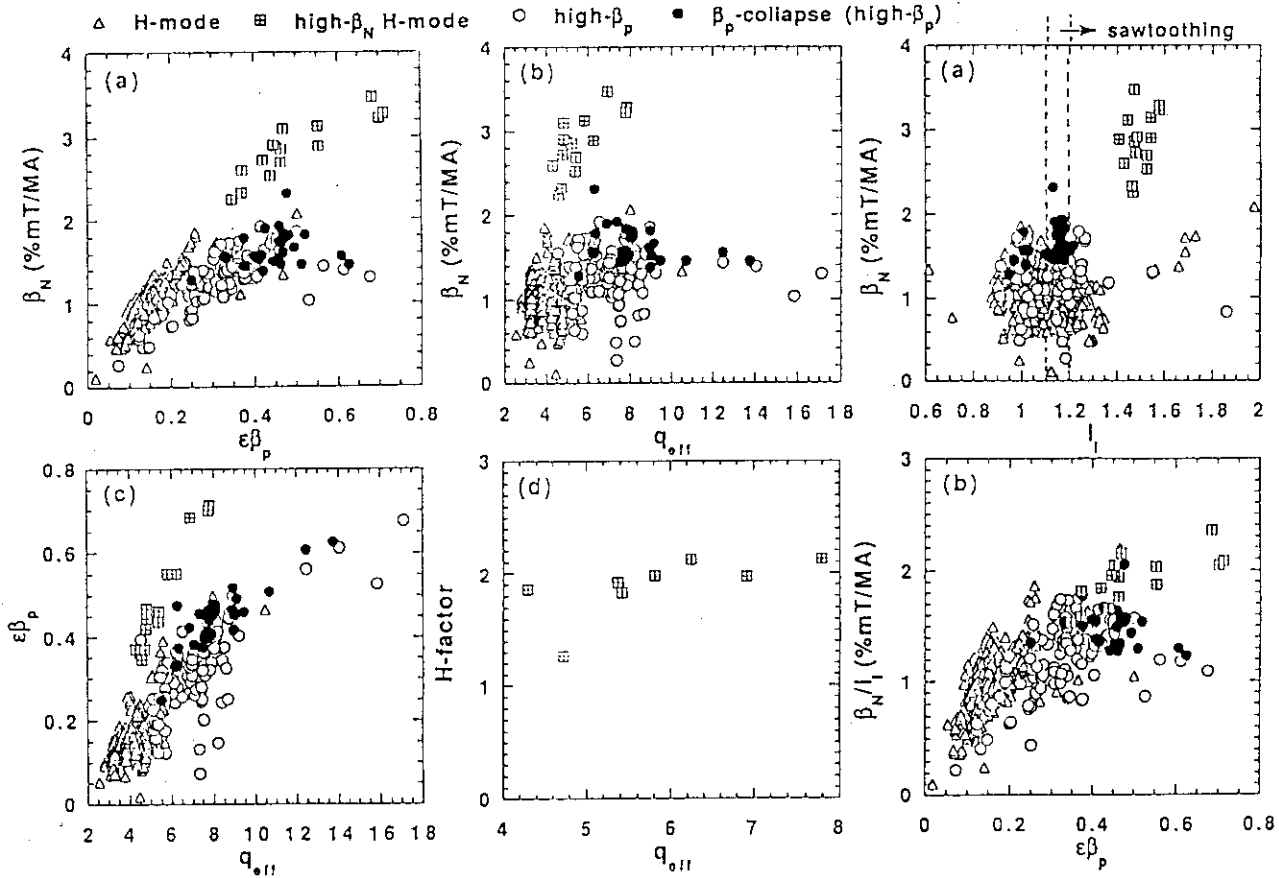


Fig.5: Achieved β_N , $\epsilon\beta_p$ and H-factor for H-mode, high- β_p mode and high- β_N discharges. The closed circles correspond to the β_p -collapse in the high- β_p mode.

Fig.6: β_N vs. l_i and β_N/l_i vs. $\epsilon\beta_p$ for H-mode, high- β_p mode and high- β_N discharges.

in H-mode, high- β_p and high β_N . In usual H-mode, ELMs limit the confinement. In high- β_p mode, $m/n=3/2$ and $4/2$ pressure driven modes (kink-balloon; see Secs.2.5,8.3,8.4) are observed. In high- β_N discharges, $m/n=2/1$ is observed to be dominant (see Sec.8.2). Also the mode structure is changing with increasing β_p (See Secs.2.5, 8.2,8.4). Therefore it cannot be concluded simply that the higher l_i is better for increasing β_N , because of the difference in dominant MHD modes in different discharge modes. In Fig.6(b), the maximum β_N/l_i is around 2 which is lower than the limiting value of 4 in DIII-D [2]. The reason of the lower limit may be that the present limit in JT-60U is that caused by internal medium m/n MHD modes and not caused by high- m/n ballooning modes or surface modes. If these medium m/n modes can be stabilized by control of $j(r)$ and $p(r)$, the maximum β_N and β_p may be increased. The further experimental study on the β -limit in JT-60U is required to clarify the effects of high aspect ratio, low triangularity (~ 0.2) and a wide vacuum region between separatrix and the resistive shell.

References

- [1] KIKUCHI, M., Nucl. Fusion 30 (1990) 265.
- [2] TAYLOR, T.S., et al., in Plasma Physics and Controlled Nuclear Fusion Research. (Proc.13th Int. Conf., Washington, 1990) Vol. I, IAEA, Vienna, (1991) p.177.

2.7 Estimation of the Bulk Ion-temperature from the Measured Carbon-temperature Using a Simple Model for the 38 keV Plasma

Y. Koide, M. Azumi, A. Van Blokland, M. Kikuchi

A. Sakasai, N. Asakura

1. Introduction

A high central ion temperature of 38 keV was measured by CXRS (charge exchange recombination spectroscopy) using carbon spectrum in high β_p experiments. Since the deuterium temperature, not the carbon temperature, is essential for the fusion reaction, a simple estimation of the bulk temperature was carried out especially for the shot with 38 keV.

2. Experimental Conditions

In this paper, JT-60U was operated in a divertor configuration, with a plasma current I_p of 1.8 MA, a toroidal field B_t of 4 T, a major radius R_p and a minor radius a_p of 3.1 m and 0.9 m, respectively, and an ellipticity of 1.7, an effective safety factor q_{eff} of 5.4, plasma volume of 53 m³. Figure 1 shows the evolution of the discharge, where the central ion temperature $T_i(0)$ reached 38 keV (E16045). Deuterium neutral beams were injected for the intensive central heating during $t=4.5$ to 6.5 s, the energy and the power of which were 90 keV and 23 MW, respectively. $T_i(0)$ increased gradually and reached 40 ± 5 keV at $t=5.19$ s, followed by an abrupt decrease. The displayed $T_i(0)$ in this figure is the apparent carbon temperature, which is not corrected for the energy dependence of the excitation cross-section $\langle\sigma v\rangle$ induced by the charge-exchange-recombination reaction. The corrected carbon temperature, where the $\langle\sigma v\rangle$ is given in ref.[1] was used for the calculations, was 38 keV. The stored energy, W_{dia} , measured with the diamagnetic loop and the neutron emission rate showed slight saturation after the drop of $T_i(0)$ and took their maxima at $t=5.4$ s when $T_i(0)$ had already dropped to 23 keV. The line-average electron density, \bar{n}_e , measured along the chord of $0.6 a_p$ was as low as $1.5 \times 10^{19} \text{ m}^{-3}$ when $T_i(0)$ took its maximum, where $n_e(0)$ was estimated to be $3 \times 10^{19} \text{ m}^{-3}$ by the combination of the equilibrium code and the measured value of $\int n_e dl$. The fact that $T_i(0)$ was at its maximum at the different time from those of the W_{dia} and the neutron emission rate may indicate the very peaked T_i profile and a large contribution of beam component to the neutron production (See ref.[2]).

3. Estimation of Bulk Ion Temperature

The transition of CVI ($n=8-7$) at 529 nm was used for the measurement of ion temperature. The measured spectrum, in which the Doppler width corresponded to 40 keV, is shown in

Fig.2. Although the measured wavelength region (the abscissa of Fig.2) covers the energy range of ± 230 keV for carbon ions, it corresponds to ± 38 keV for deuterium ions taking into account their mass ratio. Since the injected beam energy is 90 keV and n_e is low, the carbon velocity distribution can be distorted via the interaction with the slowing-down ions. Unfortunately, as seen from Fig.2, it is difficult to discuss such distortion due to the relatively large scatter of the data, which mainly comes from the attenuation of neutral beams in the central region and the small signal to noise ratio due to the broadening of the spectrum. However, the velocity distribution calculated using non-linear Fokker-Planck code [3] shows that there is no large deviation in carbon-ion velocity distribution from Maxwellian shape in the measured energy range. The error bar for the estimated T_i based on the 1- σ standard deviation becomes as large as ± 5 keV because the deduced ion temperature is sensitive to the Doppler width (T_i is proportional to the square of the Doppler width).

Next we discuss the estimation of the bulk ion temperature from the measured carbon temperature. Here we made the following assumptions for simplicity: velocity distributions of deuterium ions, impurity ions and electrons are all isotropic Maxwellians and carbon is the only impurity. We considered the energy balance for stationary conditions with negligible ohmic input,

$$g_d S_{NB} = \frac{3}{2} n_d \frac{T_d - T_z}{\tau_{eq}^{dz}} + \frac{3}{2} n_d \frac{T_d - T_e}{\tau_{eq}^{de}} + \frac{3}{2} n_d \frac{T_d}{\tau_E^d} \dots (1-1)$$

$$g_z S_{NB} = \frac{3}{2} n_z \frac{T_z - T_d}{\tau_{eq}^{zd}} + \frac{3}{2} n_z \frac{T_z - T_e}{\tau_{eq}^{ze}} + \frac{3}{2} n_z \frac{T_z}{\tau_E^z} \dots (1-2) ,$$

where d and z indicate deuterium ions and carbon ions, respectively. The factors g_d and g_z indicate the distribution rate of beam energy to deuterium and impurity ions, and these are key factors for the estimation of T_d . It should be noted that the beam energy relaxes through the classical slowing down process and then the beam component cannot be distinguished from the bulk component below a certain energy. So all the beam energy after the slowing down phase is given to bulk deuterium ions (Fig.3). We artificially introduced a energy $\alpha T_d/E_c$ (E_c is the critical energy), at which energy the beam component merges into the bulk component. The relation of $v_b \gg v_{th}^d$, v_{th}^z is also assumed for the following formulations, where $v_b = 3 \times 10^6$ m/s at 90 keV, $v_{th}^d = 1.4 \times 10^6$ m/s and $v_{th}^z = 5.5 \times 10^5$ m/s at 38 keV experimentally.

The value g_d during the slowing down, g_d' , is expressed as

$$\begin{aligned} g_d' &= \frac{-1}{E_0} \int_0^{x_b} \left\langle \frac{dE}{dt} \right\rangle_d dt \\ &= \frac{2 n_d}{n_e \tilde{Z} x_b^2} \int_{x_i}^{x_b} \frac{u du}{1 + u^3} \end{aligned} \quad (2)$$

, where $x_b^2 = E_0/E_c$ and $x_i^2 = \alpha T_d/E_c$ (E_0 : injection energy) and $\tilde{Z} = (n_d + n_z Z_z^2 m_d/m_z)/n_e$. The value $g_z' (= g_z)$ is expressed as

$$g_z' = g_d' \frac{n_z}{n_d} \frac{m_d}{m_z} Z_z^2 \quad (3)$$

The net fraction of the beam energy given to bulk deuterium ions is expressed from the previous discussions as

$$g_d = g_d' + \alpha T_d/E_c \quad (4)$$

By substituting eqs.(2,3,4) into eq.(1), T_d can be determined.

The calculated results for the discharge mentioned in Sec.2 are shown in Fig.4. T_z and T_e are measured to be 38 keV and 10 keV, respectively. In order to estimate the deuterium temperature T_d , the additional informations of τ_E^d , τ_E^z , $n_e(0)$ and Z_{eff} are necessary. \bar{n}_e was measured only along 0.6 a_p and it also leads to the difficulty in estimating the confinement characteristics in the central region. The measurement of Z_{eff} was not so certain due to the deterioration of the transmission of the vacuum window. So we carried out the sensitivity check by scanning the not exactly known plasma parameters around the following acceptable values of $n_e(0)=3 \times 10^{19} \text{ m}^{-3}$, $Z_{eff}=3$, $\tau_E^d = \tau_E^z = 0.6 \text{ s}$ and $\alpha = 1$. Figure 4(a) shows the result of $n_e(0)$ scan: at $n_e(0)=3 \times 10^{19} \text{ m}^{-3}$, $T_d(0)$ of 37.3 keV is expected (a solid line); the preferential heating of impurity ions is remarkable in low density region because the energy exchange between deuterium and carbon ions becomes small. Since the value α is critical for this analysis, the results with $\alpha=0, 1.1, 1.2$ are shown for comparison with dotted lines. With $\alpha=1.1$, $T_d(0)$ is expected to be 38.5 keV at $n_e(0)=3 \times 10^{19} \text{ m}^{-3}$, which is higher than $T_z(0)$; there is no solution of eq.(1) for $\alpha=1.2$ at the same $n_e(0)$; the value of $\alpha = 0$, which is not adequate because g_d will be under-estimated for hot-ion discharges under our consideration, gives low $T_d(0)$ of 32 keV. As shown in Fig.4(b), T_d is not very sensitive to the variation of Z_{eff} . Figure 4(c) shown the dependence on the assumed τ_E^d . The solid line shows the result when $\tau_E^z = \tau_E^d$. The parameter dependence on $\beta \equiv \tau_E^z/\tau_E^d$ is also shown with dotted lines in the same figure, which is also not very strong.

The above results indicated that the expected T_d may not deviate significantly from the measured T_z (=38 keV) even in the conditions with high power beams into low density plasmas. More detail analysis using a non-linear Fokker-Planck calculations including the deformation and anisotropy of the distribution functions is described in ref.[3].

References

- [1] FONCK, R. J., DARROW, D. S., JAEHNIG, K. P., Phys. Rev. A 29, 3288 (1984).
- [2] NISHITANI, T., et al., the paper 2.3 in this review.
- [3] AZUMI, M., YAMAGIWA, M., the paper 2.9 in this review.

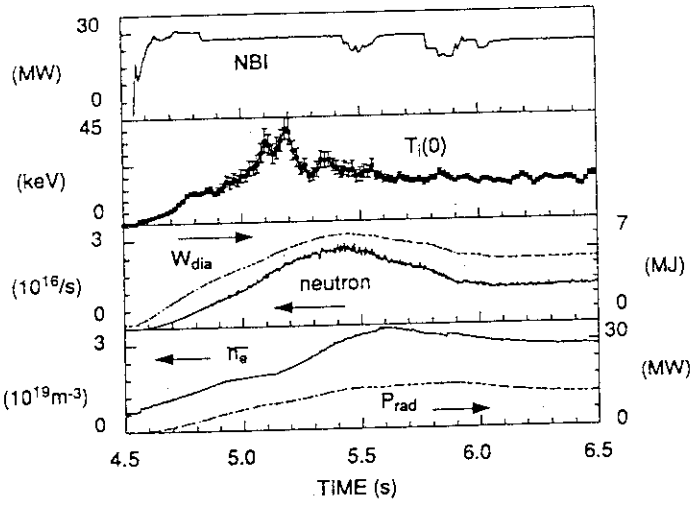


FIG. 1. Evolution of the discharge where ion temperature reached 38 keV.

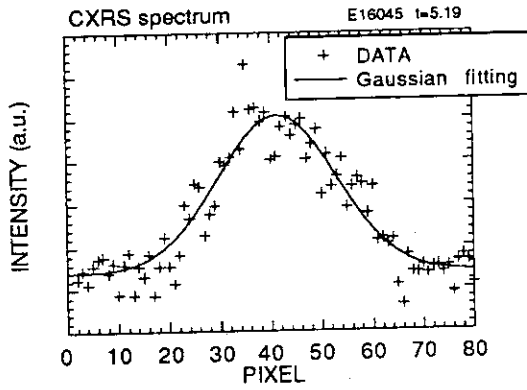


FIG. 2. Measured spectrum of CVI(n=8-7) at 529 nm. The Doppler width corresponds to an ion temperature of 40 keV (before correction of the energy dependence of the excitation rate).

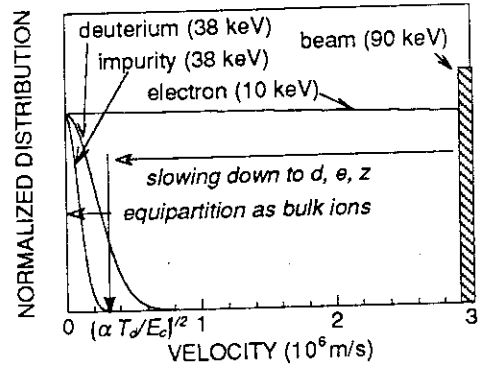


FIG. 3. Energy flow in our model calculations.

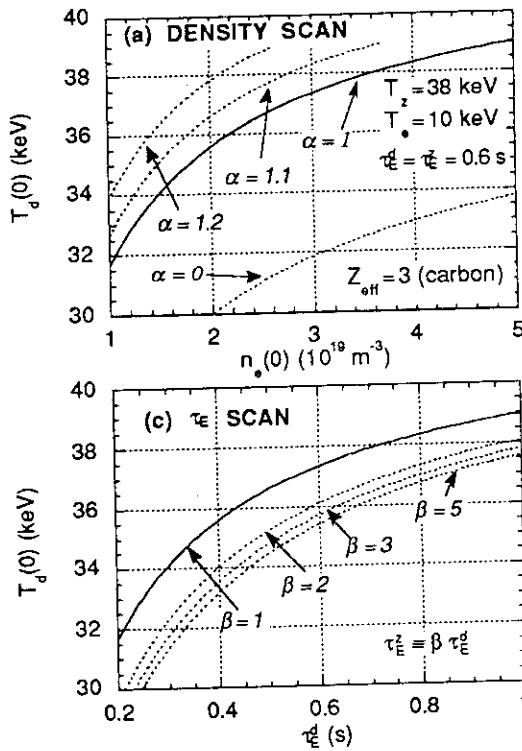


FIG. 4. Parameter scan for the estimation of the deuterium temperature from the measured carbon temperature. Scanned parameters are (a) electron density (b) effective ionic charge (c) energy confinement times for deuterium and carbon ions.

2.8 The Phenomena Associating the Crush of Central Ion Temperature of 38 Kev

Y. Koide, Y. Neyatani, S. Ishida

A. Sakasai, N. Asakura

1. Introduction

As shown in Fig.1 in ref.[1], the duration of high ion temperature $T_i(0)$ of 38 keV was as short as ~ 30 ms, followed by an abrupt termination. From the viewpoint that only $T_i(0)$ exhibited the significant deterioration, this type of collapse seems to be different from β_p -collapse, which is considered to be the most severe problem to sustain the high performance of high β_p regime [2]. It is shown in this paper that the MHD oscillation grows prior to the crush of $T_i(0)$ and that the affected region of $T_i(r)$ seems to be inside the rational surface, the safety factor of which is characterized by the mode number of the MHD oscillation.

2. MHD Oscillations Prior to the T_i -crush

Detail discharge conditions of the shot we treat here is described in ref.[1], and is not mentioned here. Figure 1 shows the evolution of this discharge (E16045) near the crush timing of $T_i(0)$. $T_i(0)$ took its maximum at $t=5.2$ s, followed by an abrupt decrease (Fig.1(a)). $T_e(0)$ showed only a slight saturation rather a crush and MHD oscillations appeared in $T_e(0.3a_p)$ as shown in Fig.1(b). ELM-like oscillations were observed in D_α emission in the divertor region (Fig.1(c)), however, its onset timing was after the $T_i(0)$ -crush. Oscillation which starts growing just prior to the $T_i(0)$ -crush was clearly detected by the magnetic probes (Fig.1(d)). The toroidal mode number 'n' of this oscillation was even and the onset of its growth is about 70 ms before the $T_i(0)$ -crush. As shown in the next section, oscillations detected in $T_e(0.3a_p)$ and the one in \tilde{B}_θ seems to be the identical MHD oscillation.

3. Characteristic of the Mode Oscillation

The upper box of Fig.2 shows the time evolution of the oscillation-frequency detected by the magnetic probe. The frequency was ~ 10 kHz at $t=5.3$ s and decreased to 7 kHz at $t=6.4$ s. The lower two boxes are the evolution of $T_e(0.3a_p)$ at $t=5.3$ and 6.4 s, showing the same frequency as that of \tilde{B}_θ . This may be understood that the both measurement of T_e and \tilde{B}_θ detected the identical MHD oscillations.

The toroidal mode number of this oscillation was even as mentioned above. In order to

know the poloidal mode number, we compared the evolution of T_e at $r=\pm 0.3a_p$ in Fig.3. The results are shown in the lower boxes of this figure. The observed in-phase evolution indicates that the poloidal mode number is also even.

Next we tried to find the q -value using the equilibrium code. In calculating the equilibrium, we scanned the value of $q(0)$ as an boundary condition in an acceptable range, i.e. $0.8 < q(0) < 2.0$, and checked whether the result was consistent or not with the even toroidal/poloidal mode numbers and the radial locations of the observed oscillation. If we set $q(0)=1.3$, the location of $q=2$ surface came to the radius which corresponded to the location of the $T_e(\pm 0.3a_p)$ -oscillations (Fig.4). So we speculate that the observed MHD is the $m/n=4/2$ mode oscillation.

4. The Crush Region

Figure 5 shows the evolution of $T_i(r)$ around the crush timing. At $t=5.19$ s, $T_i(r)$ was highly peaked and $T_i(0)$ reached 40 ± 5 keV. In the crushing phase, only the innermost two data points showed decreasing and no change was recognized in the outer region. As indicated in this figure, the location of $q=2$ surface inferred from the previous discussions almost coincides with this boundary region.

5. Frequency of MHD Oscillation and Rotation Velocity

If the MHD mode is fixed to the plasma flow, the frequency of the MHD oscillation would be expressed as follows.

$$f = \frac{1}{2\pi} \left(\frac{n}{R} V_t - \frac{m}{r_s} V_p \right)$$

In Fig.6, the measured V_t at two spatial points near the location of $q=2$ surface r_s are plotted with lines. Closed circles shows the calculated result using the above equation ($n=2$) with neglect of poloidal rotation V_p , resulting in the higher V_t than the measured one. If we assume V_p of 2.5 km/s in ion-diamagnetic direction, which is comparable to the accuracy of the measurement, calculated V_t ($m=4$) agrees with the measurement (open circles).

References

- [1] KOIDE, Y., et al., the paper 2.7 in this review.
- [2] ISHIDA, S., et al., the paper 2.5 in this review.

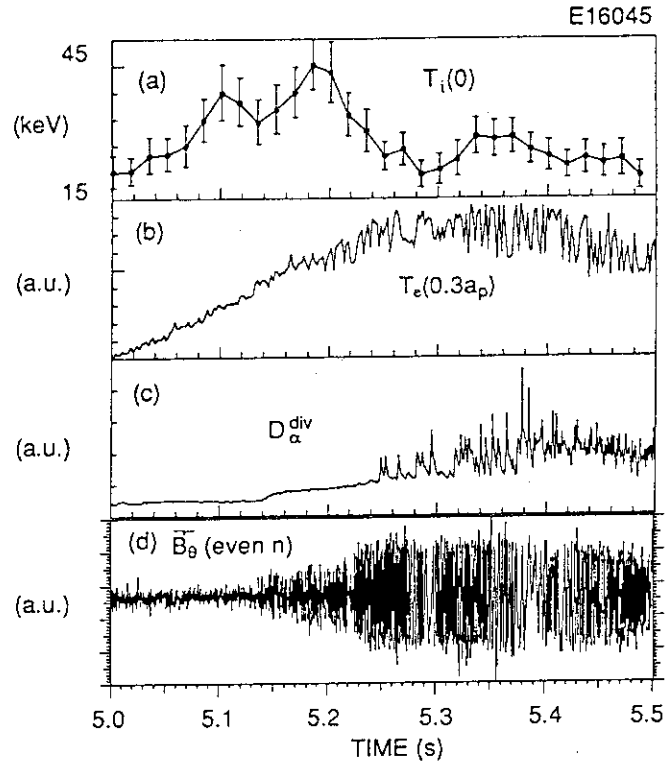


FIG. 1. Evolution of the discharge with $Ti(0)$ of 38 keV around at the crush timing. (a) $Ti(0)$ (b) $Te(0.3ap)$ (c) D-alpha emission (d) magnetic fluctuation.

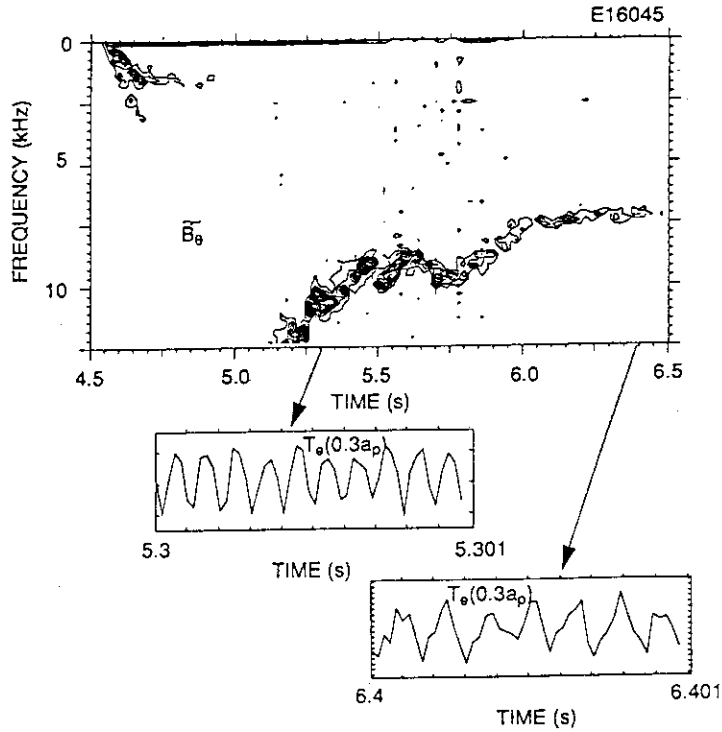


FIG. 2. Comparison of the oscillation frequency in magnetic fluctuation (upper box) and $Te(0.3ap)$

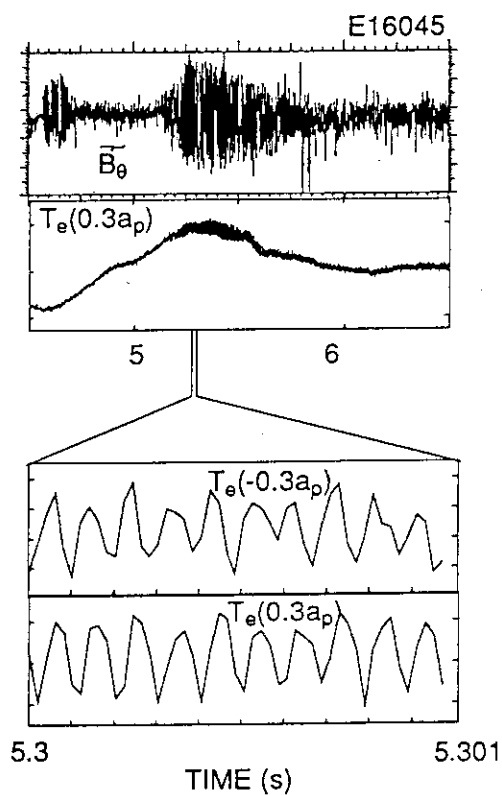


FIG. 3. Identification of the mode number by the evolution of T_e .

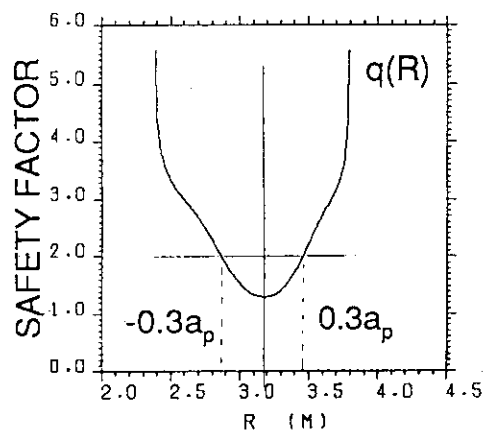


FIG. 4. Inferred q profile.

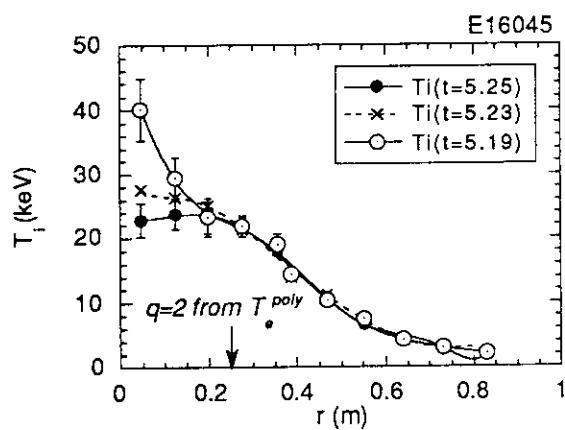


FIG. 5. $T_i(r)$ during the crushing phase.

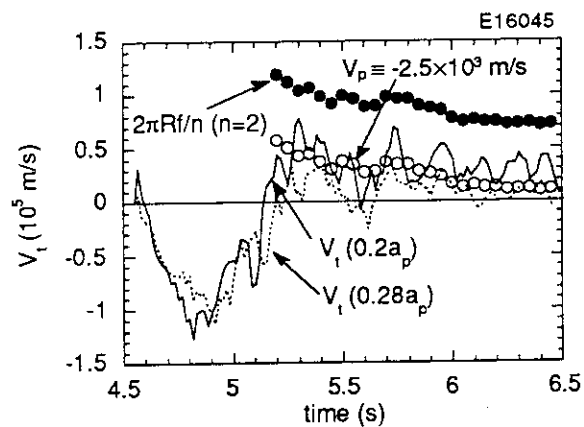


FIG. 6. V_t and frequency of MHD oscillation

2.9 Nonlinear Fokker-Planck Analysis of High Ion Temperature Plasma

M. Azumi and M. Yamagiwa

1. Introduction

In a tokamak plasma under the intensive NBI heating, the NBI power transferring to each ion component is proportional to the ratio of $Z_k^2 n_k / A_k$, where n_k , Z_k and A_k are the density, charge number and mass number of the k -species ion, respectively, when the beam energy is much higher than the ion temperature. This means that the energy input to single impurity ion is much larger than that to the hydrogen isotope ion (or, bulk ion) and that, if the energy confinement times of ion species are similar to each other, the temperature of the impurity is higher than that of the bulk ion and the energy to impurity ions is transferred back to the bulk ion through the energy exchange. This is the situation usually observed in tokamak discharges. In the hot ion mode discharges, however, the ion temperature can be increased to be comparable to the beam energy, the energy transfer from fast ions to impurity ions reduces and, moreover, it becomes difficult apparently to distinguish the bulk ion and the fast ion. In JT-60U, especially, the ion temperature of about 38 keV with comparatively low electron temperature around 10 keV was observed under the NBI heating with beam energy of 90 keV in the high β_p deuterium discharge¹⁾. The temperature was measured by the CXRS of carbon ions. In analyzing this discharge, we have to be careful for evaluating the bulk ion temperature, including the definition of temperature itself. The deformation of the velocity distribution is also to be checked. In this paper, we study the characteristics of the velocity distribution function and the deuterium (effective) temperature in this typical discharge by using the 2-D Fokker-Planck equation. In the next section, the coupled equations of energy balance for deuterium and impurity ions are studied for comparison with the Fokker-Planck solution, which is in detail described in the section 3. The results are summarized and discussed in the section 4.

2. Energy Balance Equation

The coupled equations of energy balance between deuterium ion and impurity one for the fixed electron temperature are

$$\begin{aligned} \frac{3}{2} n_D \frac{T_Z - T_D}{\tau_{fZ}^{D/Z}} + \frac{3}{2} n_D \frac{T_e - T_D}{\tau_{fZ}^{D/e}} - \frac{3}{2} n_D \frac{T_D}{\tau_E^D} + S_{NB} g_D (E_0/E_c, \alpha T_D/E_c) &= 0, \\ \frac{3}{2} n_Z \frac{T_D - T_Z}{\tau_{fD}^{Z/D}} + \frac{3}{2} n_Z \frac{T_e - T_Z}{\tau_{fD}^{Z/e}} - \frac{3}{2} n_Z \frac{T_Z}{\tau_E^Z} + S_{NB} g_Z (E_0/E_c, \alpha T_D/E_c) &= 0, \end{aligned} \quad (1)$$

where $g_{D,Z}$ are fractions of beam power density transferred to deuterium and impurity ions, respectively, and αT_D is the lower limit of the available beam energy. Other notations are conventional ones. These nonlinear equations are numerically solved for parameters at the

plasma center and $t=5.19$ sec of high Ti shot (#16045). The plasma parameter dependence of solution has been studied in detail in the ref. 1 and, in this paper, we fix the plasma parameters as follows: $n_e=3 \times 10^{19} \text{m}^{-3}$, $T_e=10 \text{keV}$, $Z_{\text{eff}}=3$, $Z_{\text{imp}}=6$ (carbon), $S_{\text{NB}}=0.58 \text{ MW/m}^3$ and $E_0=90 \text{ keV}$. The measured T_C is 38 keV (we use the suffix "C" instead of "Z" explicitly to denote the carbon, hereafter). Figure 1 shows the dependence of T_D and T_C on τ_E^D ($=\tau_E^C$) with $\alpha=1.2$. We can see that T_D exceeds T_C in the range of $T_C > 38 \text{ keV}$, or, $\tau_E^D > 0.5 \text{ sec}$, and $T_D=39 \text{ keV}$ at $T_C=38 \text{ keV}$. The value of T_D^* (T_D at $T_C=38 \text{ keV}$) can be changed by the ratio τ_E^C/τ_E^D and the parameter α . When the ratio τ_E^C/τ_E^D is increased, the value of τ_E^D necessary to attain $T_C=38 \text{ keV}$ increases and T_D^* shows the slight decrease ($T_D^*=34 \text{ keV}$ even for $\tau_E^C=\infty$) because the conductive-convective energy loss is not the main channel of impurity energy loss. On the other hand, the parameter α strongly affects the attained T_D^* . This is because the available energy for the collisional energy transfer to ions and electrons from fast ions is $E^*=E_0-\alpha T_D$ in this model. The slight increase of α decreases the energy fraction to impurity and increases τ_E^D necessary to attain $T_C=38 \text{ keV}$. The resultant value of T_D^* is much higher due to the combined effects of the increased τ_E^D and the increased direct energy input αT_D . We can not obtain the reasonable solution of T_D^* for $\alpha > 1.6$ under the present set of parameters in the energy balance equations, as seen in Fig.2. In this way, the bulk ion temperature does strongly depend on the artificial (or, unphysical) parameter α for the high ion temperature comparable to the beam energy.

3. Nonlinear Fokker-Planck Equation

The velocity distribution functions of charged particles under the binary collision process are expressed by the following steady-state Fokker-Planck equation in the 2 dimensional velocity space ($v, \theta=\cos^{-1}(v_{\parallel}/v)$)²⁾

$$\frac{df_k}{dt} = \sum_j C(f_j, f_k) + \frac{1}{2v^2} \frac{\partial}{\partial v} \left[\frac{v^3}{\tau_E^k} f_k \right] - \frac{f_k}{\tau_P^k} + S_k = 0 \quad (2)$$

where τ_E^k and τ_P^k are the energy and particle confinement time, respectively, and S_k is the particle source of the k -th particle from NBI. The energy dependence of τ_E^k and τ_P^k are assumed to take the form of $\tau_{E,P}^k = \tau_{E0,P0}^k [1 + (E/E_{*E,P}^k)^{3/2}]$, respectively, and τ_{P0}^k is adjusted such that the total number of particle is the prescribed value, while τ_{E0}^k is adjusted such that the impurity ion temperature is the measured value. The parameters, $E_{*E,P}^k$, represent the improved confinement of the high energy particle. In the following, $E_{*E,P}^k$ are fixed at 10 keV , for simplicity, and we abbreviate E_{*E}^D as E^* . We solve the coupled equations for deuterium and impurity ions with Maxwellian electron distribution by iterative procedure. Plasma parameters are the same as those used in the previous section. Figure 3 is the example of velocity distribution functions for $E^*=\infty$ (with no improvement of fast ion confinement). The symbols \diamond , \bullet and \circ represent $f(E, \theta=\pi/2)$, $f(E, \theta=0)$ and the θ -averaged f , respectively, where the NB is injected perpendicularly, $S_D = S_{D0} \delta(E-90 \text{ keV}) \delta(\theta-\pi/2)$. The impurity

distribution function is almost Maxwellian in the range of $E < 400$ keV due to the high self-collision frequency and only $f_C(E, \theta=0)$ is plotted. The confinement time τ_E^D necessary to obtain $T_C \sim 38$ keV is $\tau_E^D = 0.9$ sec with $\tau_E^C = 5.0$ sec. From the resultant energy balances between deuterium, carbon and electron, the electron global energy confinement time is evaluated $\tau_E^e \sim 0.4$ sec, which is about half of τ_E^D . We note that, even with this good deuterium energy confinement, the convection-conduction energy loss takes 70% of NBI input power density. Although the deuterium distribution function is anisotropic especially near the injection energy, the deviation from the Maxwellian one is not so large in the "thermal" energy range of $E < 40$ keV, and we define the "effective" temperature by the average slope in this energy range. This definition gives $T_D^{\text{eff}} \sim 45$ keV, which is higher than the impurity temperature. This feature is the same as the results obtained from energy balance equations. However, we stress that T_D^{eff} is not the temperature in the sense that the stored energy can not be evaluated by $(3/2)n_D T_D^{\text{eff}}$. In fact, The Fokker-Planck solution gives the average energy of 37 keV, even including the fast ion component, which is much lower than T_D^{eff} . The fast ions have experimentally shown to have the better confinement than thermal ions, partly due to the large larmor radius, by which the fluctuations driving the anomalous loss are averaged out. The result with $E^* = 40$ keV is shown in Fig. 4, and the effective temperature and the required τ_{E0}^D decreases to $T_D^{\text{eff}} \sim 41$ keV and $\tau_{E0}^D \sim 0.3$ sec. This τ_{E0}^D gives $\tau_E^D(90 \text{ keV}) = 1.3$ sec, which is much longer than the thermalization time $\tau_{th}^D(90 \text{ keV}) \sim 0.2$ sec, and the anomalous loss has little effects on fast ions. In spite of the large decrease of τ_{E0}^D , the total stored energy of deuterium ions increases a little bit ($\sim 5\%$) due to the contribution from fast ions. Figure 5 summarizes the dependence of T_D^{eff} on T_C for the different value of E^* . Here we have set $\tau_E^C \sim \infty$; that is, the energy flow from deuterium to impurity balances to that from impurity to electron. The value of T_D^{eff} is the sensitive function of T_C and increases nonlinearly in the high T_C region. The decreasing E^* reduces T_D^{eff} but still T_D^{eff} is higher than T_C except in the case of $E^* = 20$ keV, in which the distribution function is deformed even in the "thermal" region. The nonlinearity of T_D^{eff} on T_C also depends on the beam energy. In Fig. 6, the cases with beam energy of 90 keV, 135 keV and 180 keV are plotted for $E^* = 40$ keV, for comparison. It is clearly shown that the increase of the beam energy reduces T_D^{eff} , and the critical impurity temperature for $T_D^{\text{eff}} > T_C$ moves to the higher temperature side.

4. Conclusion

The deuterium temperature in the hot ion discharge in JT-60U has been analysed by using the energy balance equations and the Fokker-Planck equation. Increasing the impurity temperature to the value comparable to the beam energy, the "effective" deuterium temperature can exceed the impurity temperature. This general tendency is obtained both from the energy balance equations and from the Fokker-Planck equation. However, the temperature evaluated

by the energy balance strongly depends on the artificial parameter, while, in the case of the Fokker-Planck equation, it depends on the energy dependence of energy confinement time. The analysis in this paper shows that the experimental measurement of the deuterium temperature, or the distribution function itself, will give the good information for understanding the transport process in a tokamak.

References

- [1] KOIDE, Y., et al, the paper 2.7 in this review.
- [2] KILLEEN, J., MARX, K.D., Methods in Comp. Phys., Vol.9, Academic Press, New York (1969).

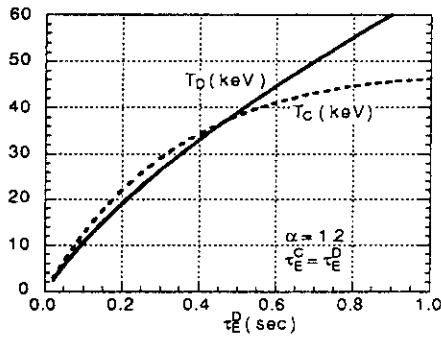


Fig.1 τ_E -dependence of T_D and T_C , calculated from Eq.(1).

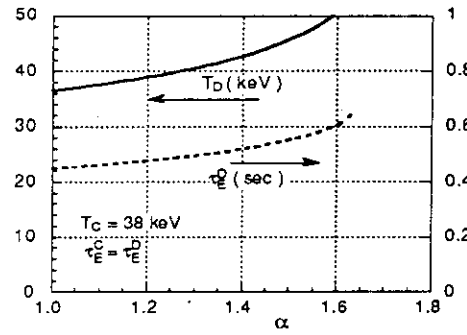


Fig.2 Dependence of T_D and τ_E on α for $T_C=38\text{keV}$, calculated from Eq.(1)

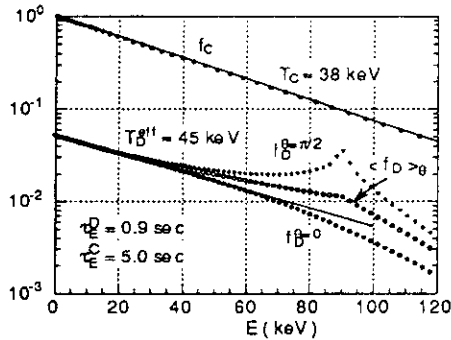


Fig.3 Fokker-Planck solutions of deuterium and carbon ions.

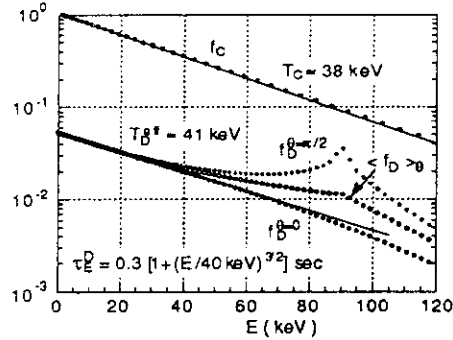


Fig.4 Fokker-Planck solutions of deuterium and carbon ions, with enhanced confinement of fast ions ($E^*=40\text{keV}$).

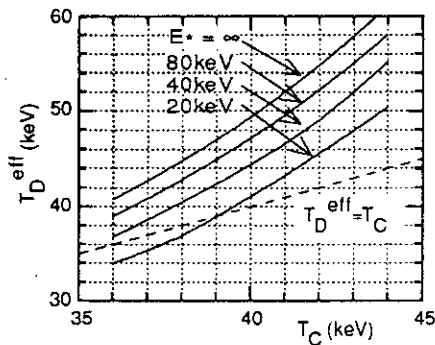


Fig.5 Dependence of T_D^{eff} on T_C for $E^*=\infty$, 80keV, 40keV and 20keV with $E_0=90\text{keV}$.

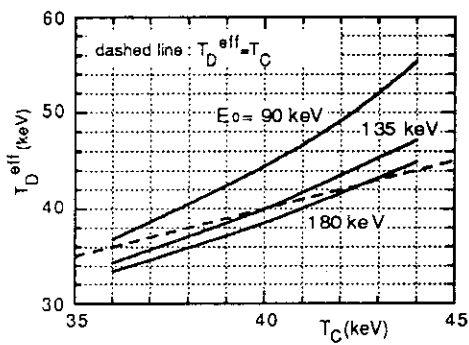


Fig.6 Dependence of T_D^{eff} on T_C for $E_0=90\text{keV}$, 135keV and 180keV with $E^*=40\text{keV}$.

2.10 Summary of the Compression Experiments

A. Tanga, R. Yoshino, N. Hosogane, Y. Kamada, K. Nagashima and Y. Koide.

1. Adiabatic and Non Adiabatic Compression.

The technique of plasma compression was devised for increasing the plasma performances: the work done to compress the plasma is equivalent the effect of additional heating. In the case of large tokamaks, such as TFTR or JT-60U the equivalent additional heating power can be as much as tens of megawatts. Most of the theoretical and experimental work on plasma compression so far has been devoted to adiabatic compression. In the adiabatic compression the poloidal and toroidal fluxes are conserved and in principle the plasma is subjected to only mechanical work [1,2]. The behavior of the plasma under adiabatic compression was theoretically studied in the pioneering work by Furth and Yoshikawa in 1970 [3].

Whilst the adiabatic compression has the advantage of relatively simple physical processes, avoiding the complications produced by the changes in the plasma current profile, caused by the currents which can be induced if the fluxes are not conserved; there are the disadvantages of the constraints on the poloidal circuit. In fact, in the case of a radial compression, by moving the plasma in the direction of the larger toroidal field, normally the inductive coupling between the equilibrium coil and the plasma causes an injection of flux in the plasma. Therefore the flux injected by the equilibrium coil must be counterbalanced by a flux removal, achieved, for example, by changing (reducing) the current in the primary coil. While this operation may be relatively easy in small size tokamak, the voltage requirement will increase greatly in larger tokamaks and the resulting scenarios may become non-practical. However in large machines such as for example JET or JT-60U it may be possible to have available compressional speed to make a compression experiment, but not the flux compensation to make the compression adiabatic. Some effects of non adiabatic compression were reported in JET [4]. In the case of divertor configuration as in the case of JT-60U it is possible to achieve a combination of radial compression and, at the same time a reduction of the plasma volume by moving the position of the x-point further into the vacuum vessel, by increasing the current in the divertor coil. Preliminary results of this combined toroidal and poloidal compression are reported here.

2. Plasma Current and Shape Control.

The plasma position was changed in time of 100-150 ms. The flux plots of the initial and final configurations are shown in fig 1. Before compression typically the plasma volume was between 75-78 cubic meters, while after the compression the plasma volume was 35-40- cubic

meters, also the major radius compression was performed by moving the position of the magnetic axis from 3.4 to 3.0m.

The value of the plasma current was maintained well constant by the feedback system, in fact the increase was only 20-40kA in a fast transient. Because of the increase of plasma elongation and of the toroidal field, caused by the plasma radial movement, the value of the edge q decreased only moderately, from typically 6-7, to values of the order of 5. The small compressed plasma was more vertically unstable than the initial one, due to the combined effects of reduced vessel shell effect and increased elongation, therefore the control of the vertical position needed to be adjusted. A vertical instability event occurred in one of the plasma discharges of the experiment.

The time evolution of the coil and control currents is shown in fig 2. A ramp was applied to the radial position and to the x-point position, which is controlled by the current of the divertor coil.

3. The Effects of Compression on Plasma Parameters

The compression both radial and poloidal had a strong effects on the plasma parameters as shown in fig.3, for an ohmic plasma discharge. It is possible to see that both the plasma energy and the neutron production double during the compression.

The time evolution of a pulse with NB heating is shown in fig 4.

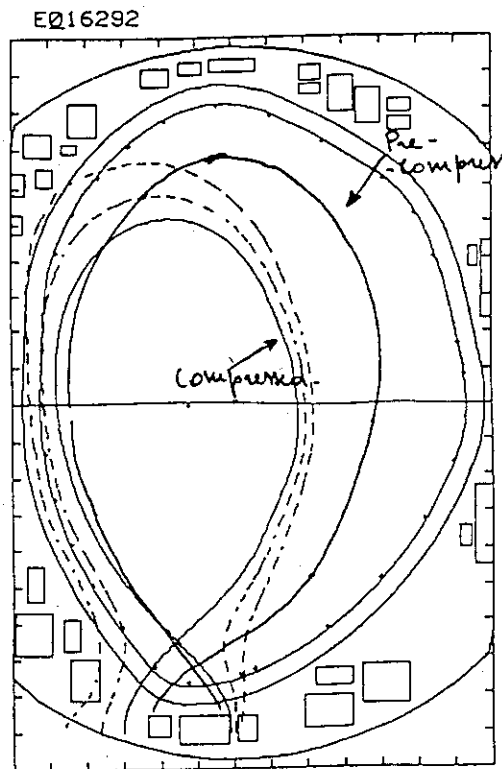


Fig. 1. Poloidal flux plot of the plasma before and after compression., plasma current= 1.9MA

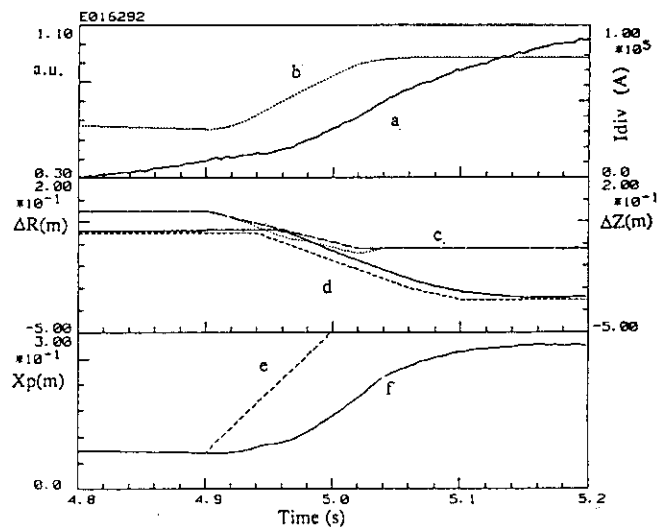


Fig. 2. Time evolution of the control signals and coil currents. a) Intensity of soft X-ray central channel, b) Divertor coil current, c) vertical displacement, d) radial displacement, e) requested X-point position, f) X-point position.

It is possible to see that in the short compression time the neutron rate increases appreciably, whilst the plasma stored energy increases by approximately 1.0 MJ.

The increase in the ion temperature is shown in fig 5. Fig 5 shows three ion temperature radial profiles taken with short time interval, during the compression.

The increase in ion temperature takes place over the whole cross section as it should be expected. The increase in neutron production, achieved with compression, plotted against NB power is shown in fig 6. In this figure the values of the neutron rate before and after the compression are reported with a time interval of 100-150ms. It is possible to see that on average plasma compression increased neutron production by approximately a factor of two. The post compression values increase approximately with the square of the injection power. Therefore it should be expected an increase in the neutron rate beyond the present limits with higher NB power.

4. Experimental Limits and Instabilities

As it has been said the compression experiments here were not adiabatic, i.e. the toroidal and poloidal fluxes were not conserved. As a consequence the plasma current profile underwent a rapid change. The time evolution of the internal inductance is obtained, for a series

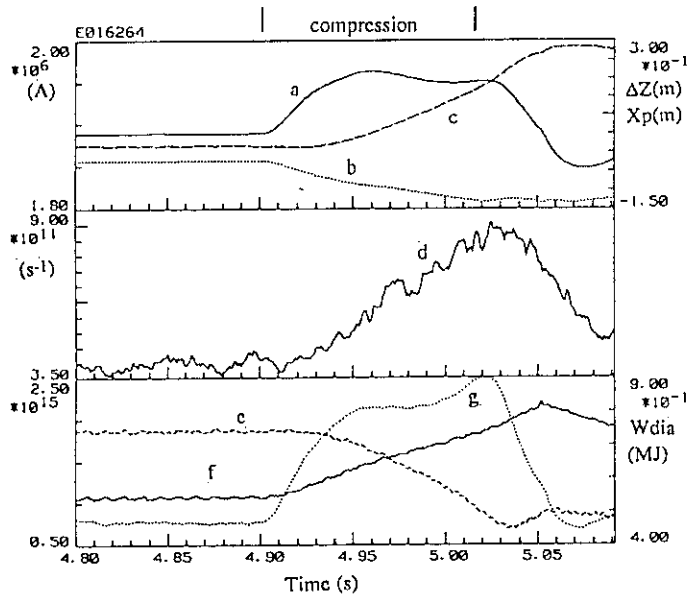


Fig. 3. Time evolution of plasma quantities during compression of a ohmic discharge: a) Plasma current, b) and c) Vertical plasma position and position of the x-point, d) Neutron rate, e and f) Line density of the two interferometer channels, g) Plasma stored energy.

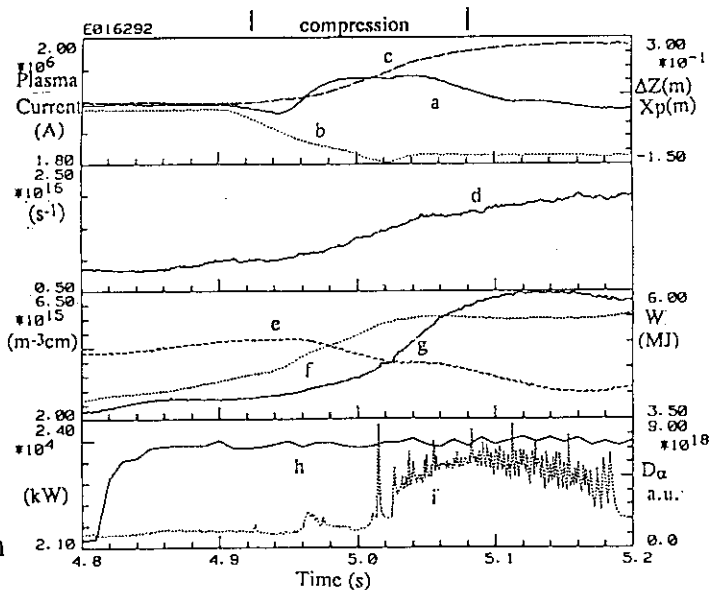


Fig. 4. Time evolution of plasma quantities during compression of a discharge with additional heating: a) Plasma current, b and c) Vertical plasma position and position of the x-point, d) neutron rate, e and f) line density of the two interferometer channels, g) plasma stored energy, h) NB injected total power, i) Intensity of $D\alpha$ light in the x-point region.

of plasma discharges. Although there are probably large error bars in the determination of the internal inductance in such conditions, however, there are indications of the rapid transient which occurred. It should furthermore be mentioned that, in several cases a MHD lock-mode appeared which further suggest the rapid changes of the plasma current profile.

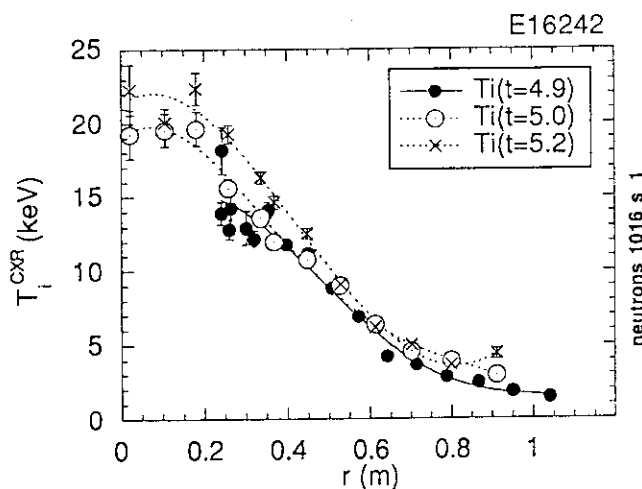


Fig. 5. Ion temperature radial profiles a) Before compression, b) After compression.

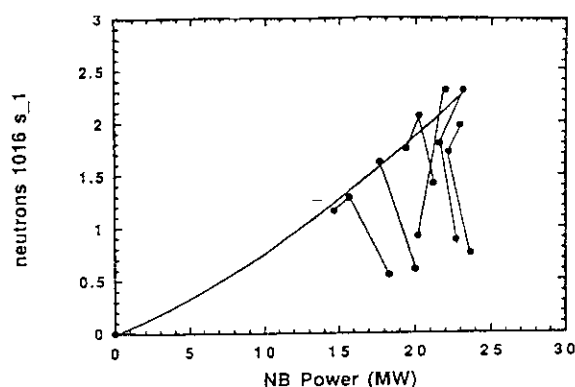


Fig. 6. Neutron rate before and after compression plotted versus NB power. The starting lower points were taken just before compression, the second points are 150-250ms later, the last point were taken at the maximum value achieved in the same discharge. In four cases the maximum neutron rate was achieved at the compression.

5. Conclusions.

The compression results shown demonstrate that non adiabatic compression increases plasma parameters. Therefore it could be a useful tool for producing and for studying thermonuclear plasmas. If the compression is not adiabatic however the plasma current profile is strongly changed during and after the compression. Furthermore the currents, induced in the plasma, because the compression is not adiabatic, have a twofold consequence: a) the induced currents may produce unstable profiles, as indeed it has happened in a few cases, and b) it could be a useful technique to produce plasma current profiles which are new and have possibly different confinement properties.

References:

- 1) Golant, V.E., Plasma Phys. Contr. Fusion 26 (1984) 77
- 2) Tait, G., Bell, J., Bell, M.G., Bitter, M., et al. in Proc. of 10th conference on Plasma Physics and Controlled Nuclear Fusion Research, London, UK, 12-19 September 1984, IAEA Vienna 1985.
- 3) Furth, H.P., Yoshikawa, S., Phys. of Fluids, 13 (1970) 2593.
- 4) Tanga, A., Gottardi, N., Hubbard, A., Lazzaro, E., Noll, P., et al. in proc. 13th European Conference on Controlled Fusion and Plasma Heating Schliersee, FRG, 14-18 April 1986, vol. 10C, Part I pag 286.

3 Transport Studies

3.1 On and Off-axis NBI Heating Experiments

K. Nagashima, H. Shirai, M. Sato, Y. Koide

In many local transport analyses, an empirical transport formula¹⁾ has been used. In this formula, particle flux consists of a diffusion and a flow (inward pinch) terms, and heat flux consists of a conduction and a convection terms (a coefficient of convection heat flux term has been a physically interesting problem, $3/2$ or $5/2$?). Lately, from several experimental results, it has been found that the empirical transport formula is not adequate to express tokamak transport. Off-diagonal flux and/or heat pinch terms have been introduced to explain the experimental results. Therefore, one of the most important issues on tokamak transport is to clarify structures of various flux (particle, heat, toroidal momentum and etc.).

On DIII-D tokamak, experimental results showed an existence of non-diffusive inward heat flux in both cases of ECH²⁾ and NBI³⁾ off-axis heating experiments. On the other hand, this non-diffusive flux was not observed in ICRF heating experiment on JET⁴⁾. In this section, on and off-axis NBI heating experiments on JT-60U will be introduced.

Figure 1 shows the plasma configuration of this discharge (E016502), which has a lower x-point divertor. In the figure, the two parabolic lines represent orbits of tangentially injected neutral beams. These beams are injected from near torus equatorial plane. The upper one passes through the plasma center and the lower one passes only in an area of $r/a > 0.5$. Therefore, on and off-axis heating can be performed using these two beam lines. The plasma parameters of this discharge are plasma current of $I_p = 1.5$ MA, toroidal field of $B_T = 4.25$ T, major radius of $R = 3.2$ m, minor radius of $a = 0.80$ m, elongation factor of $\epsilon = 1.61$, effective safety factor of $q_{eff} = 6.5$ and line averaged electron density of $n_e = 1.2 - 1.4 \times 10^{19} \text{ m}^{-3}$ using deuterium working gas. The NBI heating power is 3.2 MW in the both cases of on and off-axis heating.

In this discharge, electron and ion temperatures were measured using ECE fourier spectrometer and charge exchange recombination spectroscopy of carbon impurity. The measured T_e and T_i profiles are shown in Fig.2. T_e profiles are almost same in both cases of on and off-axis heating (a bit peaking in $r/a < 0.5$ can be seen in on-axis heating). T_i profiles has a clear response to heat sources. The heat source profiles are shown in Fig.3, where total heating profiles (thick lines) and NBI heating profiles (thin lines) on electron (solid line) and ion (dashed lines) are shown. The total heating powers were calculated from neutral beam heating, ohmic heating, energy equipartition on electron, and from neutral beam heating, energy

equipartition on ion. It should be noted that in a case of off-axis heating, the heat source to ion is almost zero in the central region but, exactly, the diagnostic beam reaches up to the center.

To analyze the transport feature, diffusion coefficients were calculated using the following formula,

$$-\nabla q_j + P_j = 0 \quad (1)$$

$$q_j = -\chi_j n \partial T_j / \partial r \quad (2)$$

where q_j , χ_j and P_j are heat flux, diffusion coefficient and total heat source, respectively. A subscript j represent a particle species of electron or ion. The calculated χ_e and χ_i are shown in Fig.4. On electron transport, χ_e of off-axis heating is small in a region of $r/a < 0.5$, which may be a result from "profile invariance" of electron temperature. On ion transport, χ_i of off-axis heating is meaningless in the region of $r/a < 0.5$ because the ion heat flux is almost zero in this region (a heating by the diagnostic beam was neglected). In the analysis, radiation energy loss was neglected, which is important in an edge region of $r/a > 0.8$.

From the analysis, it seems that there is non-diffusive inward heat flux of ion. However, if the transport of high energy ion is not negligible compared with the energy slowing down process, the source profiles are altered and it may explain the central heating of ion. On electron transport, an improvement of χ_e in the inner region of $r/a < 0.5$ can be seen in the case of off-axis heating. Two explanations can be considered. One is a decrease of micro-turbulence dominating the transport. For example, there is a possibility that the turbulence level is suppressed by a decrease of η_i parameter. The another explanation is an existence of non-diffusive heat flux. For an further understanding, more detailed experiments are needed.

As a conclusion, ion temperature profile is sensitive to the heating profile, and it seems that there is a non-diffusive heat flux, if there is no additional process to heat ion in the central region. On the other hand, electron temperature profile is not sensitive to the heating profile. But, no conclusive explanation can be obtained only from these experiments.

References

- [1] WOOTTON, A.C., et al., Phys. Fluids B 2 (1990) 2879
- [2] LUCE, T. C., PETTY, C. C., De HAAS, J. C. M., Phys. Rev. Lett. 68 (1992) 52
- [3] SCHISSEL, D. P., et al., Nucl. Fusion 32 (1992) 689
- [4] BALET, B., et al., Nucl. Fusion 32 (1992) 1261

Fig.1 Magnetic configuration and orbits of tangentially injected neutral beams.

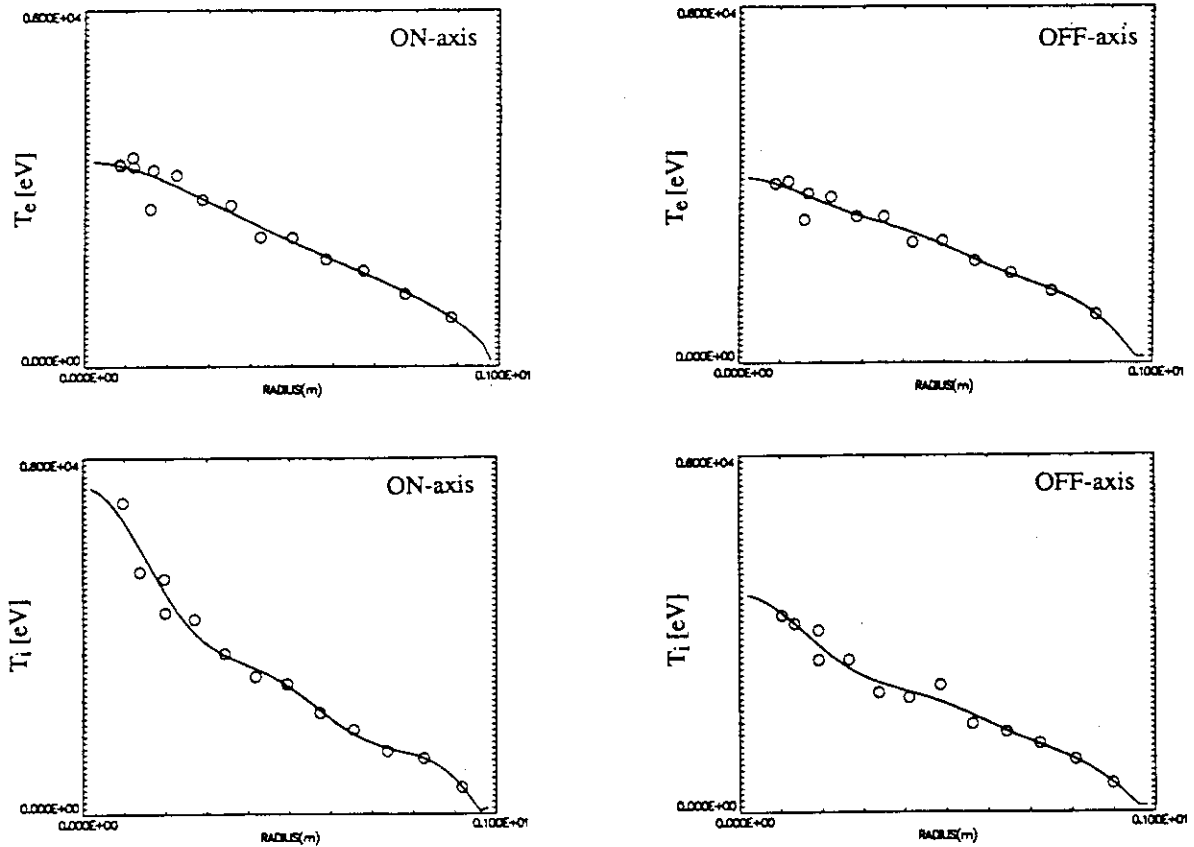
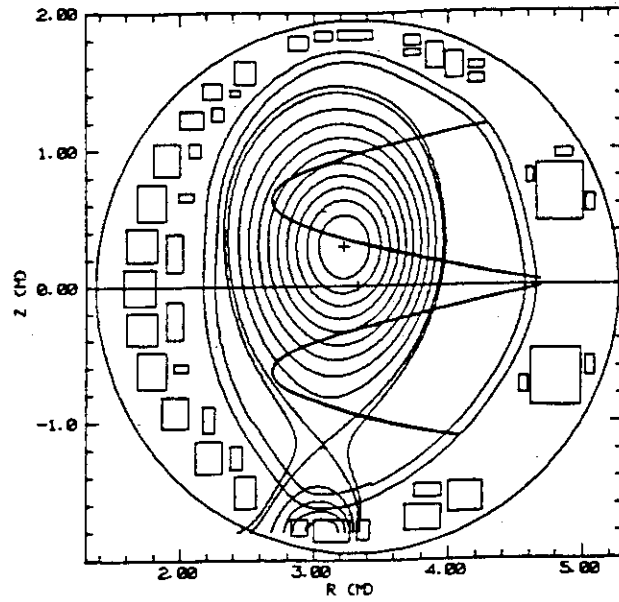


Fig.2 electron(upper figures) and ion(lower figures) temperature profiles of on(left hand side) and off(right hand side)-axis NBI heated discharges.

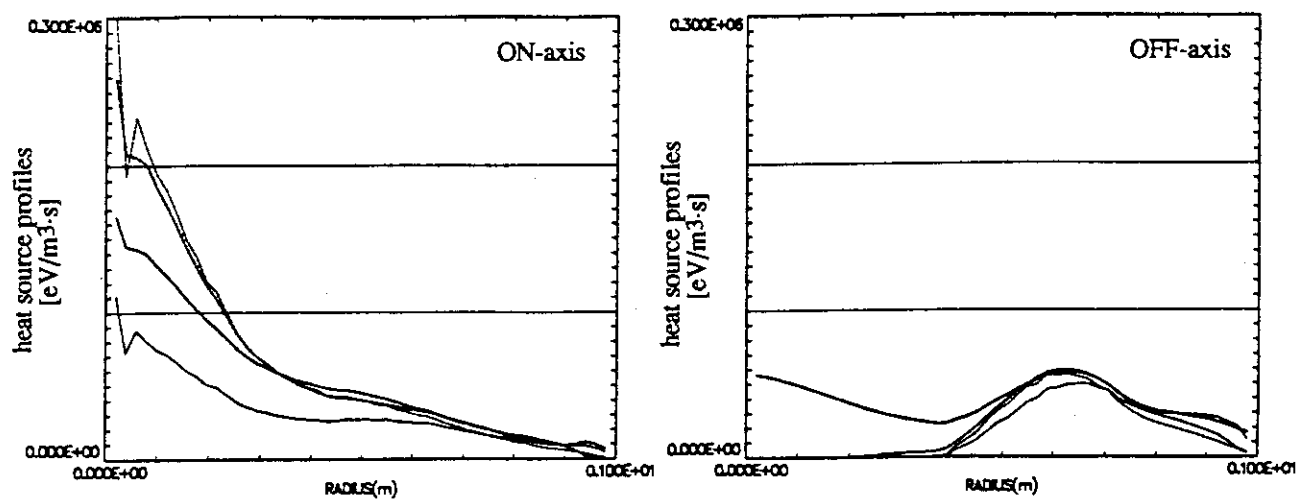


Fig.3 Heat source profiles on electron (solid lines) and ion (dashed lines). Thick and thin lines represent total and NBI heating profiles, respectively.

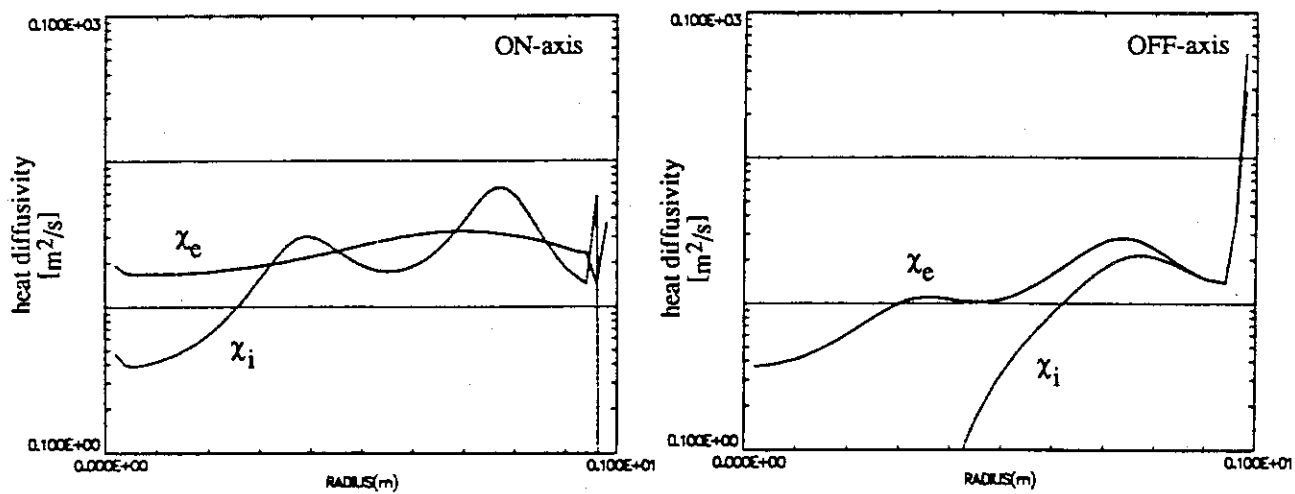


Fig.4 Electron (solid lines) and ion (dashed lines) heat diffusion coefficients calculated using power balance (Eqs.(1) and (2)).

3.2 Toroidal Momentum Transport Experiment using Tangential NBI

K. Nagashima, Y. Koide

In several tokamaks, toroidal momentum transport has been examined using steady state momentum balance. It has been found that measured toroidal momentum diffusivity is larger than neo-classical value and the absolute value is almost same to ion heat diffusivity measured from power balance analysis¹⁾. Latest several experimental results on tokamak transport show an existence of non-diffusive inward heat flux^{2, 3)}, as same as an inward pinch of particle flux. Hence, an existence of analogical momentum pinch or not is a currently interesting issue. In this section, experimental results of off-axis toroidal momentum input using tangential NBI will be introduced.

In this experiment, the counter direction (opposite to plasma current) tangential NBI was injected with a off-axis deposition profile. Almost all NBI power was deposited in an outside region of $r/a > 0.4$. Magnetic configuration of this discharge is a highly elongated lower x-point divertor, and main plasma parameters are plasma current of $I_p = 1.5$ MA, toroidal field of $B_T = 4.27$ T, major radius of $R = 3.15$ m, minor radius of $a = 0.79$ m, elongation factor of $\epsilon = 1.63$, effective safety factor of $q_{eff} = 6.5$ and line averaged electron density of $n_e = 0.9 \times 10^{19} \text{ m}^{-3}$ using deuterium working gas. Tangential NBI input power is 1.5 MW in the counter direction with an angle of 33 degree between beam and magnetic axis. The measured toroidal velocity and input toroidal momentum profiles are shown in Fig.1. In the figure, the toroidal velocity profile becomes nearly flat in a central region, where there is no momentum input. On the plasma edge, very steep velocity gradient is seen, which may be produced by some ion loss mechanism⁴⁾. From this steady state profile, it seems that there is no inward momentum pinch. Momentum diffusion coefficient is calculated from toroidal momentum balance using a following simple diffusion equation,

$$\frac{\partial(mnU)}{\partial t} = -\nabla M + S_M \quad (1)$$

$$M = -mn\chi_\phi \partial U / \partial r \quad (2)$$

where m and n are mass and density of ion. U , M , S_M and χ_ϕ represent toroidal velocity, momentum flux, momentum source and momentum diffusivity, respectively. The calculated momentum diffusivity in a steady state condition is shown in Fig.2 (solid line). In the inner region of $r/a \approx 0.5$, diffusion coefficient can not be determined because there is no momentum source. From power balance analysis, ion heat diffusion coefficient was estimated and a ratio of χ_i/χ_ϕ was about 2 in the outer half region.

In this experiment, tangential NBI with a counter direction was injected to ohmic target plasma at $t=8.06$ sec. As momentum input is limited in the outer half region, toroidal rotation starts in this region and penetrates into the inner region. It is thought that this penetration is dominated by toroidal momentum diffusion (perpendicular viscosity). Hence, the momentum diffusivity can be estimated from time evolution of toroidal velocity. This behavior is shown in Fig.3, where measured toroidal velocities at $r/a=0.11, 0.23, 0.38, 0.62$ and 0.88 are shown using asterisk symbols. The solid lines in the figure show calculated rotation velocities using Eq.(1). In this calculation, it was assumed that toroidal velocity is induced only by toroidal momentum input from NBI and that the velocity is zero at the plasma edge. A profile of momentum diffusivity was assumed as $(\chi_\phi(0)-\chi_\phi(a))(1-(r/a)^2)^\alpha + \chi_\phi(a)$, where $\chi_\phi(0)$ and $\chi_\phi(a)$ represent the central and edge values. From a comparison between the measured and calculated values, most plausible profile of momentum diffusivity was determined and shown in Fig.2 using a dashed line. The difference of diffusivities between the momentum balance and transient analysis is about 1.5-2.0 in a region of $r/a=0.6$ to 0.9 .

About the difference, it should be noted that the momentum diffusivity of transient analysis was obtained from an intermediate condition between ohmic and neutral beam heating (L-mode confinement). Generally, it is thought that tokamak transport is deteriorated by additional heating. Therefore, the difference of diffusivities may be due to the deterioration of L-mode confinement.

As a conclusion, the behavior of measured toroidal velocity was explained by only diffusive term, and non-diffusive momentum flux was not observed in the above experiments.

References

- [1] BURRELL, K. H., et al., Plasma Physics and Controlled Nuclear Fusion Research 1990, Washington, D. C., Vol.1, (1991) 123
- [2] LUCE, T. C., PETTY, C. C., De HAAS, J. C. M., Phys. Rev. Lett. 68 (1992) 52
- [3] SCHISSEL, D. P., et al., Nucl. Fusion 32 (1992) 689
- [4] KOIDE, Y., et al., Plasma Physics and Controlled Nuclear Fusion Research 1992, Wurzburg, in printing

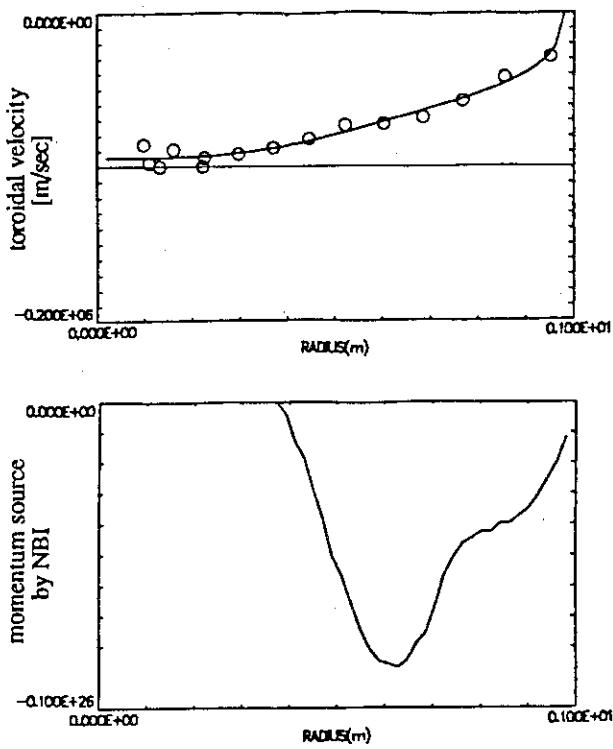


Fig.1 Measured toroidal velocity and toroidal momentum source profiles.

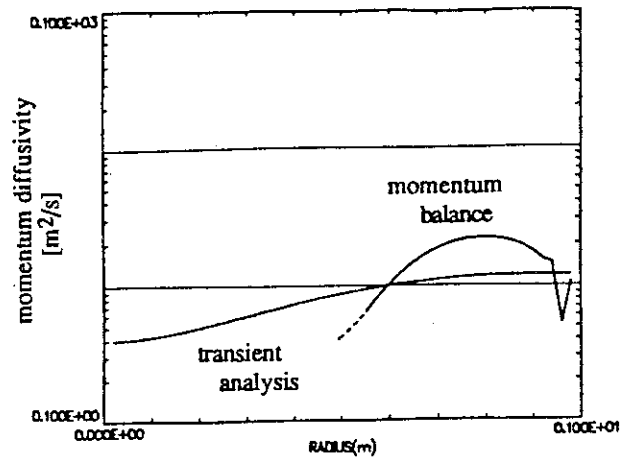
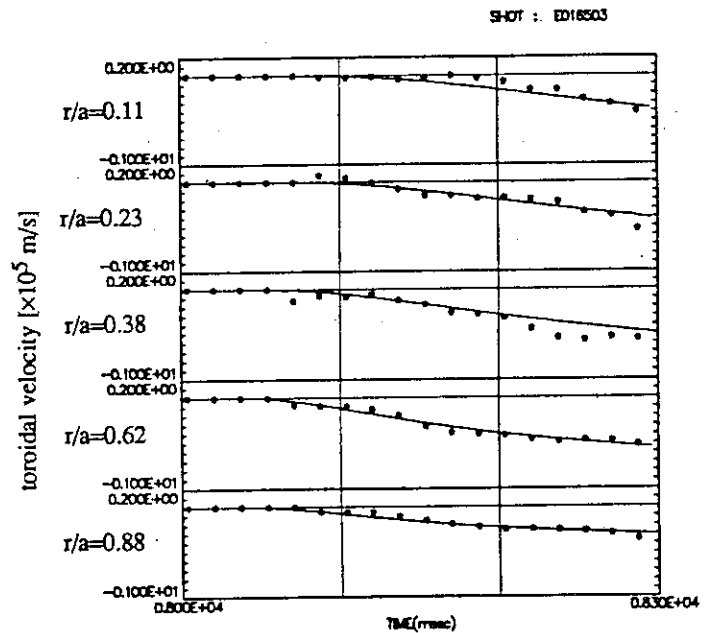


Fig.2 Calculated toroidal momentum diffusivities using momentum balance (solid line) and transient analysis (dashed line).

Fig.3 Time evolutions of measured (symbols) and calculated (lines) toroidal velocities at different five positions. Tangential NBI injection starts at $t=8.06$ sec.



3.3 Particle Transport Induced by Temperature Gradient on ICRF Experiments

K. Nagashima, M.Sato, T. Fukuda, H. Kimura

Lately, density and temperature perturbations induced by sawtooth collapse were measured simultaneously in JET¹⁾, and density flux induced by temperature gradient was recognized experimentally. This coupling between particle and heat flux was also observed in JT-60²⁾. In this section, ion cyclotron range of frequency (ICRF) central heating experiments on JT-60U will be described. In these experiments, density profile peaking seems to be coupled with temperature profile peaking. The two different phenomena, the density profile peaking in steady states and the density perturbation induced by sawtooth collapse, are analyzed using coupled transport equations including off-diagonal transport terms.

In these experiments, ion cyclotron second harmonic heating was used to heat hydrogen minority species in helium plasma. Resonance region of ICRF was located at plasma center. High energy ions generated by ICRF mainly heated electron in the central region, and electron temperature profile peaked in a region of $r/a < 0.4$. The main parameters of these discharges were plasma current of $I_p = 2.0$ MA, toroidal magnetic field of $B_t = 4.0$ T, effective safety factor of $q_{eff} = 4.5$, major and minor radii of $R = 3.50$ m and $a = 0.97$ m, plasma elongation factor of $\epsilon = 1.4$, line averaged electron density of $n_e = 2 \times 10^{19}$ m⁻³, and ion cyclotron heating power up to $P_{IC} = 3.6$ MW. Magnetic configuration was a lower x-point divertor. By the injection of ICRF, total radiation loss power increased by a factor of 1.5 to 2, and effective charge number Z_{eff} increased from 2.0 in ohmic phase to 2.0-2.5 in ICRF heating phase. Two measurement chords of FIR interferometer were located at tangential radii of $r/a = 0.08$ (inner chord) and 0.84 (outer chord).

Typical time evolutions of ICRF heating power, central electron temperature and two chord integrated electron densities are shown in Fig.1. The heating power increases gradually up to 3.6 MW at 9.3 sec, and following it, the central electron temperature increases gradually. Just after the turn-on of ICRF, the edge electron density (outer chord) increases slightly. However, during the increasing phase of heating power, it keeps almost constant. On the other hand, the central density (inner chord) increases similar to the temperature. The sawtooth oscillation becomes giant from 9.4 sec, which is clearly seen in the central density. This effect is not seen in the edge density because the sawtooth inversion radius is $r_s/a = 0.28$ and it is far away from the measurement chord ($r/a = 0.84$).

From the figure, it is found that in ICRF heating phase, the density profile becomes peaking in an inner region in spite of no particle source. The relation between density and

temperature profile peaking is clearly shown in Fig.2, where ratios of two chord integrated densities (inner chord value over outer chord value) are plotted as a function of temperature gradient at $r/a \approx 0.25$. From the measurement of visible bremsstrahlung emission profile, impurity accumulation in the central region was not observed. Therefore, this density peaking is not considered to be due to an impurity effect.

To analyze the particle balance in the steady state, we consider coupled transport equations including off-diagonal terms¹⁾

$$\begin{pmatrix} \frac{\Gamma}{n} \\ \frac{q}{nT} \end{pmatrix} = - \begin{pmatrix} D & \alpha \\ \beta & \chi \end{pmatrix} \begin{pmatrix} \frac{\partial n / \partial r}{n} \\ \frac{\partial T / \partial r}{T} \end{pmatrix} \quad (1)$$

where n , T , Γ and q represent plasma density, temperature, particle flux and heat flux, respectively. D and χ are particle and heat diffusivity, and α and β represent off-diagonal transport coefficients. On the particle flux equation, external particle source is negligible in the inside region (in these discharges, typical width of ionization is evaluated to be about 0.05-0.10 m). Hence, we can assume $\Gamma=0$ and obtain

$$\alpha/D = - \frac{\partial n / \partial r}{n} / \frac{\partial T / \partial r}{T} \quad (2)$$

Considering the plasma elongation, the peaking width is $\Delta r \approx 0.4-0.5$ m in the inner interferometer chord. Using the measurement values of $\Delta n \cdot \Delta r \approx 0.35-0.40 \times 10^{19} \text{ m}^{-2}$ and $(\partial T / \partial r / T) \approx 2$, density gradient is evaluated as $(\partial n / \partial r / n) > (\Delta n / \Delta r / n) \approx 1$, and $-\alpha/D > 0.5$ is obtained from Eq.(2).

As can be seen in Fig.1, clear density perturbations were induced by giant sawtooth oscillations in ICRF heating phase. Here, using particle and energy balance equations, we will simulate time evolution of the density perturbation and compare it with the measured one. The particle and energy balance equations are

$$\partial n / \partial t = -\nabla \Gamma + S \quad (3)$$

$$\partial W / \partial t = -\nabla q + P \quad (4)$$

where W , S and P represent heat density of $W=(3/2)nT$, particle and heat sources, respectively. All quantities are divided into the two parts, the equilibrium part and the perturbing part, like

$n(r,t)=n_0(r)+n_1(r,t)$, and Eqs.(3) and (4) are solved as an initial value problem. The detailed method of this calculation can be found in the reference²⁾. In the calculation, four transport parameters, D , α , β and χ , have to be given externally. From the results of gas puff modulation experiments^{3, 4)}, $D(r)$ and $\chi(r)$ are given as $D(r)=0.6-0.5(1-(r/a)^2)$ and $\chi(r)/D(r)=5$. Here, the effect of off-diagonal transport terms is examined, using an assumption of Onsager relation, $\alpha=\beta$ ⁵⁾.

Figure 3 shows measured and calculated evolution of the chord integrated density perturbation (inner chord) after one sawtooth collapse. Three calculated cases are $\alpha/D=\beta/D=0.0$, -0.5 and -1.0 . It should be noted that the calculated values are dependent strongly on the initial perturbed profile during a few ten milli-second after the collapse, and that if the off-diagonal terms are not included, the decay of perturbed density behaves exponentially. The measured density perturbation behaves almost similar to one calculated using $\alpha/D=\beta/D=-1.0$. The calculated perturbation is dependent on all four transport parameters. However, the behavior is not so sensitive to the ratio of χ/D , and a parameter β is not important because of $\chi \gg \beta$. Therefore, in this analysis, α is the most critical parameter and is estimated to be $\alpha/D \approx -1$.

As a conclusion, in ICRF central heating experiment, density profile peaking was found in spite of no external particle source. This density profile peaking is following to the electron temperature profile peaking. On the other hand, density perturbation induced by sawtooth collapse could be explained if the particle flux induced by temperature gradient is included. From the above two analysis, $\alpha/D \approx -1$ was obtained.

References

- [1] HOGWEIJ, G. M. D., O'ROURKE, J., SIPS, A. C. C., De HAAS, J. C. M., Proc. 17th EPS Conference on Controlled Fusion and Plasma Physics (1990), Part I, 158
- [2] NAGASHIMA, K., FUKUDA, T., JAERI-M 91-208
- [3] NAGASHIMA, K., SAKASAI, A., JAERI-M 92-057
- [4] NAGASHIMA, K., SAKASAI, A., De HAAS, J. C. M., FUKUDA, T., Proc. 19th EPS Conference on Controlled Fusion and Plasma Physics (1992), Part I, 87
- [5] O'ROURKE, J., Nucl. Fusion 27 (1987) 2075

SHOT : E015104

Fig.1 Typical time evolutions of ICRF heating power, central electron temperature, inner and outer chord integrated electron densities.

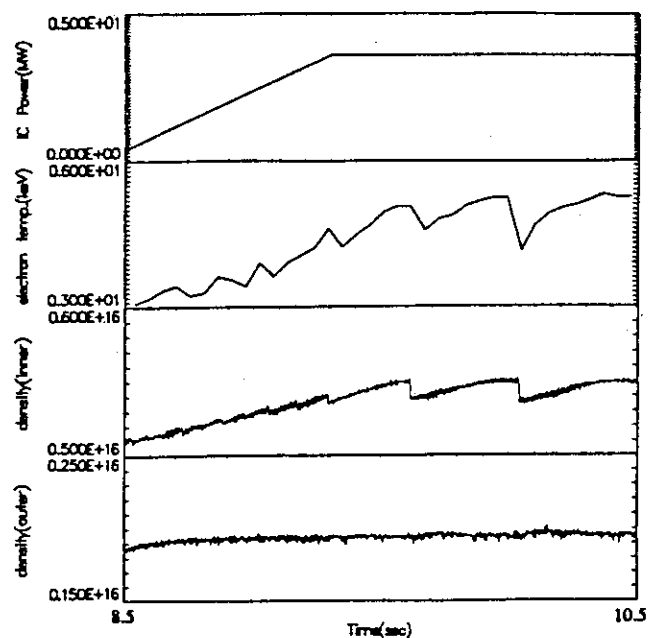


Fig.2 Relation between density and temperature profile peakings. Ratios of two chord integrated densities are plotted as a function of temperature gradient at $r/a=0.25$.

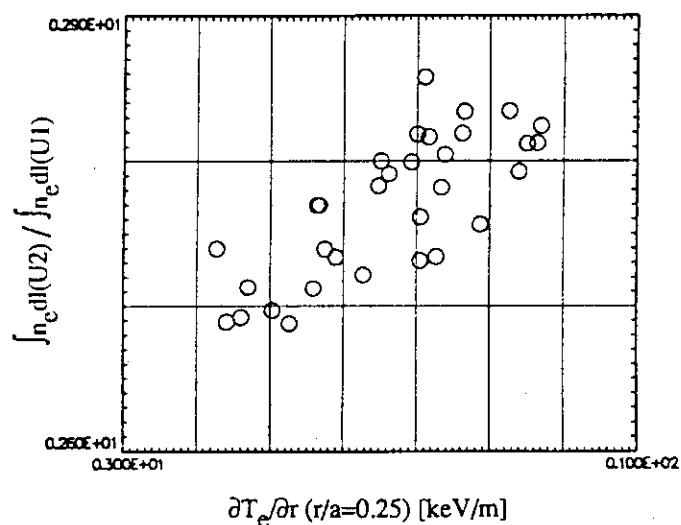
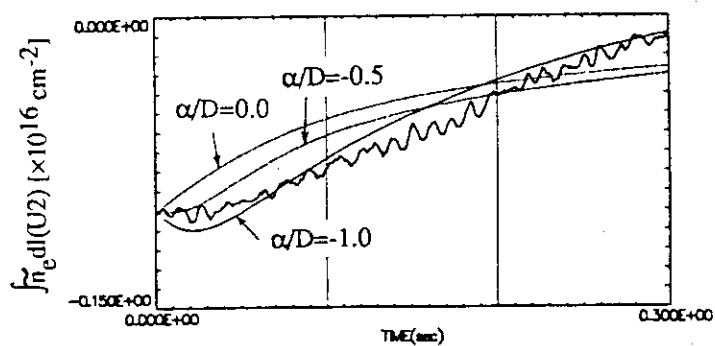


Fig.3 Measured and calculated evolutions of chord integrated density perturbation at $r/a=0.08$.



3.4 Anti-parallel Toroidal Rotation to Plasma Current during Near-perpendicular NBI

Y. Koide, T. Tuda, A. Sakasai, N. Asakura
S. Ishida, M. Kikuchi

1. Introduction

Recent experimental results, especially H-mode studies, have revealed the important role of radial electric fields on the improved transport [1]. It is essential to know not only the effect of the electric field itself but also the formation mechanisms of the electric field, including characteristic effects depending on the heating methods.

Our experiments have shown that the direction of toroidal rotation velocity during near-perpendicular NB tends to be ctr-directed and this suggest the formation of inward electric field in plasmas. In this paper, plasma rotation in L-mode plasma is discussed in relation with the ripple-loss.

2. Ctr-directed Toroidal Rotation during Near-perpendicular Neutral Beam Injection

The neutral beam heating system in JT-60U consists of 10 near-perpendicular beam injectors (6 co-injectors and 4 ctr-injectors) and 4 tangential beam injectors (2 injectors each for co- and ctr- directions), the injection angles of which are 75° and 36° to the magnetic axis, respectively. Deuterium beams accelerated to ~ 90 keV were injected, and the input power per injection unit was ~ 2 MW.

Figure 1 shows the comparison of $V_t(r)$ observed with various combinations of beam injectors. In this figure, the type of injected beam is denoted by the following symbols : T (tangential beam), P (near-perpendicular beam) ; the number of used injectors is shown in parenthesis. (The diagnostic beam is a co-directed perpendicular beam (P-co(1)), which is injected in all data shown in this figure.) In the cases with tangential beams, $V_t(r)$ showed peaked profiles with the direction in accordance with the external momentum input (shown with two sets of open circles. Plasma current $I_p=1.5$ MA, toroidal magnetic field $B_t=2$ T, line-average density $\bar{n}_e=0.6\times 10^{19}\text{m}^{-3}$). In this paper, negative V_t means ctr-directed rotation and positive V_t co-directed rotation. In contrast to results with tangential beams, perpendicular beams produced a ctr-directed uniform rotation profile (closed circles, $I_p=1.5$ MA, $B_t=2$ T, $\bar{n}_e=2.5\times 10^{19}\text{m}^{-3}$). Note that, in this case, the beams were co-directed, which was opposite to the observed rotation. The direction of V_t was reversed when plasma current was reversed, i.e. the anti-parallel relation between V_t and I_p remained. This fact shows the existence of an inward electric field as a rotation-driving source in plasmas heated by perpendicular NB injection,

which is stronger than the external momentum input.

In order to investigate the location of the above-mentioned driving source, beam perturbation experiments were carried out. The method of beam modulation is shown in Fig.2. A diagnostic beam was injected with constant power, and co-perpendicular beams were injected with a square-wave modulation of frequency 1-4 Hz into a discharge with $I_p=2$ MA, $B_t=4$ T, $\bar{n}_e=1.4 \times 10^{19} \text{ m}^{-3}$ as shown in an upper box of this figure. This modulation brought about a disturbance in \bar{n}_e less than $\pm 5\%$ (lower box of Fig.2(a)). The beam line of the modulated beams is shown with an arrow in Fig.2(b). Since these beams injected off the magnetic axis and the beam diameter was ~ 0.3 m at FWHM (full width at half maximum), the central region inside $r \sim 0.2$ m was free from direct external momentum input. Figure 2(c) shows the waveforms of modulated toroidal rotation velocity at $r/a_p=0.15, 0.6$ and 0.8 (solid lines), where a_p is a plasma minor radius. Each trace is fitted to a sinusoidal function at the modulation frequency plus a linear function (dotted lines). Note that V_t at $r/a_p=0.1$ was also modulated at the frequency of the beam modulation. However, the position of $r/a_p=0.1$ was outside the deposition region, showing that the modulated part of V_t , \tilde{V}_t , was propagating from further out. This view is supported by the fact that the phase delay of \tilde{V}_t became larger and the modulated amplitude became smaller in the inner region as shown in this figure. The phase of propagating \tilde{V}_t is almost in anti-phase to the co-beam modulation.

Next we discuss the spatial profile of above-mentioned phase delay, $\Delta\phi$, and the amplitude, $|\tilde{V}_t|$. We fitted the wave form of the beam-power to a sinusoidal function, and the fitted phase was used as the origin of phase the shift, i.e. $\Delta\phi=0$. As shown in Fig.2(d) (modulation frequency was 2.5 Hz in this discharge), the phase decreased from -210° at the edge to -330° at the center, showing the inward propagation of \tilde{V}_t . Furthermore, the modulated amplitude $|\tilde{V}_t|$ decreased as position decreased from $0.9 a_p$ to the center, as shown in Fig.2(e). It follows that the driving source of ctr-directed rotation exists in the edge region around $r \geq 0.9 a_p$. A contribution of -180° to the total phase-shift of -210° at the edge is attributable to the anti-phase response of V_t to the beam injection. The -30° remainder is indicative of a response time, which corresponds to a delay of 33 ms at 2.5 Hz modulation.

In addition to the driving source in the edge region, there are two further features which characterize the ctr-rotation. First, a q_{eff} dependence of the magnitude of this ctr-rotation which is shown in Fig.3(a): steady state $V_t(r)$ during co-perpendicular NB injection in two discharges with similar configurations and with different q_{eff} of 10 (closed circles) and 3.5 (open circles) are compared in this figure. It was found that the magnitude of ctr-rotation was larger with higher q_{eff} . Another feature is the dependence on the toroidal field ripple. The modulated amplitude $|\tilde{V}_t|$ during co-perpendicular beam modulation in two discharges with similar q_{eff} and with different magnitude of toroidal field ripple are plotted vs. major radius in Fig.3(b). The toroidal field ripple was changed by varying the position of the plasma column. Closed circles

show $|\tilde{V}_t|$ when the plasma was formed on the outer side (the shaded region schematically shows the radial position), where the maximum toroidal field ripple reached 3 %. In this case, the response of \tilde{V}_t to co-beam modulation is in the ctr-direction as mentioned above. However, the magnitude of the ctr-rotation became small or was not observed when the plasma was moved inwards while keeping the value of q_{eff} constant. Open circles show $|\tilde{V}_t|$ in a smaller plasma (hatched region) with a maximum toroidal field ripple of 0.4 %. $|\tilde{V}_t|$ monotonically increased towards the center and was small in the edge region. Note that, in this case, the response of \tilde{V}_t to co-NB modulation is in co-direction in contrast to the former case. A result of co-tangential beam modulation is shown with a dotted line for a comparison in this figure: even in a large plasma, ctr-rotation was not observed.

These observations mentioned above, i.e. driving source in the edge region, enhanced ctr-rotation with higher q_{eff} and larger toroidal field ripple, all qualitatively agree with the condition of the enhanced ripple loss mechanism [2]. We deduced that the ctr-rotation during perpendicular NB injection is driven by ripple-loss induced inwardly directed radial electric field.

References

- [1] TAYLOR, R.J., et al., Phys. Rev. Lett. **63** (1989) 2365.
- [2] TOBITA, K., et al., to be published in Phys. Rev. Lett.

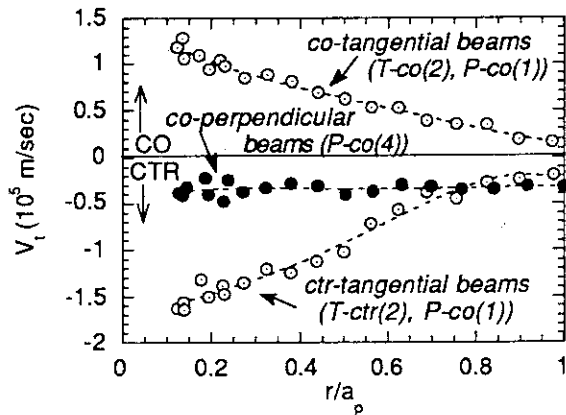


Fig. 1 Toroidal rotation profiles observed with various combinations of neutral beam injectors. The symbols 'T' and 'P' denote tangential injection and nearly-perpendicular injection, respectively. The number of injection units used is shown in parentheses. A diagnostic co-directed perpendicular beam is injected in every case for the $V_t(r)$ measurement.

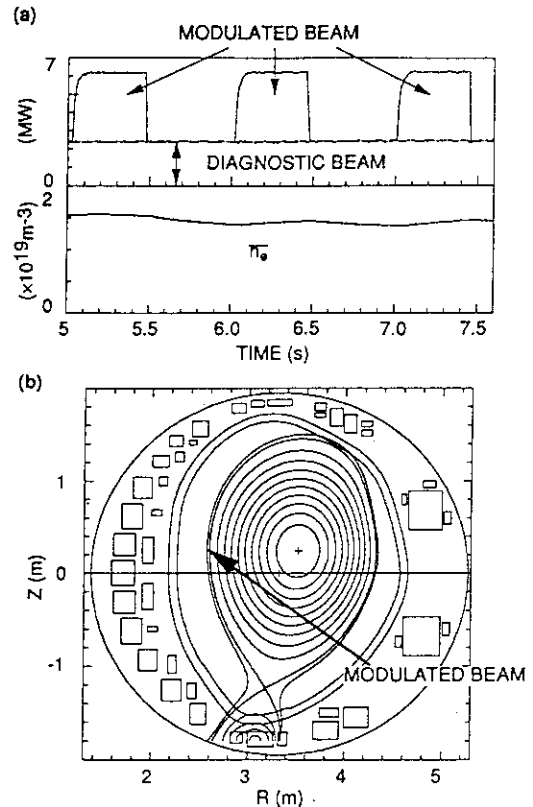


Fig. 2 Experiments with beam modulation. (a) Evolution of beam power and line-average electron density. (b) Equilibrium poloidal flux surfaces and the injection direction of modulated beams. Off-axis and co-directed perpendicular beams are modulated.

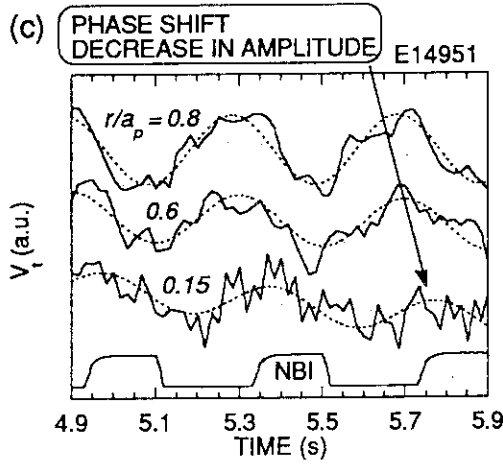


Fig. 2 (c) Response of toroidal rotation to the modulated beams. Three traces of V_t at $r/a_p=0.1$, 0.5 and 0.85 are shown. Each trace is fitted to a sinusoidal function with the modulation frequency plus a linear function (shown with dotted lines). Profiles of (d) phase delay and (e) modulated amplitude.

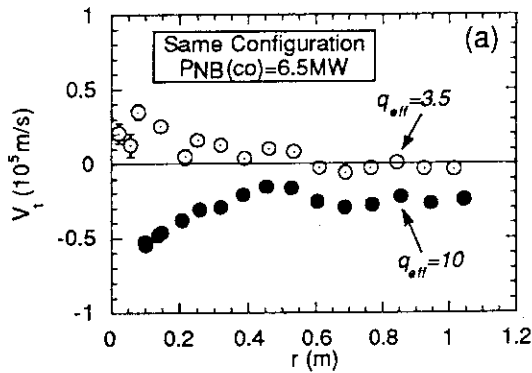
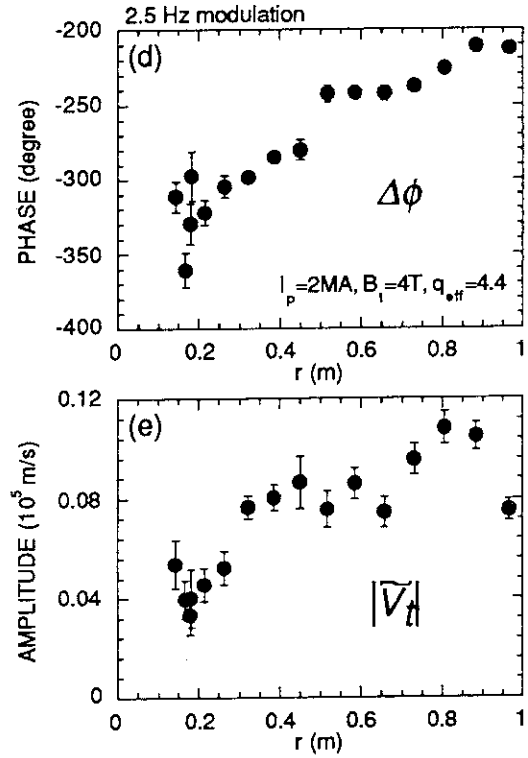
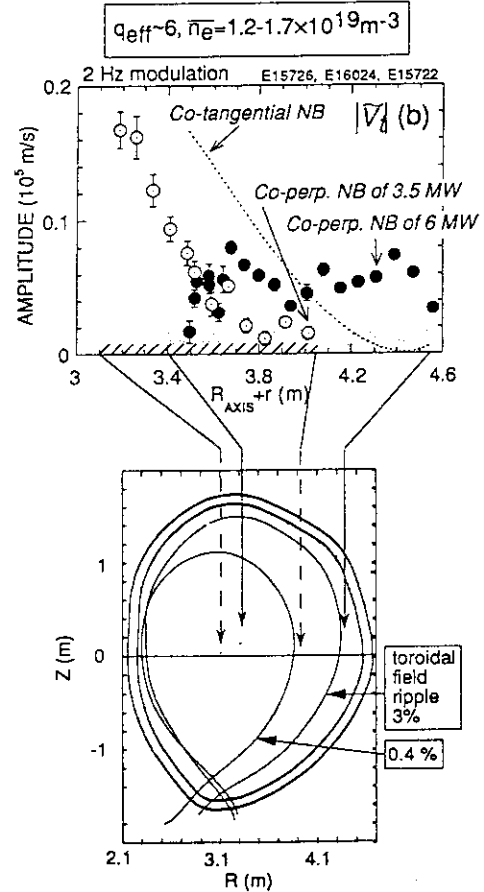


Fig. 3 (a) Comparison of steady state profiles of $V_t(r)$ with $q_{eff}=3.5$ (open circles) and with $q_{eff}=10$ (closed circles). (b) Comparison of modulated amplitude between discharges with different toroidal field ripple; 3% (closed circles), 0.4% (open circles). during co-tangential beam is shown with a dotted line for a comparison. Hatched and shaded regions show schematically the plasma positions.



3.5 Co-parallel Toroidal Rotation to Plasma Current During LHCD

Y. Koide, K. Ushigusa, S. Ide

A. Sakasai, N. Asakura

1. Introduction

In plasmas where the current is fully driven by lower hybrid waves (LHW), some special features have been reported compared with inductively driven plasmas : particle confinement was improved [1] : MHD instability was stabilized [2] : the threshold power required for the H-mode transition was lower in LHW-driven plasmas than in NB heated plasmas [3]. We found another characteristic feature of plasma rotation in discharges in which the current was almost fully driven by LHW : V_t tended to be in the direction co-parallel to plasma current. Since an external momentum input from LHW was given to electrons and the direction of the momentum input was anti-parallel relative to the plasma current, the observed co-directed plasma rotation, which mainly represents the ion flow, suggests the formation of an outward radial electric field in LHW-driven plasmas.

2. Toroidal Rotation Induced by LHCD

Figure 1 shows the characteristic direction of V_t in response to LHW injection. Two LHW pulses with a power of 1.4 MW and with peak parallel-refractive indices of $N_{\parallel}=1.44$ ($t = 6-7$ s) and $N_{\parallel}=2.24$ ($t = 8-9.5$ s) were injected. Power-limitations, due to the accessibility condition of LHW, are negligible for these values of N_{\parallel} . The loop voltage, V_L , during LHW was reduced from 0.35 V to 0.1 V at $t=6$ s (the middle box of this figure), showing that 70 % of I_p was driven by LHW. The evolution of V_t at the center and at the edge of plasma is shown in the bottom box of this figure. V_t measured at both spatial points was observed to be in the ctr-direction when the diagnostic beam was injected at $t=5.5$ s. This ctr-rotation is the effect discussed in ref.[4]. An additional co-directed contribution to V_t is observed during LHW injection ($t=6-7$ s). After the termination of LHW at $t=7$ s, V_t increased in the ctr-direction. When the second LHW pulse was injected during $t=8-9.5$ s, the magnitude of this ctr-rotation was again reduced, and the plasma edge started to rotate in the co-direction. The response time of V_t seems to be shorter than 100 ms, which was similar to the response time of the hard X-ray emission.

A typical radial profile, $V_t(r)$, during LHW, is compared with $V_t(r)$ in the Ohmic phase in

Fig.2(a). The diagnostic beam was injected 1 s after the start of LHW injection, when the plasma had already reached a steady state, and the duration of the beam-pulse was decreased to 100 ms in order to reduce the effect of NB injection on the rotation. A uniform $V_t(r)$ of $\sim -0.1 \times 10^5$ m/s was formed in the Ohmic phase (closed circles) as shown in this figure. In the LHW phase with $N_{//}=1.76$ (open circles), $V_t(r)$ changed towards the co-direction over the whole plasma region.

In Fig.2(b), V_t is plotted vs. accessible LHW power P_{LH} . We use V_t averaged over the inner and outer half of the plasma, i.e. $V_t(r < a_p/2)$ and $V_t(r > a_p/2)$, in this figure. The electron density was fixed around at $\bar{n}_e = 5 \times 10^{18} \text{ m}^{-3}$. $V_t(r < a_p/2)$ increased almost linearly with P_{LH} for $N_{//}=1.28$ (closed circles). As for the data with LHW of $N_{//}=1.92$ (open circles), $V_t(r < a_p/2)$ also increased with P_{LH} and $V_t(r > a_p/2)$ showed a similar tendency (crosses). These observations provide evidence that the observed change in plasma rotation towards co-direction is driven by LHW injection.

When energetic electrons leave the plasma, positive charges are left behind and an outward electric field is set up. As a result, V_t would be driven in the $\mathbf{E}_r \times \mathbf{B}_\theta$ direction, i.e. the co-direction, where \mathbf{E}_r and \mathbf{B}_θ are vectors of radial electric field and poloidal magnetic field, respectively. According to the soft X-ray measurements reported in ref.[5], for the range of \bar{n}_e and $N_{//}$ in these experiments, the power lost through energetic electrons to divertor plates is expressed as $P_{LOSS} = 0.36 P_{LH} \tau_{SD}^{0.86}$. Then we may regard $N_{EE} \equiv P_{LOSS}/E_{RES}$ as the number of lost energetic electrons per unit time, where E_{RES} is the resonant parallel energy of the energetic electrons, and τ_{SD} is the slowing down time of energetic electrons; E_{RES} and τ_{SD} are defined by the following relativistic formulae,

$$\tau_{SD} = \frac{4\pi \epsilon_0^2 m_0^2 c^3}{\bar{n}_e \ln \Lambda} \frac{N_{//}^3}{(Z_{eff} + 1)(1 - N_{//}^2) + \sqrt{1 - N_{//}^2}} \quad (1)$$

$$E_{RES} = mc^2 \left(\frac{1}{\sqrt{1 - N_{//}^2}} - 1 \right) \quad (2) ,$$

where m and c are electron rest-mass and velocity of light respectively. In Figs.3(a)-(d), V_t is analyzed in terms of N_{EE} . Accessibility of LH power were took into account in this figure, where more than 80 % of the injected LHW power was accessible even with $N_{//}$ as small as 1.28. Figure 3(c), for example, shows the data with a fixed $N_{//}$ of 1.92 ($P_{LH}=1.16\text{-}1.43$ MW, $\bar{n}_e=4.2\text{-}5.7 \times 10^{18} \text{ m}^{-3}$). When N_{EE} increased from 3 to $4.5 \times 10^{18}/\text{s}$, $V_t(r < a_p/2)$ increased from -0.13×10^5 m/s to 0.13×10^5 m/s (closed circles). $V_t(r > a_p/2)$ also increased towards the co-direction (open circles) as N_{EE} increased. Figures 3(a), (b) and (d) show similar plots of $V_t(r < a_p/2)$ for different $N_{//}$: (a) $N_{//}=1.28$, (b) $N_{//}=1.76$ and (d) $N_{//}=2.24$ (The ranges of \bar{n}_e and P_{LH} are comparable for Figs.3(a)-(d)).

One of the common features for these data is that V_i increased with N_{EE} , showing that the number of energetic electrons lost from the confined region was related to the observed rotation. The drive efficiency of V_i per unit loss rate of energetic electrons is represented by the slope of the plots in Figs.3(a) to (d), i.e. dV_i/dN_{EE} . For simplicity, we fitted the data to a linear function and the result is shown with a dotted line. In fact, a non-linear fitting function seems to be required to fit these data to incorporate the region of low N_{EE} taking into account the ohmic region, which was therefore excluded. (A similar non-linearity is also evident in Fig.2(b).)

It is found that larger $N_{//}$ is associated with larger dV_i/dN_{EE} . This result is clearly shown in Fig.4(a), where dV_i/dN_{EE} is plotted vs. $N_{//}$. Roughly speaking, dV_i/dN_{EE} increased with $N_{//}$. For example, dV_i/dN_{EE} at $N_{//}=2.24$ is increased by 80 % compared with that for $N_{//}=1.28$. This result means that the change in V_i due to the loss of energetic electrons depends on the $N_{//}$ of the driving waves, with larger $N_{//}$ corresponding to larger changes in V_i . The hard X-ray emission profile has a similar dependence on $N_{//}$ as shown in Fig.4(b), where the profile peaking factor of HX is defined by the ratio of hard X-ray intensities with photon energy above 150 keV (I_{HX}) measured along two chords through $r=0.33 a_p$ and $0.74 a_p$. In this figure, data in discharges at the higher end of the P_{LH} range for each $N_{//}$ are plotted. It is seen, from this figure, that peaked profiles of HX are formed by LHW with lower $N_{//}$ and broad profiles with high $N_{//}$ as has been reported in ref.[6]. The similarity of the $N_{//}$ dependence of dV_i/dN_{EE} and $I_{HX}(0.74a_p)/I_{HX}(0.33a_p)$ shown in Figs.4(a) and (b) suggests a correlation between them.

The profile of energetic electrons is also important from the viewpoint of current profile modifications and their influences on MHD stability. So a proper experimental study for the identification of loss mechanisms is needed to understand the $N_{//}$ dependence of the plasma rotation.

References

- [1] PORKOLAB, M., et al, Proc. of 10th Int. Conf. on Plasma Phys. and Controlled Nucl. Fusion Research, London (1984), Vol.1 p.463.
- [2] VAN HOUTTE, D., et al, Nucl. Fusion **24** (1984) 1485.
- [3] TSUJI, S., et al, Phys. Rev. Lett. **64** (1990) 1023.
- [4] KOIDE, Y., et al, the paper 3.4 in this review.
- [5] USHIGUSA, K., et al., Plasma Physics and Controlled Fusion Research (Proc. 14th Int. Conf. Würzburg, 1992).
- [6] KONDOH, T., et al., in Contr. Fusion and plasma Physics (Proc. 19th Eur. Conf. Innsbruck, 1992), vol.16C, Part II, Eur. Phys. Soc. (1992) 969.

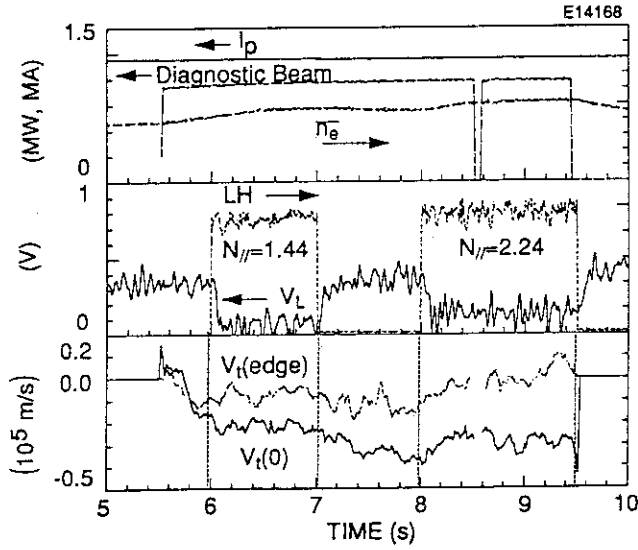


FIG. 1 Response of toroidal rotation to LHW injections. Two LHW pulses, the peak parallel refractive indices of which are ≈ 1.44 ($t = 6-7$ s) and ≈ 2.24 ($t = 8-9.5$ s), are injected (middle box). Evolutions of V_t at the center and at the edge of plasma (bottom box).

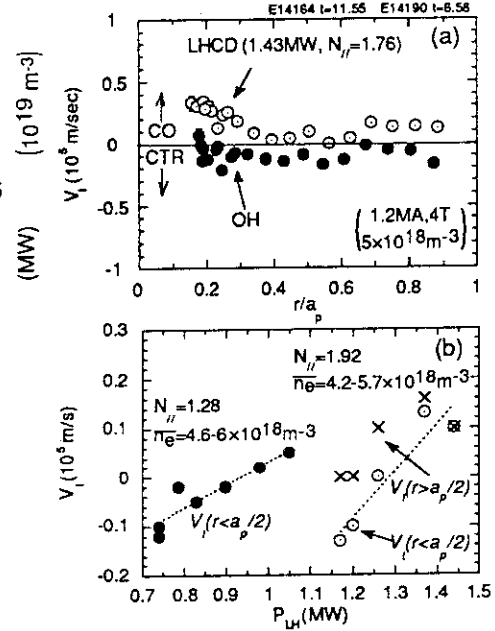


FIG. 2 (a) $V_t(r)$ during LHW injection ($N_{\parallel} = 1.76$) with a power of 1.43 MW (open circles), is compared with $V_t(r)$ in Ohmic phase (closed circles). (b) V_t averaged over the half radius of the plasma plotted vs. LHW power. Closed circles: $V_t(r < a_p/2)$ with N_{\parallel} of 1.28, open circles: $V_t(r < a_p/2)$ with N_{\parallel} of 1.92, crosses: $V_t(r > a_p/2)$ with N_{\parallel} of 1.92.

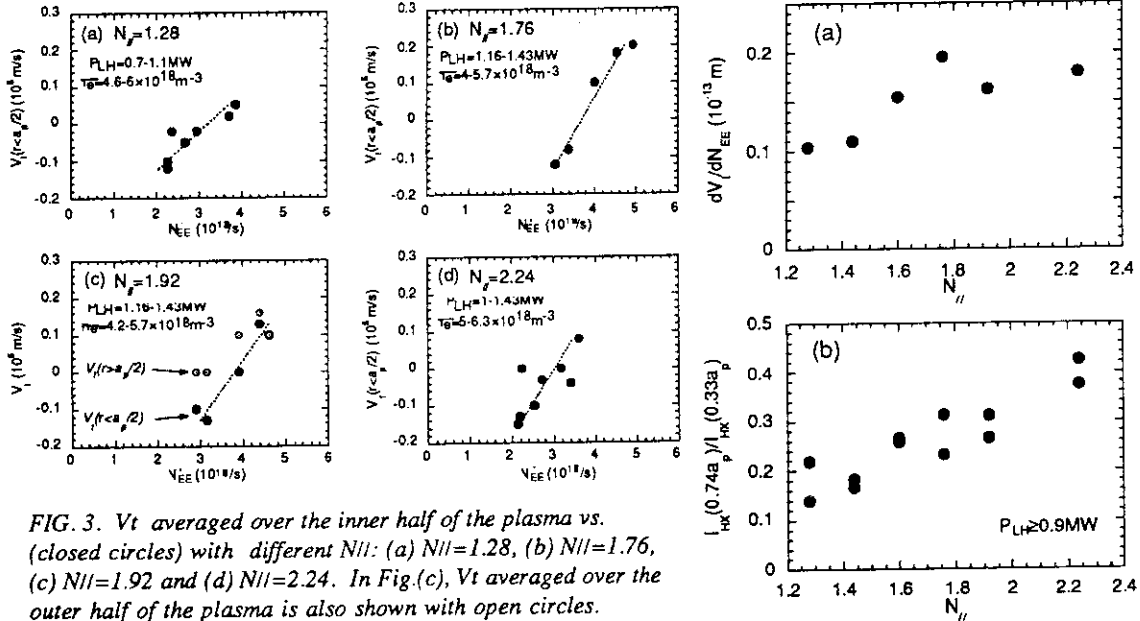


FIG. 3. V_t averaged over the inner half of the plasma vs. N_{\parallel} : (a) $N_{\parallel} = 1.28$, (b) $N_{\parallel} = 1.76$, (c) $N_{\parallel} = 1.92$ and (d) $N_{\parallel} = 2.24$. In Fig.(c), V_t averaged over the outer half of the plasma is also shown with open circles.

FIG. 4. (a) The driving efficiency of V_t per unit number of energetic electrons, dV_t/d , plotted vs. N_{\parallel} . (b) The N_{\parallel} dependence of the profile peaking factor of the hard X-ray emission profile, which is defined by the ratio of hard X-ray intensity at energies above 150 keV measured along two chords with $r/ap = 0.33$ and 0.74.

3.6 Transport Analysis of Ohmically Heated Plasmas by CXRS Measurement

Hiroshi Shirai Yoshihiko Koide, Masayasu Sato, Nobuaki Isei,
Mitsuru Kikuchi, Tomonori Takizuka, Masafumi Azumi

As a first step of transport analysis of ohmically heated plasmas in JT-60U, the dependence of the neutron emission rate and the stored energy on the density profile shape, the effective charge number, Z_{eff} , and the ion thermal diffusivity, χ_i was studied [1]. Because the neutron emission rate, in particular, depends on these parameters, the experimental data must be carefully evaluated and treated in the transport analysis of ohmically heated plasmas. In this calculation, we assume the electron density profile as some power of parabolic shape; $n_e(r) = n_e(0) (1 - r^2)^m$, and using two channels of interferometer data, the line averaged electron density, \bar{n}_e , is inferred taking into account of Shafranov shift of magnetic axis. We use Electron Cyclotron Emission (ECE) data for the electron temperature. Z_{eff} is calculated by visible Bremsstrahlung data.

As for the ion temperature, there used to be one channel of active beam probe which measured T_i value in the plasma center several years ago. However, there is no diagnostic system which can directly measure T_i profile in the present JT-60U device. Therefore T_i profile shapes were calculated by assuming $\chi_i = f \chi_i^{\text{NC}}$, where χ_i^{NC} is the neoclassical diffusivity proposed by Chang & Hinton [2]. The coefficient f is determined by comparing the measured neutron emission rate and the stored energy with the calculated values. However, it is doubtful whether the assumed χ_i reproduces the actual T_i profile, because the χ_i^{NC} profile is almost spatially constant while the experimentally evaluated χ_i increases from the plasma center toward the edge [3]. Therefore the direct measurement of T_i is necessary for the minute transport study of ohmically heated plasmas.

In this section, the T_i profiles measured by Charge Exchange Recombination Spectroscopy (CXRS) are adopted to evaluate χ_e and χ_i . We adopted two ways to utilize T_i profile data by CXRS; (1) Short pulse (≤ 100 msec) beams are injected repeatedly every 0.5 ~ 1 sec and the T_i profile data are gathered at the end of each beam pulse and treated statistically (See Fig.1; shot E15367) or (2) one unit of neutral beam is injected and the T_i profile data are gathered 100 msec after the beginning of injection (See Fig.2; shot E15721). In the former way, each beam pulse must be separated in order to get rid of the influence of slowing down fast ion due to the beam pulse just before. Still more we cannot get this type of shot too much. Therefore we utilized the latter way.

The plasma parameters other than T_i such as n_e and T_e are measured just before the beginning of neutral beam injection. The measured T_i by CXRS is expected to be somewhat higher than that of ohmically heated level. We will evaluate the increment of T_i during the 100 msec NBI heating. The increment of \bar{n}_e , the particle averaged electron temperature, $\langle T_e \rangle$, and the stored energy including beam component, W^* , of 100 msec

after the NBI in 2 MA plasma are 0.8 %, 2 % and 6.5 %, respectively. At the beginning of beam injection, heating power mainly deposits to electrons because T_e is low. It can be assumed that the increment of T_i is less than that of T_e . The increment of W^* is attributed to the beam stored energy because the slowing down time of fast ion is larger than 100 msec. If the one unit of NB is injected continuously, these increments are 6 %, 21 % and 33 %, respectively. Thus we assume that the increment of T_i at 100 msec after the injection is small. We will check this by using 1.5 dimensional transport code TOPICS.

Both χ_e and χ_i are calculated by the electron and ion energy balance equation (we set $P_{NBI}^e = P_{NBI}^i = 0$ in eqs. (1) and (2) of Sec. 3.7). The radiation loss, P_{rad} , is neglected in the calculation. We calculate the plasma current assuming neoclassical plasma resistivity. Figure 3 is the density and the temperature profiles of typical 2 MA ohmically heated plasma; shot 15721, $t = 4.5$ sec, $B_t = 4$ T, $\bar{n}_e = 1.44 \times 10^{19} \text{ m}^{-3}$. In the region of $r > 2a/3$ where the convection loss and/or the radiation loss becomes comparable to the conduction loss, χ_e and χ_i include a large error. Therefore whether χ_e decreases toward the plasma edge region is indistinct.

Figure 4 shows the \bar{n}_e dependence of χ_e and χ_i at $r = a/2$ in 2 MA ohmically heated plasmas. The internal inductance l_i is almost the same (~ 1) except for the shot of $\bar{n}_e = 1.1 \times 10^{19} \text{ m}^{-3}$ ($l_i \sim 1.2$). In the low density region ($\bar{n}_e < 1 \times 10^{19} \text{ m}^{-3}$), χ_e becomes larger than χ_i and the electron heat transport governs the energy confinement. In this density region, energy confinement time, τ_E , follows Neo Alcator scaling [4]. In the high density region ($\bar{n}_e > 1.5 \times 10^{19} \text{ m}^{-3}$), χ_i becomes larger than χ_e and the ion heat transport governs the energy confinement. In this region, τ_E saturates around 700 msec. A transport theory predicted that the dissipative trapped electron mode dominates in the low \bar{n}_e region and the ion temperature gradient mode (η_i mode) dominates in the high \bar{n}_e region in the ohmically heated plasmas [5]. The results shown here supports this prediction.

Figure 5 is the density and the temperature profiles of typical 3 MA ohmically heated plasma; shot 16129, $t = 4.5$ sec, $B_t = 4$ T, $\bar{n}_e = 1.2 \times 10^{19} \text{ m}^{-3}$. Figure 6 shows the \bar{n}_e dependence of χ_e and χ_i at $r = a/2$ in 3 MA ohmically heated plasmas. l_i is 1.15 ~ 1.2 for these shots. In the high density region of $\bar{n}_e > 1.2 \times 10^{19} \text{ m}^{-3}$, χ_i becomes larger than χ_e like 2 MA cases. Since there is no 3 MA data with low \bar{n}_e , it is unknown whether the electron heat transport governs the energy confinement in $\bar{n}_e < 1 \times 10^{19} \text{ m}^{-3}$.

In order to make clear the \bar{n}_e dependence of χ_e and χ_i shown above, the error evaluation of calculated χ_e and χ_i is required. This is an important future subject.

References

- [1] SHIRAI, H., et al., Rep. JAERI-M 92-073 (1992) Sec. 5.1, page 134
- [2] CHANG, C.S., HINTON, F.L., Phys. Fluids, **29** (1986) 3314
- [3] SCOTT, S.D., et al., Phys. Fluids, **B2** (1990) 1300
- [4] SHIRAI, H., et al., Rep. JAERI-M 92-073 (1992) Sec. 3.10, page 92
- [5] DOMINGUEZ, R.R., WALTZ, R.E., Nucl. Fusion, **27** (1987) 65

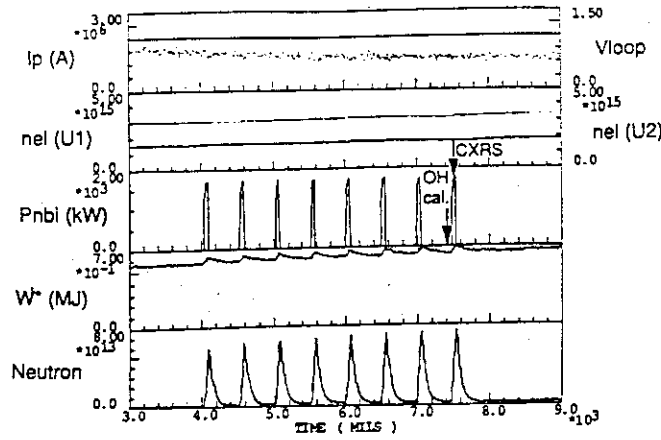


Fig. 1 Waveform of $I_p = 2$ MA ohmically heated plasma (shot E15367) with repetition of 1 unit short pulse neutral beam injection. The time of transport analysis and T_i measurement by CXRS is indicated.

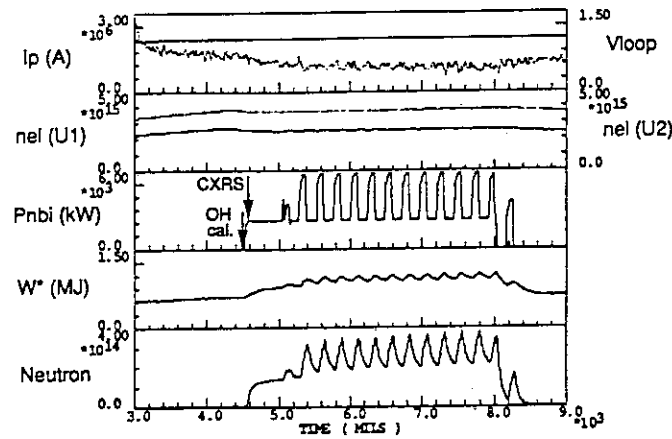


Fig. 2 Waveform of $I_p = 2$ MA ohmically heated plasma (shot E15721) with ordinary neutral beam injection. The time of transport analysis and T_i measurement by CXRS is indicated.

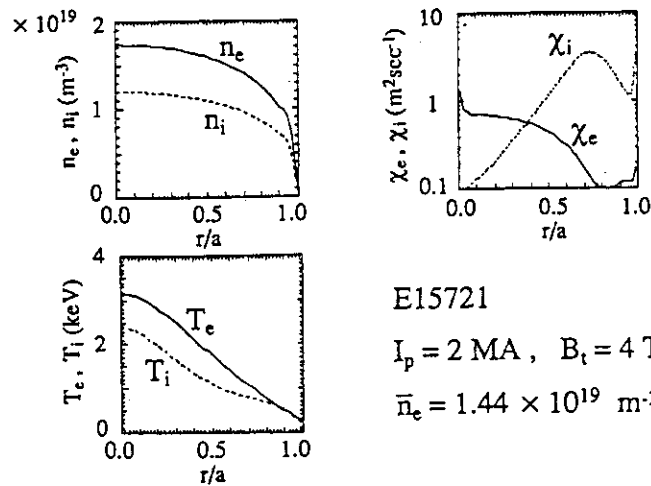


Fig. 3 The profiles of (a) n_e and n_i , (b) T_e and T_i , (c) χ_e and χ_i in $I_p = 2$ MA ohmically heated plasma (Shot E15721, $t = 4.5$ sec).

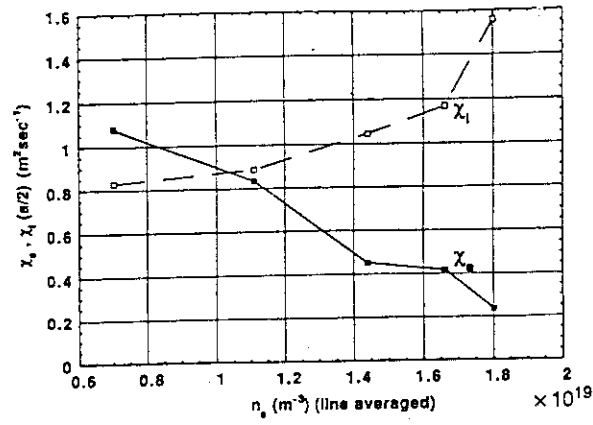


Fig. 4 The \bar{n}_e dependence of χ_e and χ_i at $r = a/2$ in $I_p = 2$ MA ohmically heated plasmas.

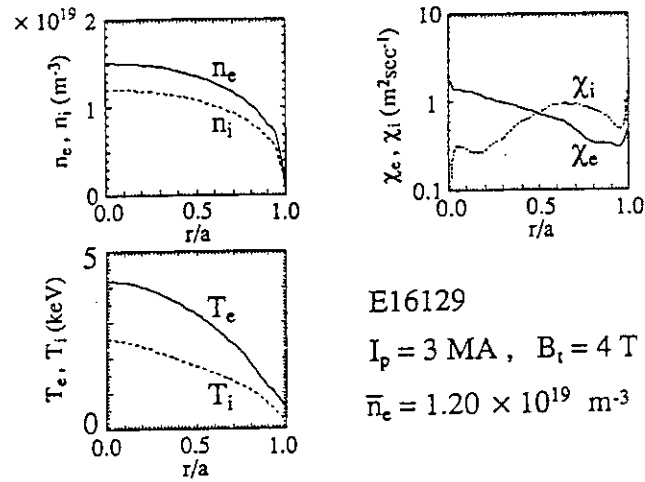


Fig. 5 The profiles of (a) n_e and n_i , (b) T_e and T_i , (c) χ_e and χ_i in $I_p = 3$ MA ohmically heated plasma (Shot E16129, $t = 9.1$ sec).

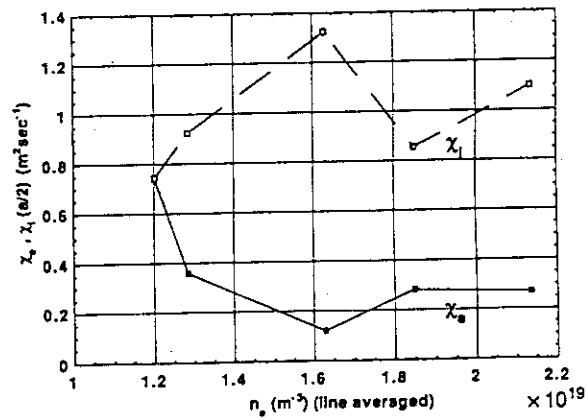


Fig. 6 The \bar{n}_e dependence of χ_e and χ_i at $r = a/2$ in $I_p = 3$ MA ohmically heated plasmas.

3.7 Transport Analysis of Low Power NBI Heated Plasmas

Hiroshi Shirai Yoshihiko Koide, Masayasu Sato, Nobuaki Isei,
Mitsuru Kikuchi, Tomonori Takizuka, Masafumi Azumi

In the previous work [1], the plasma current dependence, the absorption power dependence and the toroidal field dependence of electron and ion thermal diffusivities, χ_e and χ_i , were analyzed in the neutral beam heated L-mode plasmas of JT-60U in the high elongated configuration. For example, the absorption power dependence of χ_e and χ_i at $r = a/2$ in $I_p = 3$ MA plasmas in high elongated configuration are shown in Fig.1. It was found that χ_i is larger than χ_e in this P_{abs} range and that χ_i increases with P_{abs} while χ_e is nearly unchanged. Most of the plasmas available for the local transport analysis have high P_{abs} (> 15 MW) and the L-mode shots with small P_{abs} is very few; for example there were only two shots 7.7 and 12.9 MW for $I_p = 3$ MA plasma. Therefore it was hard to survey the overall P_{abs} dependence of heat transport from ohmically heated plasmas to high power heated plasmas. We are planning to apply theoretical (η_i mode, drift wave etc.) or semiempirical (Rebut-Lallia-Watkins [2] etc.) heat transport models to study the heat transport mechanism in the next step of study. Before that we must investigate the characteristics of χ_e and χ_i in a wide range of plasma parameters of I_p , P_{abs} , \bar{n}_e , B_t and etc.

In this section, we pay attention to the P_{abs} dependence of χ_e and χ_i . In order to compensate for the lacked low P_{abs} data, we deal with plasmas with $P_{abs} < 10$ MW. Thermal diffusivities, χ_e and χ_i , are calculated by the electron and ion energy balance equations. They are shown as follows;

$$\chi_e(r) = \frac{-\frac{3}{2} T_e \Gamma_e + \frac{1}{r \langle |\nabla r|^2 \rangle} \int_0^r (-P_{rad} + P_{eq} + P_{OH} + P_{NBI}^e) r dr}{-n_e \frac{\partial T_e}{\partial r}} \quad (1)$$

$$\chi_i(r) = \frac{-\frac{3}{2} T_i \Gamma_i + \frac{1}{r \langle |\nabla r|^2 \rangle} \int_0^r (-P_{CX} - P_{eq} + P_{NBI}^i) r dr}{-n_i \frac{\partial T_i}{\partial r}} \quad (2)$$

where Γ_i , P_{rad} , P_{eq} , P_{CX} , P_{OH} represent the ion particle flux, the radiation loss, the equilibrium energy exchange between electrons and ions, the charge exchange loss, Ohmic heating power, respectively. n_e is calculated from two channels of interferometer data. T_e is measured by ECE. T_i is measured by CXRS. Since we P_{rad} disregarded in this calculation, the χ_e and χ_i value in the peripheral region is not correct. Bracket is the average over a magnetic surface. Γ_i is defined as follows.

$$\Gamma_i(r) = \Gamma_e(r) = \frac{1}{r \langle |\nabla t|^2 \rangle} \int_0^r S(r) r dr \quad (3)$$

where S is a local particle source due to the recycling at the wall.

First, we deal with the $I_p = 3$ MA plasmas with $B_t = 4$ T in high elongated configuration. The magnetic axes of these shots are slightly shifted inward in the major radius direction. Plasma volume is about 69 m^3 , which is 10 % smaller than the previous work. Figure 2 shows the P_{abs} dependence of stored energy components (W_e , W_i and W_b) and thermal diffusivity, respectively. The line average electron density is $2.08 \sim 2.34 \times 10^{19} \text{ m}^{-3}$. The ohmic data ($\bar{n}_e = 1.85 \times 10^{19} \text{ m}^{-3}$) is also shown for reference. Internal inductance, l_i , is 1.21 except for the shot of $P_{abs} = 6.7 \text{ MW}$ ($l_i = 1.15$). It seems that this low l_i shot has smaller stored energy and larger χ_e . If we disregard this shot, χ_i increases with P_{abs} from ohmically heated level to the middle P_{abs} range, while χ_e does not have clear P_{abs} dependence or slightly increases with P_{abs} . We can see $\chi_e \sim 1 \text{ m}^2\text{sec}^{-1}$ and $\chi_i \sim 2 \text{ m}^2\text{sec}^{-1}$ at $P_{abs} = 10 \text{ MW}$, which connects to the high P_{abs} region (see Fig.1). After all, χ_e is almost insensitive to the absorption power, while χ_i value increases drastically with P_{abs} from ohmically heated plasmas to the high P_{abs} neutral beam heated plasmas. Thus we can treat heat transport without considering ohmically heated phase or neutral beam heated phase. This trend was also observed in JT-60 plasmas (hydrogen plasmas) [2]. We can assert that the energy transport in the L-mode plasma is dominated by ions.

Next, we deal with the $I_p = 2$ MA plasmas with $B_t = 4$ T in standard configuration. Plasma volume is $85 \sim 90 \text{ m}^3$. Figure 3 shows the P_{abs} dependence of stored energy components and thermal diffusivity, respectively. The line average electron density is $1.54 \sim 1.95 \times 10^{19} \text{ m}^{-3}$. The ohmic data ($\bar{n}_e = 1.66 \times 10^{19} \text{ m}^{-3}$) is also shown for reference. Internal inductance is $1.1 \sim 1.2$. Each stored energy components increases with P_{abs} . We can see that χ_i is larger than χ_e in this P_{abs} range. Different from the $I_p = 3$ MA cases, we cannot see the clear P_{abs} dependence of χ_i . Still more, if we compare Fig.2 and Fig.3 we find that χ_e of $I_p = 2$ MA case is smaller than that of $I_p = 3$ MA case, which contradicts to the better confinement of higher I_p . It is possible that χ_e is underestimated while χ_i is overestimated in $I_p = 2$ MA shots; effective thermal diffusivity, χ_{eff} [1], is similar between $I_p = 2$ MA shots and $I_p = 3$ MA shots in this P_{abs} range. In order to make clear this point, we must carry out error evaluation of χ_e and χ_i .

References

- [1] SHIRAI, H., et al., JAERI-M 92-073 (1992) Sec. 5.2, page 137
- [2] REBUT, P.H., WATKINS, M.L., GAMBIER, D.J., BOUCHER, D., Phys. Fluids, **B3** (1991) 2209
- [3] HIRAYAMA, T., SHIRAI, H., YAGI, M., SHIMIZU, K., KOIDE, Y., KIKUCHI, M., AZUMI, M., Nucl. Fusion **32** (1992) 89

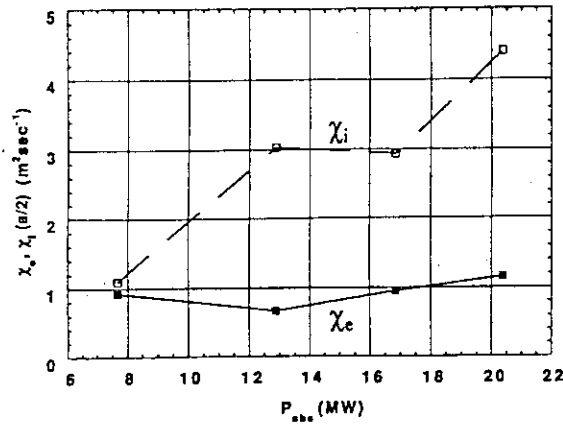


Fig. 1 The P_{abs} dependence of thermal diffusivities χ_e and χ_i at $r = a/2$ in $I_p = 3$ MA neutral beam heated plasmas. (results of previous work [1])

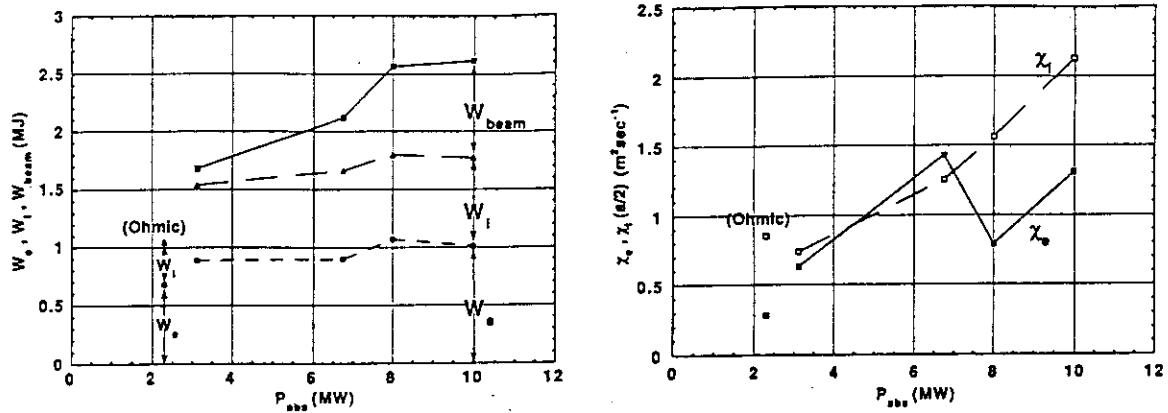


Fig. 2 The P_{abs} dependence of stored energy components; W_e (electron), W_i (ion), W_{beam} (beam) and thermal diffusivities χ_e and χ_i at $r = a/2$ in $I_p = 3$ MA neutral beam heated plasmas.

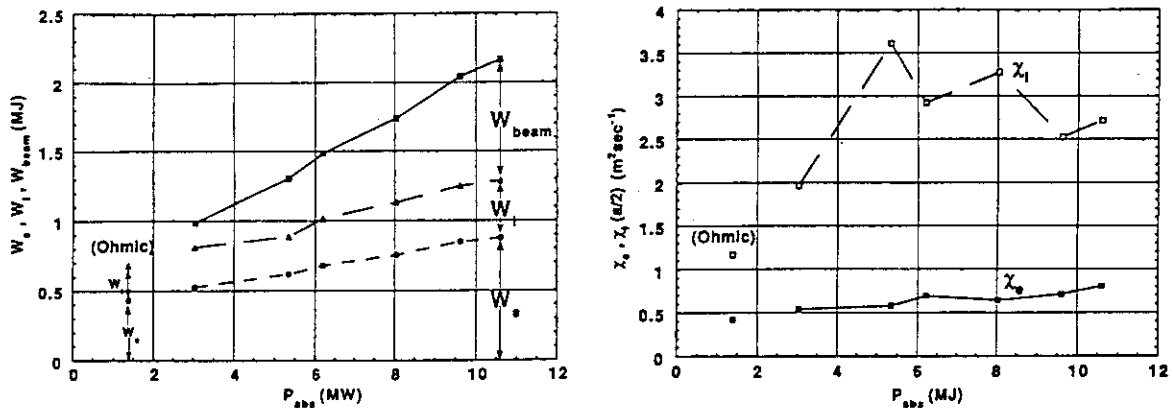


Fig. 3 The P_{abs} dependence of stored energy components; W_e (electron), W_i (ion), W_{beam} (beam) and thermal diffusivities χ_e and χ_i at $r = a/2$ in $I_p = 2$ MA neutral beam heated plasmas.

3.8 High Energy Electron Transport Induced by Pellet Injection in Lower Hybrid Current Drive Discharge

K. Nagashima, T. Kondo, T. Fukuda

On high energy electron transport in tokamak, measured amplitude of radial transport is significantly higher than neo-classical value, and it is considered that this anomalous transport is determined by some micro-instabilities. Turbulence levels of electrostatic and magnetic fluctuations are crucial issues for an understanding of transport physics. Hence, high energy electron transport is a very important subject because it is thought that the transport is mainly dominated by radial component of magnetic fluctuation. In several tokamak machines, diffusion coefficient of high energy electron has been estimated. The measured values are scattering in a large range of 0.5 to 10 m²/sec^{1, 2}). In this section, experimental result obtained from a perturbative transport of high energy electron induced by pellet injection in lower hybrid current drive discharge.

An aim of this experiment was to determine diffusion coefficient of high energy electron generated by lower hybrid radio-frequency wave (LHRF), and a steady state discharge with a long pulse LHRF were used. In this discharge, about 40 percent of toroidal current was maintained by high energy electrons induced by LHRF. In this steady state condition, a small pellet of deuterium (a cylindrical form with a diameter of 3 mm and a length of 3 mm) was injected in order to make a perturbation of high energy electron profile. The pellet penetration depth was estimated by a response of soft x-ray emission profile and was determined to be about $r/a=0.55$. It is estimated that about 70 percent of the pellet was ablated by high energy electron. The plasma parameters of this discharge (E016414) were plasma current of $I_p=1.0$ MA, toroidal field of $B_T=4.0$ T, major radius of $R=3.6$ m, minor radius of $a=0.88$ m, elongation factor of $\epsilon=1.5$, effective safety factor of $q_{eff}=8.1$ and line averaged electron density of $n_e=0.9 \times 10^{19}$ m⁻³ (before pellet injection) using deuterium working gas. The magnetic configuration was a lower x-point divertor.

A dynamics of high energy electron is dominated by three processes. The first is a generation by LHRF and the other two are a collisional slowing down and a radial transport. Therefore, the following simple equation can be used to analyze a behavior of high energy electron.

$$\frac{\partial n_h}{\partial t} = S_h - \frac{n_h}{\tau_{SD}} + \frac{1}{r} \frac{\partial}{\partial r} r D_h \frac{\partial n_h}{\partial r} \quad (1)$$

where n_h , D_h , S_h and τ_{SD} represent density, diffusion coefficient, source and slowing down time of high energy electron, respectively. τ_{SD} is determined by bulk plasma density. Hence, a dynamics of bulk plasma density should be considered. Here, particle conservation equation and a simple formula of particle flux are used as following,

$$\partial n / \partial t = -\nabla \Gamma + S \quad (2)$$

$$\Gamma = -D \partial n / \partial r - V n \quad (3)$$

where n , Γ and S represent density, flux and source of thermal particle. D and V are diffusion coefficient and inward flow velocity. Just after the pellet injection, density gradient becomes significantly large in the pellet penetration region, and the diffusion term in Eq.(3) becomes dominant. Hence, the flow velocity term is negligible during a short period after the injection. The source profile of high energy electron S_h should be determined from absorption profile of LHRF, but it is not easy to estimate real absorption profile. In this analysis, the source profile was determined from a steady state balance of Eq.(1) using the measured profile of high energy electron. (The profile of high energy electron was estimated from hard x-ray emission profile $I_{HX}(r)$, using an assumption of $I_{HX}(r) \propto n_h(r) \times \sum Z_i^2 n_i(r)$ where Z_i and n_i are charge number and density of ion.)

The measured and calculated time evolution of line integrated electron density at $r/a=0.05$ before and after pellet injection are shown in Fig.1. In the calculation, pellet ablation was determined using a theoretical formula of

$$\frac{dD_p}{dX} = -\alpha \frac{n_e^{1/3} T_e^{5/3}}{D_p^{2/3} V_p} - \beta \frac{n_h E_0^{1.549}}{D_p^{2/3} V_p} \quad (4)$$

where the two terms of right hand side represent the ablations by thermal and high energy electrons. D_p , V_p and E_0 are pellet diameter, injection speed and energy of high energy electron. A coefficient of α is 1.78×10^{-13} and an another coefficient of β was determined to adjust the experimental pellet penetration depth. The source profile S was given from this ablation profile, and the diffusion coefficient D was determined to fit the measured value of the first 20 msec after the pellet injection (a clear density decay can be seen in this period when the diffusion process is dominant).

To clarify an image of high energy electron behavior, a calculated time evolution of high energy electron profile is shown in Fig.2 (which is a calculated case using a spatially constant

coefficient of $D_h=1.0 \text{ m}^2/\text{sec}$). Just at a time of pellet injection, high energy electron decreases abruptly in the outer half region (ablation region), and decreases gradually in the central region. It is considered that the decrease in the central region is dominated by the competing two processes, the diffusion of high energy electron and the increase of slowing down time which is due to the thermal particle diffusion. Hence, the diffusion coefficient D_h can be determined from the decrease of high energy electron density in the central region, if the diffusion of high energy electron is dominant, $D_h \gg D$. (In this analysis, D was estimated to be about 1.0-1.5 m^2/sec at the edge.)

Figure 3 shows a time evolution of hard x-ray intensity before and after the pellet injection (at 6.010 sec). After the injection, hard x-ray intensity decreases about 30 percent. The hard x-ray is generated by bremsstrahlung emission of high energy electron and the measurement is a chord integrated value at $r/a=0.4$. To compare the measured hard x-ray intensity with the calculated one, the chord integrated values were calculated using the assumption of $I_{HX}(r) \propto n_h(r) \times \sum Z_i^2 n_i(r)$. These values are shown in Fig.4, using the diffusion coefficients of $D_h=10, 1, 0.1 \text{ m}^2/\text{sec}$. From the comparison between Fig.3 and 4, it can be concluded that the diffusion coefficient of high energy electron is $D_h \ll 10$.

References

- [1] CATTO, P. J., MYRA, J. R., Phys. Fluids B 3 (1991) 2038
- [2] GONDHALEKER, A., et al., 19th EPS Conference on Controlled Fusion and Plasma Physics (1992) I-147

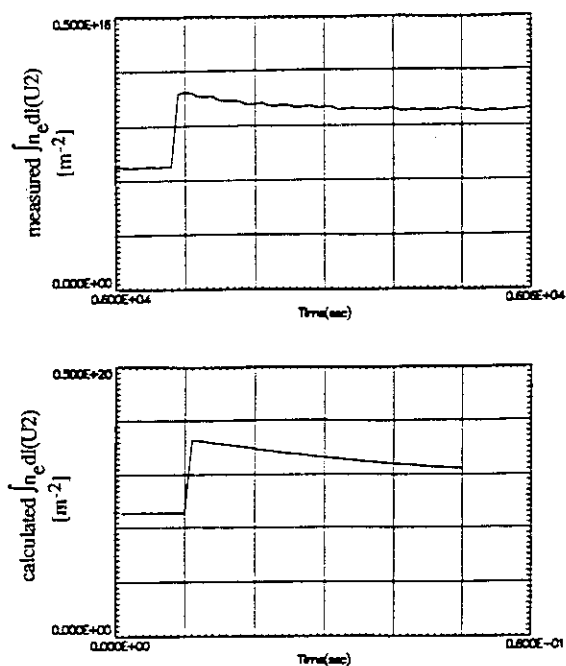


Fig.1 Measured and calculated time evolutions of chord integrated electron density ($r/a=0.05$) before and after pellet injection.

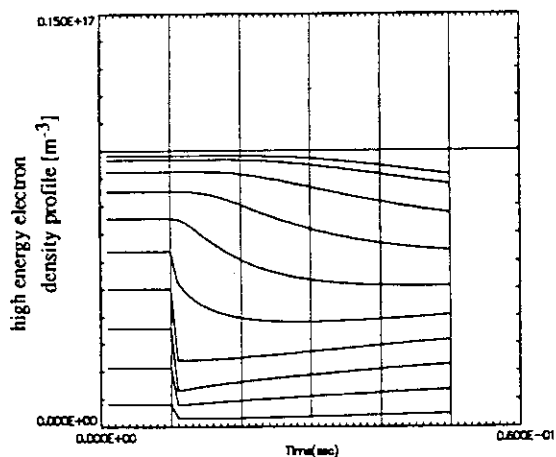


Fig.2 Calculated time evolution of high energy electron density profile using $D_h=1.0 \text{ m}^2/\text{sec}$. Ten solid lines represent densities at $r/a=0.0, 0.1, \dots, 0.9$.

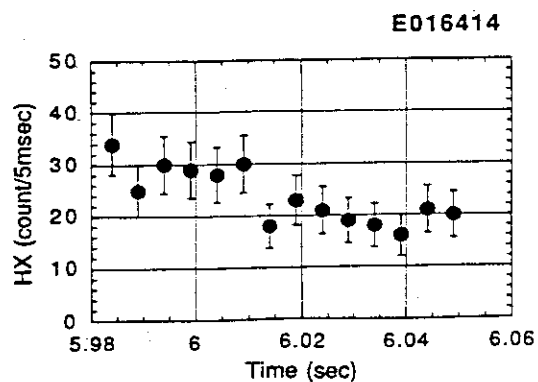


Fig.3 Time evolution of measured hard x-ray intensity at a chord of $r/a=0.4$.

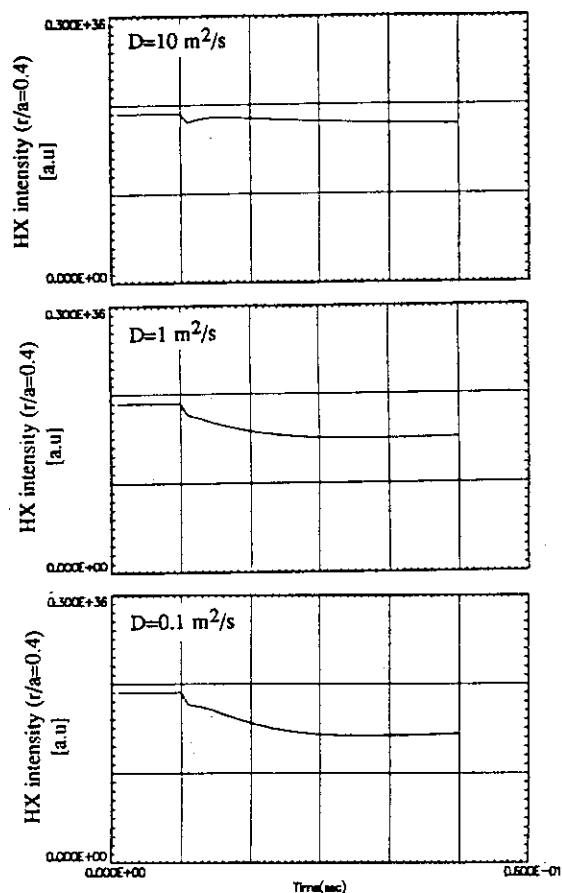


Fig.4 Calculated time evolutions of hard x-ray intensity using $D_h=10, 1, 0.1 \text{ m}^2/\text{sec}$.

4. Impurity and Divertor

4.1 Decaborane-based Boronization System and Its Operation Experience

M. Saidoh, H. Hiratsuka, T. Arai, M. Shimada, N. Ogiwara, Y. Neyatani, T. Koike,
H. Ninomiya, M. Yamage^{*1}, H. Sugai^{*1} and G. L. Jackson^{*2}

1. Introduction

A new type of boronization system using decaborane $B_{10}H_{14}$ as a substance for boronization has been installed in the JT-60U tokamak in order to reduce the influx of impurities during plasma discharges[1]. Two sessions of boronization have been carried out on July 30 and September 1, 1992. Initial results indicate that the boron film produced from decaborane shows a good performance similar to that of layers produced in the conventional way. Present paper describes the JT-60U boronization system, the boronization process and the properties of the deposited boron film. The effects of boronization on the plasma performance will be described in the following chapters.

2. The JT-60U Boronization System

Figure 1 is a schematic layout of the decaborane-based boronization system for JT-60U. This system including decaborane container can be located in the torus hall because of its safer features that decaborane is not explosive and less toxic than diborane and that the pressure of decaborane is always subatmospheric throughout the system. This enables installation of a decaborane container near the JT-60U vacuum vessel resulting in the short delivery lines from the container to the injection port of the vacuum vessel which are less than 20 m, in comparison with the conventional boronization system[2].

In order to obtain a steady decaborane gas flow, the gas feeding system including the decaborane container and the delivery lines is heated up to and kept at $100 \sim 110^\circ\text{C}$ during boronization session. Flow rates of decaborane and helium are controlled by mass controllers independently and a post-mixed gas of decaborane and helium is fed continuously into the JT-60U vessel.

The residual gas analyzer (RGA) has been used to evaluate the vacuum quality during boronization. In the RGA system, a 1 mm orifice has been added to restrict inlet flow and increases differential pumping. This limits the total pressure in the RGA to less than 1×10^{-2} Pa, which allows its periodic use during boronization. A 150 l/s turbomolecular pump backed by a rotary pump provides the differential pumping. The exhaust line from the pump is connected to the exhaust line of the tokamak vacuum system used during the boronization session.

During boronization the JT-60U vacuum vessel is evacuated by a 3000 l/s turbomolecular pump backed by a 1340 l/min rotary pump whose oil is continuously filtrated with an oil filtration system used in semiconductor industries. A decaborane filter is connected to the rotary pump. A dedicated exhaust line conducts all vacuum pump exhaust out of the building with help from a fan located at the end of the exhaust line on the roof. A nitrogen purge is connected to the inlet of the rotary pump to dilute the boronization byproducts below the explosion limit for hydrogen.

For safety a stationary air monitoring system and an exhaust line monitoring system sample two points in the torus hall and two points in the two vacuum pump exhaust lines, respectively. These are sensitive to decaborane concentrations of as low as 10 ppb. In addition, portable detectors sensitive to a range of toxic gases including decaborane are carried during hazardous operations.

3. The Boronization Process

Prior to boronization a helium glow discharge was carried out in order to clean up the plasma facing surfaces. The glow discharge was maintained in JT-60U using two graphite anodes spaced 140 degree toroidally, while the tokamak wall was the cathode (Fig. 1). After the glow discharge cleaning, decaborane gas was injected into the JT-60U tokamak under helium glow discharge in order to carry out the boronization. The injected gas molecules are decomposed into boron and hydrogen and ionized borons are accelerated towards the first wall to coat it with boron. Byproducts, mainly hydrogen and helium are pumped away by the special decaborane pumping system. Increment of RGA signal of H_2 due to the decomposition of decaborane under glow discharge is clearly seen in Fig. 2. When we take into account of the amount of helium and decaborane gases fed into the vessel mentioned below, the increment of RGA signal of H_2 indicates the almost complete decomposition of decaborane into boron and hydrogen. To improve the deposition of boron film with high quality the vessel walls were heated to 300 °C. A typical session consisted of 10 hours of glow discharge, consuming 15 grams of decaborane. Typical glow discharge parameters were 270 to 310 volts, with 3 amps of current drawn by each electrode, maintaining a total pressure of 2×10^{-1} Pa with helium (380 SCCM (standard cm^3/min)) and decaborane (5.5 SCCM) flow.

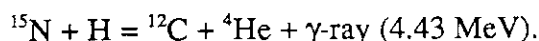
4. The Properties of The Deposited Boron Film

Probe samples were inserted in two positions (P-4 section and P-13 section) of the plane of the outer wall during second boronization session in order to examine the deposited boron films. Polished molybdenum, and polished and as-received graphite were used as the probe samples. Atomic composition depth profiles of deposited films on molybdenum and graphite have been measured by means of Auger electron spectroscopy (AES) and simultaneous Ar^+ -ion sputtering. The results obtained for molybdenum and graphite substrates of P-4 probe samples are shown in Figs. 3 and 4, respectively. The followings are clearly found. For molybdenum

the interface between boron deposit and molybdenum substrate is very sharp, while for graphite it becomes broad even when the graphite surface is smooth. The deposited films are over 90% boron as seen from Fig. 3 and Fig. 4(a). More than 15% carbon exists in the film on the as-received graphite as shown in Fig. 4(b), which clearly indicates that the deposited boron film in the present boronization can not cover all of the graphite surfaces, because of their surface roughness.

The film thicknesses shown in the figures are obtained from scanning electron microscopy (SEM) observation of the cross-section of the films deposited on the P-4 probe sample supposing that the film width, at which the AES intensity of boron becomes 50%, is a film thickness of deposited boron film. For P-13 section the thickness of deposited boron film is obtained to be 2 nm. The area of the plasma facing surfaces in JT-60U is approximately 200 m². 15 gram of decaborane, therefore, gives a boron deposit with an average thickness of 46 nm. The present experimental results clearly show that the deposited boron films are toroidally nonuniform.

Depth profiles of hydrogen concentration in the boron films were also measured by means of nuclear reaction analysis using ¹⁵N as follows[3].



Results are shown in Fig. 5. Hydrogen concentrations in the films on both substrates are obtained to be 10%, which is low compared with that produced in the conventional boronization[4]. The depth at which hydrogen concentration is half of the 10% concentration are also obtained to be 100 nm and 140 nm for molybdenum and graphite substrates, respectively, which agree with the thicknesses of the boron films on molybdenum and graphite measured by AES and simultaneous Ar⁺-ion sputtering, respectively.

Plasma performance has been improved after boronization compared with the previous one, details of which will be discussed in the following chapters, although the present two boronizations did not produce enough thickness of deposited boron layer to cover all of the carbon tiles. Therefore more powerful and uniform boron coating is required and some improvements of the boronization system for this purpose are in preparation.

*1 Nagoya University

*2 General Atomics

References

- [1] SAIDOH M. et al., Accepted for publication in Fusion Eng. & Des..
- [2] WINTER J. et al., J. Nucl. Mater. **162-164** (1989) 713.
- [3] LANFORD W. A. et al., Appl. Phys. Lett. **28** (1976) 566.
- [4] Von SEGGERN J. et al., J. Nucl. Mater. **176&177** (1990) 357.

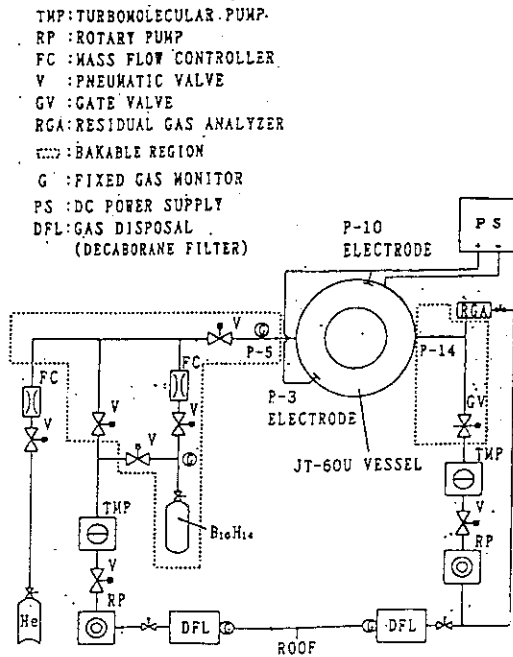


Fig. 1 Simplified schematic layout of JT-60U boronization system.

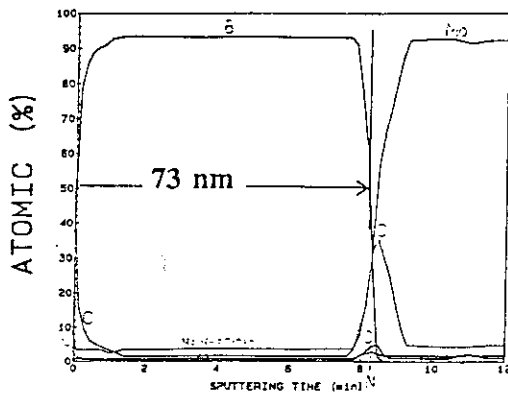


Fig. 3 The AES depth profile of the atomic composition of deposited film on molybdenum after second boronization of JT-60U.

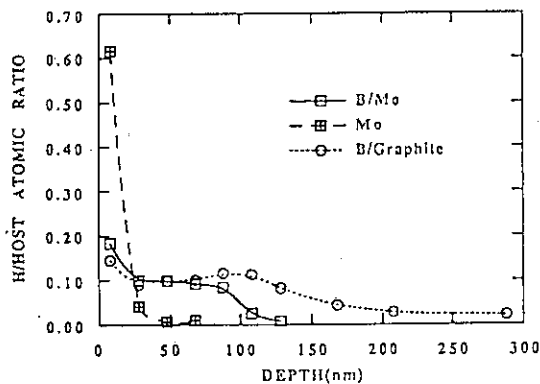


Fig. 5 Depth distribution of the relative hydrogen content in deposited films on molybdenum and graphite after second boronization. Depth distribution of the relative hydrogen content in non-coated molybdenum is also shown in comparison. Hydrogen concentrations are obtained by means of nuclear reaction analysis using ^{15}N .

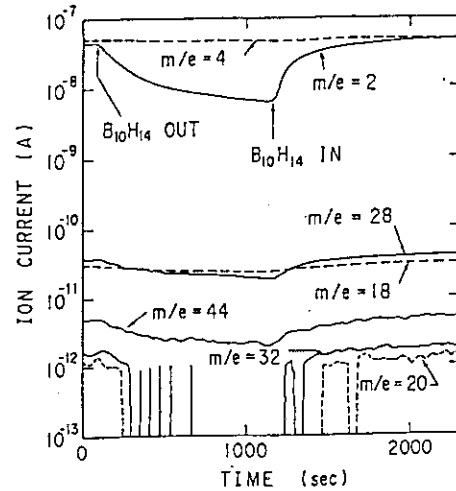


Fig. 2 Mass spectrometer signals of masses 2(H_2), 4(He), 18, 20, 28, 32 and 44 as a function of time during glow discharge with and without a decaborane injection.

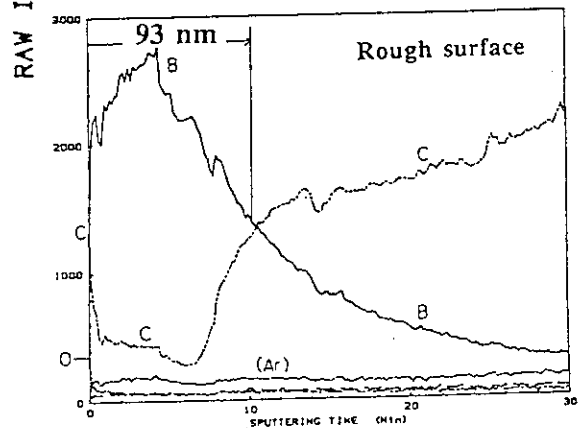
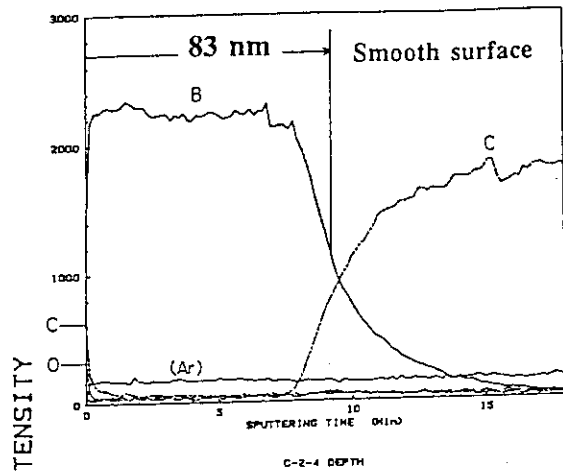


Fig. 4 The AES depth profiles of the atomic composition of deposited films on graphite with smooth surface (a) and rough surface (b) after second boronization of JT-60U.

4.2 Effects of Boronization and Wall Conditioning on H-mode

M.Shimada, H.Ninomiya, R.Yoshino, Y.Kamada, M.Saidoh, H.Nakamura and S.Tsuji

1. Introduction

This chapter describes the effects of boronization and wall conditioning on H-mode. The purpose of boronization and wall conditioning is reduction of impurity and particle recycling. Excessive amount of impurities and particle recycling is detrimental to confinement and stability. Accessibility to H-mode is also affected by impurities and particle recycling. Two sessions of boronization have been carried out in 1992. The first session took place on July 31 and the second session on Sept. 1. Approximately 10g and 15g of decaborane was processed in these sessions. Details of the hardware and procedures are described in section 4.1. Effects on impurity levels were discussed in section 4.3. This section discusses changes in particle recycling and confinement. Critical issues are also discussed and schemes for solution are presented.

2. Results

Shown in Fig. 1 are two discharges: one before the first boronization and the other after the second boronization. Toroidal field and plasma current were similar: both 4T and 2.5 MA. The neutral beam power was roughly the same. In both cases, a clear LH transition was not observed, but HL transition was very clear. The D_α traces show that after the boronization, the particle recycling flux was reduced by an order of magnitude. The rate of electron density increase was also lower after the boronization; dn/dt during the ELM-free phase was $2.8 \times 10^{19} \text{ m}^{-3}\text{s}^{-1}$ before the boronization, and was $1.4 \times 10^{19} \text{ m}^{-3}\text{s}^{-1}$ after the boronization. The electron density at the ELM onset was similar for both cases. The lower target density and the lower rate of density rise after the boronization extended the period of the ELM-free phase by a factor of 2.5.

Changes of discharge characteristics by boronization are discussed in Fig. 2. Discharge parameters are: $B_t=4\text{T}$, $I_p=2.5\text{MA}$ and $P_{in}=15\text{-}20 \text{ MW}$. Fig. 2(a) shows that D_α emissivity is systematically reduced by an order of magnitude by boronization. An explanation of particle recycling reduction is change of density range, which can be discussed by Fig. 2(b). The density range of pre-boronized discharges is higher than those after boronization. However, there is systematic reduction seen between data after the first boronization and data after the second boronization. As a result of the particle recycling reduction, confinement time increased significantly, which is shown in Fig. 2(c). H factor is defined as $\tau_E/\tau_E(\text{ITER-89P})$. In Fig. 2(d), H factor is plotted against the particle recycling at the divertor, which suggests that particle recycling has some threshold value under which confinement is improved with reduced recycling. Fig. 3 shows a plot similar to Fig. 2(d), with plasma parameters more extended in B_t , I_p and P_{in} .

showing an H factor of 2.2 after the second boronization. Fig. 3 also shows that for each boronization stage, the range of Da and H factor is very wide, but a trend of higher H-factor with lower particle recycling is obvious, suggesting that wall conditioning at each stage of boronization is very important in reducing particle recycling and in improving confinement. Fig. 4 presents H factors against I_p for constant $B_t=4T$, and $P_{in} = 15-20MW$. This figure indicates a steady improvement after each boronization session and also expansion of operation space with improved confinement.

3. Discussion of Experimental Results and Critical Issues

After boronization, oxygen levels in joule heating phase were reduced, but the oxygen levels in NB-heating phase were not. Carbon levels were not reduced either in joule heating or in NB-heating phases. Boronization and subsequent wall conditioning reduced particle recycling, which resulted in improvement of confinement. This result indicates that reduction of particle recycling alone can improve confinement. However, reduction of particle recycling is not advantageous from the viewpoint of making a dense and cold divertor, because the temperature at the divertor can be roughly given as the ratio of the divertor heat load to the particle flux. The divertor density can be given as the ratio of the particle flux to the square root of the divertor temperature. Therefore, for a given divertor heat load, reduction of divertor particle flux contradicts with formation of a dense and cold divertor. This poses the most serious problem in the tokamak confinement study. Furthermore, in low-recycling discharges, remote radiative cooling is small compared with main plasma radiation power. Demonstration of enhanced confinement compatible with a high recycling divertor and remote radiative cooling is a crucial issue.

In the boronization sessions carried out so far, the boron coating was thin(maximum:80 nm), and was highly localized(decay length was 1-2 m), which is the most plausible explanation for little reduction in impurity levels. During the vent in Nov.-Dec. 1992, a new boronization system with 12 injection inlets was installed in the machine. These inlets were designed to supply decaborane vapor almost uniformly around the torus. With this system, we aim to coat the first wall with more uniform, and thicker boron film. Reduced impurity levels with this new boronization system may alleviate the requirement on the particle recycling.

In recent tokamak experiments, most divertors have been designed with an open geometry to maximize flexibility in shaping. In this configuration, enhancement in particle recycling in the divertor inevitably deteriorates energy confinement, since neutral particles freely flow back to the main plasma through the aperture between the scrape-off layer and the wall. In a closed divertor configuration, the neutral particles are impeded from returning to the main plasma, which results in

maintaining good confinement and in enhancing divertor particle recycling and remote radiative cooling.

Requirements for the design of a closed divertor include:

- (1) The minimum particle recycling flux for reducing divertor temperatures below 20 eV, and for reducing the divertor heat load below 10MW/m^2 by remote radiative cooling.
- (2) The maximum ionization source inside the separatrix for maintaining good confinement and good current drive efficiency. The maximum ionization source required to prevent MARFE and detaching should also be investigated, but this value is expected to be well below the limit imposed by confinement and current drive.
- (3) The minimum impurity levels in the divertor for remote radiative cooling.
- (4) The maximum impurity neutral particle flux allowed to the main plasma scrape-off layer for maintaining impurity contamination in the main plasma below 0.2 % for light impurities.
- (5) The heat flux distribution and particle flux distribution in the scrape-off layer.

The maximum neutral particle conductance can be derived for simultaneous demonstration of (1) and (2). A similar consideration is required for simultaneous satisfaction of (3) and (4). Both consideration should include the effects of ionization by plasma. Further consideration must include the backflow of impurity ion, and the wall source of impurities. Experimental evaluation of (5) enables estimation of the minimum aperture for reducing the throat heat load below an engineering limit and for reducing the particle recycling on the throat. The minimum divertor length can be derived from the requirement on the divertor conductance and the minimum divertor aperture. The neutral particle pressure derived from (1) and the particle input (by beams and gas-puffing) should provide the requirement for pumping. Experimental documentation of (1)-(5) is very important in establishing a firm basis for optimizing the performance of JT-60U and future machines such as ITER. Consideration of ELMs, requiring dynamic treatments of (1)-(5), should also be important. The long range experimental program of JT-60U and the divertor design of JT-60SU should reflect such a consideration.

4. Conclusion

Conclusions on boronization and wall conditioning studies are summarized as follows.

- (1) Two sessions of boronization have reduced particle recycling, which improved confinement.
- (2) Impurities were not reduced by boronization, probably due to localized and thin boron layer.
- (3) Confinement improvement by reduction of particle recycling is contradictory to high recycling divertor scheme in an open divertor geometry; more uniform, thicker boron layer might reduce the requirement on particle recycling. Long-term solutions including a closed divertor should be investigated.

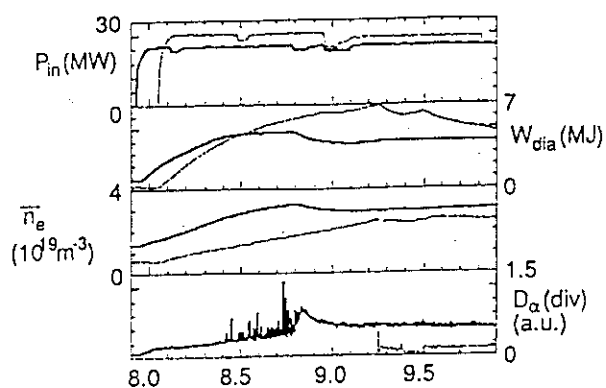


Fig. 1 Time evolution of two discharges: one before the 1st boronization and the other after the 2nd boronization. Shown are neutral beam power, diamagnetic stored energy, line-average electron density ($r/a=0.5$), and divertor $D\alpha$ emission.

Fig. 2 Changes of discharge characteristics by boronization. Shown are data from H and L mode discharges with $B_t=4T$, $I_p=2.5MA$ are $P_{in}=15-20$ MW.

(a) $D\alpha$ emissivity vs. shot number

(b) $D\alpha$ emissivity vs. line-average density

(c) H factor vs. shot number

(d) H factor vs. $D\alpha$ emissivity

The solid squares denote values before the 1st boronization, the open circles values after the 1st boronization, the solid circles values after the 2nd boronization.

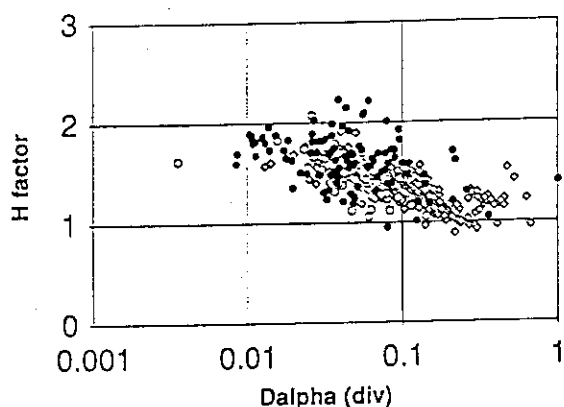


Fig. 3 H factor vs. $D\alpha$ emissivity. Open diamonds denote values before the first boronization, open circles values after the 1st boronization, the solid circles values after the 2nd boronization.

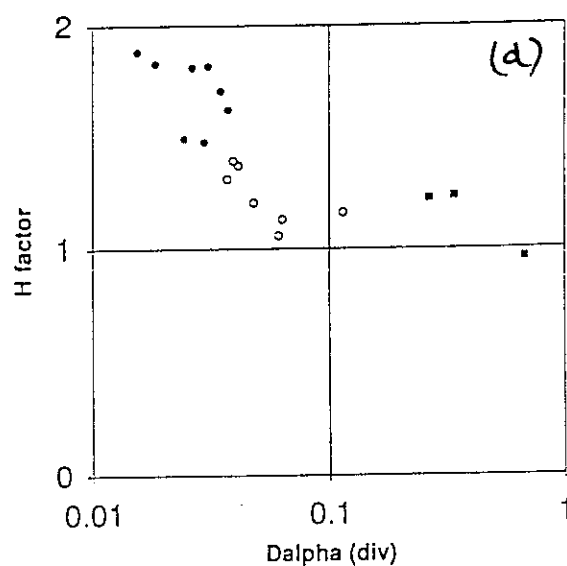
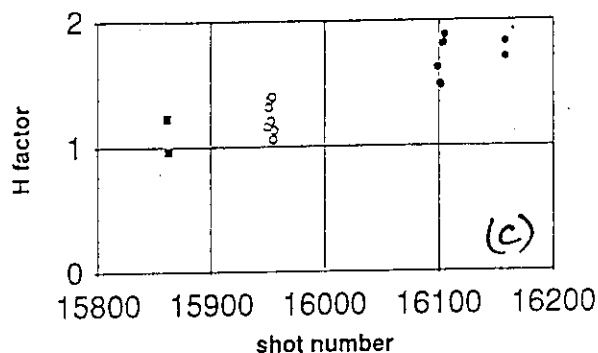
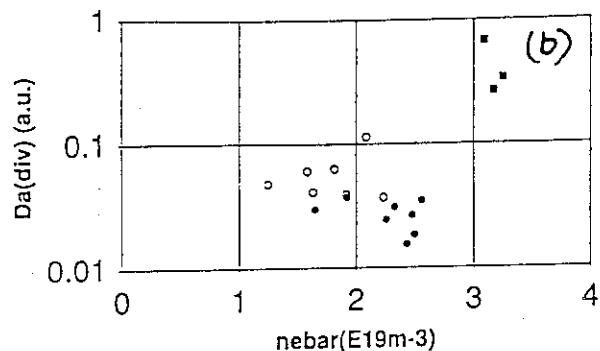
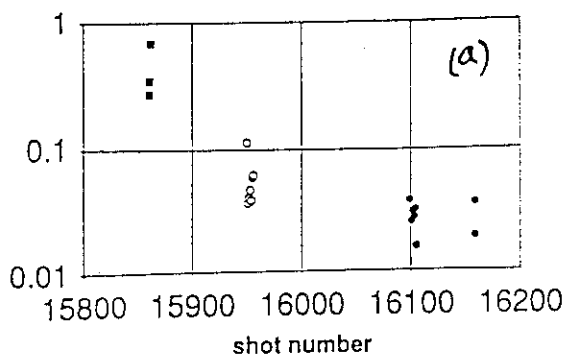
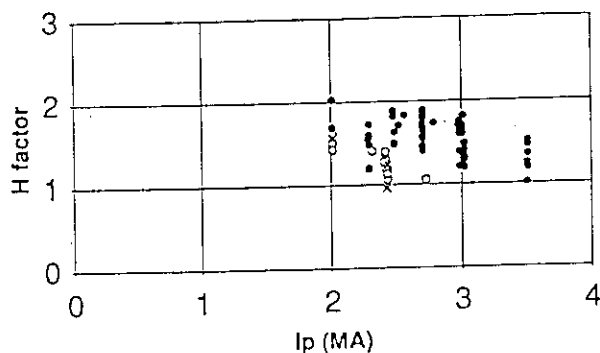


Fig. 4 H factor vs. I_p . X's denote values before the first boronization, open circles values after the 1st boronization, the solid circles values after the 2nd boronization.

4.3 Impurity Concentration and Radiation Loss in the Main Plasma

T. Sugie, H. Kubo, M. Shimada, H. Nakamura, A. Sakasai, K. Hill, K. Itami, N. Asakura, Y. Kawano, S. Numazawa, T. Hirayama, N. Hosogane, S. Tsuji and JT-60 Team

Wall conditioning has been carried out with deuterium TDC, helium TDC, disruptive cleaning and helium GDC. With these conditioning methods, we obtained Z_{eff} of 1.6 and the oxygen / carbon concentrations of 0.5% / 1.2% in OH discharges. In addition, we installed a boronization system for more powerful wall conditioning[1]. But it is difficult to reduce the carbon impurity, originated from the first wall materials, only with these wall conditioning methods in the high power NB heated discharges. We confirmed that the high density operation is useful to reduce carbon concentration, and the divertor shielding efficiency of impurity ions increases with the electron density[2].

1. Impurity Reduction by Wall Conditioning

Concentrations of oxygen, carbon and boron have been derived from the Z_{eff} and the intensity ratio of OVIII (1s-2p; 19 Å), CVI (1s-2p; 33.7 Å) and BV (1s-2p; 48.6 Å) measured with a grazing incidence spectrometer. Radiation losses were also measured with a 32ch bolometer array.

Figure 1 (a) and (b) show the long term histories of Z_{eff} and impurity concentrations in OH discharges at the line averaged electron density of $2 \times 10^{19} \text{ m}^{-3}$. After the 1st vent of a vacuum vessel, the Z_{eff} gradually decreased from 3.4 to 2 by ~200 tokamak discharges with D_2 / He TDC, disruption cleaning and He glow discharge, and the oxygen concentration also decreased 3.6 % to 0.8 %. On the other hand, boronization reduced Z_{eff} and oxygen concentration in a short time. After the 1st boronization of just after the 2nd vent, the Z_{eff} decreased from 3.5 to 2. And after the 2nd boronization, the Z_{eff} and oxygen concentration decreased more. Figure 2 (a) and (b) show the impurity concentrations and radiation loss power as a function of line averaged electron density before and after 1st boronization. In this figure, the oxygen concentration decreased from 3.5 % to 0.4 % at $\bar{n}_e = 3 \times 10^{19} \text{ m}^{-3}$, but the carbon concentration did not decrease with boronizations. Boron concentration was around 0.4%. The radiation loss power of main plasma also decreased from 0.65 MW to 0.15 MW in accordance with the decrease of oxygen.

In NB heated discharges ($P_{\text{NB}}=17\text{-}23.5 \text{ MW}$, $B_T=3\text{-}4 \text{ T}$, $I_p=1.8\text{-}2.4 \text{ MA}$), the effect of boronization was not so clear as shown in Fig.3 (a) and (b). The oxygen concentration slightly decreased after the 2nd boronization, but the effect of boronization was not so clear in comparison with the concentration before the boronization. Oxygen still survive 0.8% of

the electron density. The carbon concentration did not change before and after the boronizations. Z_{eff} also did not change after the boronizations. Radiation losses of main and divertor plasmas also had no change after the boronizations as shown in Fig. 4(a) and (b). These results suggest that the boronizations were insufficient and/or the boron film was weak under the high power NB heating. According to the thickness measurement of boron film, the thickness was toroidally non uniform such as 75 nm near the injection port of decaborane vapor and only 2 nm at the opposite side [1]. From these results, more powerful and uniform boronization is required.

2. Impurity Behavior in High Density NB Heated Plasmas

Z_{eff} and impurity concentrations increased with the NB injection power (P_{NB}) as shown in Fig. 5(a) and (b). Especially, the carbon concentration increased steeply with the injection power and reached to $\sim 3.5\%$ of the electron density at 24 MW. That is, it is difficult to reduce the carbon impurity originated from the first wall materials in high power NB heated plasmas.

Figure 6 (a) and (b) show Z_{eff} and impurity concentrations as a function of line averaged electron density. Those values were clearly decreased with the electron density. Especially, the carbon concentration decreased remarkably and held around 1.5% of electron density during high power NB heating (23 MW, 2.5 sec) at $\bar{n}_e = 5 \times 10^{19} \text{ m}^{-3}$. And also, we confirmed that impurity shielding efficiency increases with electron density since the ratio of carbon concentration to carbon influx decreased with electron density [2]. From these results, high density operation is promising to reduce impurity concentrations of main plasma even in a high power NB heating.

References

- [1] SAIDOH, M., et al., Section 4.1, in this review.
- [2] SAKASAI, A., et al., Proc. 14th Int. Conf. on Plasma Physics and Controlled Nuclear Fusion Research, Würzburg (1992).

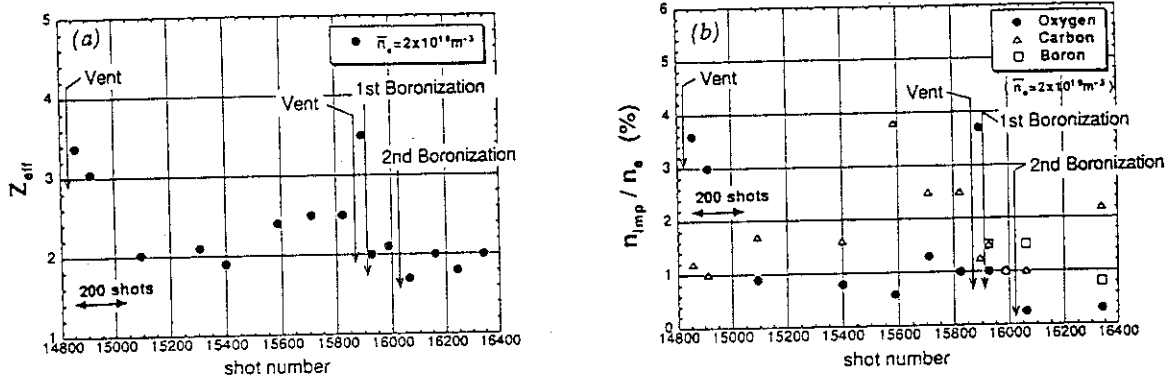


Fig.1 Long term histories of (a) Z_{eff} and (b) impurity concentrations in OH discharges at the line averaged electron density of $2 \times 10^{19} \text{ m}^{-3}$.

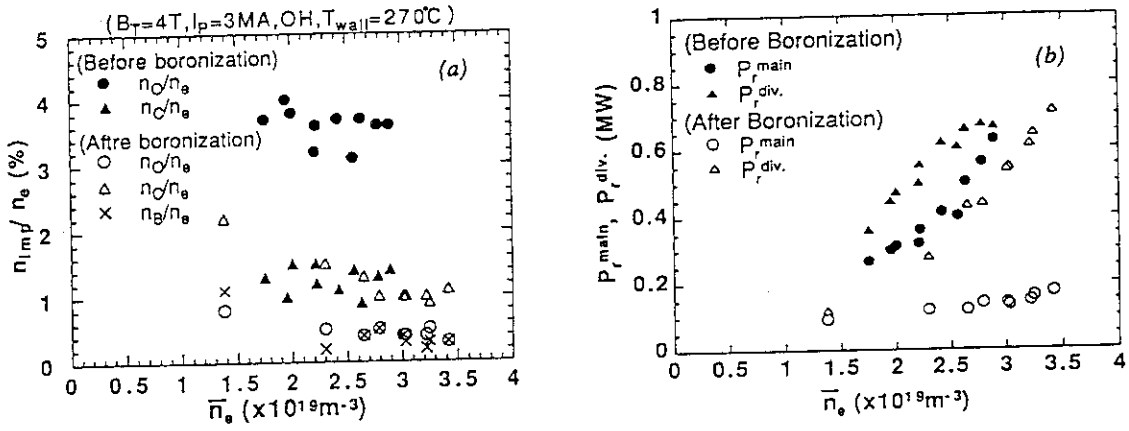


Fig.2 (a) Impurity concentrations and (b) radiation loss power as a function of line averaged electron density \bar{n}_e before and after 1st boronization in OH discharges.

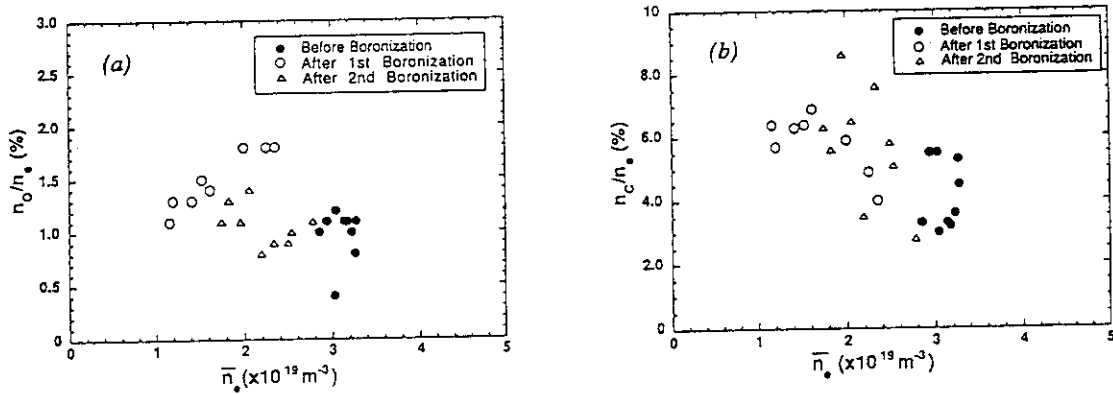


Fig.3 (a) Oxygen and (b) carbon concentrations in NB heated discharges as a function of line averaged electron density \bar{n}_e before and after (1st and 2nd) boronizations. ($P_{NB} = 17 - 23 \text{ MW}$, $B_T = 3 - 3.4 \text{ T}$, $I_p = 1.8 - 2.4 \text{ MA}$)

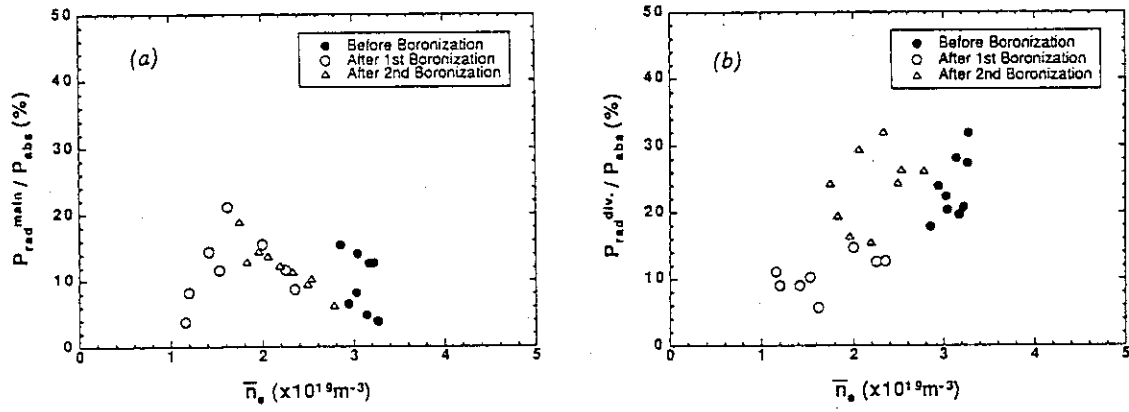


Fig.4 Rate of radiation loss power of (a) main and (b) divertor plasma to absorption power as a function of line averaged electron density \bar{n}_e . ($P_{NB}=17-23$ MW, $B_T=3-34$ T, $I_p=1.8-2.4$ MA)

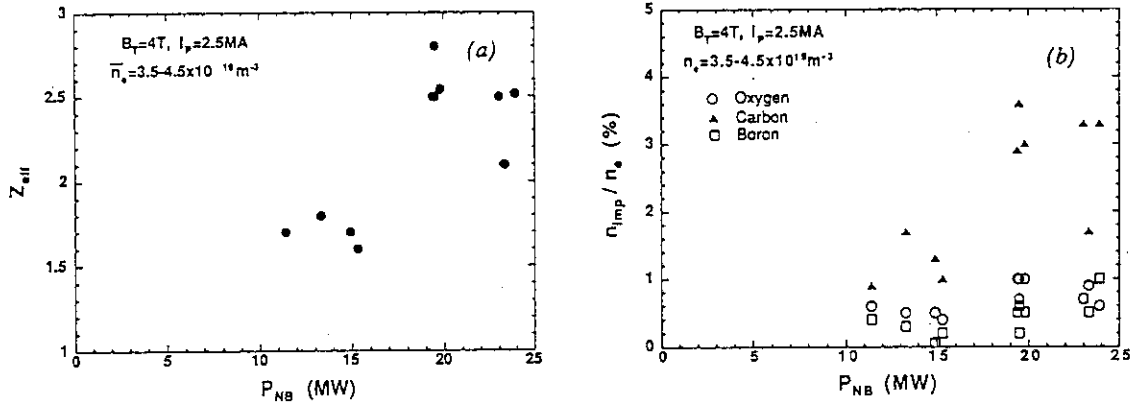


Fig.5 (a) Z_{eff} and (b) impurity concentrations as a function of NB injection power.

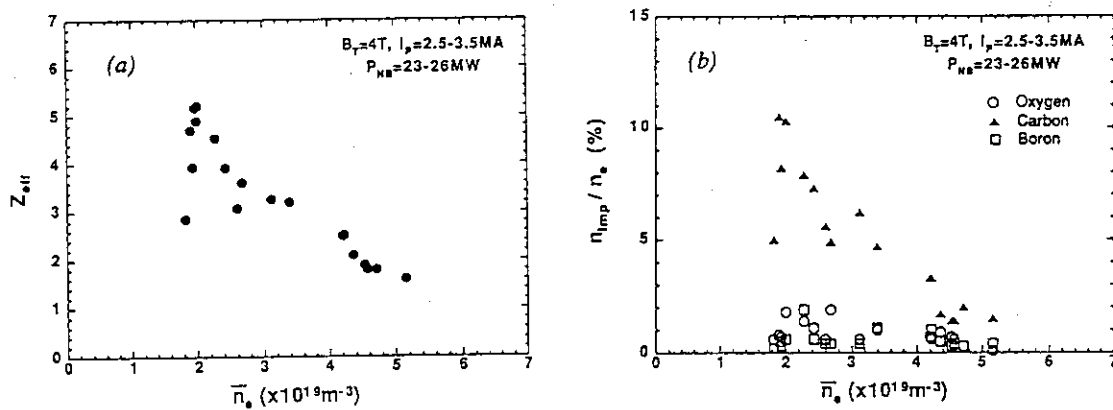


Fig.6 (a) Z_{eff} and (b) impurity concentrations as a function of line averaged electron density under the condition of $B_T=4$ T, $I_p=2.5-3.5$ MA, $P_{NB}=23-26$ MW.

4.4 Distributions of Divertor Radiation Loss in Ohmic Discharges

N.Hosogane, N.Asakura, H.Kubo, K.Itami, K.Shimizu,
S.Tsuji, T.Sugie, A.Sakasai and M.Shimada

1. Introduction

The understanding of the characteristics of divertor radiation loss is very important to establish a remote radiative cooling method for suppressing heat load to the divertor tiles in fusion reactors. The divertor radiation loss varies with the main or divertor electron density, heating power, impurity species and equilibrium configuration parameters such as safety factor and height of X-point. These characteristics may depend on the type of divertor, that is, open or closed divertor. In case of open divertor like JT-60U, besides the separatrix strike zones, neutral particles and impurities are distributed around the X-point or the lower half of the main plasma, which may result in the distribution of divertor radiation loss different from that in the closed divertor. Therefore, with an 32-channel bolometer array, the distribution of the radiation loss in the divertor region was investigated for ohmic discharges.

2. Distribution of Divertor Radiation Loss

Figure 1 show the viewing lines of a 32-channel bolometer array in the divertor region. Divertor configurations with heights of X-point are 8 cm (solid line) and 12 cm (dotted line), which are discussed in this paper, are described to show the geometrical relationship between the divertor region and these viewing chords. To obtained the radiation loss only from the divertor region, it is necessary to subtract the contribution of the main radiation. To do this, the up-down symmetry of the main radiation loss profile is assumed, and the divertor radiation loss is defined as a sum of the residuals obtained by excluding the contribution of the main plasma along the viewing chord.

Figure 2 shows the distributions of divertor radiation loss for two series of ohmic discharges with different heights of X-point, 4-8 cm and 11-14 cm and the ohmic power as a function of main electron density. The plasma current is 1.2-3 MA and the toroidal magnetic field is 2.5-4 T for the former series and 4 T for the latter series. The ohmic power changes step by step with the change in plasma current, and is almost linearly proportion to the plasma current. The main electron density was scanned by the gas puff, but the range scanned for each plasma current was limited by the locked mode at the low density side and the occurrence of the MARFE at the high density side. It is interesting to note that the divertor radiation $P_{\text{rad}}^{\text{div}}$ measured in the stable phase of discharges appears to continuously increase with the main electron density, although the density scan was carried out for different plasma currents. It is

found in this figure that the radiation loss is mainly distributed to the three regions measured by ch.28, ch.29 and ch.30, which respectively correspond to 1) the SOL and main plasma surface in the inboard side above the X-point, 2) the inboard separatrix strike zone and the proximity of the X-point, and 3) the outboard separatrix strike zone and the SOL and main plasma surface in the outboard side above the X-point. The distributions are not almost changed for configurations with different height of X-point investigated here.

In order to see the variation of the distribution of the divertor radiation loss against the main electron density scan in detail, the fraction of these radiation loss normalized by the total divertor radiation loss was plotted as a function of the main electron density in Fig.3. The equilibrium configurations are limited to those with $X_p=11.5-12.5$ cm to exclude ambiguities of the measurement due to the movement of the separatrix lines. It is seen in this figure that the radiation loss at ch.30, which corresponds to the outboard separatrix strike zone, is only 20-30 %, and is comparable with that at ch.28. This means that the divertor radiation loss defined as the above contains a significant contribution, order of 50%, from the SOL and/or the plasma surface near the X-point. This is because the radiating region is expected to spread from the X-point region. Therefore, to discuss the characteristic of divertor radiation loss on the basis of the divertor parameters such as electron density and temperature in front of divertor tiles, it is necessary to separate the radiation loss at the divertor tiles from the total divertor radiation loss. Besides, as shown by the behavior that ch.29 increases with the increase in electron density, and ch.28 decreases, this plot suggests that the radiative region gathers around the X-point with the increase in electron density. Because it is considered that the fraction of the radiation loss at the inboard separatrix strike zone is unchanged like that at the outboard one, and the increase in ch.29 is caused by the radiation loss around the X-point. (If it is not, it is suggested that there is a strong in-out asymmetry in the divertor radiation loss.) The opposite behavior of ch's 28 and 29 may be explained as a result of impurity shielding by the divertor plasma. In case of low electron density, impurity gases or ions generated at the divertor tiles can spread over the above of the X-point, but in case of high electron density, they are ionized near the divertor tiles. This behavior possibly changes the distribution of the divertor radiation loss.

3. Fraction of the Divertor Radiation Loss Against the Ohmic Power

Figure 4 shows the electron density dependence of the fraction of total divertor radiation loss against the ohmic power for the discharges discussed above. It is seen in this figure that at the same electron density, the fraction of divertor radiation losses for lower q discharges, that is, discharges with larger plasma current or lower toroidal magnetic field, tend to be smaller than those for higher q discharges. This dependence of the total divertor radiation loss is well summarized as a function of a parameter of $n_e^{\text{main}} q_{\text{eff}}$ as shown in Fig.5. Also, the radiation loss at the outboard separatrix strike zone obtained by ch.30 is found to obey the same

parameter dependence. In the qualitative sense, this dependence probably comes from that the divertor plasma is cooled by increasing the electron density or the connection length of the scrape-off layer between the main plasma and the divertor tiles. It is interesting to note that the radiation loss at the separatrix strike zone and around the X-point have the same parameter dependence, although the electron temperatures and densities are expected to be different. To understand it quantitatively, it is necessary to investigate it with simulation codes which treat impurity transport and generation. Because, as the radiation loss is expressed as $\Sigma n_z n_e^{\text{div}} L(T_e^{\text{div}})$ (n_z : impurity density, n_e^{div} : divertor electron density, T_e^{div} : divertor electron temperature and L : cooling parameter), the radiation loss depends on various things such as impurity levels, divertor plasma parameters, particle confinement time, spatial distribution of these parameters etc.

Summary

The distribution of the divertor radiation loss was investigated for ohmic discharges with a 32-channel bolometer array. The fraction of the radiation loss at the outer separatrix strike zone is 20-30 % against the radiation loss measured in the divertor region. Almost the half of the radiation in the divertor region is considered to be radiated from the SOL and/or the main plasma surface around the X-point, the distribution of which tends to gather around the X-point as the electron density increases. The fraction of the total divertor radiation loss and the radiation at the outboard separatrix strike zone against the ohmic power are found to vary as a function of a parameter $n_e^{\text{main}} q_{\text{eff}}$.

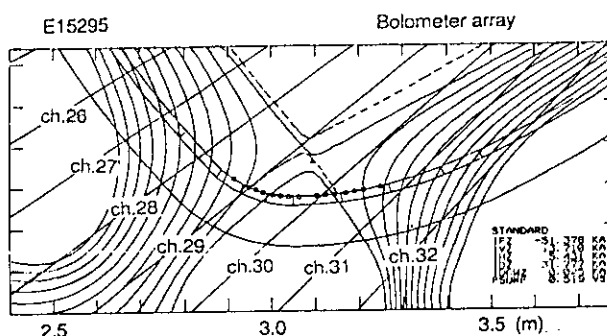


Fig.1 Viewing chords of the bolometer array in the divertor region. The divertor configurations described show the relationship between these viewing chords and the configurations discussed (solid: $Xp=8\text{cm}$, dotted: $Xp=12\text{cm}$)

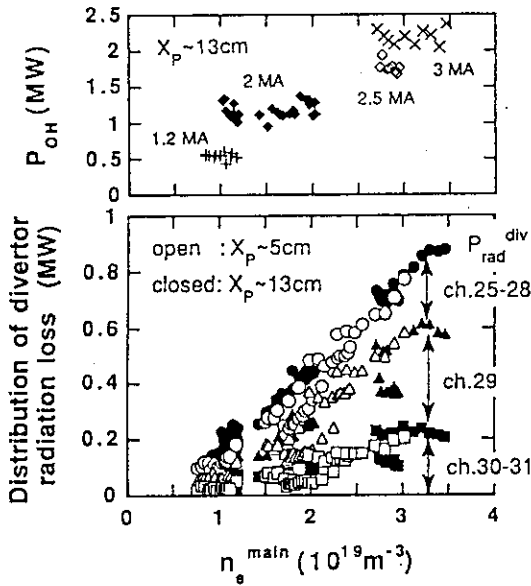


Fig.2 Distribution of the radiation loss and ohmic power plotted as a function of main electron density for different ohmic discharges. Discharges parameters are: $I_p=1.2-3$ MA, $B_T=2.5, 3, 4$ T for $X_p=4-8$ cm, and $I_p=1.2-3$ MA, $B_T=4$ T for $X_p=11-14$ cm.

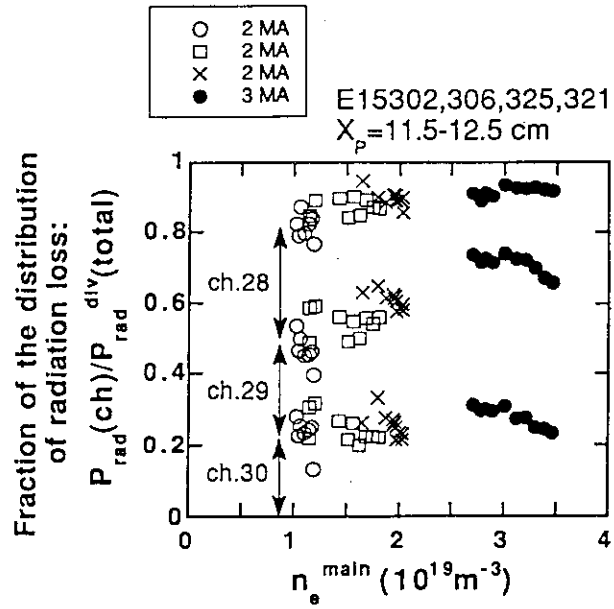


Fig.3 Dependence of the distribution of the divertor radiation loss on the main electron density.

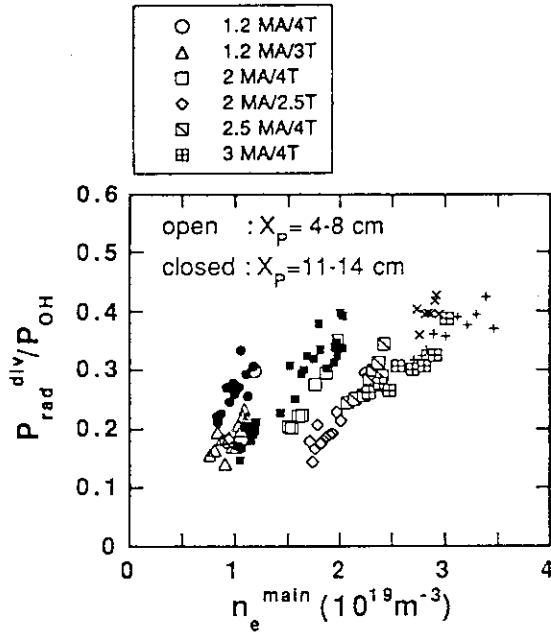


Fig.4 Fraction of the radiation loss against the ohmic power plotted as a function of main electron density.

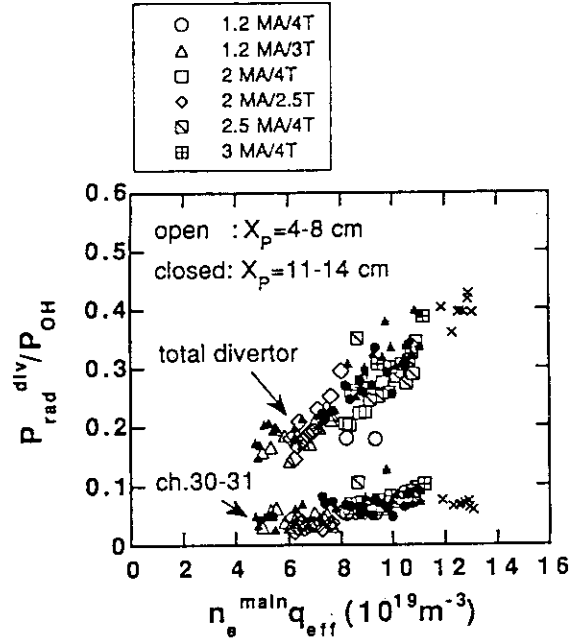


Fig.5 Fraction of the radiation loss against the ohmic power plotted as a function of parameter $n_e^{\text{main}} q_{\text{eff}}$.

4.5 Heat Flux in Divertor Plasmas

K. Itami, M. Shimada, N. Asakura, K. Shimizu, S. Tsuji,
N. Hosogane, H. Kubo

1. Introduction

In order to estimate impurity generation and material performance of the first wall in fusion reactors, it is necessary to predict the temperature of the divertor and the heat flux to the divertor. The divertor system for ITER represents one of the most difficult design tasks for ITER. The peak power loads on the divertor plates of $< 15 \text{ MW/m}^2$ are acceptable for steady state operation. Hence maximum value of heat flux density at the divertor is an important parameter and an experimental scaling is required to predict the first wall behaviour in high density and high power beam heated discharges. It is expected that divertor conditions close to the conditions of fusion reactors will be realized under the full performance of JT-60U. The study of the heat and particle transport in JT-60U will provide a basis for the prediction in these devices.

2. Characteristics of Steady State Heat Flux in H-mode and L-mode

In H-mode, the steady state heat flux (steady state for $\sim \tau_E$) is obtained during the high T_i operation. A typical heat flux profiles in high T_i H-mode and L-mode are shown in Fig. 1(a). In H-mode phase, heat flux profile is symmetric or the maximum heat flux at the inner divertor is larger than that of the outer divertor. In L-mode, heat flux profile exhibits asymmetry. The maximum heat flux density at the outer divertor is two to three times larger than that in the inner divertor. When the effective safety factor increases, the peak heat flux density decreases. In Fig. 1(b), the heat flux profile at the timing of L-mode and the heat flux profile in another L-mode discharge with $q_{eff} = 6.5$ are compared. The main plasma density and total heat load to the divertor and the configuration is almost same in these cases. The broadening of heat flux is due to the longer connection length in the discharges with $q_{eff} = 6.5$.

3. Scaling of Heat Flux in NB heated Plasmas

To investigate the transport in the scrape-off layer, the power scaling of the decay length in the scrape-off layer and the decay length at the divertor have been studied[1,2]. To predict the boundary plasma parameters in the fusion device, we pay attention to the peakedness of heat flux at the divertor and investigate the transport of heat flux as a function of the global parameters in JT-60U.

The peakedness of heat flux (in other words the inverse width of the heat channel) is determined by the competing processes of transport along the magnetic field and the perpendicular diffusion of particles and heat. The heat flux and particle flux to the divertor and the connection length dominate the scaling by determining electron temperature and density in the scrape-off layer and the divertor plasma. Then the peaking factor of heat flux at the outer strike point of separatrix (the outer divertor) Y is described by the total heat flux to the outer divertor P_{HEAT} , the line averaged density \bar{n}_e and the effective safety factor q_{eff} . The peaking factor Y , defined by $Y = 2\pi R f q_{max} / P_{HEAT}$, is effectively the inverse of the width of scrape-

off layer. Here $2\pi R$ is the toroidal circumference, $f q_{\max}$ is the product of the expansion of magnetic flux tube and the maximum heat flux density at the divertor. From a statistical analysis of database, we obtained the scaling of the peaking factor scaled as [3]

$$Y = 6.09 P_{HEAT} [\text{kW}]^{0.49} \bar{n}_e [\times 10^{19} \text{m}^{-3}]^{0.45} q_{eff}^{-0.67}.$$

A database of steady state heat flux was assembled from discharges with $1.2 \text{ MA} \leq I_p \leq 3 \text{ MA}$ (plasma current), $1 \times 10^{19} \text{m}^{-3} \leq \bar{n}_e \leq 7 \times 10^{19} \text{m}^{-3}$ (averaged density of the main plasma), $4 \text{ MW} \leq P_{NB} \leq 16 \text{ MW}$ (NBI heating power), $2.5 \leq q_{eff} \leq 13$ (effective safety factor).

In addition to the original database, discharges with high power beam heating data is plotted, as shown in Fig. 2. Neutral beam power is extended up to $P_{NB} = 25 \text{ MW}$ and $\bar{n}_e = 8 \times 10^{19} \text{m}^{-3}$. The new data points are indicated by the larger symbols in the figure. As shown in the figure, the scaling is still valid. The reduction of peaking factor of heat flux due to continuous ELMs is up to $\sim 40\%$.

4. Effect of Radiation Loss to Peak Heat Flux Density

The most important purpose for establishing scaling about heat flux is to predict the peak heat flux in fusion devices from the global plasma parameters. Total heat flux to the scrape-off layer is estimated from the energy balance in the main plasma. To predict peak heat flux density around each hitting points of separatrix at the divertor, which is refereed as target, it is necessary to take into account of the asymmetry of heat flux between the inner target plates and the outer target plates and the radiation loss near the divertor. When the ion grad-B direction is toward the divertor plates, it has been observed that heat flux is larger at the outer target than the inner target. In JT-60U experiment, about 70% of total heat flux is deposited at the outer target. When the ion grad-B drift direction is away from the divertor plates, the asymmetry of heat flux becomes small.

The effect of radiation loss on the peak heat flux density is included by describing the scaling as a function of the scrape off layer heat flux, rather than total heat flux to the divertor. We assume the heat flux to the scrape-off layer P_{SC} is given by

$$P_{SC} = P_{HEAT} + \frac{P_{RAD-DIV}}{2}.$$

Here $P_{RAD-DIV}$ is the radiation power from the divertor. The same data set with the scaling of Y is used to obtain the scaling of the peak heat flux density. Since toroidal field, plasma current, beam power of the new data points are limited in the narrow range, we roughly estimated the scaling of the peak heat flux as the function of P_{SC} , \bar{n}_e and q_{eff} , rather than statistically analyzed. As shown in Fig. 3, the peak heat flux density q_{max} scales with the product $P_{SC}^{1.5} \bar{n}_e^{-1} q_{eff}^{-1} / f$. This scaling has a larger dependence on the inverse of \bar{n}_e and q_{eff} than the scaling of Y . The larger dependence on the inverse of \bar{n}_e and q_{eff} is attributed to the tendency that a fraction of $P_{RAD-DIV}$ scales with $\bar{n}_e q_{eff}$.

5. Discussions

Here we apply the scaling of the peaking factor of heat flux to the plasmas with the different major radius R and minor radius a . From the heat conduction along the magnetic

field,

$$P = 2N [q_{||} \frac{B_P}{B_T} 2\pi R \Delta]$$

is obtained. P is the total power to the scrape-off layer. $q_{||}$ is heat flux along the magnetic field and given by $q_{||} = \frac{\kappa_{||}^0}{L_{||}} [T_s^{7/2} - T_{div}^{7/2}]$. $L_{||}$ is the connection length to the divertor and is given by $L_{||} = \pi R q_{eff} / N$. N is number of null points; i.e. $N = 1$ is single null and $N = 2$ is double null. The subscripts s and div denotes the scrape-off layer and divertor, respectively. The power flow from the main plasma is given by

$$P = \chi_{\perp} \frac{n_s T_s}{\Delta} S / 2N$$

Here χ_{\perp} is thermal diffusivity coefficient and S is the surface area. From these two equations,

$$\Delta^{-1} \propto \chi_{\perp}^{-7/9} (NP/S)^{5/9} n_s^{-7/9} (q_{eff} R/N)^{4/9}$$

is obtained. Assuming $n_s \propto \bar{n}_e$ for simplicity, the right hand side can be replaced with $(NP/S)^{0.49} \bar{n}_e^{-0.45} (q_{eff} R/N)^{0.67}$. Then the generalized form of the scaling will be

$$Y = 28 P_{HEAT} [\text{kW}]^{0.49} \bar{n}_e [\text{m}^{-3}]^{-0.45} q_{eff}^{-0.67} R [\text{m}]^{-1.65} \left(\frac{2A}{1+\kappa} \right)^{0.49} N^{1.38},$$

where A and κ are aspect ratio and ellipticity of the plasma cross section.

The major interest to this scaling is the application to the design of fusion reactors. The plasma parameters in the ITER ignition phase ($P = 40\text{MW}$, $\bar{n}_e = 1.4 \times 10^{20}\text{m}^{-3}$, $R = 6\text{m}$, $q_{eff} = 3$) gives the width of heat channel $\Delta = 8\text{mm}$, if $P = P_{HEAT}$ is assumed. The $\Delta = 5\text{mm}$ estimation in ref. [4] seems to be pessimistic, since a larger value than $\Delta = 8\text{mm}$ is expected due to the reduction of $P = P_{HEAT}$ by the radiation loss at the divertor.

6. Conclusions

Characteristics of heat flux to the divertor is investigated in the H-mode and L-mode discharges. A database analysis has shown the scaling of the peaking factor of heat flux on $P_{HEAT}^{0.49} \bar{n}_e^{-0.45} q_{eff}^{0.67}$ for NB heated discharges in JT-60U is extended to the discharges with up to $P_{NB} = 25\text{MW}$ and $\bar{n}_e = 8 \times 10^{19}\text{m}^{-3}$.

Acknowledgments

The authors wish to thank the members of Japan Atomic Energy Research Institute who have contributed to the JT-60U project.

REFERENCES

- [1] MCCORMICK K., Proceedings of 19th EPS Conference
- [2] BUCHENAUER, D., to be published in J. Nucl. Mater.
- [3] ITAMI, K. et al. to be published in J. Nucl. Mater.
- [4] ITER CONCEPTUAL DESIGN REPORT. NO.18.

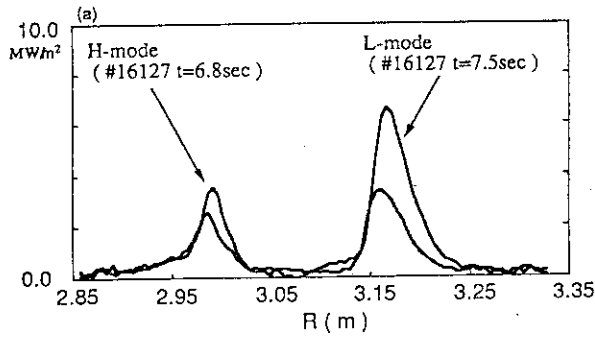


Fig. 1(a)
Heat flux profiles in L-mode and H-mode.

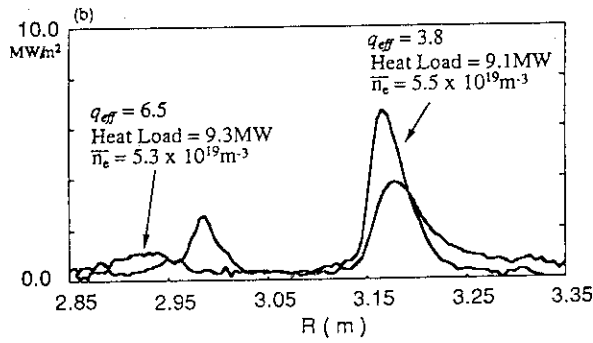


Fig. 1(b)
Heat flux profiles in the beam heated and discharges with $q_{eff} = 3.8$ with $q_{eff} = 6.5$.

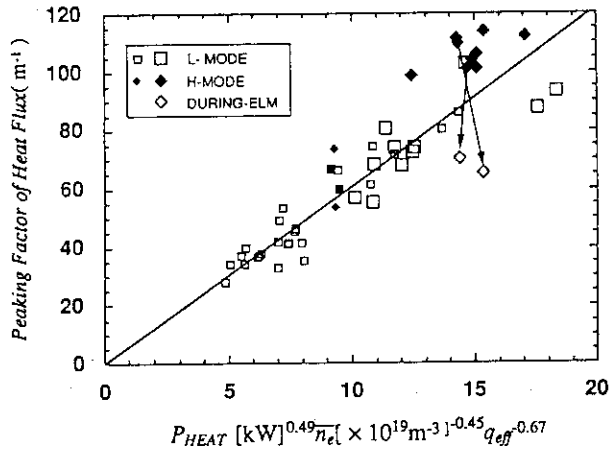


Fig. 2
Scaling law of the peaking factor of heat flux for NB heated discharges. In addition to the original database, discharges with up to $P_{NB} = 25\text{MW}$ and $\bar{n}_e = 8 \times 10^{19}\text{m}^{-3}$ are plotted.

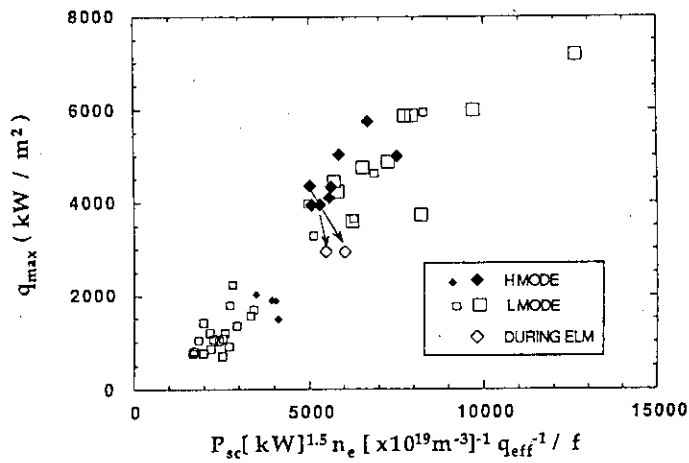


Fig. 3
Scaling law of the peak heat flux density. The peak heat flux density scales with the product $P_{sc}^{1.5} \bar{n}_e^{-1} q_{eff}^{-1} / f$.

4.6 Heat Flux in ELMy Discharges and High Beta Poloidal Discharges

K. Itami, N. Hosogane, M. Shimada

1. Introduction

ELMy H-mode is the most promising confinement since the good confinement in the core plasma and the moderate divertor conditions can be achieved at the same time. In JT-60U, it is estimated from the monitor video signal that a major part of the energy is released in few scans of IRTV camera (less than a millisecond) at each ELM. This study investigates behaviors of time averaged heat flux during ELMy phase rather than transient heat flux at each ELM activity.

1. Heat Flux Measurement during ELM Activity

Surface temperature of divertor tile increases rapidly at each ELM (~several hundreds of micro seconds) and reduces gradually due to heat conduction until the next ELM. This sequence is repeated during ELMy H-mode. When ELM frequency is high or ELM activity is regular, average heat flux during ELM can be estimated. When ELM frequency is higher than several kHz, pulsed heat flux at each ELM may be treated as semi-continuous heat flux. In the case of ELMy discharge with low frequency (> 40 Hz) of ELMs, we can estimate heat flux, only if sample timings synchronize with perturbations of temperature. In the discharge #16157, for example, ELM activity is regular with the frequency of about 80Hz. ELM activity and the sampled temperature is almost synchronized.

In order to estimate errors in calculating time averaged heat flux during ELMy phase, we carried out simulations of IRTV measurement. Heat flux during ELMy phase is modeled by $P_{HEAT} = P_S + P_{ELM}$, as shown in Fig. 1. Here P_S and P_{ELM} are steady state heat flux during ELMy phase and pulsed heat flux due to ELM, respectively. A pulse width of heat flux due to ELM is assumed to be $\delta t = 1$ msec. Temperature sampled by IRTV camera system is simulated by calculating surface temperature of a tile and then acquiring the values every 25 msec. Figure 2a shows simulated time traces of temperature sampled at the timing of T1, T2, T3 and T4. The time averaged heat flux density $\bar{P}_{HEAT} = 5$ MW/m² and the ELM power ratio $P_{ELM} / \bar{P}_{HEAT} = 0.5$ are assumed. Figure 2b shows time traces of P_{cal} which is heat flux density calculated from the data shown in Fig. 2a. Since the sampling frequency and ELM frequency is exactly same, the peak temperature just after each ELM is always taken if the sampling timing happens to be T4. In this case P_{cal} is far from \bar{P}_{HEAT} . If the data is taken more than 5msec later than T4, the error of calculated heat flux is small.

If the ELM frequency is n times higher than the sampling frequency, the peak temperature just after ELM is sampled every n ELMs at the timing of T4, the timing of just after an ELM. Fig 3 shows P_{cal} / \bar{P}_{HEAT} as a function of the ELM power ratio. As shown in this figure, the error of calculation become smaller as the ELM frequency is high and ELM power ratio is small. In reality, ELMs are not so accurate as sampling clocks and sudden jumps of temperature are sampled at several sampling time. It is still possible to obtain \bar{P}_{HEAT} with good accuracy by excluding few data of sudden jump in temperature from the calculation, if ELM frequency is approximately n times ELM frequency and heat flux at each ELM is approximately equal.

3. Broadening of Heat Flux Profile due to Continuous ELM Activity

When the particle recycling level is relatively large, the pulsed heat flux at each ELM is mainly deposited to the inner divertor. As the particle recycling is reduced by wall conditioning, the fraction of the pulsed heat flux deposited to the outer divertor increases along with the improvement in the H-mode confinement [1].

A significant broadening of heat flux due to continuous ELM activity is observed in ELMy H-mode discharges with $I_p = 3\text{MA}$, $B_T = 4\text{T}$ and $P_{NB} \geq 20\text{MW}$, when the level of the particle recycling is low. Fig. 4 shows the time evolution of a typical H-mode discharge with continuous ELM activity. With the onset of the continuous ELM activity with frequency of $\sim 80\text{Hz}$, the peak heat flux is reduced about 30% than before the onset of ELM activity. The profiles of heat flux and particle flux before ELM and during continuous ELMs are shown in the Fig. 5. The heat flux profile broadens and the peak heat flux density is significantly reduced at both the inner divertor and the outer divertor. The particle flux doubles over the divertor. The H-factor estimated at $t=7.2\text{sec}$ is 1.4. The broad heat flux profile is maintained until the end of the neutral beam injection, while no serious degradation of H-mode confinement is observed.

Low particle recycling and regular ELMs are prerequisite to achieve the broadening of heat flux. The low level of recycling is required to get H-mode plasma with good confinement and in-out symmetry of pulsed heat flux. Although higher frequency of ELM is good to smooth the pulsed heat flux during ELMy phase, it degrades the H-mode confinement [2]. The observed ELM frequency of $\sim 80\text{Hz}$ seems to be compatible with improved H-mode confinement. The broadening of the heat flux due to the continuous ELM points out the importance of ELMs control and demonstrates the advantage of ELMy H-mode over L-mode from the point of heat flux control.

heat flux during high beta-p disruption

4. Heat Flux during High Beta Poloidal Mode

It has been observed that the peak heat flux density at the inner target is larger than the peak heat flux at the outer target during high beta poloidal mode. While the magnetic flux expansion factor at the inner target is approximately twice as large as that at the outer target, the peak heat flux density at the inner divertor is larger than the peak heat flux density. This indicates the heat flux density along the magnetic at the outer target is at least $\sqrt{2}$ times larger than that at the outer target, even if the difference of magnetic field geometry around the divertor is taken into account. This in-out asymmetry of heat flux in high beta poloidal mode is opposite to the asymmetry in L-mode discharges. Figure 6. shows a typical discharge of which high beta-p mode is terminated by a beta collapse. The beta collapse occurred at $t=5.95\text{sec}$ and a half of the stored energy is released within 100 milliseconds. In the IRTV measurement the heat flux suddenly disappear at the beta collapse for the period of about 100 milliseconds. Although heat flux begun to recover after $t=6.0\text{sec}$, the magnetic stored energy had been released. H alpha signal viewing the divertor region showed a large spikes of signal at the beta collapse and then decreases to zero level, indicating little particle recycling at the divertor, until $t=6.0\text{sec}$. Increase in the radiation loss power after the beta collapse is mainly from the main plasma and a major part of the energy is released by radiation loss from the main plasma during the beta-p collapse.

Figure 7 shows profiles of heat flux for the period of $t=5.9\text{sec}$ to $t=6.2\text{sec}$. At $t=6.0\text{sec}$ peaks of heat flux disappeared in both the inner and the outer target. Figure 8(a) shows time traces of the peak heat flux in the inner target and the outer target. Figure 8(b) shows time traces of the total heat flux around the inner target and the outer target. The inner peak heat flux density q_{max}^{in} is twice as large as the outer peak heat flux density q_{max}^{out} before the beta collapse. Since the inner hit point of separatrix at the target is on the boundary of the IRTV sight before the beta collapse, more than half of the heat flux to the inner targets is not included and P_{HEAT}^{in} is estimated to be twice as large as P_{HEAT}^{out} . After the beta collapse, the peak value of heat flux at the outer target surpass the peak heat flux at the inner target.

5. Discussions

Although the opposite asymmetry of heat flux to that in L-mode discharges is only observed in high beta poloidal discharges, the difference may be partly explained from the understanding of heat flux behaviors in H-mode and L-mode discharges. The high beta poloidal discharges are operated under the low recycling wall conditions. The lower recycling at the divertor reduce the electron density gradient along the scrape-off layer, resulting in the reduction of asymmetry in particle flux, heat flux and radiation loss which are observed in L-mode discharges. Even in similar recycling conditions, the more symmetric heat flux profile is observed in H-mode discharges than L-mode discharges[this review]. The peak heat flux at the inner target is as large as the peak heat flux at the outer target. Reduction of heat flux at the outer target is possibly correlated to the good core confinement.

6. Conclusions

A significant broadening of time averaged heat flux profile is observed during continuous ELM activity in H-mode discharges with $I_p = 3\text{MA}$, $B_T = 4\text{T}$ and $P_{NB} \geq 20\text{MW}$. From the simulation study, it is confirmed that the averaged heat flux can be estimated within a good accuracy, since the frequency of ELM activity approximately synchronizes with the sampling frequency of IRTV system. In high beta poloidal mode, the heat flux to the inner target is twice as large as the heat flux to the outer target. This asymmetric behavior relaxes to that of L-mode after beta collapses.

Acknowledgements

The authors wish to thank the members of Japan Atomic Energy Research Institute who have contributed to the JT-60U project.

References

- [1] SHIMADA, M. et al. " JT-60U High Power Heating Experiments" 14th IAEA-CN-56/A-1-3.
- [1] ITAMI, K. et al. " Heat Transport and Electric Current in Tokamak Boundary Plasmas of JT-60U" 14th IAEA-CN-56/A-6-5.

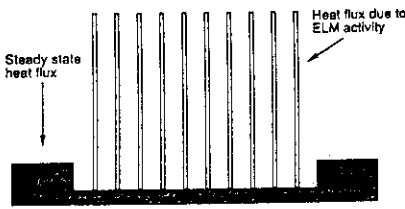


Fig.1 Heat flux model during ELM phase.

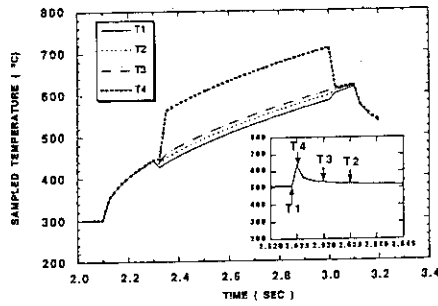


Fig.2(a) Simulated time traces of temperature sampled at the timings of T1, T2, T3 and T4.

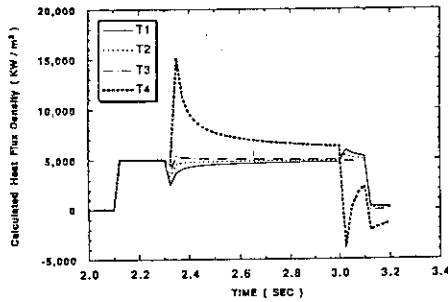


Fig.2(b) Time traces of the calculated heat flux from the data shown in Fig.2(a).

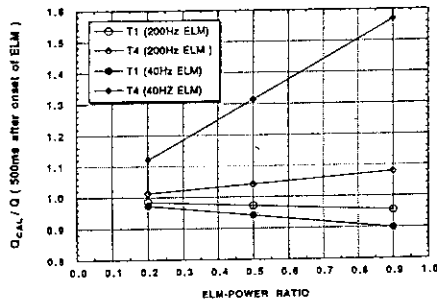
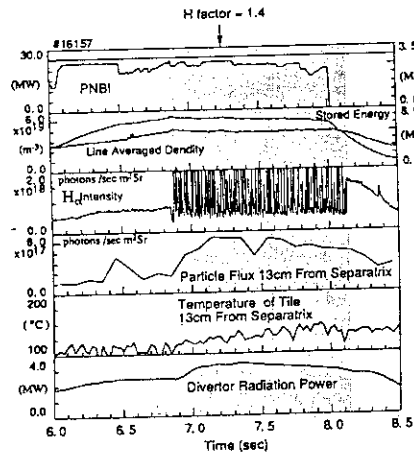
Fig.3 P_{ELM} / P_{HEAT} as a function of the ELM power ratio.

Fig.4 Time evolution of a typical H-mode discharge with continuous ELM activity.

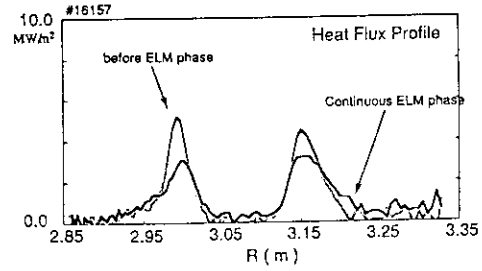


Fig.5 Profiles of heat flux before ELMs and during continuous ELMs.

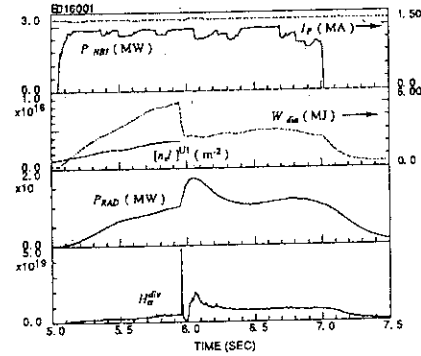


Fig.6 Time trace of a typical discharge of high beta poloidal mode.

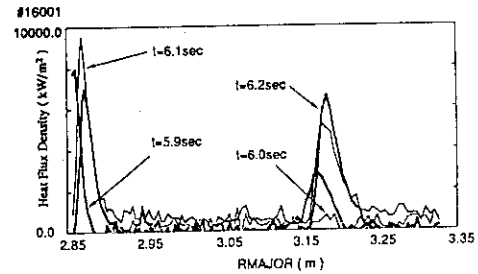
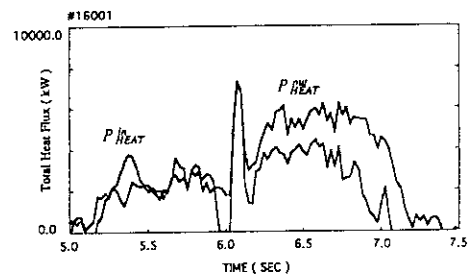
Fig.7 Heat flux profile on the divertor for $t=5.9\text{sec}$ to $t=6.2\text{sec}$ in #16001.

Fig.8(a) Time traces of the peak heat flux density at the inner target and at the outer target

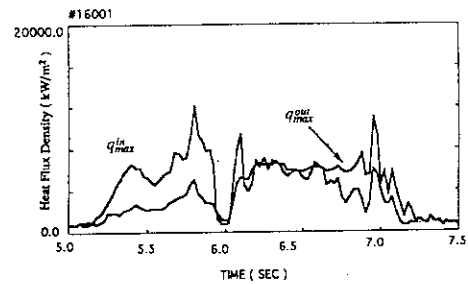


Fig.8(b) Time traces of the total heat flux at the inner target and at the outer target

4.7 Carbon Generation Mechanism

A. Sakasai, H. Kubo, M. Shimada, K. Itami, T. Sugie,
N. Asakura, S. Numazawa, S. Tuji, N. Hosogane

1. Introduction

Carbon impurities are inevitably generated at graphite divertor plates in high power heated diverted tokamaks. The influx of deuterium, carbon and oxygen into the divertor region was measured by spectroscopic diagnostics in JT-60U. The generation mechanism of the carbon impurities was investigated [1] with high power NB heated and high density diverted discharges. In JT-60U, divertor plates made of carbon-fiber composites (C/C) were installed with an accuracy of 0.5 mm, and their edges were bevelled in order to prevent localized heat flux onto the plates. No carbon bloom was observed at a neutral beam power level of 20-25 MW for 2 s.

2. Carbon Impurity Generation Mechanism

In JT-60U, spectrometers, a Langmuir probe array and an infrared television (IRTV) camera were installed for divertor diagnostics to study the divertor characteristics. The influxes of deuterium, carbon and oxygen ions were derived, respectively, from the measured line intensities of D_{α} , C II 657.8 nm and O II 441.5, 441.7 nm. In order to calculate the carbon influx by sputtering at divertor plates, electron temperature and density profiles on the divertor plates and the surface temperature of the divertor plates were measured independently [2].

Considering a steady state, we can assume that the outflux is equal to the spectrometrically measured influx. Then the carbon influx Γ_C can be expressed as

$$\frac{\Gamma_C}{\Gamma_D} = \frac{Y_D}{1-Y_C} + \frac{Y_O}{1-Y_C} \times \frac{\Gamma_O}{\Gamma_D} \quad (1)$$

where Γ_D , Γ_O and Γ_C are the fluxes of deuterium, oxygen and carbon ions onto the divertor plates, respectively. Y_D , Y_O and Y_C are the sputtering yields of carbon by deuterium, oxygen and carbon ions, respectively [3]. Physical and chemical processes are considered for the deuterium and oxygen sputtering. The carbon sputtering (self-sputtering) is a physical process. The physical sputtering yield depends on the incident energy of the ions. The incident energy was assumed as given in ref. [4]. The ion temperature was assumed to be equal to the electron temperature. In experiments with ion beams, the chemical deuterium sputtering yield is much larger than the physical deuterium sputtering yield.

The impurity generation mechanism has been studied by considering the spatial distributions of the deuterium, carbon and oxygen influxes[5] because only total influxes were discussed in a former study [1]. Figure 1(a) shows the spatial distributions of the measured carbon influx and the calculated carbon influxes by self-sputtering, physical and chemical oxygen ion sputtering and physical deuterium ion sputtering at the outer strike point of the separatrix in NB heated discharges with $I_p = 2.5$ MA, $B_T = 4.0$ T and $P_{NB} = 23$ MW. The deuterium and carbon flux at the inner strike point on the divertor plates is larger than that at the outer strike point. On the other hand, electron temperature, pressure and heat load at the outer strike point are higher than at the inner strike point [2]. The calculated carbon influx is in a good agreement with the measured carbon influx. The ratio of the measured to the calculated influx which was averaged spatially is 1.2 near the outer strike point. The contributions of carbon, oxygen and deuterium sputtering are about 38%, 1% and 61% of total carbon influx near the outer strike point. The carbon and deuterium sputtering is dominant, and oxygen sputtering is very small, because of $\Gamma_O / \Gamma_D \approx 10^{-4}$ in this discharge. The ratio of the measured to the calculated influx is from 1.0 to 2.0 near the outer strike point in high density ($\bar{n}_e = 4 - 6 \times 10^{19} \text{ m}^{-3}$) and neutral beam heated discharges ($P_{NB} = 8 - 25$ MW) considering the spatial distribution as shown in Fig. 1(b). The calculated and the measured carbon influxes normalized to the deuterium influx are nearly constant and 0.015 to 0.035 up to $\bar{n}_e = 6.2 \times 10^{19} \text{ m}^{-3}$ as shown in Fig. 1(c).

The spatial distribution measurement of the influxes and electron temperature in the divertor improves the agreement as compared with the result considered only total influxes. However, the ratio in the case of high electron temperature ($T_e \approx 100$ eV compared with $T_e < 50$ eV), low density ($\bar{n}_e < 3 \times 10^{19} \text{ m}^{-3}$) and high power NB heated discharges ($P_{NB} \approx 20$ MW) has a tendency to be less than 1.0. The difference in the case of high electron temperature in the divertor probably suggests that the incident ion energy in the divertor region is different from the assumption made in ref. [4].

This result indicates that carbon impurities generated by the chemical deuterium ion sputtering does not any problem. No carbon bloom was observed in high power NB heated discharges. The surface temperature of the divertor plates measured by IRTV did not exceed 800°C, and the concentration of heat deposition at the edges of the carbon tiles would be reduced by high thermal conductivity of the tiles (C/C), good alignment of the surface and edge bevelling of the tiles. Therefore, radiation enhanced sublimation might not play an important role in JT-60U, so far.

The empirical law of relation between concentration of carbon ions in the divertor plasma and in the main plasma is very important to study impurity shielding and transport. The carbon concentration in the main plasma can be estimated using calculated value of carbon influx in the divertor plasma to find the empirical law. The concentration of carbon ions

(carbon influx / deuterium influx) in the divertor plasma is compared with that (carbon density / deuterium density) in the main plasma as shown in Fig. 2. The ratio of carbon concentration in the divertor plasma to that in the main plasma depends on the electron density in the main plasma. The ratio is about 40% at $n_e = 1.5 \times 10^{19} \text{ m}^{-3}$ in OH plasmas and from 15 - 45% at $n_e = 5 \times 10^{19} \text{ m}^{-3}$ in NB heated plasmas. This result suggests that shielding becomes more effective as electron density increases. This knowledge is important from a viewpoint of impurity control.

3. Conclusions

The impurity generation mechanism, the remote radiative cooling and the spectroscopic aspects of divertor radiation were studied in JT-60U.

The dependence of the carbon influx on the electron density can be explained by deuterium (physical sputtering), oxygen and carbon sputtering. The contribution of the chemical deuterium sputtering is small. The importance of the oxygen sputtering is clear in the low density discharges. The decrease in relative carbon flux in the high density region is explained by the reduction in the relative oxygen concentration and the decrease in the electron temperature in the divertor region. The carbon and deuterium sputtering is dominant in the high density ($n_e = 4 - 6 \times 10^{19} \text{ m}^{-3}$) NB heated discharge. The relation between concentration of carbon ions in the divertor plasma and in the main plasma was obtained to study impurity shielding and transport.

References

- [1] KUBO, H., et al., Proc. 10th Intern. Conf. on Plasma-Surface Interaction in Controlled Fusion devices, Monterey 1992, J. Nucl. Mater. to be published.
- [2] ITAMI, K., et al., paper IAEA-CN-56/A-6-5, *ibid*.
- [3] ROTH, J., VIETZKE, E. and HAASZ, A.A. Supplement to the Journal Nuclear Fusion, Vol.1 (1991) 63.
- [4] CHODURA, R., J. Nucl. Mater. 111&112 (1982) 420.
- [5] SAKASAI, A., et al., paper IAEA-CN-56/A-7-12, in Plasma Physics and Controlled Nuclear Fusion Research (to be published in Proc. 14th Int. Conf. Würzburg, 1992).

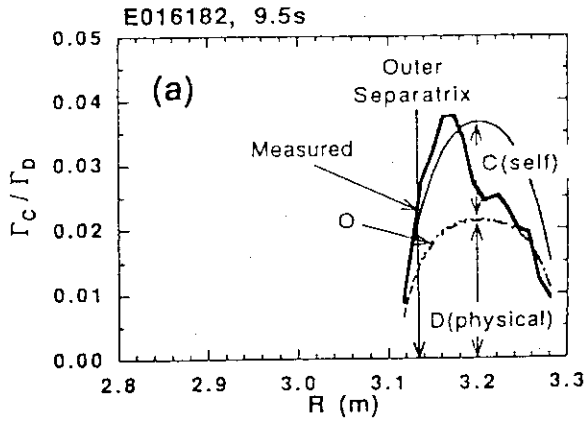


Fig. 1(a) The spatial distributions of the measured carbon influx and the calculated carbon influxes by self-sputtering, physical and chemical oxygen ion sputtering and physical deuterium ion sputtering at the outer strike points of the separatrix in NB heated discharges with $I_p = 2.5$ MA, $B_T = 4.0$ T and $P_{NB} = 23$ MW.

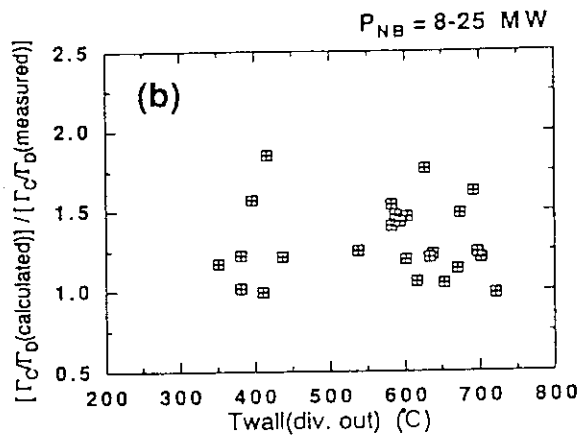


Fig. 1(b) The values of the calculated carbon influx normalized to the measured carbon influx as a function of the surface temperature of the divertor plates near the outer strike points in high density ($\bar{n}_e = 4 - 6 \times 10^{19} \text{ m}^{-3}$) and neutral beam heated discharges ($P_{NB} = 8 - 25$ MW) considering the spatial distributions.

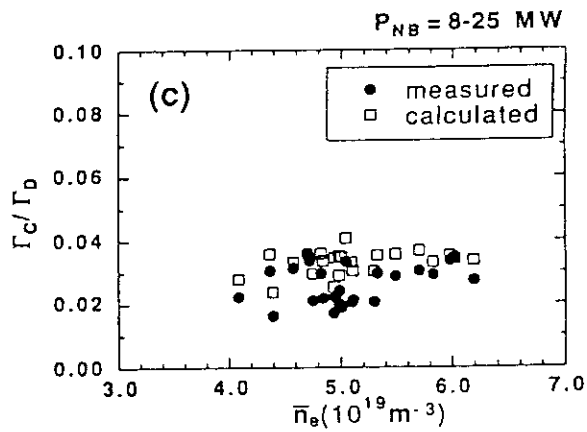


Fig. 1(c) The calculated and the measured carbon influxes normalized to the deuterium influx as a function of the line averaged electron density in the main plasma in the same discharges as Fig. 1(b).

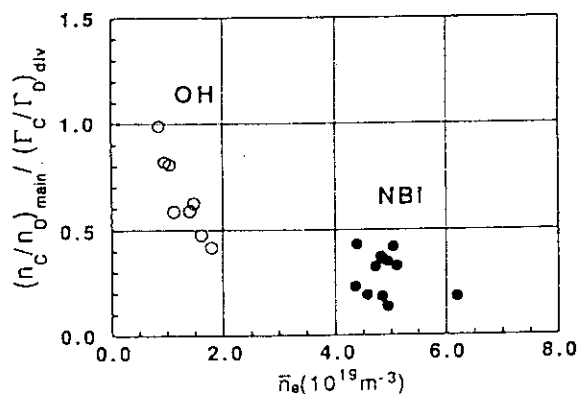


Fig. 2 The concentration of carbon ions (carbon influx / deuterium influx) in the divertor plasma is compared with that (carbon density / deuterium density) in the main plasma as a function of line averaged electron density in the main plasma.

4.8 Ion Temperature Characteristics and Impurity Behavior in Divertor Region

A. Sakasai, T. Sugie, H. Kubo, K. Itami, N. Asakura, N. Hosogane

1. Introduction

Ion temperature in the divertor is a very important plasma parameter with electron temperature and density there to study the divertor of large tokamak. So ion temperature in the divertor region of JT-60U has been spectroscopically measured. It is difficult to measure directly ion temperature in the divertor region of large tokamak. Some spectral lines from divertor plasma are measured using spectroscopic measurement of vacuum ultra violet (VUV) wavelength range in JT-60U.

2. Spectroscopic Measurement

A normal incidence VUV spectrometer with the Roland circle diameter 1.2 m is installed to view divertor plasma bending VUV light by tungsten mirror as shown in Fig. 1. The information from the spectroscopic measurement occupies spectral intensity and ion temperature of inner divertor at this viewing arrangement. The VUV spectrometer has a high wavelength resolution of 0.5 nm/mm to measure the Doppler broadening of VUV spectral lines. Figure 2 shows VUV spectra of NB heated hydrogen plasma. C IV 154.822 nm \times 4th order, C IV 155.077 nm \times 4th, D Ly α 121.534 nm \times 6th and H Ly α 121.567 nm \times 6th are measured in Fig. 2. H/D ratio is measured from intensities of D Ly α and H Ly α . Ion temperature of C³⁺ in the divertor region is obtained from the Doppler broadening of C IV 155.077 nm as shown in Fig. 3.

3. Ion Temperature Characteristics in Divertor Region

Ion temperature in the divertor region is depend on electron density of main plasma, height of X-point and NB heated power. Figure 4 shows the dependence of ion temperature in the divertor region on electron density of main plasma. As electron density of main plasma increases $\bar{n}_e = 1 \times 10^{19} \text{ m}^{-3}$ to $3 \times 10^{19} \text{ m}^{-3}$, the divertor cools down and the ion temperature decreases from $T_{i\text{div}} = 35 \text{ eV}$ to 20 eV in an OH discharge. The ion temperature has a strong dependence on electron density of main plasma in NB heated discharges ($P_{\text{NB}} = 7 - 10 \text{ MW}$) as shown in Fig.5. $T_{i\text{div}}$ decreases about 5 eV as electron density of main plasma increases from $\bar{n}_e = 2.0 \times 10^{19} \text{ m}^{-3}$ to $2.4 \times 10^{19} \text{ m}^{-3}$. The ion temperature decreases in OH

discharges as X-point becomes higher. Then the ion temperature decreases in OH discharges as q_{eff} becomes smaller.

Figure 6 shows the dependence of ion temperature in the divertor region on NB heated power. The ion temperature increases in NB heated discharges ($P_{\text{NB}} = 0 - 15$ MW) as NB heated power increases. The scatter of the ion temperature in the same NB power is caused by including the dependence on electron density. The dependence on q_{eff} is also indicated because the ion temperature in the discharge of $I_p = 2.0$ MA, $B_T = 4.0$ T is higher than T_i^{div} in that of $I_p = 1.3$ MA, $B_T = 2.0$ T.

Figure 7 shows comparison between ion temperature in the divertor region and electron temperature on the divertor plate from Langmuir probe measurement. The ion temperature is a little lower than the electron temperature in high density ($\bar{n}_e = 4 - 6 \times 10^{19} \text{ m}^{-3}$) and high NB power ($P_{\text{NB}} = 11 - 23$ MW) heated discharges. This is caused by the difference of measuring positions and the line integral effect along to the line of sight.

4. Ion Temperature and Impurity Behavior in Divertor Region on H-mode

Ion temperature in the peripheral region of main plasma on high T_i H-mode increases and makes a pedestal, and global confinement is improved. Also ion temperature in the divertor region on ELM free H-mode is higher than that on ELMy H-mode as shown in Fig. 8. The ion temperature decreases from $T_i^{\text{div}} = 33 - 37$ eV on ELM free H-mode to 26 eV on ELMy H-mode.

It is also observed that C VI intensity increases rapidly and carbon impurity is generated at a burst in ELMy H-mode phase. This is a very interesting phenomena concerning to carbon impurity generation mechanism on H-mode.

5. Conclusions

Ion temperature in the divertor region has been measured using the Doppler broadening of VUV spectral lines. The ion temperature is depend on electron density of main plasma, height of X-point, q_{eff} and NB heated power.

Ion temperature in the divertor region on ELM free H-mode is higher 10 eV than that on ELMy H-mode. It is also observed that carbon impurity is generated at a burst in ELMy H-mode phase. It is required to study carbon impurity generation mechanism on H-mode understanding this phenomena.

The ion temperature in the divertor region obtained from the spectroscopic measurement has a line integral effect along to the line of sight across the divertor. Therefore it is necessary to evaluate the line integral effect using 1.5 dimensional Monte Carlo code to identify the ion temperature on the magnetic surface.

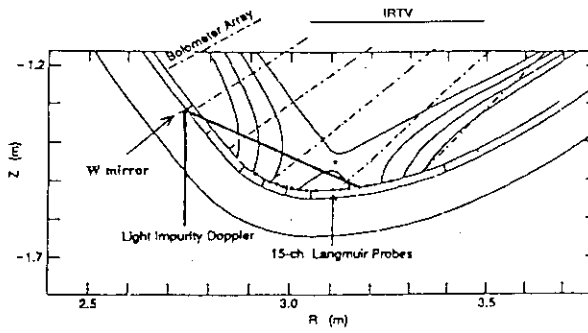


Fig. 1 The line of sight of a normal incidence VUV spectrometer bending VUV light by tungsten mirror.

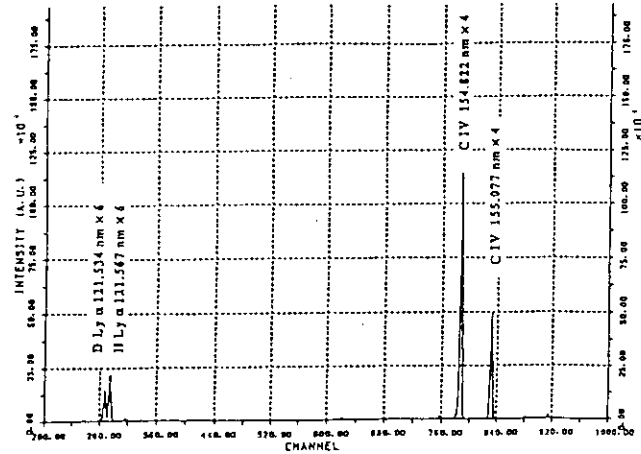


Fig. 2 VUV spectra of NB heated hydrogen plasma.

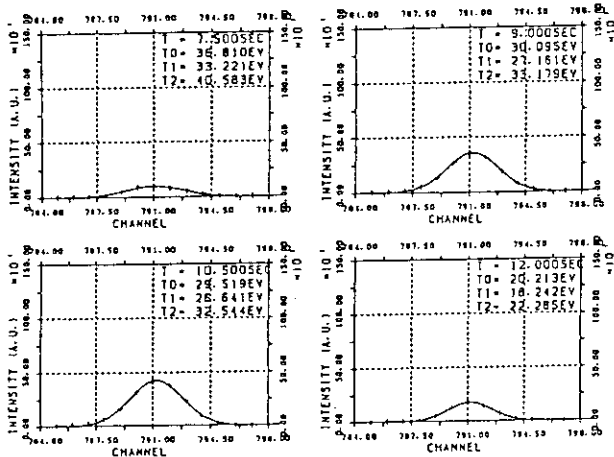


Fig. 3 Ion temperature of C^{3+} in the divertor region obtained from the Doppler broadening of C IV 155.077nm.

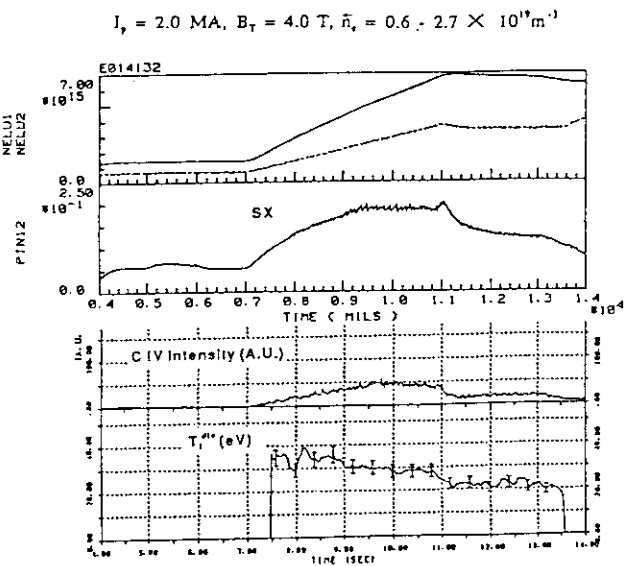


Fig. 4 The dependence of ion temperature in the divertor region on electron density of main plasma in OH discharges.

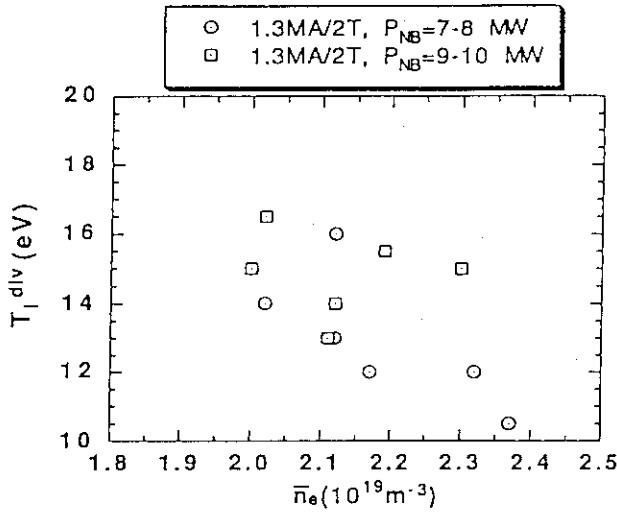


Fig. 5 The dependence of ion temperature in the divertor region on electron density of main plasma in NB heated discharges ($P_{NB} = 7 - 10$ MW).

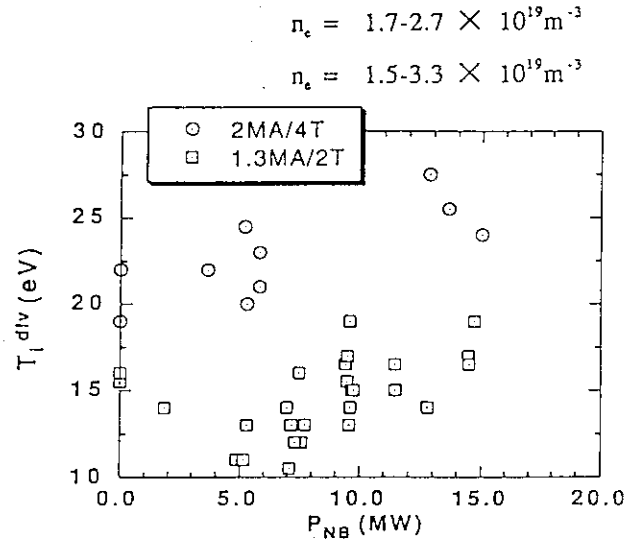


Fig. 6 The dependence of ion temperature in the divertor region on NB heated power.

$I_p = 2.5$ MA, $B_T = 4.0$ T, $\bar{n}_e = 4.6 \times 10^{19} \text{ m}^{-3}$
 $P_{NB} = 11-23$ MW

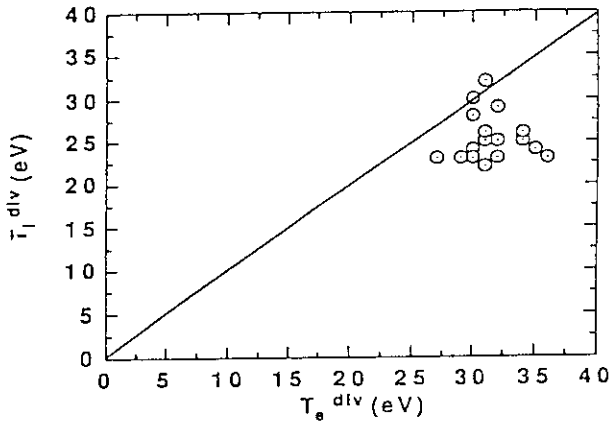


Fig. 7 Comparison between ion temperature in the divertor region and electron temperature on the divertor plate from Langmuir probe measurement.

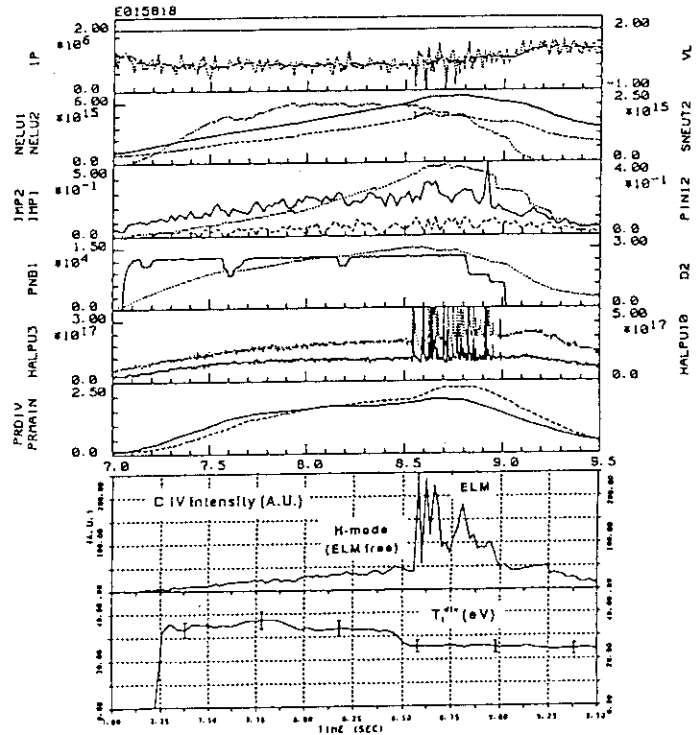


Fig. 8 Ion temperature and impurity behavior in the divertor region on ELM free and ELM H-mode.

4.9 Study of Impurity and Radiative Loss in Divertor Plasmas with Absolutely Calibrated VUV Spectrometers

H. Kubo, T. Sugie, M. Shimada, N. Hosogane,
A. Sakasai, S. Tsuji, K. Itami, and S. Numazawa

1. Introduction

For study of impurity behavior, it is important to measure the charge state distributions of impurities in divertor plasmas. However, such measurements have not been performed up to now. Remote radiative cooling is the most straightforward way to reduce the heat load onto the divertor tiles. The nature of the radiative losses has not been entirely clear, because spectroscopic observation in the VUV region has been poor. This work presents spectroscopic study of impurities and deuterium in divertor plasmas. Line intensities of D I, C II - IV, and O III - VI were simultaneously measured with absolutely calibrated VUV spectrometers. The charge distributions for carbon and oxygen and radiative losses were estimated from the measured line intensities.

2. Experimental Procedures

Figure 1 shows a schematic diagram of a cross-section of the JT-60U tokamak and the viewing chords of the important diagnostics in this work. VUV spectrometers (a grazing incidence spectrometer [1] and a normal incidence spectrometer [2]) observed the divertor plasma through the main plasma. In Fig. 1 (b), the relative solid angles of the spectrometers are shown as functions of the major radius. Because the viewing areas of the spectrometers were small, we discuss divertor discharges with the null point near the surface of the divertor tiles as shown in the figure. The radiative losses were measured with bolometers, and the electron temperatures were measured with Langmuir probes.

The grazing incidence spectrometer and the normal incidence spectrometer covered the wavelength regions of 300 - 1300 Å and 970 - 1560 Å, respectively. As an example, spectra observed in an ohmically heated discharge are shown in Fig. 2. The spectral lines of D I Lyman- α and 2s - 2p of C II - IV and O III - VI, which were the most important lines with a view to studying the radiative power losses, were observed simultaneously. The sensitivities of the spectrometers were calibrated using the branching ratio method and an calibrated Ar mini-arc [3].

When the plasma configuration was switched from limiter to divertor, the line intensities of D I, C II - IV, and O III - V increased rapidly. Therefore, it was concluded that these spectral lines came from the divertor plasma although the viewing chords of the spectrometers passed through the main plasma. On the other hand, the time evolution of the line intensity of O VI differed from that for these lines. It was expected that the line of O VI was a mixture of the emissions from the divertor plasma and the main plasma.

3. Results and Discussion

From intensities of C II 904 Å, C III 977 Å, C IV 1548 Å, O III 704 Å, O IV 555 Å, O V 630 Å, and O VI 1032 Å, charge state distributions for carbon and oxygen in divertor plasmas were derived by assuming the corona population equilibrium. Figure 3 shows the charge state distributions ($n_{A+z} n_e dl$) for an ohmically heated discharge. Here, n_{A+z} and n_e is the density of the ion A^{+z} and the electron density in the divertor plasma, respectively. dl is the length of the divertor plasma along the viewing chords of the spectrometers. The Li-like ion was dominant for carbon and the B- and Be-like ions were dominant for oxygen.

Radiative power loss in units of W/m^2 is given by

$$P_{\text{rad}} = \sum R_{A+z} n_{A+z} n_e dl,$$

where R_{A+z} is the rate coefficient for radiative power loss. The radiative power losses calculated from the spectroscopic measurements are shown in Fig. 4. The loss of neutral deuterium atoms was calculated by assuming $T_i = T_e$ and $n_{D^+} = n_e$. The ratio of the power loss due to each ion to the total power loss can be found on the right vertical axis. Here, the total radiative power loss refers to the sum of the power losses shown in the figure. The missing power loss due to unobserved ions was expected to be less than 5% of the total power loss. The radiative power losses were consistent with those measured with the bolometers, typically by a factor of 2. Fig. 4 (a) shows the radiative power losses for the ohmically heated discharge discussed previously (Fig. 3). The contributions of deuterium, carbon, and oxygen in the total power loss were 34%, 28%, and 39%, respectively. The radiative power losses for an neutral beam heated discharge with the neutral beam power of 12 MW is shown in Fig. 4 (b). The contributions of deuterium, carbon, and oxygen were 58%, 39%, 3.4%, respectively. The loss of neutral deuterium atoms was dominant. And the line radiations from C IV and D I were also important processes.

References

- [1] KUBO, H., et al., Rev. Sci. Instrum. **59** (1988) 1515.
- [2] KUBO, H., et al., Jpn. J. A. Phys. **28** (1989) 2610.
- [3] SUGIE, T., et al., Calibration of VUV Spectrometers, in this report.

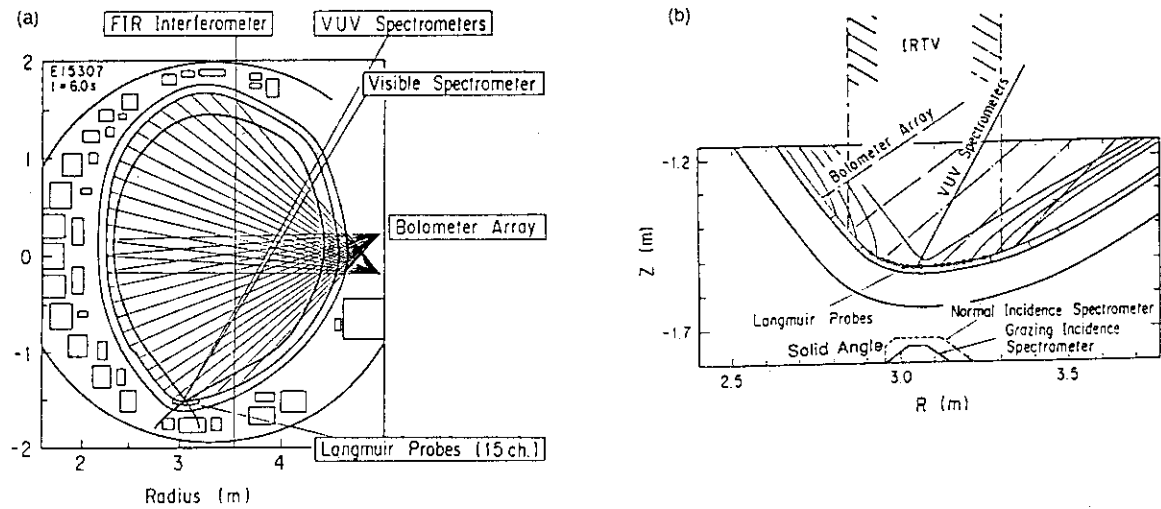


Fig. 1. (a) Schematic diagram of a cross-section of the JT-60U tokamak and the viewing chords of diagnostics. (b) Schematic diagram of the viewing chords of the diagnostics for divertor investigation. The solid angles of the spectrometers are shown as functions of the major radius.

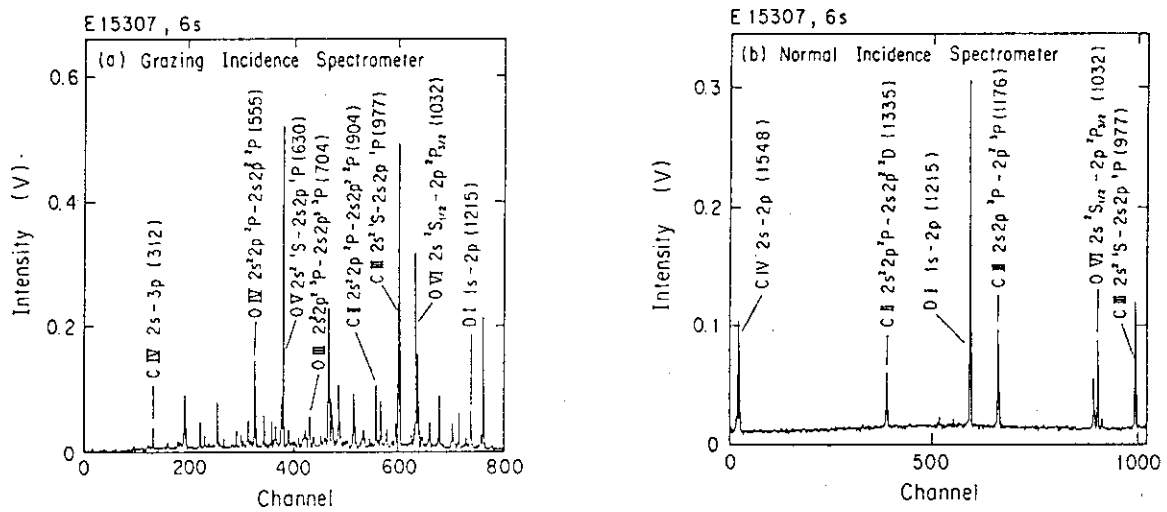


Fig. 2. Spectra in an ohmically heated discharge observed with (a) the grazing incidence spectrometer and (b) the normal incidence spectrometer. The wavelengths are shown in units of Å in parentheses.

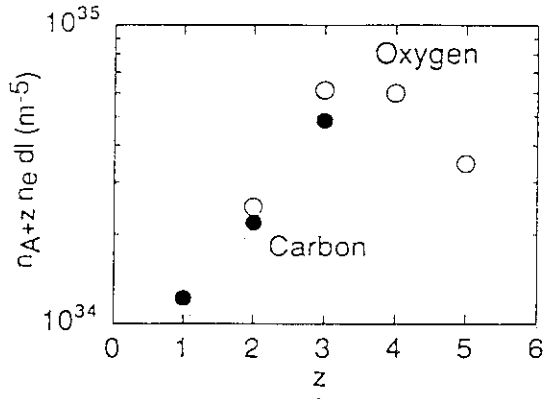


Fig. 3. Charge state distributions for carbon (closed circles) and oxygen (open circles) in a divertor plasma. They were obtained in an ohmically heated discharge (The plasma current I_p was 2 MA, the toroidal field B_T was 4 T, the line average electron density n_e was $3.1 \times 10^{19} \text{ m}^{-3}$, the effective ionic charge Z_{eff} was 2.0, and the radiation from the divertor plasma $P_{\text{rad}}^{\text{div}}$ was 0.19 MW.). The values for O VI were overestimated, because the observed O VI line included the emission from the main plasma.

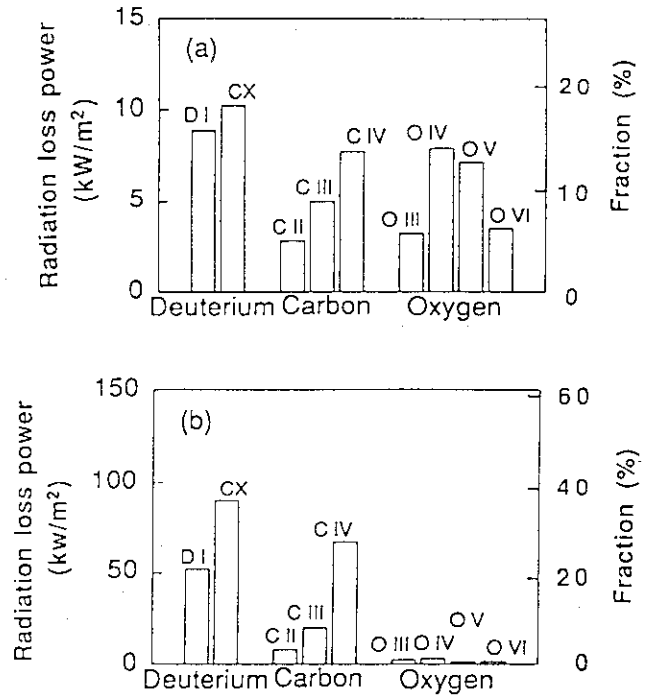


Fig. 4. Radiative power losses from the divertor plasmas (a) for the ohmically heated discharge (see the caption of Fig. 3) and (b) for a neutral beam heated discharge ($I_p = 2.4 \text{ MA}$, $B_T = 4 \text{ T}$, $n_e = 3.9 \times 10^{19} \text{ m}^{-3}$, $Z_{\text{eff}} = 3.3$, and $P_{\text{rad}}^{\text{div}} = 2.8 \text{ MW}$.). The loss of neutral deuterium atoms was indicated as CX.

4.10 Recycling Study in High Density Discharges

N. Asakura, N. Hosogane, S. Tsuji, M. Shimada

1. Introduction

One of the key issues for designing the large-scale and long-pulse tokamak such as ITER is the control of the heat flux to the divertor target plates. A possible solution is the high recycling divertor (gas target divertor) formed by the strong gas puff or gas pumping, where the heat flux can be reduced on the target plates though the radiative loss in the divertor region. Performance of the high recycling divertor has been studied in JT-60U in order to produce the cold and dense divertor plasma. In this paper, the particle recycling in the high density discharges provided by the strong gas puff are reported.

2. Recycling Measurements

The H_α/D_α poloidal scopes are installed on the same up-oblique port and they view the plasma cross-section perpendicularly. The chords of the sight-line are shown in Fig. 1. The 15 absolutely-calibrated channels are used for the poloidal cross-section measurement. The best spatial resolution over the divertor plates is designed to be about 4 cm. The signals of line-integrated H_α/D_α emission are guided through 200 m optical fibers to the PMT array and an interference filter is placed in front of each PMT. The data are sampled with the sampling period of 1 ms, which is restricted by the response of the pre-amplifier.

The ionized deuterium neutral influx Φ_{D_α} , where deuterium is used for beam and plasma species in the series of the experiments, is calculated by integrating the signals along the poloidal circumference as following,

$$\Phi_{D_\alpha} = \sum_{j=1}^{17} I_j \cdot \varepsilon_j \cdot 2\pi R_j \cdot \Delta l_j \quad (\text{n} \cdot \text{s}^{-1}), \quad (1)$$

where I_j (photons $\text{s}^{-1} \text{m}^{-2}$), ε_j (ionized neutrals/photon), Δl_j (m) are the H_α/D_α photon signal, the "ionization events per photon" and the representative path over j -th section. The plasma poloidal boundary is divided into 17 sections as is schematically shown in Fig. 1 and the line-integrated emission signals of S_1 to S_{15} are distributed to I_j in each section. Following three assumptions are made for this calculation; First, ε_j of 15, according to the empirical function of $\varepsilon(n_e, T_e)$ [1] for the plasma edge condition of $n_e \sim 0.5 \times 10^{19} \text{m}^{-3}$ and $T_e \geq 15 \text{eV}$, is used. Second, toroidal symmetry of the emission profile is assumed. Third, the outboard emission I_{17} , which can not be measured by the scope, is replaced by the inboard emission corresponded to the vertical location I_2 .

3. Recycling and Divertor Plasma

All NBI injected high density experiment were performed in the high elongation plasma configuration with the ion grad B drift pointing toward the target. The wall conditioning such as He TDC/GDC was not carried out between the discharges, the first wall runs in a saturated mode. The time evolution of the plasma parameters in the representative

discharge at $I_p/B_t = 1.2 \text{ MA}/4 \text{ T}$ and X_p height of 10 cm is shown in Fig. 2. The pre-programmed gas puff was applied though the ohmic phase to maintain the steady-state ohmically heated discharge, and it was stepped up with increasing the NBI power. The radiation from the divertor region and the X_p vicinity was increased rapidly with the strong gas puff, leading to the radiative divertor. The particle recycling in the divertor region was enhanced simultaneously, and the distribution is shown in Fig. 3. The inboard recycling is seen significantly up to far inboard of the strike point. The high recycling zone near the strike points spreads both inboard and outboard from the divertor region with the increase in the density and injection power. The excessive gas puff triggered the MARFE at the outer strike zone, starting at 9.6 s, and it was expanding into the inboard divertor region. The asymmetry of the recycling distribution is reduced to be even. The fluctuations was observed in $\Phi_{D_\alpha}^{\text{inboard}}$ when the discharge entered from L-mode to ELMy H-mode during the high power injection.

Total recycling Φ_{D_α} with varying of $I_p = 1.2/1.7 \text{ MA}$ and $B_t = 2.7/4.0 \text{ T}$ are plotted in Fig. 4(a) as a function of \bar{n}_e . Φ_{D_α} rises with increase in \bar{n}_e along the different trajectory depending on the q_{eff} value. Here, during the ELMy H-mode, Φ_{D_α} is reduced off the trajectories. This database can be scaled on the curve of $\Phi_{D_\alpha} \propto (\bar{n}_e \times q_{eff})^{4.5}$, and it is shown in Fig. 4(b).

Local n_e^{div} and T_e^{div} profiles on the target plates were measured by the 15 channel Langmuir probe array, and the location are shown in Fig. 2(a). Figure 5 plots the peak values of n_e^{div} on the outboard target plates, and T_e^{div} corresponding to the locations of the n_e^{div} measurement as a function of $\bar{n}_e \times q_{eff}$. Here, the peak value of n_e^{div} on the inboard target plates could not be measured due to the damages of the probes. It is found that n_e^{div} for the different q_{eff} rose along the same trajectory with increase in $\bar{n}_e \times q_{eff}$, and that local T_e is slightly reduced with $\bar{n}_e \times q_{eff}$ at the same injection power. Cool ($T_e^{\text{div}} \sim 20\text{-}40 \text{ eV}$) and dense ($n_e^{\text{div}} \leq 6 \times 10^{19} \text{ m}^{-3}$) divertor plasma is observed in higher $\bar{n}_e \times q_{eff}$.

During ohmic high density discharges ($\bar{n}_e \leq 3.5 \times 10^{19} \text{ m}^{-3}$), Φ_{D_α} is much (10 - 100 times) smaller than that during the high recycling L-mode discharges. In contract to the L-mode discharges, Φ_{D_α} increases with \bar{n}_e independent of q_{eff} .

4. Asymmetry of Recycling

Asymmetries in the heat flux and recycling profiles have been seen during the high density discharges. Inboard recycling was seen significantly not only by using inboard gas inlets but also by outboard ones. Figure 6 shows the ratio of inboard recycling to the total recycling as a function of $\bar{n}_e \times q_{eff}$. Asymmetry of the recycling distribution near the target plates is also increased with $\bar{n}_e \times q_{eff}$ following the same trajectory. While, the outboard heat flux is dominant for all cases.

The preliminary calculation result by using 2-D SOL/divertor simulation code, UEDA-code, shows that D_α emission distribution extends, in particular, to the inboard surface of the first wall rather than outboard one with increase in the particle outflux to the divertor plate. The D_α emission distribution corresponds to the expanse of the neutral particle distribution. It is determined that narrower geometrical space in inboard divertor may produce the asymmetries of the neutral particle and D_α emission distribution. However, q_{eff} dependence can not be seen strongly in the simulation results.

5. Summary

The high recycling divertor experiment provided by the strong gas puff has been performed with the ion grad B drift pointing toward the target. Results of the particle recycling are summarized.

1. $\bar{n}_e \times q_{eff}$ dependence of Φ_{D_α} and n_e^{div} is determined, in particular, during NBI discharges.
2. T_e^{div} is slightly reduced with $\bar{n}_e \times q_{eff}$ at the same NBI power. Cool ($T_e^{div} \sim 20\text{-}40\text{ eV}$) and dense ($n_e^{div} \leq 6 \times 10^{19}\text{ m}^{-3}$) divertor plasma is observed in higher $\bar{n}_e \times q_{eff}$.
3. Asymmetry of the recycling distribution near the target plates is also increased with $\bar{n}_e \times q_{eff}$. Inboard recycling is seen significantly in high $\bar{n}_e \times q_{eff}$ discharge. Simulation result shows that narrower geometrical space in inboard divertor may produce the asymmetries of the neutral particle and D_α emission distribution.

The distance to the X-point X_p was scanned vertically from 1 cm to 20 cm at the high recycling discharges. Φ_{D_α} does not change with X_p height at the same $\bar{n}_e \times q_{eff}$. The asymmetry of Φ_{D_α} was slightly reduced at high X_p ($\sim 20\text{ cm}$). While, the heat flux to the outboard target plates was always dominant.

The heat flux to the outboard target plates can not be reduced in the high recycling divertor experiment because of inboard-dominant asymmetry of the particle recycling distribution. Reversed field experiment is scheduled in 1993 in order to reduce the particle and heat flux asymmetries.

References:

- [1] JONSON L.C., HINOV. E., J. Quant. Spectrosc. Radiat. Transfer, **13** (1973) 333.

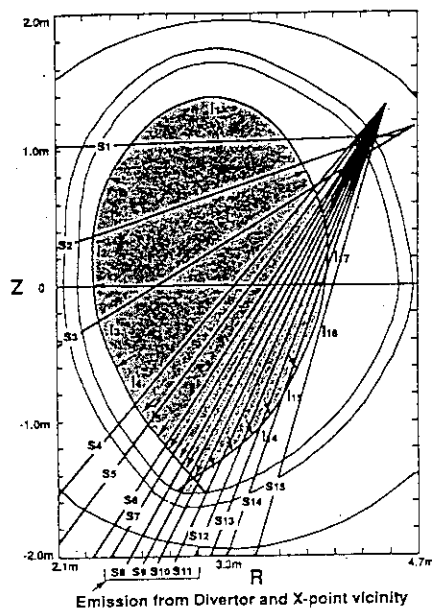


Fig.1 15 sight-lines of the H_α/D_α scopes, viewing poloidal cross-section, are shown by solid lines. Emission signals S_i are used to calculate 17 representative emissivities I_i for the circumferences shown by between two arrows.

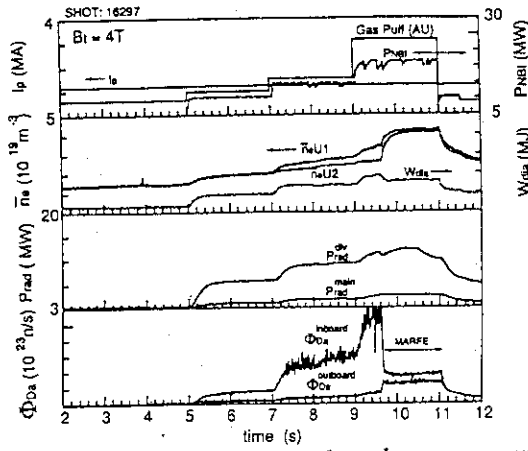


Fig.2 Time evolution of the plasma parameters in the high recycling discharge at $I_p/B_t = 1.2\text{MA}/4\text{T}$ and X_p height of 10 cm.

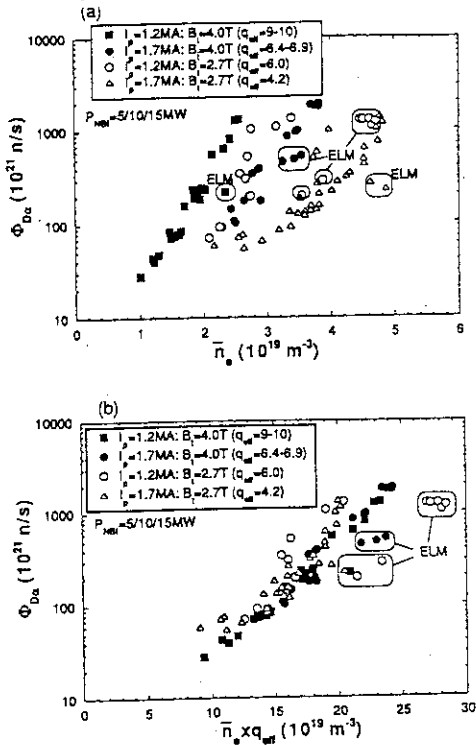


Fig.4 $\Phi_{D\alpha}$ at the four combination of $I_p = 1.2/1.7\text{MA}$ and $B_t = 2.7/4.0\text{T}$ as a function of \bar{n}_e for (a) and $\bar{n}_e \times q_{eff}$ for (b); $\Phi_{D\alpha}$ follows the same curve of $\Phi_{D\alpha} \propto (\bar{n}_e \times q_{eff})^{4.5}$.

Asymmetry of Particle Influx

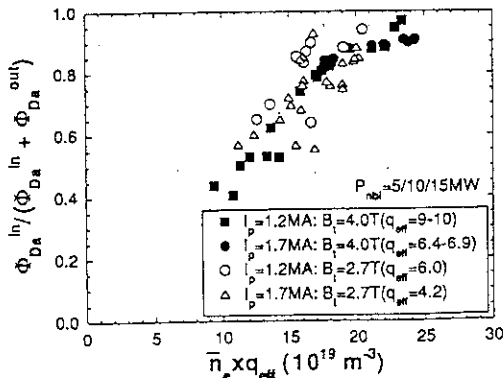


Fig.6 Ratio of inboard recycling to the total recycling as a function of $\bar{n}_e \times q_{eff}$. Asymmetry of the recycling profile near the target plates is also increased with $\bar{n}_e \times q_{eff}$ following the same curve.

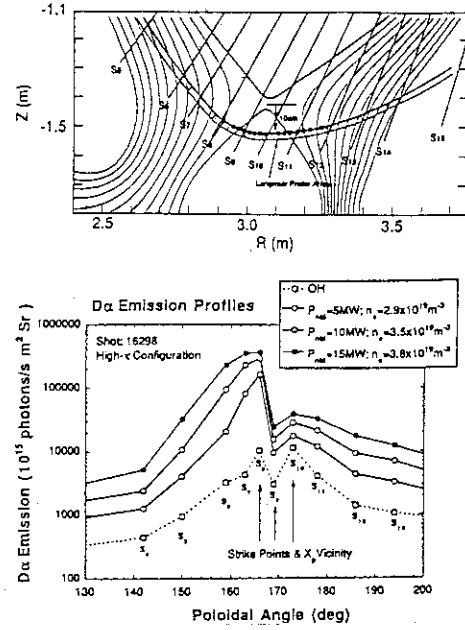


Fig.3 (a); Enlarged sight-lines of $H\alpha/D\alpha$ scopes in the vicinity of the target plates and the poloidal flux surface for the high elongation plasma configuration shown in Fig. 1. (b); $D\alpha$ distributions for increasing gas puff and input power are shown;

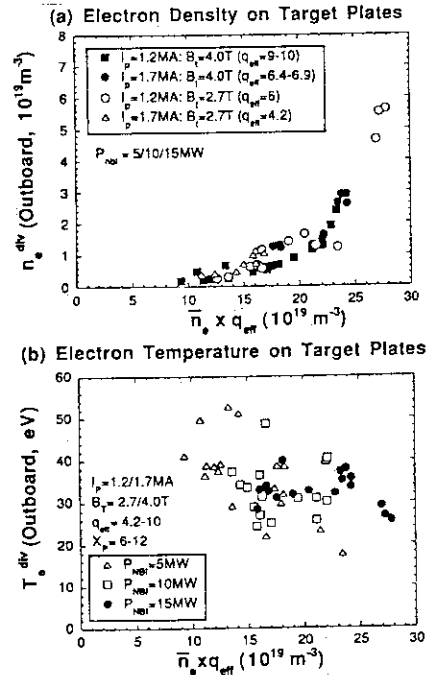


Fig.5 Peak values of n_e^{div} on the outboard divertor plates for (a), and T_e^{div} corresponding to the locations of the n_e^{div} measurement for (b) as a function of $\bar{n}_e \times q_{eff}$.

4.11 Recycling in H-mode and High β_p Discharges

N. Asakura, S. Tsuji, S. Ishida, N. Hosogane, M. Shimada

1. Introduction

The high performance discharges such as H-mode and high β_p plasma have been operated in relatively low electron density regime ($\bar{n}_e \leq 3.5 \times 10^{19} \text{ m}^{-3}$), and high NBI power ($P_{NBI} \geq 10 \text{ MW}$) in JT-60U. One of the key issues to produce the high performance discharges reproducibly and to extend the operation regime is the reduction of the recycling neutrals from the target plates and the first wall. In this paper, the particle recycling in the high performance discharges is reported.

The particle recycling is measured by the 15 channel H_α/D_α scopes, which are installed on the same up-oblique port and viewing the plasma poloidal cross-section perpendicularly. The diagnostic and the calculation of the ionized neutral influx Φ_{D_α} were mentioned in the previous paper.

2. Wall Conditioning and H-mode Discharge

H-mode discharges have been operated in the relatively low density regime because of the low threshold density of ELM starting ($\bar{n}_e^{ELM} = 2 - 3.5 \times 10^{19} \text{ m}^{-3}$). Figure 1 shows time evolution of plasma parameters for the H-mode discharge with $I_p = 1.5 \text{ MA}$ and $B_t = 2.5 \text{ T}$. The first H-mode with the duration of 150 ms and the second one with 70 ms started at 8.73 s and 8.93 s, respectively. Coherent fluctuations were seen in the poloidal D_α distribution for 400 ms prior to the first H-mode transition. During the H-mode, \bar{n}_e started to increase rapidly, while the radiation from the divertor zone P_{rad} was saturated due to the reduction of the particle recycling. The second H-mode was terminated at $\bar{n}_e = 1.7 \times 10^{19} \text{ m}^{-3}$ and ELM started associated with the saturation of W_{dia} .

Particle recycling is determined by several factors; 1) wall condition (wall temperature, TDC/GDC or disruptive cleaning and boronization); 2) fueling (gas puff and pellet); 3) plasma position in vacuum vessel (X_p height and plasma shape); 4) plasma parameters (\bar{n}_e , q_{eff} and P_{NBI}). The first wall is covered by the graphite and CFC tiles except the diagnostic and auxiliary heating equipment ports. In particular, effective and durable wall conditioning method is essential to maintain the low recycling wall condition and to achieve the better qualities such as confinement and stability for a series of discharges.

Wall conditioning methods were combined in order to reduce the recycling neutrals into the plasma, and the additional gas fueling was cut after the initial pre-puffing for the break-down. It was found that the lower wall temperature T_{wall} was favorable to reduce the recycling, and that Φ_{D_α} was decreased at $T_{wall} = 70 - 100^\circ\text{C}$ to be about the half of that at $T_{wall} = 200 - 300^\circ\text{C}$ during the NBI injection. He GDC cleaning was temporal and it was routinely done during lunch time(12 - 1pm), during dinner time(6 - 7pm) and overnight(10pm - 9am). In addition, the inter-shot He TDC of 10 minutes has been done to repeat the reproducible low recycling discharges.

Boronization has been applied twice in 1992 by using the He GDC after evaporating 10g and 15g Decaborane($B_{10}H_{14}$) for the first and second time, respectively. The Φ_{D_α} reduction is plotted in Fig. 2. The database includes Φ_{D_α} both during H-mode and L-mode

before the L-H transition. T_{wall} ranges in 70 - 120°C for the database and the ELM free H-mode discharge with higher B_t and I_p could not be seen before the first boronization due to the large recycling and density build-up during L-mode. More reproducible and lower recycling H-mode discharges with the larger confinement time have been derived in the higher density regime with increasing Decaborane[1].

Hot ion H-mode discharge with the high field of $B_t = 4$ T, high power of $P_{NBI} \geq 20$ MW and $T_i(0) \leq 32$ keV has been derived after the boronization due to the reduction of the recycling and oxygen influx. Time evolution of the parameters for the high I_p and high field H-mode discharge is shown in Fig. 3. The increase in recycling Φ_{D_α} and P_{rad} were suppressed during the high power beam injection and \bar{n}_e started to increase up to \bar{n}_e^{ELM} . The H-mode started at the unclear transition of 8.5 s, and the fluctuations of Φ_{D_α} were seen continuously during the H-mode. The H-mode discharge "without clear L-H transition" in D_α signal was often seen for the case of the high B_t H-mode discharge.

Figure 4 shows the D_α emission distributions during OH, L-mode and H-mode of the high B_t H-mode discharge. The profiles are symmetry in the strike zone. The recycling is reduced in all poloidal portion at the L-H transition. Even in the low recycling H-mode discharges Φ_{D_α} is dominated 3 - 6 times than the first particles supplied by NBI Φ_{NBI} and density rise dN_e/dt .

I_p dependence of Φ_{D_α} is plotted in Fig. 5(a). Here, database for $I_p = 2$ MA is taken about 100 shots after the others, and boronization was not effective any longer. Φ_{D_α} , in particular, for the higher \bar{n}_e regime can be reduced with increase in I_p up to 3 MA. The density of the starting ELM activity \bar{n}_e^{ELM} is extended to be higher. Fig. 5(b) shows the particle confinement time including divertor and SOL effects such as the flux amplification given by

$$\tau_p^{wall} = \frac{N_e}{\Phi_{D_\alpha} + \Phi_{NBI} - dN_e/dt} \quad , \quad (1)$$

where N_e is defined by $\bar{n}_e V_p$ and the plasma volume V_p is about 70 m³. τ_p^{wall} is higher than that for OH phase of 150 ms and it is increased and saturated with \bar{n}_e , in contrast to the L-mode discharge, where τ_p^{wall} is decreasing with \bar{n}_e . The large τ_p^{wall} of ~800 ms are measured during 20 ms.

3. High β_p Discharge

The high β_p discharge experiments were performed with $B_t = 4$ T, $P_{NBI} = 20 - 28$ MW and $I_p = 1.2 - 1.8$ MA after the first boronization. The high-elongated shape plasma was positioned inboard compared to the H-mode discharge in order to heat the plasma center effectively. The plasma volume of 50 m³ is smaller. He TDC was not always carried out between the discharges. He GDC cleaning was routinely done and T_{wall} ranges from 260 - 300°C. Figure 6 shows time evolution of plasma parameters for the high β_p discharge with $I_p = 1.8$ MA and $P_{NBI} = 25$ MW. The central plasma density $\bar{n}_e U1$ started to increase during NBI leading to the peaked density profile. T_i profile also peaked and $T_i(0)$ raised up to 38 keV. Φ_{D_α} and P_{rad} were increased with \bar{n} . The recycling, in particular, in the divertor zone seems to be larger compared to that for the series of the H-mode discharges. It is difficult to identify whether it is caused by the smaller I_p or by the worse wall condition such as the lack of inter-shot TDC, higher T_{wall} and losing boron-coated

layers on the graphite tiles. The short H-mode with the duration of 20 ms started at 5.35 s, following the fluctuations of Φ_{D_α} from 5.2 s to 5.3 s. W_{dia} was saturated at 5.43 s during ELM activity. The D_α emission distributions are shown in Fig. 7. Asymmetry of the recycling profiles were seen in divertor zone during NBI and the recycling at the inboard strike point is about 2-3 times larger than outboard.

I_p dependence of Φ_{D_α} is plotted in Fig. 8(a). Here, all database is taken after the first boronization. Φ_{D_α} is reduced with increase in I_p . Noted that low Φ_{D_α} shots at $I_p = 1.5 - 1.7$ MA have been derived after He GDC or He TDC cleaning, and the H-mode phase of 20 - 30 ms appeared in the discharges. The density of the starting ELM activity \bar{n}_e^{ELM} is extended higher. \bar{n}_e^{ELM} at $I_p = 1.7-1.8$ MA is comparable to that at $I_p = 2$ MA for the high B_t H-mode discharge. Fig. 8(b) shows τ_p^{wall} , and it is lower than that for the ohmic phase of 80-100 ms. However, it is constant in $\bar{n}_e = 0.8 - 2.4 \times 10^{19} \text{ m}^{-3}$ instead of that in the L-mode discharge. The highest τ_p^{wall} of ~ 120 ms was measured in the short H-mode phase.

4. Summary

Particle recycling of the hot ion H-mode and high β_p discharges, which are operated in the relatively low density regime and high NBI power, were reported. Particle recycling can be reduced with increase in I_p at the same \bar{n}_e for both discharges, and the density of the starting ELM activity \bar{n}_e^{ELM} is extended with I_p . The energy confinement in the H-mode plasma is improved in the plasma peripheral region, where both the temperature and density are increased and the steep pressure gradient is created. The particle confinement is determined by the edge plasma condition, and large τ_p^{wall} in the H-mode is associated with better τ_E . While, the good energy confinement in the high β_p plasma is characterized by the peaked T_i and n_e profiles in the core plasma. The smaller τ_p^{wall} is determined by the edge plasma. However, the reason could not be identified whether the smaller I_p or the worse wall condition.

References:

- [1] SHIMADA M., *et al.*, in Plasma Physics and Controlled Nuclear Fusion Research (Proc. 14th Int. Conf. Wurzburg, 1992) IAEA-CN-56/A-1-3.

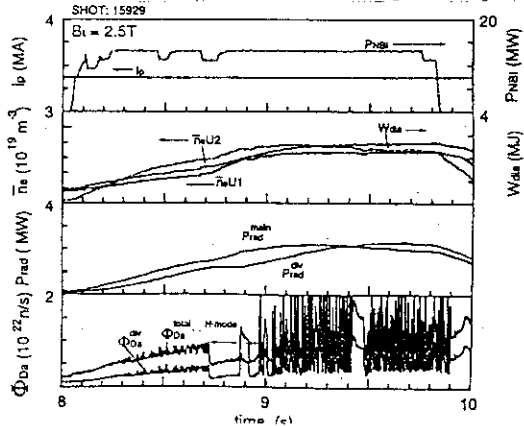


Fig.1 The time evolution of the plasma parameters in H-mode discharge at $I_p/B_t = 1.5\text{MA}/2.5\text{T}$.

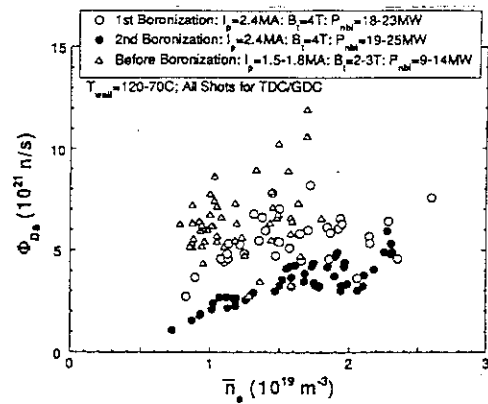


Fig.2 Reduction of $\Phi_{D_\alpha}^{div}$ by boronizations are shown, and all data are used during H-mode.

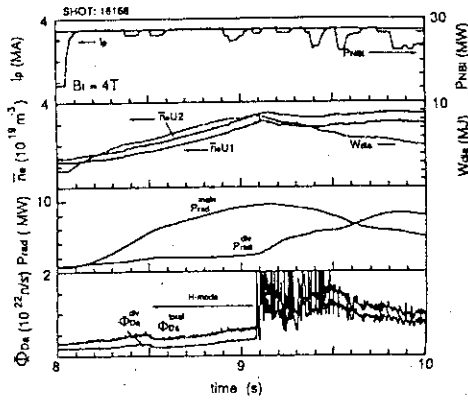


Fig.3 The time evolution of the plasma parameters in high B_t and high I_p H-mode discharge at $I_p/B_t = 3.5\text{MA}/4\text{T}$.

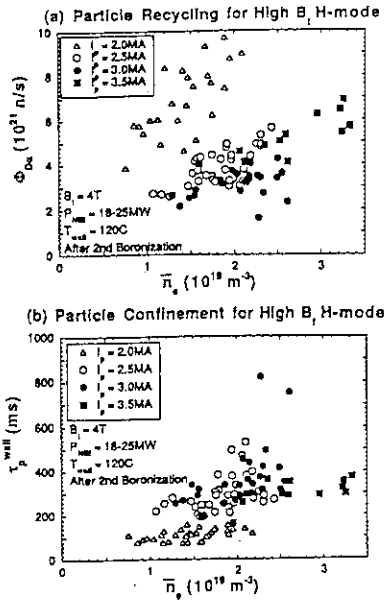


Fig.5 Φ_{D_α} at $I_p = 2.0\text{--}3.5\text{ MA}$ and $B_t = 4\text{ T}$ as a function of \bar{n}_e for (a) and particle confinement time τ_p^{wall} for (b).

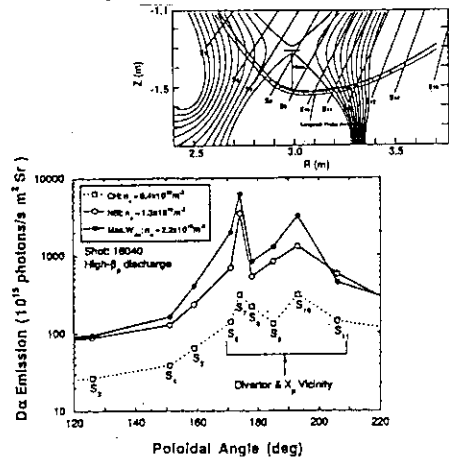


Fig.7 (a); Enlarged sight-lines of the H_α/D_α scopes in the vicinity of the target plates and the poloidal flux surface for the high β_p discharge. (b); D_α distributions during OH and NBI are shown:

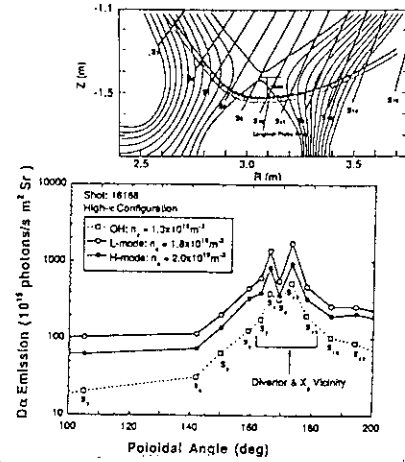


Fig.4(a); Enlarged sight-lines of the H_α/D_α scopes in the vicinity of the target plates and the poloidal flux surface for the high B_t H-mode discharge. (b); D_α distributions during OH and NBI are shown:

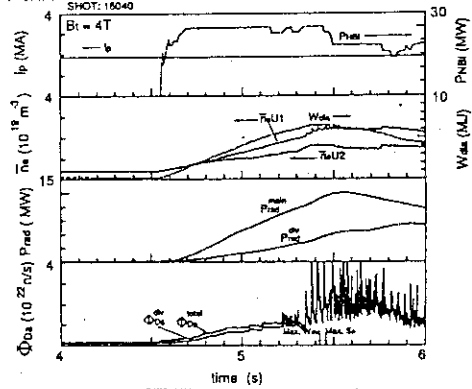


Fig.6 The time evolution of the plasma parameters in high β_p discharge at $I_p/B_t = 1.8\text{MA}/4\text{T}$.

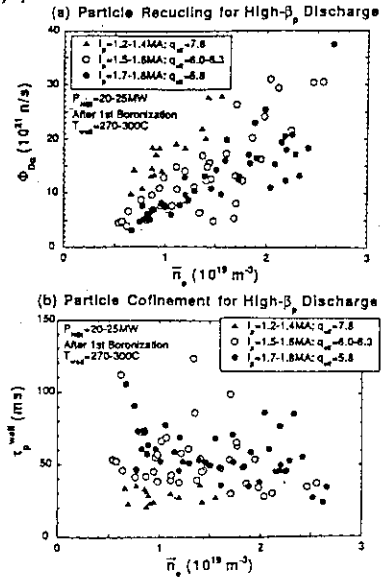


Fig.8 Φ_{D_α} at $I_p = 1.2\text{--}1.8\text{ MA}$ and $B_t = 4\text{ T}$ as a function of \bar{n}_e for (a) and particle confinement time τ_p^{wall} for (b).

4.12 Modelling of Impurity Transport

K. Shimizu, T. Takizuka, M. Azumi, M. Shimada

1. Introduction

An excessive amount of impurities in the main plasma degrades energy confinement, triggers disruption and dilutes the fuel. On the other hand, impurity radiation in the divertor region is useful for reducing the heat load of divertor plates. Impurity control, therefore, is one of the crucial issues for fusion research. Understanding of the mechanism of impurity generation and impurity transport is indispensable to impurity control.

A two dimensional impurity code based on the Monte Carlo technique has been developed in order to study the impurity behavior in the divertor plasma. This code requires plasma parameters in the scrape-off layer as input data. They are obtained from an interpretative divertor code where the fluid equations along the magnetic field are solved numerically by using the Langmuir probe data and IRTV data as the boundary conditions at the divertor plates. The relation between the divertor code, the impurity code and the measurements is illustrated in Fig. 1.

2. Interpretative Divertor Code

The divertor code [1] has been improved in the following aspects,

- * The momentum conservation is solved without the assumption of $v_{||} \ll C_s$.
- * The convection term is added to the energy conservation equation.

$$\nabla_{||} q_{||} = \nabla_{||} \left\{ (5T + \frac{1}{2} m_i V_{||}^2) n \vec{V}_{||} - \kappa_{||} \vec{\nabla}_{||} T \right\} = S_E$$

- * The code is extended to treat the inside and outside divertor plasmas simultaneously.

This code enables us to evaluate the particle confinement time in the main plasma, τ_p , and the heat diffusivity in the scrape off layer, χ_{\perp} . These transport parameters are evaluated in JT-60U ohmic divertor plasmas ($I_p = 2$ MA, $B_T = 3.5$ T, $\bar{n}_e = \sim 0.8 - 3 \times 10^{19} \text{ m}^{-3}$). Figure 2 shows that the calculated neutral density profile is consistent with the measured H_{α} distribution. The particle confinement time evaluated from the total ionization source inside the separatrix surface is about 90 ~ 100 msec, while τ_p including the divertor region is about 45 ~ 55 msec. Neglecting the energy source term such as the ionization loss and the impurity radiation loss in SOL, we evaluate χ_{\perp} from the calculated radial profiles of $T(x)$ and $q_{||}(x)$ at the upstream. It is found that χ_{\perp} increases from 2 m²/s to 5 m²/s radially, as shown in Fig. 3 [2].

3. Impurity Transport Modelling

Impurity transport in the divertor region should be treated in two dimensions. The motion of neutral impurities is intrinsically two dimensional at least, and the motion of impurity ions has also a two dimensional structure because of cross-field diffusion. The 2-D fluid equations for the conservation of particle and momentum contain various characteristic time, i.e. diffusion time, parallel transit time along the magnetic field line and ionization time. Such equations are called stiff system and are very difficult to solve. It requires considerable efforts not only to

develop a fluid model but also to modify the code to add new effects. Furthermore, the fluid description is valid for the plasma where the transit time of the parallel motion is much longer than the collision time between the impurity ions and the background plasma ions. The application of the fluid model is questionable for low recycling divertor plasma, where the parallel motion has a strong interaction with the velocity change due to Coulomb collision because of low collision frequency for low charge state impurities. (Typical plasma parameters are $n_{ed} = 1 \times 10^{19} \text{ m}^{-3}$, $T_{ed} = 30 \text{ eV}$.) The Monte Carlo approach is beneficial for incorporating the parallel motion and various collisional effects, and for modelling impurity generation and the interactions between impurities and walls.

We solve the kinetic equations with the Coulomb collision operator for the distribution functions $f_1(\vec{r}, \vec{v}, t)$ using the orbit following Monte Carlo technique. The model includes the following processes.

1. An impurity neutral is sputtered from a divertor plate. The particles moves with a constant velocity until it is ionized. The ionization point can be determined from the relation of $\int_0^1 ds/\lambda = -\ln \xi$ where $\lambda(s)$ is local ionization mean free path, s is the distance from the divertor plate along the straight line, and ξ is an uniform random number.

An Impurity ion is followed with the specified time interval Δt , typically 10^{-6} sec.

2. The parallel motion along the field line is determined by the electric force, the friction force and the thermal force with the plasma,

$$m_I \frac{dv_z}{dt} = F_z = ZeE + m_I \frac{V_{//} - v_z}{\tau_z} + \alpha_z \frac{\partial T_e}{\partial s} + \beta_z \frac{\partial T_i}{\partial s}$$

where v_z is the velocity of the impurity ion with the charge state Z and $V_{//}$ is the flow velocity of the background plasma ions. The impurity-ion collision time τ_z and the coefficients, α_z and β_z , are described in ref. [3]. The toroidal effect is neglected at present.

3. The deflection and energy transfer due to Coulomb scattering are simulated by the Monte-Carlo technique, which is similar to that in ref. [4]. The background plasma flows along the field line with the velocity of $V_{//}$. The scattering is computed in the moving coordinate system with $V_{//}$ along the field line; as a result, the velocity change due to the friction force is incorporated in this step.

4. The diffusion across the flux surface is simulated by adding the random displacement,

$$(\Delta x, \Delta y) = \sqrt{2D_{\perp}\Delta t} \cdot (R_x, R_y)$$

where (x, y) is the Cartesian coordinate, (R_x, R_y) is normal random numbers, and D_{\perp} is the cross field diffusion coefficient. The pinch effect across the flux surface is also applied by $\Delta r = -V_p \cdot \Delta t$.

5. The charge state of impurity ion changes through atomic processes. We take only the direct ionization. For the ionization rate coefficients, a code developed by Kato [5] is used. A simple hit-or-miss Monte-Carlo method is employed for the ionization process, that is, the impurity ion is ionized further when $\xi \leq \Delta t/\tau_I$, where ξ is an uniform random number and $\tau_I = 1/n_e \langle \sigma v \rangle_I$.

6. When the impurity ion hits the divertor plate or walls, it is assumed to be absorbed.

A new test particle is launched from the divertor plate.

Many test particles (for example, 5000) are launched from the divertor plates at first in the simulation and are followed until the spatial distribution of impurity ions becomes almost stationary. Typically, the calculation has been executed for 0.1~0.2 sec. We obtain the steady state density for each charge state of impurity, and calculate the radiation profile and the line intensity of the visible spectroscopic lines. Comparing such quantities with the measurements, we can evaluate the absolute density of impurity and investigate impurity generation mechanism from the divertor plate or walls and the impurity shielding and transport.

4. Calculation results

Calculations have been carried out for carbon impurity in JT-60U ohmic divertor plasmas ($I_p = 2$ MA, $B_T = 3.5$ T). We employ $D_{\perp} = 1$ m²/s and no pinch velocity $V_p = 0$ m/s. We investigate the density dependence of the impurity shielding efficiency. The destination to the main plasma of impurity ions launched from outer divertor plate are shown in Fig.4. The peak values of n_{ed} and T_{ed} at divertor plates used in the calculations are also plotted. The probability of entering the main plasma increases significantly with reducing the main plasma density below $\bar{n}_e \approx 1 \times 10^{19}$ m⁻³ (from 0.6 % at $\bar{n}_e = 1.5 \times 10^{19}$ m⁻³ to 2.2 % at 1.0×10^{19} m⁻³). The mean free path, $\lambda_{mfp} = v_z \tau_z$, of C^{4+} is about 5.4 m for $\bar{n}_e = 1 \times 10^{19}$ m⁻³ and 0.8 m for $\bar{n}_e = 1.5 \times 10^{19}$ m⁻³. (The distance from the X-point to the divertor plate along the field line, L_d , is about 5 m.) The density dependence of the destination fraction to the main plasma is consistent with the carbon concentration in Fig. 2 of ref. [6]. For detailed comparison with the experimental data, however, a more realistic sputtering model must be incorporated into our impurity model. Figure 5 shows the steady state distribution of carbon impurities along the field line for $\bar{n}_e = 1.5 \times 10^{19}$ m⁻³. The density is integrated radially in SOL. The impurities are localized near the divertor plate. Most of impurity ions are pushed back to the divertor plate by the friction force. When the force acting the impurity ions is artificially set to be zero ($F_z = 0$), the probability of entering the main plasma increases from 0.6 % to 17 %.

References

- [1] SHIMIZU, K., et al., JAERI-M 91-161 (1991).
- [2] SHIMIZU, K., et al., J. Nucl. Mater. 196-198 (1992) 476.
- [3] NEUHAUSER, J., et al., Nucl. Fusion 24 (1984) 39.
- [4] TANI, K., et al., J. Phys. Soc. Japan 50 (1981) 1726.
- [5] KATO, T., private communication (1992).
- [6] SHIMADA, M., et al., sec. 8.10, JAERI-M 92-093 (1992) 230.

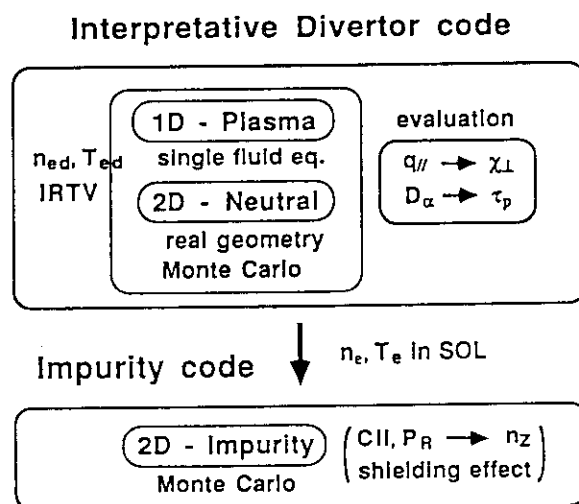


Fig. 1 Data flow between interpretative divertor code, impurity code and measurements.

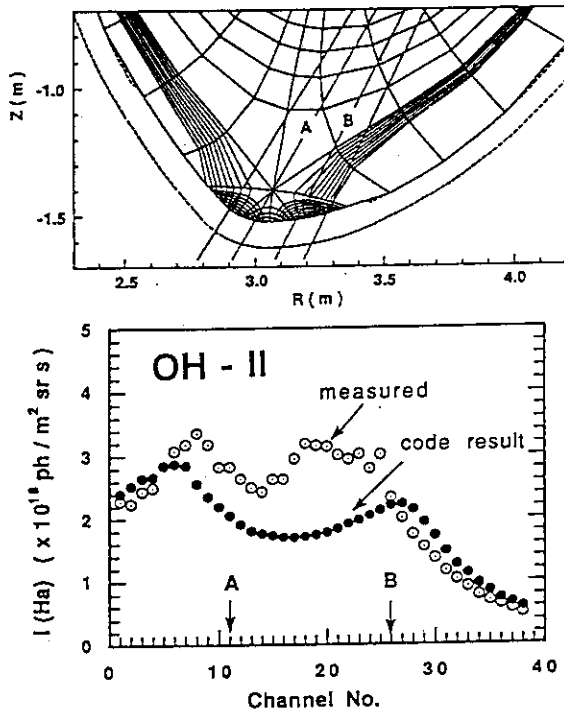


Fig. 2 (a) 2-D calculation mesh and H α monitor array.
(b) Comparison between measured and calculated H α profiles.

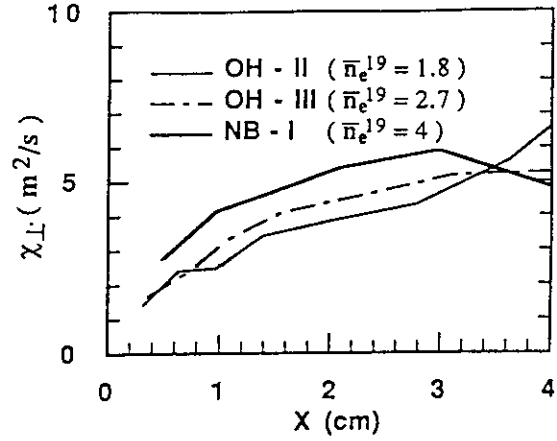


Fig. 3 Radial profiles of the evaluated cross field heat diffusivity in SOL.

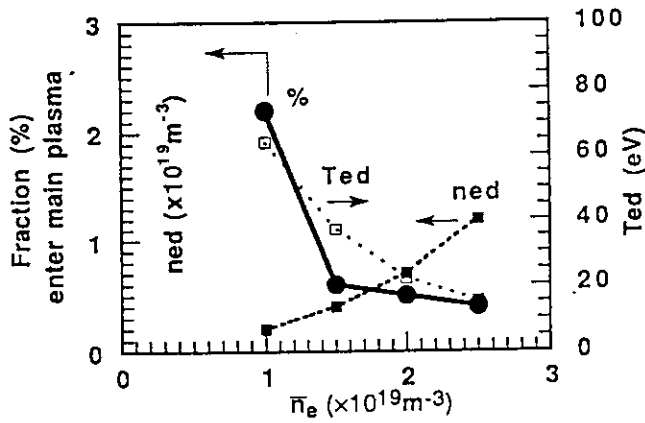


Fig. 4 Density dependence of the destination to the main plasma of impurity ions launched from outer divertor plate.

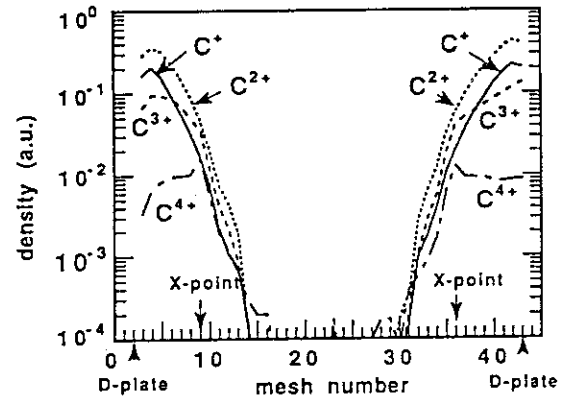


Fig. 5 Distribution of carbon impurities along the field lines in the steady state. Plasma parameters are $\bar{n}_e = 1.5 \times 10^{19}$, $n_{ed} = 0.4 \times 10^{19}$, $T_{ed} = 37$ eV.

4.13 Divertor Analysis with the UEDA Code

S. Tsuji, K. Shimizu, T. Takizuka, N. Asakura, K. Itami, M. Shimada

1. Introduction

Reduction in sputtering and erosion of divertor plates is the most crucial issue for fusion experimental reactors such as ITER. The heat flux profile and its peak value are determined in competing processes between parallel and cross-field transport, the latter of which is anomalous. Hence edge data base, in particular, those on the cross-field transport coefficients D_{\perp} and χ_{\perp} are required to predict divertor performance.

Formation of cold and dense divertor plasma is indispensable to alleviate heat load on target plates. It is of interest to investigate how cold divertor plasmas can be achieved in the open divertor configuration of JT-60U. The divertor and scrape-off layer (SOL) plasmas are simulated in real geometry with the UEDA code, which is a two-dimensional time dependent fluid code with a Monte Carlo method for neutral gas behavior [1]. Although the UEDA code can include drift heat flux and impurities, we simulated pure deuterium plasmas without the drift heat flux in this study.

2. Comparison with Experimental Profile Data

The cross-field transport coefficients in the SOL are important parameters for the simulation. In the UEDA code, D_{\perp} and χ_{\perp} can be specified as constant or Bohm-like diffusivities. The parallel diffusivity is assumed to be classical. Experimentally measured T_e and n_e profiles with 15-ch Langmuir probes and heat flux profile with an IRTV camera at the divertor plates (closed circles) are compared with calculated ones (open symbols) to estimate χ_{\perp} in Figs. 1 and 2. D_{\perp} is always assumed to be $1 \text{ m}^2/\text{s}$ since the measured n_e profile may have some systematic errors due to uncertainties in the effective cross sections of probe tips. The calculated profiles are almost symmetric while the experimental profiles are in-out asymmetric; the electron temperature and heat flux are higher at the outer strike point. Thus the comparison are chiefly made concerning the outboard profiles. Both in ohmic (Fig. 1) and beam-heated (Fig. 2) cases, the measured profiles are globally fit well with $\chi_{\perp} = 2 \sim 4 \text{ m}^2/\text{s}$. However the cross-field heat diffusivity may be lower near the peaks where spatial resolutions both in experiments and calculation are not high enough to study.

3. Particle Flux Amplification

The conditions to achieve cold and dense divertor plasmas are numerically investigated in an open divertor configuration of JT-60U shown in Fig. 3. The divertor electron and ion temperatures and electron density in the magnetic flux tube adjacent to the separatrix surface are plotted as a function of particle outflux from the main plasma Γ_P in Figs. 4 and 5. The power outflux from the main plasma was taken to be 10 MW (circles) and 20 MW (squares). We assumed the diffusivity as $D_{\perp} = 1 \text{ m}^2/\text{s}$ and $\chi_{\perp} = 4 \text{ m}^2/\text{s}$. The closed and open symbols denote inboard and outboard sides, respectively. The particle amplification factor G_i and G_o were calculated as the ratios of the inner and outer divertor fluxes to $\Gamma_P/2$. The electron temperature at the outer strike point drops exponentially with Γ_P as shown by the straight lines in Fig. 4. The electron density and the flux amplification factor are maximized when $T_e^{\text{div}} \sim 10 \text{ eV}$. Further

increase in Γ_p results in lowering the divertor temperature below 10 eV so that the divertor plasma becomes less opaque to neutral particles as seen in Fig. 6.

The calculated plasma parameters are almost the same between inner and outer strike points when Γ_p is low. However the plasma temperature at the inner strike point drops faster with Γ_p due to enhanced inboard particle recycling. This is presumably because the conductance along the inner wall is much lower than that along the outer wall. Incidentally n_e^{div} plotted in Fig. 5 does not necessarily give the peak values since the density peak shifts from the separatrix due to the cross-field diffusion.

4. Discussion

The peak electron temperature decreases as $\propto 10^{**}(-4 \Gamma_p[10^{22}/s] / P[\text{MW}])$ in Fig. 4. This fast drop leads to penetration of neutral to the X-point, which may be related to the MARFE occurrence near the density limit. Actually MARFE was observed in JT-60U when the divertor electron temperature decreases to around 10 eV [2], which is consistent with the density limit model in ASDEX [3]. The dependence of divertor temperature on \bar{n}_e becomes stronger since $\Gamma_p = N / \tau_p \propto \bar{n}_e^2$ because $\tau_p \propto 1 / \bar{n}_e$. Thus the operation window for cold divertor plasmas is considered to be narrow, which is confirmed by the experimental difficulty in maintaining the peak electron temperature at the divertor below 20 eV. This situation partly arises from the relatively shallow divertor configuration of JT-60U with $X_p = 5 \sim 13$ cm.

The cross-field heat diffusivity in the SOL appears to increase with the distance from the separatrix surface. This tendency is consistent with the results by a simple divertor code [4]. Thus a Bohm type ($\chi_{\perp} \propto T_e$) dependence does not describe the spatial behavior. As far as we compares profiles at the divertor like Figs. 1 and 2, their shapes are not so sensitive to χ_{\perp} as the SOL falloff lengths. Hence a reciprocating Langmuir probe installed at the end of 1992 will enable a more accurate estimation of χ_{\perp} .

The in-out asymmetries in T_e^{div} , n_e^{div} and heat flux profiles were not reproduced since the drift heat flux $q_{\perp} \propto B \times \nabla T$ was not calculated. Additional terms, $\Gamma_{\perp} \propto B \times \nabla T$, $E \times B$ drift and SOL current have been incorporated into a new version of the UEDA code, which will provide a tool to investigate the cause of the asymmetry.

5. Summary

The divertor plasmas in JT-60U were simulated with the UEDA code. The measured profiles at the divertor both in ohmic and L-mode discharges were reproduced with $D_{\perp} = 1 \text{ m}^2/\text{s}$ and $\chi_{\perp} = 2 \sim 4 \text{ m}^2/\text{s}$. The heat diffusivity in the SOL appears to increase radially. Inboard particle recycling was enhanced with increasing particle outflux due to geometrical effects. Simulation of pure deuterium plasmas showed that the particle flux amplification factor was maximized when $T_e^{\text{div}} \sim 10$ eV. The calculation also suggests that $G \geq 20$ is possible in the open divertor configuration of JT-60U. Neutral particles penetrate to the X-point when $T_e^{\text{div}} \leq 10$ eV, which may trigger MARFE. Hence operational window for cold divertor plasmas is narrow in terms of particle flux for given heat flux.

References

- [1] UEDA, N., KASAI, M., TANAKA, M., et al., Nucl. Fusion **28** (1988) 1183.
- [2] HOSOGANE, N., ASAKURA, N., et al., J. Nucl. Mater. **196-198** (1992) 750.
- [3] BORRASS, K., Nucl. Fusion **31** (1991) 1035.
- [4] SHIMIZU, K., ITAMI, K., KUBO, H., et al., J. Nucl. Mater. **196-198** (1992) 476.

Ohmic: $I_p = 2.5$ MA, $B_T = 4$ T, $\bar{n}_e = 2.1 \times 10^{19} \text{m}^{-3}$
 $\Gamma_p = 1.4 \times 10^{22}/\text{s}$, $Q_T = 1.0$ MW, $D_{\perp} = 1 \text{ m}^2/\text{s}$

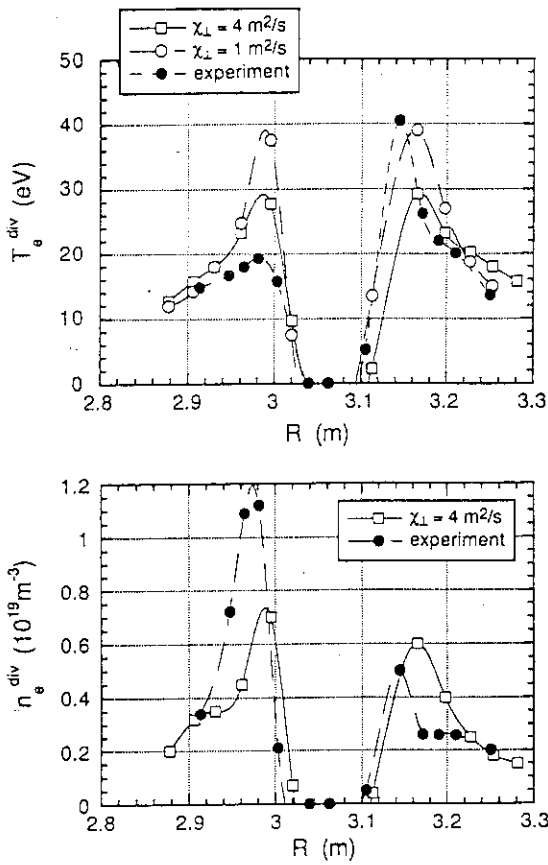


Fig. 1 Comparison between measured and calculated T_e and n_e profiles at the divertor plates. The discharge and calculation parameters are listed above.

$I_p = 2$ MA, $B_T = 4$ T, $P_{NB} = 17$ MW, $\bar{n}_e = 2.2 \times 10^{19} \text{m}^{-3}$
 $\Gamma_p = 3.0 \times 10^{22}/\text{s}$, $Q_T = 8.0$ MW, $D_{\perp} = 1 \text{ m}^2/\text{s}$

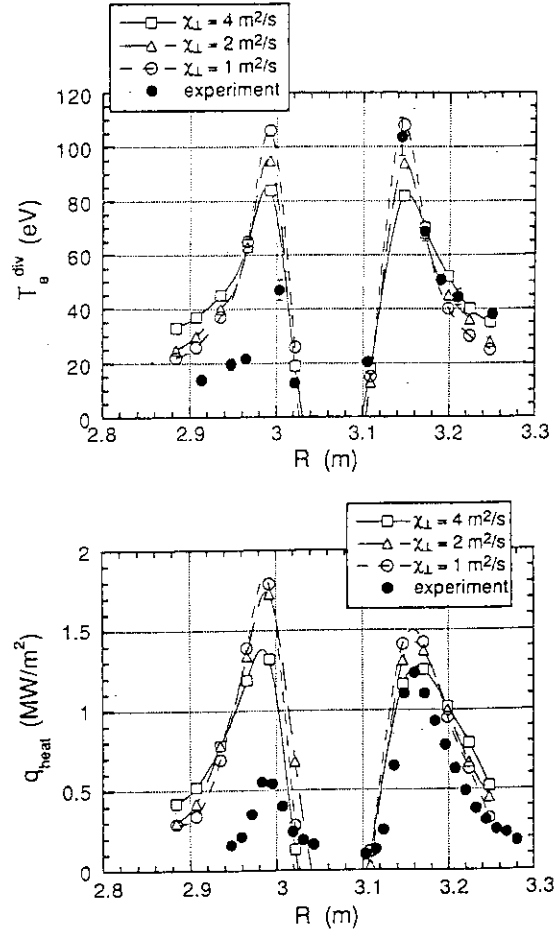


Fig. 2 Comparison between measured and calculated T_e and heat flux profiles at the divertor plates in beam heated L-mode.

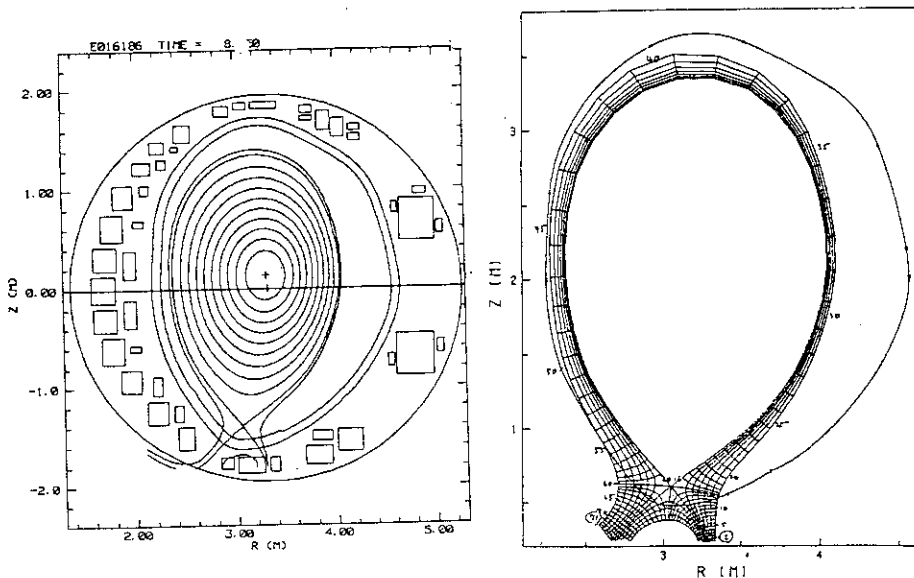


Fig. 3
MHD equilibrium configuration and calculation mesh for Figs. 4 ~ 6.

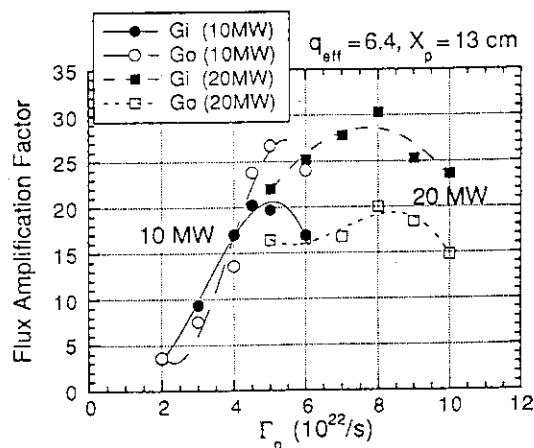
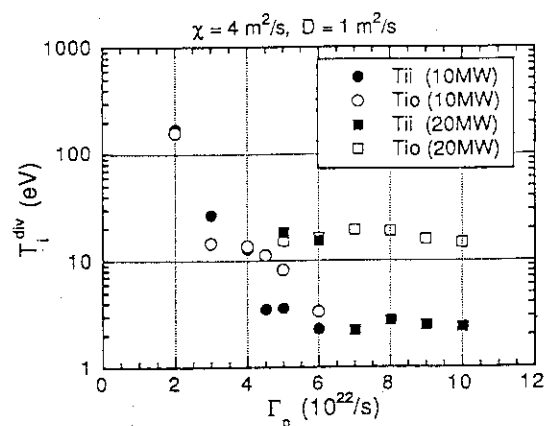
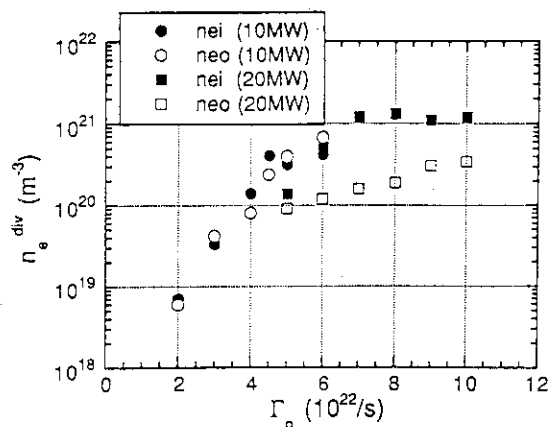
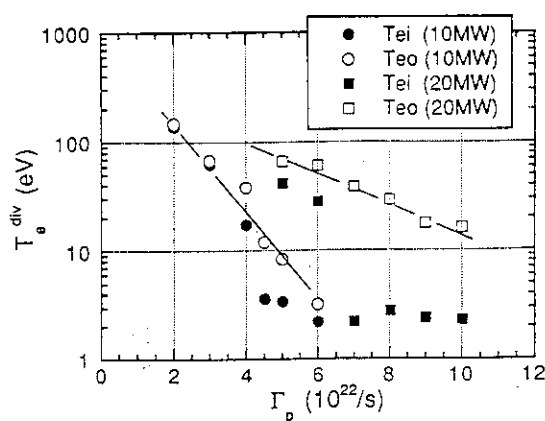


Fig. 4 The calculated electron and ion temperatures at inner (i) and outer (o) meshes adjacent to divertor plates and the separatrix surfaces as a function of particle outflux from the main plasma.

Fig. 5 The calculated electron density and flux amplification factor as a function of particle outflux from the main plasma.

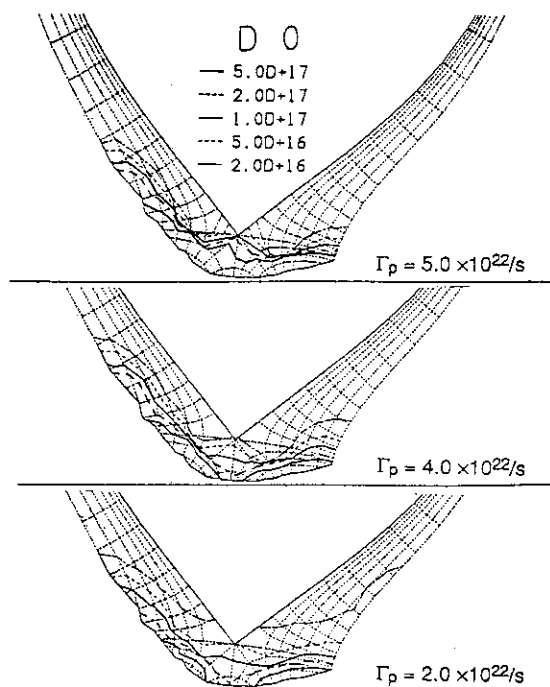


Fig. 6 Two dimensional distribution of neutral particles near the divertor plates when $Q_T = 10$ MW. The divertor plasma becomes less opaque to neutral particles with increasing Γ_p .

4.14 Helium Ash Experiment with He Beam Fuelling in Divertor Discharges

H.Nakamura, H.Kubo, H.Kimura, A.Sakasai and T.Sugie

1. Introduction

Previous studies in JT-60 L-mode discharges with He beam fueling demonstrated that He ash can be easily exhausted in high density operation[1]. However, in case of H-mode discharge, control of He ash in core plasma is crucial issue because of its good particle confinement. Recently, He exhaust from core plasma by ELMs activities is demonstrated in DIII-D with He gas puffing[2]. Therefore, in JT-60U, He ash study with He beam fueling has been started in ELMy H-mode discharges. In addition to these NB heated discharges, ICRF heating experiment has been done for initial study of He ash control. In this section, initial results of He ash studies with He beam fuelling in NB- and ICRF-heated discharges are described.

2. Experimental Apparatus

The JT-60U device is a large tokamak with a single-null poloidal divertor at the bottom of the torus. Typical parameters are a major radius of 3.1 m, a minor radius of 1.5 m, a maximum plasma current of 6 MA, a toroidal field of 4.5 T and a discharge duration of 15 s. Deuterium plasmas are heated by deuterium NB with heating powers of 20 MW. Instead of ^4He beam, ^3He beam with a beam energy of 70 keV is used because He beam injection was planned in connection with D- ^3He ICRF experiment. ICRF wave power and frequency is 3 MW and 116 MHz, respectively. Charge exchange recombination spectroscopy (CXRS) is used to measure the He^{2+} ion density profile in the main plasma by observing the transition at 4686\AA ($n=4-3$) of He^+ . However, the He density profile is not yet available because data analysis of the CXRS measurement is not completed. In the divertor region, intensities and profiles of $\text{D}\beta$ emissions and He I (6378\AA) ones are measured by 38 channel spectrometers. Although a residual gas analyzer to measure neutral pressure in outer divertor region has been installed, it is not operating because of control trouble.

3. Results and Discussion

3.1 NB Heating

Typical wave forms in ELMy H-mode discharge are shown in Fig.1. Plasma parameters are plasma current of 1.5 MA, toroidal field of 2 T and heating power of 15 MW, respectively. During $t=5.5\text{ s}$ to 7.55 s , ELMy H-mode is observed. ^3He beam was

injected during $t=5.5$ s to 7 s. He emission measured by divertor spectroscopy increases monotonically. Figure 2 shows spatial profiles of He and $D\alpha$ emissions in divertor region. According to divertor simulation of ITER conditions, outward shift of He profile is predicted. However, significant difference of peak position is not observed between He and $D\alpha$ emissions considering 1.1 cm of spatial resolution of the spectrometer. On the other hand, significant difference of spatial profiles is observed between He and $D\alpha$ emissions. In case of the $D\alpha$ emission, the emission intensity in inner divertor is usually higher than one in outer divertor. Contrary to the $D\alpha$ emission, the He emission intensity in outer divertor is same as the one in inner divertor. Considering ratio of ionization rate/excitation rate (I/E), significant asymmetries of He particle flux (Γ) can be obtained. In case of He, the I/E value shows linear dependence on electron temperature (T_e). On the other hand, in case of $D\alpha$, the I/E value has weak dependence on T_e . In typical case, T_e^{OUT}/T_e^{IN} is around 2. Therefore, Γ^{OUT}/Γ^{IN} of He and $D\alpha$ are 2 and 0.4 for D, respectively. This asymmetry of Γ_{He} is promising for efficient He pumping in fusion reactor because divertor pumping is performed in outer divertor region. To measure He neutral pressure near outer divertor, a RGA is under installation.

3.2 ICRF Heating

In D- ^3He fusion experiments, ICRF heating was performed in 3rd harmonics resonance condition ($B_t=4$ T, $I_p=2.5$ MA) and 4th harmonics resonance condition ($B_t=3$ T, $I_p=1.9$ MA). Maximum power of ^3He beam and ICRF wave are 10 MW and 3 MW, respectively. In case of 4th harmonics resonance condition ($B_t=3$ T, $I_p=1.9$ MA), raw data of He CXRS did not show significant increase during ICRF heating. However, in case of 3rd harmonics resonance condition ($B_t=4$ T, $I_p=2.5$ MA), significant increase in raw data of He CXRS is observed during ICRF heating phase. In this case, ^3He beam (99 keV) acceleration was also observed in vertical charge exchange diagnostics. At present, effect of ICRF heating condition on He CXRS data is not understood. However, further experiment is planned because ICRF wave has a possibility of enhanced He exhaust in fusion reactor.

4. Summary

In ^3He beam fuelling into ELMy H-mode discharge, difference of peaks position was not observed between He and $D\alpha$ emissions. Considering ratio of ionization rate/excitation rate of He and $D\alpha$, He flux in outer divertor is higher than one in inner divertor. This is desirable characteristics for efficient He pumping in fusion reactor. In D- ^3He fusion experiment, difference of response of He CXRS raw data was observed between 3rd and 4th harmonics resonance conditions.

Reference

- [1] NAKAMURA, H., et al. Phys. Rev. Lett. **67**(1991)2658.
- [2] Hillis, D. L., et al., J. Nucl. Mater. **196-198**(1992)35.

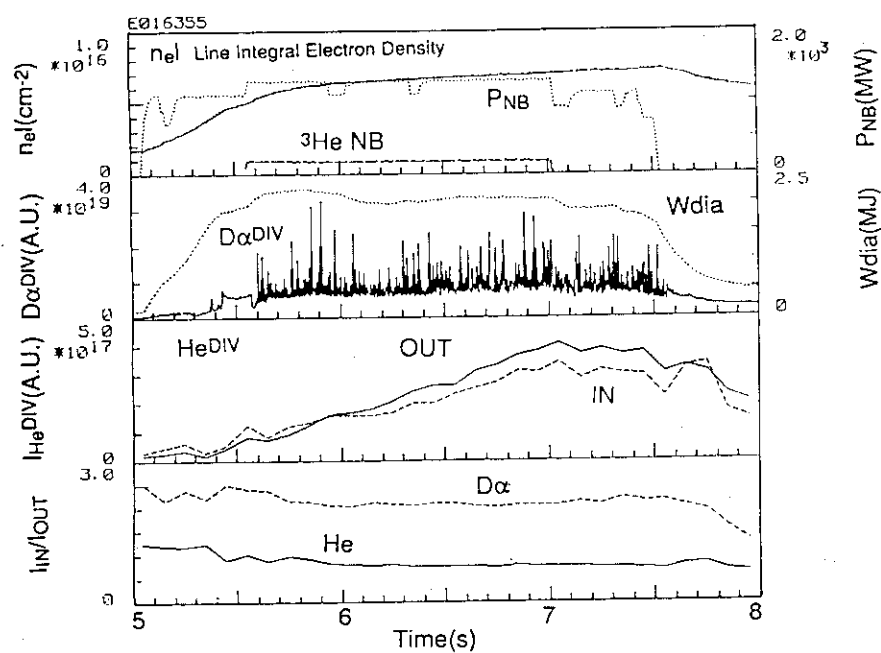


Fig.1 Typical wave forms of ELMy H-mode discharge with He beam fuelling.

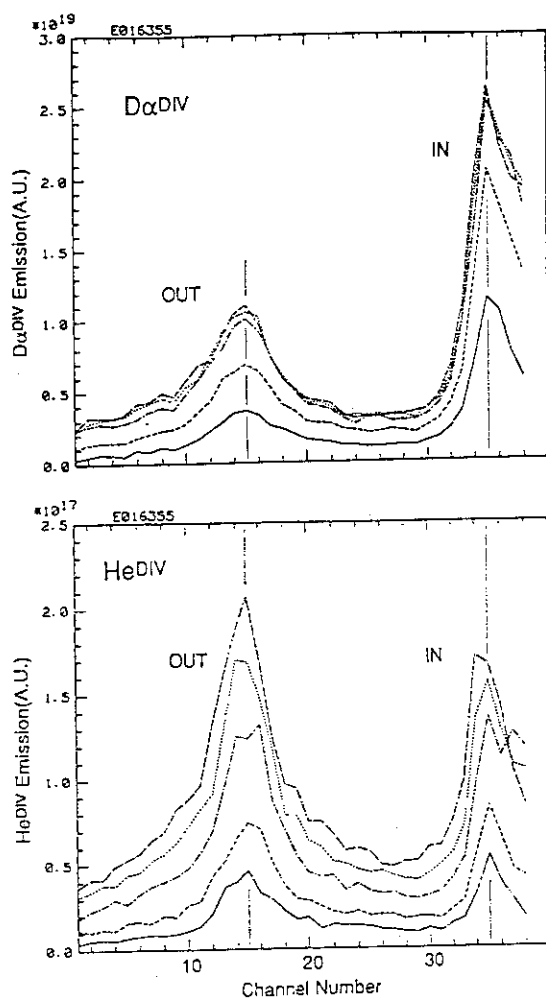


Fig.2 Spatial profiles of He and D_α emissions in divertor.

4.15 Investigation of First Wall Damage

T. Ando, M. Matukawa, K. Kodama, S. Oguri,
Y. Ouchi, T. Arai, J. Yagyu, A. Kaminaga, T. Sasajima, K. Yamane, F. Niino

1. Erosion of Divertor Plate due to Field Ripple

In the post-experiment investigation in November, 1992, no serious damage (cracking or fracture) was observed on the C/C composite divertor plate and the graphite first wall. Figure 1 shows the typical view of divertor tiles after operations until October, 1992, where the surface temperature of the center tiles (P-1 section) was measured using IRTV during the operations. However, as shown in Fig. 2, shallow erosions were observed on a large number of divertor tiles (mainly tile row : e) which were located at the outboard striking point in low X-point, low density and high power operations for H-mode study performed in the last year. Erosion patterns show clear toroidal periodicity, as shown in Fig. 3, which suggests that the heat flux is enhanced at these eroded positions due to the field ripple. The poloidal field perpendicular to the divertor plate is considerably small in these operations, so that the field line near the divertor plate is significantly affected by the ripple of toroidal field coils. Simple explanation of this erosion behavior is given in Fig. 4. For example, in the typical H-mode discharge (E16116; at 8 s), the poloidal magnetic field perpendicular to the divertor plate is about 0.08 T at the outboard separatrix-intercepting point. The toroidal field and its ripple at this point are 4.32 T and $\sim 2\%$, respectively, which gives the maximum poloidal field of ~ 0.08 T perpendicular to the divertor plate. In this case, the toroidal field ripple is comparable to the poloidal field produced by the plasma and poloidal field coils. Therefore, the combined poloidal field varies from \sim zero to \sim twice of the poloidal field without ripple. The gradient of the incident field line also varies from \sim zero to $\sim 1/30$, correspondingly.

The heat flux on the tile flat surface can be given approximately as follows;

$$q \sim q_0 \times B_p / B_t,$$

where q : heat flux on the tile surface, q_0 : heat flux perpendicular to the field line, B_p : poloidal field perpendicular to the tile surface, B_t : toroidal field.

Thus, the heat flux on the tile surface varies in the toroidal direction, from \sim zero in the reduced poloidal field region to \sim twice in the enhanced field region compared to the non-ripple heat flux. Further analysis should be made in future.

Figure 5 shows an example of the erosion profile measured using 3-D Laser Sensor. The left-hand tile was not taper-shaped before the operation because these tiles were attached to the single backing plate. The measured tile height yields the level difference between these tiles of 0.38 mm, and the gradient of the eroded surface is approximately $1/50$. All eroded edges were

taper-shaped using filing tools during the vent to decrease the development of erosion .

2. Radioactive Analysis of Divertor Plate

Radioactive analysis of several removed divertor tiles was carried out. As shown in Fig. 6, preliminary results show that Be-7 is the main residual radionuclide and two peaks appear at the inboard and outboard striking zones. Especially, the significant peak is observed at the inboard zone. Be-7 is produced from the photonuclear reaction of carbon and hard X-rays which are produced by runaway electrons, however the inboard zone is ion drift side in the JT-60U operations. If the measured Be-7 is produced by the runaway electrons, it is rather reasonable that higher peak appears at the outboard striking zone (electron side). Hence, there might be other reason, for example, nuclear reaction of carbon-12 and He-3 which is one of the product of D-D fusion reaction. This possibility has been reported in the radioactive analysis of the JET carbon materials [1]. Further investigation is necessary.

3. Others

Several loose-jointed divertor tiles were observed. The inspection revealed that the bolts became loose during operations because of imperfect spot welding to stop their rotation. In one of these tiles, extraordinary thick erosion was observed. The measured thickness was 1.4 mm, which can not be explained by the misalignment of tiles. The possible reason is that the eddy current induced in the loose-jointed tiles produces rotating electromagnetic moment, which happened to cause the protrusion of the tiles because there is 1~2 mm gap between tiles. In this case, the protruded edge is easily eroded. All loose-jointed tiles were screwed with suitable torque and the bolts were welded tightly.

Several small craters were observed on the graphite first wall tiles which were placed at the opposite side of the pellet injector. Figure 7 shows the view of the damaged tiles. The pellets were not injected into the vacuum vessel without plasma, so that the penetration through the plasma causes this damage. The damaged graphite tiles were changed to C/C composite ones with superior mechanical shock properties.

CVR (Chemical Vapor Reaction) B₄C-converted graphite tiles were exposed to the actual plasma to examine its material behavior. The edge of these tiles was melted due to high heat concentration, but B₄C-converted layer, about 100 μ m thick, was not exfoliated and still remained after one-year operations.

Reference

- [1] CHARUAU, J., et al., to be published in Proc. 17th Symp. Fusion Technol., Roma, Italy, September 14-18, 1992.

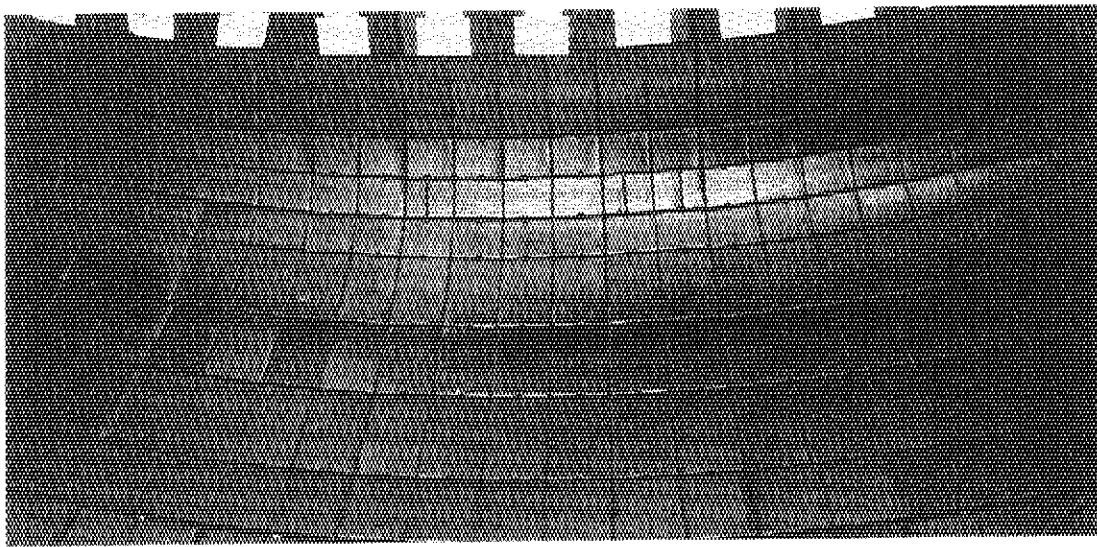


Fig. 1 Typical view of divertor plate after operations in 1992 (P-1 section, typical tile size (row : f) 107 x 80 mm)

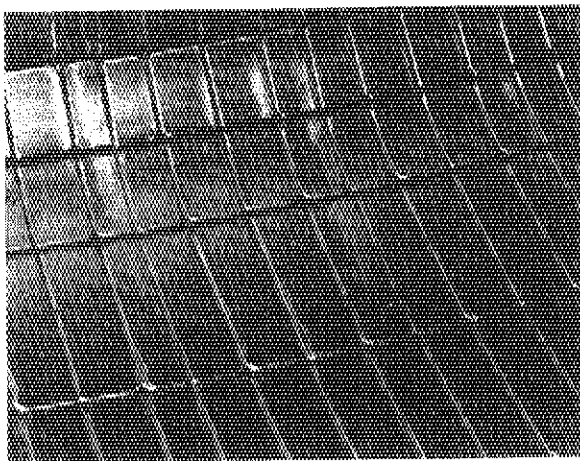


Fig. 2 Typical erosion observed on the divertor tiles
(row : e, typical tile size 107 x 40 mm)

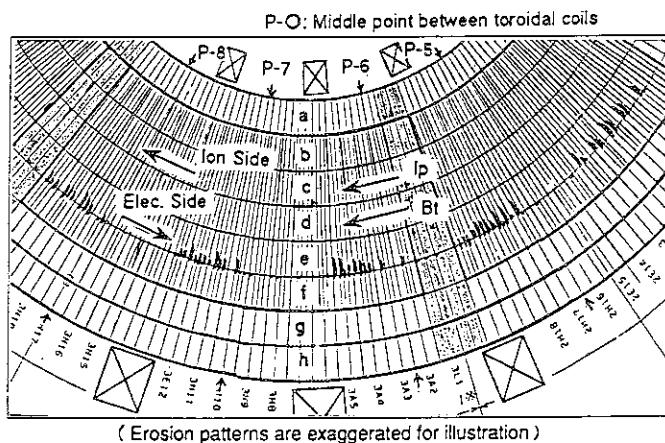


Fig. 3 Erosion pattern observed on the divertor plate,
showing clear toroidal periodicity due to field ripple

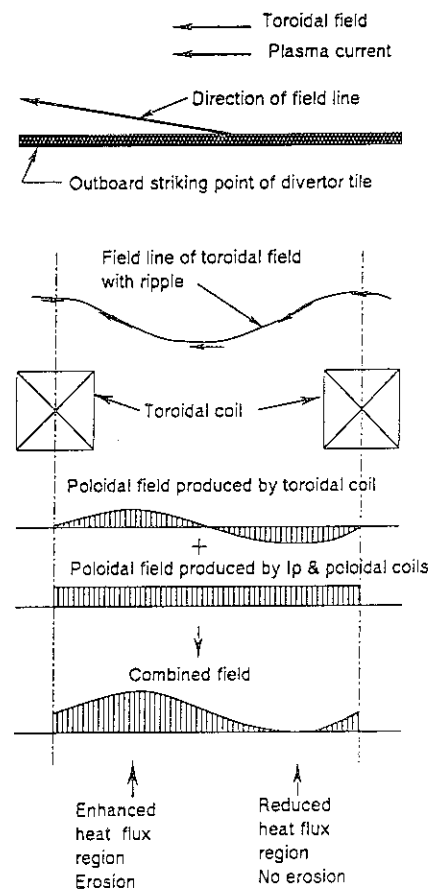


Fig. 4 Picture of the ripple effect on the enhancement
and reduction of the heat flux on the divertor plate

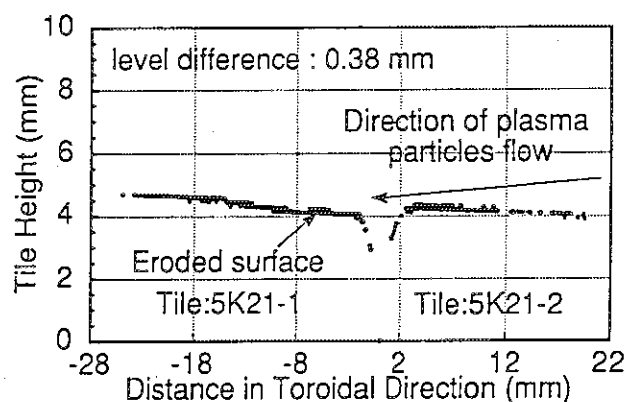


Fig. 5 Example of the erosion profile of divertor tiles obtained from in-situ measurement using 3-D Laser Sensor

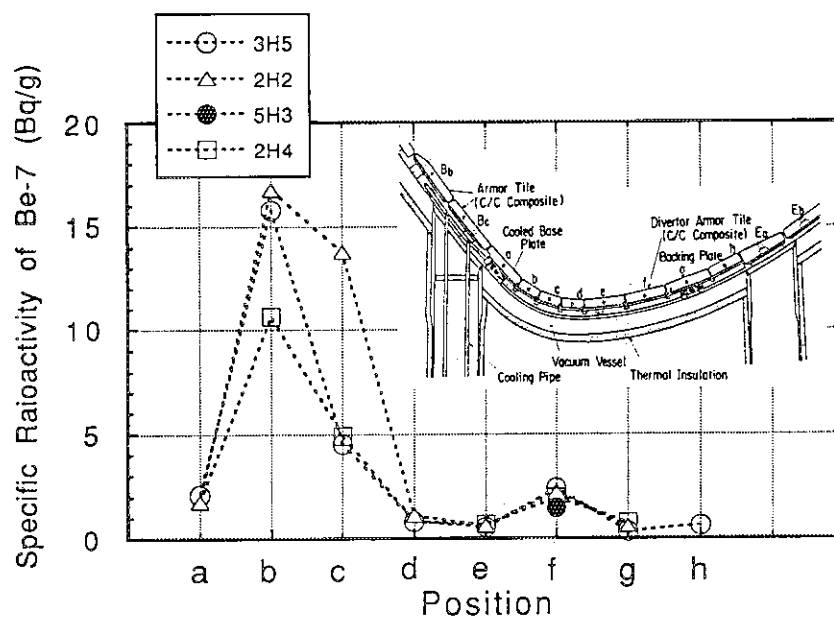


Fig. 6 Residual radioactivity of Be-7 of the removed divertor tiles

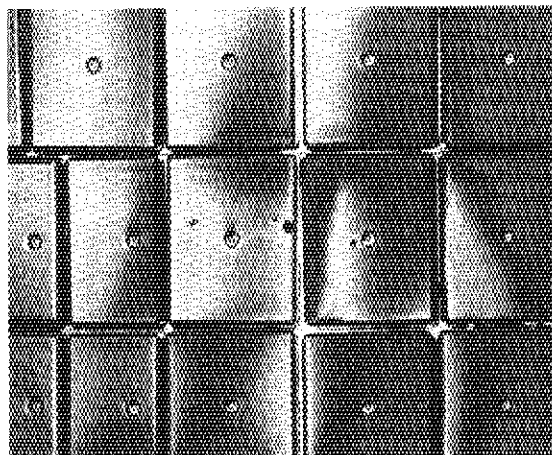


Fig. 7 View of pellet-bombarded graphite tiles, showing several small craters (Size of the tile : 107 x 126 mm)

5. Current Drive

5.1 Progress in LHCD Experiments

K. Ushigusa, T. Imai, Y. Ikeda, T. Kondoh, O. Naito, M. Nemoto, M. Sato, S. Ide, M. Seki, S.W. Wolfe, T. Fukuda

Abstract

Performances in the lower hybrid current drive (LHCD) experiments on JT-60U was compared with other machines. Highly recharged discharges by a high power LH injection were analyzed to study an effect of the DC electric field on the CD efficiency. Impacts of experimental results on the basic studies of LHCD physics were overviewed.

1. LHCD Performance in JT-60U

Several progresses on LHCD experiments has been reported in the 14th IAEA conference on Würzburg. In JET, a full CD plasma was achieved at 0.4MA by LHCD alone and at 2MA with a combination of 2.3MW of LHCD and 3MW of fast wave power[1]. A synegetic effect between LHCD and ICRF was clearly demonstrated in these experiments. The plasma current of 0.8MA has been fully driven by 2.9MW LHCD in Tore Supra[2]. By suppressing sawteeth and $m=1$ mode, a high central electron temperature of $T_{eo} = 8-10\text{keV}$ in LHCD plasma was maintained for $\sim 8\text{sec}$. A short pulse LH injection at a frequency of 8GHz was performed in FT-U and CD experiments in PBX-M was started for aiming the current profile control. LHCD experiments are also proposed in ALCATOR-Cmod and DIII-D. These facts indicate that an important role of LHCD in the steady state study for a tokamak reactor are commonly recognized again.

Performances in JT-60U LHCD experiments were shown in Fig.1 and 2 with results from other machines. Figure 1 shows the driven current by LHCD against the CD efficiency. In JT-60U, the full CD plasma at 2MA was achieved at the efficiency of $2.5 \times 10^{19} \text{m}^{-2} \text{A/W}$. The CD efficiency in LHCD experiments is plotted against the JT-60 scaling on LHCD efficiency in Fig. 2. Recent results from JT-60U, JET and ASDEX were all consistent with the scaling. It should be noted that the volume averaged electron temperature in JT-60U is smaller than that in JT-60. At the electron density of $n_e \sim 0.7 \times 10^{19} \text{m}^{-3}$, the diamagnetic stored energy W^* is $\sim 0.47\text{MJ}$ in JT-60U full CD plasma at $I_p = 1.2\text{MA}$ with the plasma volume V of $\sim 90\text{m}^3$, while $W^* \sim 0.28\text{MJ}$ in JT-60 CD plasma at $I_p = 1\text{MA}$, $n_e = 0.8 \times 10^{19} \text{m}^{-3}$ and $V = 32\text{m}^3$. This indicates that the volume averaged electron temperature in JT-60U full CD plasma is $\sim 60\%$ of

that in JT-60 at the same density and current. To achieve higher CD efficiency in JT-60U, we have to operate in higher density and higher current with high power LH injection. These experiments will be performed in 1993 by adding a new large multijunction launcher which has a potentiality to inject $\sim 7\text{MW}$ of LH power.

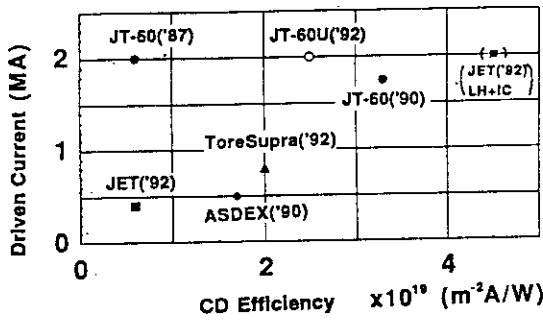


Fig.1 Driven current versus the current drive efficiency for various machines.

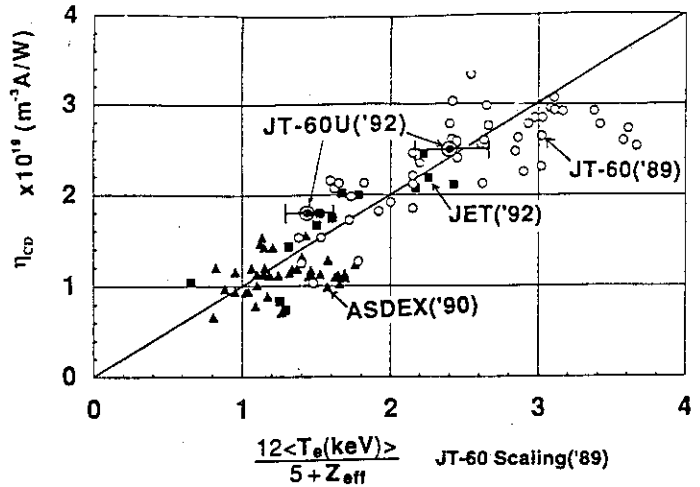


Fig.2 The current drive efficiency against the JT-60 Scaling for CD efficiency

2. Analysis of Highly Recharged Discharges

The CD efficiency is strongly affected by the DC electric field. A comparison of the CD efficiency with the DC electric field between the experiments and the theory has been studied in ASDEX[3]. An analysis of highly recharged discharge by high power LH injection is important because LHCD is suitable method to recharge the primary power supply. Figure 3 shows the time evolution of the loop voltage for different LH power injections at a low density plasma. At $P_{LH} \sim 0.9\text{MW}$, the full CD plasma is achieved; the DC electric field disappears. When we increase the injection power up to $P_{LH} \sim 2.2\text{MW}$, this is ~ 2.5 times of the power required for zero loop voltage, the loop voltage becomes negative. The decrease in the loop voltage is plotted against the injected LH power divided by the LH power without DC electric field in Fig. 4. The decrease in the loop voltage saturates at high power injection is clearly shown in Fig. 4. This means that the recharging efficiency of the primary power supply is limited. Reference[3] has derived the following relation between the loop voltage and the injected power in LHCD plasma with DC electric field;

$$\frac{P_{LH}}{P_{LH0}} = \left(1 - \frac{R_{OH}}{R_{LH}} \frac{V_{LH}}{V_{OH}}\right) \frac{1}{\eta/\eta_0} \quad (1)$$

where P_{LH0} , R_{OH} and R_{LH} are the LH power without electric field, the plasma resistance in OH phase and LH injected phase, respectively. $\eta/\eta_0 = \ln\{(1-X_2)/(1-XX_2)\}/\{(X-1)X_2\}$, $X = (N_{||min}/N_{||max})^2$, $X_2 = 12/(Z_{eff}+5)(v_{||min}/v_{te})^2(E/E_{CD})$, v_{te} is the electron thermal velocity and E_{DC} is the Dricer field. Broken line in Fig. 4 shows the theoretical curve from Eq.(1) with the same assumption in Ref.[3]; the ratio R_{OH}/R_{LH} set to be constant (a free parameter). This theory does not agree with experimental results in highly recharged cases. The ratio R_{OH}/R_{LH} can be described by the ratio of the electron temperature of LH and OH phases. Since the electron density is almost constant in these experiments, the ratio of electron temperature is replaced by the ratio of the stored energy. Therefore, the ratio R_{OH}/R_{LH} can be described by the the injection power; $R_{OH}/R_{LH} \propto (T_{eLH}/T_{eOH})^{1.5} \propto (W_{LH}/W_{OH})^{1.5} \propto (P_{LHabs}/P_{OHabs})^{3/4}$ where $P_{LHabs} = P_{LH} + V_{LH} I_p$ and $P_{OHabs} = V_{OH} I_p$. Putting this relation into Eq.(1), $\Delta V/V_{OH}$ is plotted against P_{LH}/P_{LH0} by the solid line in Fig. 4. The experimental data agrees well with this curve. It can be concluded that the theory derived in Ref.[3] can be applied for a highly recharged cases by a small modification.

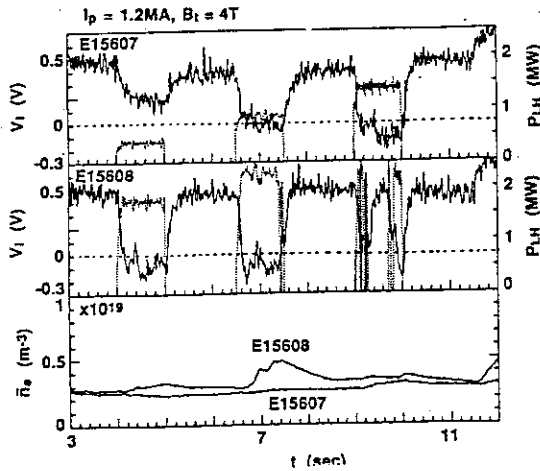


Fig.3 Example of the LH power scan at the low density discharges.

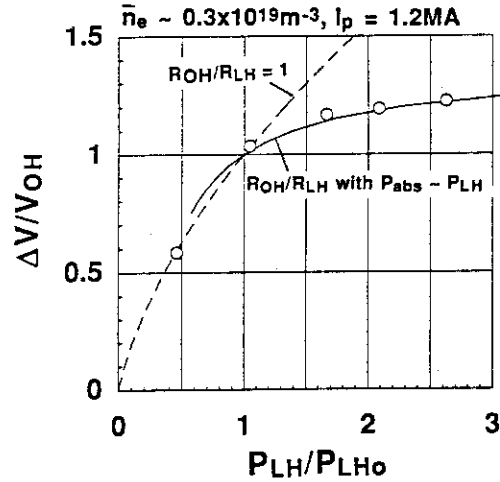


Fig. 4 The decrease in the loop voltage normalized by the OH voltage against the injected power divided by the full CD power.

3. Progresses in Basic Studies of LHCD Physics

Various basic studies in LHCD physics were performed in 1992 experiments. The accessibility condition has been checked by measuring the hard x-ray spectrum, the non-thermal electron cyclotron emission (Sec. 5.5), the non-accessible wave power and the increase in the radiated power (Sec. 5.4). All these results indicated the validity of the accessibility condition in tokamak plasmas. These studies are important for coming high power LHCD experiments in 1993 to obtain a high CD efficiency without causing catastrophic discharges by the accessibility limit. Studies on behaviors of energetic electrons in LHCD plasmas are also developed by measuring the hard x-ray signals (Sec. 5.2), the direct loss power through energetic electrons (Sec. 5.6), by studying the pressure anisotropy (Sec. 5.7) and by analyzing the hard x-ray signals in pellet injected plasma (Sec. 5.8). All these studies indicate that the slowing down is dominant process in JT-60U LHCD plasmas. Other basic studies such as the LH dispersion relation (Sec. 5.3), the change in the plasma rotation velocity in LHCD plasmas (Sec. 3.5), the divertor plasma in LHCD discharges and a fast loss of energetic electrons during LHCD are also important in an application of high power LHCD.

Based on these basic studies of LHCD physics for past two years, a high power LHCD experiments will be performed in 1993 by adding a new large multijunction launcher, which consists of toroidally 4 and poloidally 4 modules and each module has 12 sub-waveguides. Total injection power of $\sim 10\text{MW}$ and the driven current of higher than 3MA can be expected in these experiments. The parameter range in LHCD experiments will be largely expanded and various application of LHCD may be possible.

Reference

- [1] The JET Team, Proc. of 14th Int. Conf. on Plasma Physics and Contr. Fusion Research, Würzburg, Germany, (1992), IAEA-CN-56/E-1-1.
- [10] MOREAU, D., et al., Proc. of 14th Int. Conf. on Plasma Physics and Contr. Fusion Research, Würzburg, Germany, (1992), IAEA-CN-56/E-2-1.
- [3] LEUTERER, F., et al., Nuclear Fusion 31(1991) 2315.

5.2 Behavior of High Energy Electrons during LHCD

T. Kondoh, T. Imai and K. Ushigusa

1. Introduction

Steady state operation is a key issue to realizing a commercial fusion reactor. Lower Hybrid Current Drive (LHCD) is one of the most promising method for non-inductive current drive.

We study basic characteristics of high energy electrons by means of hard x-ray (HX) measurement to understand the physics of LHCD plasma. Confinement, distribution function and anisotropy of high energy electrons are investigated by means of hard x-ray measurement that is emitted by coulomb collision of fast electrons with ions.

We describe confinement of the fast electrons in section 3 and distribution function of fast electrons as a function of RF spectrum and anisotropy are described in section 4 and 5, respectively. Finally, a summary and conclusions are given in section 6.

2. Hard x-ray Measurement System

Hard x-ray emissions are detected by 8-channel sodium-iodide (NaI(Tl)) detector (Fig. 1). Seven channels look radial profile perpendicularly to the magnetic axis (Perpendicular array) and the other looks forward direction to the electron (Tangential detector). The detected HX signal is processed by CAMAC and pulse height analyzed into 256 channels every 50 msec. To measure the fast time response, single channel analyzers (SCA) are employed collecting x-ray signal energy range of 60-250 keV and above 250 keV every 1 msec.

3. Confinement of Fast Electrons

To investigate loss mechanism of the fast electron, we compare the time response of hard x-ray intensity with slowing down time of the fast electrons.

The slowing-down time of the resonant electrons with LH wave of refractive index $N_{//}$ is given by

$$\tau_{sd} = \frac{4\pi\epsilon_0^2 m_0^2 c^3}{n_e e^4 \ln \Lambda} \frac{1}{N_{//}^3} \frac{1}{(Z_{eff} + 1)(1 - 1/N_{//}^2) + \sqrt{1 - 1/N_{//}^2}}$$

where $\ln \Lambda$ is the Coulomb logarithm, n_e is electron density and Z_{eff} is effective charge of the ions.

Figure 2 (a) shows temporal evolution of plasma parameters. LH power is modulated by 2 Hz rectangular wave to measure rise and decay time of HX intensity. Peak refractive index of LHW is $N_{//peak} = 1.29$ which corresponds to resonant electron energy of 300 keV. Density rises up from 0.4 to $2.5 \times 10^{19} \text{ m}^{-3}$ in order to measure rise and decay time dependence on density during discharge.

Figure 2 (b) shows reciprocal of rise and decay time versus calculated slowing down time. Difference between rise time and decay time is caused by variation of loop voltage. The loop voltage is changed by LH caused by the non-inductive plasma current. Rise and decay times are affected by loop voltage. Rise and decay time subtracted the OH-field effect exists between the two experimental values. This effect is about 10 m sec as we can read from fig. 2 (b).

As a consequence, confinement of the fast electron is dominated by the slowing down process.

4. Distribution Function of High Energy Electrons

Figure 3 (a) represents temporal evolution of plasma parameters of LHCD experiment. Three LHW pulses with different $N_{//}$ are injected in a shot. Resonant electron energy with LHW of $N_{//} = 1.92, 1.61$ and 1.44 are 88, 141 and 200 keV, respectively. $N_{HX\perp}$ indicates hard x-ray intensity measured by perpendicular detector and $N_{HX//}$ is measured by tangential detector. Figure 3 (b) shows hard x-ray spectra of tangential detector with various $N_{//}$ spectra when line averaged electron density is $0.4 \times 10^{19} \text{ m}^{-3}$ (low density) and (c) shows when $1.8 \times 10^{19} \text{ m}^{-3}$ (high density).

We define hard x-ray temperature THX by the function $\exp(-E/THX)$ using the least squares method fitting 100 to 200 keV energy range. Figure 4 (a) shows hard x-ray temperature $THX_{//}$ versus electron density n_e as a parameter of $N_{//}$. As the $N_{//}$ decreases (phase velocity increases), $THX_{//}$ increases. $THX_{//}$ also increases as density increases. This is because loop voltage V_L increases as density increases (Fig. 4 (b)) and fast electrons are accelerated by the electric field.

5. Anisotropy of Fast Electrons

Since high energy electrons (energy range of several hundred keV) emit Bremsstrahlung strongly directionally to forward direction, intensity ratio $I_{HX//} / I_{HX\perp}$ indicates anisotropy of fast electrons. Though it does not indicate anisotropy of distribution function directly, we adopt it because of simplicity.

The dependence of anisotropy on $N_{//}$ and electron density is shown in Fig. 5 (a) and (b). The anisotropy increases at low $N_{//}$ (fast phase velocity) as qualitative expectation. However the anisotropy increases as density increases against the results of Fokker-Planck code and magnetic measurements[1]. These results may arise from residual ohmic field.

6. Summary

Experimental results are summarized as follows;

(1) Confinement of the fast electrons produced by LHW is dominated by slowing down process by comparing time response of hard x-ray and calculated slowing down time.

(2) Change of hard x-ray temperature is explained by the phase velocity of LHW and loop voltage.

(3) Large anisotropy is shown when phase velocity of LHW is large. Anisotropy of fast electron is also effected by residual ohmic field.

Because such characteristics of fast electrons are affected by ohmic field, it is necessary to reduce this effect for the investigation of LHW and electron interaction.

Reference

[1] Wolf, S.W, this report, Sec. 5.7

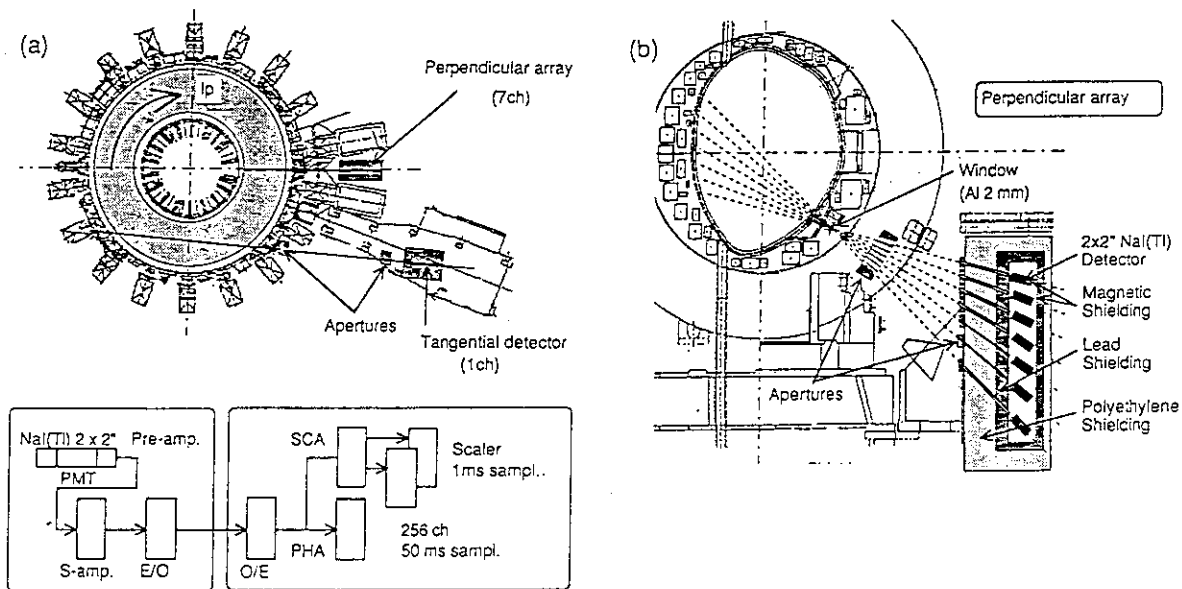


Fig.1 Schematic diagram of the hard x-ray detector. (a) Tangential detector used to collect hard x-ray spectra emitted to the forward direction to the electrons. (b) Seven channels detectors perpendicular detector to the magnetic axis.

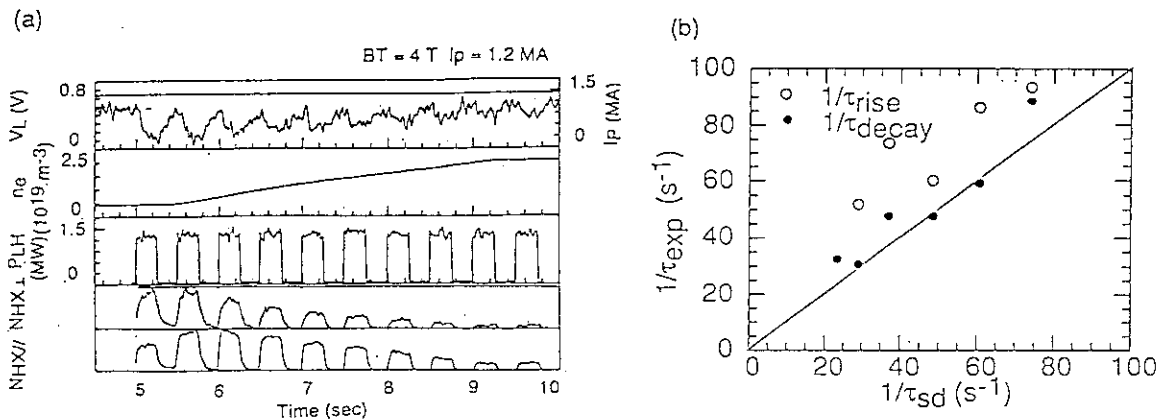


Fig.2 Measurement of rise and decay time of the hard x-ray intensity as a functions of electron density. (a) Temporal evolution of plasma parameters (b) Rise and decay time versus calculated slowing down time.

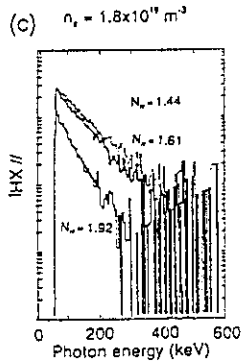
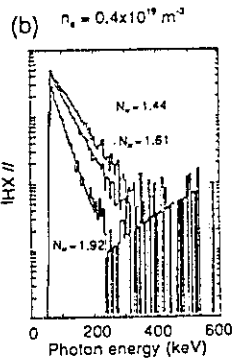
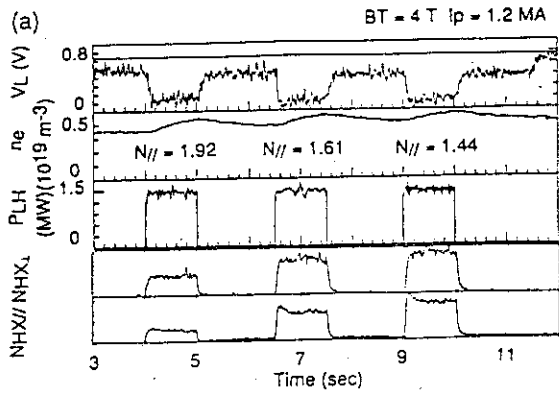


Fig. 3 (a) Temporal evolution of the loop voltage V_L , plasma current I_p , line averaged electron density n_e , the hard x-ray intensity perpendicular to the magnetic surface $N_{HX\perp}$ and forward direction to the plasma current $N_{HX//}$. (b) Hard x-ray spectrum as parameters of $N_{//}$ spectra. $n_e = 0.4 \times 10^{19} \text{ m}^{-3}$ (c) Hard x-ray spectra. $n_e = 1.8 \times 10^{19} \text{ m}^{-3}$

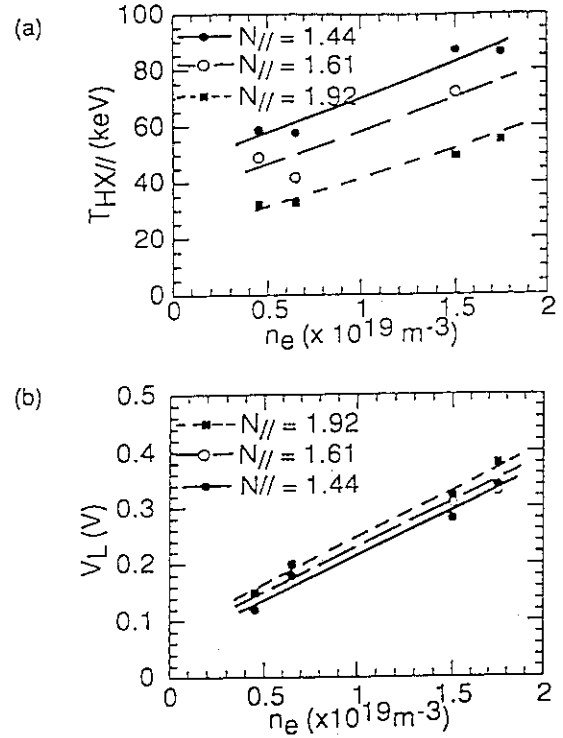


Fig. 4 (a) Hard x-ray temperature versus electron density as a parameter of $N_{//}$ spectrum. (b) Loop voltage as a function of electron density.

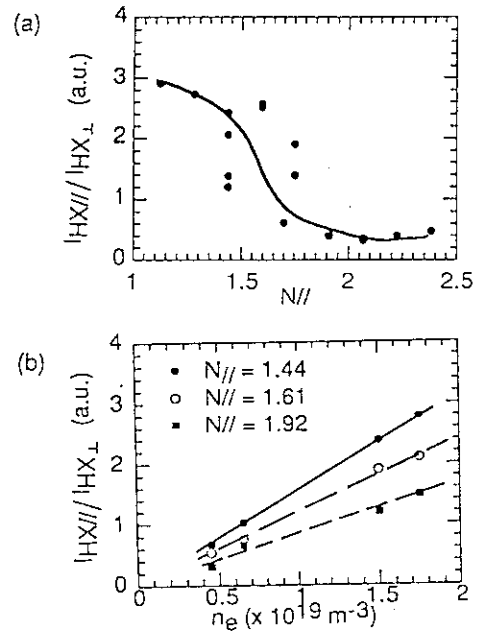


Fig. 5 (a) Anisotropy of hard x-ray intensity as a function of $N_{//}$. (b) Anisotropy of hard x-ray intensity as a function of electron density.

5.3 Verification of LH Wave Dispersion Relation

M. Nemoto, T. Imai, K. Ushigusa and M. Sato

1. Introduction

Coupling between Lower Hybrid (LH) wave and high energy ion assuming α particle in D-T plasmas has been investigating for establishment of more efficient current drive on JT-60U. Since actual burning plasmas consist of many kinds of ions, we have to verify mass dependence in a simple dispersion theory predicted in the previous study [1,2].

In this paper, a characteristic of coupling between deuterium ion and LH wave is described comparing with the previous experimental result with hydrogen beam ion.

2. Experiment and Discussion

The dispersion theory gives an equation of a critical density n_e^c of LH absorption from electron to ion

$$n_e^c = \frac{2.28f^2}{\frac{E_B}{F_8^2 A_B T_e} + \gamma - 2.34\left(\frac{f}{B_T}\right)^2},$$

where, f is LH wave frequency in GHz, energy of particle absorbing LH power E_B and T_e are in eV, B_T is in Tesla, A_B is atomic number of injected beam species, F_8 is a factor with respect to ratio of electron thermal velocity to phase velocity of LH wave parallel to the toroidal magnetic field and γ is a factor defined by Z_{eff} .

Experimental parameters are the same as the previous experiment with hydrogen [2], i.e., $I_p=1.2\text{MA}$, $B_T=4\text{T}$, the parallel refractive index of LH wave $N_{//\text{peak}}=1.39$, frequency of LH wave $f=1.74\text{GHz}$ and helium gas is fueled to increase electron density linearly. Energy range of deuterium neutral beam (NB) which is injected simultaneously with LH wave is from 40keV to 90keV. In this experiment, two charge exchange (CX) analyzers of NPA2 and NPA3 shown in Fig.1 are used to observe behavior of beam ion acceleration. Both analyzers are able to measure deuterium and hydrogen energy spectra simultaneously in good signal to noise ratio due to thick neutron shields. One of them (NPA3) is installed on JT-60U after the previous experiment and its sight line is viewing plasma core perpendicularly from a bottom port of the JT-60U vacuum vessel, as shown in Fig.2. Although the sight line is including a NB line for the active CX measurement, the NB unit is not used to reduce injecting NB power in this experiment. Therefore NPA3 observes ion energy spectra passively. The other one (NPA2) is a tangentially viewing CX analyzer which is used in the previous experiment, and NB units which beam lines cross a sight line of NPA2 are operated.

Fig.3 shows typical time evolution of LH wave absorption by deuterium ion when beam energy E_{B0} is 70keV. Each column from the top shows line averaged electron density \bar{n}_e , LH

wave P_{LH} and NB power P_{NBI} , a product of nonthermal frequency signal ($1.5\omega_{ce}$) measured by ECE system times electron density as a measure of the electron absorption. Average energy E_{ave} shown in lower two columns is defined as an energy value normalized by ion flux in Naperian logarithm unit over beam energy. E_{ave} measured by the parallel CX of NPA2, shown in the forth column from the top, arise at 7.3sec gently when electron density is $1.79 \times 10^{19} m^{-3}$. On the other hand, arising time of E_{ave} by the perpendicular CX of NPA3 is 6.3sec and it is corresponding to $1.35 \times 10^{19} m^{-3}$. Difference of arising time is due to coupling region of LH wave and ions. As given by the equation, the critical density is roughly proportional to the electron temperature. Therefore, if there is a region in outer plasma, where $n_e(r=r) > n_{ec}$ condition is satisfied, LH wave power is absorbed by ions of energy E_B there, the same as core plasma. Those ions change to high energy neutral particles by CX collision between low energy neutral particles from out of plasma and those are emitted without higher energy loss by collision between electron and other ions. In region near X point of diverter configuration plasmas, low energy neutral particles are dense due to backflow of neutral particles between the first wall of the vacuum vessel and the outermost magnetic surface from diverter plates. Since viewing line of NPA3 is through there, it measures CX neutral particle energy spectra influenced significantly ion energy distribution of outer plasma in comparison to the spectra measured by NPA2. Moreover, in the case of higher critical density in the central region, opacity of CX neutral flux from inner plasma becomes higher. Therefore, the lower critical density obtained by NPA3 suggests that weak absorption of LH wave in outer plasma occurs. Fig.4 shows ion energy dependence of the critical densities measured by both analyzers. One by NPA2 is in good agreement with a prediction by the dispersion relation with parameters of $F_8=2.75$, $\gamma=0.8$ and $T_e=1.4keV$. Energy of particle absorbing LH power is substituted $E_B=E_{B0}+5keV$, it is the same as before. Critical density determined by those parameters is a little lower than predicted one with parameters of the hydrogen discharges ($F_8=2.75$, $\gamma=0.8$ and $T_e=2.0keV$). Obtaining profile data of the accurate electron temperature is necessary to specify the causes for the difference between those critical densities. The good agreement indicates that the dispersion relation explains the mass dependence well, although more accurate determination of the electron temperature remains. On the other hand, the dependence by NPA3 disagrees with a predicted curve with constant values. Larger difference between obtained data of NPA2 and NPA3 in higher density region suggests that occurrence region of LH wave absorption in outer plasma shifts outward according to increase of electron density.

We should estimate a radial distribution of high energy CX particles emission after obtaining detail profiles of electron density and the electron temperature to compare with energy spectra measured by both analyzers and to evaluate more accurate LH absorption.

3. Conclusion

Deuterium beam ion acceleration due to the LH wave absorption in JT-60U plasmas was studied to prove a mass dependence of critical density estimated from the dispersion relation. The obtained acceleration characteristic could well explain the dependence. This result will give a useful measure to study the LH wave absorption in actual reactor plasmas.

We should measure n_e , T_e and Z_{eff} profiles in order to obtain more accurate and detailed evaluation of the LH absorption.

References:

- [1] NEMOTO, M., et al., Phys. Rev. Letter **67**(1991)70.
- [2] NEMOTO, M., et al., JAERI-M report **92-073**(1992)304.

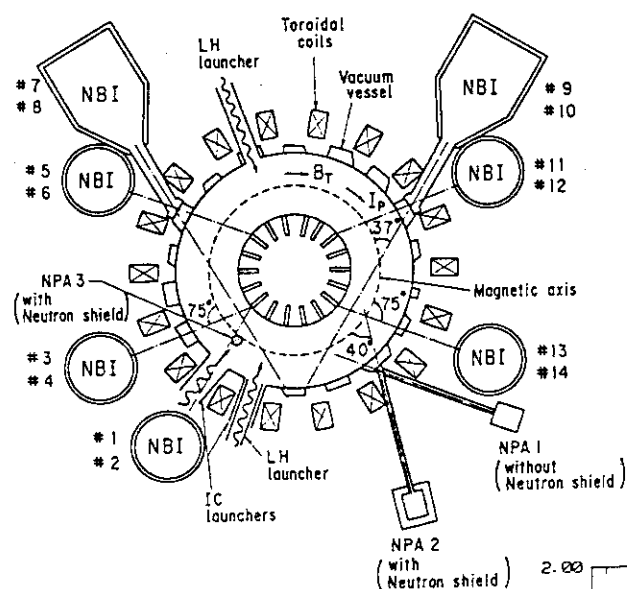


Fig.1 Arrangements of CX analyzers and NBI units.

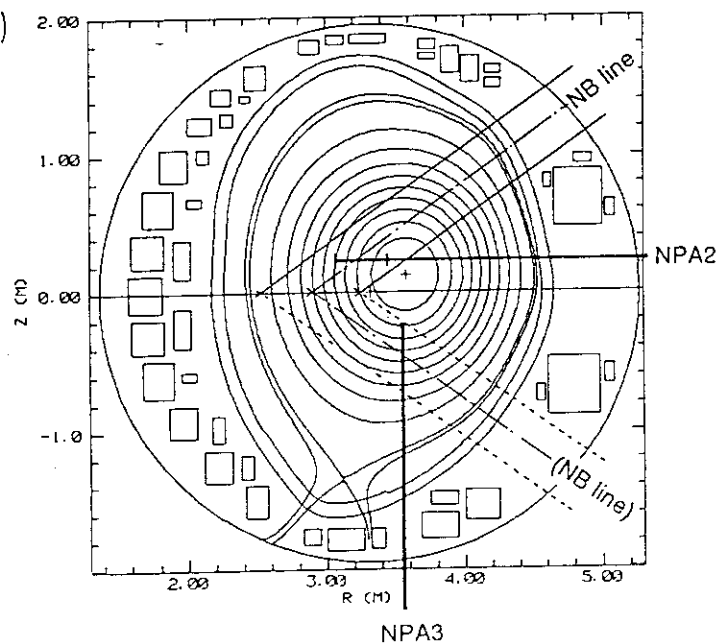


Fig.2 Viewing lines of CX analyzers and neutral beam lines on cross-sectional view of typical divertor configuration.

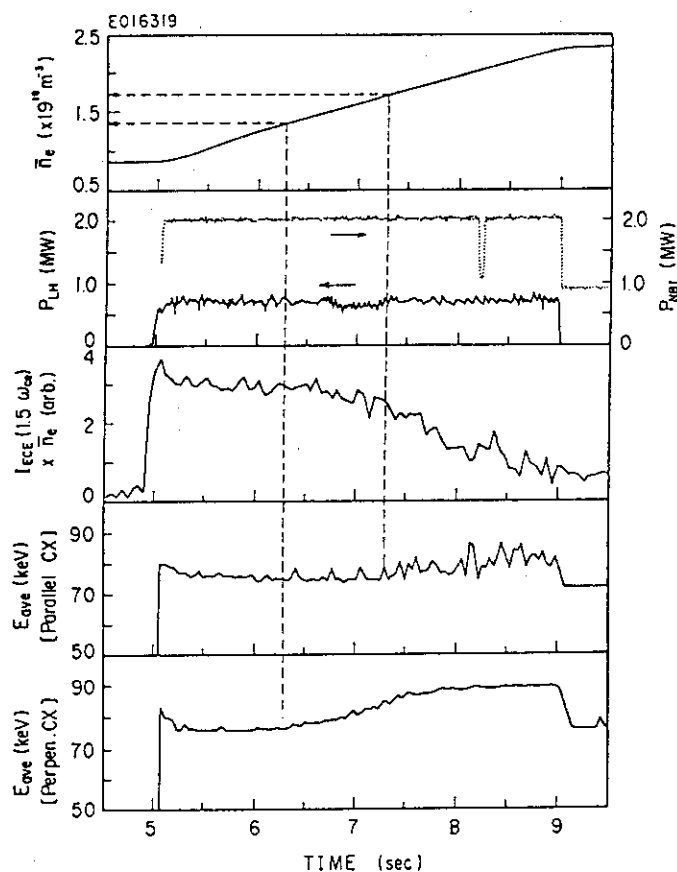


Fig.3 Typical time evolution of the simultaneous injection of LH wave and NB.

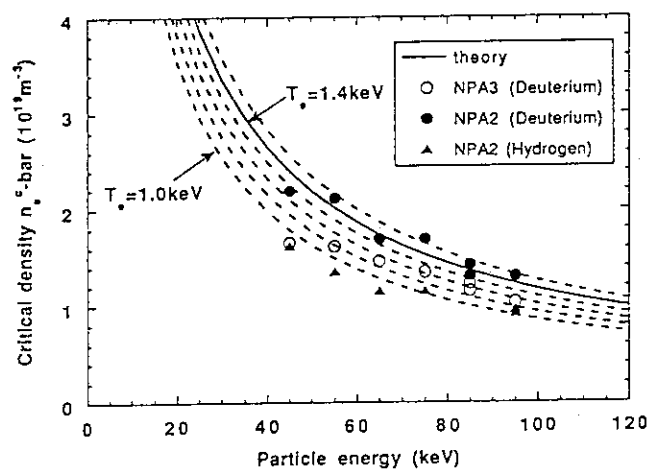


Fig.4 Comparison between the theoretical critical density and experimental data obtained with NPA2 and NPA3.

5.4 Detection of Non-accessible Wave

Y.Ikeda, K.Ushigusa, T.Imai

1. Introduction

In an application of LHCD in a future steady state tokamak machine, the launched LH wave should have a very narrow and fast phase velocity spectrum within the accessibility condition is satisfied. On the operation of a very narrow spectrum, the most of the launched power, which is optimized for current drive, may easily turn to an non-accessible power due to the change of the plasma parameters. This situation is very dangerous because a large RF power is not absorbed in plasma core and stays in the scrape off layer (SOL), and may enhance the plasma-wall interaction [1]. We study in detail the accessibility condition of a very narrow spectrum on JT-60U LHCD experiments by using a 24x4 multijunction grill.

2. Experimental Setup

The launched wave spectrum is very sharp (half-width: $\Delta N_{//}^{\text{half}} \sim 0.4$) and is controlled in the wide range of $N_{//\text{peak}} = 1$ to 3 at the frequency of 2GHz by changing the phasing between adjacent multijunction module in the grill. The power rate of mainlob ($N_{//\text{peak}}$) is more than $\sim 80\%$ in the excited wave. A Langmuir probe on the divertor plate is connected to two frequency analyzers to detect the LH pump frequency of the signal at the divertor plasma. Figure 1 shows the typical plasma configuration and the location of the probe on the divertor plate. The Langmuir probe for measuring RF signal is located at the inner side (ion drift side) of the divertor plate, which is not fed a high voltage to measure plasma density in these experiments. The probe is in the divertor plasma, therefore, the RF signal may be caused by the density perturbation at the pump wave frequency in the divertor plasma. The RF signal detected by this probe is transmitted though a 2GHz band waveguide for filtering lower frequency ($\sim 1.7\text{GHz}$) and is connected to the spectrum analyzers. One spectrum analyzer measures the time evolution of the RF intensity at 2GHz with the frequency resolution of 3 MHz, and the other is used to measure the frequency spectra with the frequency resolution of 10 kHz at every 100 ms during RF injection to check the frequency spectral broadening. The other Langmuir probes on the divertor plate are operated to measure divertor plasma density during LH experiments.

3.Experimental Results

The effect of three parameters on the accessibility condition are studied by using the RF probe: wave spectrum, plasma density, and toroidal magnetic field. The dependence of the

wave spectrum on the RF signal normalized injected power ($P_{LH} \approx 0.6\text{MW}$) are examined by scanning the $N_{//\text{peak}}$ from 1.2 to 2.2 during LH injection as shown in Fig. 2. The plasma parameters are $B_t=4\text{T}$, $I_p=2\text{MA}$, $\bar{n}_e=1.8 \times 10^{19}\text{m}^{-3}$, and the accessibility condition $N_{//\text{acc}}$ is estimated 1.35 from the center toroidal field and the average density. Though the plasma current is not fully driven by LH waves, more than 50% ~ 30% of plasma current are exchanged by RF driven current. The intensity of the probe signal at 2GHz decreases with increasing the $N_{//\text{peak}}$. The spectral broadening is in the range of $\sim 1\text{MHz}$ at -20dB from the peak frequency and the profile of the frequency spectrum dose not depend on the $N_{//\text{peak}}$. Therefore, the frequency resolution of 3 MHz in the RF intensity measurement is much enough to measure the time evolution of intensity of the pump wave frequency. The edge plasma density measured by Langmuir probe array on the divertor plate shows the plasma density at the RF probe position is $\sim 1 \times 10^{19}\text{m}^{-3}$ and there is no significant difference in the divertor plasma density between various wave spectra.

Figure 3 shows the density dependence of the RF signal normalized by P_{LH} . In the density range of $\bar{n}_e = 0.6 - 1.8 \times 10^{19}\text{m}^{-3}$, the accessibility condition changes from $N_{//\text{acc}} = 1.2$ to 1.34 at $I_p=1.2\text{MA}$, $B_t=4\text{T}$, and $P_{LH} \approx 1.2\text{MW}$, while the $N_{//\text{peak}}$ of the launched waves are 1.44, 1.6 and 1.92, respectively. The increase of the RF signal at high density is observed only with lower $N_{//}$ spectrum, where the wave spectrum does not satisfy the accessibility condition. The spectrum is slightly broadened at higher density as reported in ASDEX [2], however, the spectral broadening is in the range of $\sim 1\text{MHz}$ at -20dB from the peak frequency and there is no strong effect of the wave spectrum on the frequency broadening as shown in Fig. 4.

The intensity of RF signal also depends on the toroidal field. Figure 5 shows the intensity of RF signal normalized by P_{LH} as a function of the toroidal field at the $N_{//\text{peak}}$ of 1.44, 1.6 and 1.92, respectively. The plasma density is $0.9 \sim 1.1 \times 10^{19}\text{m}^{-3}$, $I_p=1.2\text{MA}$, and $P_{LH}=1.2\text{MW}$. In the magnetic field range of $B_t=2.5\text{--}4\text{T}$, the accessibility limit $N_{//\text{acc}}$ changes from 1.27 to 1.45. The intensity of the RF signal increases at the low toroidal field operation when the wave spectrum is close to the accessible limit. The spectral broadening is observed at the lower field operation, and the broadening is in the range of $\sim 1\text{MHz}$ at -20dB from the peak frequency.

3. Discussion and Conclusion

It is shown that the intensity of RF signal is closely related with the wave spectrum, plasma density and toroidal field. A LH wave injection with lower $N_{//}$ spectrum into higher density and lower toroidal field plasma gives a higher intensity of the RF signal at the divertor plasma. Though the frequency spectral profile is slightly affected by the plasma density and toroidal field, the frequency spectral broadening is negligible to measure the wave power of the RF pump frequency at the divertor plasma.

In the calculation of ray trajectory of LH waves, it is known the non-accessible waves accumulate at the plasma surface through the mode conversion to fast waves and is reflected at the cut-off point of the fast wave in the scrape off layer, and finally enters the divertor region [3]. Therefore, the intensity of the pump frequency at the divertor region may be correlated with the accessibility condition of the launched waves. The accessible power rate of the launched power is given by

$$P_{acc} = \left(\int_{N_{//}^{acc}}^{\infty} P(N_{//}) dN_{//} + \int_{-\infty}^{-N_{//}^{acc}} P(N_{//}) dN_{//} \right) / \int_{-\infty}^{\infty} P(N_{//}) dN_{//} \quad (1)$$

Since the launched wave spectra are narrow and with small sidelob in these experiments, the power rate sharply drops when the $N_{//}^{acc}$ becomes beyond the $N_{//}^{peak}$. If the wave spectrum is approximated by the Gaussian profile around $N_{//}^{peak}$, the accessible power rate is described by,

$$P_{acc} = 1 - \frac{1}{\sqrt{\pi}} \frac{P_{main}}{\Delta N_{//}} \int_0^{N_{//}^{acc}} \exp \left(- \frac{(N_{//}^{peak} - N_{//})^2}{\Delta N_{//}^2} \right) dN_{//} \quad (2)$$

where $\Delta N_{//} = \Delta N_{//}^{half} / 2\sqrt{\ln 2}$, and P_{main} is the power rate of the mainlob of launched wave spectrum. The $N_{//}^{peak}$ is shifted with the $\Delta N_{//}^{half} = \sim 0.4$ and P_{main} of ~ 0.8 by changing the phasing in the JT-60U LHCD grill, therefore, the accessible power rate of various wave spectra can be roughly estimated by the value of $(N_{//}^{peak} - N_{//}^{acc}) / \Delta N_{//}^{half}$.

Figure 6 shows the all previous data as a function of the non-accessible power rate ($1 - P_{acc}$) calculated by equ. (2). The behavior of RF signal is well explained by the accessibility parameter, where the wave spectra, density and toroidal field widely change. Although there are some open questions concerning a gain of the RF probe for the slow and fast waves in plasmas, the RF signal detected at the divertor plasma may give a good method to measure the non-accessible wave power.

It has been shown that the accessibility condition is clearly verified by injecting a very narrow wave spectrum. The signal of pump frequency detected by the RF probe at the divertor plasma is enhanced when the launched wave does not satisfy the accessibility condition. The intensity of RF signal is well explained by the power rate of accessibility parameter. This result indicates that the RF probe at the divertor plasma is a good method to identify the accessibility condition.

REFERENCES

- [1] JT-60 Team, "Review of JT-60U experimental results from March to October, 1991", JAERI-M(92-073).
- [2] PERICOLI-RIDOLFINI V., et al., Nucl. Fusion **32**(1992) 286.
- [3] USHIGUSA K., et al., Nucl. Fusion **22** (1982) 33.

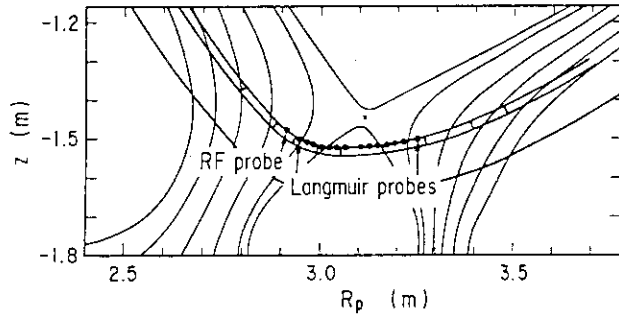


Fig. 1 Location of RF probe and Langmuir probes on the divertor plate.

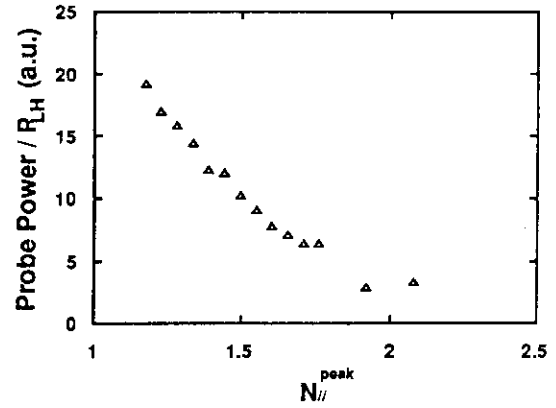


Fig. 2 Intensity of RF signal as a function of $N_{||}^{peak}$. The accessibility condition $N_{||}^{acc}$ is at $Bt=4T$, $\bar{n}_e = 1.8 \times 10^{19} m^{-3}$.

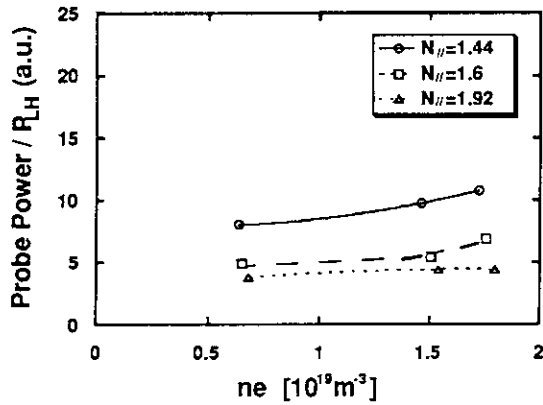


Fig. 3 Intensity of RF signal as a function of line average density. The accessibility condition changes from 1.2 to 1.34 for $\bar{n}_e = 0.6$ to $1.8 \times 10^{19} m^{-3}$ at $Bt=4T$.

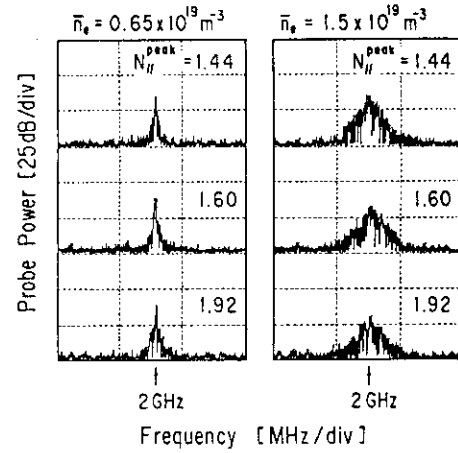


Fig. 4 Spectrum around the 2GHz pump frequency in low ($\bar{n}_e = 0.65 \times 10^{19} m^{-3}$) and medium ($1.5 \times 10^{19} m^{-3}$) density.

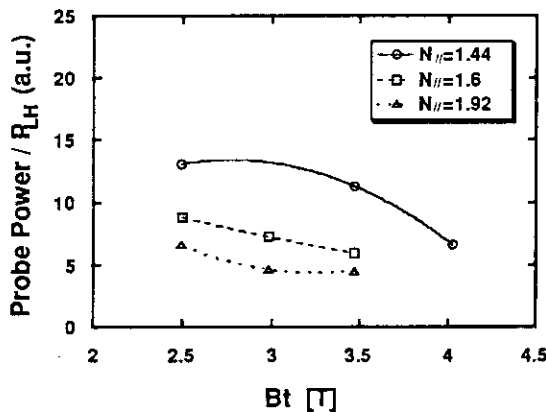


Fig. 5 Intensity of RF signal as a function of toroidal magnetic field. The accessibility condition changes from 1.27 to 1.45 for $Bt=2.5T$ to $4T$ at $\bar{n}_e \approx 1 \times 10^{19} m^{-3}$.

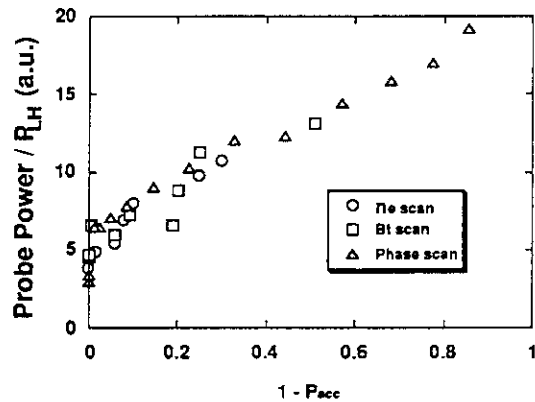


Fig. 6 Intensity of RF signal as a function of non-accessible power.

5.5 Effects of Accessibility on ECE Signal in LHCD Experiments

M. Sato, T. Imai and K. Ushigusa

1. Introduction

The study of supra-thermal electrons is important for understanding the mechanism of Lower Hybrid Current Drive (LHCD). One of the interesting features of the Lower Hybrid Wave (LHW) is an accessibility condition which limits the lowest N_{\parallel} ($N_{\parallel}^{\text{acc}}$) to penetrate to the core of the plasma. Accordingly, supra-thermal electrons produced by the LHW are limited correspondingly by the value of $N_{\parallel}^{\text{acc}}$. Therefore the study of the supra-thermal electrons gives information on the accessibility in tokamak plasmas. Here, the observed electron cyclotron emission (ECE) is analyzed from the point of view of accessibility in LHCD.

2. Accessibility Condition

The accessibility condition limits the lowest N_{\parallel} of the wave launched to penetrate to the core of the plasma. It is

$$N_{\parallel} > N_{\parallel}^{\text{acc}}(n_e, B_t, Z_{\text{eff}}, f) \\ = f_{\text{pe}}/f_{\text{ce}} + (1 + (f_{\text{pe}}/f_{\text{ce}})^2 - (f_{\text{pi}}/f)^2),$$

where f , f_{ce} , f_{pe} and f_{pi} are the launched wave, electron cyclotron, electron plasma and ion plasma frequencies, respectively. It originates from the existence of a turning point between the slow wave and the fast wave. The launched LH power depends on N_{\parallel} , frequency (f) and the phase difference of the LH wave ($\Delta\phi$): $P_{\text{LH}} = P_{\text{LH}}(N_{\parallel}, f, \Delta\phi)$. The supra-thermal electrons produced by the LHW are limited according to the $N_{\parallel}^{\text{acc}}$. The energy (E_{sp}) of the supra-thermal electrons is related to N_{\parallel} as $E_{\text{sp}}(N_{\parallel}) = m_e c^2 [1/(1 - 1/N_{\parallel}^2)^{1/2} - 1]$. When the electron density is increased, the accessibility condition is changed and the behavior of the supra-thermal electron may be changed. That is, as $N_{\parallel}^{\text{acc}}$ is increased, the allowed N_{\parallel} is limited, and the maximum energy of the supra-thermal electron may be decreased.

3. Experimental Apparatus and Results

The launcher of the lower hybrid heating system in JT-60U is the multi-junction type[1]. It can produce sharp power spectra in broad N_{\parallel} region, which is appropriate to study the impact of the accessibility condition on the supra-thermal electrons. The peak of the spectrum depends on $\Delta\phi$, as shown in the LH power spectra of Fig.1. Information on the supra-thermal electrons may be obtained from measurement of the ECE spectra. The ECE spectra are measured by a Fourier transform spectrometer (FTS) along a horizontal line of sight in JT-60U[2]. The frequency of ECE from the supra-thermal electrons is relativistically shifted to a lower frequency.

The typical time evolution of the plasma parameters in LHCD is shown in Fig.2. The plasma parameters are as follows; $I_p=1.2\text{MA}$, $B_t=4\text{T}$, $P_{LH}=1.3\text{MW}$, $\Delta\phi=120^\circ$ ($N_{||\text{peak}}=1.29$). The line averaged electron density increases from $0.6 \times 10^{19}\text{m}^{-3}$ to $3 \times 10^{19}\text{m}^{-3}$. When the LH power is chopped, the ECE at $1.0f_{ce}^0$, $1.5f_{ce}^0$ and $3f_{ce}^0$ respond quickly, but the ECE at $2f_{ce}^0$ responds slowly, where f_{ce}^0 is the electron cyclotron frequency at the plasma center. The ECE at $2f_{ce}^0$ is mainly the second harmonic ECE from the thermal electrons. The ECE at f_{ce}^0 and $1.5f_{ce}^0$ are relativistically shifted second harmonic ECE, but the ECE at f_{ce}^0 may be absorbed by the thermal electrons. The ECE at $1.5f_{ce}^0$ is not affected by the absorption so it is used for the study.

A physical quantity which is the product of the line electron density and ECE emissivity is defined by the following equation; $J_{NEC} = n_{edl} \times I_{ECE}(1.5f_{ce}^0)$, where $I_{ECE}(nf_{ce}^0)$ is the ECE emissivity at nf_{ce}^0 . The density dependence of J_{NEC} is shown in Fig. 3. The following two facts are found:

- (1) J_{NEC} is drastically decreased at the density where the accessibility condition is marginally satisfied in cases of $\Delta\phi=120^\circ$ and 150° .
- (2) J_{NEC} is not drastically decreased in case of the $\Delta\phi=210^\circ$ (the highest $N_{||}$).

4. ECE Analysis Model

The supra-thermal electrons produced by the LH wave collide with the bulk plasma and their number decreases in a characteristic time of slow-down time (τ_{sd}). Then the density of the supra-thermal electron (n_{sp}) is linear with τ_{sd} : $n_{sp} \propto \tau_{sd} * P_{LH}$. Since the emissivity of ECE is proportional to the supra-thermal electron density and τ_{sd} which is inversely proportional to the electron density, then

$$I_{ECE} * n_e \propto P_{LH} \quad (1).$$

The LH power which produced the supra-thermal electrons is calculated taking into account the accessibility condition. Using eq.(1) a comparison between experiment and calculation may be made. The following assumptions are used. (1) The supra-thermal electrons are uniform from R1 to R2. (2) $I_{ECE}(1.5f_{ce}^0)$ is relativistically shifted the second harmonic ECE, then the supra-thermal electrons from R1 to R2 with energy (E) of $E_1 < E < E_2$ may emit the $I_{ECE}(1.5f_{ce}^0)$ where the second harmonic ECE from the electron with energy (E) at R_i is shifted to $1.5f_{ce}^0$. The supra-thermal electron emitted the $I_{ECE}(1.5f_{ce}^0)$ may be responded to the LH power with $N_1 < N_{||} < N_2$. In the experiment, $N_{||}^{acc}$ is increased by increasing the electron density where N_i is correspondent to the $N_{||}$ for E_i .

The LH power which produces the supra-thermal electrons emitting $I_{ECE}(1.5f_{ce}^0)$ is calculated taking into account the accessibility condition. The procedure for calculating in the case of $N_{||} \sim N_{||}^{acc}$ is the following;

$$\begin{aligned} P_{ECE} &= P_{acc}(N_1) - P_{acc}(N_2) & \text{for } N_{||}^{acc} < N_1 \\ P_{ECE} &= P_{acc}(N_{||}^{acc}) - P_{acc}(N_2) & \text{for } N_1 < N_{||}^{acc} < N_2 \end{aligned}$$

$$P_{ECE}=0 \quad \text{for} \quad N_2 < N_{//}^{acc},$$

where P_{acc} and P_{ECE} are the total power satisfying the accessibility condition and The power which is related to $I_{ECE}(1.5f_{ce}^0)$, respectively. Here $R_1=-0.12m$ and $R_2=0.3$ are assumed, $E_1=230keV$, $N_1=1.38$, $E_2=160keV$ and $N_2=1.55$. The schematic diagram of R_i and E_i is shown in Fig.4.

The electron density dependence of P_{ECE} is shown in Fig.5. The starting point of the decrement of P_{ECE} depends on the value of N_1 , and the points of $P_{ECE}=0$ depends on the value of N_2 . The values of R_1 and R_2 are selected taking into account of the above reason. The experimental electron density dependence of J_{NEC} is shown in Fig.6. The agreement between the experimental results and calculation is qualitatively good. This means that the LH accessibility condition affects the behavior of the supra-thermal electrons.

5. Summary

By changing electron density the response of the ECE is measured in order to investigate the accessibility condition of the LHW. The LH power which is related to the emitted ECE is calculated taking into account the accessibility condition. A comparison between experiment and calculation is made. The agreement between experimental results and calculation results is qualitatively good.

This means that the LH accessibility condition affects the behavior of the supra-thermal electron.

References

- [1]Ushigusa, K. et al, this issue 5.1
- [2]Sato, M. et al, this issue 9.4

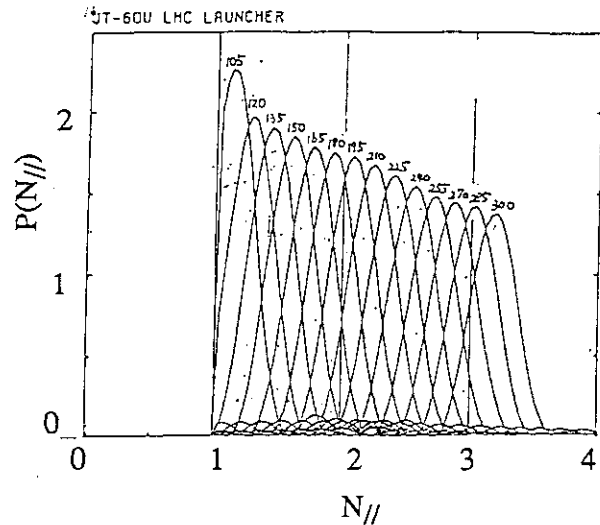
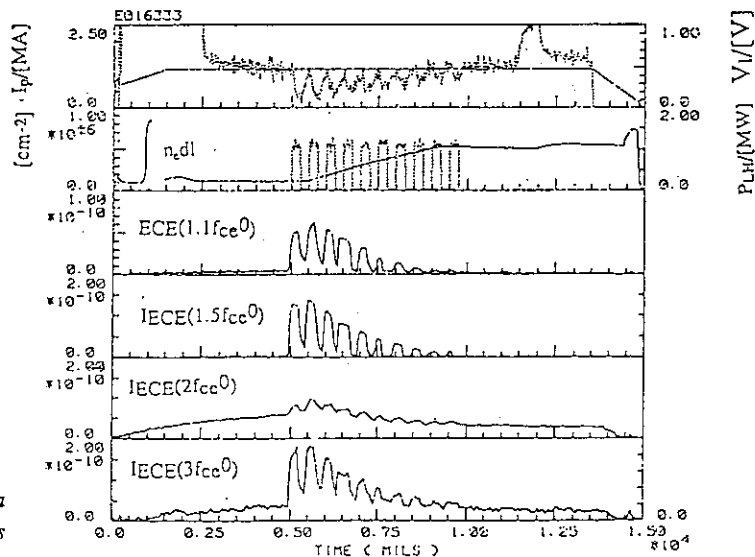
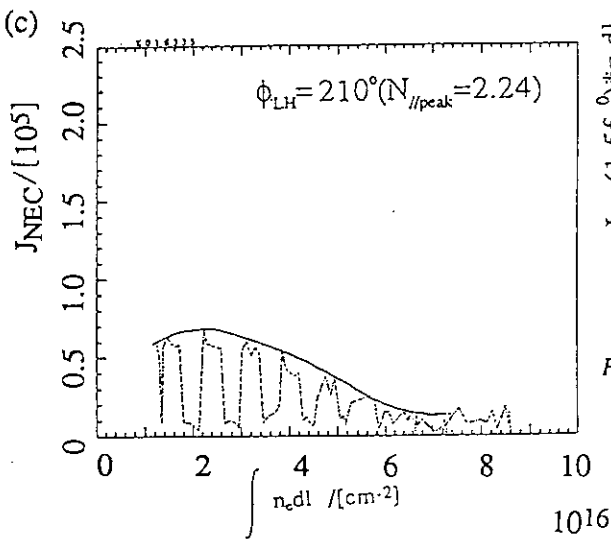
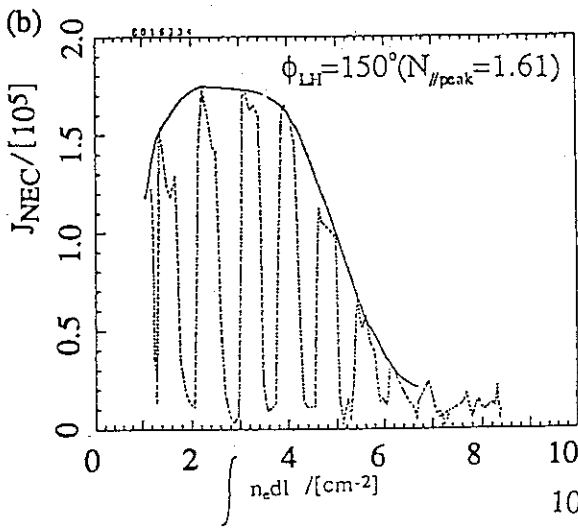
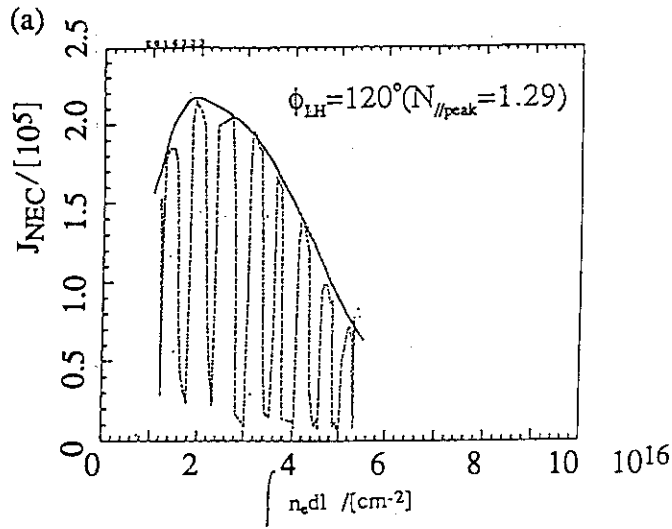
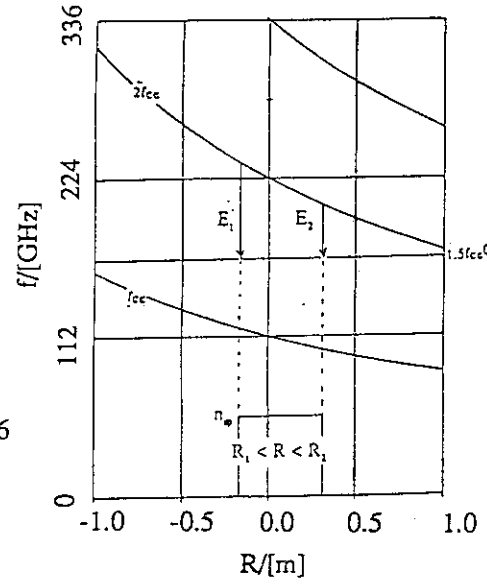
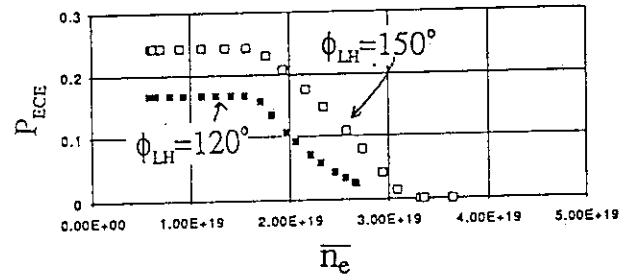
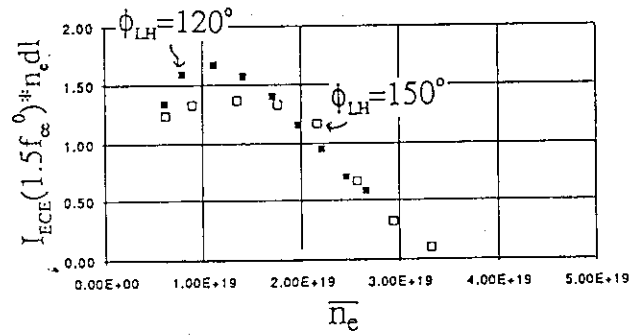


Fig.1. Power spectra of LH multi-junction launcher

Fig.2. Typical time evolution of plasma parameters. I_{ECE} unit is $W/Hz/m^2/1sr$.




Fig.3. Density dependence of J_{NEC} .

Fig.4. Schematic diagram of R_i and E_i .

Fig.5. Calculated electron density dependence of P_{ECE} .

Fig.6. Experimental electron density dependence of J_{NEC} .

5.6 Identification of the Direct Loss of Energetic Electrons During LHCD

K. Ushigusa, T. Kondoh, O. Naito, T. Imai, Y. Ikeda, M. Satou, Y. Kamada

Abstract

The absolute value of the direct lost power through energetic electrons during LHCD discharges is measured by the calibrated divertor x-ray signal. Measured loss is fairly low as suggested in last experiments. The relation between the accessibility condition and the directly lost power, and the profile of energetic electron on divertor plates are discussed. Frequency response of direct loss power is analyzed by a simple model.

1. Direct Loss Power and the Slowing Down Time

In last review of 1991, it has been reported that the soft x-ray signal from the divertor plates during LHCD discharges is a good measure of the direct loss of energetic electrons[1]. However, there was no proof of the proportionality between the divertor x-ray signal and the directly lost power through energetic electrons. The recent experiments carried out by D. Ress et al. [2] has shown that the thick target x-ray flux is directly proportional to the electron power loss with little dependence on the electron distribution function when x-ray flux is measured by an x-ray diode sensitive at photon energy much less than the characteristic energy of the electron distribution. In LHCD experiments, resonant energy of electrons accelerated by LH waves ranges from 60 to 700keV. Since the photon energy measured in the divertor x-ray detector (typically < 15keV) is much less than that of electrons accelerated by LH waves in present experimental conditions, we can use the divertor x-ray signal to obtain the power lost directly through energetic electrons. The calibration was performed by using a transient loss of energetic electrons (the EEP)[3].

In Fig. 1, the directly lost power through energetic electrons is divided by the injected LH power and plotted against the slowing down time[1], which is estimated at the velocity corresponding to the $N_{||peak}$. The direct loss power is roughly proportional to the slowing down time for wide range of τ_{SD} and indicating that the slowing down is dominant in JT-60U LHCD plasmas. It is worthwhile to extrapolate the direct loss of energetic electrons in ITER based on the JT-60U results. In ITER, steady state operation is expected at $n_e \sim 8.3 \times 10^{19} \text{m}^{-3}$ with $N_{||} \sim 1.8$ ($P_{LH} \sim 50 \text{MW}$). Corresponding slowing down time becomes 2 - 3 ms. Then the lost power rate through energetic electrons in ITER can be estimated to be $P_{Loss}/P_{LH} \sim 0.2\%$ as shown in Fig. 1. When we consider the confinement improvement of energetic electrons due to the higher plasma current[1,3], the direct loss power in ITER may be negligibly small.

Since almost all of the launched wave used in the experiments discussed in Fig.1 satisfies the accessibility condition, there is no necessity to take this into account. When the launched

peak $N_{||}$ is close to the minimum accessible $N_{||}$ ($N_{||}^{acc}$), a significant fraction of the launched power may be lost. The direct loss of energetic electrons also must be affected by the accessibility condition. To study this effect, we will compare two different cases where the electron density was increased linearly with time during the LHCD pulse. In the first case, waves with $N_{||}^{peak} > N_{||}^{acc}$ were injected and therefore almost all injected power satisfies the accessibility condition. In the second case, waves with $N_{||}^{peak} \sim 1.3$ were injected, and the minimum accessible $N_{||}$ becomes higher than the launched $N_{||}^{peak}$ during the LH pulse. This second case must be affected significantly by the accessibility condition. In Fig. 2, the direct lost power normalized by the injected power is plotted against the slowing down time of the electron velocity corresponding to $N_{||}^{peak}$. Results for the first case are shown as open squares, and for the second case as open circles. There is a large difference between these two plots. Solid circles in Fig. 2 are the results of the second case with the direct lost power divided by the accessible power. The accessible power is estimated using the launched spectrum and the accessibility condition calculated for the line average density and the central toroidal field. The slowing down time which corresponds to the larger of $N_{||}^{acc}$ and $N_{||}^{peak}$ is used as the abscissa in Fig. 2. By employing these corrections, the set of data appears almost on the same line. This suggests that the inaccessible power is not absorbed by energetic electrons and the estimation of the accessible power employed here is not inconsistent to the experimental results.

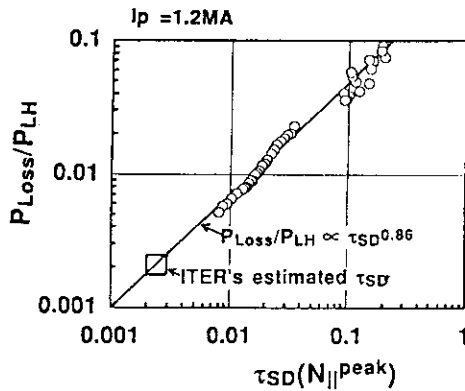


Fig.1 Direct loss power of energetic electron power against the slowing down time.

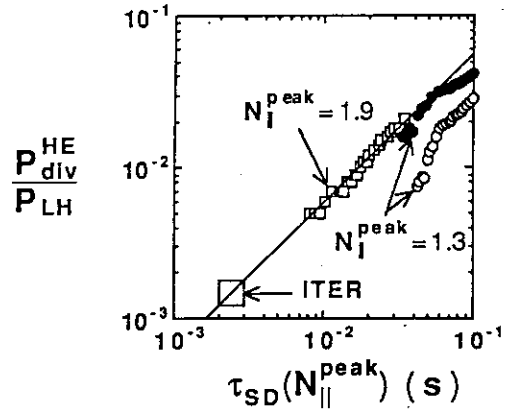


Fig.2 Same plot as Fig. 1. Effect of the accessibility condition on the direct loss where the accessibility condition is taken into account in solid circles

2. Distribution of Energetic Electrons on the Divertor Plates

Energetic electrons which cross the separatrix go to the divertor plate along with the magnetic field line and reach the divertor plate quickly. Therefore the profile of energetic electrons on the divertor plate may be very narrow compared with the thermal particles. It is important to study the width of reached energetic electrons on the divertor plates because its peakness is important factor of the heat flux density. In order to study the profile of energetic

electrons on the divertor plates, the height of null-point was swept during the LH pulse with a constant clearance between the launcher and the outermost plasma surface. And the time evolution of the divertor x-ray signal was measured. Figure 3a shows the change in the configuration of this null-point sweep where the solid line is the viewing chord of the divertor x-ray detector. The profile of divertor x-ray signal is easily obtained from the time evolution of divertor x-ray signal and plotted in Fig. 3b where the horizontal axis is the relative distance on the divertor plate (positive is outside). Figure 3b indicates that the profile of energetic electrons on the divertor plates has a typical half width of around 2cm. This width is apparently narrow compared with the thermal particles. The half width of the divertor heat flux measured by IRTV, which is though to be mainly the thermal heat load, is $\sim 5\text{cm}$ at $n_e = 0.4 - 0.5 \times 10^{19}\text{m}^{-3}$ in LHCD discharges (see Sec. 4.12). The poloidal Larmor radius of energetic electron which has the velocity corresponds to the wave phase velocity $c/N_{||}$ is $\rho_e(\text{cm}) = 0.85/N_{||}/(1-1/N_{||}^2)^{0.5}$ for $I_p = 1.2\text{MA}$. With $N_{||} = 1.2$, which corresponds the accessibility condition in this case, the poloidal Larmor radius becomes $\sim 1.2\text{cm}$. This is almost half of the measured half-width of energetic electron profile on the divertor plates. The profile of energetic electrons on the divertor plates may depends on the plasma current, the electron energy, the magnetic turbulence at the plasma edge and so on. Further studies should be performed to understand the profile of energetic electrons at scrape-off layer.

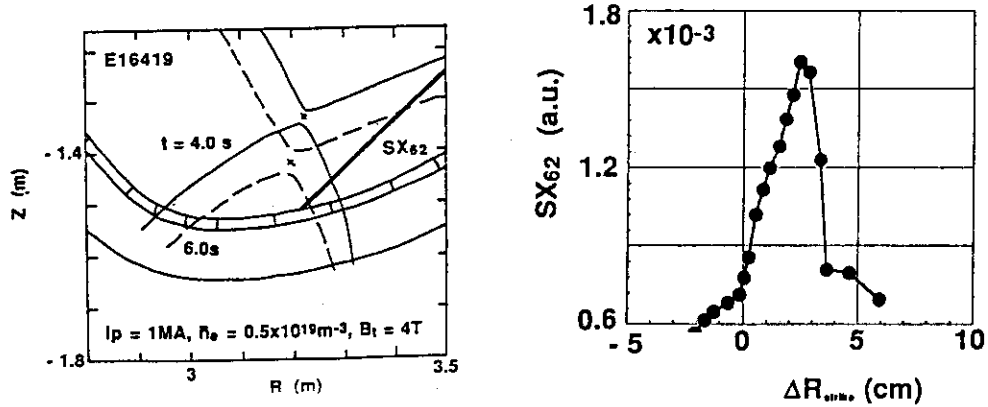


Fig.3 (a) Configurations of null-point sweep and the viewing chord of the divertor x-ray detector.

(b) Radial profile of divertor x-ray signal.

3. Response of Divertor X-ray Signal in Modulated RF Injection

To study the time response on the divertor x-ray signal, a sinusoidally modulated LH power was injected. A typical example is shown in Fig.4a where the LH power with $N_{||\text{peak}} = 2.24$ is modulated at a frequency of 5Hz. The divertor x-ray signal oscillates with the same frequency. Using numerical fitting, the phase difference between the modulated power and the fitted x-ray signal, and the oscillating amplitude of x-ray signal are determined from these time evolutions. Figure 4b shows the relative oscillating amplitude at modulation frequency, and the

phase difference against the modulation frequency. The phase difference increases and the amplitude decreases with increasing the modulation frequency. These responses can be understood by a simple model. From energy balance of energetic electrons, the electron tail energy is described by $W = P_{LH} / (i\omega - 1/\tau_{SD} - 1/\tau_{Loss})$, where ω , τ_{SD} and τ_{Loss} are the angular frequency of modulated LH power, the slowing down time and the characteristic time of energetic electron loss, respectively. The lost power is given by $P_{Loss} = W/\tau_{Loss} = A \exp(-\phi)$ where $A = 1/(1+\omega^2\tau_a^2)^{0.5}/(1+R)$, $\phi = \tan^{-1}(\omega\tau_a)$, $\tau_a = \tau_{SD}R/(1+R)$ and $R = \tau_{Loss}/\tau_{SD}$. Curves in Fig. 4b show the amplitude A and the phase difference ϕ in above equations with an appropriate slowing down time ($\tau_{SD} \sim 20\text{ms}$), where the solid and broken lines are calculated with τ_{Loss}/τ_{SD} of ∞ and 1, respectively. Experimental results indicates that the characteristic loss time of energetic electrons in this case is much longer than the slowing down time. The slowing down process is dominant compared with the loss of energetic electrons. This conclusion is consistent with the parameter dependence of direct loss power[3]. Although the phase difference is limited at $\phi = \pi$ in this simple model, we observed the phase difference larger than π in low $N_{||}$ injection with a high frequency modulation. This fact indicates the limit of this simple zero-dimensional model. More accurate model which contains both radial and velocity space diffusion should be used to analyzing these experiments.

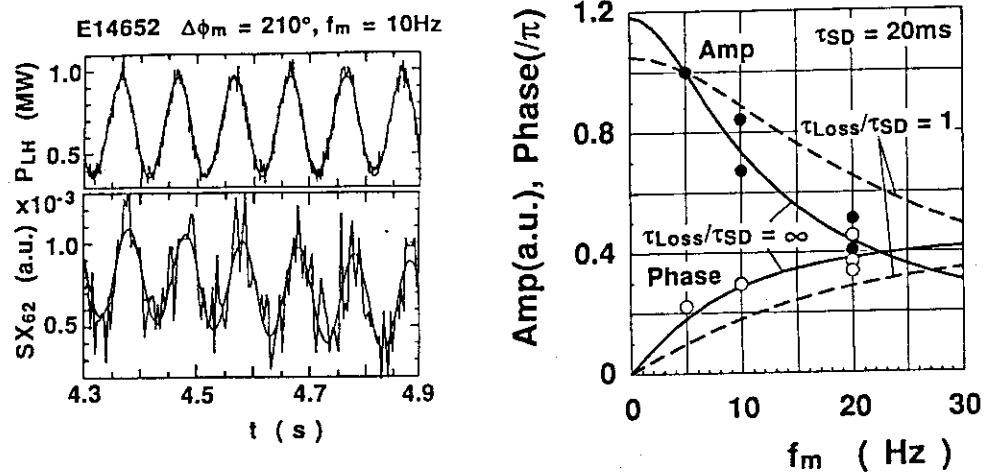


Fig. 4 (a) Time evolution of modulated LH power and the divertor x-ray signal.

(b) The phase difference between LH power and divertor x-ray signal and the relative amplitude of oscillating div. x-ray signal against the modulation frequency. Solid and broken lines show the calculated results for $\tau_{SD}=20\text{ms}$ with $\tau_{Loss}/\tau_{SD} = \infty$ and 1, respectively.

References

- [1] JT-60 Team, JAERI-M 92-073, (1992) Sec. 11.11.
- [2] RESS, D., RICE, B.W. and HORTON, R.D., Rev. Sci. Instrum., 61(1990)2777.
- [3] USHIGUSA, K., KONDOH, T., NAITO, O., et al., Nucl. Fusion 32(1992)1977.

5.7 Measurement of Pressure Anisotropy in LHCD Discharges

S W Wolfe, K Ushigusa, T Imai, T Kondoh

1. Introduction

To optimise the lower hybrid current drive (LHCD) efficiency for possible application to a future fusion reactor, a thorough understanding of the electron distribution function is desirable. The lower hybrid wave propagating parallel to the magnetic field interacts with high energy electrons to produce an enhanced fast electron population and anisotropy in velocity space. This interaction, and factors which counteract it, have complicated dependencies on parameters of the launched wave and target plasma, such as injection angle, parallel index of refraction $N_{||}$, electron temperature and density profiles, effective charge number Z_{eff} , and current profile. Quantifying the effects on the electron distribution function is therefore important. The simplest method of obtaining crude information on averaged quantities such as plasma beta, anisotropy, and internal inductance is to use magnetic measurements [1-3]. These can be supplemented by measurements of hard x-ray emission profiles, which can provide insights into the power deposition profile and fast electron distribution (see Kondoh *et al.*, Section 5.2 of this report; also [4,5]).

2. Calculation of Anisotropy

On JT-60U, measurements of the diamagnetic flux and plasma equilibrium have been used to determine pressure anisotropy in the following way: A boundary identification code incorporating data from magnetic probes and flux loops on the vacuum vessel gives estimates of equilibrium parameters, including Shafranov Λ ($= \beta_p^{eq} + l_i/2$, where β_p^{eq} is the average of perpendicular and parallel β_p , and l_i is the plasma internal inductance coefficient). Data from diamagnetic loops are used along with these equilibrium estimates to give β_p^\perp . Therefore the quantity $D = \Lambda - \beta_p^{dia} = (\beta_p^\parallel - \beta_p^\perp + l_i)/2$ may be calculated. Its value will in general contain information about the anisotropy (through the difference between parallel and perpendicular beta) as well as the internal inductance.

The evolution of these quantities is shown for the typical LHCD discharge of Figure 1. The total plasma current of 1.2 MA was driven non-inductively at a toroidal field $B_T = 4$ T and a central line-averaged electron density n_e of less than $0.3 \times 10^{19} \text{ m}^{-3}$. The phasing $\Delta\phi$ between the modules of the multi-junction launcher was 135° , corresponding to a parallel index of refraction for the wave at the peak of the spectrum of 1.44. The quantity D shows an increase when LH power is applied, but there is also a slow downward trend in the waveform. This trend is due mainly to the expected slow change in l_i . Changes in the bulk plasma pressure will contribute little to this behaviour because of the tendency for the bulk to have an isotropic

distribution of pressure. Therefore, if D is measured a short time after LH switch-on, that is, before I_i has changed appreciably, then the increment ΔD will characterise the anisotropy of the fast electron population. An anisotropy parameter can be defined as $A = \Delta\beta_p^{\parallel}/\Delta\beta_p^{\perp} = 2\Delta D/\Delta\beta_p^{\perp} + 1$. In these experiments, a time of 0.3 s after the start of the LH was found to be sufficient to allow the fast electron population to respond while allowing only small changes in bulk plasma parameters and current profile.

3. The Database

Data from more than 100 LH discharges in 1992 were analysed to give a good statistical base. Plasma parameters were as follows: current $I_p = 1.2$ MA, toroidal field $B_T = 4$ T, and line-averaged electron density n_e from 0.4 to $2.4 \times 10^{19} \text{ m}^{-3}$, with Z_{eff} ranging simultaneously from 9 to 4. Lower hybrid power input to the torus P_{LH} ranged from 0.9 to 2.5 MW at 2 GHz, and the phasing $\Delta\phi$ between multi-junction modules was varied from 135° to 270° to give a range in N_{\parallel} , taken at the peak of the LH wave spectrum, of 1.4 to 2.9. The parameter ranges allowed dependencies on parallel index, density, and power to be investigated.

Since the precision of the equilibrium estimates and the diamagnetic data may be 10% or worse, the calculations are subject to large uncertainty. To maintain faith in at least the qualitative parameter dependencies, the discharges were discriminated as follows: 1) the plasma equilibrium parameters for all shots appearing on the same plot were similar (an indication of this was the proportionality constant between diamagnetic energy and beta); and 2) the residual toroidal electric field E_{OH} for all shots was much less than the critical field E_c for electrons resonant with the wave to run away ($E_{\text{OH}}/E_c < 0.1$). This is given by $E_c = m\gamma V / e\tau_{\text{SD}}$, where $m\gamma V$ is the momentum of electrons with speed V ($=c/N_{\parallel}$), γ is the relativistic gamma given by $\gamma = (1 - N_{\parallel}^{-2})^{-1/2}$ and τ_{SD} is their collisional slowing down time, given by

$$\tau_{\text{SD}} = \frac{4\pi\epsilon_0^2 m^2 \gamma^2 c^3}{\bar{n}_e e^4 \log\Lambda \cdot N_{\parallel}^3 (Z_{\text{eff}} + 1 + \gamma)}$$

For the calculation here, $Z_{\text{eff}}=5$ and the Coulomb logarithm $\log\Lambda=19$.

4. Parameter Dependence

Figure 2 shows the dependence of the anisotropy on parallel index (launcher phasing) for electron densities in the range 0.9 to $1.2 \times 10^{19} \text{ m}^{-3}$. The anisotropy (closed circles) decreases slightly as N_{\parallel} increases, but the dependence is weak. For comparison, the results of a two-dimensional Fokker-Planck code used to model the current drive process are also shown (the line labelled FP). The computation shows a stronger anisotropy, but the qualitative dependence is similar. Intuitively, one expects the anisotropy to decrease with index, since at

high $N_{||}$ the phase velocity of the wave is closer to the electron thermal velocity so that the slowing down process should be more effective in reducing the anisotropy.

Figure 3 shows the dependence on electron density at a fixed $N_{||}$ of 1.6 ($\Delta\phi=150^\circ$). Here, the anisotropy is seen to decrease with density. This behaviour disagrees with the hard x-ray measurements of Kondoh *et al.* (Section 5.2 of this report). The model, on the other hand, predicts little, if any, dependence on density, except at densities less than about $1 \times 10^{19} \text{ m}^{-3}$, when the anisotropy is seen to increase. Again, this agrees qualitatively with the experimental results, while there is a substantial disagreement in the magnitude of the anisotropy.

More investigation is needed to be able to explain the difference between the experimental results and the model, but it should be noted that any contribution to $\Delta\beta_p$ from the bulk plasma will tend to decrease the value of $\Delta\beta_p^{||}/\Delta\beta_p^\perp$ and wash out any parameter dependencies. Furthermore, the disagreement of the density dependence with the hard x-ray measurements may arise from differences in E_{OH}/E_c , because residual OH field is expected to enhance anisotropy. Other factors which should be considered when interpreting the results are the effects of non-negligible changes in internal inductance and variations of the driven current profile with $N_{||}$. These factors would affect the validity of the initial assumption of $\Delta I_1 \approx 0$.

5. Summary

In summary, the anisotropy in the pressure distribution during LHCD on JT-60U has been deduced using the magnetic measurements (estimates of equilibrium parameters and diamagnetic beta). It is seen to decrease with parallel index and density, although the dependencies are weak. This agrees qualitatively with the results of a 2-D Fokker-Planck code, but quantitatively the measured magnitude is about a factor of two smaller than the prediction. The density dependence disagrees with hard x-ray measurements, and residual electric field may explain this. Other factors which may affect the measurements and which are presently not completely controllable or not well-determined are the precision of the equilibrium estimates, Z_{eff} , driven current profile, bulk plasma changes, and wave accessibility. More work is necessary in order to take these effects into account.

References:

- [1] WOOTTON, A.J., COOPER, W.A., Plasma Phys. **24** (1982) 1183.
- [2] USHIGUSA, K. *et al.*, Nucl. Fusion **29** (1989) 1052.
- [3] LEUTERER, F *et al.*, in Controlled Fusion and Plasma Physics (Proc. 19th EPS Conf. Innsbruck 1992) Vol. 16C Part II, European Physical Society (1992) 957.
- [4] von GOELER, S. *et al.*, in Controlled Fusion and Plasma Physics (Proc. 19th EPS Conf. Innsbruck 1992) Vol. 16C Part II, European Physical Society (1992) 949.
- [5] FROISSARD, P. *et al.*, in Controlled Fusion and Plasma Heating (Proc. 18th EPS Conf. Berlin 1991) Vol. 15C Part III, European Physical Society (1991) 389.

FIG. 1: Evolution of plasma parameters during LHCD: a) plasma current I_p and loop voltage V_{loop} ; b) LH power P_{LH} and central line-averaged electron density n_e ; c) Shafranov lambda from magnetic measurements, β_p^{dia} from diamagnetic flux, and their difference.

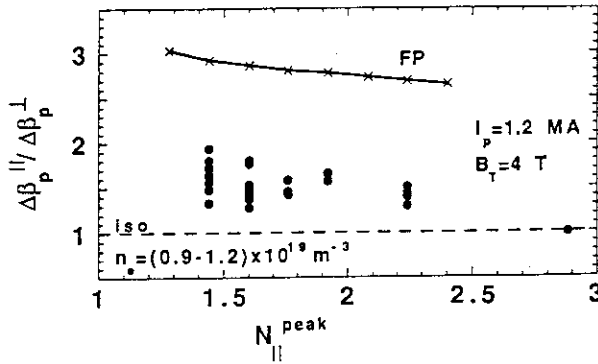
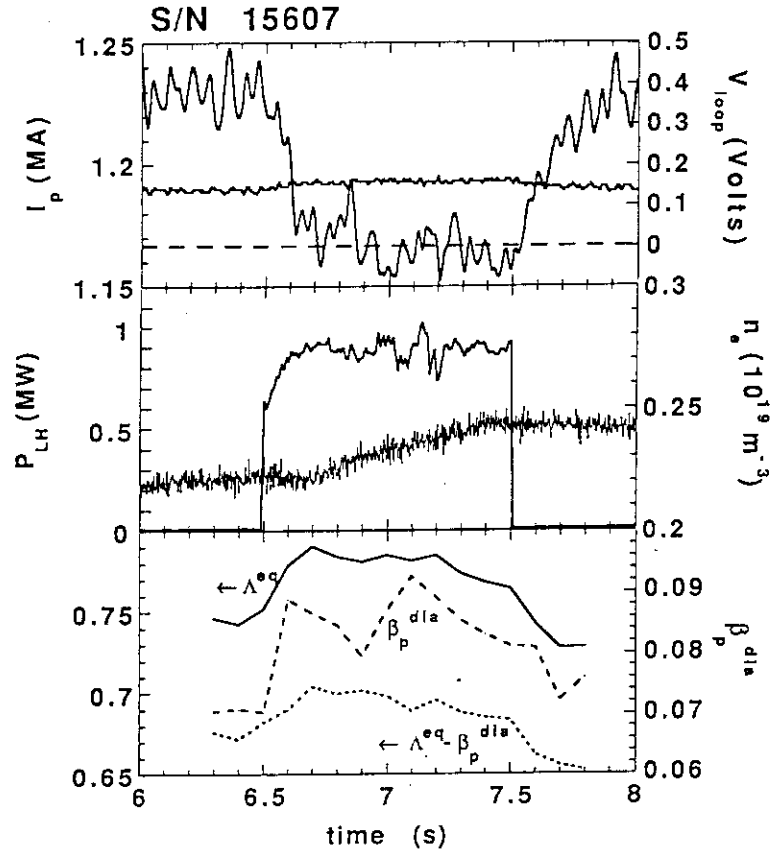


FIG. 2: Dependence of pressure anisotropy on parallel index of refraction of the launched wave. Closed circles are from the magnetic measurements; the line labelled FP shows the 2-D Fokker-Planck calculation.

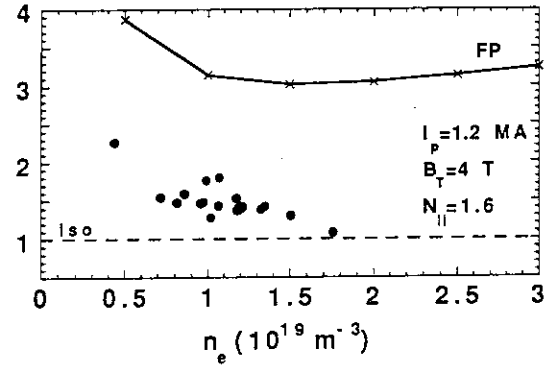


FIG. 3: Dependence of pressure anisotropy on plasma density. Closed circles are from the magnetic measurements; the line labelled FP shows the 2-D Fokker-Planck calculation.

5.8 Combined Fast Wave and Lower Hybrid Wave Experiment

T. Fujii, H. Kimura, T. Kondoh, M. Saigusa, Y. Ikeda, T. Imai,
S. Moriyama, M. Nemoto, K. Ushigusa

1. Introduction

Recently, the current drive mechanism by using a fast wave (FW) in the ion cyclotron range of frequencies (ICRF) are intensively investigated in tokamaks [1, 2], because their power is more absorbed by electrons via Landau damping and transit time magnetic pumping (TTMP) in hotter and denser plasmas and therefore ICRF fast wave current drive is quite attractive in a reactor grade tokamak. However, the power absorption of the ICRF fast wave is not strong in the present tokamaks since the electron temperature is not sufficiently high, and then the demonstration of the fast wave current drive is difficult even in JT-60U where the central electron temperature in target ohmic discharge plasmas is as low as about 3 keV. Accordingly, expecting enhancement of fast wave-electron coupling by high energy electrons generated by LH waves, the combined ICRF fast wave and LH wave experiment has been carried out on JT-60U at $B_T = 3.2$ T so that ion cyclotron harmonic resonance layers are off-axis. The fast wave-electron coupling properties are investigated by scanning the peak $n_{//}$ value of power spectrum of the fast waves as well as of the LH waves at low electron densities.

2. Experimental Conditions

We examine the electron heating by off-axis ICRF heating in combination with low power LHRF heating at $B_T = 3.2$ T and $f = 116$ MHz in helium discharges. In this condition the second and third harmonic resonance layers of hydrogen, which remains in the helium plasma, are off-axis at $x = -0.6$, 0.75 m, respectively, as shown in Fig. 1. Small power absorption by ions may be expected from the results of the previous experiments on JT-60 in Ref. [3] so that resulting FW power may couple to electrons in the plasma core. Target ohmic plasma parameters are : the line-averaged electron density $\bar{n}_e = 0.4 - 1.5 \times 10^{19} \text{ m}^{-3}$, the plasma

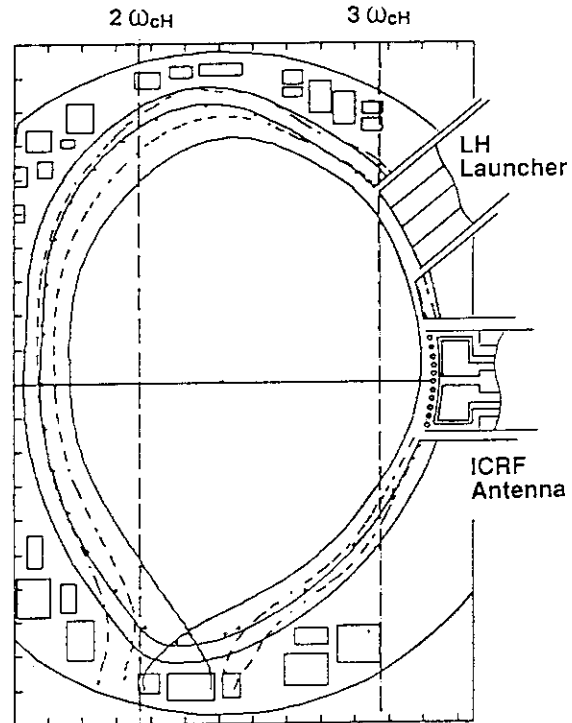


Fig. 1 Ion cyclotron resonance layers for $B_T = 3.2$ T and the applied ICRF frequency $f = 116$ MHz.

current $I_p = 1.2$ MA, the effective safety factor $q_{\text{eff}} = 7.4$. Applied wave powers are: ICRF power $P_{\text{IC}} = 0.8 - 1.8$ MW and LH power $P_{\text{LH}} = 0.9 - 1.5$ MW at 2 GHz. A multijunction type of LH launcher is installed into the vacuum vessel at a poloidal angle of 40m degrees. The radiated power n_{\parallel} spectrum of the LH waves is 1.3 to 2.5 by changing the toroidal phase difference $\Delta\phi$ of the LH launcher from 120 to 240 degrees. On the other hand two ICRF antennas are located at equatorial ports. The radiated power n_{\parallel} spectrum of the ICRF fast waves is changed by phasing the antenna currents toroidally by 0, 90 and 180 degrees, that is, (0, 0), $(\pi/2, 0)$ and $(\pi, 0)$ modes. The JT-60U ICRF antenna has a poloidal septum at the center position to decoupling between toroidally adjacent current straps. So that its peak k_{\parallel} value is not exactly calculated by the present code, but it is approximately 0 for (0, 0) mode, 1.5 - 2 for $(\pi/2, 0)$ mode and 2 - 3 for $(\pi, 0)$ mode.

3. Experimental Results

Although we have conducted the combined heating with scanning the LH phasing from 120 to 240 degrees, we focus the data for $\Delta\phi = 150$ degrees ($n_{\parallel/\text{peak}} = 1.6$) in this section. Typical results, time evolution of the stored energy W_{DIA} , \bar{n}_e , the radiation loss P_{rad} , one turn loop voltage V_L , P_{IC} and P_{LH} for the $(\pi, 0)$ mode at the target plasma densities of $\bar{n}_e = 1 \times 10^{19} \text{ m}^{-3}$ and $0.4 \times 10^{19} \text{ m}^{-3}$ are shown in Fig 2 (a) and (b), respectively. In the higher density case the electron density increases by 40 % during ICRF pulse of 1.7 MW applied at 1 sec later LH pulse of 1 MW. The loop voltage also increases by about 0.06 V of 10% of the total value. On the other hand, in the low density case the loop voltage does not change although the electron density increases by about 100% in combination of 1.8 MW ICRF and 1.5 MW LHRF powers.

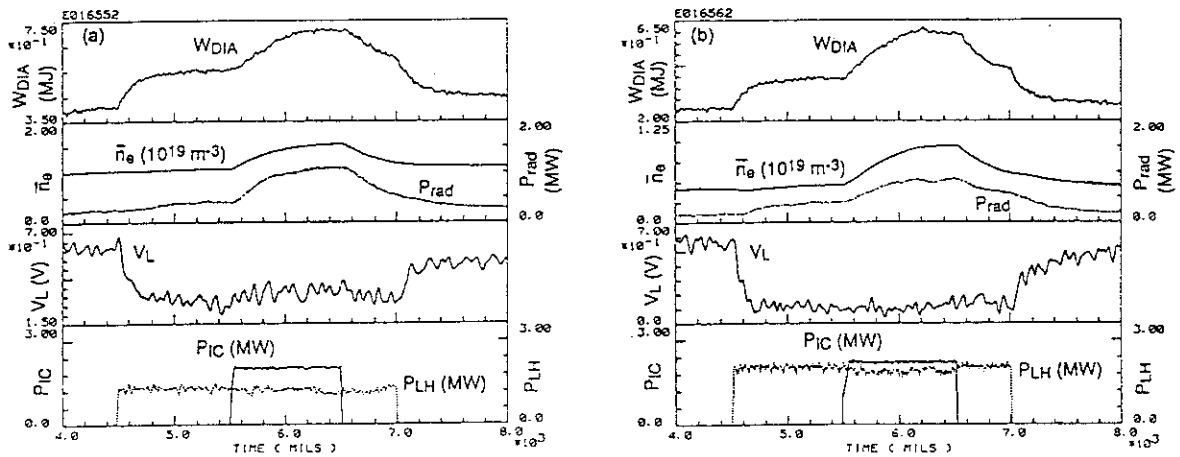


Fig. 2 Time evolution of W_{DIA} , \bar{n}_e , P_{rad} , V_L , P_{IC} and P_{LH} for $(\pi, 0)$ mode in combined ICRF and LH wave heating at target plasma density of (a) $1 \times 10^{19} \text{ m}^{-3}$ and (b) $0.4 \times 10^{19} \text{ m}^{-3}$.

Figures 3 (a) and (b) show time evolution of Hard X-ray (HX) emission for the shots shown in Fig. 2 (a) and (b) respectively. Signals coming from 1 to 7 channel indicate $T_{HX\perp}$ in photon energy range of 100 - 200 keV at $r/a = 0.7$ to 0.2 and a signal from 8 channel $T_{HX\parallel}$. In comparison of figures, $T_{HX\perp}$ tends to increase in the higher density case, increasing loop voltage during ICRF pulse, while it tends to decrease or be constant in the low density case, unchanging loop voltage. $T_{HX\parallel}$ increases in both cases but smaller in the low density case. Considering that $T_{HX\perp}$ and $T_{HX\parallel}$ increase with increasing loop voltage after LH pulse, it is inferred that the ICRF fast waves couple to fast electrons in the low density case so as to keep the loop voltage constant.

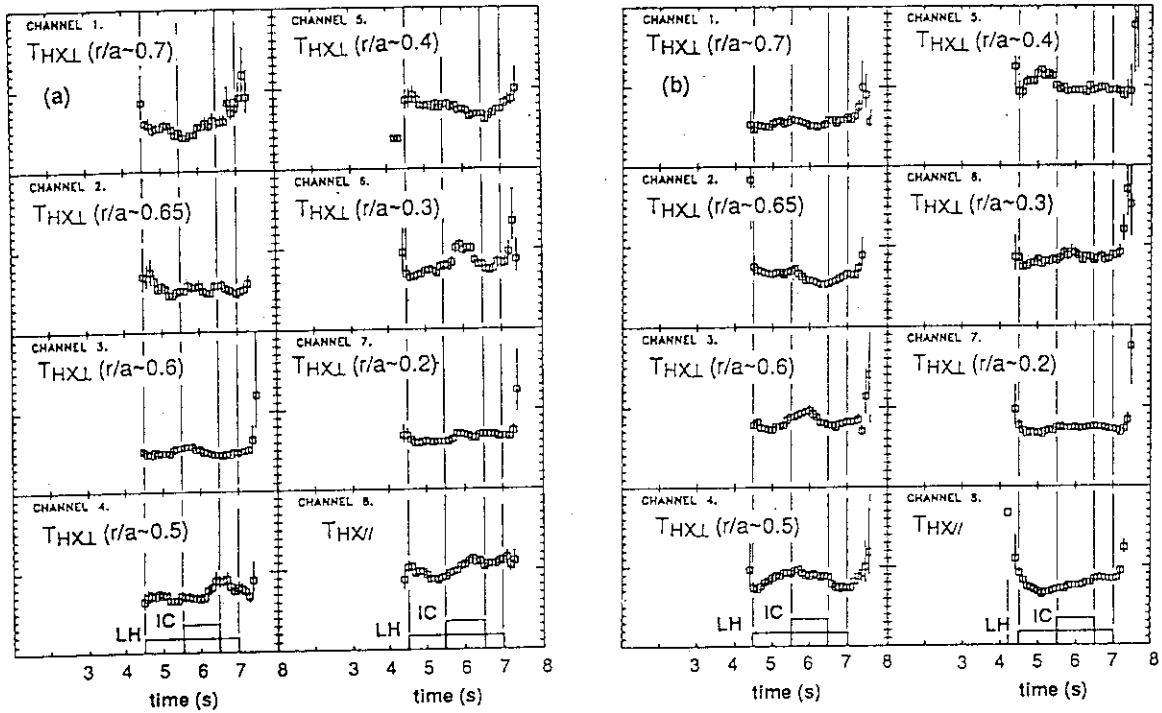


Fig. 3 Time evolution of Hard X-ray emission at target plasma density of (a) $1 \times 10^{19} \text{ m}^{-3}$ and (b) $0.4 \times 10^{19} \text{ m}^{-3}$ for the shots shown in Fig. 2 (a) and (b), respectively.

Figure 4 shows the increase in the loop voltage as a function of target plasma density for three ICRF phasing modes. Here, (0, 0) phasing data is obtained at $B_T = 4 \text{ T}$ different from others. The loop voltage increases clearly at target plasma densities more than $1 \times 10^{19} \text{ m}^{-3}$ for $(\pi, 0)$ mode. The increase in the loop voltage does not seen for any phasing mode at least in low densities. However, it is unclear whether the change in the loop voltage between phasing modes is different.

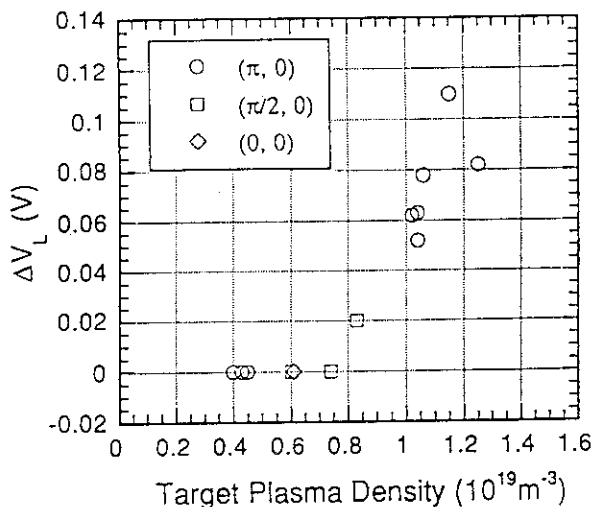


Fig. 4 Increase in the loop voltage as a function of target plasma density for three ICRF phasing modes. Here, $(0, 0)$ phasing data is obtained at $B_T = 4 \text{ T}$ different from others at $B_T = 3.2 \text{ T}$.

4. Summary and Discussion

We have examined the fast wave-electron coupling by the combined ICRF fast wave and LH wave heating in helium discharges at power levels of $P_{IC} = 0.8 - 1.8 \text{ MW}$ and LH power $P_{LH} = 0.9 - 1.5 \text{ MW}$. The different change in loop voltage is observed for $(\pi, 0)$ mode between target plasma densities of $\bar{n}_e = 1 \times 10^{19} \text{ m}^{-3}$ and $0.4 \times 10^{19} \text{ m}^{-3}$. From HX measurements, the fast wave-fast electron coupling may take place somewhat in the lower density case, but the quantitative estimation is quite difficult.

In further investigation, we should condition the wall, for example by boronization, and condition the antennas sufficiently so that the electron density keeps constant in application of ICRF power. Moreover, the higher electron temperature conditions, such as smaller plasma volume and higher plasma currents, are better for fast wave-electron coupling because it seems that the change in loop voltage does not become smaller and further the interaction between ICRF waves and the wall and the resulting electron density increase may reduce as the ICRF power absorption increases with the electron temperature.

References

- [1] START, D.F.H., et al., Nucl. Fusion **30** (1990) 2170.
- [2] PINSKER, R.I., et al., 14th Int. Conf. Plasma Phy. and Cont. Nucl. Fusion, Wurzburg (1992) IAEA-CN-56/E-2-4.
- [3] FUJII, T., et al., JAERI-M 90-066 (1990) pp115 - 118.

5.9 Hard X-ray Measurement in Combined Fast Wave and Lower Hybrid Wave Experiment

T. Kondoh, T. Imai, K. Ushigusa, T. Fujii and H. Kimura

1. Introduction

Theories predict fast waves in ion cyclotron range of frequency (ICRF) can drive non-inductive current in high density region through electron Landau damping (ELD) or transit-time magnetic pumping (TTMP). It is expected to be used as current drive or current profile control method in the central region of the reactor plasma.

Details of the combined fast wave (FW) and lower hybrid wave (LHW) experiment is described in previous section [1]. Thus, we emphasize on hard x-ray measurement of these experiments in this section. To investigate synergistic effects between fast waves and lower hybrid waves on current drive efficiency we measure hard x-ray spectrum. Hard x-ray spectra are measured by 7-channel sodium-iodide (NaI(Tl)) array and a tangential NaI(Tl) detector.

First experiment is to study the synergistic effect between TTMP and LHCD. In this experiment, there are no resonance in the core plasma.

The second experiment is to investigate the synergistic effect between LH wave and second harmonic ion cyclotron regime. In this shot hydrogen resonance is located near the center of the plasma. Fast wave with low parallel index of refraction should be mode converted into ion Bernstein waves (IBWs) if the hydrogen beta were sufficiently high. These electrostatic waves are expected to interact with fast electrons.

2. Results of TTMP and LHCD Combination

First experiment is to study the synergistic effect between TTMP and LHCD. Electrons directly absorb fast waves via TTMP when resonance condition is satisfied.

Figure 1 shows temporal evolution of plasma parameters. Phasing of ICRF antenna is $(\pi, 0)$ and peak refractive index of excited wave $N_{\parallel \text{peak}}$ is 2.2. Working gas is helium with residual hydrogen and deuterium. Toroidal magnetic field B_T is 3.2 T and there is no ion cyclotron resonance in the core plasma. Before ICRF injection, LHW is applied to generate fast electrons which should interact with fast waves through TTMP. Peak refractive index of LHW is 1.77. After IC is applied, electron density and loop voltage rise up. Hard x-ray temperature $T_{HX\parallel}$ rises up from 60 keV to 85 keV.

Hard x-ray temperature is strongly influenced by loop voltage [2] as shown in Fig. 2. Triangle, square and closed circle indicate $T_{HX\parallel}$ versus loop voltage V_L when $N_{\parallel \text{peak}} = 1.44, 1.61$ and 1.92 , respectively. Large circles indicate $T_{HX\parallel}$ when LH only and combination of LH+IC.

Though THX is increased after IC injection, increase of THX may be caused by increase of loop voltage from Fig.2. Thus, we can not conclude that synergistic effect between IC and LH on hard x-ray temperature exists or not.

3. Results of ICH and LHCD Combination

The second experiment is to study the synergistic effect between FW and LHCD through mode conversion to IBW. Toroidal magnetic field B_T is 4T. There is second harmonic hydrogen resonance near the center of the plasma. Theoretical prediction shows if the hydrogen beta were high, fast waves with low parallel refractive index should be converted into IBWs. Fast electron produced by LHW can interact IBWs through Landau damping as a result.

Figure 3 shows temporal evolution of plasma parameters. Phasing of ICRF antenna is (0,0). Working gas is hydrogen with residual deuterium. Before ICRF injection, LHW is applied to generate fast electrons. Peak refractive index of LHW is 2.24 corresponding energy of resonant electron is 60 keV.

Figure 4(a) shows hard x-ray spectra during LH ($t = 4.7 - 5.5$ sec) and LH+FW phase ($t = 5.7 - 6.5$ sec). Slope of the HX spectrum during LH+FW is smaller than LH only. We should pay attention to effects of neutron yield because second harmonic resonance exists near the center of the plasma and residual deuterium is heated. Influence of neutron is negligible in LH phase. Solid curve in Fig. 4 (a) indicates x-ray spectrum due to g-ray caused by (n,γ) reaction. This curve is estimated using another shot heated by ICRF without LHW.

Figure 4 (b) shows HX spectra which is subtracted neutron effect. The slopes of the spectra agree within statistical errors. Thus, we conclude from this experiment that we can not observe the difference between slope of spectra during LH and LH+FW.

4. Summary

Unfortunately, in these preliminary experiments we can not observe synergistic effect between LH and FW on hard x-ray spectrum. Further investigation is needed avoiding neutron influence and loop voltage effects on hard x-ray spectrum.

References

- [1] Fujii, T., this report, Sec. 5.8
- [2] Kondoh, T., this report, Sec 5.2

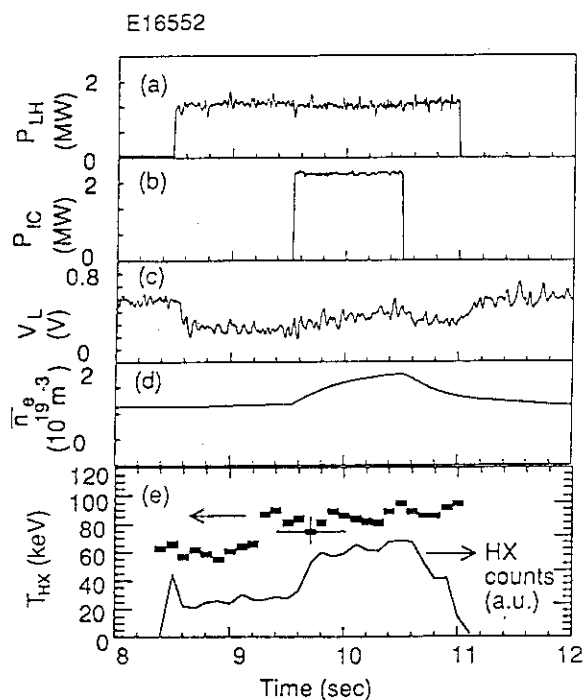


Fig.1 Temporal evolution of plasma parameters. (a) P_{LH} , (b) P_{IC} , (c) V_L , (d) hard x-ray temperature T_{HX} and hard x-ray counts of the parallel detector. Phasing of IC is $(\pi, 0)$ and peak refractive index of LH is 2.2

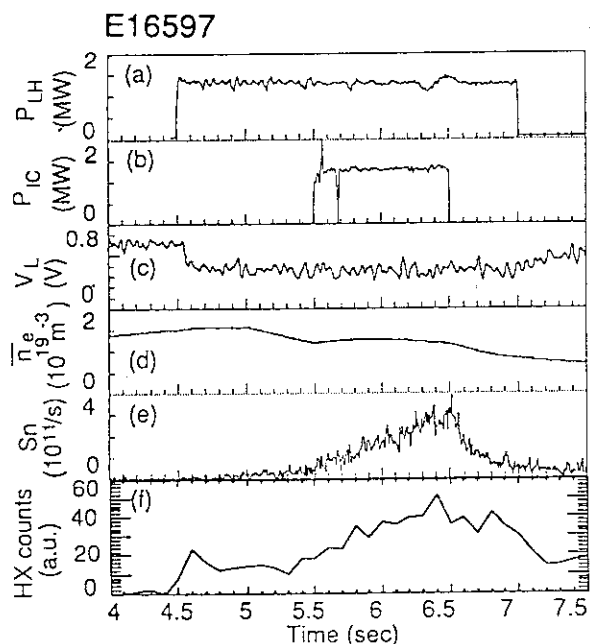


Fig.3 Temporal evolution of plasma parameters. (a) P_{LH} , (b) P_{IC} , (c) V_L , (d) neutron yield S_n , (e) hard x-ray counts. Phasing of IC is $(0, 0)$ and peak refractive index of LH is 2.24.

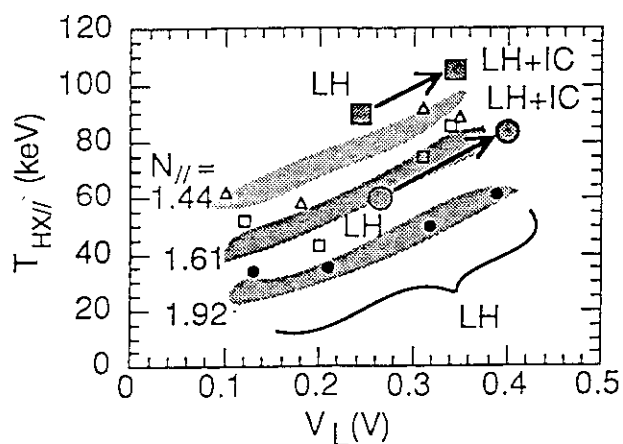


Fig.2 Hard x-ray temperature $T_{HX//}$ versus loop voltage V_L . Open triangle, open square and closed circle indicate $T_{HX//}$ when $N_{//peak} = 1.44, 1.61$ and 1.92 , respectively (LH only). Large circle indicate $T_{HX//}$ when LH only and combination of LH+IC (refractive index of LHW $N_{//peak}$ is 1.77) and large square indicate $N_{//peak}$ of LHW is 1.61.

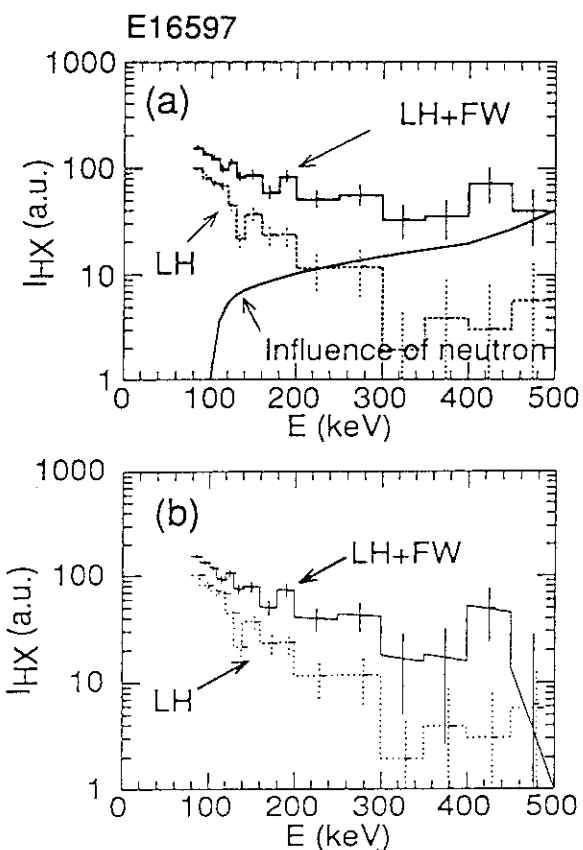


Fig.4 (a) Pulse height analysis of hard x-ray of parallel detector at $t = 4.7-5.5$ sec (LH) and $t = 5.7-6.5$ sec (LH+FW). Solid curve indicates influence of γ -ray caused by D-D neutron on HX spectrum while $t = 5.7-6.5$ sec. (b) HX spectrum which is subtracted γ -ray effects.

5.10 Progress in Bootstrap Current Study

M. Matsuoka, S. Ishida, Y. Kamada, and M. Kikuchi

1. Introduction

Bootstrap current was analyzed for both high poloidal beta β_p and high normalized beta β_N shots. In the high β_p experiment, relatively small plasma ($\sim 50 \text{ m}^3$) was produced at the inboard side to heat the central part of the plasma with high power density. The high β_p plasma is characterized by high temperatures ($T_{e0} \sim 10 \text{ keV}$, $T_{i0} \sim 30 \text{ keV}$), peaked density profile, and β_p collapse within 1 sec after beam initiation. The high β_N was obtained with similar plasma configuration but with lower toroidal field. The characteristics of these shots are described in chapter 2 in detail.

2. Bootstrap Current in High β_p Plasma

Figure 1 shows the plasma stored energy W_s , β_p from diamagnetic measurement, surface plasma voltage V_s , and estimated bootstrap current of a typical high β_p shot. Solid lines and open circles are the experimental and the numerical result using 1.5D time-dependent code. The operating conditions are: $I_p = 1.3 \text{ MA}$, $B_T = 4.4 \text{ T}$, $P_{NB} = 18 \text{ MW}$, $q_{eff} = 7.8$. Beams were initiated at $t = 5 \text{ sec}$ and β_p collapse was occurred at $t = 5.75 \text{ sec}$. During this phase, the plasma stored energy increased almost linearly. Since a code-integrated value is available for the plasma density, we assumed the density profile with peaking factor which was obtained by matching both the plasma stored energy and the neutron production. The resultant time-evolution of V_s agrees well with the experimental data. The estimated bootstrap current just before β_p collapse is 0.65 MA , which is 50% of the total plasma current.

Bootstrap current in high β_p plasma mainly flows at $\rho \sim 0.5$ due to

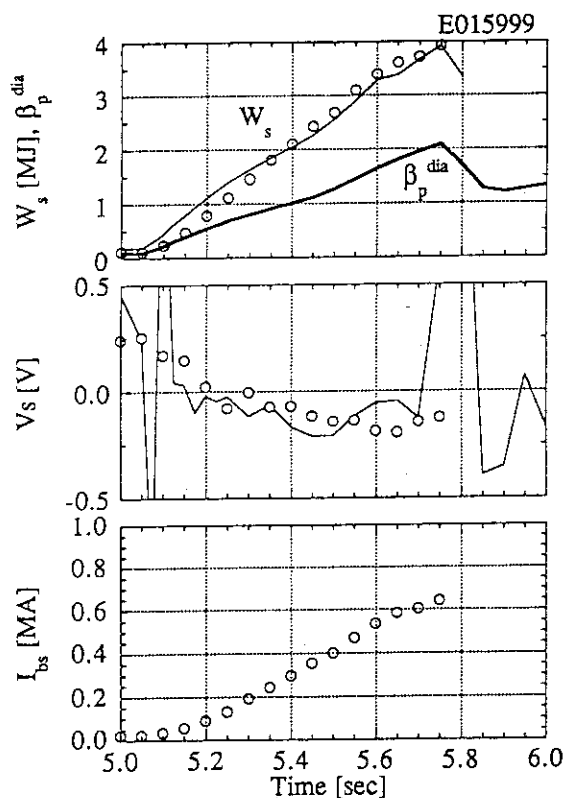


Fig. 1 Plasma stored energy W_s , diamagnetic poloidal beta β_p^{dia} , surface plasma voltage V_s , and estimated bootstrap current I_{bs} of a typical high β_p shot.

peaked density profile. This is in contrast to that in H-mode plasmas where bootstrap current mainly flows at the periphery of the plasmas. The numerical code predicts that, in the half way of the plasma minor radius, the electron temperature is still sufficiently high so that the profile of the total plasma current is almost unchanged due to long skin time in high β_p plasmas. This tendency can be seen from the evolution of the internal inductance l_i , which is obtained from magnetics. The upper graph in Fig. 2 shows l_i of the medium β_p shot in which no β_p collapse occurred. The central electron temperature was 7 keV just before beam termination and 2 keV at ohmic phase. We see that l_i was almost

unchanged just before and after beam injection. This indicates that the current profile was not modified by bootstrap current. Note that l_i during beam injection is not reliable since l_i from magnetics has less accuracy in high β_p phase. The lower graph in Fig. 2 shows l_i in a high β_N shot, which has lower electron temperature. The central electron temperature during beam injection was about 3.5 keV and decreased to 1.2 keV in later ohmic phase. On the contrary to the upper graph, the internal inductance after beam injection substantially decreased from that just before beam initiation in this case. In addition, the internal inductance recovered after beam injection very slowly, though the shot had a lower electron temperature than the upper graph shot.

3. Bootstrap Current in High β_N Plasma

Figure 3 shows loop voltage V_{loop} , line averaged electron density \bar{n}_e , and beam injection power P_{inj} of a typical high β_N shot, which is identical to the shot in the lower graph in Fig. 2. The loop voltage was kept negative during beam injection, which suggests a substantial part of the plasma current was replaced by bootstrap current. The loop voltage in the periods shown by arrows should be excluded from the present consideration since the plasma shape was changed in these periods. Both quasi-perpendicular and tangential beams were used in this shot but the tangential beams were balanced so that the beam driven current can be neglected.

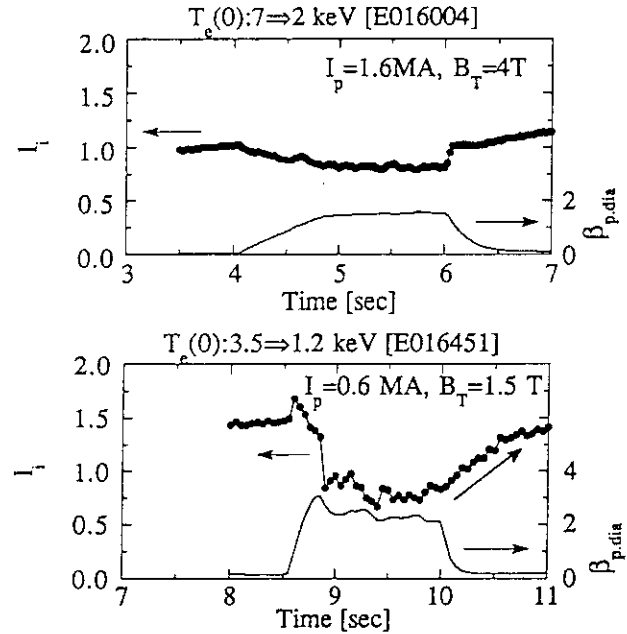


Fig. 2 Internal inductance l_i and diamagnetic poloidal beta β_p^{dia} of high β_p shot (upper graph) and high β_N shot (lower graph).

The poloidal flux function Ψ and the 'resistive' poloidal flux function Ψ_r of this shot are plotted in Fig. 4. The definition of Ψ_r is;

$$\Psi_r \equiv \Psi - \frac{1}{2\pi} \frac{1}{4} \mu_0 R_p I_p l_i.$$

Since surface loop voltage V_s and surface resistive loop voltage V_r were obtained by the following relations;

$$V_s = 2\pi \frac{d\Psi}{dt}$$

and

$$V_r = 2\pi \frac{d\Psi_r}{dt},$$

the gradient of each plot reflects V_s or V_r . The curve of Ψ is almost flat after $t=9$ sec, which indicates V_s is almost 0. Though the absolute value of l_i deduced from magnetics is not reliable in high β_p

phase, time-derivative of l_i can still be used if the plasma state is almost steady. In the period $t=9.5\sim 9.8$ sec, the plasma was fairly steady-state (see Figs. 2 and 3). If we consider Ψ_r in this period to be flat, the resistive loop voltage was 0, which means the current was fully driven by bootstrap current. If we consider the average in the period $t=9\sim 10$ sec (a straight line in Fig. 4), the resistive loop voltage becomes 0.1 V.

The analysis using ACCOME, a steady-state non-inductive current analysis code [1], predicts bootstrap current of 0.3 MA (50% of the total plasma current) and the resistive loop voltage of 0.11 V. If bootstrap current is neglected, the resistive loop voltage should be 0.22 V. Consequently, bootstrap current in the high β_N shot is equal to or higher than that predicted from the present theory.

3. Conclusion

The surface loop voltage of a high β_p shot reasonably agrees with the numerical result using 1.5D time-dependent code. The resistive loop voltage of a high β_N shot is equal to or

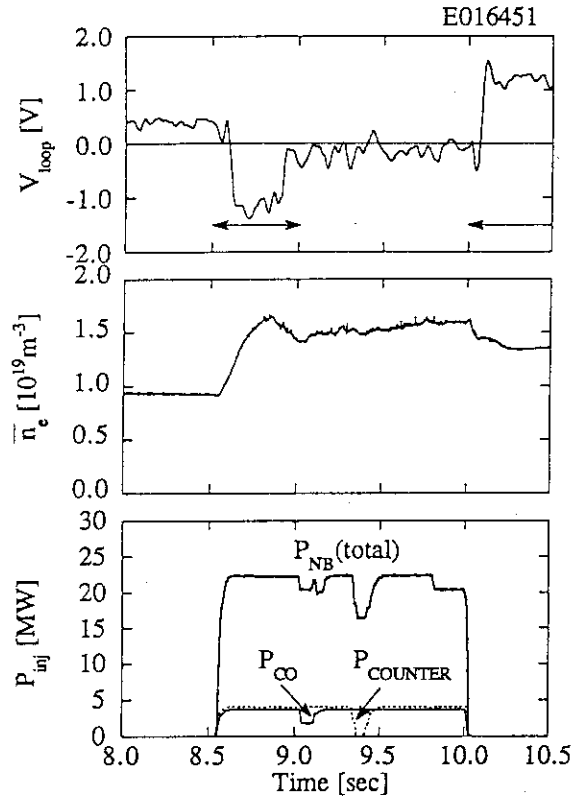


Fig. 3 Loop voltage V_{loop} , line averaged electron density \bar{n}_e , and beam injection power P_{inj} of a typical high β_N shot.

lower than that predicted using a steady-state code. In both cases, the bootstrap current is about 50% of the total plasma current. The total current profile was almost unchanged in the high β_p shot due to high electron temperature, while it was substantially changed in the high β_N shot.

References

- [1] TANI, K., AZUMI, M., and DEVOTO, R., S., J. Comp. Phys. **98** (1992) 332.

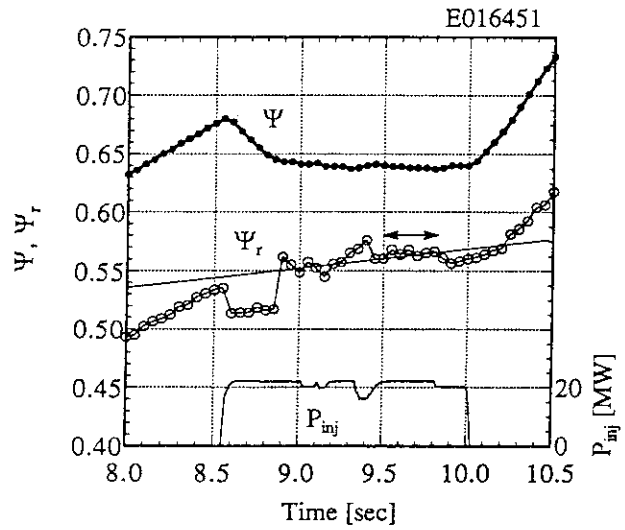


Fig. 4 Poloidal flux function Ψ and the 'resistive' poloidal flux function Ψ_r of a typical high β_N shot.

5.11 Current Drive by Using Tangential Neutral Beams

M. Matsuoka, M. Kuriyama, and K. Nagashima

1. Introduction

In a neutral-beam current-drive experiment, the poloidal beta often increases substantially since high power beams are injected. Consequently, the amount of beam-driven current is unclear since to separate beam-driven current from bootstrap current is difficult.

A sophisticated experiment on neutral-beam-driven current was performed in JT-60U, by comparing co- and counter-injected shots. In this method, the contribution of bootstrap current is nearly canceled out so that the amount of beam-driven current can be estimated directly from the experiment.

2. Comparison of Experimental and Numerical Results

Recently re-oriented beamlines from quasi-perpendicular beamlines were used in this experiment [1]. A pair of upper and lower beamlines are co-directed, and another pair are counter-directed with 2.86 m of tangential radius. The elevation angles of beam axis are $\pm 9^\circ$. A pair of upper and lower axes merge at the injection ports and diverge in the tokamak vacuum vessel so that the heating profile becomes off-axis with usual plasma configuration. Figure 1 shows the tangential beam axes and the plasma configuration ($R=3.4$ m, $a=0.9$ m) in this experiment.

Two successive shots are compared in Fig. 2. In the first shot (E016345, solid lines), counter beams (CTR) were injected first and later co beams (CO) were injected. In the next shot (E016346, dotted lines), the sequence for beams was reversed. The loop voltage V_l with counter beams is always higher than that with co beams, which indicates the existence of beam driven current. The condition for beam energy is same between co- and counter-injection phases; beam energies of the upper and lower beams were 90

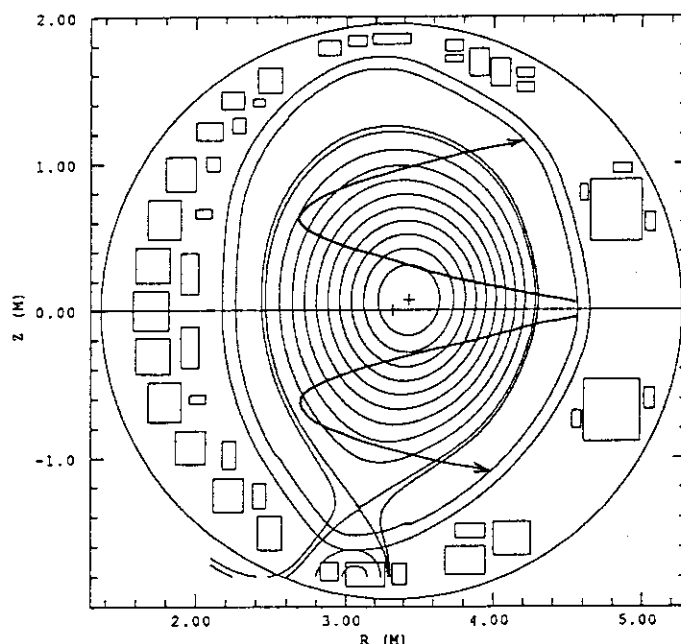


Fig.1 Tangential beam axes and plasma configuration.

and 85 keV, respectively. The beam power P_{inj} is about 3.6 MW for all cases. The central electron temperature evolved from 4 to 5 keV and the difference between shots is small (2 to 5%). The effective plasma charge was high (~ 4) due to low density operation.

Beam-driven current I_{nb} can be estimated from the average loop voltage V_l of two shots and the plasma current I_p ($=1.5\text{MA}$);

$$I_{nb} = I_p \times \frac{|\Delta V_l / 2|}{V_l} \quad (1)$$

where ΔV_l is the difference in V_l between two shots. The estimated beam-driven current and current drive efficiency $n_e I R / P_{inj}$ are also shown in the figure. The line averaged electron density \bar{n}_e^{U2} ($\rho_{min}=0.05$) was used in the calculation of the current drive efficiency. Solid circles in the figure are the values evaluated from the plasma surface loop voltage. The beam-driven current and the current drive efficiency are estimated to be 250-400 kA and $0.2-0.4 \times 10^{19} \text{ m}^{-2}$, respectively.

This experimental result was compared with the prediction of ACCOME code, a numerical code for steady-state, non-inductive plasma currents [2]. The predicted beam-driven and bootstrap currents for $t=6.75$ sec are 350 kA and 80 kA, respectively. The beam-driven current evaluated from the experiment is smaller than that from the

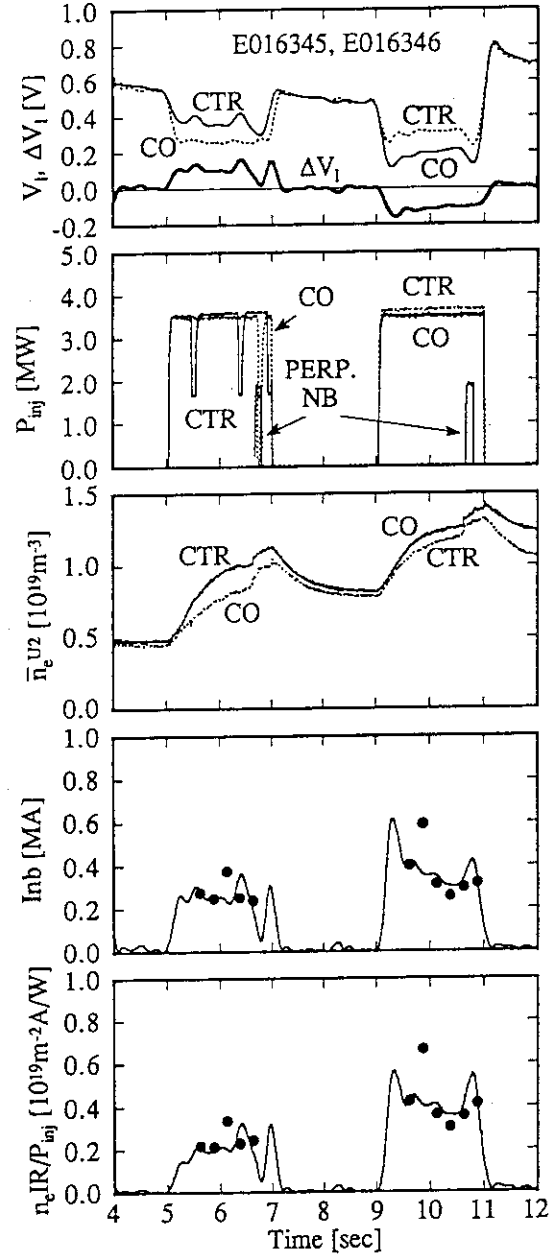


Fig. 2 Loop voltage V_l , beam power P_{inj} , and line averaged electron density \bar{n}_e^{U2} in successive shots (solid and dotted lines). Beam-driven current I_{nb} and current drive efficiency $n_e I R / P_{inj}$ are evaluated from ΔV_l , the difference in V_l . Solid circles are the values evaluated from the surface loop voltage.

numerical code by about 40%. If the bootstrap current of 80 kA is taken into account to the evaluation of the experimental result, the beam-driven current becomes smaller by 5%. In eq. (1), the change of the internal inductance is neglected. The internal inductance deduced from the magnetics increases linearly before and after the first beam injection and its contribution to loop voltage is 0.1 V. If we take this contribution, the beam-driven current becomes larger by 30%. As a result, the difference between the experimental and the numerical is about 15%, if both contributions are taken into account.

Sawtooth activity appeared after $t=9$ sec in these shots, that is, the first and second beam injection phases are without and with sawtooth, respectively. The sawtooth period was longer with co-injection (~ 220 ms) than that with counter-injection (~ 100 ms). This result is consistent with those obtained in JT-60 [3] and JET [4] and contradict with that obtained in ASDEX [5]. The plasma stored energy was similar between co- and counter-injected plasmas in sawtooth-free phase but in sawtooth phase the plasma stored energy for the co-injected plasma is larger by 20% than that for the counter-injected plasma. As for toroidal rotation, the counter-injected plasma has faster rotation speed than the co-injected plasma by 50%.

3. Conclusion

We evaluated the beam-driven current by comparing the loop voltage of the plasmas with co- and counter-beam injections. The maximum beam-driven current is 400 kA, which is 25% of the total plasma current. The current drive efficiency is $0.4 \times 10^{19} \text{ m}^{-2}$. This result agrees with the numerical prediction within 15%. The plasma behaves differently in several aspects with co- and counter-beam injections.

References

- [1] KURIYAMA, M., AKIBA, M., AKINO, N., et al., Proc. 13th Symposium on Fusion Engineering, Vol. 2, IEEE, (1989) 996.
- [2] TANI, K., AZUMI, M., and DEVOTO, R., S., J. Comp. Phys. **98** (1992) 332.
- [3] ISHIDA, S., NAGASHIMA, K., NISHITANI, T., KUSAMA, Y., and MATOBA, T., Nucl. Fusion **30** (1990) 552.
- [4] EDWARDS, A.W., BICKLEY, A., BÜCHSE, R., et al., Proc. 19th Eur. Conf. Innsbruck, Vol. I, European Physical Society (1992) 379.
- [5] GEHRE, O., GRUBER, O., MURMANN, H.D., et al., Phys. Rev. Lett. **60** (1988) 1502.

6. Fast Ion Study

6.1 Sawtooth Stabilization Experiments by Second Harmonic Minority Ion ICRF Heating

H. Kimura, T. Fujii, M. Sato, D.J. Campbell, K. Hamamatsu, S. Moriyama,
M. Nemoto, M. Saigusa, H. Takeuchi

1. Introduction

In 1992, the JT-60U ICRF experiment using two new antennas started. The maximum coupled power to plasmas so far reached 3.6MW for 1.4 sec [1]. ICRF heating is to be generally utilized on JT-60U as unique central heating method for high performance confinement study and current drive study as well as high energy particle study with coupled power up to 5MW (eventually 8MW) in combination with NBI, LHCD and pellet. Specific subjects for the ICRF study on JT-60U for a near term are as follows;

- Extension of operation range for sawtooth stabilization to high \bar{n}_e , high I_p and low- q by second harmonic minority ion heating for confinement improvement.
- D-³He fusion with 4th harmonic ICRF wave acceleration of ³He beam in high density regimes for alpha particle study [2, 3].
- Synergistic effects on current drive between ICRF and LHCD for improvement in current drive efficiency [4, 5].
- Local current profile control by minority ion current drive and its combination with tangential NBI for sawtooth control.
- Helium ash exhaust by edge ICRF acceleration or sawtooth activity control.

In this section, experimental results on sawtooth stabilization for ohmically heated target plasmas are presented. In JT-60 ICRF experiment, we already obtained clear symptoms of the sawtooth stabilization in the high electron density and low- q regime [6]. In JT-60U experiments, we are demonstrating more firmly the sawtooth stabilization for high electron density and relatively low- q discharges. Overall characteristics on the sawtooth stabilization and conditions for the stabilization are discussed. Results on the sawtooth stabilization experiments with NBI or LHCD target plasmas are presented in the next section (6.2).

2. Typical Shot of Sawtooth Stabilization

Typical example of the sawtooth stabilization by the second harmonic minority ion ICRF heating is shown in Fig. 1, where time evolution of the diamagnetic plasma stored energy, the line-average electron density, the central electron temperature by an ECE polychromator and

the ICRF power is indicated. The present experiments were done mainly with helium discharges containing residual minority hydrogens. The longest sawtooth period of this shot reached 0.87sec with 2.8MW of ICRF power (P_{IC}), which corresponds to 2.1 times energy confinement time (τ_E) of this shot. The central electron temperature of 5.5keV and the profile peaking factor ($T_e(0)/\langle T_e \rangle$) of 2.8 were obtained [7]. Incremental energy confinement time was 0.3sec, which is similar to JET results with the same plasma current [8]. The fact implies that the ICRF central heating does not suffer from the large toroidal field ripple of JT-60U.

3. Power-dependence of Sawtooth Period

Figure 2 indicates sawtooth period as a function of P_{IC} for the toroidal field at the vessel center ($R=3.32m$), B_{T0} , of 4.05T (open circle) and 3.97T (closed circle). Sawtooth period (τ_{ST}) tends to increase with increasing heating power. We found that optimization of the cyclotron resonance layer position against the plasma center ($R=3.46m$) is important for the stabilization. τ_{ST} increases remarkably at 2.8MW for B_{T0} of 3.97T, while it tends to saturate for B_{T0} of 4.05T. The electron temperature profile was also more peaked for the 3.97T case. The vacuum toroidal field at the plasma center is 3.81T for B_{T0} of 3.97T and 3.89T for B_{T0} of 4.05T, while the magnetic field giving the hydrogen second harmonic cyclotron resonance for the frequency of 116MHz is 3.82T. Therefore the experimental results are consistent with the fact that the resonance layer is closer to the plasma center for B_{T0} of 3.97T than for B_{T0} of 4.05T. However, we should also take into account of the paramagnetic effects of the low β_p plasma. A room for the optimization of the cyclotron resonance layer position may be still left, which will be checked shortly.

It is worth noting here that stabilization is also obtained with 2.8MW at relatively high density ($\bar{n}_e \sim 3.8 \times 10^{19} m^{-3}$) and low- q ($q_{eff}=4$, $I_p=2.4MA$), which is indicated by a diamond in Fig. 2.

4. Operation Range for Sawtooth Stabilization

Figure 3 indicates operation range for the sawtooth stabilization in $1/q_{eff} - \bar{n}_e/P_{tot}$ plane, where data points (closed circle) whose sawtooth periods are longer than 0.5sec are plotted. The operation range for JET ICRF experiment [9] is added for comparison. On JT-60U, sawtooth stabilization is obtained in the region of higher value of \bar{n}_e/P_{tot} , notably at $\bar{n}_e/P_{tot} \sim 0.9 \times 10^{19} m^{-3} MW^{-1}$ (the diamond in Fig. 2), than on JET, where fundamental resonance minority ion heating is employed. This is considered to be due to the fact that JT-60U employs second harmonic minority ion heating, which is favourable for producing energetic ions in high density regimes.

5. Conditions for Stabilization

We found that the sawtooth stabilization can be obtained only when a size of the inversion radius (r_{inv}) exceeds a critical value. An example is shown in Fig. 4. A monster sawtooth appeared in the late phase of the three seconds pulse, although the ICRF power and the

electron density were constant throughout the pulse and were almost the same as those of the shot in Fig. 1. Stabilization occurs after the inversion radius expands sufficiently as shown in the bottom box in Fig. 4. Trajectories in the plane defined by a sawtooth period and r_{inv}/a are shown for several cases having similar ICRF power and electron density in Fig. 5. The stabilization is found to occur only after the inversion radius exceeds a threshold value, i.e., $r_{\text{inv}}/a \geq 0.2 \sim 0.23$. This is probably due to the need for confinement of energetic ions inside $q=1$ surface. Further discussion will be given in the next section (6.2).

6. Impact on Energy Confinement

Figure 6 shows the diamagnetic stored energy versus the loss power ($P_{\text{tot}} - dW_{\text{dia}}/dt$). At $B_{T0}=4.05\text{T}$ (quasi-central heating case), the experimental data almost agree with ITER-89P scaling, where we assume 10% hydrogen component in helium plasma. By fine tuning of the resonance position ($B_T=4.05\text{T} \rightarrow 3.97\text{T}$), the energy confinement time increases by about 20%, accompanied with extension of the sawtooth stable period as shown in Fig. 2.

7. Conclusions

- (1) Sawtooth stable periods of 0.9sec for OH target plasmas were obtained by the minority second harmonic ICRF heating.
- (2) Sawtooth stabilization is obtained at $\bar{n}_e/P_{\text{tot}} \sim 0.9 \times 10^{19} \text{m}^{-3} \text{MW}^{-1}$, which is notably larger than the value achieved on JET, where fundamental resonance minority ion heating is employed.
- (3) Stabilization occurs only after the inversion radius expands sufficiently, i.e., $r_{\text{inv}}/a \geq 0.2 \sim 0.23$.
- (4) The energy confinement time is improved by about 20%, accompanied with sawtooth stabilization.
- (5) The incremental energy confinement time reached 0.3sec.

References

- [1] MORIYAMA, S., et al., Sec. 10.2 in this Review.
- [2] FUJII, T., et al., Sec. 6.4 in this Review.
- [3] NEMOTO, M., et al., Sec. 6.5 in this Review.
- [4] FUJII, T., et al., Sec. 5.11 in this Review.
- [5] KONDO, T., et al., Sec. 5.12 in this Review.
- [6] KIMURA, H., et al., Proc. EPS Top. Conf. on RF Heating and Current Drive of Fusion Devices (Brussels, 1992), EPS, 93.
- [7] SATO, M., et al., Sec. 6.3 in this Review.
- [8] BHATNAGAR, V.P., et al., Plasma Phys. Contr. Fusion **31** (1989) 333.
- [9] CAMPBELL, D.J., et al., Proc. 15th Eur. Conf. on Contr. Fusion and Plasma Heating (Dubrovnik, 1988), EPS, Vol. 12B, Part I, 377.

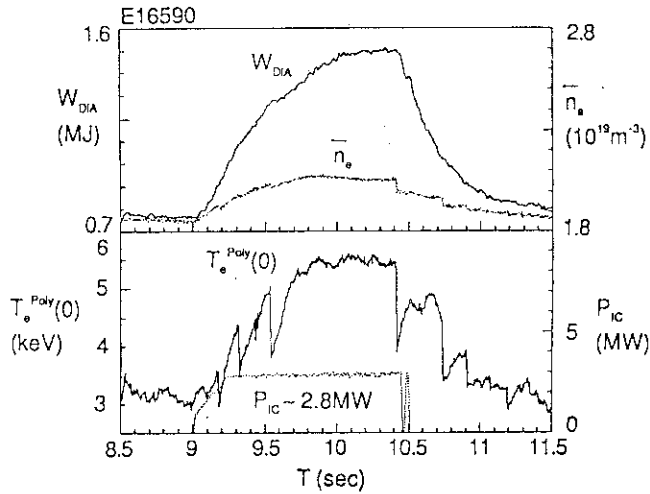


Fig.1 Typical waveform of sawtooth stabilization by second harmonic minority ion ICRF heating. $I_p=2\text{MA}$, $B_T=3.97\text{T}$, $q_{eff}=5.3$, $\bar{n}_e=2\times 10^{19}\text{m}^{-3}$, $P_{IC}=2.8\text{MW}$, He discharge.

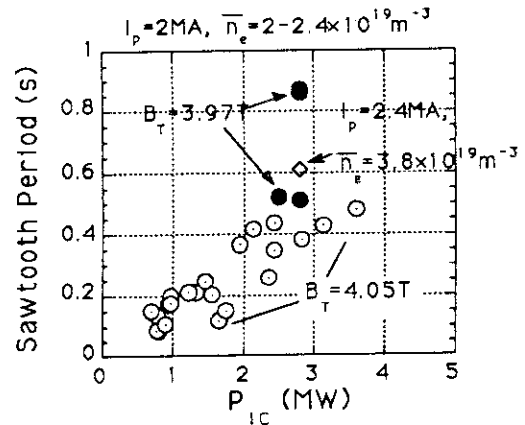


Fig.2 Dependence of sawtooth period on ICRF heating power.

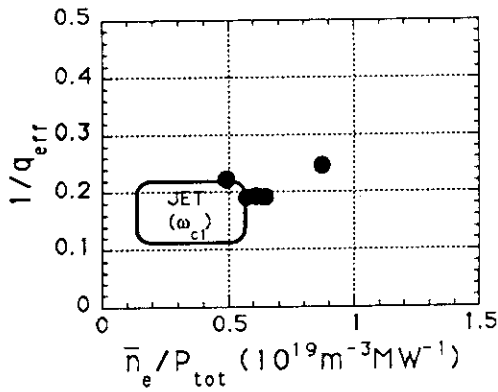


Fig.3 Operation range for sawtooth stabilization

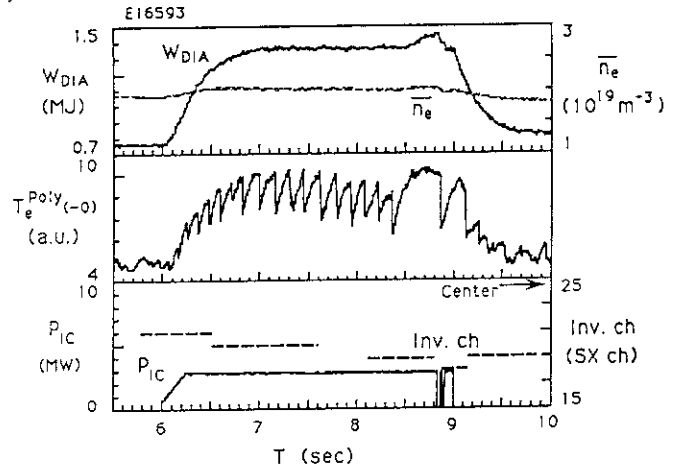


Fig.4 A shot example showing that the sawtooth stabilization occurs after the inversion radius exceeds a threshold value. $I_p=2\text{MA}$, $B_T=3.97\text{T}$, $q_{eff}=5.3$, $\bar{n}_e=2\times 10^{19}\text{m}^{-3}$, $P_{IC}=2.8\text{MW}$, He discharge.

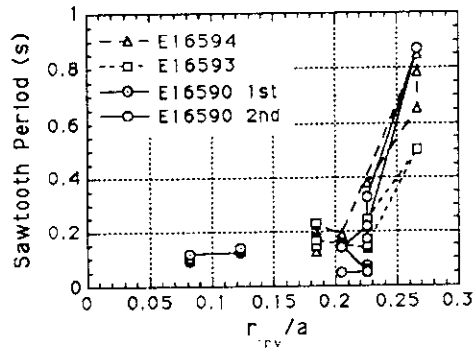


Fig.5 Trajectories of a sawtooth period as a function of r_{mv}/a

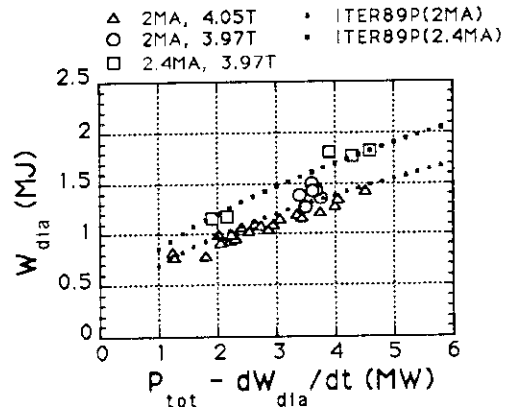


Fig.6 Diamagnetic stored energy versus loss power

6.2 Sawtooth Stabilization Experiments by ICRF Heating in Combination with NBI or LHCD

H. Kimura, T. Fujii, M. Sato, M. Nemoto, T. Kondoh, D.J. Campbell, K. Hamamatsu, Y. Ikeda, T. Imai, M. Matsuoka, S. Moriyama, M. Saigusa, H. Takeuchi, K. Ushigusa

1. Introduction

This section describes experimental results on sawtooth stabilization by ICRF heating combined with NBI heating or lower hybrid current drive (LHCD). In JT-60, we had already carried out combined ICRF and NBI heating experiments with emphasis on the sawtooth stabilization, where we found that the dependence of the sawtooth stabilization on P_{NBI}/\bar{n}_e was opposite between a low density case and a high density case. In JT-60, ICRF waves and beam ions strongly coupled because the hydrogen beam was used and hydrogen is main resonant species for ICRF heating. This is the reason of somewhat complicated behaviours of the sawtooth stabilization observed in combined ICRF and NBI heating on JT-60 [1]. On the other hand, in JT-60U, deuterium beam is employed, while the main resonant species of ICRF heating are still hydrogen. Thus ICRF waves and beam ions decouple in JT-60U. In this case, role of the NBI heating becomes simple, that is to heat bulk plasmas and to lengthen the slowing-down time of the fast protons produced by ICRF heating. We indeed observed more efficient sawtooth stabilization by ICRF heating with NBI heated plasmas than with ohmically heated target plasmas.

LHCD is also expected to assist sawtooth stabilization by ICRF heating through broadening the current profile. Preliminary experiments of combined ICRF and LHCD were carried out to check the effects. However, the sawtooth period became rather short in combined ICRF and LHCD scheme than in ICRF heating alone. Conditions for the sawtooth stabilization by ICRF heating are discussed taking all those experimental results including ICRF heating alone case described in the previous section (6.1).

2. Combined ICRF and NBI Heating

Typical example of the combined ICRF and NBI heating experiment is shown in Fig. 1 (shot E16376), where time evolution of the diamagnetic plasma stored energy, the line-average electron density, the central electron temperature by an ECE polychromator, the ICRF power, the NBI power and a channel number of a soft X-ray detector array in the poloidal cross-section corresponding to the sawtooth inversion is indicated. The present experiments were performed with deuterium discharges containing residual minority hydrogen. ICRF heating regime was minority hydrogen second harmonic heating. The

toroidal field at the vessel center ($R=3.32\text{m}$), B_{T0} , was 4.05T. So, the resonance position was slightly off-axis (about 10cm out from the axis). Total neutral beam power was $\sim 9.6\text{MW}$, which consisted of 5.4MW perpendicular D beam, 1.7MW co-directed tangential D beam and $\sim 2.5\text{MW}$ perpendicular ^3He beam. We obtained stable period of 1.74sec by 3.1MW of ICRF power, as shown in the electron temperature trace in Fig. 1. The central electron temperature was almost constant during the stabilized period, although \bar{n}_e went up from $1.8 \times 10^{19}\text{m}^{-3}$ to $3.1 \times 10^{19}\text{m}^{-3}$. At $t=8\text{sec}$, we had $T_{eo} \sim 6.6\text{keV}$, $T_{io} \sim 5\text{keV}$ and $\bar{n}_e \sim 3 \times 10^{19}\text{m}^{-3}$. The electron temperature profile was somewhat broader ($(T_e(0)/\langle T_e \rangle) \sim 2.5$) than the one with ICRF heating alone ($(T_e(0)/\langle T_e \rangle) \sim 2.8$ [2]). A slowing-down time of fast protons in the plasma center was estimated to be considerably long, ranging from 420ms to 240ms during the stable period for 200keV protons. A remarkable high energy tail of protons was indeed observed by an active charge exchange neutral particle analyzer whose line of sight is about 40 degree to the magnetic axis, as shown in Fig. 2. Figure 3 indicates maximum sawtooth period during the combined IC and NB heating (open square) as a function of the ICRF power together with the data of the ICRF heating alone. Considering B_{T0} of 4.05T for the present combined IC+NB experiment, sawtooth stabilization by ICRF heating is realized more easily with NBI-heated target plasmas than with ohmic target plasmas.

3. Combined ICRF Heating and LHCD

The combined ICRF and LHCD experiments were conducted with helium discharges with minority hydrogen, i.e., conditions similar to those in Fig. 1 of Sec. 6.1 except application of LHCD. B_{T0} was 3.97T, so the ICRF resonance position was almost on-axis. Figure 4 shows time evolution of the combined ICRF and LHCD experiment. Peak refractive index of LH waves ($N_{||}^{\text{peak}}$) is 1.6 and injected power (P_{LH}) was 1.5MW. Reduction of the loop voltage ($\Delta V_L/V_L$) by LHCD was -0.39 and it was further reduced to -0.55 by ICRF heating. The line-average electron density was $1.9 \times 10^{19}\text{m}^{-3}$ at LH only phase and slightly increased to $2.1 \times 10^{19}\text{m}^{-3}$ in combined IC+LHCD phase. Apparently sawtooth stabilization by the ICRF heating could not be obtained with the LHCD target plasma in the present experiment. Similar result was obtained with higher value of $N_{||}^{\text{peak}}$ ($=2.3$) of LH waves. We found that the sawtooth inversion radius became short in application of the LH waves than without them. Figure 5 indicates time variation of the sawtooth period and r_{inv}/a for (a) the combined ICRF and LHCD case and (b) ICRF alone case. In the former case, r_{inv}/a is limited less than 0.19, while it remains a value more than 0.2 in the latter case, before ICRF injection. As pointed out in Sec. 6.1, there exists a lower limit of r_{inv}/a for the sawtooth stabilization. This is the reason why the stabilization could not be obtained with the LHCD target plasma. Measurement of hard X-ray emission shows that hard X-ray intensity decreases after injection of ICRF waves only in the plasma core, suggesting absorption of LH waves by fast protons produced by ICRF waves in the plasma core. The incremental energy confinement time of

ICRF heating with LHCD target plasma was limited at 200ms because of lack of sawtooth stabilization, while it reached 300ms associated with the sawtooth stabilization with ohmic target plasmas [2]. Global energy confinement time of the combined ICRF heating and LHCD agree with ITER-89P scaling.

4. Discussion

Figure 6 illustrates variation of r_{inv}/a during the sawtooth stabilization as a function of \bar{n}_e for some typical examples. Here we should note that the stabilization could not be obtained for IC+LH case. Arrows indicate direction of time passage in stable periods. As described in the previous section (6.1), lower limits of r_{inv}/a for the stabilization of IC only cases are considerably large, although the resonance position was near on axis. The reason can be understood from following consideration. For efficient stabilization, fast protons should be confined inside $q=1$ surface [3]. The condition can be represented as

$$2\delta_b \leq r_{inv} - r_{res},$$

where δ_b is a banana half width which is given approximately by $\rho_i(R_0/r)^{1/2}$, ρ_i is a Larmor radius and r_{res} is the resonance layer position. We take $r=(r_{inv}+r_{res})/2$ for the critical orbit. We found that a maximum energy of fast protons which can be confined inside $q=1$ surface (E_i^{max}) is $\sim 550\text{keV}$ for $r_{inv}/a=0.23$ corresponding to IC alone case and $\sim 300\text{keV}$ for $r_{inv}/a=0.19$ corresponding to IC+LH case, with $r_{res}/a=0$ corresponding to $B_{T0}=3.97\text{T}$. Furthermore, E_i^{max} is $\sim 350\text{keV}$ for $r_{inv}/a=0.23$ with $r_{res}/a=0.07$ corresponding to $B_{T0}=4.05\text{T}$. Those estimations are consistent with the present experimental trend on the stabilization. In this connection, an average energy of fast protons calculated by a local Fokker-Planck code is 270keV , order of which is consistent with the above estimations. One finds that for IC+NB case the stabilization is obtained from much smaller value (0.13) of r_{inv}/a and hence variation range of r_{inv}/a is quite large in comparison with IC alone case. E_i^{max} is estimated to be 40keV and 1MeV at the start and the end of the stable period respectively. E_i^{max} of 40keV is too low for the stabilization by ICRF. This suggests that NBI heating and/or current drive played a role in the stabilization in the early stage of the stable period.

5. Conclusions

- (1) Sawtooth stable period of 1.7sec was obtained in combined second harmonic minority ion ICRF heating and NBI heating. Stabilization effects by NBI can not be excluded.
- (2) Sawtooth stabilization by the ICRF heating could not be obtained with the LHCD target plasmas.
- (3) Lower limits of r_{inv}/a for the stabilization observed in ICRF alone and ICRF+LHCD can be explained by the condition required for fast ions to be confined inside $q=1$ surface.

References

- [1] KIMURA, H., et al, et al., "Higher Harmonic ICRF Heating Experiments in JT-60", submitted to Plasma Phys. Contr. Fusion.

[2] KIMURA, H., et al, Sec. 6.1 in this Review.

[3] PORCELLI, F., Plasma Phys. Contr. Fusion 33 (1991) 1601.

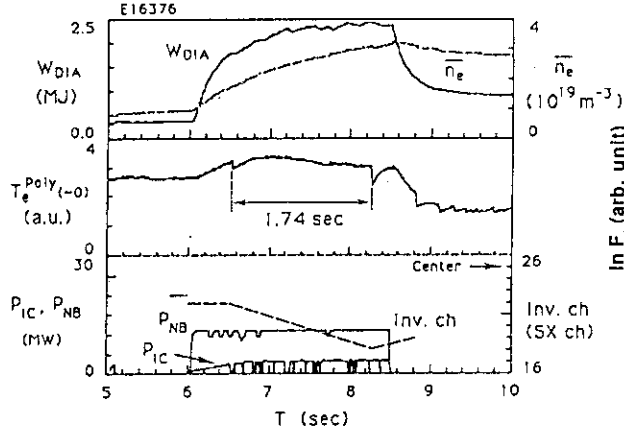


Fig.1 Time evolution of combined ICRF and NBI heating. $I_p=2.5\text{MA}$, $B_T=4.05\text{T}$, $q_{\text{eff}}=4$, $\bar{n}_e \sim 3 \times 10^{19}\text{m}^{-3}$, $P_{\text{IC}}=3.1\text{MW}$, $P_{\text{NB}} \sim 10\text{MW}$, D2 discharge.

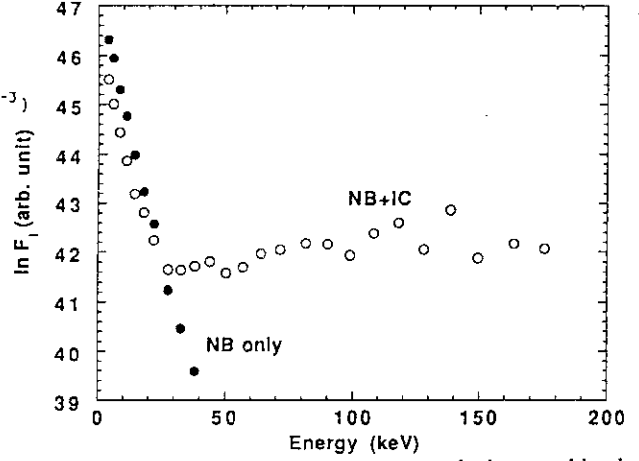


Fig.2 Charge exchange energy spectra during combined ICRF+NBI heating and NBI heating alone (shot E16370). similar experimental conditions as in Fig. 1.

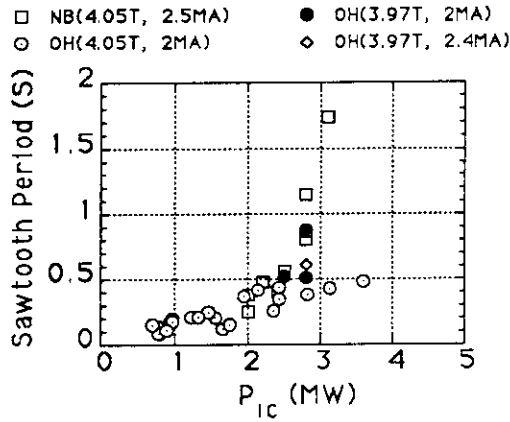


Fig.3 Maximum sawtooth period during combined IC and NB heating as a function of the ICRF power together with data of ICRF heating alone.

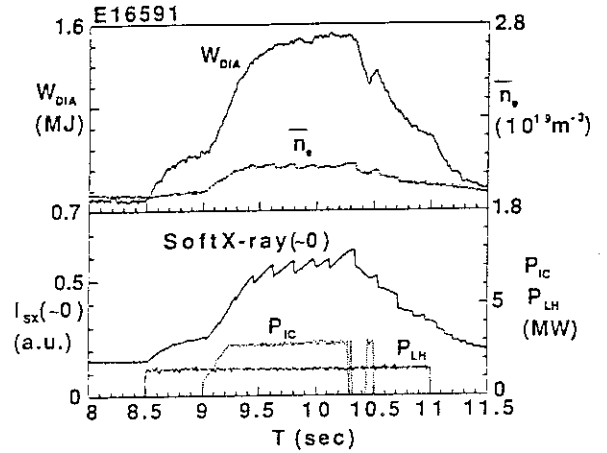


Fig.4 Time evolution of the combined ICRF and LHCD experiment. $I_p=2\text{MA}$, $B_T=3.97\text{T}$, $q_{\text{eff}}=5.3$, $\bar{n}_e \sim 2 \times 10^{19}\text{m}^{-3}$, $P_{\text{IC}}=2.8\text{MW}$, $P_{\text{LH}}=1.5\text{MW}$, He discharge.

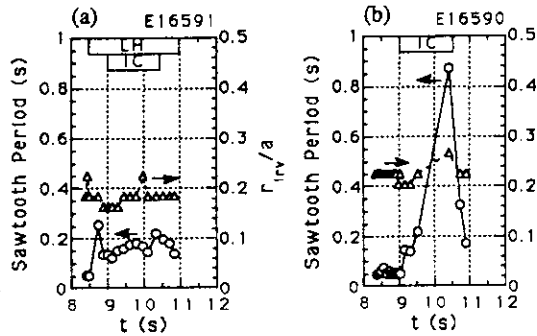


Fig.5 Time variation of the sawtooth period and r_{inv}/a for (a) combined ICRF and LHCD case and (b) ICRF alone case.

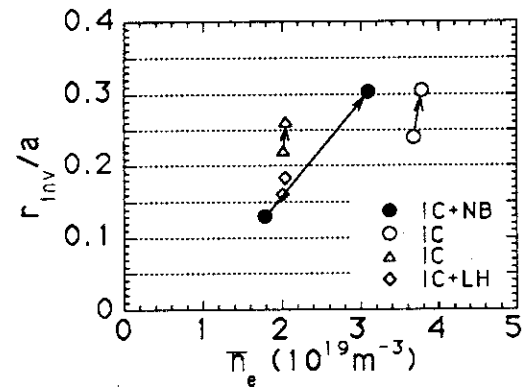


Fig.6 Variation of r_{inv}/a during the sawtooth stabilization as a function of \bar{n}_e for some typical examples.

6.3 Electron Temperature Profiles in Sawtooth Stabilization Experiment

M. Sato, H. Kimura and T. Fujii

1. Introduction

Sawtooth relaxations prevent the increase of electron temperature in tokamaks. Recently a decrease of the central neutron emission was observed after sawtooth collapse in JET [1]. The sawtooth relaxations influence the central plasma parameters, and so the control of the sawtooth relaxation may increase the fusion performance. The control can be done using the techniques such as pellet injection and ICRF heating [1]. In JT-60U [2,3], the second harmonic minority ion ICRF heating is used for central heating resulting in sawtooth stabilization. Here the time evolution of the electron temperature profiles during sawtooth stabilization for ohmically-heated target plasmas and resonance optimization position experiments are studied.

2. Electron Temperature Profiles in Sawtooth Stabilization Experiments

2.1 Sawtooth Stabilization for Ohmically Heated Target Plasmas

The typical time evolution of the plasma parameters during sawtooth stabilization for an ohmically-heated target plasma [3] is shown in Fig. 1. The plasma parameters are as follows; $I_p=2\text{MA}$, $B_t=4\text{T}$, $P_{IC}=3.6\text{MW}$. When the line averaged electron density is $2.2 \times 10^{19} \text{m}^{-3}$, the electron temperature reaches to 5keV . The electron temperature is determined from the ECE measured with an absolute-calibrated Fourier transform spectrometer system (FTS) [4]. The peaking factor of the electron temperature ($T_e(0)/\langle T_e \rangle$) in the ohmic phase is about 2. When the sawteeth are stabilized after the injection of ICRF power, the peaking factor increases up to 2.8; after a sawtooth crash the peaking factor falls to 2. Typical electron temperature profiles in the sawtooth stabilization experiment are shown in Fig. 2. The electron temperature in the region of $r/a < 0.5$ is increased due to the ICRF heating. The inversion radius is about 0.35. After the sawtooth crash the electron energy is transported from the central region ($r/a < 0.35$) to the medium region ($0.35 < r/a < 0.85$). The dependence of the increment in electron temperature at the crash on the sawtooth period and ICRF power are shown in Fig. 3 and 4. The increment of the electron temperature linearly increases as the sawtooth period increases. The relationship between the peaking factor of the electron temperature and the sawtooth period is shown in Fig. 5. The peaking factor at the top of the sawtooth increases as the period of the sawtooth increases but the peaking factor saturates at 2.8.

2.2 Optimization of the Resonance Position

Optimization of the cyclotron resonance position is important for sawtooth stabilization [3]. Here its effect on the electron temperature profile is discussed. The electron temperature profiles in the cases of $B_t(R_{axis}=3.55m) = 3.89T$ and $3.81T$ are shown in Fig. 6, where R_{axis} is the plasma center. Discharge conditions of these two shots are quite similar except small difference in B_t . ICRF power is injected at the early phase of the discharge in order to minimize the sawtooth effects. The frequency of the injected ICRF is 116MHz. The magnetic field giving a second harmonic cyclotron resonance in hydrogen at the injected frequency is 3.82T. The arrows indicate the position of the resonance. The resonance position is calculated taking into account the internal fields [5]. The resonance position difference between B_t of 3.89T and B_t of 3.81T is about 0.12m in ρ .

The increment of the electron temperature at the center and the peaking factor are 1.4keV, 2.5 and 1.9keV, 2.8 in the cases of $B_t=3.89T$ and $3.81T$, respectively. The relationship between sawtooth and ICRF power is shown in Fig.2 of ref. 3. The sawtooth period in the case of $B_t=3.89T$ is limited around 0.4sec at P_{IC} of 2.8MW, while it reached 0.9sec with the same power. A small difference in the resonance position thus results in a remarkable difference in central electron temperature.

3. Summary

During minority second harmonic ICRF heating, the increment of the electron temperature at the crash after a period of the sawtooth stabilization reaches 2keV and the peaking factor reaches 2.8. Optimization of the resonance position is important for getting peaked of the profile of the electron temperature and the sawtooth stabilization.

References

- [1]The JET Team (presented by D J Campbell) : Proc. 13th Int. Conf. Plasma Phys. and Contr. Nucl. Fus. Res., (1990, Washington, USA) IAEA-CN-53/A-6-3
- [2]FUJII, T., et al; JAERI-M 92-073 p280
- [3]KIMURA, H., et al; this issue 6.1
- [4]SATO, M., et al., this issue 9.4
- [5]SATO, M., et al, JAERI-M 92-073 p342

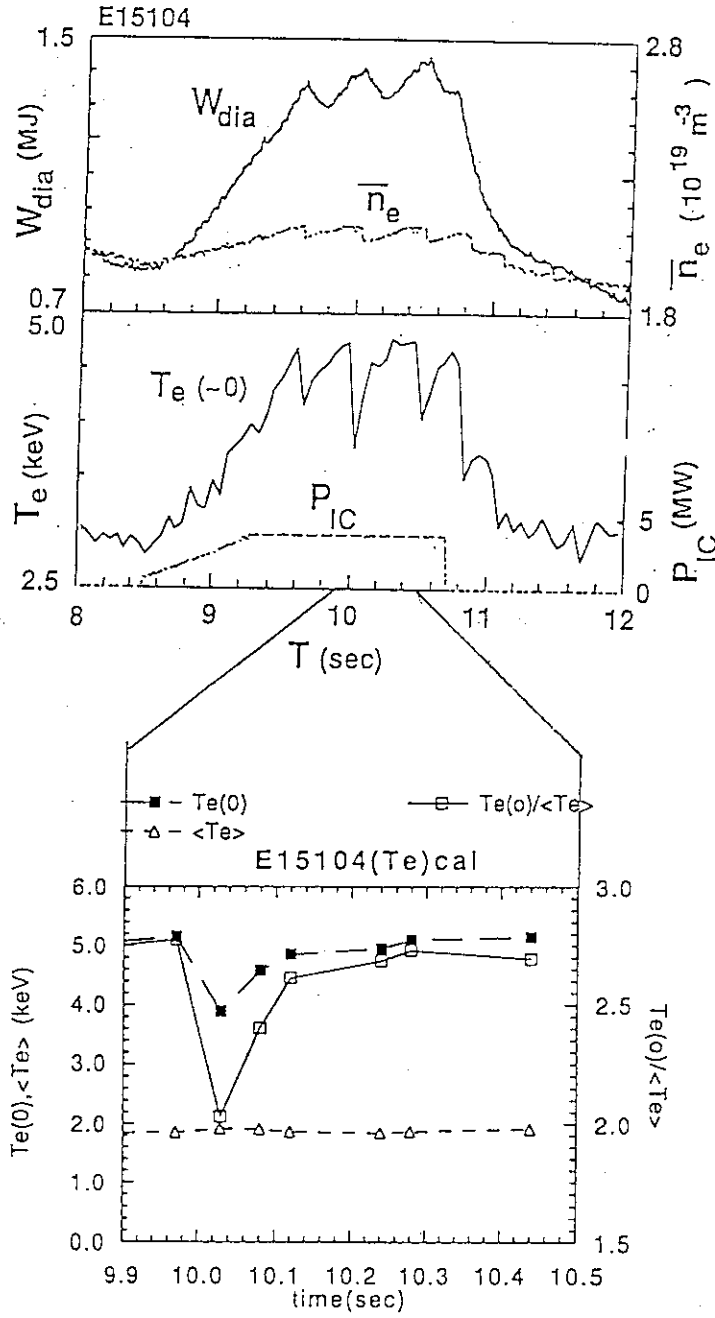


Fig.1. Typical time evolution of plasma parameters in the sawtooth stabilization experiment.

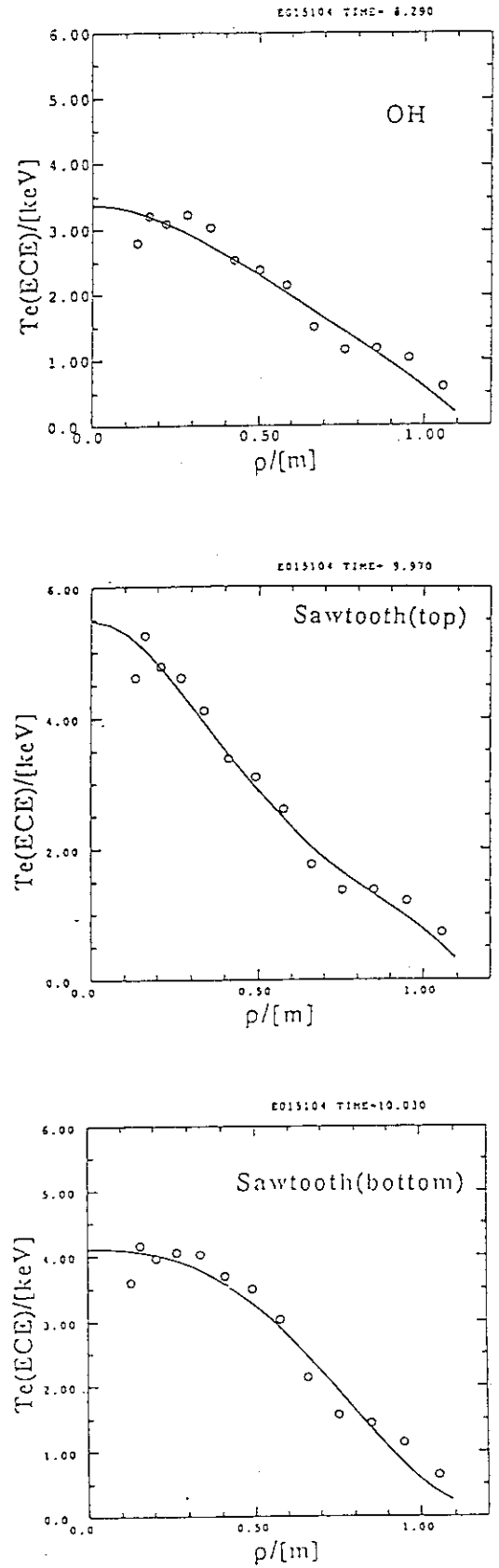


Fig. 2. Typical time evolution of the electron temperature profile in the sawtooth stabilization experiment.

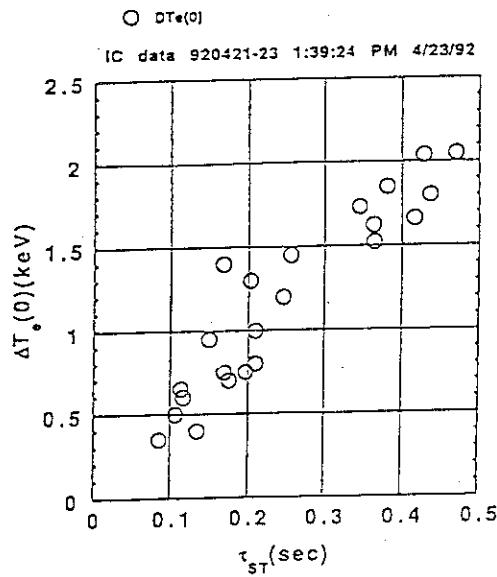


Fig.3. Increment of the electron temperature vs sawtooth period

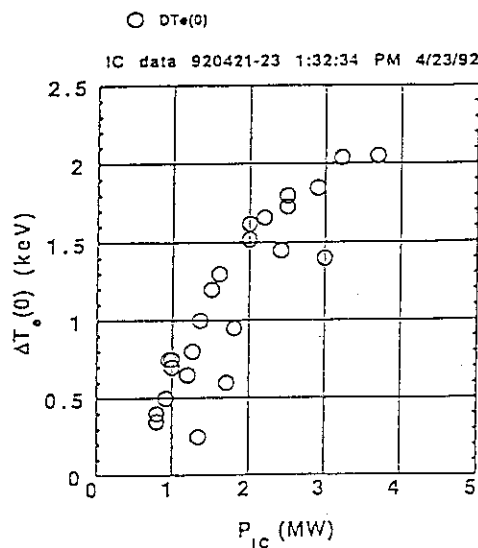


Fig.4. Increment of the electron temperature vs ICRF power

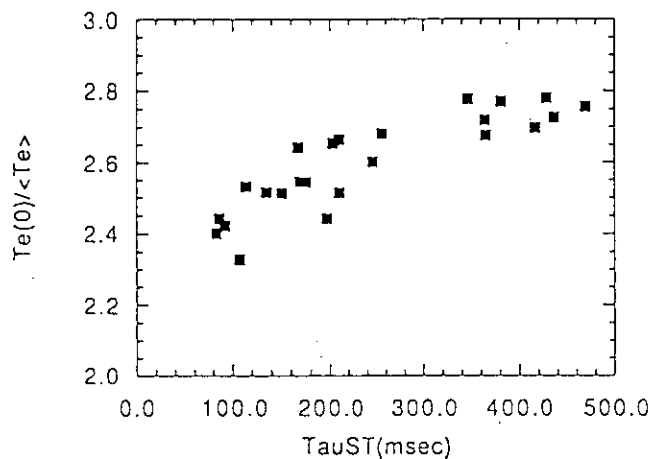


Fig.5. Peaking factor $T_e(0)/\langle T_e \rangle$ at the top of the sawtooth

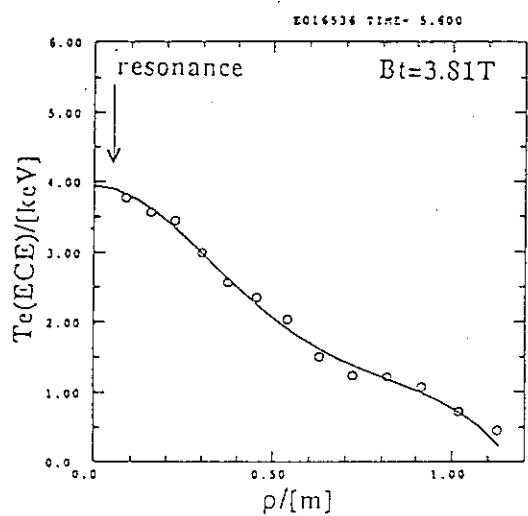
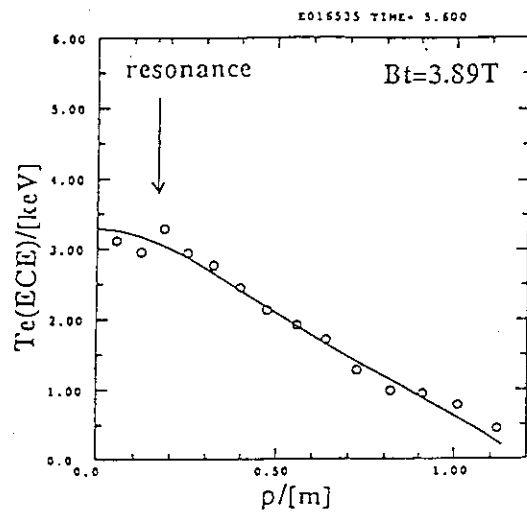
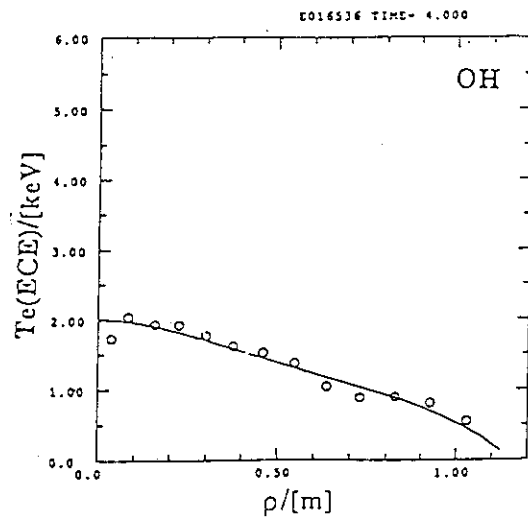


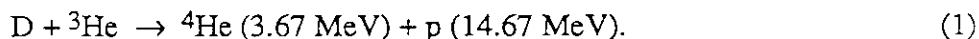
Fig.6. Electron temperature profiles in the cases of 3.89T and 3.81T in optimization of cyclotron resonance experiment. The power of ICRF is 3MW, for 3.89T case and 2.9MW for 3.81T case. $I_p=2.5$ MA, line averaged $n_e=3.7 \times 10^{19} m^{-3}$.

6.4 D-³He Experiments by ICRF Heating

T. Fujii, H. Kimura, M. Nemoto, M. Saigusa, S. Moriyama, H. Takeuchi, K. Tobita,
Y. Koide, K. Nagashima, A. Sakasai, A. Van Blokland, M. Kuriyama, Y. Kusama

1. Introduction

High energy (3.5 MeV) α particles are generated in a D-T reactor and should heat a plasma so as to maintain D-T fusion reaction. They should be confined in a sufficient time and should bring about no serious MHD instabilities. Therefore, the investigations on behaviours and confinement of high energy α particles is one of the most important issues in JT-60 U. If we use the D-T plasma, we have a serious radio-activation problem because many neutrons are generated on the reaction. On the other hand, if we use the D-³He plasma, we can investigate behaviours and confinement of α particles with similar energy to that of the D-T reaction without actual difficulties with respect to the radio-activation because D-³He fusion reaction is given by



Experiments of α particle generation have been performed in JET by fundamental minority ICRF heating to heat ³He and then rise the D-³He reactivity. Higher harmonic ICRF heating of ³He (third, fourth harmonics at $B_T = 4 \text{ T}$, 3 T , respectively) has been chosen in JT-60U since a frequency range of its ICRF heating system is 110-130 MHz. Higher harmonic heating has advantage that it is insensitive to minority ³He concentration and is efficient for the D-³He reaction at higher densities in contrast with fundamental heating. ICRF power in the higher harmonic regime is coupled efficiently with ³He of higher energy so that we have performed D-³He experiments in combination with ³He NBI.

2. Experimental Setup

First D-³He experiments have been performed in two available ICRF heating regimes on JT-60U as the applied frequency of the ICRF heating system is 116 MHz. One regime is on-axis heating by third harmonic heating of ³He at $B_T = 4 \text{ T}$ where a third harmonic resonance layer of ³He is indeed on-axis and also resonance layers of second harmonic of H and fourth harmonic of D are the same position, and further third and fifth resonance layers of D are at both inner and outer plasma edges, as shown in Fig. 1 (a). Then, if H ion concentration is high, ICRF power is absorbed by H and therefore D-³He reaction is reduced. The other regime is on-axis heating by fourth harmonic heating of ³He at $B_T = 3 \text{ T}$ where a fourth harmonic resonance layer of ³He is on-axis, and several other resonance layers of ³He, D and

H are near the axis and near the plasma edges, as shown Fig. 1 (b). In this case, it is possible that ICRF power absorption by ^3He , D and H is competitive at the plasma core.

ICRF antennas are located at P11 and P12 equatorial ports shown in Fig. 1 (a), which are a 2×2 loop array type with a solid poloidal septum. ^3He perpendicular beams are injected from five upper beam units of #2, 4, 6, 10, 12, as shown in Fig. 1(b). Its beam trajectory is off-axis shifted upper by 0.3 m at the plasma center. D perpendicular beams are injected from an upper beam unit of #14, which is also used for charge exchange recombination spectroscopy (CXRS) to measure the ion temperature, and lower beam units of #1, 3, 5, 11, 13. An ion energy spectrum is measured by three types of charge exchange (CX) neutral analyzers. A NPA3 is a CX \perp analyzer and a NPA2 is a CX// analyzer. Their signal reflects the ion energy spectrum at the plasma core because their sight line intersects the NB trajectory. The other analyzer is a passive type of CX \perp which gives an ion energy spectrum of a peripheral plasma. The CXRS is also enable to obtain the ^3He energy spectrum if SN ratio is sufficient. Fast ion loss by ripple loss is examined only by a far-infra-red camera which sights the area of poloidal angle about 30 degrees. A NaI scintillate for g-ray measurement is provided in order to estimate the fusion power by D- ^3He reaction because the γ -ray of 16.6 MeV is emitted in the coincident process of D- ^3He reaction with probability of 3×10^{-5} of the formula (1).

3. Experimental Results

Experimental data are obtained in the following plasma parameters : $I_p = 2.5$ MA, $n_e = 2.9 - 3.6 \times 10^{19} \text{ m}^{-3}$, $P_{IC} = 2.3 - 3.1$ MW, $P_{NB}(^3\text{He}) = 1.8 - 4.1$ MW, $P_{NB}(\text{D}) = 1.8 - 7.2$ MW for $B_T = 4$ T, $I_p = 1.9$ MA, $n_e = 2.1 - 2.9 \times 10^{19} \text{ m}^{-3}$, $P_{IC} = 2.6 - 3.1$ MW, $P_{NB}(^3\text{He}) = 1.8 - 2.7$ MW, $P_{NB}(\text{D}) = 1.8 - 6$ MW for $B_T = 3$ T, and Beam energy $E_b(^3\text{He}) = 73 - 78$ keV and $E_b(\text{D}) = 80 - 88$ keV. Typical results for $B_T = 4$ T and $B_T = 3$ T are shown in Fig. 2 (a) and (b), respectively. We should pay attention to high energy ions, especially ^3He ions because they enhance D- ^3He reactivity. The data of fast ions by the active CX analyzers are shown in the figures. The detailed description of the CX measurements in D- ^3He experiments is given in section 6.5. High energy ^3He ions of 100 keV are observed only for $B_T = 3$ T while high energy D ions are observed both for $B_T = 3$ T and $B_T = 4$ T. Also ^3He tail formation is observed only for $B_T = 3$ T by the passive CX \perp analyzer. Strong H tail is observed for $B_T = 4$ T by the active CX \perp analyzer, and good heating efficiency of $\tau_E^{\text{inc}} = 200$ ms is achieved. Moreover sawtooth period is extended up to 1.7 sec which is the longest value up to date. On the other hand, for $B_T = 3$ T heating efficiency is small as $\tau_E^{\text{inc}} = 50$ ms and sawtooth behaviour does not strongly change.

Total emmissivity of ^3He line spectrum measured by CXRS are shown in Fig. 3 (a) and (b) for $B_T = 4$ T and $B_T = 3$ T, respectively. The intensities, measuring at spatial four points, has no response to ICRF pulse for $B_T = 4$ T. Fast drops during ICRF pulse in Fig. 3 (a) is due to

breakdowns of the NB #14 beam line which is use for the CXRS measurement. On the contrary, the intensities change in response to the ICRF pulses for $B_T = 3$ T as shown in Fig. 3 (b). Their decay time is about 40 ms which is close to slowing-down time of 100 keV ^3He fast ions. Thus, this indicates that ^3He beam is accelerated by ICRF waves only for $B_T = 3$ T, which agrees with the measurements by the CX analyzers.

These fast ion generation gives changes in ripple loss, but no change in 16.6 MeV γ -ray emission. The ripple loss measured by the FIR camera increases for $B_T = 3$ T while it slightly increases for $B_T = 4$ T. The sixth harmonic and seventh harmonic resonance layers of D are located at $R - 3.91 = 0.4$ m and $R = 4.56$ m, respectively, at $B_T = 3$ T so that this may enhances fast ion ripple loss. The intensity of 16.6 MeV γ -ray emission is not at a measurable level although some adjustment of the NaI scintillator system is still needed for further measurement.

4. Summary and Discussion

First D- ^3He experiments are carried out in two higher harmonic ICRF heating regimes, third harmonic at $B_T = 4$ T and fourth harmonic at $B_T = 3$ T in combination with NBI heating of ^3He and D beams. Fast ion generation of each species and related results are summarized in the following table. ^3He tail was observed as well as D tail for $B_T = 3$ T while D and H tails were observed for $B_T = 4$ T. High energy ions which enhance D- ^3He reactivity were generated, but 16.6 MeV γ -ray emission was not at a measurable level.

The experimental conditions in further investigations must be optimized to obtain the sufficient γ -ray emission. The H concentration should be reduced substantially for $B_T = 4$ T because it is predicted that D- ^3He reaction decreases in high H concentration regimes. The plasma position is shifted to inside by about 0.2 m and further B_T is chosen at about 2.9 T so that both ^3He beams deposition and the fourth harmonic resonance layer of ^3He are on the axis and therefore D- ^3He reactivity is substantially increased.

	4 T			3 T		
	^3He	D	H	^3He	D	H
CX_{\perp}	no tail	tail	tail	tail	—	—
CX_{\parallel}	—	tail	tail	—	tail	no tail
Passive CX_{\perp}	no tail	—	—	tail	—	—
CXRS	small increase in intensity of ^3He line			increase in intensity of ^3He line		
Ripple Loss	small increase			increase		
γ -ray Emission	no signal			no signal		

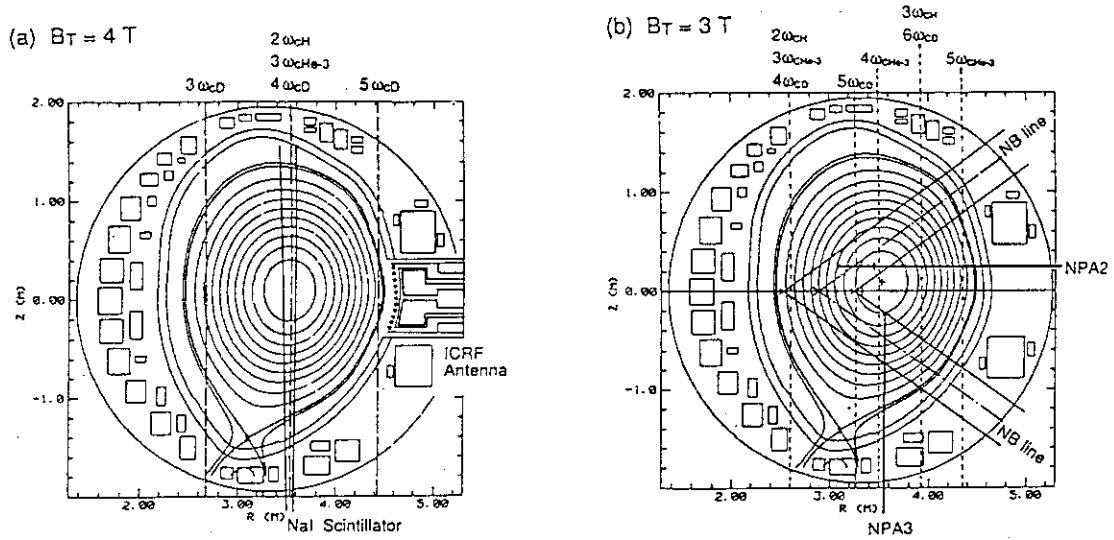


Fig. 1 Higher harmonic resonance layers (a) for $B_T = 4$ T and (b) for $B_T = 3$ T.

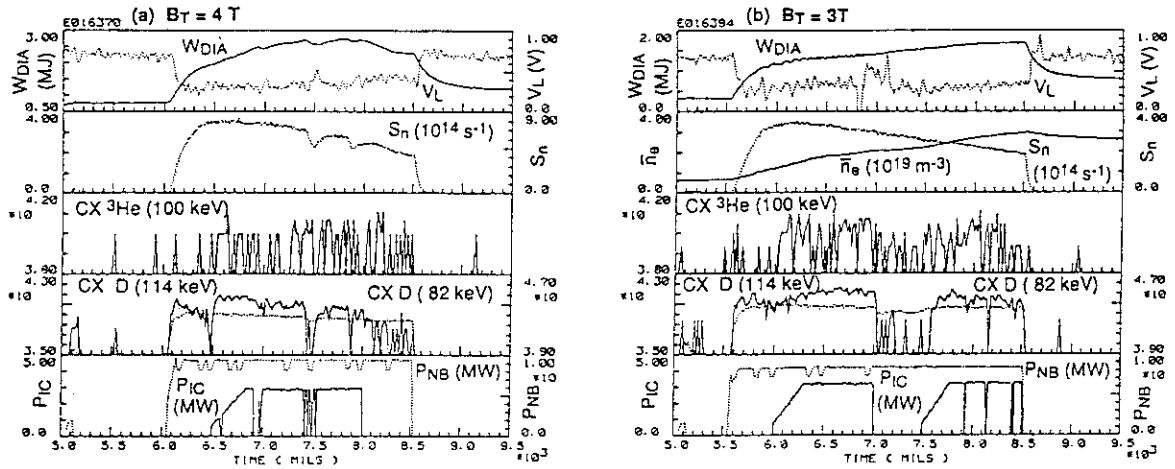


Fig. 2 Typical results obtained (a) for $B_T = 4$ T and (b) for $B_T = 3$ T.

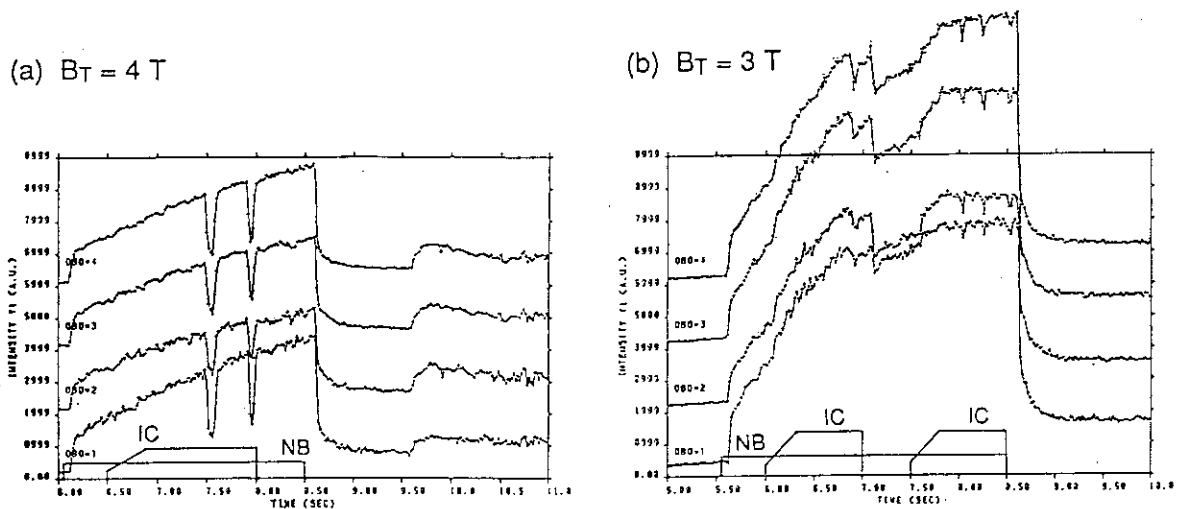


Fig. 3 Intensities of ^3He line spectrum measured by CXRS at special four points (a) for $B_T = 4$ T and (b) for $B_T = 3$ T.

6.5 CX Measurement of High Energy Ions in D-³He Experiments

M. Nemoto, H. Kimura, T. Fujii and K. Hamamatsu

1. Introduction

Understanding of α particle behavior in D-T plasma is one of the important issues for the establishment of burning plasmas. If ³He beam ions of around one hundred keV energy are able to be accelerated up to a few hundred keV by ICRF wave absorption, generation of α particle of 3.67MeV by D-³He reaction is expected easily. We carried out the first D-³He experiment according to the previous experimental plan on JT-60U[1]. In this paper, the primary results of deuterium, ³He and hydrogen ions behavior measured by charge exchange(CX) analyzers are described.

2. Experimental Apparatus and Results

The first D-³He experiment on JT-60U was carried out in the standard diverter plasmas with quasi-perpendicular neutral beam injection (NBI) units which arrangement is shown in Fig.1. Prepared NBI units were five ³He NBI units and four deuterium ones that were applied to increase the electron temperature. Upper beam units, except for one unit (#1) as a probe beam for the active CX measurement with a perpendicular CX analyzer (NPA3), were used for ³He NBI, because these beam lines are very close to plasma center as shown in Fig.2. Therefore high production rate of α particles is expected. On the other hand, deuterium beam units were selected from lower ones, except for #14 unit for the active CX measurement by a tangential CX analyzer (NPA2). ³He and deuterium beam energy are 78keV and 82keV, respectively. Frequency of ICRF wave was 116MHz, and it is corresponding to the forth harmonic of ³He ion resonance ($4\omega_{\text{CHe-3}}$) around plasma center of $R=3.50\text{m}$ where $B_T=2.85\text{T}$, as shown in Fig.2. Parameters' regions of D-³He experiments are $I_p=1.7\text{-}2.5\text{MA}$, $B_T=2.7\text{-}4.0\text{T}$ at $R=3.32\text{m}$ where is center of the JT-60U vacuum vessel, $\bar{n}_e=(0.6\text{-}3.8)\times 10^{19}\text{ m}^{-3}$, ICRF wave power $P_{\text{IC}}=1.8\text{-}3.3\text{MW}$, frequency of ICRF wave $f=116\text{MHz}$ and ³He beam power $P_{\text{He3}}=2.0\text{-}5.5\text{MW}$.

In discharges of $B_T=3.80\text{T}$ at plasma center, clear deuterium beam ion and thermal hydrogen ion acceleration by absorption of ICRF wave were measured by NPA2. Resonance layers of ICRF wave are located at plasma center, where the second harmonic of hydrogen ion resonance ($2\omega_{\text{CH}}$), the third harmonic of ³He ion resonance ($3\omega_{\text{CHe-3}}$), and the forth harmonic of deuterium ion resonance ($4\omega_{\text{CD}}$) are overlapping. Since hydrogen and deuterium ions absorb most of ICRF power, ³He beam ion is hardly accelerated by the interaction with ICRF wave there. However, in the case of $B_T=2.85\text{T}$, it is expected that ³He beam ions will be accelerated by the absorption of most of ICRF power if wave injection from right direction in Fig.2 does

not lose power at resonance layers of $3\omega_{CH}/6\omega_{CD}$ and $5\omega_{He3}$. Fig.3 shows a typical time evolution of discharge of $B_T=2.85T$ and $I_p=1.9MA$. Electron density in the top column increased linearly due to 3He beam injection. In this discharge, ICRF power was injected twice during 3He and deuterium beam injection. High energy 3He ion flux of 99keV, shown in the third column from the upper, increased during ICRF wave injection, and deuterium ions of which energy is more than injection energy increase clearly just after ICRF wave injection, as shown in the fourth column.

We measured 3He ion energy spectra with NPA2 in good signal to noise ratio, and deuterium and hydrogen ones were measured simultaneously with NPA3. Fig.4 (a) and (b) show energy spectra of 3He and deuterium measured by NPA3 and NPA2, respectively. Both of the tail temperatures of 3He and deuterium energy spectra are around 10keV, and those are higher than the electron temperature and the ion one by charge exchange recombination spectroscopy measurement. It means that ICRF wave and beam ions are in some coupling. 3He flux less than about 40keV increase during ICRF wave injection as shown in the third column in Fig.3. This means that confinement of slowing down 3He ion improves more or less, although expected increase of stored energy due to the coupling is not clear. On the other hand, as shown in Fig.4(c), higher energy hydrogen ions due to absorption of ICRF wave were not detected by NPA3. These results suggest that injected ICRF power is absorbed by 3He in the $4\omega_{He-3}$ layer and deuterium ion in the fifth deuterium one ($5\omega_{CD}$), mainly.

Since γ ray of 16.6MeV due to $D-^3He$ reaction occurrence was not detected by a perpendicular γ -ray measurement system viewing plasma core, that coupling condition did not bring about $D-^3He$ reaction in spite of 3He beam ion acceleration.

3. Discussion

To estimate absorption power of ICRF wave at resonance layers and enhancement of high energy ions for each ion species, we simulate CX energy spectra with experimental parameters at 6.9sec in the discharge shown in Fig.3 with a one-dimensional global wave code incorporating Fokker-Plank code self-consistently[2]. Those parameters are shown in Table1. The code is able to calculate a radial distribution of absorbed ICRF wave power density and an ion energy distribution with respect to resonance layers of one ion species. In the case of $B_T=2.85T$, preliminary calculation results show that the larger part of ICRF wave power is absorbed at the layers of $4\omega_{He-3}$ and $3\omega_{CH}$ and acceleration of 3He and hydrogen ions occur clearly over the injected beam energy and over about 30keV, respectively. However, the calculation result for deuterium shows unclear acceleration and it is not consistent with experimental result. Hydrogen energy spectra obtained by the calculation are not able to compare with experimentally obtained one, since energy region of good signal to noise ratio is less than about 30keV as shown in Fig.4 (c). Although accurate comparison of 3He ion energy

spectra is impossible due to treatment of only one ion species in the code, these results are consistent with the experimental results of CX measurement qualitatively. For more accurate and quantitative estimation, we should modify the simulation code in order to treat multi-ion species simultaneously.

4. Conclusion

According to the previous plan, we carried out the first D- ^3He reaction experiment with ICRF wave. ^3He beam ion acceleration by ICRF wave power absorption was observed, although γ ray of 16.6MeV proving the α particle generation was not detected. A reason of this conflict seems that ^3He beam ions do not absorb ICRF wave power more efficiently since ^3He beam axis is not through the plasma center where overlaps with resonance layer of $4\omega_{\text{CHe-3}}$. Also the absorption by deuterium beam ion lowered the wave power density in the plasma core.

We expect that generation of α particle will be brought about by optimizing resonance position and ^3He beam deposition in the next experiment. Moreover, we should estimate relation between the generation and ^3He beam ion acceleration with a modifying program code which is able to calculate ICRF wave absorption at resonance layers of some ion species simultaneously.

References:

- [1] FUJII, T., et al, JAERI-M 92-073(1992)276.
- [2] HAMAMATSU, K., et al, Nucl. Fusion, 29(1989)147.

1. Toroidal magnetic field at plasma center $B_T=2.85\text{T}$	4. Neutral beam ^3He ; power 3.7MW Energy 78keV D ; power 7.0MW Energy 82keV
2. Density profiles $n_e(r)=2.7\times 10^{19} \cdot (1-(r/a)^2)^{0.25} \text{ m}^{-3}$ $n_H(r)=2.18\times 10^{-2} \cdot n_e(r)$ $n_D(r)=2.18\times 10^{-1} \cdot n_e(r)$ $n_{\text{He3}}(r)=3.50\times 10^{-1} \cdot n_e(r)$ $n_C(r)=1.0\times 10^{-2} \cdot n_e(r)$	5. ICRF wave frequency 116MHz power 3.2MW
3. Temperature profiles $T_e(r)=3.1(1-(r/a)^2)^{0.73} + 0.22 \text{ keV}$ $T_i(r)=T_e(r)$	

Table 1: Experimental parameters of calculation for ICRF power density in resonance layers

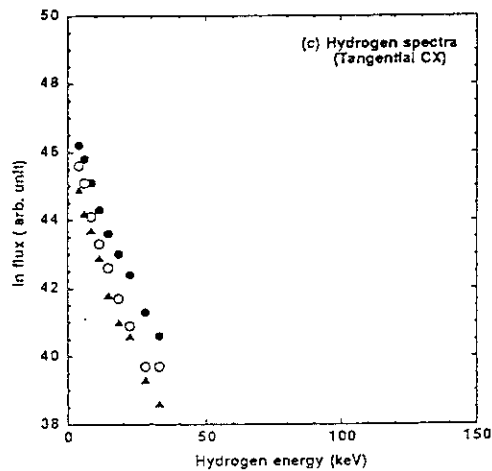
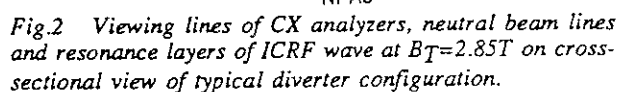
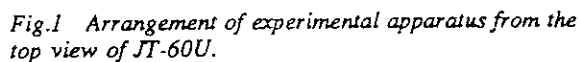


Fig.4 Typical energy spectra of (a) ^3He , (b) Deuterium and (c) Hydrogen measured by CX analyzers.

6.6 Ripple-Induced Fast Ion Losses

K. Tobita, K. Tani, Y. Neyatani, H. Takeuchi, A. van Blokland and T. Fujita

In JT-60U, a few 10 % of near-perpendicularly injected fast ions can be lost to the first wall by the toroidal field (TF) ripple. The ripple-lost fraction has been deduced from the temperature rise of the first wall. An infrared TV (IRTV) camera introduced recently has provided us fast wall temperature measurements with good spatial resolution and has enabled us to estimate reliable ripple loss power. In this section, we summarize the results of the ripple loss experiments after the introduction of the IRTV.

1. Detection of Ripple-Trapped and Ripple Banana Drift Losses

Orbit following Monte Carlo (OFMC) calculations [1] indicate that the heat load due to ripple-trapped appears on the lower (∇B ion drift direction) outboard and that the heat load due to banana drift appears on the upper outboard. The expected areas are illustrated in Fig. 1. The location of the heat load due to banana drift is determined by the the TF ripple distribution and the shape of the vacuum vessel.

By changing the field of view (FOV) of the IRTV camera, we measured the wall temperature rise in the areas. Infrared images obtained from the TV are shown in Fig.2. The heat load due to both processes is observed in the locations expected from the calculations. We can see a localized heat spot for ripple-trapped loss in Fig.2 (a). In the heat load due to banana drift, we can see large temperature rise at the tile edges (Fig.2(b)), which indicates that the heat load is attributed to banana drift. Because banana particles impinge on the wall at shallow angles because of their guiding-center orbits.

2. Toroidal Periodicity

The primary banana tips of neutral-beam-injected fast ions are out of the ripple-trapping region in JT-60U. As a consequence, the banana particles must circumnavigate the torus several times before they become ripple-trapped. This requirement leads to the toroidal periodicity of the heat load due to the ripple-trapped loss. The toroidal periodicity means that the heat load appears between every TF coil at the same heat flux.

A possible approach for confirming the toroidal periodicity experimentally using the only IRTV camera is to indicate that there is no difference in the heat flux between the NB injection close to the FOV of the IRTV and distant NB injection. In fact, the experimental heat flux was independent of the position of the injected NB. This result indicates the toroidal periodicity of the heat load in our case. The toroidal periodicity make possible to estimate the overall ripple-trapped loss power from the measurements of a period of the heat load.

3. Parametric Dependence

The OFMC code indicates that key parameters determining the ripple loss are TF ripple magnitude, safety factor, elongation, aspect ratio, and so on [2]. Of these parameters, the effect of the ripple magnitude and the safety factor is straightforward. Ripple wells are formed in the region where the effective ripple well parameter α^* ($\equiv (\partial \bar{B}/\partial l) / (\partial \tilde{B}/\partial l)$) satisfies $|\alpha^*| < 1$, where we express the toroidal magnetic field as $\partial B_\phi(r, \theta, \phi)/\partial l = \partial \bar{B}(r, \theta)/\partial l + \partial \tilde{B}(r, \theta)/\partial l \cos N\phi$. Here, \bar{B} , \tilde{B} , θ and ϕ stand for the axisymmetric and non-axisymmetric components of the toroidal magnetic field, the poloidal angle and the toroidal angle, respectively, and N is the number of TF coils. For a plasma with circular cross section, the ripple trapping condition can be simplified to $|\alpha^*| = r|\sin\theta|/(Nq\delta) < 1$ [3]. As expected from this condition, the ripple trapping region extends with δ and q .

By changing the plasma size and position, we obtained a relation between the ripple loss fraction and the ripple magnitude δ_{mid} , where δ_{mid} denotes the toroidal ripple on the outermost magnetic surface on the midplane. As plotted in Fig.3, the ripple loss fraction increased with ripple size. Here, the ripple loss fraction is defined as the ratio of the total ripple loss power to the NBI power. The total ripple loss power is estimated by assuming the toroidal periodicity of the heat spot. Radiation and charge exchange (CX) losses can also be part of the heat deposition on the wall. We estimated the loss power due to these processes from the temperature rise of the first wall near the TF coils and corrected for their contribution: part of the heat load near TF coils, however, may be attributed to the ripple loss. The error bars shown in the figure are mainly determined from the ambiguity in the estimation of radiation and CX loss power.

The poloidal distribution of the heat load is shown for different values of the effective safety factor q_{eff} in Fig. 4. Here, the q_{eff} scan is performed by changing I_p . As expected, the experimental data showed a strong dependence of q_{eff} on the ripple loss.

(4) Comparison Between Experiments and Calculations

An important question on the ripple loss is whether available codes predict the ripple loss quantitatively or not. The code adopted here was the OFMC code without including radial electric field (E_r). Since the radial component of the $\mathbf{E} \times \mathbf{B}$ drift is not zero in a non-axisymmetric system, the neglect of the electric field can affect the ripple loss fraction. According to several runs of the OFMC code with inclusion of E_r , the effect of E_r on the ripple loss was within the statistical error of the Monte Carlo calculations when E_r is of the order of kV/m.

The comparison between the experiments and the OFMC calculations of the ripple-trapped loss is shown in Fig. 5. Good agreement between both is seen. Here, discharge parameters for the plotted data were $I_p = 2.5 - 4.0$ MA, $B_T = 4.0$ T, $q_{\text{eff}} = 2.9 - 4.7$, $\delta_{\text{mid}} =$

0.2 - 0.5 % and line-averaged electron density $\bar{n}_e = (2.5 - 4.5) \times 10^{19} \text{ m}^{-3}$. The error in the computation is attributed to the statistical error caused by the finite number of test particles used in the Monte Carlo calculations. These results indicate that the OFMC code predicts the ripple-trapped loss quantitatively.

References

- [1] Tani, K., Azumi, M., Kishimoto, H., Tamura, S., J. Phys. Soc. Japan **50** (1981) 1726.
- [2] Putvinskij, S., et al., ITER-IL-PH-1-9-1 (1989).
- [3] Anderson, O.A., Furth, H.P., Nucl. Fusion **12** (1972) 207.

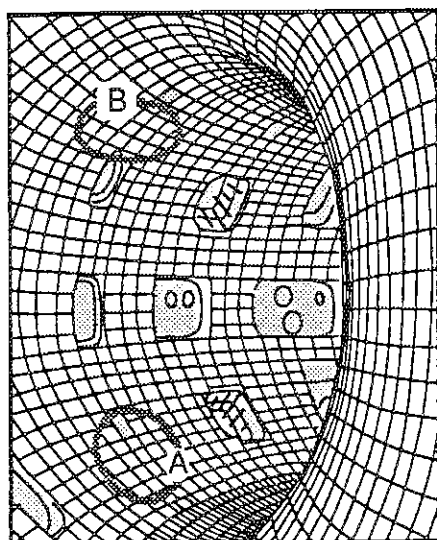
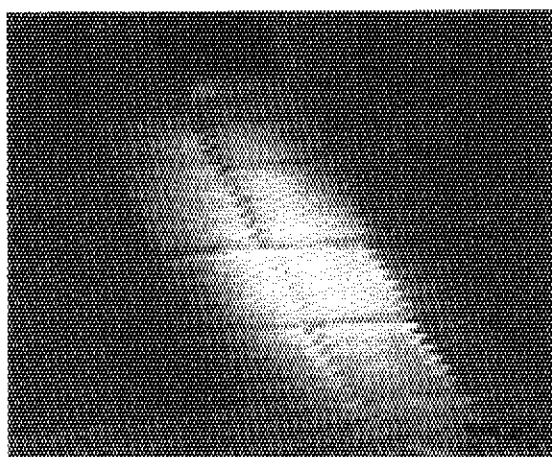
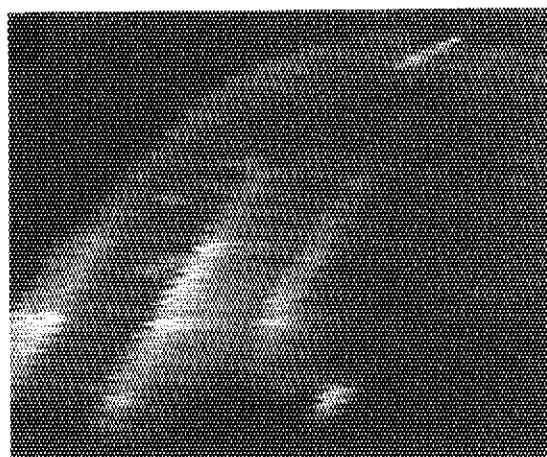


Fig. 1 Interior of JT-60U and the locations where the heat load due to ripple-trapped (A) and banana drift loss (B) is expected to appear.



(A)



(B)

Fig. 2 Photographs of infrared images of ripple-trapped loss (A) and banana drift loss (B) on the first wall. Whiter color corresponds to higher surface temperature.

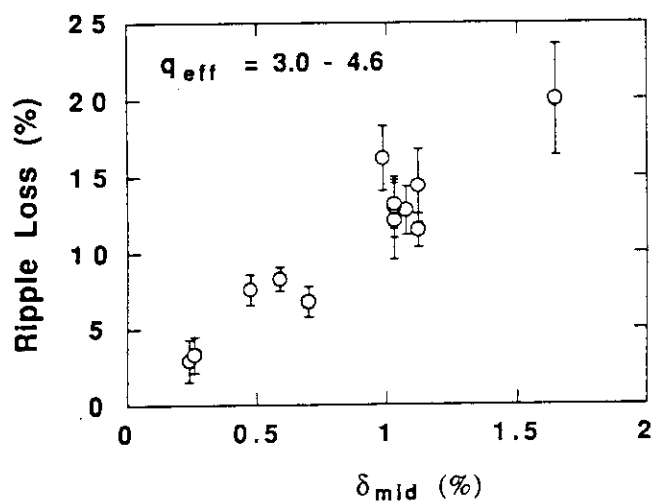


Fig. 3 Ripple-trapped loss vs. δ_{mid} which is the ripple magnitude at the plasma edge on the midplane.

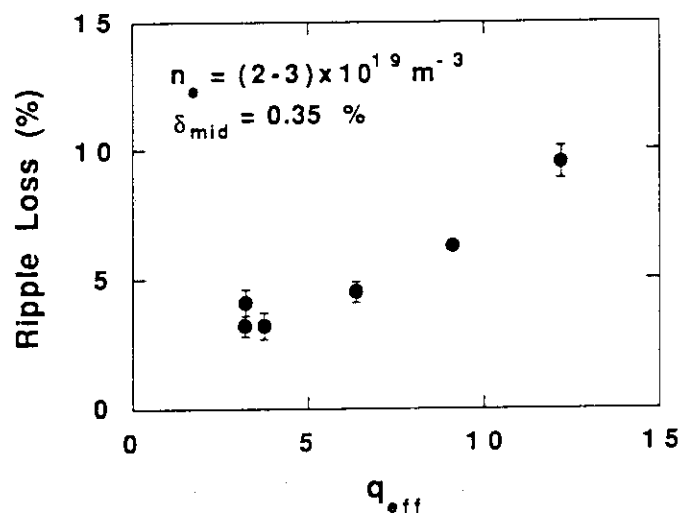


Fig. 4 Dependence of ripple-trapped loss on the effective safety factor q_{eff} .

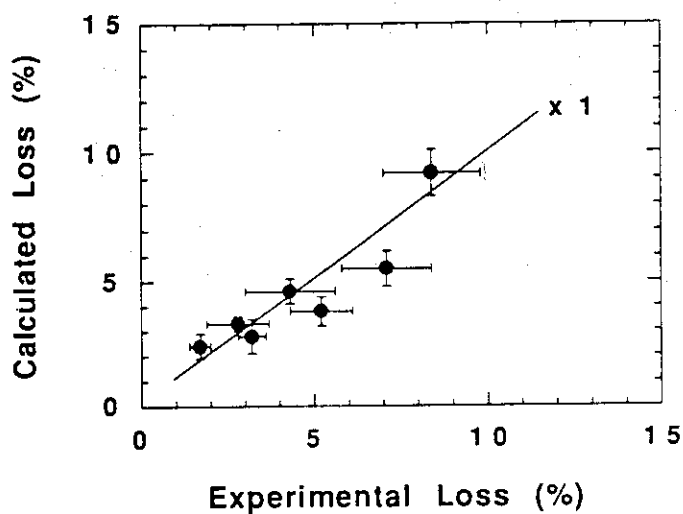


Fig. 5 Comparison of the ripple loss between the experiment and the calculations. The solid line represents agreement between both.

6.7 Triton Burnup

T. Nishitani, A. Morioka and Y. Ikeda

1. Introduction

The behavior of 1 MeV tritons produced in the $d(d,p)t$ reaction is important to predict the properties of D-T produced 3.5 MeV alphas because 1 MeV tritons and 3.5 MeV alphas have similar kinematic properties such as Larmor radius and precession frequency. The confinement and slowing down of the fast tritons were investigated by measuring the ratio of the 14 MeV and the 2.5 MeV neutron production rates. Tritons of 1.0 MeV are produced in the $d(d,p)t$ reaction at the same rate as the 2.5 MeV neutrons from the $d(d,n)^3\text{He}$ reaction. The majority of these tritons will remain confined in the plasma and slow down and a small fraction will undergo the fusion reaction $t(d,n)^4\text{He}$, in which 14 MeV neutrons are produced. Experiments in TFTR[1] and JET[2,3] indicated that the confinement and slowing down of tritons were consistent with the classical predictions. In JT-60U, the loss of tritons is expected to be larger than in TFTR and JET because of its large toroidal field ripple and the orientation of the neutral beam injection systems which is nearly perpendicular to the toroidal magnetic field. Time resolved triton burnup measurements were carried out by a 14 MeV neutron detector and they are compared with classical slowing down calculations.

2. Diagnostics

The time-resolved 14 MeV emission rate was measured with the silicon surface barrier diode (SBD) [4]. The 14 MeV neutrons entering a silicon diode may undergo the following nuclear reactions: $^{28}\text{Si}(n,p)^{28}\text{Al}$ and $^{28}\text{Si}(n,\alpha)^{25}\text{Mg}$, which have effective thresholds of about 7 MeV. Thus, the above reactions do not occur for the far more abundant 2.5 MeV neutrons. The SBD is mounted in the 20 cm-thick lead cylinder to shield gamma-rays from neutron capture events in the surrounding structure. The detector was installed just outside the JT-60U vacuum vessel on the midplane but inside the toroidal field coils, as close to the plasma as possible. The SBD used in this work has an area of 300 mm², and a nominal depletion depth of 1500 μm , which is sufficient to stop the 10 MeV protons and alphas produced in the nuclear reactions mentioned above. A thin disk with a ^{241}Am alpha particle source is mounted in front of the SBD to make an energy calibration of the detector possible using 5.486 MeV alphas. The 14-MeV neutron yield integrated over several weeks was measured by the activation foils using the $^{93}\text{Nb}(n,2n)^{92\text{m}}\text{Nb}$ reaction, which has a threshold energy of 9 MeV, a flat response function around 14 MeV, and a large cross-section. Because a pneumatic foil transfer system was not available, a half-life time of 10.15 days is suitable for one week of irradiation. The foil

was irradiated in the re-entry port only 16 cm outside the typical plasma surface [4]. The foil activation for the total 14 MeV yield was calibrated by a Monte Carlo simulation using the Monte Carlo Neutron and Photon transport code (MCNP)[5]. The absolute error in the 14 MeV emission rate was estimated to be $\pm 30\%$ including the calibration uncertainty of $\pm 20\%$.

3. Analysis

The time-dependent 14 MeV neutron emissivity was simulated by a simple classical slowing down model. The plasma was divided into 11 annular shells in the calculation. In each shell, the tritons were divided into 400 groups according to their birth time, with 10 ms time bins. The number of tritons in a group is proportional to the 2.5 MeV neutron emissivity at the birth time of the tritons. Tritons were allowed to slow down in each shell according to the classical energy loss formula[2] as

$$\frac{dE}{dt} = -\frac{\alpha}{\sqrt{E}} - \beta E \quad (1)$$

$$\alpha = 1.81 \times 10^{-7} \ln \Lambda_{ii} A^{1/2} Z^2 \sum_j \frac{n_j Z_j^2}{A_j}$$

$$\beta = 3.18 \times 10^{-15} \ln \Lambda_{ei} \frac{Z^2}{A} \frac{n_e}{T_e^{1.5}},$$

where E is the triton energy and T_e the electron temperature in eV, n_e is the electron density in cm^{-3} , A and Z are the triton mass and charge numbers, while n_j , A_j , and Z_j are the ion density and charge numbers. Finally, the $\ln \Lambda$'s are the Coulomb logarithms for ion-ion and ion-electron collisions. The loss of confined tritons was taken into account assuming an exponential decay of the number of tritons of the form $e^{-t/\tau}$ where t and τ are the time since the birth and the confinement time of the tritons, respectively. The diffusivity, D , was estimated by using the relation for the confinement time $\tau = a_p^2 / 5.8D$ to reproduce the experimental triton burnup ratio. The time history of the 14 MeV neutron emission rate was calculated by using the electron temperature profile from ECE measurement, the ion temperature profile from charge exchange recombination spectroscopy, and the electron density profile from the FIR interferometers as the time dependent plasma parameters. The triton birth profile was calculated using the steady state tokamak code TOPICS[6] for a typical time and the shape of the profile was assumed to be constant during the period of the triton burnup. The angular distribution of the tritons was assumed to be isotropic.

4. Results

Figure 1 shows the temporal evolution of the 2.5 MeV and 14 MeV neutron emission rates in a plasma with NBI heating of 18.7 MW. The peak of 14 MeV neutron emission was delayed due to the slowing down of the tritons from 1 MeV to the peak of $d(t,n)\alpha$ reactions at 170 keV of the triton energy. The delay is very sensitive to the slowing down process of the

triton, but not to the confinement time. The calculated 14 MeV emission rate is also shown in Fig. 1. There is good agreement between the measured and the calculated temporal evolution of the 14 MeV emission rate, indicating that the slowing down process of the 1 MeV tritons is classical.

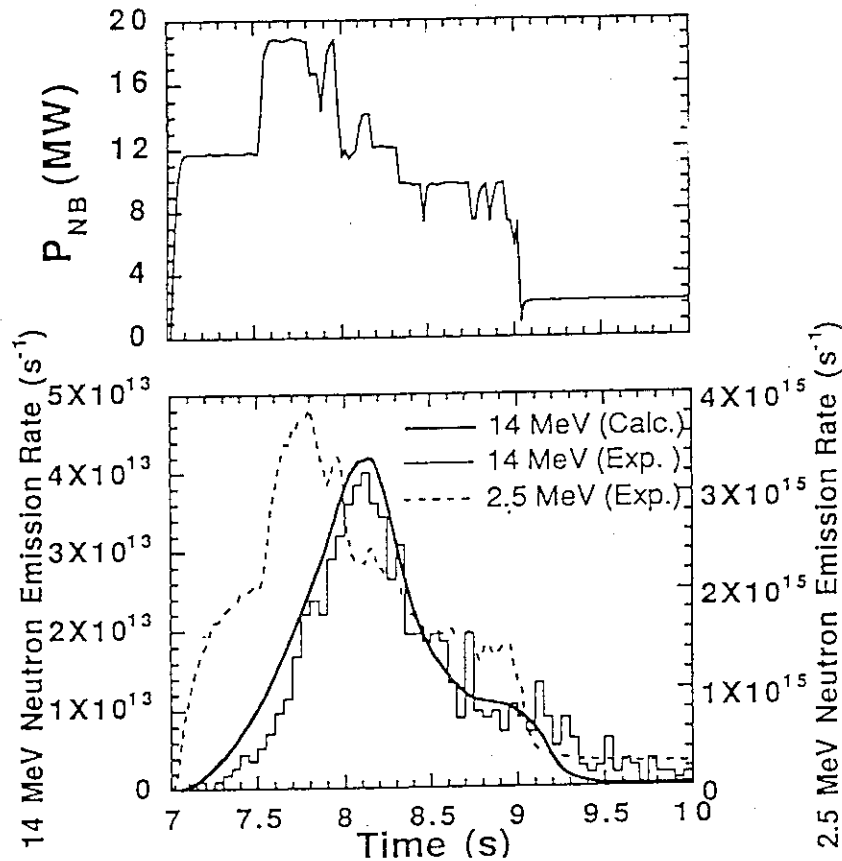


Fig.1 Comparison of predicted and measured 14 MeV neutron emission rate for the D° beam-injected D-D plasma.

The measured and calculated triton burnup ratios are plotted against the plasma current in Fig. 2. The triton burnup ratio is in the range 0.2-1.0 % which is 20-30% less than calculated except some point in high I_p discharges. This difference is as large as the 30% uncertainty of the measurement. It was expected that the orbit loss of the 1 MeV tritons was enhanced by the large anisotropy of the birth tritons in near perpendicular NB injection due to the large anisotropy of $d(d, p)t$ reactions. Figure 3 shows the fractional loss of the 1 MeV tritons predicted by the OFMC calculations. The prompt loss and the orbit loss in the slowing down process go up to be 40 % in the I_p of 1.5 MA. The ripple loss is 10-12 % in the range of I_p 1.5-2.5 MA. The total loss of the 1 MeV tritons does not contradict the discrepancy between the measured and calculated triton burnup ratios. If we explain the discrepancy by the triton diffusivity, $D \sim 0.2 \text{ m}^2/\text{s}$ is needed to reproduce the experimental triton burnup ratios.

It is reported in TFTR that the fast ions are lost according with the intense MHD activity[7]. So the Large discrepancy between the measured and calculated triton burnup ratios in some discharge with high I_p is probably due to the MHD activity.

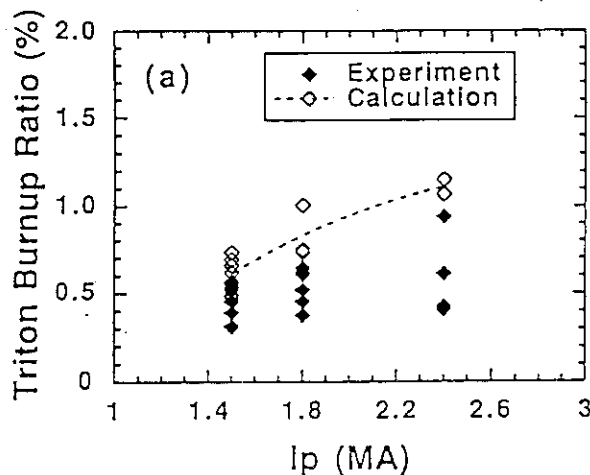


Fig.2 Comparison of the predicted and the measured triton burnup ratio averaged during the shot as a function of the plasma current

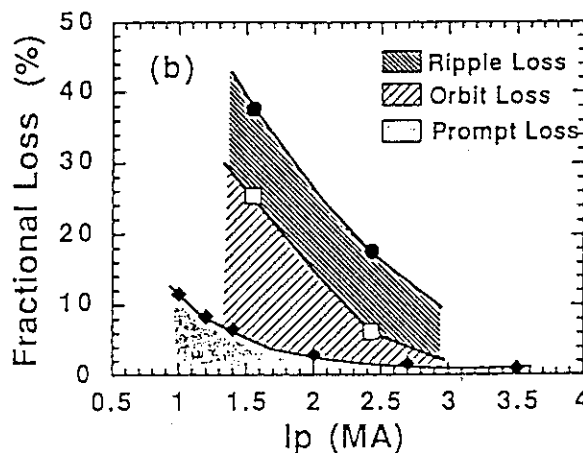


Fig. 3 Loss of the 1MeV tritons predicted by the OFMC calculation as a function of the plasma current

4. Conclusion

The confinement and slowing down of the 1 MeV tritons was investigated through the burnup of the 1 MeV tritons in the D-D plasma. The slowing down process of the 1 MeV tritons was found to be classical. The triton burnup ratio was measured to be in the range 0.2 - 1.0 % which was 20 -30 % smaller than the calculated values using the classical slowing down model. The discrepancy does not contradict the toroidal ripple loss and the orbit loss of the tritons predicted by the OFMC calculation.

References

- [1] STRACHAN, J.D., *et al.*, in Plasma Physics and Controlled Nuclear Fusion Research 1988 (Proc.12th Int. Conf. Nice,1988) Vol.1, IAEA, Vienna (1990) 257.
- [2] CONROY, S., JARVIS, O.N., *et al.*, Nucl. Fusion **28** (1988) 2127.
- [3] JET TEAM, in Plasma Physics and Controlled Nuclear Fusion Research 1988 (Proc.12th Int. Conf. Nice,1988) Vol.1, IAEA, Vienna (1990) 247.
- [4] JT-60 TEAM, Japan Atomic Energy Research Institute Report JAERI-M 92-073 (1992).
- [5] LOS ALAMOS MONTE CARLO GROUP, LANL Report LA-7396-M, Rev. 2 (1986).
- [6] NAKA FUSION RESEARCH ESTABLISHMENT, Japan Atomic Energy Research Institute Report JAERI-M 91-159 (1991).
- [7] ZWEBEN, S.J., Boivin, R., *et al.*, in Plasma Physics and Controlled Nuclear Fusion Research 1992, IAEA-CN-56/A-6-3.

6.8 Neutron Spectrometry with a ^3He Gas Ionization Chamber

T. Iguchi, N. Nakayamada and T. Nishitani

1. Introduction

Neutron energy spectrum produced from D-D and/or D-T burning plasmas reflects many useful informations on ion energy distribution, and high energy resolution neutron spectrometry is expected to be one of the most promising technique for ion temperature diagnostics. In particular, a ^3He gas ionization chamber (^3He I.C.) was proved as a successful tool for D-D plasma neutron diagnostics in the large tokamak machines such as JET and TFTR [1],[2]. At JT-60U, the same type of ^3He I.C. has been installed and applied to D-D plasma neutron spectrometry. This report gives an outline of the present neutron spectrometry system and some results obtained from ohmic and neutral beam heating D-D plasma experiments.

2. Neutron Spectrometry System

The ^3He I.C. used in JT-60U is the same type fast neutron spectrometer as already experienced in many other tokamaks, which is called FNS-1 on the market[3]. For 2.45MeV D-D neutrons, the energy resolution of this detector can be 50 keV FWHM, while the detection efficiency is also comparatively high, about 1.3 counts/(neutron/cm²). Fig.1 shows a flowchart of the present data analysis to estimate ion energy distribution from the measured pulse height spectrum of the ^3He I.C.. An adequate unfolding code with the detector response functions is needed to obtain neutron spectrum from the measured pulse height data. In this study, the response functions of the ^3He I.C. in the energy range between 0.1 and 5.0MeV were prepared through Monte Carlo calculation. These calculational results were adjusted to agree with the measured response data for several kinds of monoenergetic neutron sources. The spectrum unfolding code was based on the maximum likelihood and the maximum entropy method[4]. On the other hand, the FPS code was adopted to interpret the measured neutron spectra. This Monte Carlo code calculates the energy spectrum of a fusion product for given energy distribution functions, such as Maxwellian distribution, solutions of Fokker-Planck equation etc., of the primary reacting ions in a tokamak plasma[5]. The reasonable ion energy distribution can be estimated by searching the best agreement between experimental and theoretical neutron spectra.

3. Experiments

The ^3He I.C. was placed at about 15 m distance under the center level of the vacuum chamber. Through a collimator, the view area is subtended around 10 cm in diameter at the position of 10 cm outside the plasma center. The performance of the present neutron

spectrometry system were checked for some ohmically and beam heated D-D plasmas, of which average neutron emission rates were limited low to suppress the pile-up effect in pulse height measurement, about 5×10^{12} n/s in ohmic heating only and 4×10^{14} n/s in 4MW neutral beam additional heating, respectively. The measured pulse height data were summed up over several shots to improve the counting statistics.

4. Results and Discussion

Fig.2 shows an example of measured pulse height and unfolded neutron spectra obtained from ohmically heated D-D plasmas. It is well known that, for a purely Maxwellian distribution of the plasma ions with temperature $T(\text{keV})$, the Doppler broadening of the 2.45 MeV D-D neutrons is expressed by $82.5\sqrt{T}$ (keV) FWHM in a Gaussian distribution[6]. In the case of Fig.2, Gaussian fitting for the unfolded neutron spectrum gives the mean energy of 2.47 MeV and standard deviation of 45.9 keV, which corresponds to the ion temperature of 1.73 keV with uncertainty of $\pm 30\%$. This value is consistent with the maximum ion temperature estimated as 2.0-2.3 keV from total neutron yield because the ion temperature from neutron spectrum is considered a time and space averaged value a little outside the plasma center.

Fig.3 shows an example of neutron spectrum data from beam heated D-D plasmas. Neutral beam deuterons of 90 keV are injected into the main plasma under an incidence angle of 75 deg. to the magnetic axis, while, to this axis, the viewing angle of the neutron spectrometer is 90 deg.. Due to the beam-plasma interaction, the neutron spectral line shift was observed in the measured pulse height data. Assuming the background ion temperature of 4.0 keV combined with the analytical solution of Fokker-Planck eq. in the FPS code, good agreement is found between the calculated and the unfolded neutron spectra as shown in Fig.3(b), which was also consistent with the result from CXRS diagnostics.

5. Conclusion

Neutron spectrometry using a ^3He gas ionization chamber system has been successfully applied to JT-60U D-D plasma experiments. Under the condition of low neutron emission rates in ohmic and low power additional heating, this system has been verified very useful for the ion temperature diagnosis. However, in order to expand the applicability of this system to higher power level experiments, it is necessary to be able to control counting rates and reject pile-up effects in the pulse height measurement, for example, by remotely adjusting the collimator size.

References

- [1] JARVIS, O.N., et al., Rev.Sci.Instrum., 57 (1986) 1717.
- [2] NISHITANI, T., and STRACHAN, J.D., J.J. Appl. Phys., 29(3) (1990) 591.
- [3] JORDAN VALLEY APPLIED RADIATION LTD., 'FAST NEUTRON SPECTROMETER MODEL FNS-1 Instrument Manual' (1985).
- [4] ITOH, S., and TSUNODA, T., J. Nucl. Sci. Tech., 26(9) (1989) 833.
- [5] VAN BELLE, P. and SADLER, G., Proc. Workshop on Basic and Advanced Fusion Plasma Diagnostic Technique, Varenna (1986) 50.
- [6] BRYSK, H., Plasma Phys., 15 (1973) 611.

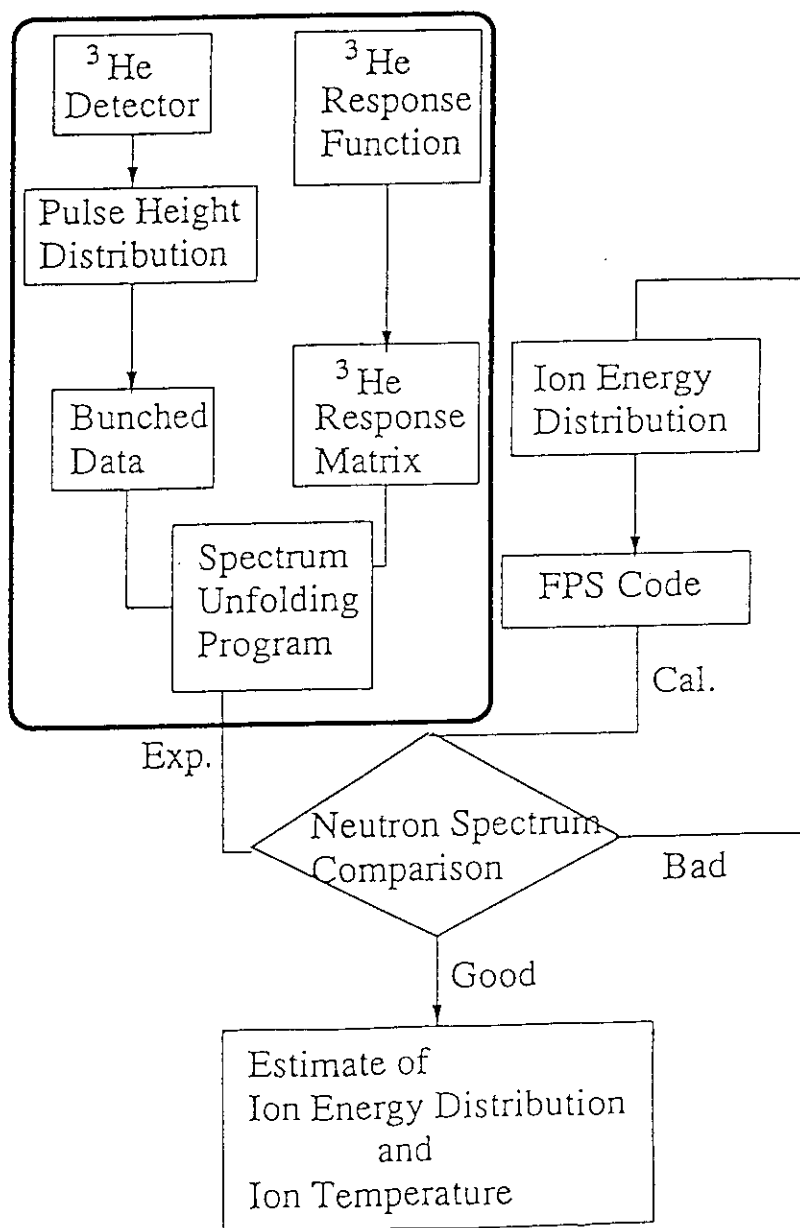


Fig.1 Flow chart of the data analysis for neutron spectrometry system with a ^3He gas ionization chamber.

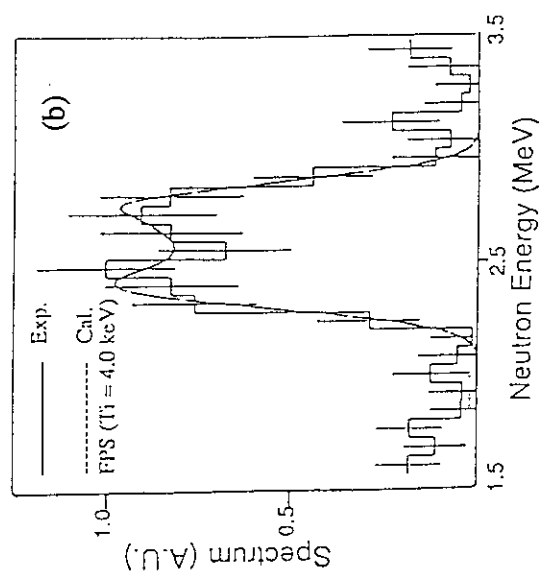
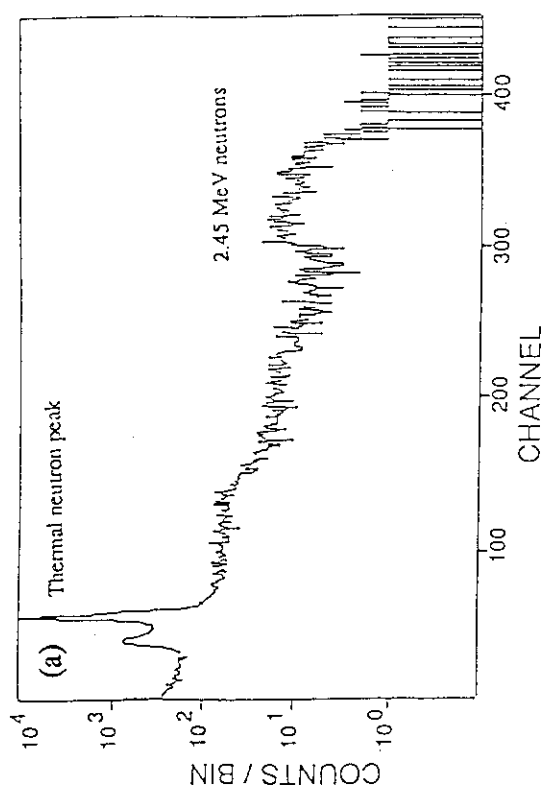


Fig. 3 Neutron spectrum in NB heated D-D plasma: (a) Measured pulse height spectrum and (b) Unfolded neutron spectrum.

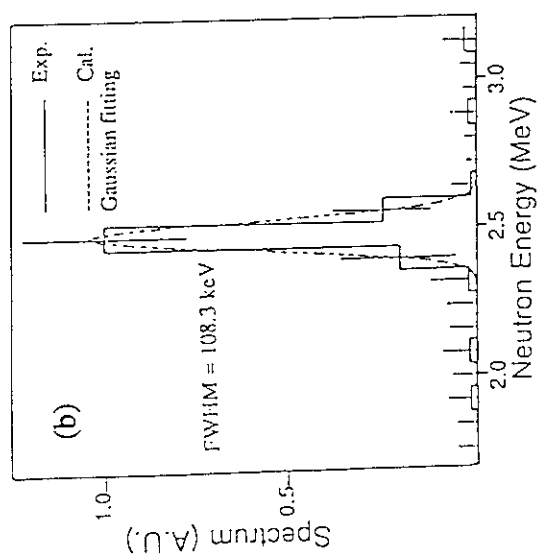
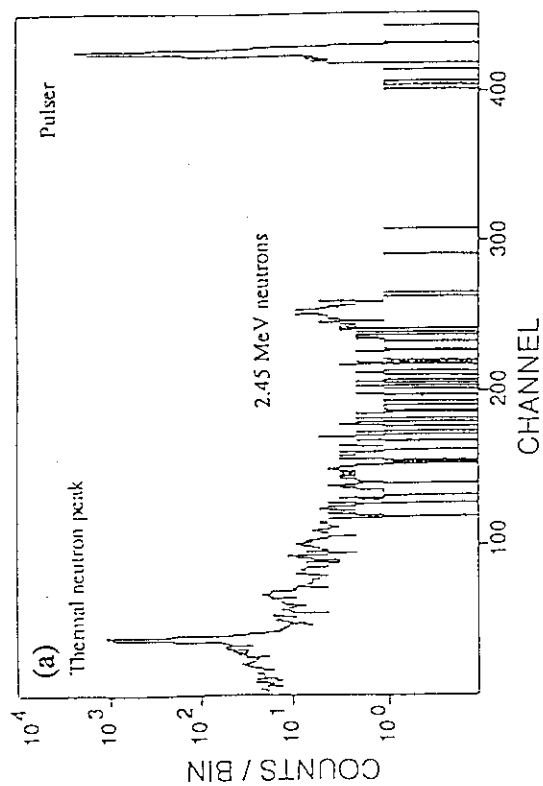


Fig. 2 Neutron spectrum in ohmically heated D-D plasma: (a) Measured pulse height spectrum and (b) Unfolded neutron spectrum.

6.9 Activation Analysis with 1-D Code in D-D Discharges

N. Miya , Y.Ikeda, N. Toyoshima, T. Nishitani and H. Takeuchi.

1. Introduction

Evaluation of dose rate after shutdown of D-D plasma discharge operations associated with neutron production is of importance to estimate personal exposures during maintenance of the machine. A one-dimensional calculation code was employed to identify radionuclides and to assess a level of radioactivity in JT-60U. The calculation is compared with the measurement of dose rate as well as activation rate caused in experiments of the first 39 D-D operation weeks.

2. D-D Operation and Neutron Production

The D-D operation in JT-60U began from June 1991. Neutron production in the initial 39 operation weeks is shown in Fig.1. JT-60U had two shutdowns after operation phases marked 'Operation A' and 'Operation B' in the figure for in-vessel work or maintenance of the machine to be conducted after each phase. The calculation has been carried out for the dose rate and the activation rate during the shutdown times in two cases: Case#1 after the operation phase A(after week #11 in Fig.1), and Case#2 after the B(after #39). The corresponding total neutron productions are listed in Table 1.

Table 1 The D-D neutron productions in the case#1 and the case#2.

Case	Operation Phase	Weeks	Total neutron Yield
#1	A (June19-Oct.4 1991)	#1-10	7×10^{17}
#2	B (June19 1991-Apr.24 1992)	#1-39	1.7×10^{18}

3. Calculation

A one-dimensional transport code ANISN is used. Adopted nuclear group constant set is FUSION-40¹⁾. Legendre polynomial order in scattering cross section P5 and the order of angle dividing number S8, the isotopic division in space, are applied. A one-dimensional torus model shown in Fig.2 is used for the calculation. Number of radial meshes is 105. A code system CINAC-V4 is used to calculate the radioactivity and dose rate around the device. An averaged neutron yield in each operation week is adopted for the code. D-T neutron fraction due to triton burn-up is assumed to be 1% of D-D neutron. Used chemical compositions (weight %) of structures and materials around the device are shown in Table 2.

4. Measurement

Time dependencies of dose rates are measured by the gamma-dosimeter (GM survey meter) at a position of a vacuum vessel surface of mid-plane in P-3 section. A γ -ray spectrum of a support structure (type SS-316 stainless steel sample) of carbon first wall tile was measured with a Ge detector at a cooling time of 63 days after the shutdown of phase A.

5. Results and Discussion

The calculation results of dose rate on the vacuum vessel (position A in Fig.2) are shown in Fig. 3 for the case#1 and the case#2 with the data measured by the GM survey meter during the shutdowns after each phase. Increment of dose rate is identified in case#2 at the time from two days to one month. It is caused by the accumulation of long half-life nuclide of ^{58}Co generated by $^{58}\text{Ni}(n,p)$ reaction which derived from a large composition of Ni in Inconel-625. The experimental values agree well with the calculation results although the data are restricted within about one month. Accuracy of calculation is considered to be not satisfactory within a week because of the use of averaged neutron yield.

A spectrum of SS-316 (position B in Fig.2) sample is shown in Fig.4 in which radioactivities of ^{58}Co , ^{51}Cr , ^{60}Co , ^{54}Mn , ^{59}Fe , ^{57}Co are identified. They have relatively long half-lives of 70.8d, 27d, 5.4y, 312.5d, 271d, respectively. This sample is irradiated over D-D discharge for 10weeks (Phase A). Cobalt-58, ^{54}Mn and ^{57}Co are produced via threshold reaction of $^{58}\text{Ni}(n,p)$, $^{55}\text{Mn}(n,2n)$ and $(^{58}\text{Ni}(n,np)+^{58}\text{Ni}(n,2n)^{57}\text{Ni}\rightarrow^{57}\text{Co})$, respectively, although the others were due to (n,γ) . Radioactivities via threshold reactions are associated with the primary D-D neutrons. In the previous report²⁾, the dominant (n,γ) reactions are observed in the SS-316 sample located outside the vessel near the TF-coil of P-3 section. This difference in reaction between the two samples is attributable to the location of the sample. It can be interpreted in terms of an enhanced low energy neutron flux distribution in the region outside the vacuum vessel. Calculation result of ^{60}Co differs relatively from that of the measurement. This discrepancy is probably due to a large contribution of the thermal neutrons in the calculation. Further studies are needed to make the 1-D code most suitable conditions: D-T neutron fraction (assuming 1% of D-D neutron), and modelling of TF-coil structure.

6. Summary

In this work the one-dimensional neutron transport code ANISN and the induced radioactivity calculation code CINAC provided a sufficient prediction for the dose rate and the activation on the tokamak machine. Further studies are needed to make the calculation most suitable conditions for the effects by the thermal neutrons.

- References;** 1) K.MAKI, et. al., JAERI M 91-072,1991.
2) JT-60 Team, JAERI M 92- 140,1992,pp250-259.

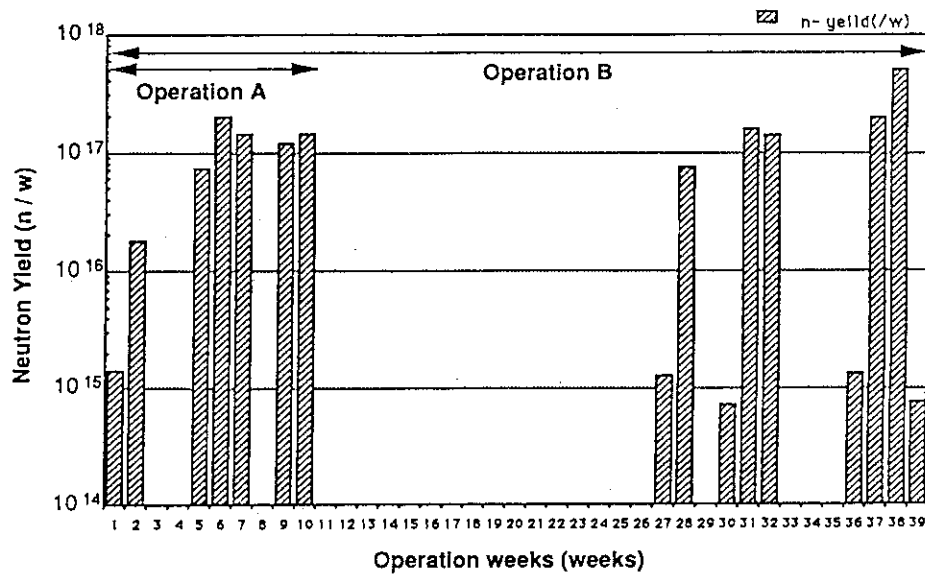


Fig.1 Neutron Yield in JT-60U D-D Operation.

Table 2 Chemical compositions of the materials around the device.

Material (%)	First Wall	SUS316	Inco625	HighMn	TF Coil
C	100	0.08	0.02	0.5	
Mn		2	0.07	18	
Fe		65.145	4.32	74.4	
S		0.03	0.001		
Si		1	0.14	0.4	
Ni		12	60.78	2	
Cr		17	22.02	4.7	
Al			0.2		
Ti			0.23		
Co		0.2	0.06		
Mo		2.5	8.58		
P		0.045	0.006		
CB(+TA)			3.57		
Cu					99.8
Ag					0.2

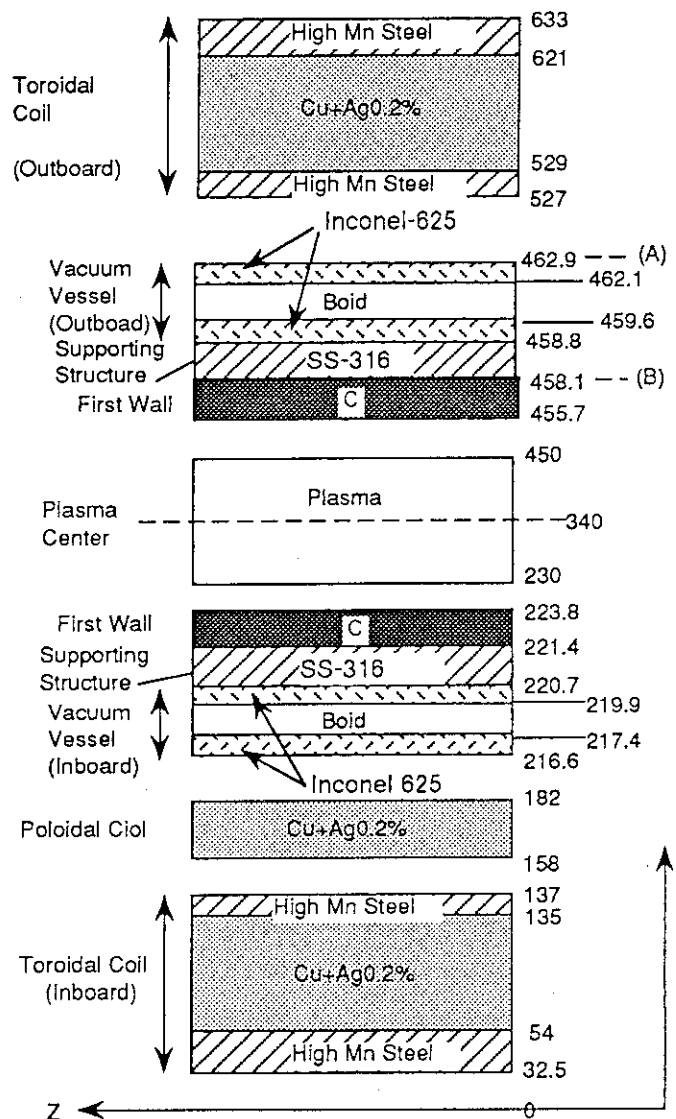


Fig.2 One-dimensional torus model (cm).

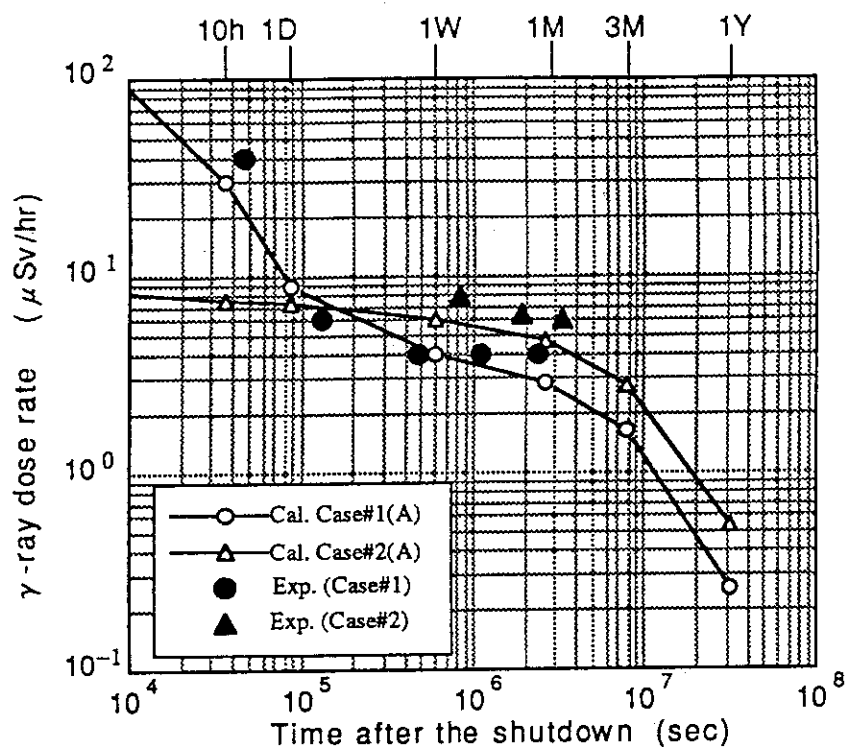


Fig.3 Comparison of the measured results (Exp.) with calculated results (solid lines) in γ ray dose rate on the vessel (Case#1,2,A-point).

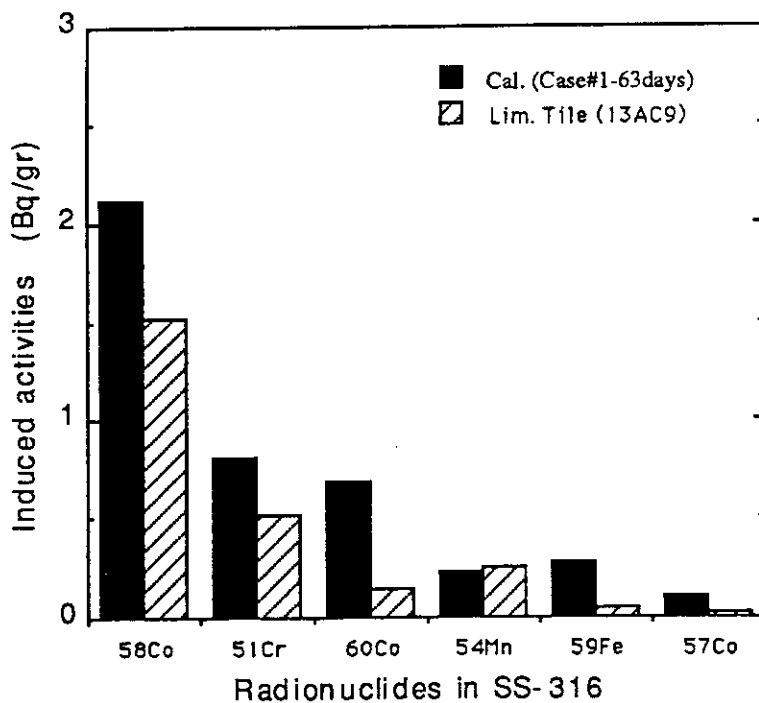


Fig.4 Comparison of the measured results with calculated results (B-point, Case#1-63days after the shutdown) in induced activities on the first wall material SS-316 (limiter tile 13AC9).

7. Disruption and Plasma Control

7.1 Review of Disruptions

R.Yoshino, Y.Neyatani, N.Hosogane, Y.Kamada, S.W.Wolfe, M.Matsukawa and S.Miura

1. Introduction

In tokamak fusion reactors, disruptions will determine the lifetime of the first wall and divertor plates, and the resultant high electromagnetic stress on the structure will impose severe constraints on the design. Reduction of the plasma current decay rate will reduce the electromagnetic forces on in-vessel components, will improve the maintenance of plasma position control following the energy quench, and reduce the production of nonthermal (runaway) electrons owing to relatively higher electron temperature. Furthermore suppression of disruptions can extend the operational limit. Stable and fast plasma current ramp-up and ramp-down will be indispensable to decrease the dwell time in pulsed reactors.

To develop the avoidance and softening techniques of disruptions, investigations of them are indispensable. In JT-60U, three types of disruptions were mainly observed in divertor plasmas. They are locked mode disruption, density limit disruption, and high I_i disruption. The last one was observed for low density plasmas during the plasma current ramp-down owing to high I_i , that may be caused by the tearing instability. Characteristics and avoidance techniques of these three disruptions are reviewed in this paper.

Besides these disruptions, a few disruptive terminations caused by the vertical positional instability were observed in the high β_p experiments[1]. However this instability was perfectly stabilized by an optimization of the feedback control gain of the vertical plasma position, owing to the relatively small plasma elongation of 1.5~1.7 defined at the outermost flux surface and high stabilizing effect of vacuum vessel. High β_p collapse caused a few disruptive terminations owing to the plasma attachment to the inner board first wall, but data points are not enough to be analyzed.

2. Locked Mode Disruption

Locked mode disruptions are observed during the plasma current ramp-up and flattop. Crossing of $q_{\text{eff}}=4$ or 5 with low I_i causes minor or major disruptions as observed in other tokamaks. In JT-60U, plasma current ramp-up with constant plasma minor radius is limited to $<0.5\text{MA/s}$ by locked mode disruptions. The locked mode disruptions are believed to be a consequence of the error field produced mainly by the divertor coil, since they are observed only when the divertor coil is excited. The $m/n=2/1$ component of this field at the plasma surface may be $\sim 1\text{Gauss}$. Rotating modes are observed prior to the locked mode disruption at

q_{eff} slightly larger than 4 or 5. Locked modes occurred crossing $q_{\text{eff}}=4$ after the excitation of the divertor coil cause minor disruptions with a sudden increase in I_i , and sometimes terminated the discharge.

In JT-60U, to obtain plasmas of $3 < q_{\text{eff}} < 4$ without the locked mode disruptions, q_{eff} was reduced to a value lower than 4.0 just after the plasma initiation (e.g. 0.2 s) by strong compression of the plasma on the inboard side with a plasma minor radius $a_p=0.6\text{m}$ as presented in Fig.1. While plasma current was ramped up with 1MA/s, a_p was expanded to 0.9~1.0m keeping $3 < q_{\text{eff}} < 4.0$. Even though the divertor coil current was excited to change the plasma configuration from limiter to divertor during this ramp-up, locked modes were perfectly suppressed. This operational scenario substantially reduces the skin current leading to higher values of I_i for the divertor plasma and improving the MHD stability. By using this ramp-up method, ramp rates as high as 2.0MA/s were obtained from 0.5MA to 3.5MA without additional NB heating or the use of a helical field as presented in Fig.2. Minor disruptions caused by locked modes without rotating precursors were observed at $I_p > 1\text{MA/s}$, but they did not cause a current quench.

Low density locked mode[2] was observed at $q_{\text{eff}} < 3.7$ for $n_e < 0.9 \times 10^{19} \text{m}^{-3}$ only with the excitation of the divertor coil as presented as presented in section 7.3. In the case of divertor plasmas without exciting the divertor coil, that can be produced by the stray field of OH coil current, discharges were stable and low density locked mode was not observed.

3. Density Limit Disruption

Density limit disruptions were observed during a whole discharge, that may be triggered by the tearing mode due to the strongly peaked current profile. The lack of power balance in the plasma periphery causes the shrinkage of a plasma current channel at high plasma densities or an intense influx of impurity. Energy quench and current quench in the density limit disruption is investigated in section 7.9.

In the density limit disruption of JT-60U divertor plasmas, MARFE and the detached plasma were always observed before the current quench at $q_{\text{eff}} > 3$. The duration of MARFE was $> 1\text{s}$ for OH and NB plasmas, and was not a function of q_{eff} as presented in Fig.3. Stable MARFE of $\sim 4\text{s}$ was observed at any q_{eff} . For OH plasmas, the duration of the detached plasma phase was 0.1~0.6s at $3 < q_{\text{eff}} < 5$, and increased a little by decreasing I_i at the start of the detached plasma phase as presented in Fig.4. This may be explained by the larger stability margin of $m/n=2/1$ or $3/2$ modes owing to the smaller $q=1$ radius[3]. At $q_{\text{eff}} > 7$, no current quench was observed after the detached plasma phase as presented in Fig.5. Plasmas survived changing the plasma state frequently as detached or attached until the end of the programmed shutdown. These disruption-free discharges at high q_{eff} may be obtained by high impurity-shielding effect of the divertor, and/or high MHD stabilizing effect of large magnetic shear.

A MARFE or a detached plasma can be returned to a divertor plasma by high power NB heating or LHRF heating in JT-60U. A slow positive plasma current ramp with 0.2MA/s also produced a long detached plasma phase of >1 s for $q_{eff}>3$ owing to the flattening of the plasma current profile (lowering I_i) and the heating of the plasma periphery. In a MARFE or a detached plasma the heat flux to the divertor plate can be reduced to very small value due to nearly 100% radiation of the input power by the main plasma. This drastic reduction of the heat flux to the divertor plate is a good precursor of the density limit disruption, and will offer a way to avoid melting the divertor plate in an emergency such as a loss of coolant accident (LOCA)[4], where the detached plasma can be generated by impurity pellet injection or intense gas puffing, and can be maintained by additional heating.

4. High I_i Disruption

High I_i disruptions were observed during a plasma current ramp-down, that may be triggered by the tearing mode due to the strongly peaked current profile caused by the long diffusion time of plasma current owing to high electron temperatures at low plasma densities of $<1 \times 10^{19} \text{m}^{-3}$. Generation of runaway electrons are observed during the current quench in high I_i disruptions as presented in section 7.9. Low plasma density may be the principal cause. To get the stable plasma current ramp-down, I_i must be lower than some limiting value.

In JT-60U, the plasma minor radius was reduced during the current ramp-down to broaden the plasma current profile by decreasing the skin time. The I_i was controlled lower than the limit value during the lowering of q_{eff} to ~ 3 as presented in Fig.6, where plasma minor radius was reduced from 1.1m to 0.7m. This ramp-down scenario was tried in many shots without no major disruption for $I_p > 0.5\text{MA}$. Furthermore fast ramp-down from 2.0MA to 0.5MA with $dI_p/dt = -4.0\text{MA/s}$ was obtained successfully. A helical field with a principal mode number of $m/n=3/2$ produced by DCW(Disruption Control Winding)[5] was excited to broaden the plasma current profile and obtained the stable plasma current ramp-down as presented in section 7.5.

5. Conclusions

In JT-60U, three types of disruptions were observed in divertor plasmas. They were investigated to suppress them. Stabilization techniques were developed, and fast plasma current ramp-up of 2MA/s and ramp-down of -4MA/s were obtained without disruptions.

References

- [1] ISHIDA, S., et al., section 2.5
- [2] La HAYE, R.J., et. al., Phys. Fluids B 4 (1992) 2098
- [3] SHIMIZU, K., JAERI-M 89-165 (1989)
- [4] POST, D.E., et al., ITER DS 21 (1991)
- [5] NINOMIYA, H., et al., Plasma Devices and Operatio, 1 (1990) 43

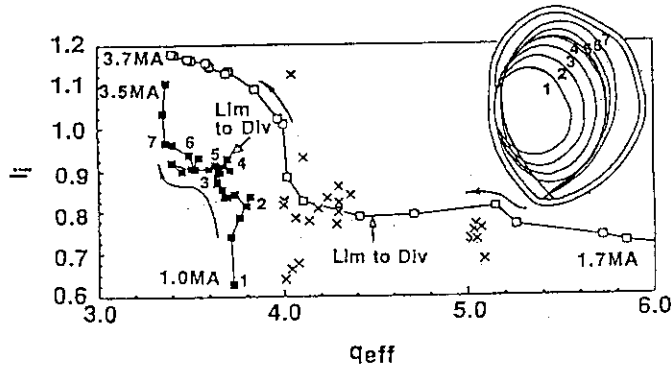


Fig.1 Time behavior of q_{eff} and l_i during 1.0MA/s plasma current ramp-up with expanded a_p (■), and 0.5MA/s ramp-up with constant a_p (□). Expansion of the plasma is presented in a figure with each time point number. X is the start of the rotating mode prior to the locked mode disruption.

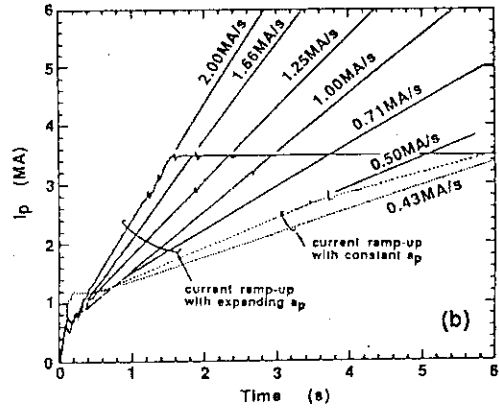


Fig.2 Plasma current ramp-up with/without expanding plasma minor radius. Plasma current ramp-up with 2MA/s is obtained.

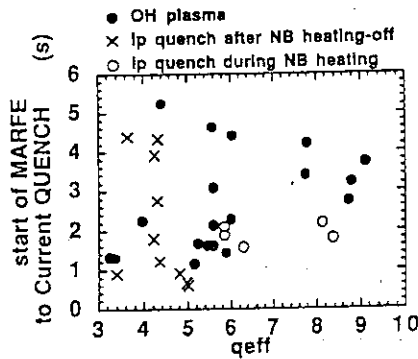


Fig.3 Time delay of the plasma current quench from the start of MARFE in the density limit disruption.

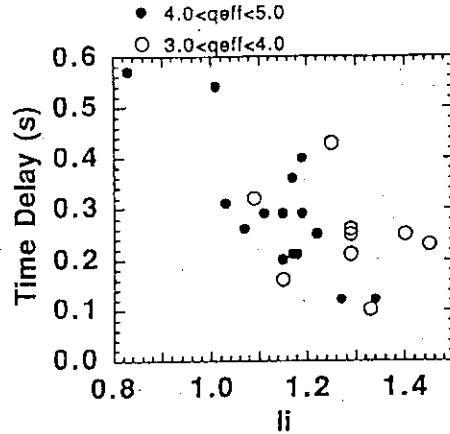


Fig.4 Time delay of the plasma current quench from the start of the detached plasma in the density limit disruption versus l_i .

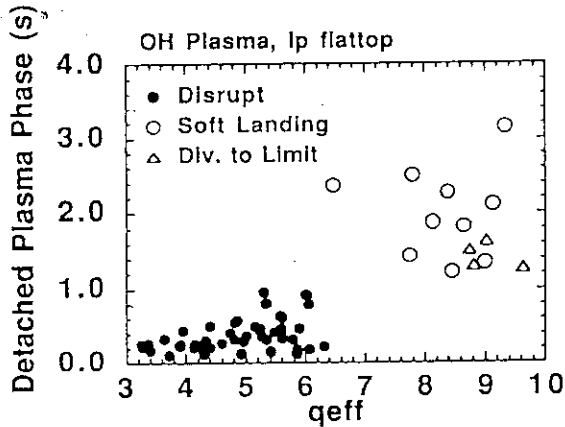


Fig.5 Time delay of the plasma current quench from the start of the detached plasma in the density limit disruption versus q_{eff} .

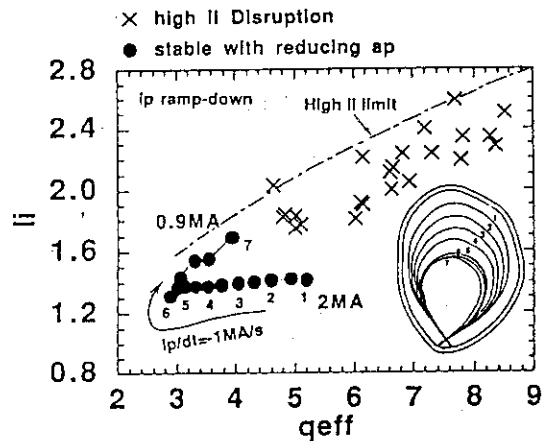


Fig.6 q_{eff} and l_i of high l_i disruption, and a trajectory of q_{eff} and l_i during the plasma current ramp-down with reducing the plasma minor radius.

7.2 Identification of a Low Density Locked Mode

S W Wolfe, R Yoshino, Y Kamada

1. Introduction

Certain confinement regimes in tokamaks require stable low-density plasmas. For example, hot ion regimes ("supershots" in TFTR, hot ion H-modes), the VH mode (DIII-D) and LHCD experiments all require low density Ohmic target plasmas. However, low density tokamak plasmas are susceptible to MHD instability, usually in the form of large amplitude coherent modes which are locked in spatial phase. Disruptive activity, confinement degradation, and, at worst, discharge termination are inevitable results of locked mode activity. To improve low density operation, the MHD activity must be fully characterised and understood.

2. Instability at Low Density

Observations on JT-60U have demonstrated that, at a sufficiently low density, discharges are often unstable. The impact on the performance depends on the value of the effective surface safety factor q_{eff} and whether the plasma is in a limiter or divertor configuration. After the divertor coil has been excited (20 to 30 kA), if q_{eff} is between 3 and 4 and the line-averaged electron density at the current flat-top is less than about $0.8 \times 10^{19} \text{ m}^{-3}$, the discharge almost always terminates disruptively, as shown in Figure 1a). Under the same conditions, but in a limiter configuration with no divertor coil excitation, the discharge is also unstable but does not terminate. In this case, the instability often manifests itself as a slow (≈ 2 Hz) oscillation in the soft x-ray emission and synchronous spikes in the H_{α} emission.

Plasma performance in the divertor configuration is thus degraded compared to the limiter case. This dependence of stability on divertor coil excitation has previously been observed for locked modes in the current ramp-up [1], which suggested that error fields (non-axisymmetric components of the vacuum magnetic field--see Miura *et al.*, Section 7.3 of this report) arising from the divertor coil were playing a rôle. Experiments on other machines have shown that error fields are important for low density operation also (DIII-D [2], JET [3], COMPASS-C [4]). Those investigations showed that a density threshold exists below which a locked mode is driven nonlinearly unstable by the error field. This threshold depends on the magnitude of the error field and the value of q_{eff} . Therefore, to determine whether this type of instability was affecting low density operation on JT-60U, it was necessary to search for 1) threshold behaviour, and 2) a locked mode.

A clear threshold has been observed for q_{eff} between 3 and 4, as mentioned above. At lower values, data are sparse, and at higher q_{eff} , very low densities are possible and a threshold is not observed. A dependence on divertor coil current requires more data to be conclusive.

Detecting the expected locked mode has been attempted. It has proven to be difficult, however, because JT-60U has no saddle loops dedicated to monitoring locked modes, and a rotating precursor (which would be easy to detect on, for example, the Mirnov coils) has never been observed prior to low density disruptive activity. As an alternative, the magnetic probe system meant for plasma control is used. It consists of three poloidal arrays: two of them (TC) measure the field tangential to the wall (approximately B_θ) at 17 poloidal positions and at toroidal locations 180° apart, and the third (N) measures the field normal to the wall (approximately B_r) at 16 poloidal positions. The relative amplitude of a magnetic field perturbation is given by $b_\theta = \tilde{B}_\theta / B_{\theta 0} = B_\theta / B_{\theta 0} - 1$, where $B_{\theta 0}$ is the unperturbed field. In the presence of a locked mode, the unperturbed field is impossible to deduce, so that it is approximated by $B_{\theta 0}(t) \approx B_\theta(t_0) I_p(t) / I_p(t_0)$, where t_0 is a time when the plasma is unperturbed, usually just before the mode appears. Note that this method only takes into account the change in current in the approximation of the unperturbed field. If the plasma changes shape or moves appreciably (more than about 1 cm) the approximation will be poor.

Furthermore, a conclusive experiment has been operationally difficult to carry out because low density usually leads to a locked mode in the current ramp-up (regardless of configuration), and the effects of this mode later on in the discharge are unknown. The discharge shown in Figure 1 was one of the few where no locked mode was observed in the current ramp-up, and a clear locked mode was seen just prior to the disruptive activity. The divertor coil current, proportional to the magnitude of the error field, was increasing when the instability started, while the density was decreasing (see Figure 1b). A polar plot of the magnetic field perturbation at 4.51 s (compared to conditions at 4.50 s) shows a predominantly $m=3$ structure (see Figure 1c). Note that the discharge terminates about 0.9 s later.

3. Interpretation Difficulties

Good statistics for these experiments are still lacking; there have not been many observations of unstable low density discharges at low q_{eff} . Furthermore, most of these exhibit "conventional" locked mode activity in the current ramp-up, which makes interpretation of the results difficult. Also, a locked mode is usually not detectable prior to the start of disruptive activity at low density. This may be due to the measurement difficulties mentioned above.

In particular, it may be important to distinguish those cases where a conventional locked mode has appeared in the current ramp-up. It should be noted that this locking sometimes occurs before divertor coil excitation, which means that the perturbation is not locking to the divertor coil error field, but to another error field or some wall structure. When this happens, it can be assumed that the plasma, or some part of it, has stopped rotating. When an external helical perturbation is applied to this stationary plasma, theory predicts [5] that a tearing mode can be driven; whether the perturbation is resonant with the pre-existing mode is irrelevant.

The plasma response to this perturbation will be to amplify the resulting island. In any case, theory does not predict any threshold behaviour, except possibly through the parameter dependence of Δ' (the tearing stability parameter).

Thresholds are expected when the plasma is rotating, because then the external perturbation will only penetrate the plasma if conditions on viscosity or inertia are met. For a given perturbation amplitude, this translates to a threshold on plasma density. Once this threshold is crossed, the external perturbation is able to penetrate the plasma and drive a locked island. This locked mode will grow while the plasma rotation in the vicinity of the island gradually stops. It is obvious that since the mode grows from an externally-applied magnetic structure, no rotating precursor is expected.

Measurements on DIII-D [2], JET [3], and COMPASS-C [4], using dedicated locked mode monitoring systems, show that this error field driven locked mode grows at a rate about an order of magnitude slower than conventional locked modes until it saturates. Thereafter, it usually persists until a change in the bulk plasma conditions (for example, ramping down the plasma current) drives the mode unstable and leads to disruption.

4. Recommendations and Summary

Based on these considerations, the following recommendations can be made concerning the detection of an error field driven low density locked mode on JT-60U:

- 1) The persistence of locked modes should be verified somehow, both to ensure that a locked mode originating in the current ramp-up does not exist, and to follow the low density locked mode to its end (discharge termination, damping, etc.);
- 2) Care should be taken to detect the locked mode at its onset. Only then will thresholds be clear. Measurements taken at the start of disruptive activity may not be so reproducible.

In summary, low density operation on JT-60U leads to disruptive activity. Circumstantial evidence from the existence of thresholds in density and divertor coil current suggests that a low density locked mode may be affecting confinement. A locked mode is usually not detectable, however, and further improvements in measurement technique and operation are required.

References:

- [1] YOSHINO, R *et al.*, paper IAEA-CN-56/G-3-1 to be published in proc. of 14th IAEA Conf. on Plasma Physics and Contr. Nuclear Fusion Research (Würzburg, Oct. 1992).
- [2] SCOVILLE, J T *et al.*, Nuclear Fusion 5 (1991) 875.
- [3] FISHPOOL, G M *et al.*, in *Avoidance and Control of Tokamak Disruptions* (papers presented at the IAEA Technical Committee Meeting, Culham, 1991) IAEA, Vienna (1991) 84; FISHPOOL, G M, Ph. D. thesis, Imperial College, London (1992).
- [4] MORRIS, A W *et al.*, in *Controlled Fusion and Plasma Physics* (Proc. 18th EPS Conf. Berlin 1991) Vol. 15C Part II, European Physical Society (1991) 61.
- [5] FITZPATRICK, R, and HENDER, T C, Phys. Fluids B 3 (1991) 644.

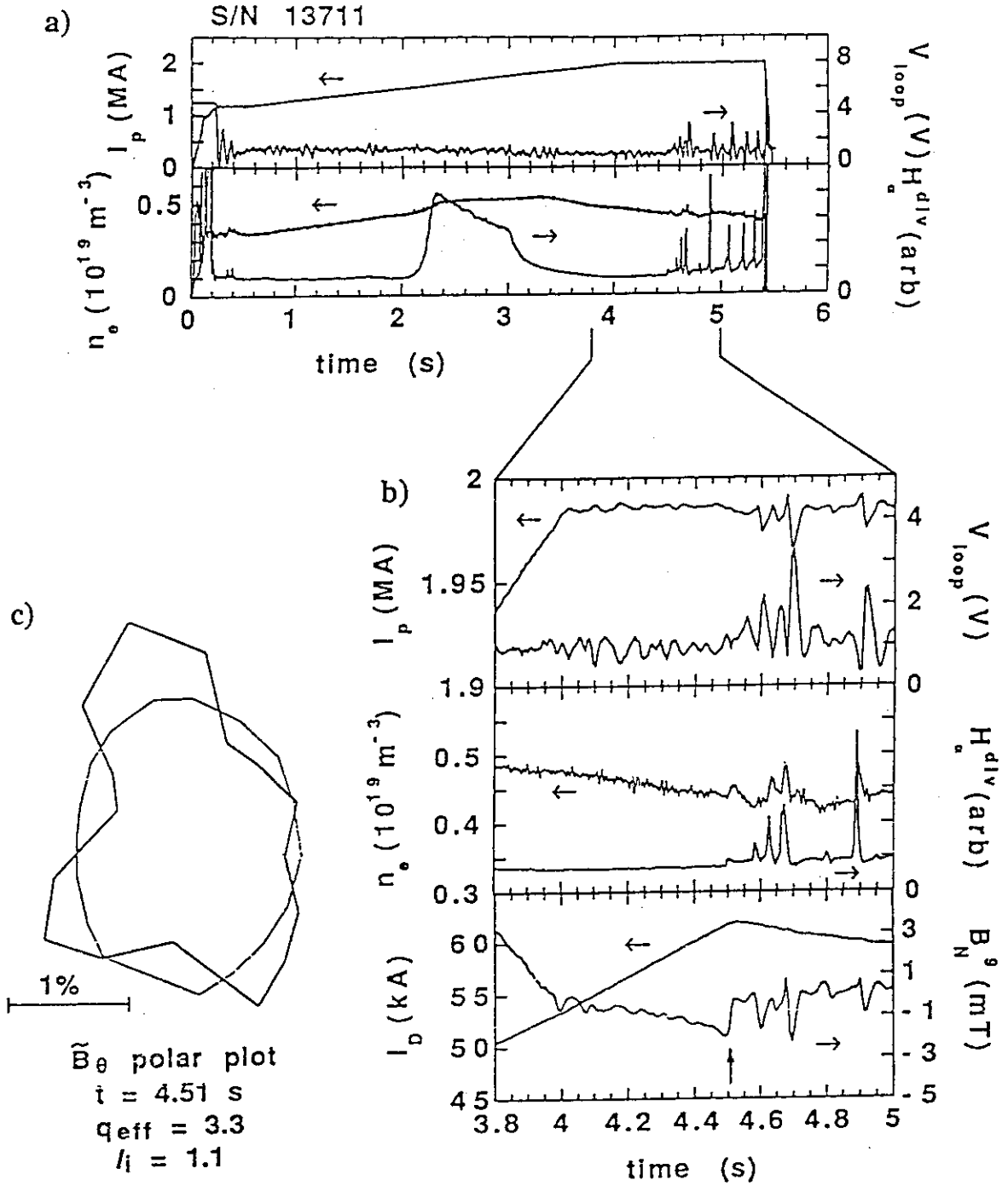


FIG. 1: Time evolution of a discharge with a locked mode appearing at low density:
 a) overview of plasma current I_p , one-turn voltage V_{loop} , line-averaged electron density n_e and H_α emission from the divertor;
 b) detail near the appearance of the mode, showing I_p , V_{loop} , n_e , H_α , divertor coil current I_D and magnetic field normal to the wall on the inboard midplane B_N^0 ;
 c) polar plot of the fluctuation in magnetic field tangential to the wall B_θ at 4.51 s (referred to "unperturbed" state at 4.50 s).

7.3 Error Field Analysis of Magnetic Coils

S.Miura, R.Yoshino, H.Ninomiya and M.Matsukawa

1. Introduction

We describe basically the numerical solution for error fields in the presence of resonant magnetic field perturbations. Although the tokamak is nominally an axisymmetric resonant fields errors of order $\delta B/B_t \approx 10^{-4}$, where B_t is the toroidal field. We will see that perturbations of this magnitude can have a significant effect on the plasma equilibrium, producing magnetic islands that short-circuit the confinement properties of the magnetic fields. The poloidal and toroidal mode numbers (m,n) of a resonant perturbation satisfy the resonance condition $m=nq$ for a rational surface in the plasma with safety factor q . Such a perturbation produces islands whose width scales as $\sqrt{\Psi}$.

2. Magnetic Field of JT-60U Device

The major elements device which produce the magnetic error fields of JT-60U are illustrated in Fig.1. Plasma current up to about 6MA will be induced by the F-coil. An sector coil(DCW-coil) produces helical magnetic fields of $m/n=3/2, 2/1, 1/1$. The plasma loop will be kept in radial and vertical equilibrium initially by a conducting shell and later in time by a vertical magnetic field and a horizontal magnetic field generated by the V-coil and the H-coil. Bending a straight, helically symmetric system into a torus results in a system that is neither helical nor axisymmetric. This, in general, leads to complicated and usually detrimental modifications of the magnetic surfaces near the separatrix.

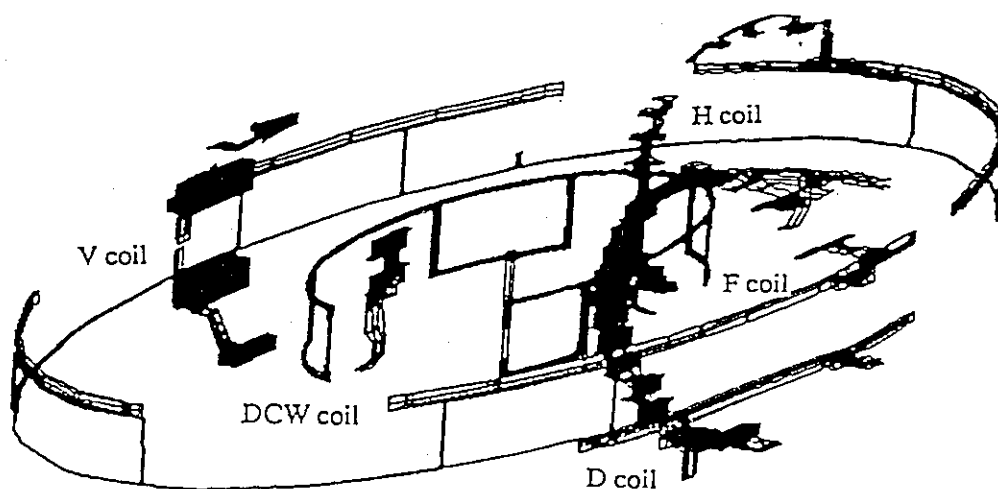


Fig.1 The feeder diagram of the JT - 60U tokamak, showing all all poloidal field coils

3. Magnetic Field Model and Field-line Tracing

The flux loops, poloidal flux data can be used as constraints for the MHD equilibrium calculation. Accordingly results from a fast boundary identification(FBI) code which approximates the plasma current as six filaments are required to get the fixed boundary. The Grad-Shafranov equation is solved using the fast Buneman method and Picard iteration scheme. The plasma current density profile is assumed as (1).

$$\begin{aligned} f(\bar{\psi}) &= 1 + \alpha\bar{\psi} + \gamma\bar{\psi}^2 - (1+\alpha+\gamma)\bar{\psi}^3 \\ j(\bar{\psi}) &= j_0[\beta_p^* R/R_p + (1-\beta_p^*)R_p/R]f(\bar{\psi}) \\ \bar{\psi} &= (\psi - \psi_{axis}) / (\psi_{surf} - \psi_{axis}) \end{aligned} \quad \dots (1)$$

The axisymmetric magnetic field is given by the derivatives of poloidal flux function ψ which is obtained by FBEQU[1]. The purpose of our investigation was to study the magnetic error fields effects in JT-60U, particularly the reduction in the obtainable pitch reversal compared with idealized straight feeders system. The feeder current is assumed to be a filament current, the field error is derived by the Biot-Savart law, using a second-order Runge-Kutta-Gill method. The errors in magnetic fields which result from coil leads and coil feedpoints around the tokamak are not so large. In simulations, a slight shift of one of the large outer field shaping coils, however, would produce basically results to the mode locking phenomena observed.

Field line tracing is then used to produce a puncture plot of the various flux surface. The flux surfaces predicted by this model are intended to represent a generic single-null of the actual JT-60U plasma used in the experiment. All poloidal modes presented in Fig.2 are less than about 1gauss by calculated the island width.

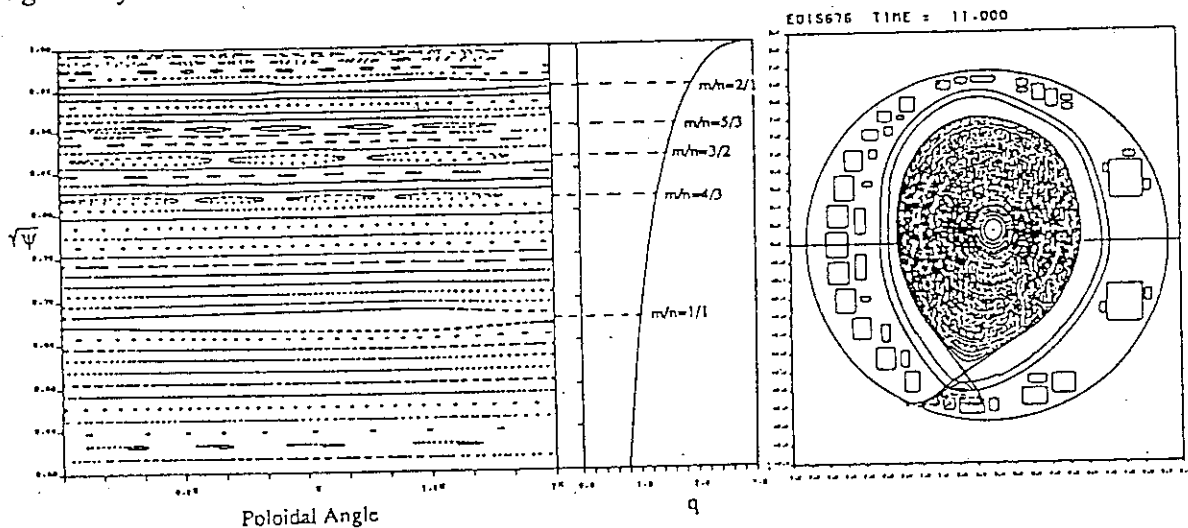


Fig.2 Non-axisymmetric radical field spectrum from a slightly shifted, elliptical poloidal coils in JT-60U. The F-coil with -84.2KA turn, the V-coil with 13.5KA turn, the H-coil with 2.6KA turn, the D-coils with 19.6KA turn and DCW-coils with 13.6KA turn, is given an ellipticity of 1.50. The spectrum is evaluated at a minor radius of 1.01m, a major radius of 3.24m and $q_{surf} = 3.24$.

4. Magnetic Field Error of Each Coil

The analysis by the field line tracing code described by the section 3 (referee to Fig.2) was carried by including the each poloidal coils(Fig.3). Current of each poloidal coils are the following.

The F-coil with -84.2KA/turn the V-coil with 13.5KA/turn, the H-coil with 2.6KA/turn, the D-coils with 19.6KA/turn and DCW-coils with 13.6KA/turn.

An ellipticity of plasma is 1.50. The spectrum is evaluated at a minor radius of 1.0m.

F-coil

The flux surface near the separatrix is ergodic.

H-coil and V-coil

The effect of the non-axisymmetric magnetic field is very small.

D-coil

An island for mode $m/n=1/1$ is clearly appeared.

DCW-coil

Modes of $m/n=3/2, 4/3, 4/2$ are clear. The flux surface inside the separatrix, shows the ergodic region.

Toroidal field ripple

The magnitude of 'Toroidal field ripple' is typically much larger than the magnitude of the other magnetic fields. But it is non-resonant and does not produce islands.

We can neglect this non-resonant part of the non-axisymmetric magnetic field.

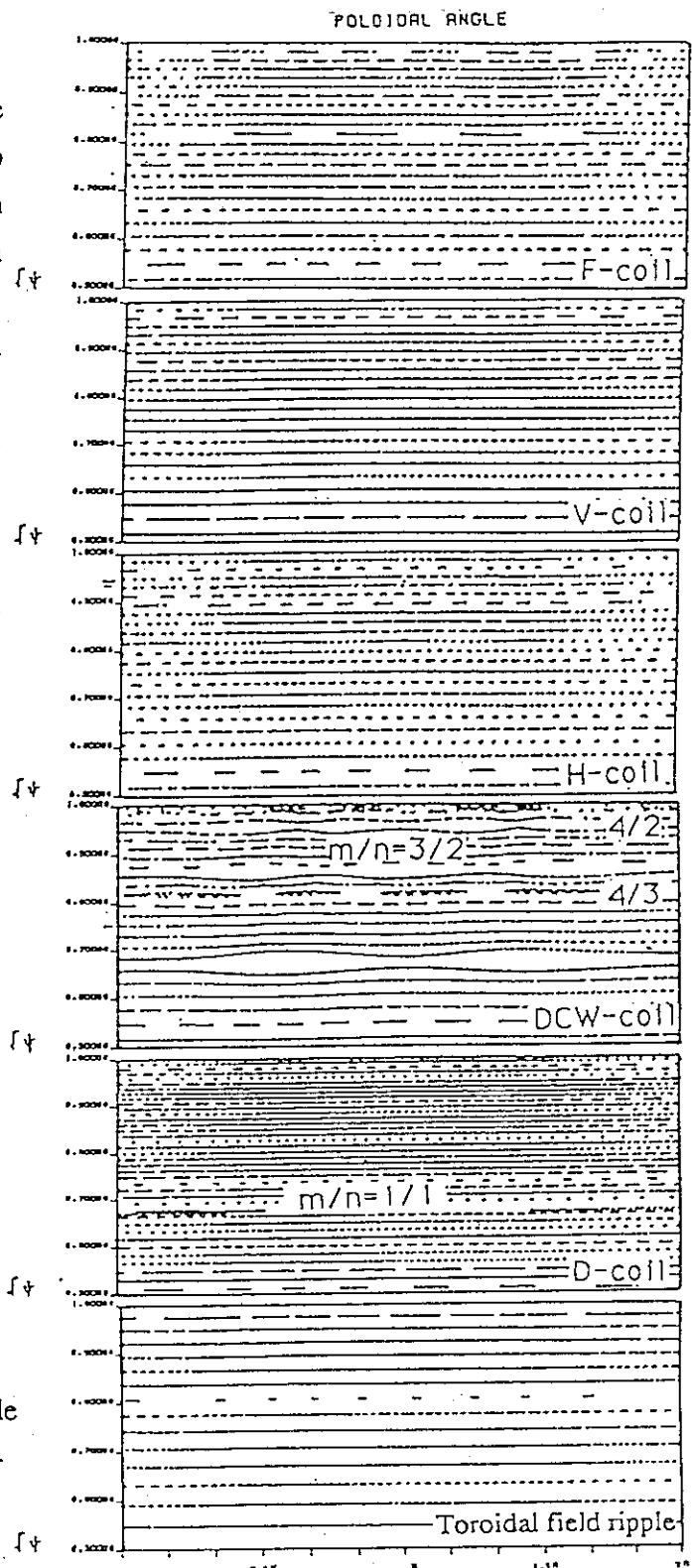


Fig 3 Flux surfaces with islands due to the non-axisymmetric field by each poloidal fields.

Another effect of the magnetic perturbation caused by F-coil is revealed in the expanded view shown in Fig.4, depicting the ergodic region which appears 200 - 300 degrees. For clarity, the separatrix has been deleted; only the surfaces outside the separatrix are shown. The island calculated inside here are a result of D-coil or DCW-coil fields error. The analysis by the field line tracing code described above was carried by including all poloidal coils. The line tracing is calculated 0 - 360 degrees of the poloidal angle, which is near the divertor x-point steeped by 1mm.

The calculated flux surface near the separatrix is shifted about 1mm and the modulated number of the flux surface has a relation of q_{surf} .

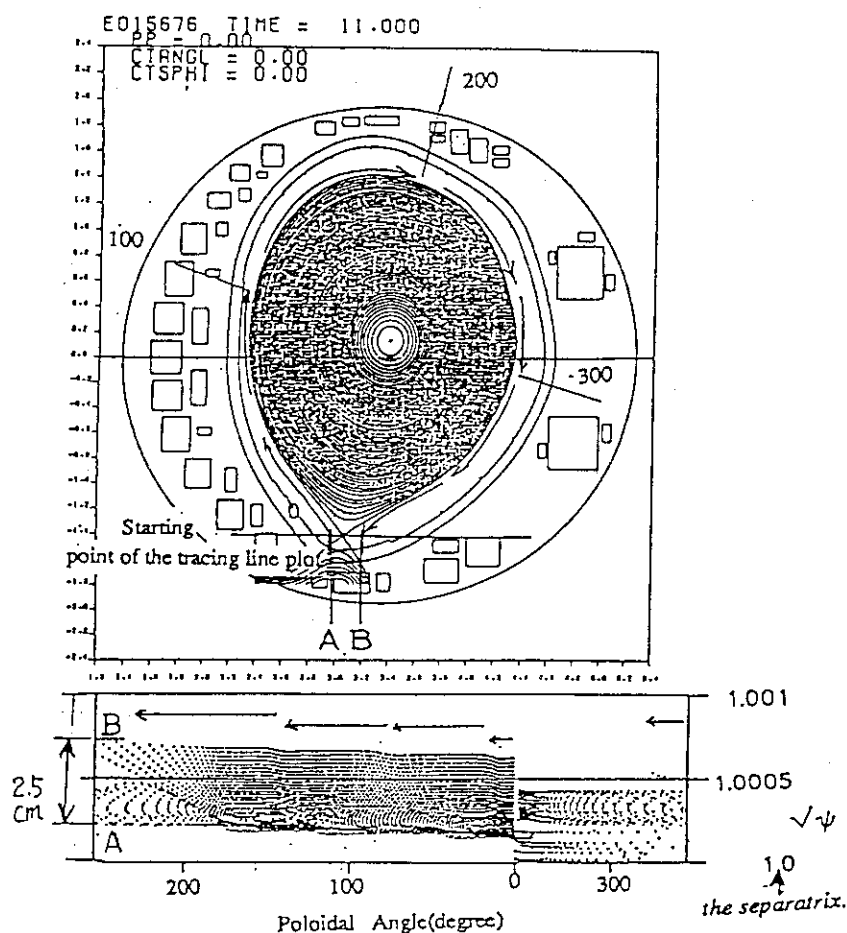


Fig.4 Expanded view of flux surfaces outside near the separatrix.

5. Summary

Magnetic islands ($m \geq 1/n=1$) result from resonant fields errors caused by small irregularities in feeders or leads of the poloidal coils. The DCW-coil produces $m/n=3/2$ islands and the ergodic region near the flux surface. The Runge-Kutta-Gill analysis and field line tracing with perturbations caused by both D-coil and F-coil suggests to set an optimum coil currents for the minimization of magnetic islands widths for the given flux function. Further experimentation is necessary to determine if reducing the resonant field errors with each poloidal coil can also affect confinement and the high beta plasma of JT-60U.

6. Reference

- [1] TSUJI, S., et al., JAERI-M 92-073 (1992) Sec.4.2

7.4 DCW Effect on Density Limit

Y. Neyatani, R. Yoshino

1. Introduction

At density limit disruptions, tearing types of fluctuations were observed before current quench in some tokamaks [1,2]. The theory predicts that the tearing type of $m/n=2/1$ mode couples with $3/2$ mode and it triggers to the current quench [3]. In order to improve density limit, additional external fields were utilized to suppress the $2/1$ and $3/2$ mode. Experiments with additional $2/1$ external field experiment were performed by DITE et al.[4], and obtained increasing density limit. However, the effect of $3/2$ external field was not clear. In JT-60U, as DCW (Disruption Control Winding) coil can be excited a principal $3/2$ component, we check the effect of the $3/2$ mode to density limit.

2. MHD Behavior in High Density Region

Density limit experiments were performed in OH phase with $I_p=2\text{MA}$, $B_T=2.8\text{T}$, $q_{\text{eff}}=3.3$. These parameters were determined by the DCW effective region of $0.2 \leq r_{\text{inv}}/a_p \leq 0.3$ [5], where r_{inv} is the sawtooth inversion radius. Internal inductance (l_i) is round 1.2 which is almost high l_i limit in $q_{\text{eff}}-l_i$ diagram. Helium and deuterium were utilized for operational gas. Density limit of He discharge ($\sim 8.1 \times 10^{19} \text{m}^{-3}$) was twice larger than that of D_2 discharge ($\sim 4.1 \times 10^{19} \text{m}^{-3}$), which will be caused by difference of the operational gas.

In He discharges, periodical $m/n=4/1$ mode was observed when electron density exceeded the critical value of $5.5 \times 10^{19} \text{m}^{-3}$. This mode was not correlated by sawtooth period, hence, may be attributed to surface mode. In D_2 discharge, no $4/1$ mode appeared, it may be caused by lower density. The $4/1$ mode continues until $2/1$ mode turns on. A $n=2$ mode appears with exciting the $4/1$ mode [Fig.1]

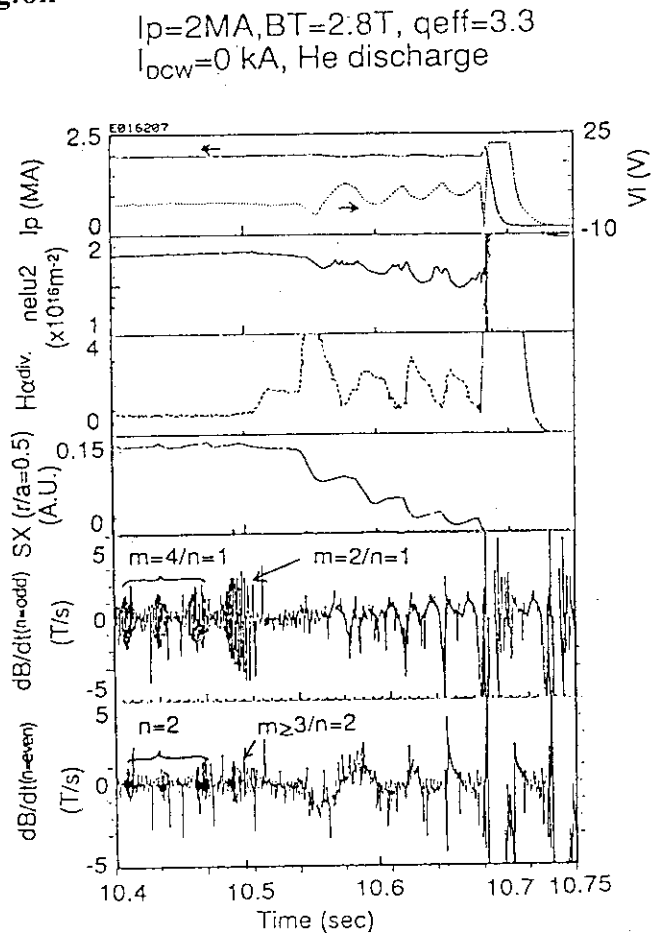


Fig.1 Time evolution of the density limit discharge with He gas operation.

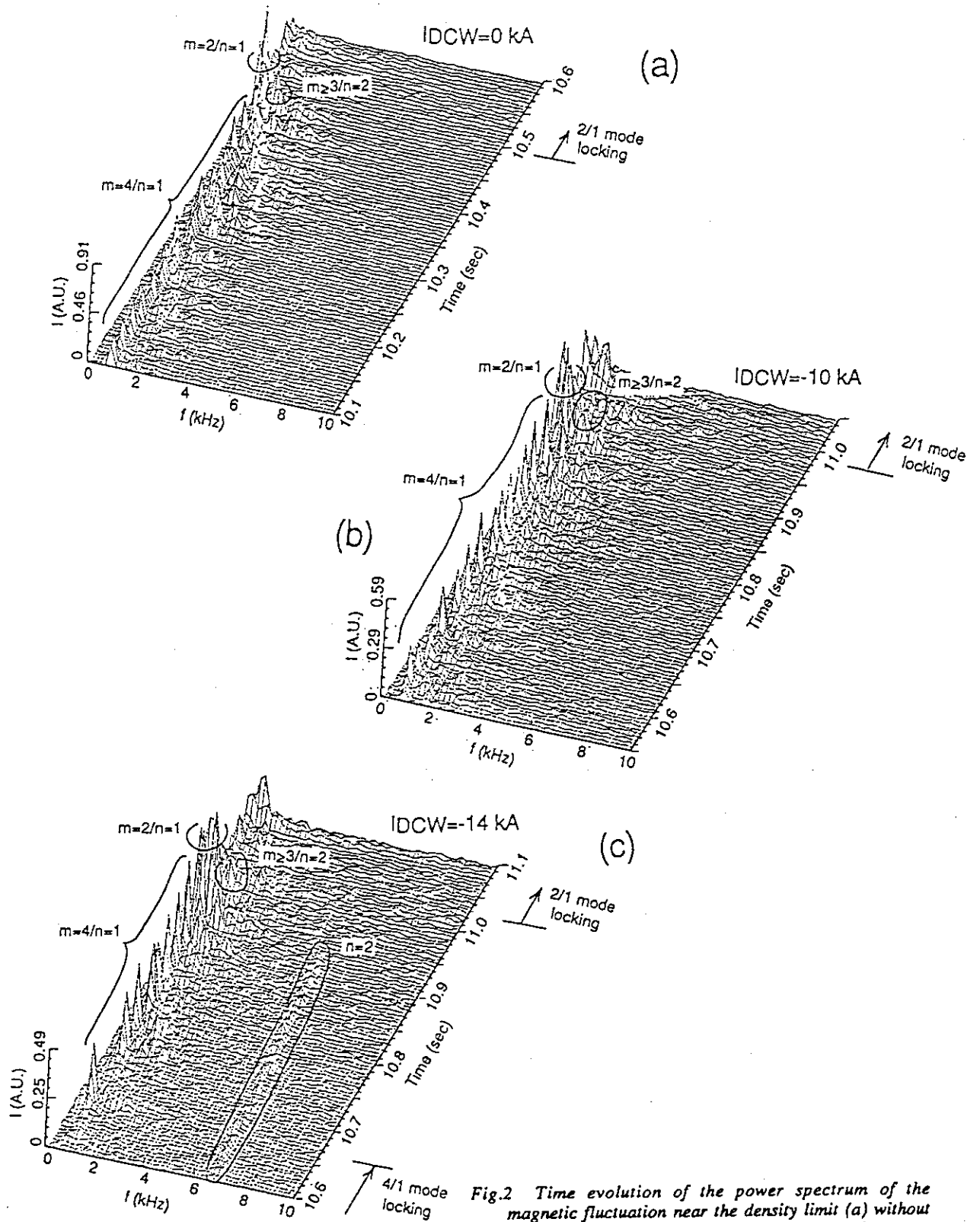


Fig.2 Time evolution of the power spectrum of the magnetic fluctuation near the density limit (a) without DCW, (b) with $IDCW=-10$ KA and (c) with $IDCW=-14$ KA.

A $m/n=2/1$ mode correlating disruption became unstable before 200~250 ms of a current quench. This 2/1 mode was observed in all density limit discharges. After the 2/1 mode grew, $m \geq 3/n=2$ mode was increased. The 2/1 mode locked after 25 to 60 ms of the fluctuation increased. After that, plasma energy exhausted stepwise with $n=1$ burst. Finally, plasma current terminated.

3. DCW Effect

A helical field produced by DCW was added with density limit discharge, and coil current was scanned from 14kA to -14kA. With/without DCW coil exciting, no difference of density limit was observed [Fig.1]. The $m=2/n=1$ and $m \geq 3/n=2$ mode was still observed. The intensity of $m \geq 3/n=2$ mode, coupled to 2/1 mode, reaches ≥ 8 gauss, in contrast, $m/n=3/2$ magnetic fields produced by DCW is up to 4 gauss near the separatrix on the outer midplane. It suggests that the DCW coil current is not enough to suppress the $m \geq 3/n=2$ mode. However, some interactions have been observed between DCW magnetic field and magnetic fluctuations.

Figure 2 shows the time evolution of the power spectrum of the magnetic fluctuation. With DCW discharge, an $n=2$ mode with frequency of ~ 6 kHz was observed in the case of $I_{DCW}=14$ kA. The frequency continuously decreased until the 2/1 mode increasing. The amplitude of this mode is small and no difference of the density limit was observed with/without this mode, so, the $n=2$ mode is not correlated the density limit.

The locking phase of the 2/1 mode is changed when $I_{DCW} > 0$ kA [Fig.3]. With $I_{DCW} < 0$ kA, no change of locked phase observes. Since the error field without DCW is mainly originate by D-coil feeder, we checked the location of DCW coils and D-coil feeder [Fig.4]. For the 2/1 mode, when a additional field excited by DCW shown by squares of closed line in Fig.4, has a same sign of the error field produced by D-coil feeder, the error field caused by locking

increases, but the locking phase of the mode is same compared the case of D-coil error field (e.g. 2/1 mode locks when +line shown in Fig.4 reaches at the location of the D-coil feeder). When the additional field by DCW has a opposite sign of the D-coil error field, the error field caused by mode locking reduces and locking phase of the mode changes, which depends on the currents of DCW and D coil. If DCW current is large, locking phase will change 180 degrees (in this case, mode lock occurs when

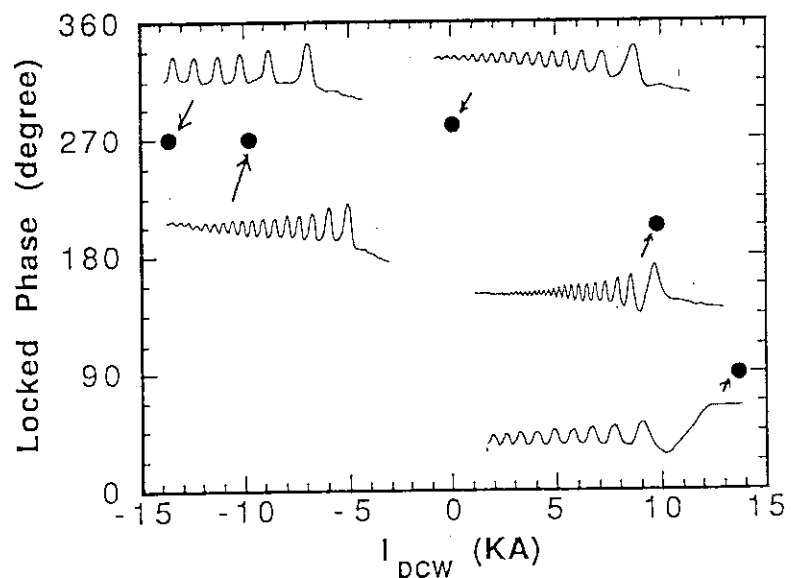


Fig.3 Locked phase of $m/n=2/1$ mode v.s. DCW coil current. Time scale of the waveform is same.

+line reaches at the location of DCW indicated by squares of dotted line in Fig.4).

A mode locking of 4/1 mode was observed in the case of $I_{DCW} < -10\text{kA}$ [Fig.3]. With $I_{DCW} = -14\text{kA}$ and $I_{DCW} = -10\text{kA}$, the 4/1 mode locks at $t = 10.46\text{ sec}$ with $B_{tild} \sim 3\text{ gauss}$ and at $t = 9.46\text{ sec}$ with $B_{tild} \sim 2.3\text{ gauss}$, respectively. In these two cases, the mode locks when $B_{tild}/I_{DCW} \sim 2.3$, and after 300 ms, rotates again. Locking phase is not changed by I_{DCW} . No locking is observed in the case of

$I_{DCW} > 0\text{kA}$. It will be depend on the phase of the DCW error field. In the case of 4/1 mode, closed and hatched lines expressed magnetic islands, as shown in Fig.4, have same islands phases. So, when $I_{DCW} < 0\text{kA}$, the error field increases by DCW. As a result, the locking phase is the same with $I_{DCW} = 0\text{kA}$. When $I_{DCW} > 0\text{kA}$, the error fields reduced by DCW, and in not enough to lock the 4/1 mode.

4. Summary

With/without DCW, no difference of the density limit is obtained at density limit experiment. The DCW coil current is not enough to suppress the $n=2$ mode correlated with the mode coupling. It is necessary to the density limit experiment with lower plasma current and toroidal field to obtain more investigation of DCW effect.

Mode locking phase of $m/n=2/1$ mode changed with $I_{DCW} > 0\text{kA}$. No change was observed at $I_{DCW} < 0\text{kA}$. It is consistent with the relation between two phases of the error fields produced by DCW and D-coil feeder.

References

- [1] WESSON J.A. et al.: Nucl. Fusion **29** (1989) 641.
- [2] ALLADIO F. et al.: Nucl. Fusion **26** (1986) 11.
- [3] BONDESON A. et al.: Nucl. Fusion **31** (1991) 1695.
- [4] MORRIS A.W. et al.: Phy. Rev. Lett. **64** (1990) 1254.
- [5] YOSHINO R. et al.: in Plasma Physics and Controlled Nuclear Fusion Research 1992 (Proc.14th Int. Conf. Wurzburg, 1992) IAEA-CN-56/G-3-1

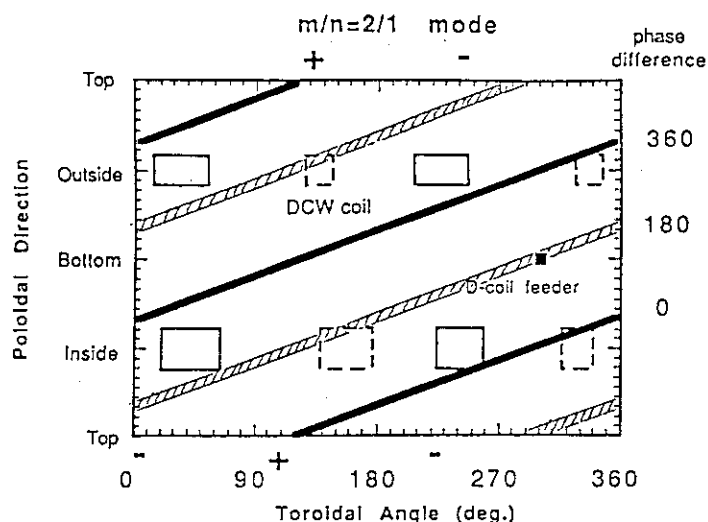


Fig.4 Relation between 2/1 mode and DCW and D-coil feeder, which originates to error field caused by mode locking. Closed square shows the location of D-coil feeder, Squares of closed lines and dotted lines show the DCW coils. Diagonal closed and hatched lines model the $m/n=2/1$ magnetic islands. The number of right hand side show the positional mode difference from an island.

7.5 Effects of DCW on Disruptions

R.Yoshino, Y.Neyatani

1. Introduction

The effects of the helical magnetic fields produced by DCW (Disruption Control Winding)[1] on the density limit disruption and the locked mode disruption, and the avoidance of the high I_i disruption during the plasma current ramp-down by the excitation of DCW are presented in this paper. Principal mode of DCW is $m/n=3/2$, and broad band modes are excited by this coil as presented in section 7.3. Then transport and MHD stabilities in the plasma core region can be modified by the generation of magnetic islands, and those in the plasma peripheral region can be changed by the ergodization. In this paper confinement degradation during the detached plasma phase, modification of the $m=1$ erosion, softening of the plasma current decay, and broadening of the plasma current profile during the plasma current ramp-down are presented.

2. Effect on the Density Limit Disruption

1) Confinement Degradation and Softening of the Current Quench

During the detached plasma phase in the density limit disruption, the plasma stored energy decreases drastically as presented in section 7.7. This confinement degradation can be enhanced by DCW as presented in Fig.1. Plasma stored energy just before the energy quench can be lowered drastically from that at the start of the detachment by exciting DCW. Low stored energy just before the energy quench is useful to decrease the rise in the radiation loss at the energy quench in the density limit disruption and to reduce the plasma current decay rate. Long current decay time (defined by $I_p/(dI_p/dt)$) of 65ms was obtained for a 2MA divertor plasma with $q_{eff}=3.2$ by exciting DCW, in which the rise in the radiation loss at the energy quench is lowered to 1~2MW. The maximum rise in the radiation loss at the energy quench increases with the decrease in the effective safety factor q_{eff} as presented in Fig.2. However the rise in the radiation loss of 1~2MW is the minimum rise at $q_{eff}=3.2$. The heat flux to the divertor plate may become broader owing to the ergodization of the plasma peripheral region by DCW, that will be measured by IRTV with the short time resolution in the next experimental period. Another cause of the low rise in the radiation loss is the low plasma temperature of 150eV at the start of the energy quench. The maximum plasma current decay time rises with lowering the plasma temperature as presented in Fig.3. Here the plasma temperature is defined by $W_{dia}/(3knV_p)$. W_{dia} is the plasma stored energy just before the energy quench, n is the

electron density, and V_p is the plasma density. Physical sputtering yield of carbon by deuterium ion decreases with lowering the energy at $<500\text{eV}$, then low plasma temperature can decrease the generation of impurities. Plasma current decay time of $>30\text{ms}$ is obtained only at the plasma temperature of $<500\text{eV}$ as presented in Fig.3. Then both of the low plasma temperature and the broadening of the heat flux by DCW may decrease the rise in the radiation loss at the energy quench and soften the current quench. On the other hand there are two shots with the short plasma current decay time of $10\sim20\text{ms}$ in spite of the excitation of DCW as presented in Fig.3. The cause of this fast plasma current decay is not clear yet. The helical magnetic field may degrade the energy confinement after the energy quench. Then experiments with a little higher q_{eff} of $4\sim6$ is planned in the next experimental period.

Degradation of the confinement is also observed in the the normal plasma discharge. Plasma density decreases by the excitation of DCW with the decrease in the stored energy. The drop in the plasma density becomes large with lowering q_{eff} from 4.2 to 2.7. The investigations of the decay rate of the plasma density after the intense gas puffing with and without DCW suggest 20% degradation of the particle confinement at $q_{\text{eff}}=3.35$ by the 14kA excitation of DCW.

2) Modification of $m=1$ Erosion

Location of $m=1$ erosion shifts to the plasma center by the positive excitation of DCW with $10\sim14\text{kA}$ as presented in Fig.4, that may be same with the cold bubble observed in TFTR[2]. However this location shift of the $m=1$ erosion is not observed with the negative excitation of DCW coil, that is consistent with the no change in the phase of the $m/n=2/1$ mode lock with the negative excitation of DCW coil as presented in section 7.4. The plasma current decay rate at the current quench was not reduced by the shift in the location of the $m=1$ erosion. Long duration of the $m=1$ erosion of $6\sim8\text{ms}$ was obtained with the long plasma current decay time of $60\sim65\text{ms}$. However the plasma current decay rate was not reduced after the same long duration of the $m=1$ erosion without exciting DCW. Then the the long current decay time may be obtained by the ergodization of the plasma periphery with the excitation of DCW as discussed above.

Modification of the sawtooth activity by the excitation of DCW was obtained in the normal discharge with $q_{\text{eff}}<3$, in which lock of $m=1$ activity and $m=1$ shift were observed.

3. Effect on the Low Density Locked Mode

Low density locked mode is observed with the excitation of divertor coil at q_{eff} of <3.7 and plasma density of $<0.8\times10^{19}\text{m}^{-3}$ as presented in section 7.1, and is avoided

without the excitation of the divertor coil. However low density locked mode can be excited by DCW. Furthermore disruptive plasma termination can be obtained at $q_{\text{eff}} < 3$ by the excitation of DCW after the degradation of the plasma confinement with the increase in the heat flux to the inboard divertor plate. The threshold on the plasma density at $q_{\text{eff}} < 3$ has not been obtained yet.

The reduction of the plasma current decay rate by the excitation of DCW is small in these locked mode disruptions with large rise in the radiation loss at the energy quench.

4. Avoidance of High I_i Disruption during the Plasma Current Ramp-down

High I_i disruption during the plasma current ramp-down was avoided by the decrease in I_i caused by the MHD activity after the excitation of DCW as presented in Fig.5. The radial field component of $m/n=3/2$ is 7 Gauss at the plasma center with a coil current of 14kA. Typical case is shown in Fig.6(b), in which helical field degrades the energy confinement gradually at $t=13.15\sim 13.4\text{s}$ ($q_{\text{eff}}=6\sim 7$) with MHD activities outside of the sawtooth inversion radius observed by a soft X-ray array. The obtained I_i is 0.2 lower than the higher I_i limit at $q_{\text{eff}} > 7$ (see Fig.6(a) Δ). On the other hand current quench is observed in a shot without the drop in I_i (see Fig.6(a) X, (b)). This broadening of the current profile by the excitation of DCW was obtained for $0.2 \leq r_{\text{inv}}/a_p \leq 0.3$ as presented in Fig.7, where r_{inv} is the sawtooth inversion radius. However this helical field had no effect on plasmas with $r_{\text{inv}}/a_p < 0.2$, and caused a current quench at $r_{\text{inv}}/a_p > 0.3$. Where current profile is not a strong function of q_{eff} during the plasma current ramp-down, so that r_{inv}/a_p cannot be presented by q_{eff} .

5. Conclusions

Effects of DCW on the density limit disruption are observed in the energy confinement degradation during the detached plasma phase, modification of the location of the $m=1$ erosion (cold bubble), and softening of the plasma current decay. Especially softening of the current decay at the current quench was obtained at $q_{\text{eff}}=3.2$. Particle and energy confinement degradation is observed by the excitation of DCW at low q_{eff} of < 4.2 . Plasma current ramp-down was stabilized by the broadening of the current profile owing to MHD activities triggered by DCW.

References

- [1] NINOMIYA. H., et al., Plasma Devices and Operations, 1 (1990) 43
- [2] JANOS.A., et al., 14th IAEA, Wurzburg (1992) IAEA-CN-56/A-3-15

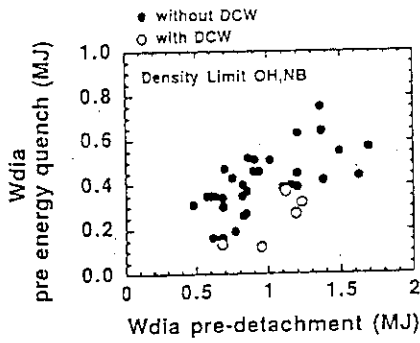


Fig.1 Confinement Degradation during the detached plasma phase. Plasma stored energy at the start of the detachment, and that just before the energy quench are presented. Closed points are without the excitation of DCW, and open points are with DCW.

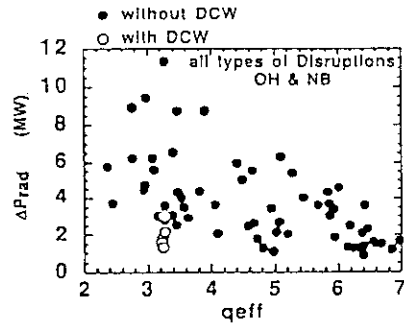


Fig.2 The rise in the radiation loss at the energy quench versus q_{eff} for all types of disruptions. They are density limit disruptions, locked mode disruptions, high I_i disruptions.

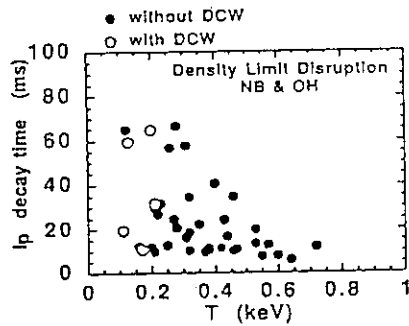


Fig.3 The plasma current decay time versus the plasma temperature defined by $W_{dia}(3nkV_p)$.

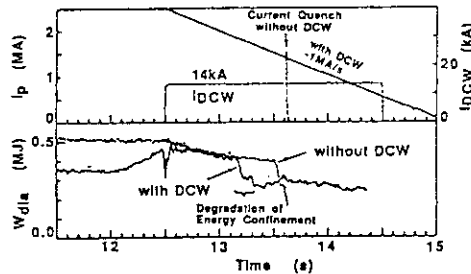


Fig.5 DCW effect on I_p ramp-down. Plasma stored energy is degraded by the excitation of DCW at 13.15-13.4s. High I_i disruption occurs without the excitation of DCW.

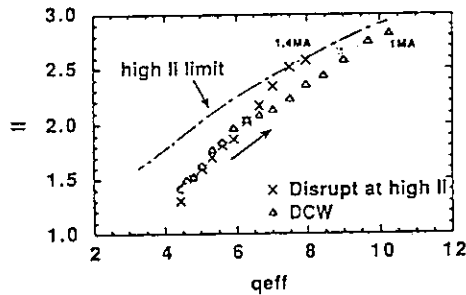


Fig.6 Trajectory of q_{eff} and I_i during I_p ramp-down. X; a disrupted shot with the constant a_p during I_p ramp-down. Δ ; DCW excitation of 14kA maintains I_i lower than the limit value.

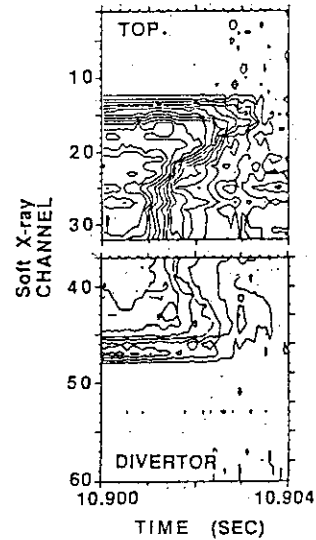


Fig.4 Contour map of the soft X-ray emission at the energy quench with the DCW current of 14kA. Cold plasma region is observed at the plasma center.

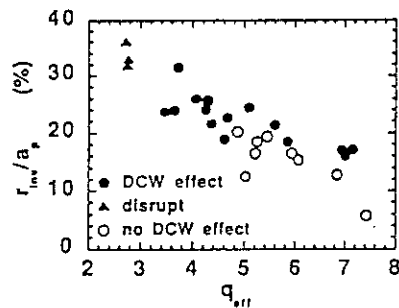


Fig.7 The region of r_{inv}/a_p versus q_{eff} , where broadening of the plasma current profile was obtained with the excitation of DCW (closed points). Open points are no broadening, and triangle points are disrupted.

7.6 MARFE Limit of Ohmic Divertor Discharges

N.Hosogane, N.Asakura, H.Kubo, K.Itami, K.Shimizu,
S.Tsuji, T.Sugie, A.Sakasai and M.Shimada

1. Introduction

MARFE is a kind of thermal instability generated at the inboard side of the wall or in the divertor region, and usually appears as a precursor before density limit of tokamak discharges. The critical density for the onset of MARFE (MARFE limit) is very important not only from operational limit, but also from divertor study, because the MARFE limits high density operations necessary for establishing a sufficient remote radiative cooling effect in the divertor region. In case of beam heated discharges, the MARFE often occurs just after the sudden drops in neutral beam (NB) power due to the breakdowns, which makes it difficult to study the critical phenomena near the MARFE limit. At this point, ohmic plasmas are favorable because the ohmic power moderately varies during the discharges. This paper presents the results of investigations on the MARFE limit in ohmic discharges from the standpoint of divertor studies.

2. MARFE Limit in the Hugill Diagram

The Hugill diagram for the ohmic discharges investigated is shown in Fig. 1. The discharge parameters scanned are $I_p=1.2-3$ MA, $B_T=2-4$ T and X_p (height of X-point) = -5 (touching at the bottom wall) - 14 cm. It is seen in this figure that most of the MARFEs occur in the narrow range of a parameter $n_e^{\text{main}} R_{q_{\text{eff}}} / B_T$. These results indicate that in the approximate sense, $n_e^{\text{main}} R_{q_{\text{eff}}} / B_T$ is a good index composed of global parameters for the MARFE limit. Since the electron density continued to be increased by the gas puff after the onset of MARFE, some discharges became to be detached as shown by symbols , which formed the boundary for density limit disruptions in this experiment.

3. Characteristics of Radiation Losses and Divertor Parameters

In divertor discharges, the MARFE is generated in the divertor region when the radiation loss increases up to a critical level. The onset of the MARFE should be closely related with divertor electron density, electron temperature and the radiation loss. Therefore, the relationships among these parameters are investigated for divertor discharges with $X_p=4-8$ cm.

3.1 Radiation Losses

As shown in Fig. 2, the total radiation loss increases with the increase in main electron density. The dominant portion is the divertor radiation loss, which increases in the weak non-linear manner, compared with the divertor electron density. The fraction of the total radiation

loss against the ohmic heating power also increases with the main electron density, and the MARFEs occur when the total radiation loss increases up to 40-50% of the ohmic heating power. The total radiation loss during the MARFE increases along the same curve of the radiation loss. This is because the radiation loss changes its profile when the MARFE occurs, but the total amount does not increase so much due to the MARFE.

3.2 Divertor Electron Densities and Temperatures

Figures 3(a),(b),(c) and (d) show the divertor electron densities and temperatures at the inside and outside separatrix strike zones as a function of main electron density. Here, these values plotted are those at the peak of the divertor electron density profiles. As shown in Fig.3 (a) and (c), both divertor electron densities at the inside and outside separatrix strike zones non-linearly increase with the increase in main electron density for discharges with $I_p=1.2-3$ MA. For each plasma current, there is an upper limit in electron density determined by the onset of the MARFE. A strong in-out asymmetry is seen in divertor electron density in the stable phase, and the electron densities at the inside separatrix strike zone is two times or more larger than those at the outside one. However, the in-out asymmetry disappears during the MARFE. At the onset of the MARFE, the outside electron density increases at a jump up to the level of the inside electron density, and both electron densities begin to decrease in the symmetric manner as shown in Fig.4.

There is also a strong in-out asymmetry in behavior of divertor electron temperatures. The inside divertor electron temperature is insensitive to the change in main electron temperature, and remains to be 10-30 eV. The changes in inside electron temperatures before and after the onset of the MARFE are small. On the other hand, the outside divertor electron temperature varies with the change in main electron density n_e^{main} in the manner stronger than the rate of $1/n_e^{\text{main}}$, and when it decreases down to a level of 20 eV, the MARFE is generated. The outside divertor electron temperature during the MARFE phase remains to be at the same level as the inside one, 5-20 eV. From the temperature dependence of the radiative cooling rate L , the radiation loss is more sensitive to the electron temperature than the electron density, so that the outside electron temperature rather than the inside one should be responsible for the onset of the MARFE.

4. Relationship between MARFE Limit and Divertor Electron Temperatures

In order to understand the MARFE limit shown in Fig.1, the outside divertor electron temperatures are plotted as a function of $n_e^{\text{main}}Rq_{\text{eff}}/B_T$ in Fig.5. In this case, $n_e^{\text{main}}Rq_{\text{eff}}/B_T$ shows the variation of $n_e^{\text{main}}/P_{\text{OH}}$ (P_{OH} : ohmic heating power), since the plasma cross-section is not scanned in these discharges and P_{OH} is approximately proportional to I_p as shown in Fig.2. From this figure, it is understood that the outside divertor electron temperature

apparently changes as a function of $n_e^{\text{main}}/P_{\text{OH}}$, and when it decreases to a level of 20 eV, the MARFE is generated. Actually, the divertor electron temperature depends on the impurity contents, maybe, height of X-point, in-out asymmetries etc., which affect the MARFE limit. To discuss the behavior of the divertor electron temperature, it is necessary to use a local parameter of divertor electron density, rather than a global parameter of main electron density, and to take other effects into consideration. Here, taking the effect of the radiation losses, the outside divertor electron temperature is investigated as a function of $(P_{\text{OH}} - P_{\text{rad}}^{\text{total}})/n_e^{\text{div}}$ (outside). As shown in Fig.6, the outside divertor electron temperature is found to decrease as the heating power per unit divertor electron density decreases. This temperature remains at a level of lower than 20 eV during the MARFE due to the increase in divertor electron density as seen in Fig.2(c).

5. Summary

The MARFE limit for ohmic discharges is investigated. It is found that the MARFE occurs when the outside divertor electron temperature decreases to a level of 20 eV and the radiation loss increases up to 40-50% of the ohmic heating power. The outside divertor electron temperature appears to decrease as a function of $n_e^{\text{main}}Rq_{\text{eff}}/B_T$, so that this parameter is a good index for the MARFE limit for ohmic discharges as long as impurity levels are not significantly changed. This comes from that the divertor electron temperature is approximately a function of $(P_{\text{OH}} - P_{\text{rad}}^{\text{total}})/n_e^{\text{div}}$. To discuss the MARFE limit in detail, it is important to investigate the effects of impurities, height of X-point, in-out asymmetries, etc..

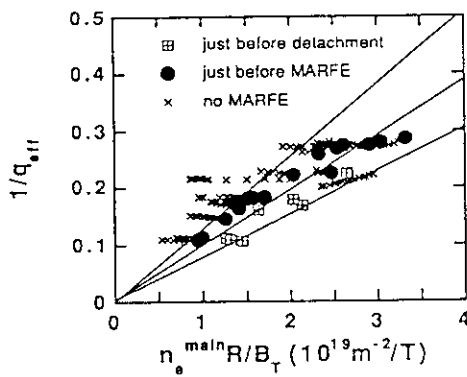
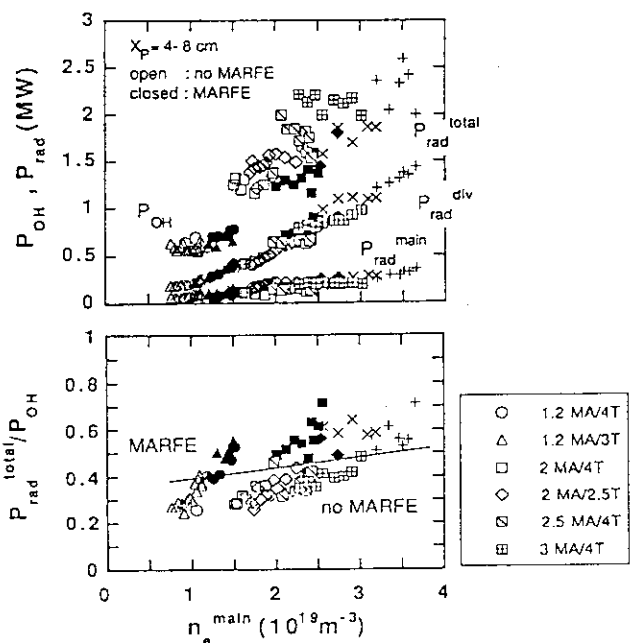


Fig.1 Hugill diagram of ohmic divertor discharges. The time evolution of the discharges are plotted in the diagram.

Fig.2 Ohmic heating power, radiation losses and the fraction of the total radiation loss against the ohmic heating power.



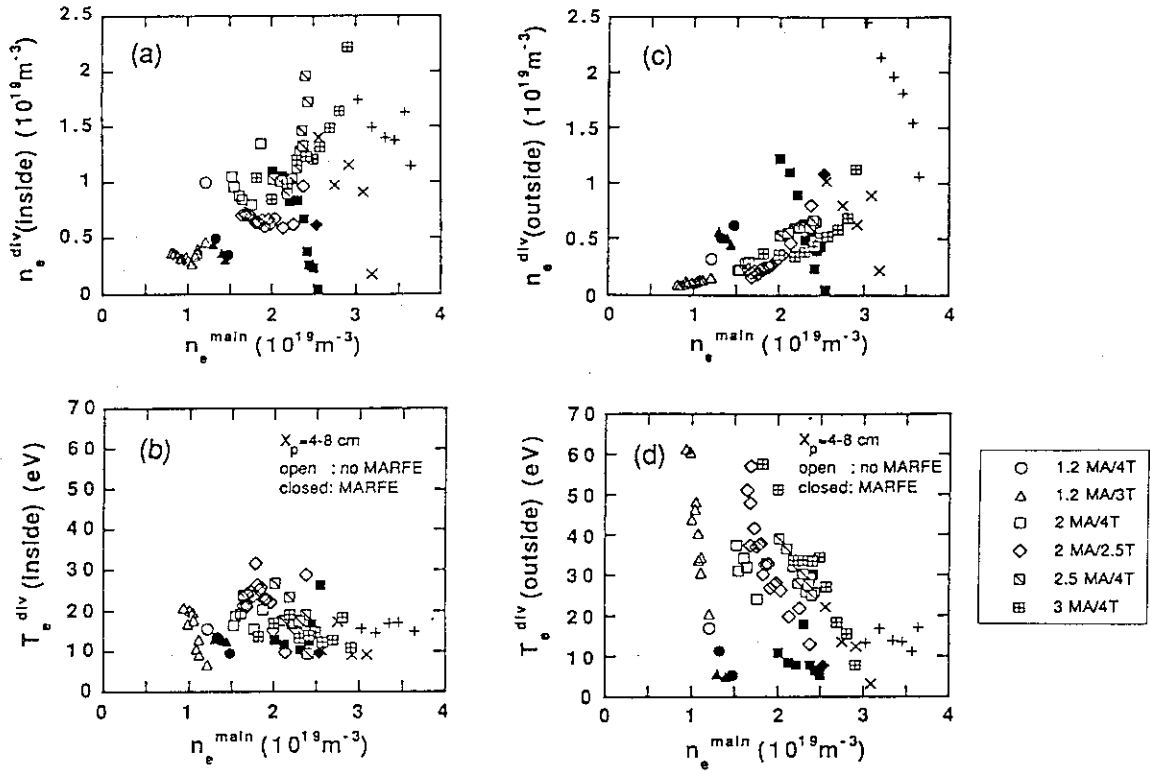


Fig.3 Plots of divertor electron density and temperatures at the inside and outside separatrix strike zones as a function of main electron density for ohmic discharges with $X_p=4-8$ cm.

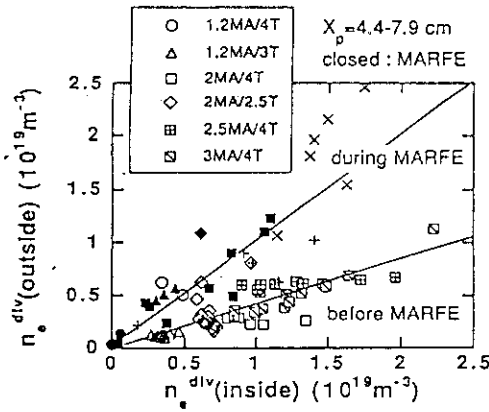


Fig.4 Relationship between inside and outside divertor electron densities before and after the onset of the MARFE.

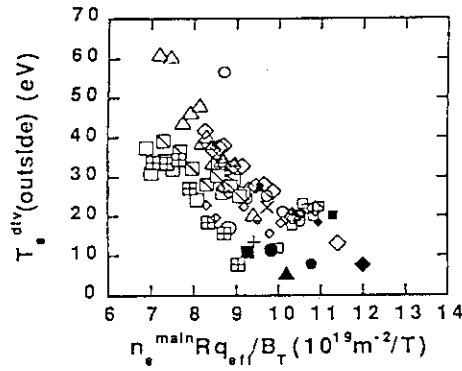
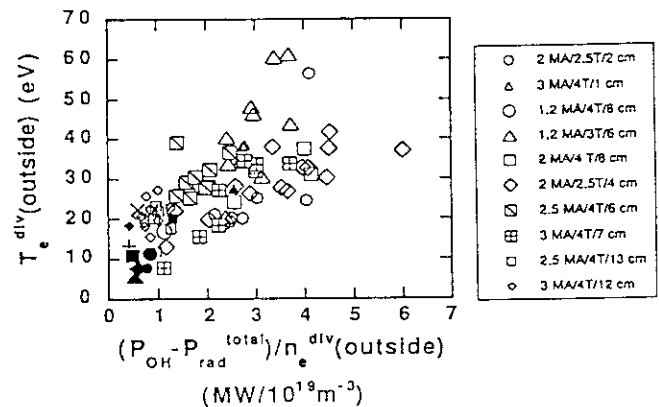


Fig.5 The outside divertor electron temperature as a function of $n_e^{\text{main}} Rq_{\text{eff}}/B_T$.

Fig.6 The outside divertor electron temperature as a function of $(P_{\text{OH}} - P_{\text{rad}}^{\text{total}})/n_e^{\text{div}}(\text{outside})$.



7.7 The Current Quench in the Disruptive Termination

R.Yoshino, Y.Neyatani

1. Introduction

To raise the reliability of the tokamak fusion reactors, both of fast plasma current decay and generation of the runaway electrons in the disruptive plasma termination must be avoided. Fast quench of the plasma current induces high eddy currents in the vacuum vessel[1], and makes the positional control of the plasma hard. An uncontrolled plasma touches the unexpected first wall with an intensive plasma wall interaction, that decreases the life time of the first wall material drastically. Furthermore the halo current induced by this attachment flows in the plasma periphery and the vessel components raising the stress on the vacuum vessel extremely. Runaway electrons generated during the current quench decreases the life time of the first wall material drastically. From the design of fusion reactors, the development of control methods to slow the plasma current decay rate without generating runaway electrons is one of urgent issues. In this paper, the current quench in disruptions in JT-60U divertor plasma are investigated. They are density limit disruptions, locked mode disruptions, high I_i disruptions during the current ramp-down with low density[2]. Various methods tried in JT-60U to reduce the current decay rate are presented in section 7.8. Then conditions required to suppress the generation of runaway electrons during the current quench is investigated in section 7.9.

2. Current Decay in the Density Limit Disruption

For density limit disruptions of OH divertor plasmas with $I_p > 1.5\text{MA}$, the plasma current decay time defined by $I_p / (dI_p/dt)_{av}$ increases with the decrease in the stored energy just before the energy quench as presented in Fig.1. Here $(dI_p/dt)_{av}$ is the time averaged current decay rate between the flat-top plasma current and the 50% of it. Circle points are current quenches without runaway electrons at I_p of $>0.5\text{MA}$, and cross points are those with generating runaway electrons at I_p of $>0.5\text{MA}$. The current decay time is determined by the electron temperature. So Fig.1 suggests that slow current decay with higher electron temperature is obtained for low stored energy just before the energy quench. This result is surprising. Because higher stored energy was expected better to get the slow current decay with higher electron temperature at the current quench. Then another process of the confinement degradation enhanced at high stored energy should be considered. The stored energies and current decay times for high I_i disruptions are on the same scaling with the density limit disruptions as presented in Fig.1.

One of possible mechanisms of the confinement degradation is the sudden influx of impurities, that is measured by the soft X-ray spike[3] after the $m=1$ erosion as presented in Fig.2. After this spike, one-turn voltage drops to negative, and plasma current rises a little. This delay of the negative voltage spike from the energy quench observed by soft X-ray spike may be same with that in JET[4]. The time resolution of the spectrometer is poor, and it is hard to get the information of impurities. On the other hand the bolometric measurement is performed each 4ms. So the increase in the radiation loss during the energy quench was investigated as the first step. Nearly linear relation is obtained between the plasma stored energy just before the energy quench and the rise in the radiation loss at the energy quench as presented in Fig.3. If the dropped electron temperature just after the energy quench is almost same for each stored energy just before the energy quench, the rise in the radiation loss does not depend on the stored energy. Then it may be possible to assume that the plasma stored energy flows to the divertor region at the energy quench and impurities (maybe mainly carbon) are generated by this high heat flux. Here the heat flux to the divertor plate must be measured to get the countability of the energy balance. In JT-60 the plasma energy, that flowed to the divertor plate at the energy quench, was almost same with the stored energy just before the energy quench[5].

The current decay time increases with the decrease in the rise in the total radiation loss at the energy quench as presented in Fig.4. Runaway electrons are observed at higher radiation rise of $>4\text{MW}$. Figure 4 shows that the reduction of the increase in the radiation loss is necessary to get slow plasma current quench. In the detached plasma state observed prior to the energy quench, the input power is almost equal to the radiation power. So the additional radiation loss during the energy quench is owing to the dropped electron temperature by the energy quench and the sudden influx of the impurities. The current decay time is determined by the electron temperature. So it is reasonable that the slower current decay with higher electron temperature is obtained for smaller rise in the radiation loss at the energy quench. This relation can be obtained for all three type of disruptions as presented in Fig.5.

3. Current Decay in the locked Mode Disruption

Current decay rate of locked mode disruptions for OH divertor plasmas is fast in spite of the low plasma stored energy of $0.1\sim0.2\text{MJ}$ just before the energy quench as presented in Fig.6 by triangle and star points. Runaway electrons are not generated in the triangle points, but are generated in star points. Here the relation between the plasma current decay time and the rise in the radiation loss at the energy quench is same with those of the density limit disruption as presented in Fig.4. Then in the locked mode disruptions the rise in the radiation loss is larger than those with the same stored energy in the density limit disruptions. One of

the possible reasons of this higher rise in the locked mode disruption may be the low plasma density of $<1\sim2\times10^{19}\text{m}^{-3}$ just before the energy quench. Because in the steady state the influx of impurity generated at the divertor plate to the main plasma increases with the decrease in the main plasma density[6] owing to the loss of the impurity influx shielding with low plasma density. However no clear dependence on the plasma density is observed in the density limit disruption. So low plasma density is not the cause. Another possibilities are the localization of the heat flux to the divertor plate as observed in TFTR limiter plasma[7], the higher degradation of the stored energy at the energy quench, or the low q_{eff} of 2.5~3.5. The second is expected from the decrease in the soft X-ray emissions as presented in Fig.6, in which all channel decrease at the same time without $m=1$ erosion.

4. Conclusions

Plasma current quench in the disruptive termination was investigated for various types of disruptions in JT-60U divertor plasmas to reduce the current decay rate. The reduction of the impurity effect is essential to slow the current decay in the current quench, that is confirmed by the following experimental results. 1) The current decay rate decreased with lowering the rise in the radiation loss at the energy quench for all types of disruptions. 2) Slow plasma current decay were obtained with low stored energy just before the energy quench in the density limit disruption. 3) In the locked mode disruptions the current decay rate is fast in spite of the low stored energy just before the energy quench. The reason of this fast current decay is not clear yet.

References

- [1] NEYATANI, Y., 19th EPS, Innsbruck, vol I (1992) 447
- [2] YOSHINO, R., section 7.1
- [3] WESSON, J.A., et al., Nuclear Fusion **29** (1989) 641
- [4] WESSON, J.A., et al., Nuclear Fusion **30** (1990) 1011
- [5] HOSOGANE, N., et al., Kakuyugo-kenkyu **65** (1991) 323 (in Japanese)
- [6] SAKASAI, et al., 14th IAEA, Wurzburg (1992) IAEA-CN-56/A-7-12
- [7] JANOS, A., et al., 14th IAEA, Wurzburg (1992) IAEA-CN-56/A-3-15

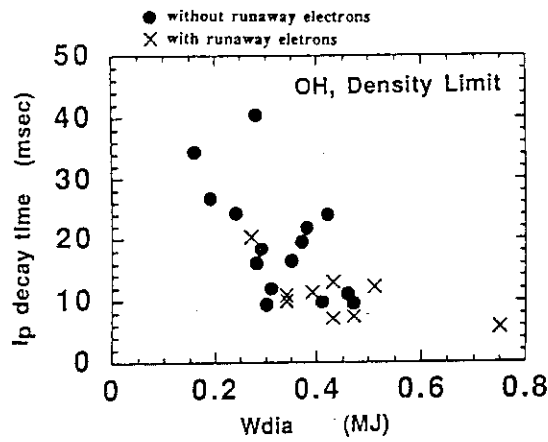


Fig.1 Plasma current decay time versus the plasma stored energy just before the energy quench for density limit disruptions for OH divertor plasmas of $I_p > 1.5$ MA.

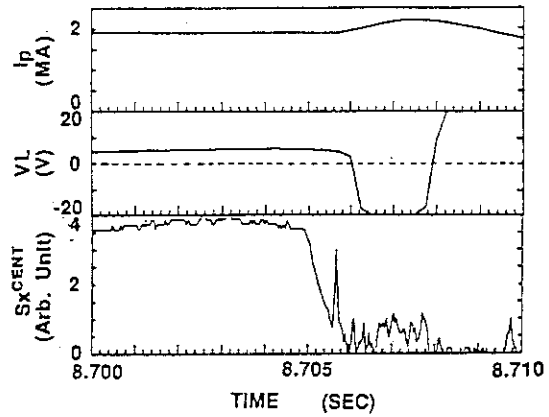


Fig.2 Time evolution of the density limit disruption. Soft X-ray spike is observed at 8.705s, after that plasma current rises with the negative one-turn voltage.

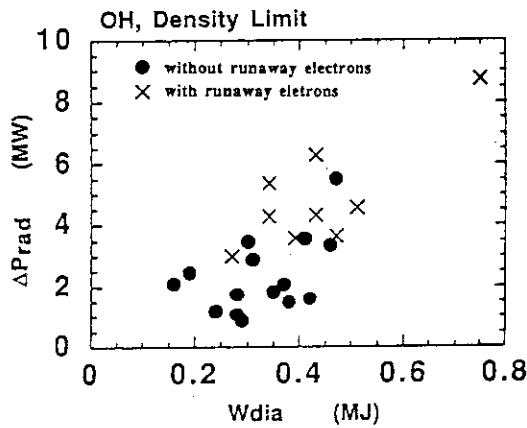


Fig.3 The rise in the radiation loss during the energy quench versus the stored energy just before the energy quench for the same disruptions in Fig.1.

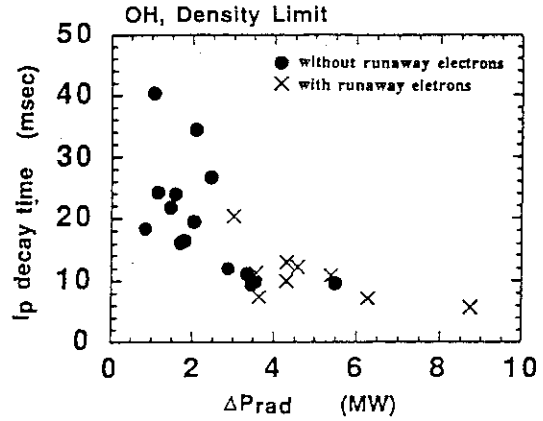


Fig.4 Plasma current decay time versus the rise in the radiation loss during the energy quench for the same disruptions in Fig.1.

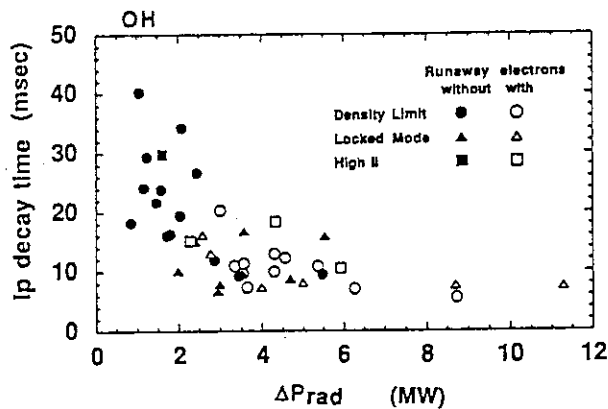


Fig.5 Plasma current decay time versus the rise in the radiation loss during the energy quench for three type of disruptions. Density limit disruptions, locked mode disruptions, and high I_i disruptions.

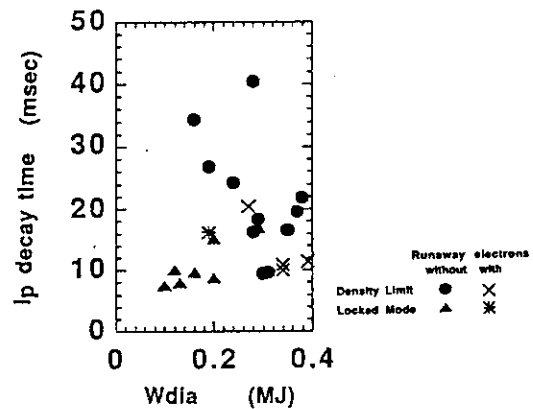


Fig.6 Plasma stored energies just before the energy quench and plasma current decay times for locked mode disruptions compared with those for density limit disruptions. OH divertor plasmas with $I_p > 1.5$ MA.

7.8 Softening of the Current Quench in the Disruptive Termination

R.Yoshino

1. Introduction

An investigation in JET comparing wall materials made of carbon and beryllium shows that the plasma current decay rate in the current quench can be decreased with beryllium wall drastically with reducing the drop in the electron temperature at the energy quench[1]. In JT-60U with carbon wall, the maximum plasma current decay time at the early phase of the current quench is 5ms as presented in section 7.11. Here disruptions with slow current decay rate (or long decay time) must be investigated to develop methods for softening the current quench. Experimental results presented in section 7.7 suggests that the reduction of the impurity influx caused by the energy quench is essential to reduce the drop in the electron temperature and the current decay rate for the density limit disruption of OH divertor plasmas. In this paper the reduction of the current decay rate is investigated.

2. Softening of the Current Quench

1) Reduction of Heat Flux to the Divertor Plate

Figures 1 in section 7.7 suggests the necessity of the low stored energy just before the energy quench to decrease the current decay rate for the density limit disruption. In the density limit disruption, a detached plasma contracting from the outermost magnetic flux surface is observed after a MARFE. After 100~600ms from the start of the detachment, a plasma is terminated by the energy quench and the current quench. During this short time period of detachment confinement degradation occurs by the enhancement of the radiation loss, MHD activities, and the shrinkage of the plasma core. The comparison of the stored energy at the start of the detachment and just before the energy quench is presented in Fig.1. Large decrease in the stored energy can be obtained during the detached plasma phase both for joule and NB heated plasmas. The detachment is produced by the power balance at the plasma periphery. So the detached plasma can be produced under high power NB heating with the intense gas puffing or the impurity injection. However Fig. 1 shows that the stored energy just before the energy quench increases with that at the start of the detachment. So more intense degradation of the stored energy is required. DCW(Disruption Control Winding) has the possibility of this degradation as presented in section 7.5.

2)Suppression of the Impurity Influxes at the Energy Quench

No current quench is observed for divertor plasmas with $q_{\text{eff}} > 7$ in spite of many minor disruptions as presented in Fig.5 in section 7.1. Here q_{eff} is the effective safety factor. However disruptive plasma terminations are still observed in limiter plasmas at $q_{\text{eff}} > 7$. Comparison of the density limit phenomena at $q_{\text{eff}} \sim 9$ for the divertor plasma and limiter plasma is presented in Fig.2. Density limit disruption is observed after the change in the plasma configuration from a divertor plasma with the null point height X_p^{FIT} of 8.5cm to a limiter plasma (see Fig.2(a)). X_p^{FB} is the null point height from the divertor plate calculated in the real time feedback control, and X_p^{FIT} is obtained by a magnetic equilibrium code. The configuration change at 5.5 s is caused by the miss calculation of X_p^{FB} caused by the drop in Shafranov lambda. X_p^{FB} becomes much higher than the reference value of 0cm, so that the divertor coil current is dropped to zero with becoming the limiter configuration. On the other hand no current quench is observed in the divertor configuration with X_p^{FIT} of 23cm (see Fig.2(b)). Higher impurity shielding can be obtained in the divertor plasma with higher q_{eff} due to the longer connection length from the divertor plate to the main plasma. This suggests higher null point height enables no current quench for divertor plasmas with lower q_{eff} of < 7 , that will be studied in the next experimental period. Broadening of the heat flux with higher q_{eff} observed in the steady state[2] may occur at the energy current quench, and decrease the generation of impurities from the divertor plate.

In the density limit disruptions for OH and NB heated divertor plasmas with $I_p > 1.5\text{MA}$, longer current decay time was obtained at q_{eff} of 5~6.5 as presented in Fig.3 by square points. Here plasma current decay time is estimated from 50% drop of the plasma current, and current quenches with runaway electrons are included. Because no generation of runaway electrons is observed in current quenches with long plasma current decay time of $> 20\text{ms}$ as presented in Fig.4 in section 7.2. According to Fig.3 high q_{eff} is not a decisive cause of long current decay time, because short current decays exist still at high q_{eff} . Then high q_{eff} may be one of necessary conditions. Same behavior is observed in the locked mode disruption presented by triangle points in Fig.3. Current decay times of them are short with $\sim 10\text{ms}$ at q_{eff} of ~ 3 , but increases to 30ms at q_{eff} of ~ 5 . However more data points are required to mention about the effect of q_{eff} .

3) Additional Heating of the Main Plasma Core

The direct heating of the plasma core is another way to avoid the drop in the electron temperature during the current quench. Plasma was heated by NB during the energy quench phase in the density limit disruptions. The effect of NB heating is presented in Fig.4. The current decay rate decreases drastically from 150MA/s with joule heating alone to 25MA/s with 8MW NB heating. The command value of the plasma current is decreased with the drop in the measured plasma current. With this reduction of the command, the generation of

runaway electrons can be avoided. With 8MW NB heating, a hot plasma core is observed during the current quench phase, that is measured by visible light TV with 1ms time resolution. The electron temperature at the plasma core may be kept much higher than 10eV. The plasma core is detached from the outermost flux surface, and its shape changes largely for each 1ms during the current quench. In the detached plasma state the degraded plasma stored energy can be also obtained with NB heating as presented in Fig.5. The plasma stored energies are 0.1~0.5MJ just before the energy quench, and the current decay time increases with NB heating power as presented in Fig.6 by closed points. NB heating power higher than 8MW is not tried yet. The direct NB heating of the locked mode disruption was also tried upto 25MW for $q_{\text{eff}}=4\sim5$ as presented in Fig.6 by open points. Reduction of the plasma current decay rate was obtained, but a little small at high power NB heating. The reason of this weaker NB heating effect may be same with the locked mode disruption for OH plasmas as presented in section 7.2.

3. Conclusions

In the density limit disruption small rise in the radiation loss was necessary to get slow plasma current decay, and was obtained with low stored energy just before the energy quench. Low stored energy can be obtained by fast degradation of the confinement during the detached plasma state. Slower plasma current decay was obtained with higher q_{eff} of 4~6 for divertor plasmas, and no current quench at $q_{\text{eff}}>7$. However current quenches were observed for limiter plasmas at $q_{\text{eff}}>7$. Divertor plasmas with higher q_{eff} may have the shielding effect of the impurity influx owing to the longer connection length. Direct NB heating of the core plasma detached from the outermost flux surface was also useful to reduce the drop in the electron temperature caused by the intensive impurity influx just after the energy quench. In the locked mode disruptions NB heating had weak effect to reduce the current decay rate, reason of that is not clear yet.

References

- [1] TANGA, A., private communication
- [2] TANGA, A., et al., will be submitted to Nuclear Fusion.
- [3] ITAMI, K., et al., 14th IAEA, Wurzburg (1992) IAEA-CN-56/A-6-5

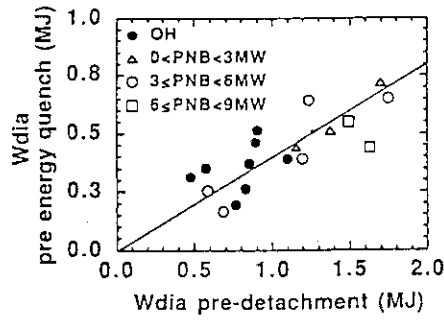


Fig.1 Comparison of the stored energies at the start of the detachment and just before the energy quench.

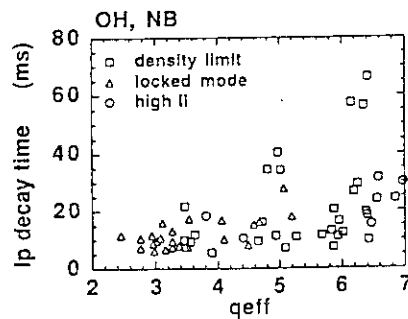


Fig.3 Plasma current decay time versus q_{eff} . OH and NB heated divertor plasmas with $I_p > 1.5$ MA. Three type of disruptions are presented, that are density limit disruptions, locked mode disruptions, and high li disruptions.

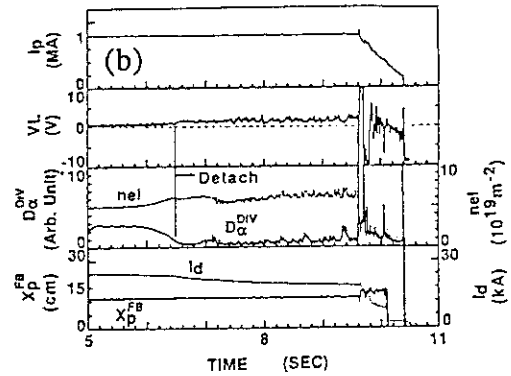
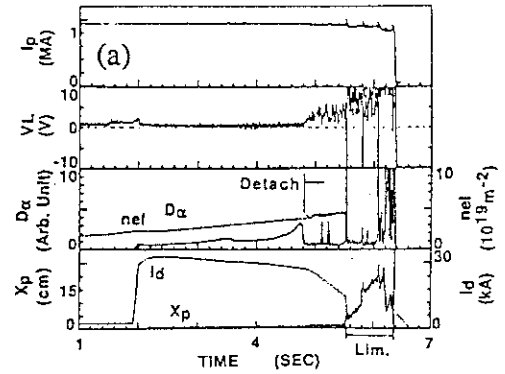


Fig.2 Density limit phenomena in high q_{eff} discharges with $q_{eff} = -9.0$.

(a) Disrupted at $t = 6.4$ s after the change in the configuration from divertor plasma to the limiter plasma at $t = 5.5$ s.

(b) Plasma is terminated without the current quench for the divertor plasma.

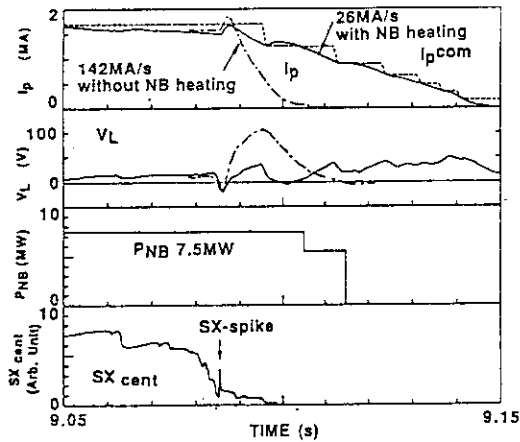


Fig.4 Softening of the current quench by 7.5MW NB heating for the density limit disruption. $q_{eff} = 6.0$

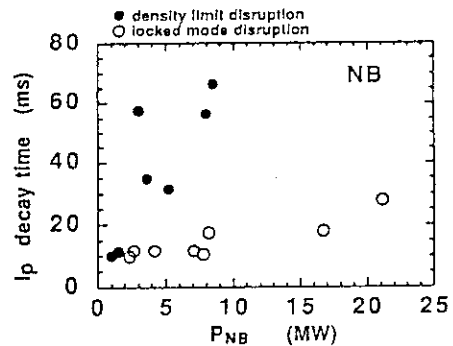


Fig.5 Plasma current decay rate versus stored energy just before the energy quench for OH plasmas and NB heated plasmas.

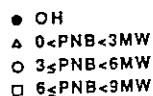


Fig.6 Plasma current decay time versus NB heating power for density limit disruptions and locked mode disruptions.

7.9 Suppression of Runaway Electrons

R.Yoshino

1. Introduction

Runaway electrons generated during the current quench in the disruptive termination decreases the life time of the first wall material drastically. Thus the suppression of runaway electrons is one of urgent issues for the design of fusion reactors. Dreicer field for the generation of runaway electrons is proportional to n_e/T_e . Then the runaway parameter can be presented by $ET_e/n_e = \eta j T_e/n_e \propto 1/(T_e^{0.5} n_e)$ [1]. This suggests high plasma density with high electron temperature is necessary to avoid the generation of runaway electrons. In this paper parameter regions of the generation of runaway electrons for the density limit disruption and the locked mode disruption are investigated, and preliminary study on the suppression of runaway electrons by NB heating is presented.

Typical case of the generation of runaway electrons in the density limit disruption is presented in Fig.1. D_α emission from the divertor plasma drops 230ms before the current quench owing to the plasma detachment. Plasma current has a tail. Runaway electrons measured by hard X-ray emission are generated just after the start of the plasma current quench, and are observed until the plasma current termination. The maximum difference between the command value of the plasma current (I_p^{com}) and the real plasma current value (I_p) is 1.2MA, and one turn-voltage rises to 214V.

In this paper density limit disruptions and locked mode disruptions for divertor plasmas with $I_p > 1.5\text{MA}$ are investigated. Current quenches with runaway electrons at $I_p > 0.5\text{MA}$ are recognized as those with the generation of runaway electrons.

2. Region of the Generation of Runaway Electrons

Plasma density and electron temperature during the current quench are important parameters to investigate the generation of runaway electrons. However measurements of the plasma density by the interferometer during the current quench are hard owing to the fringe losses, and that of electron temperature by ECE polychrometer has large ambiguity owing to the drastic change in the poloidal magnetic field. Thomson scattering measurement is a powerful method to measure them. However a timing system triggered by a negative one-turn voltage spike is required and is not established yet. From the stand point to suppress runaway electrons, the plasma density just before the energy quench is useful to search the operational space to avoid runaway electrons, and the plasma current decay time is useful to assume the electron temperature during the current quench. Then these are investigated to clarify the threshold required to suppress the generation of runaway electrons for the density limit

disruptions for OH divertor plasmas as presented in Fig.2 a). Closed circle points are disruptions without runaway electrons, open circle points are with runaway electrons at $I_p < 0.5\text{MA}$, and cross points are with runaway electrons at $I_p > 0.5\text{MA}$. In this figure current quenches with runaway electrons are limited at low plasma densities of $< 3 \times 10^{19}\text{m}^{-3}$ and at short current decay time of $< 20\text{ms}$. Runway electrons are still observed at long plasma current decay time of 40ms , if plasma density is $< 3 \times 10^{19}\text{m}^{-3}$. Data points are not enough yet, but no runaway electron is observed for $n_e > 3 \times 10^{19}\text{m}^{-3}$ at the minimum current decay time of 5ms . This result suggests intense gas puffing or pellet injection is beneficial to avoid runaway electrons with high density.

Threshold value cannot be obtained in locked mode disruptions for OH plasmas as presented in Fig.2 b). Because current quenches without runaway electrons are obtained at low plasma densities of $< 1 \times 10^{19}\text{m}^{-3}$ and short plasma current decay time. Plasma movement during the current quench is very fast at plasma current decay time of $< 10\text{ms}$. Interactions between plasmas and the first wall may be much larger than those in density limit disruptions, that can be assumed from the larger rise in the radiation loss at the energy quench as presented in section 7.7.

3. Suppression of Runaway Electrons by NB heating

NB heating during the energy quench and the current quench is useful to raise both of the plasma density and the electron temperature, and to suppress runaway electrons. Plasma density and plasma current decay time are larger than the threshold values for OH plasmas as presented in Fig.3 a). In locked mode disruptions effect of NB heating is not clear as presented in Fig.3 b). However no runaway electron is observed at plasma densities of $> 3 \times 10^{19}\text{m}^{-3}$ for OH and NB heated plasmas as presented in Fig.2 and 3. Then much higher rise in the plasma density may be required to suppress runaway electrons perfectly. Pellet injection will be tried in the next experiments.

4. Conclusions

To suppress runaway electrons in the density limit disruption and locked mode disruptions, higher plasma density of $> 3 \times 10^{19}/\text{m}^3$ may be required. Pellet injection just before the energy quench will be tried in the next experimental period.

References

- [1] WESSON, J.A., et al., Nuclear Fusion **29** (1989) 641

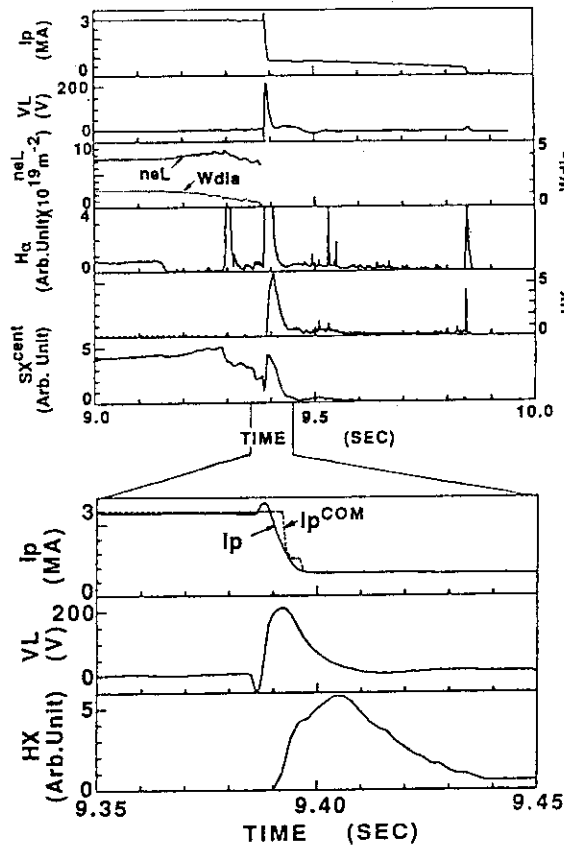


Fig.1 Plasma current quench with the generation of runaway electrons.

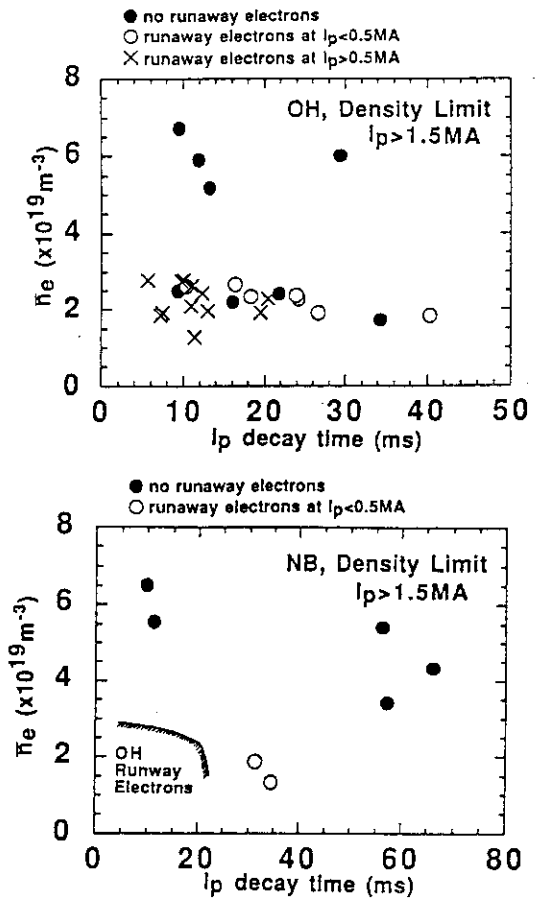


Fig.2 Plasma density just before the energy quench versus plasma current decay time in the density limit disruption for a) OH plasmas and b) NB heated plasmas.

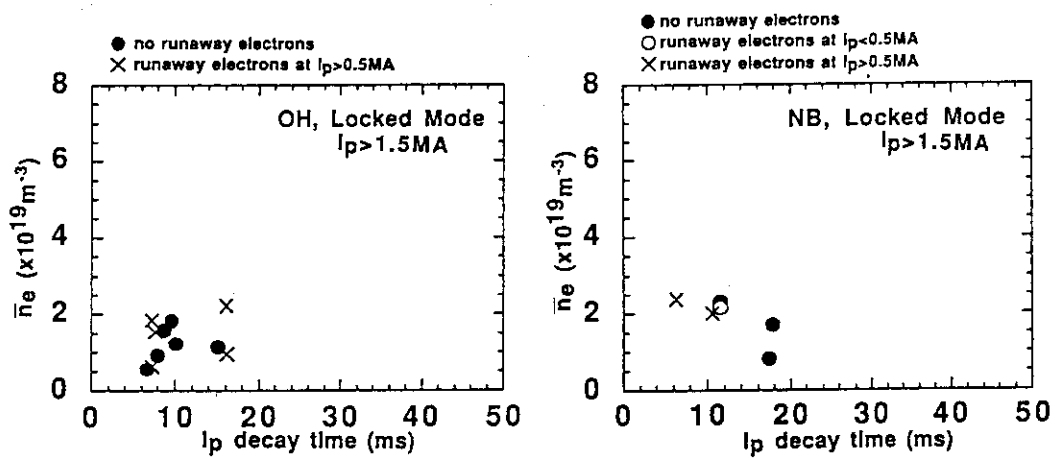


Fig.3 Plasma density just before the energy quench versus plasma current decay time in the locked mode disruption for a) OH plasmas and b) NB heated plasmas.

7.10 Stable Fast Plasma Shutdown

R.Yoshino

1. Introduction

Fast plasma shutdown of 5~10MA/s without disruptive termination and runaway electrons is required in tokamak fusion reactors to raise the reliability and safeness of the plant as discussed in ITER-CDA[1], however no systematic study has been performed yet. The controlled plasma termination without the energy quench was limited to be -4MA/s in JT-60U owing to the increase in I_i as presented in section 7.1. Then the development of a new method was required to get the plasma current ramp-down of <-5MA/s.

The avoidance of the current quench after the energy quench was observed in about 20 shots. So the required condition to avoid the current quench was investigated in these shots. According to this analysis, fast controlled plasma shutdown with the energy quench and without the current quench was tried by the intense helium gas puffing, and plasma current ramp-down of -6MA/s was demonstrated successfully from 2MA to 0MA as presented in this paper.

2. Disruptions during Plasma Current Ramp-down

In JT-60U, two types of disruptions were observed mainly during the plasma current ramp-down. They are the density limit disruption at high plasma density and the high I_i disruption at low plasma density as presented in section 7.1. Both of these disruptions may be caused by the tearing instability owing to the current profile peaking. Furthermore in these disruptions the plasma current decay time defined by $I_p/(I_p/dt)$ increases with the decrease in the stored energy just before the energy quench. The reduction in the impurity generation at the divertor plate is obtained by small heat flux for the low stored energy, so that the electron temperature during the current quench may be kept much higher than ~10eV. Here the divertor plasma configuration is maintained at the energy quench in a disruption of the divertor plasma. On the other hand runaway electrons are generated in high I_i disruptions owing to low plasma density as presented in section 7.9. These results suggest the usage of the density limit disruption to get fast controlled plasma shutdown without generating runaway electrons.

3. Avoidance of the Current Quench

If intense helium gas puffing is performed at the plasma current flattop, plasmas are disruptively terminated with the current quench. On the other hand the plasma current decay

rate in the current quench decreases with lowering the rise in the radiation loss at the energy quench as presented in section 7.7. Furthermore the current quench was avoided for the small rise in the radiation loss at the energy quench as presented in Fig.1. The energy quench, soft X-ray spike, small rise in the plasma current with the negative one-turn voltage spike, and the decay of the plasma current are observed, but the plasma current returns to the pre-energy-quench value at $t=7.58$ s. The same avoidance of the current quench were observed in about 20 shots for q_{eff} of 2.5~6 as presented in Fig.2. The threshold value of $\leq \sim 1\text{MW}$ on the rise in the total radiation loss at the energy quench to avoid the current quench can be obtained from Fig.3, in which inverse of the plasma current decay times are presented for all types of disruptions in OH plasmas at $I_p > 1.5\text{MA}$.

4. Fast Plasma Shutdown with -6MA/S

In the density limit disruption, low rise in the radiation loss can be obtained at low plasma stored energy just before the energy quench as presented in section 7.7. Then that fast degradation of the energy confinement is indispensable to avoid the current quench, that can be obtained during both of the detached plasma phase and the energy quench phase.

According to these investigations, plasma shutdown of -6MA/s from 2MA to 0MA was tried with intense helium gas of $30\text{Pam}^3/\text{s}$ during the plasma current ramp-down as presented in Fig.4. The pre-programmed plasma current decay rate is -6MA/s. Higher decay rate than -6MA/s cannot be obtained owing to the voltage-limit on a power supply. The effective safety factor q_{eff} at the plasma current flattop is 3.4, and is 4.1 at $t=12.1\text{s}$. The detached plasma was produced by this intense helium gas puffing, and fast degradation of the stored energy was obtained during the detached plasma phase from 0.6MJ to 0.4MJ and the following slow energy quench with 8ms. Plasma detachment and slow energy quench were measured by soft X-ray emission as presented in Fig.5. The start of the current quench is observed at $t=12.098\text{s}$ with the negative spike of the one-turn voltage and the small rise in the plasma current. However the current quench is returned to the controlled plasma current ramp-down as presented in Fig.4. Hot plasma core was observed by TV measurement during the plasma current decay, that suggests high electron temperature of $>10\text{eV}$ was obtained. The small rise in the radiation loss of 0.8MW at the energy quench suggests that the large impurity influx was successfully suppressed.

5. Conclusions

Small rise in the radiation loss of $\leq \sim 1\text{MW}$ at the energy quench is required to avoid the following current quench. Fast degradation of the energy confinement with lowering

the stored energy just before the energy quench is necessary to get this small rise in the radiation. This degradation was demonstrated in the fast plasma shutdown of -6MA/s from 2MA to 0MA without the current quench, in which the detached plasma state was actively produced by the intense helium gas puffing. The stored energy was degraded from 0.6MJ to nearly zero within the detached plasma phase of 15ms and energy quench phase with the $m=1$ erosion of 7ms . The start of the current quench was observed, but the plasma current decay returned to the programed one. The small rise in the radiation loss of 0.8MW obtained at the energy quench suggests the suppression of the impurity influx and the reduction of the drop in the electron temperature.

References

[1] POST, D.E. et al., ITER DS 21 (1991)

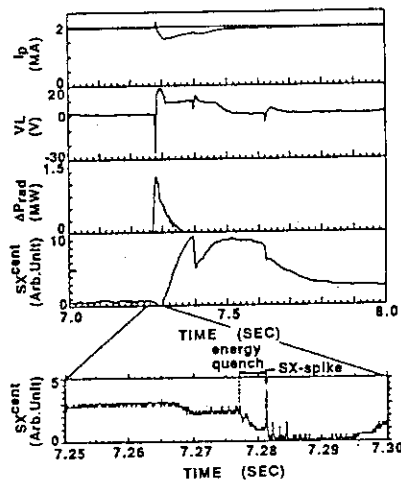


Fig.1 Typical time evolution of the energy quench without the following current quench.

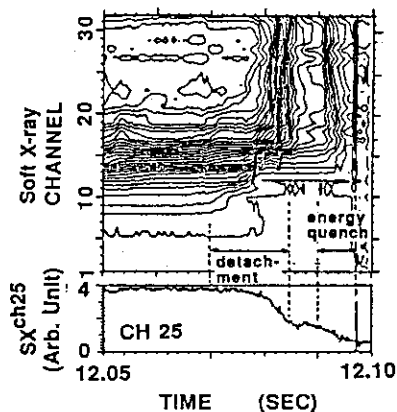


Fig.5 Degradation of the energy confinement in fast plasma shutdown (Fig.4) measured by the soft X-ray array.

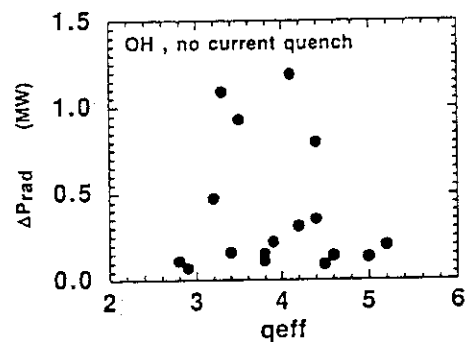


Fig.2 The rise in the total radiation loss at the energy quench versus q_{eff} for OH divertor plasmas with $I_p > 1.5\text{MA}$ and without the following current quench

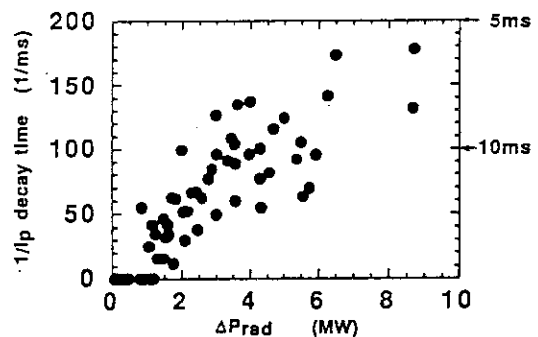


Fig.3 Inverse of the plasma current decay time versus the rise in the total radiation loss at the energy quench for OH divertor plasmas with $I_p > 1.5\text{MA}$

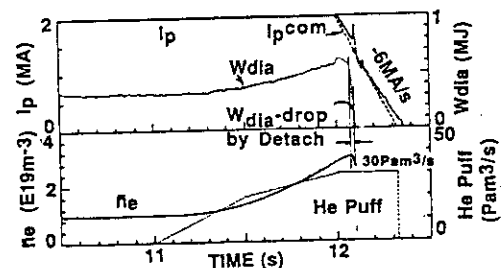


Fig.4 Fast plasma shutdown with $dI_p/dt = -6\text{MA/s}$.

7.11 Statistical Analysis of Disruptions

Y. Neyatani, R. Yoshino and N. Hosogane

1. Introduction

From the beginning of JT-60U experiment, the statistical analysis of disruption is continued to evaluate the frequency and the discharge phase of the disruptions in order to continue the plasma operations without catastrophic damages. In 1992, we separate the three periods to this year's experiment by an one month shut down in May for a regular examination and the boronization in July, i.e. January to April, May to July and August to October. In the next section, the frequency of the disruptions is described for each operational period. The rate of disruption for some operational phases is also discussed. The decay rate of the plasma current is discussed in the following section including boronization effect. The summary is described in the last section.

2. Frequency of the Disruptions

In 1992, the total shots of 1866 were discharged during January to October. The first and second boronization were performed in July and August in order to reduced oxygen. The average frequency of the disruptions of this year is 17.7% of total discharge during the operation as shown in Fig.1(a), which is 2% less than the result of the last year experiment [1]. Where the disruption is defined as follow conditions; 1) plasma current just prior to disruption is larger than 0.5 MA; 2) plasma current terminate before 14 sec of discharge. The frequencies of disruptions of three periods described above are 22.7%, 14.3% and 15.4% respectively (Fig.1(b)-1(d)). The last period is after boronization. The effect of boronization is not so clear because the disruption frequency is not so change before and after boronization.

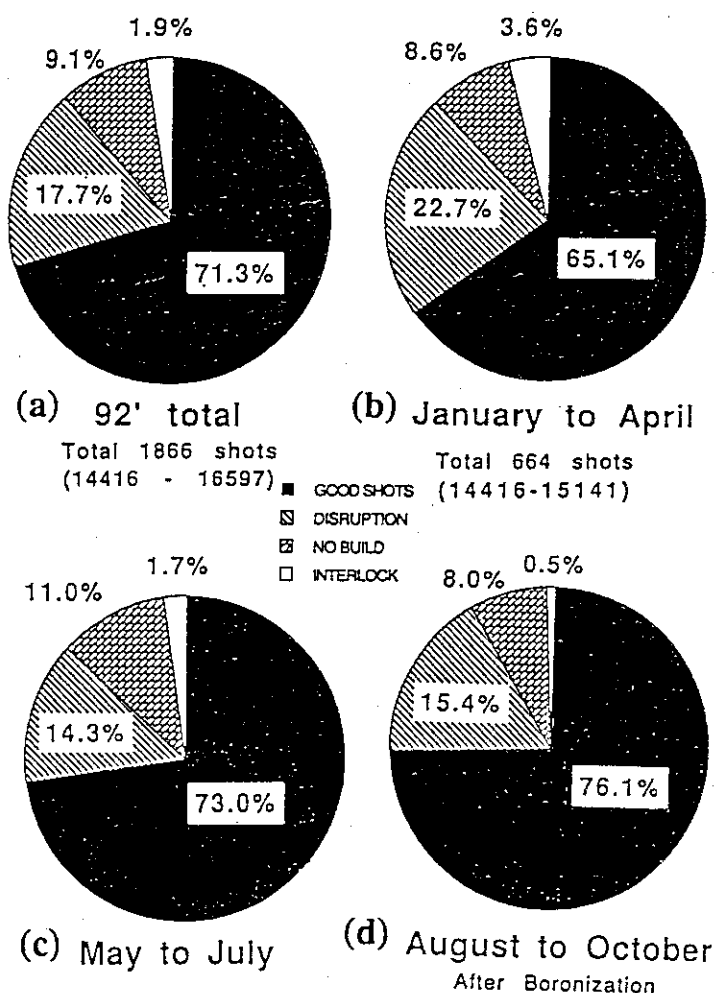


Fig.1 Histogram of the discharge in 1992

The disruption frequency of the current ramp up phase of 1992 is drastically reduced about one third than that of 1991. The disruption in ramp up phase are only 13.6% of all disruption shots (31% in 1991) (Fig.2). Most of the ramp up disruption is occurred in the NB port aging phase just after the vacuum vent (Fig.3) to withdraw metal impurities on

the carbon tiles. Another disruptions during ramp up phase are also observed large impurity content from the plasma initiation. The reduction of frequency of the current ramp up phase is mainly due to improvement plasma build up process including growing plasma method [2]. The current ramp down disruption has a major part of disruptions of 51.2% of total disruptions. The large fraction of the current ramp down disruption causes by the stable and fast plasma shut down experiment using current ramp down phase in large part of shots. A half of disruption in this phase occurred $t > 13$ sec and plasma current < 2 MA. The disruptions are mainly caused by high li or density limit. These types of disruptions can be avoided by a careful plasma position and current profile control, for example using dwindling plasma method, DCW coil, gas puffing to make a detached plasma etc [2].

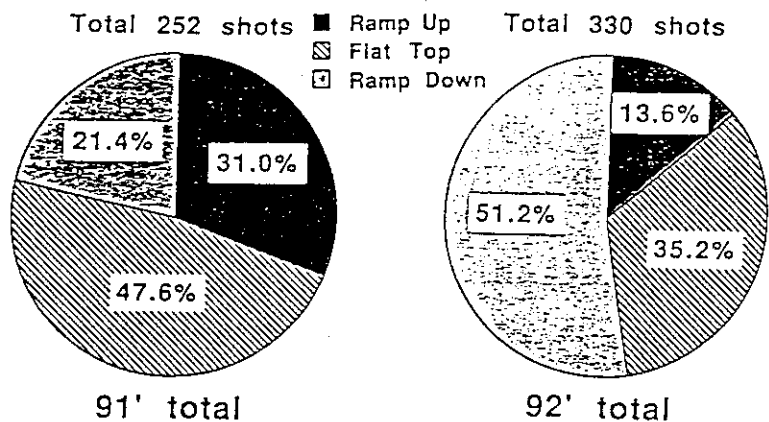


Fig.2 Comparison disruption rate between 1991 and 1992 discharges for each phases.

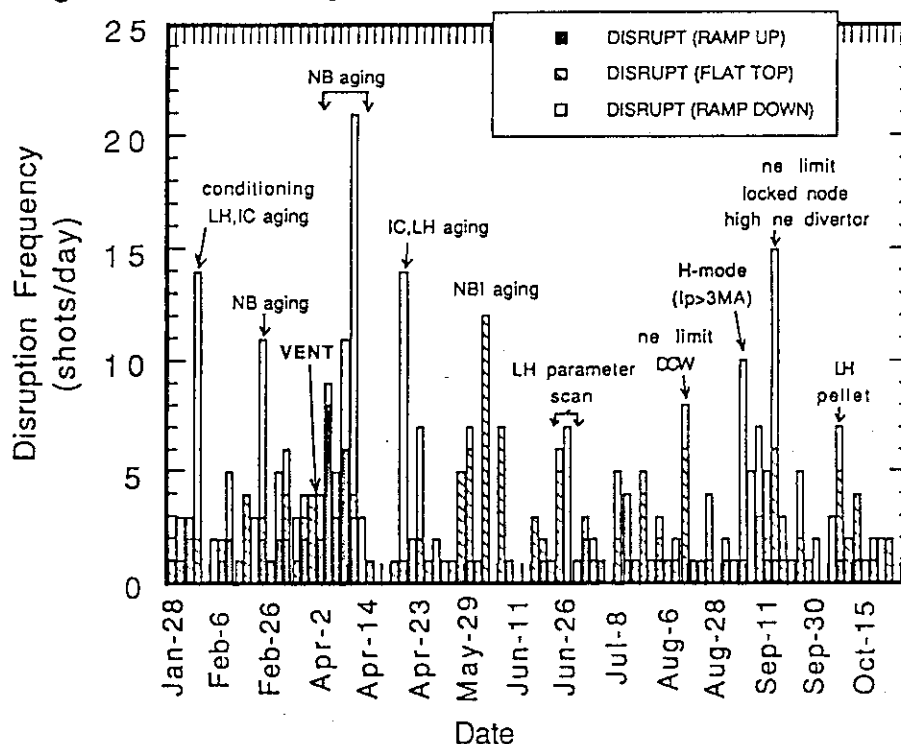


Fig.3 Disruption frequency of each experimental days. Major part of disruption occurs in aging phase.

3. Decay Rate of Plasma Current

The electromagnetic force induced by the disruptions is increased with the decay rate of plasma current. Hence, it is important to estimate the decay rate for the design of the next generation devices. Figure 4(a) shows the maximum decay rate of the disruptions with the flat top, I_p ramp up and down phases. The fastest decay has $I_p/(dI_p/dt)_{\max} \sim 5\text{ms}$, which is the same result of last year. No difference of the decay rate is also obtained for each discharge phases. The 50% decay rate ($I_p/(dI_p/dt)_{50\%}$), which was defined as the time when the plasma current decay until 50% of plasma current before disruption, is approximately 20% greater than the maximum decay rate (Fig.4(b)).

In the beryllium bounded disruption in JET, the current decay rate is about 6 times greater than that carbon bounded disruptions [3]. Hence, as the wall material may attributes the current decay rate, reducing the decay rate was expected by boronization. Figure 5 shows the 50% decay rate of density limit disruptions before and after boronization. After the boronization, the 50% decay rate became slightly large, but no clear difference was observed. Two reasons are considered. One is that at the boronization in this year, the

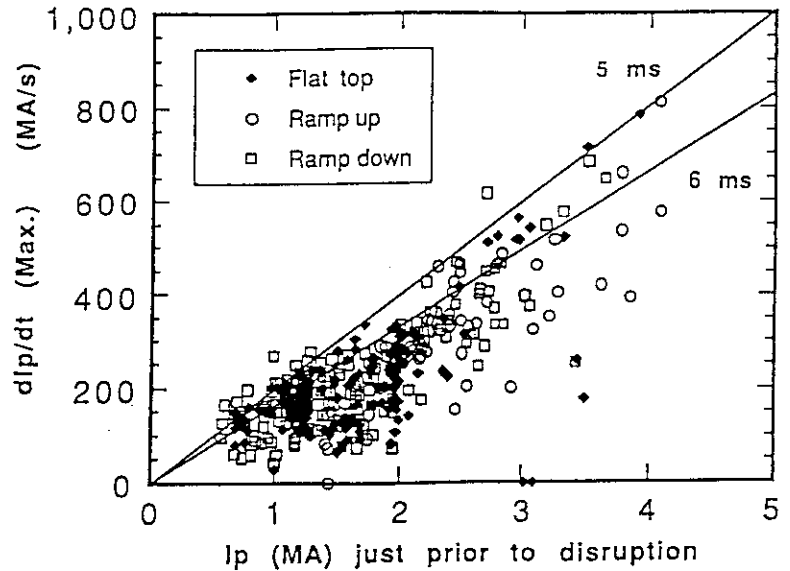


Fig.4 (a) The maximum current decay rate of disruptions. The fastest decay rate is 5ms.

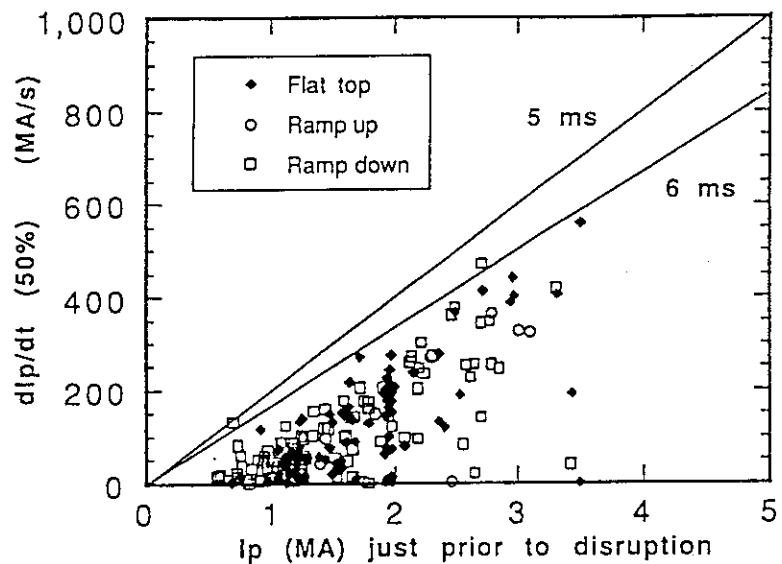


Fig.4 (b) The 50% current decay rate of disruptions. The fastest decay rate become 20% greater than the maximum decay rate.

boron layer was not made enough thickness and was localized toroidally [4]. Another reason is that if the current decay time can be assumed to be characterized by the spitzer resistive time, which correlated the radiative cooling rate by a impurity during the energy quench, the effect of boronization is not so expected because the radiative cooling rate of boron is almost as large as that of carbon [5]. As the improvement boronization system will be able to make the uniform and thick boron layer next year, it should be a future work after the next boronization.

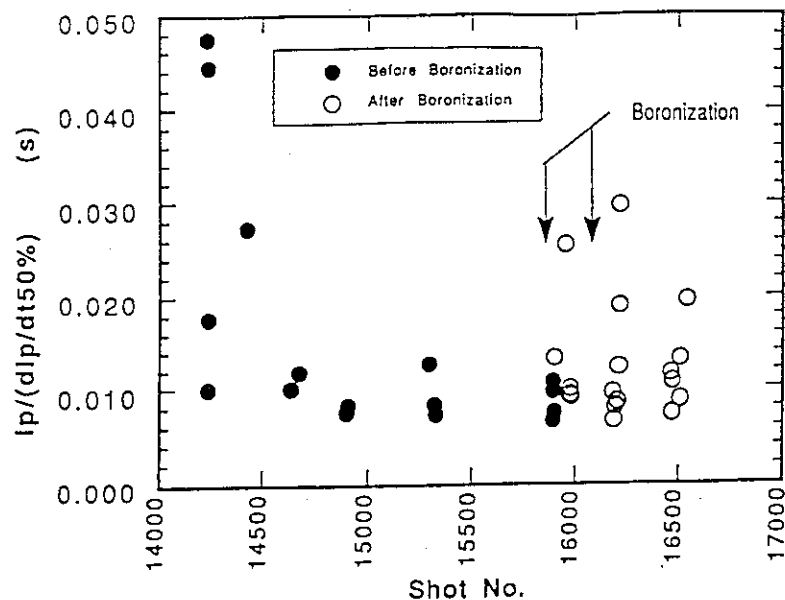


Fig.5 The 50% of current decay time of density limit disruptions which is the same before and after boronization.

4. Summary

The average frequency of the disruptions of 17.7% is surveyed at the JT-60U experiment in 1992. Disruption in current ramp up phase reduced about one third by the improvement plasma operations. A half of disruptions occurred in current ramp down phase. They are mainly caused by high li and high density. These types of disruption can be avoided by a careful plasma position and current profile control. The most fraction of the other disruption except low density locked mode has correlation to impurity influx produced at plasma initiation, and agings of NB, IC and LH.

The maximum decay rate of disruption is 5 ms which is the same results in 1991. The boronization effect is not so clear. It may be caused by an ununiformity of the boron layer and/or the less difference of the radiative cooling rate of boron and carbon.

References

- [1] NEYATANI Y. et al. : JAERI-Report, JAERI-M 92-073 p.178-181.
- [2] YOSHINO R. et al. : in Plasma Physics and Controlled Nuclear Fusion Research 1992 (Proc. 14th Int. Conf. Wurzburg, 1992), IAEA-CN-56/G-3-1
- [3] HARRIS G. R. : JET-Report, JET-R (90) 07
- [4] SAIDOH M. et al. : In this review paper
- [5] POST D.E. et al. : Atomic Data and Nuclear Data Tables, Vol.20, 5, November 1977 P.397

7.12 A Possibility Study of High Triangularity Operation

M.Matsukawa, T.Taylor, R.Yoshino, Y.Kamada, M.Kikuchi, H.Ninomiya

1. Introduction

VH-mode discharge, which has much enhanced energy confinement time rather than H-mode, was observed in DIII-D[1]. It was observed that the confinement time of VH-mode has tend to increase with the triangularity. However, it is not still confirmed clearly in other tokamaks. JT-60U has introduced the boronization system using decaborane gas in 1992. Therefore, it is very important to compare the confinement with DIII-D plasmas under the closed operational condition. This is a short report regarding to the high triangularity operation in JT-60U.

2. High Triangularity Plasma Configuration.

The vertical field coil (V-coil) of JT-60U are divided to four coil blocks and could be reconnected according to the various experimental requirements using the connection changer located in the torus hall. Figure 1 shows the poloidal field coil configuration of JT-60U. The V-coil block near the outboard, V1 and V7, has a basic function of plasma radial position control. Also, upper and lower blocks, V2, V3 and V6, could control the elongation. To control the triangularity, we need principally the independent current control for each coil blocks. However, it is very difficult to feed the electrical power into the torus hall. Therefore, we have to compromise with the two power supplies.

Figure 2 shows the new V-coil connection (hybrid connection 4) for high triangularity operation. Here, the present V-coil power supply has divided to two parts and those are controlled independently. The rating of PSV1 is 3kV/60kA and PSV2 is 2kV/60kA. It has been possible from the experimental results of plasma initiation in JT-60U which indicated that 3kV of V-coil power supply is enough for stable plasma initiation. The power transmission feeder is planned to use the present DCW-coil feeder. It does not have large rating so that the operation may be limited by the thermal increase.

A typical equilibrium of the high triangularity operation is shown in Fig.1 The major parameters are plasma current of 2MA, volume of 70m³, elongation of 1.4 and triangularity of 0.38. The triangularity of ~0.7 is required to study the VH-mode, but it is very difficult.

3.Summary

The hybrid connection of V-coil can expand the operational regime of JT-60U. It could be done by minimum cost because the control system modification is only required to the present

existing power supply. The boronization and high triangularity operation enable to study VH-mode.

REFERENCES

- [1]. T.TAYLOR, T.S., et.al., 14th IAEA Würzburg IAEA-CN-56/A-3-1.

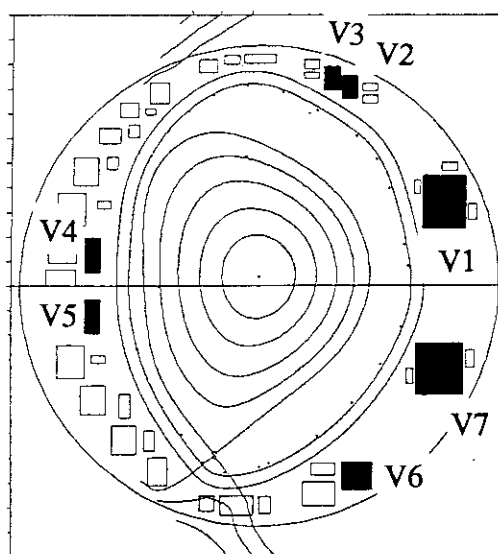


Fig.1 Poloidal field coil configuration and a typical equilibrium with the high triangularity.

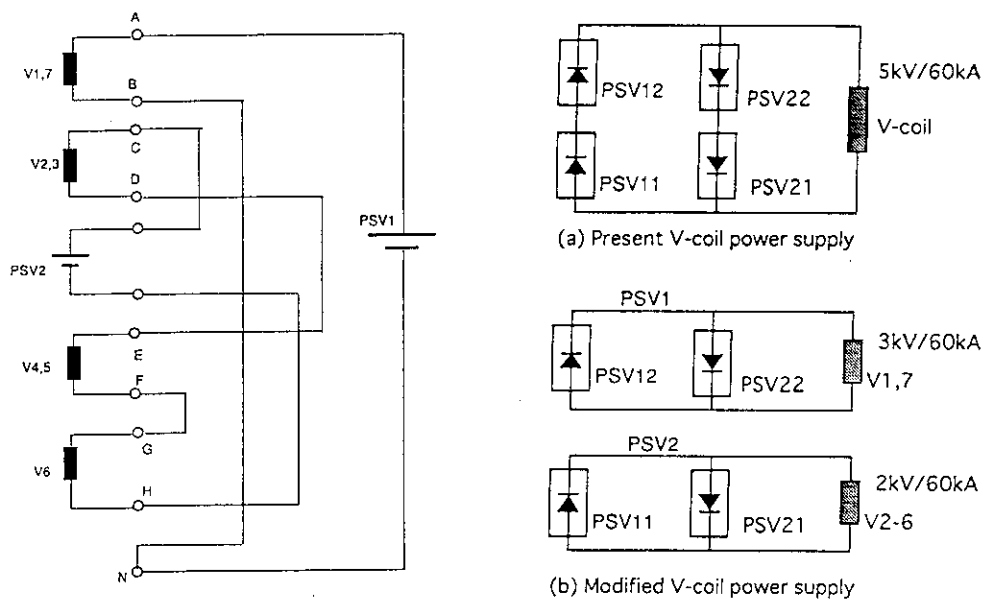


Fig.2 Reconnection of the vertical field coil (hybrid connection 4) and the modification design of V-coil power supply.

7.13 Plasma Behavior During the Plasma Termination and Initiation Procedure Observed by the Density Measurement

T. Fukuda, R. Yoshino, Y. Kamada, S. Miura, K. Ushigusa

1. Introduction

As an alternative to the RF or beam induced current sustainment, AC i. e. alternating plasma current operation has recently been recognized as one of the effective techniques to realize the steady state operation of the tokamak discharge. Eight years after the first demonstration of the AC operation on the STOR - 1M tokamak in 1984 [1], much larger scale ± 2 MA AC operation has been accomplished at JET [2]. The residual component of the plasma density is indispensable for the plasma re-startup. An inductive current drive by the ohmic transformer has the highest efficiency and it is most reliable among other various current drive schemes. In addition, it is practically independent of the plasma density. Inductively driven higher density operation in tokamak reactors relaxes the thermal loading of divertors and reduces impurity content. The potential problems associated with the mechanical fatigue of the toroidal coil, however, still remains to be controversial. This paper addresses the existence of the residual density after the plasma termination and the possibility of AC operation on JT-60 Upgrade.

2. Operation Method

In the AC operation, the plasma current is ramped down and then up in the opposite polarity during the current reversal phase. Even if the plasma current is extinct during the current reversal phase, the subsequent negative plasma current can evolve as demonstrated in JET. However, the plasma current ramp-up is facilitated only when the plasma is not completely lost and the high purity level is maintained. This is significant, since the radiation barrier can affect the subsequent current evolution. Therefore, non-disruptive plasma current termination is indispensable for the smooth current restart. This endeavor has been successfully carried on JT-60 in 1992 [3]. The residual plasma will remove the voltage spike for break down, which saves the volt-second consumption.

Operation scheme employed at JET was, in principle, constant-q operation; the plasma major radius was continuously increased as the minor radius monotonously decreased. Practically the plasma was attached to the outer limiter all the time during the current ramp phase. Presumably, most of the plasma current was carried in the surface area of the plasma. The important point is that the residual density should remain in the area where the minimum magnetic field exists in order to reduce the voltage required for

the breakdown of the succeeding plasma. Actually, in the case of JET, the loop voltage of ~ 10 V was accompanied by small scale disruptions. The minimum dwelling time which was actually achieved was 0.5 s. The dwelling time is dependent on the capability of the vertical field coil.

3. Residual Density Measurement

In order to find the possibility of the AC operation on JT-60, we focused on how long the density remains after the plasma termination. For the density measurement, reflectometric technique was employed. When the reflectometer loses the reflection layer in the plasma, it turns out to be a Michelson type interferometer for the JT-60 reflectometric system [4]. Since the absolute value of electron density can be detected by finding the intensity loss which is apparently observed as the fringe counting error, we can easily find the line integrated electron density in the termination phase. Since the diagnostic chord was situated only on the midplane, vertical interferometer chords at $R=2.68$ and 3.55 were also utilized to understand where the plasma is situated in the horizontal direction. These two chords are denominated as U1 and U2 here, respectively.

Fig. 1 shows the evolution of the line integrated electron density measured by the interferometer at the initiating phase and the terminating phase. The plasma dealt with here is a 2 MA ohmic discharge with the central toroidal magnetic field strength of 4 T. 7 Pa helium gas was injected during the current ramp down to reduce the electron temperature, which presumably enable the non-disruptive plasma termination. The plasma size was also dwindled, shifting the plasma down toward the divertor to eliminate the disruption. It is clearly documented that the plasma initiates in the inbound side of the vacuum vessel, where the minimum magnetic field exists [5]. The estimated magnetic field strength at this position is 0.005 T. The plasma then flows outward as the plasma evolves to enlarge the line density at U2 over U1. The plasma current completely diminishes at 13.82 s. However, the density remains for 180 ms after the current termination, which is of the order of the classical estimate. The robust positional fluctuation is observed in the termination phase. The phase difference of π between two interferometer chords indicates the horizontal shift of the plasma. The magnetic probe and the soft X-ray measurement also reveal the concomitant vertical oscillation. In the terminating stage, the plasma shifts inward to retain the residual density component. This is clearly shown in the figure, where the decay of density at U1 occurs after that at U2. This feature is due to the vertical field configuration. The fact that the region where the plasma terminates coincides with that of termination is utterly favorable to eliminate the voltage spike. The abrupt density increase seen in the U1 chord is due to the increase of the electron density in the divertor region as Fig. 2 indicates that the diagnostic chord does not intersect with the main plasma but with the inner leg of the divertor.

Fig. 3 is the result of the reflectometric line density measurement, which depicts the decay of the density after the loss of the reflection layer. As was observed in the boundary fitting code and the visible TV picture, the plasma disappears from the line of sight at around 13.75 s. Accordingly, the line density observed in the reflectometer vanishes. If we assume the sight length of the reflectometer over the plasma cross section to be 0.9 m, which is consistent with the result of the boundary code, the line density reasonably returns to zero at 14 s.

The Hugill diagram which documents the ratio of the current density to the electron density is shown in Fig. 4. The previous density limit obtained in JT-60 Upgrade before the boronization in July is also depicted in the figure. The data points plotted in the termination phase clearly well exceeds the limit, which documents the sustainment of the electron density while the current density is scarce. The modified boundary code which includes the eddy current effect indicates the reduction in the electron density of approximately 25 to 30 %. Since negative loop voltage was observed in the terminating phase, we can deduce the reason of exceeding the density limit as the transient rearrangement of the current density profile; i.e., negative $j(r)$ at the edge plasma region.

4. Possibility of the AC operation on JT-60

The results described above indicates the favorable prospect of the AC operation on JT-60. In the recent survey, it has been found that the AC operation can also be performed on JT-60 without any nontrivial modifications in the circuits including those of ohmic heating primary, vertical magnetic field, and position control system. Actually on JT-60, since vertical field coil current ranges from + 50 kA to - 8 kA, the inverse plasma current of 500 kA can possibly achieved. However, in order to establish the negative current, the control programme has to be modified. Even without this modification, the investigation of the plasma break down and the current build up process can be pursued with the second pulse having the same positive plasma current.

References

- [1] MITARAI, O. , WOLFE, S.W. , HIROSE, A. et al., Bull. Am. Phys. Soc. 29, 1337(1984)
- [2] TUBBING, B. J. D. , GOTTARDI, N. A. C. , GREEN, B. J. , HOW J. A. , HUART, M. et al. , Nucl. Fusion 32 (1992) 967.
- [3] YOSHINO, R. , HOSOGANE, H. , NEYATANI, Y. , WOLFE, S. W. , MIURA, S. et al. , Proc. 14 th IAEA Conference, Germany, CN-56 / G-3-1 (1992).
- [4] FUKUDA T. , NAGASHIMA, K. , KONOSHIMA et al., Rev. Sci. Instrum. 61 (1990) 3524.
- [5] JT-60 Team, JAERI-M 92-073 (1992) 24.

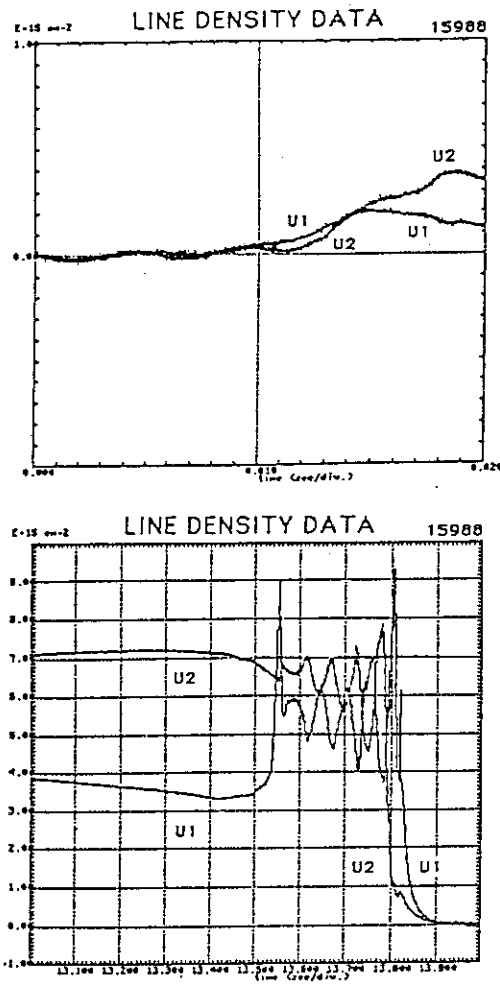


Fig. 1 Evolution of the line electron density at the initiation phase (upper figure) and the terminating phase (lower figure).

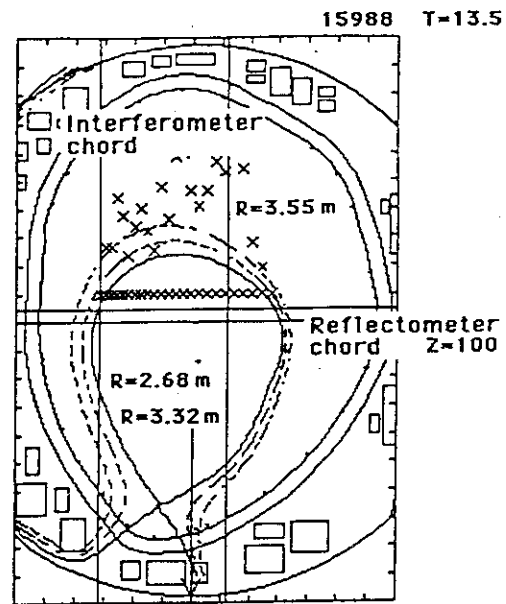


Fig. 2 Diagnostic layout plotted on the identified plasma boundary at 13.5 s.

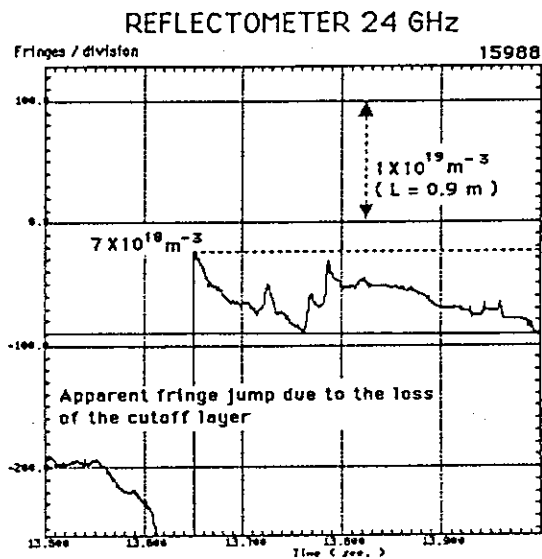


Fig. 3 Evolution of the line density measured by the reflectometer.

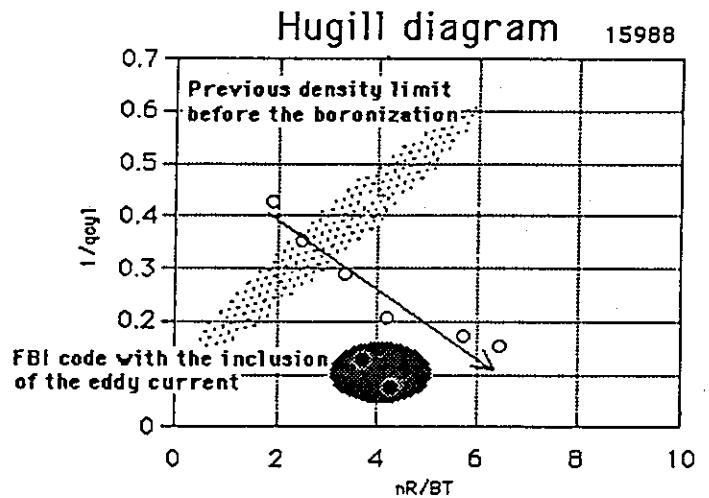


Fig. 4 Murakami-Hugill diagram depicted for the terminating plasma.

8. MHD

8.1 Overview of The Study on MHD Activities

Y.Kamada, R.Yoshino, H.Ninomiya, S.Ishida, Y.Neyatani, T.Ozeki, M.Azumi,
S.W.Wolfe, T.S.Taylor, D.J.Campbell and MHD group

1. Introduction

To demonstrate the attractiveness of the tokamak fusion reactor, the following conditions should be satisfied steadily at the same time; high- β , high bootstrap current I_{BS} fraction, long τ_E , short τ_p , disruption-free and a realistic divertor condition. Since MHD activities play important roles for all of these conditions, the final goal of MHD research is to optimize the above performance by control of MHD activities. In particular from the view point of steady state, active control of the instabilities (viz. frequency, perturbed area etc.) is necessary rather than suppression of the instabilities. Many types of MHD instabilities were reported in the history of the tokamak research [1] and recent studies in many tokamaks reported that the highest fusion parameters and sustainment of good performance was almost always limited by MHD instabilities [2]. However, it has not been completed to construct the systematic foundation of MHD activities including the relation to global/local confinement. Therefore the objectives of the MHD studies in JT-60U are i) identification of the characteristic MHD activities in the discharge regions and ii) clarification of the relationship between MHD activities and confinement. In this section, we report the outline of the MHD research in JT-60U until 1992. From 1993, the main work is to expand the systematic MHD study toward the high- β region with high I_{BS} and to optimize the reactor relevant steady condition with active MHD control by $p(r)$ and $j(r)$ control (NBCD, LHCD, sawteeth and ELM control etc.).

2. Regions of MHD Activities Related to q_{eff} , I_i and β

For the overview of MHD activities, we start from a simple categorization of discharge regions using the fundamental parameters for the MHD research, namely q_{eff} [4], I_i and β . At first, MHD regimes in the low- β region is presented in Fig.1 on the q_{eff} - I_i plane which treats OH and NB-heated L-mode discharges at low β ($\beta_p < 1$ and $\beta_N < 1.5$). This figure summarizes the current driven type instabilities and does not express high β conditions where pressure driven instabilities and I_{BS} play crucial roles in determining stability [3]. Regions of plasma parameters are: $I_p = 1\text{-}5\text{MA}$, $B_t = 1.7\text{-}4\text{T}$, $q_{eff} = 2\text{-}15$, plasma volume $V_p = 45\text{-}90\text{m}^3$, $\epsilon \sim 0.23\text{-}0.3$, $\kappa \sim 1.4\text{-}1.8$ and triangularity $\delta \sim 0.05\text{-}0.2$. Since locked modes tend to appear when q_{eff} becomes integer, q_{eff} is a good measure of safety factor at the edge for MHD instabilities. The safety factor at 95% of the outermost flux surface q_{95} is given by $q_{95} \sim 0.8q_{eff}$ in JT-60U. In Fig.1, closed squares indicate the high- I_i (including high n_e) disruptions which are observed usually during I_p ramp down in the final phase of the discharge and can be triggered even at low density, if I_i is higher than a threshold value for a given q_{eff} . In case of high n_e disruptions, the dominant MHD modes (mainly 2/1, 3/1) also grows when I_i is increased above the same threshold value by quench of the current channel. Therefore, these disruptions can be included

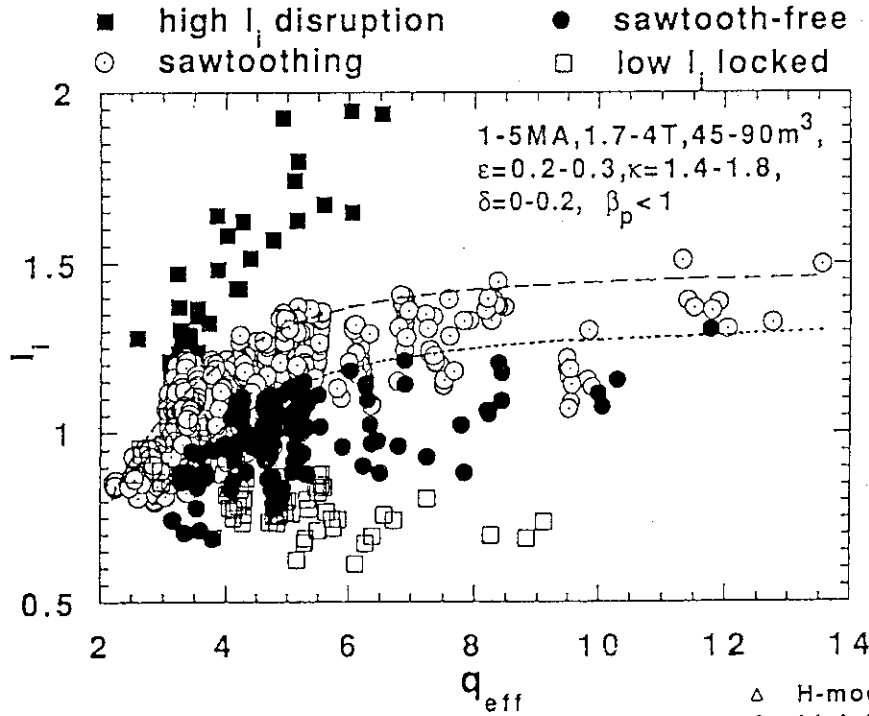


Fig.1: Discharge regions characterized by MHD activities on the $q_{\text{eff}}-l_i$ plane for $\beta_p < 1$ deuterium discharges. Dashed and dotted curves correspond to the quasi-stationary current distribution and the sawtooth boundary, respectively.

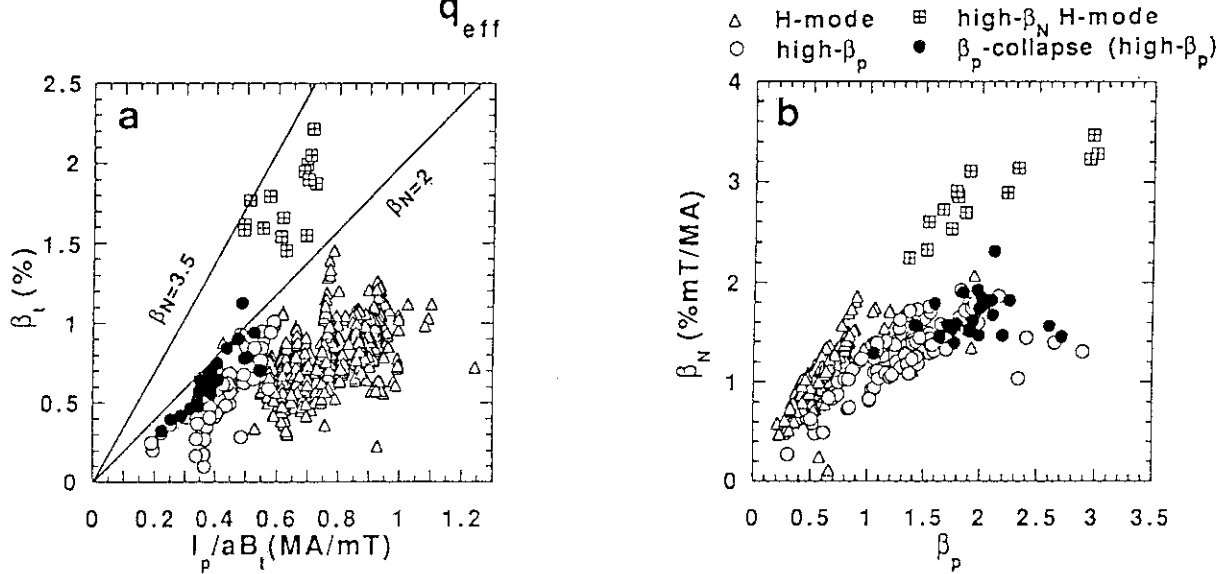


Fig.2: (a) Troyon diagram and (b) β_p - β_N diagram for JT-60U discharges.

in the same category 'high- l_i disruptions'. Sometimes high n_e disruptions can be observed in the region below the boundary. In those cases, strong detachment of plasma column is observed before the dominant MHD mode evolves. These data are not plotted in Fig.1 because precise calculation of q_{eff} and l_i for the detached plasmas has not been established. Open and closed circles correspond to sawtoothing discharges and sawtooth free discharges, respectively. The dotted line indicates the boundary of l_i below which sawtooth-free discharges appear. The open squares correspond to low- l_i locked modes (major and minor disruptions). Generally, high- l_i disruption is believed to be caused by tearing modes, and low- l_i locked modes are related to external kink activities or double tearing modes. In the low- q_{eff} region ($q_{\text{eff}} < 4$), locked modes or QSM (quasi stationary modes) are excited at low n_e even when the l_i -value is inside the stable

region. This type of instability can be related to the error magnetic fields (Sec.7.2). In the sawtooth region, we can observe the boundary of I_i corresponding to the quasi stationary state given by the dashed line (Sec.1.9). If I_p is kept constant stably (except active current drive), the value of I_i increases asymptotically toward this boundary and does not increase beyond this line (Sec.8.5). In some experiments, by rapid current ramp down or rapid increase in plasma minor radius, I_i was increased above the dashed line and decreased asymptotically toward the boundary. The empirical expressions for the dashed and dotted lines are given in Sec.8.5. In H-mode discharges, I_i is smaller than the dashed line in Fig.1, which may be because of the edge pedestal of electron temperature and pressure.

Figure 2 shows the discharge regions of JT-60U on the $I_p/aB_t-\beta_t$ plane (a) and on the $\beta_p-\beta_N$ plane (b). The closed circles in Fig.2(b) correspond to the β_p -collapse in the high β_p -mode ([5], Secs.2.1-2.5). The squares correspond to the high- β_N experiments where $\beta_N=3.5$, $\beta_p=3$ and H-factor=2 was obtained in a 0.6MA ELMy H-mode discharge and the sudden β_p -collapse was suppressed by relatively broad pressure profiles $p(r)$ and peaked current profiles $j(r)$ (Sec.2.6). However, the steady state in high- β_p and high- β_N regions has not been obtained because of appearance of pressure driven medium m/n modes (Sec.8.2-8.4).

3. Outline of MHD effects on Confinement in JT-60 and JT-60U

There are two types of effects of MHD instabilities on confinement. The first type is the disruptive phenomena which play fatal roles in the energy and particle transport. The second type is the gradual enhancement in diffusivity or repetitive release of kinetic energy. Typical disruptive events observed in JT-60 and JT-60U are major and minor disruptions (triggered at high I_i , low I_i , low n_e , $q_{eff}=2$) and β_p -collapse [5] (The important aspect is that the β_p -collapse is generally not followed by major disruption except a few cases.) The non-disruptive degradation is, in many cases, caused by sawteeth and $m/n=1/1$ activities [6-9], medium m/n activities, ELMs [7] and ballooning modes [6,7,10]. The result of the ballooning analyses [10] suggests that the ideal high- n ballooning limit is the soft limit which saturates pressure gradient. The effects of the central MHD activities are particularly apparent when the discharge has a peaked pressure profile (e.g. in pellet injected discharges [6,7] and high- T_i discharges [11]). For the achievement of high- T_i and/or high- β_p discharges [11], avoidance of the central MHD is indispensable. According to refs.[6,7] which reported characteristics of the central MHD activities for pellet fuelled plasmas, reduction in the sawtooth frequency resulted in enhanced confinement, where the effects of sawteeth on τ_E increased systematically with decreasing q_{eff} .

4. Summary of MHD-related works in JT-60U

1) sawteeth and $m/n=1/1$ mode

A scaling of τ_{inv} , parameter dependence of τ_{sw} and τ_{crash} was reported. [8,9] [Sec.8.5,1.17]
 Monster sawteeth ($\tau_{sw}\sim 2s$) were studied by ICRH experiment. [Sec.6.1, 6.2]

Behavior of fishbone activity was given. [12]

2) medium m/n modes

Systematic works of minor and major disruptions were reported. [13] [Secs.7.1-7.13, 8.1]

Disruptive regions were categorized on the q-l_i plane. [8,9,13] [Sec.8.1]

High-l_i and low-l_i disruptions were avoided by growing and dwindling a_p. [13] [Secs.7.1]

Locked modes and QSM at low n_e were studied including error field effects. [Secs.7.1-7.3]

Effects of DCW coil excitation were given. [Secs.7.4, 7.5]

Pressure driven type medium m/n modes were studied. [Secs.2.5,8.2-8.4]

3) ELMs

ELM frequency and n_e (or W)-threshold for ELM-on condition were related to the ballooning parameter. [9] [Secs.1.4, 1.11]

4) β -limit; ($\beta_N=3.5$, $\beta_p=3$; H-factor=2; ELMy H-mode) [Sec.2.6]

The β -limit was increased by broad p(r) and peaked j(r) (increase in l_i). [Secs.2.2, 2.6]

Confinement was limited by pressure driven medium m/n modes. [Sec.8.2]

5) high- β_p mode; ($\beta_p=3$, $\epsilon\beta_p<0.7$, bootstrap fraction (~58%)) [11] [Secs.2-1,2-2]

Achievable β_p was limited by the β_p -collapse under peaked p(r) with broad j(r), [11]

which is caused by kink-balloon type medium m/n modes [Secs. 2.5, 8.3, 8.4]

Sawtooth-free target is required. [11] [Sec.2-1, 2-2]

An MHD design for optimized high β_p reactors was calculated. [14]

6) L-mode and H-mode

A systematic study of l_i and sawteeth effects on τ_E was given (L-mode), [8] [Sec.1.9, 1.10]

and the study was expanded to H-mode including ELM effects. [9], [Sec.1.11]

Effects of sawteeth on T_e-profiles was reported. [Sec.1.17]

References

note: 'Plasma Phys. Controlled Nucl. Fusion Research (Proc. n-th Int. Conf. place, year) Vol. m, IAEA Vienna, (year) page' is simplified as 'Proc. n-th IAEA (place, year) Vol.m page'.

- [1] AZUMI, M., et al., Kakuyugo Kenkyu **66** (1991) 494
- [2] see papers reported in Proc. 14th IAEA (Wurzburg, 1992) IAEA-CN-56.
- [3] TAYLOR, T.S., et al., in Proc. 13th IAEA (Washington, 1990) Vol. I, p.177.
- [4] TODD, T.N., in Proc. Second Europ. Tokamak Programme Work-shop, Sault-Les-Chartreux, 1983, European Physical Society (1983) 123.
- [5] ISHIDA, S., et al., Phys. Rev. Lett. **68** (1992) 1531.
- [6] KAMADA, Y., et al., in Proc. 13th IAEA (Washington, 1990) Vol. I, p.291;
- [7] KAMADA, Y., et al., Nucl. Fusion **31** (1991) 23.
- [8] KAMADA Y., et al., 'Effects of the safety factor and the internal inductance on MHD activities and energy confinement in JT-60U' to appear in Nucl. Fusion.
- [9] KAMADA Y., et al., in Proc. 14th IAEA (Wurzburg, 1992) IAEA-CN-56/A-7-13.
- [10] OZEKI, T., et al., Nucl. Fusion **31** (1991) 51.
- [11] ISHIDA, S., et al., in Proc. 14th IAEA (Wurzburg, 1992) IAEA-CN-56/A-3-5
- [12] JT-60 Team, 'Review of JT-60U Experimental Results from March to October, 1991' JAERI-M 92-073, Japan Atomic energy Research Institute (1992), Sec.6.
- [13] YOSHINO, R., et al., in Proc. 14th IAEA (Wurzburg, 1992) IAEA-CN-56/G-3-1.
- [14] OZEKI, T., et al., ibid. IAEA-CN-56/D-4-1.

8.2 Magnetic Fluctuation in High Troyon Factor Discharges

Y. Neyatani, Y. Kamada, S. Ishida and T. Ozeki

1. Introduction

In high performance plasmas, parameters such as stored energy, beta, neutron yields, are limited by MHD phenomena in several operational regimes. Hence, identifying MHD modes is important to improve plasma parameters and to extend operational regions. In this paper, the characteristics of two types magnetic fluctuations which restrict the stored energy in high Troyon factor discharges are described. One is the continuous mode in the range of $4 < q_{\text{eff}} < 6$ and the other is a precursor to the neutron yield collapse observed in the maximum Troyon factor discharge ($q_{\text{eff}} = 7.8$).

2. Characteristics of Magnetic Fluctuations

The operational region with high Troyon factor ($g = \beta_T(\%) a(m) B_T(T) / I_p(\text{MA})$) is shown in Fig. 1. The internal inductance measured just before additional heating is 1.3 to 1.6, higher than high β_p discharges, and the toroidal magnetic field is 1.5 Tesla. The range of plasma current is 0.6 to 0.9 MA [1]. Figure 1 shows the data at the start of $n=1$ or $n=2$ modes. When $4 < q_{\text{eff}} < 6$, a large amplitude $m/n=2/1$ mode (~ 20 gauss on the outside midplane) restricts the stored energy (Fig. 2). The mode rotational frequency increases from 0 to 3 kHz. The location of the rational surface was determined to be $r/a \sim 0.66$ by soft X-ray signals (Fig. 3(a)). The central ion temperature continuously decreases to one half of its maximum during the 2/1 mode, while T_i at $r/a > 0.6$ does not change so much. After $t = 6.14$ sec, the mode rational surface moves inward to

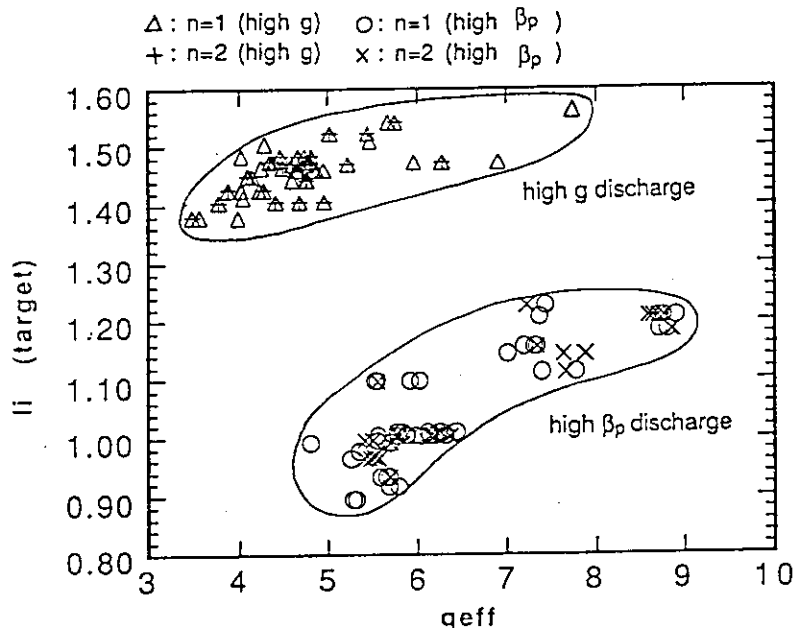


Fig. 1 q_{eff} v.s. li (target) diagram at the $n=1$ or $n=2$ mode starts in the high Troyon factor and high beta discharges in JT-60U.

$r/a \sim 0.5$ (Fig.3(b)), while the central ion temperature decreases more rapidly. The 2/1 mode has poloidal asymmetry, suggesting it may be associated with a pressure driven mode. Its growth time is of the order of 1 ms, which is $\sim 10^4 \tau_A$ (τ_A is Alfvén time) [2]. Since the growth time of the ideal kink-ballooning mode is $10^{-1} \sim 10^{-3} \tau_A$, the observed mode is probably not of this type. After the 2/1 mode locks at $t=6.3$ sec, the T_i profile becomes more flat at $r/a < 0.5$ (closed circles in Fig.4). After the stored energy drops with an H α burst at $t \sim 6.5$ sec, T_i at middle r/a decreases and changes the profile as shown by 6.7 s curve in Fig.4. The stored energy increases again since additional heating still continues and another type of $n=1$ and $n=2$ mode becomes unstable (Fig.2). The mode rational surfaces of these mode cannot be identified because of the low amplitude SX signal from the low T_e edge. The $n=1$ mode is more symmetric suggesting it may not be attributed to a pressure driven mode.

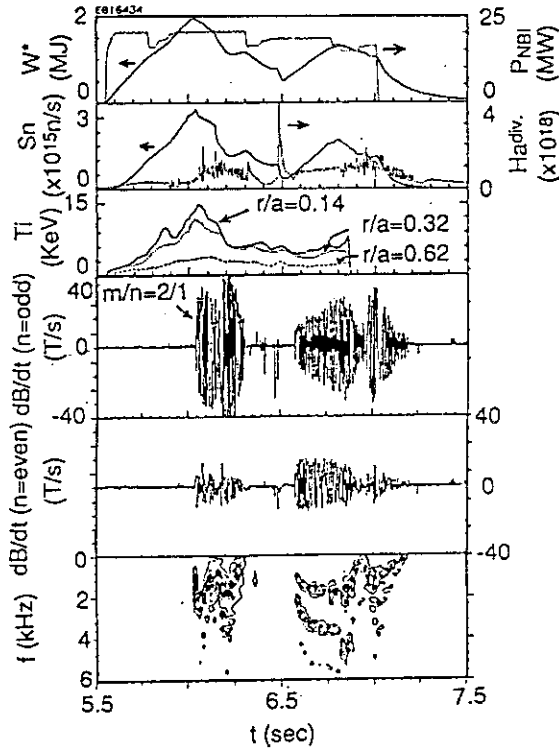


Fig.2 Waveform for a high g discharge with $I_p=0.9$ MA, $B_T=1.5$ T and $q_{eff}=4.8$. Stored energy decreases as the 2/1 mode glows.

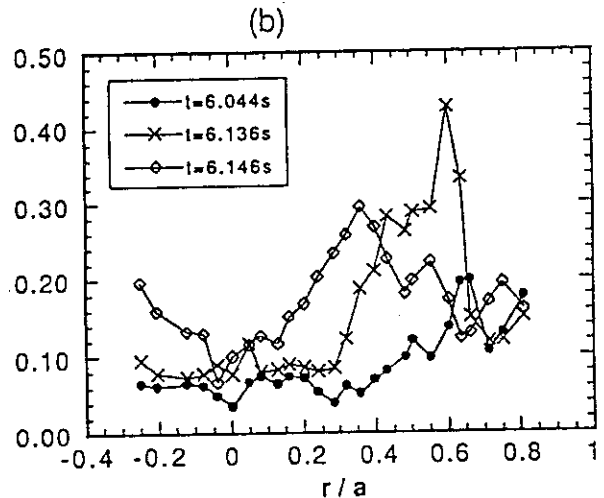
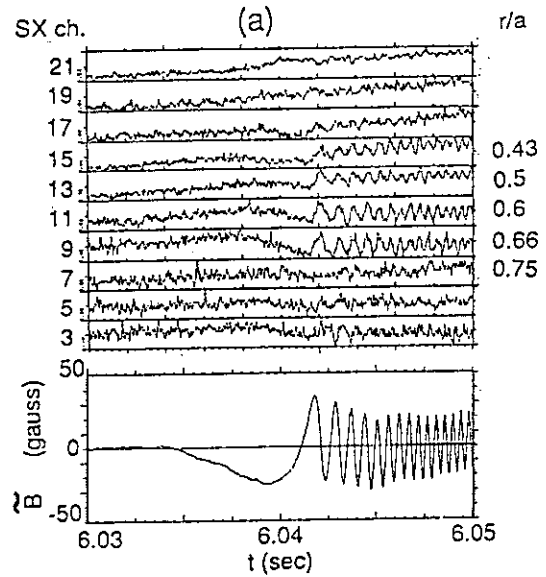


Fig.3 (a) The 2/1 mode correlates with soft X-ray signals at $r/a=0.66$. The mode frequency increases as the mode grows. (b) At $t=6.14$ s, the mode rational surface moves inside from $r/a \sim 0.6$ to $r/a \sim 0.4$.

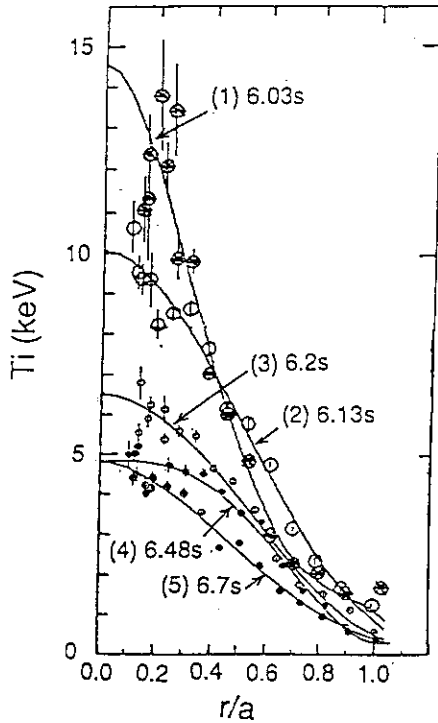


Fig.4 Radial distribution of ion temperature for several time slices : before 2/1 mode unstable ($t=6.03s$), just after 2/1 mode growth ($t=6.13s$), during 2/1 mode after mode rational surface changes ($t=6.2s$), just before Ha spike ($t=6.48s$) and during $n=1$ mode ($t=6.7s$). As 2/1 mode grows, central T_i continuously decreases and the profile become broader.

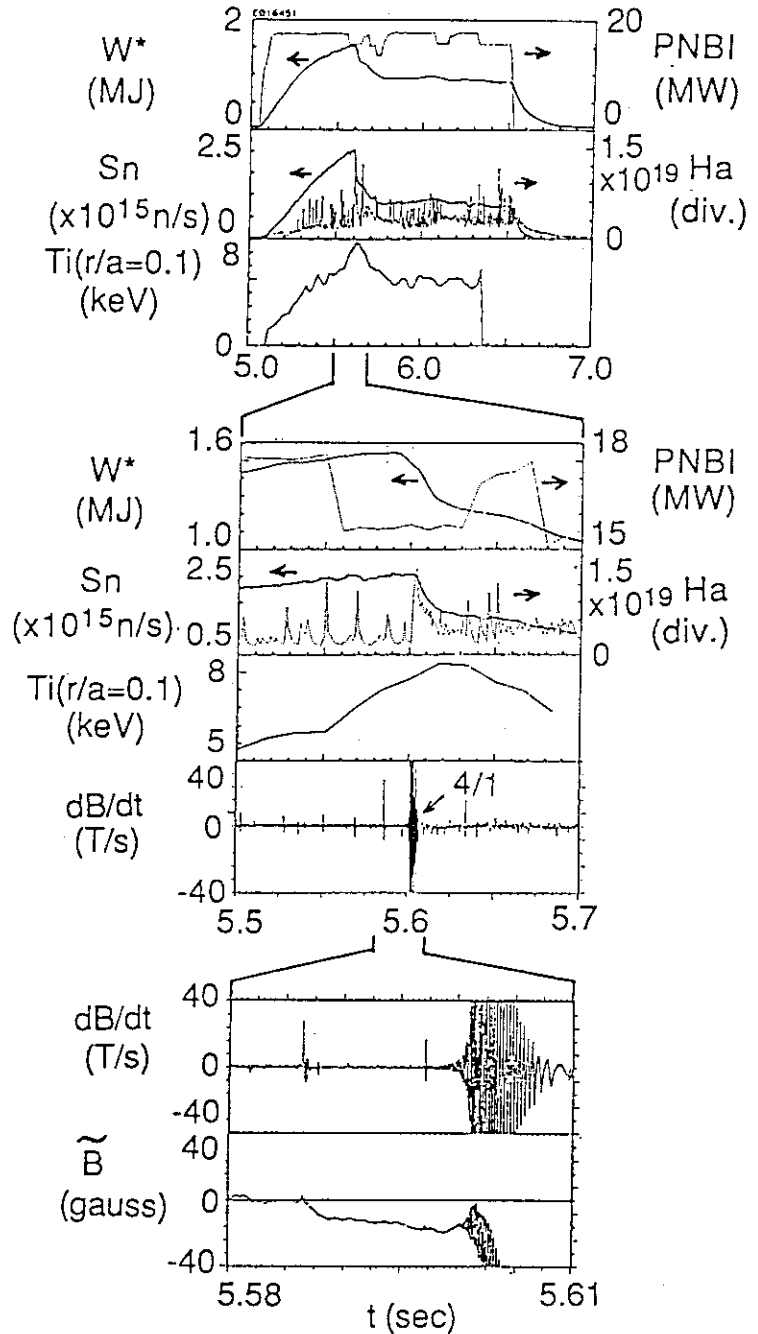


Fig.5 Waveform for the maximum g discharge in hot ion H-mode with $I_p=0.6MA$, $B_T=1.5T$ and $q_{eff}=7.8$. Locked mode at $t=5.587s$ limits the stored energy and $m/n=4/1$ mode restricts the neutron emission rate.

In the hot ion H-mode with the maximum g, a kind of beta collapse is observed (Fig.5). The discharge parameters are $I_p=0.6$ MA, $B_T=1.5$ Tesla, $q_{eff}=7.8$ with 18MW of NBI heating. In this discharge, the stored energy starts to drop as an $n=1$ locked mode grows to ~ 10 gauss over an interval of 40ms. After that, a rotating $m/n=4/1$ mode grows to a maximum amplitude of 10 gauss at a frequency of 8 kHz. The neutron emission rate drops even as $T_i(0)$ is increasing. Figure 6 shows the radial distribution of SX emission. As the 4/1 mode grows, the edge temperature decreases at first, and then, a reduction of central temperature was observed. The

mode rational surface exists at $r/a \sim 0.7$. This mode also has strong poloidal asymmetry, suggesting a pressure driven mode. The growth time is three order magnitude larger than τ_A , so the ideal kink-ballooning mode is not associated with this mode.

The ion temperature gradient at the 2/1 rational surface is $\sim 20 \text{ KeV/m}$, which is twice as large as that at the 4/1 surface. Although the density profile is unknown, the pressure gradient at the 2/1 surface is certainly larger than at the 4/1 surface. However, the normalized pressure gradient parameter α defined by $-(2\mu_0 R q^2 / B^2)(dp/dr)$, which is related to ballooning stability, has a q dependence so that, it is not inconsistent that both modes may be attributed to the resistive ballooning mode.

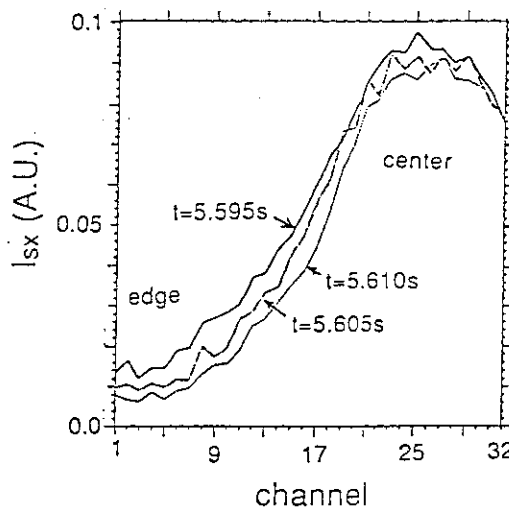


Fig.6 Spatial distribution of the SX signals before ($t=5.595\text{s}$) and after ($t=5.605, 5.610\text{s}$) the $m/n=4/1$ mode unstable in maximum g discharge.

3. Summary

In high Troyon factor discharges with low B_T (1.5 Tesla) and high li ($1.3 < li_{\text{target}} < 1.6$), magnetic fluctuations were observed near the maxima in stored energy and neutron yield. A pressure driven type $m/n=2/1$ mode restricts the stored energy in the range of $4 < q_{\text{eff}} < 6$. In the high q region ($q_{\text{eff}}=7.8$) with maximum g in a hot ion H-mode, a pressure driven 4/1 mode (not ideal mode) restricts the neutron emission rate. Neither mode is considered to be ideal because of the large growth time. The most likely candidate for these modes is the resistive ballooning mode.

References

- [1] KAMADA Y. et al. : in this review paper.
- [2] OZEKI T. et al. : JAERI Report , JAERI-M 90-180.

8.3 MHD Stability Analyses for β_p Collapse

T. Ozeki, M. Azumi, and S. Ishida

1. Introduction

In high β_p experiments of JT-60U, β_p collapses were observed [1] same as in JT-60. The results of the stability analysis using the equilibria of JT-60 high β_p experiments show that the value of β_p observed[2] in the β_p collapse is consistent with the critical β_p of the $n=1$ kink mode, where the stability boundary is reduced by the hollow q -profile[3]. In JT-60U, however, the q -profile seems to be rather flat than hollow because the temperature of the heated plasma is about two times higher than that of JT-60 so that the current decay time is longer. Therefore, we re-analyze the ideal MHD stability of high β_p plasmas in JT-60U assuming the flat q -profile and discuss the stabilization. The plausible candidates for the β_p collapse of JT-60U high β_p plasmas are the ideal ballooning, kink and infernal modes.

2. Ballooning and Low- n Mode Stability Analyses

Our procedure is to reconstruct the MHD equilibrium of the experimental discharge from the experimentally measured data using the assumption of q -profile and then analyze them for the stabilities. We choose the typical high β_p discharge of E15014 in which the β_p collapse occurred at $\beta_p=1.44$. The equilibrium is made by the MEU-DAS code from the geometric data and two profiles parameter of $\langle J_{\parallel} \rangle$ and $dp/d\psi$. Here, we assume the up-down symmetry because of the restriction of the stability code. The high β_p discharges were carried out in a highly elongated configuration shifted inward. The pressure profile is estimated from the ion temperature of CXRS, the electron temperature of ECE and the ion density. The ion density is estimated as $n_i = n_{i0} [0.83(1 - \rho^2)^{5.15} + 0.17]$ from a kinetic analysis of line-density, neutron rate and stored energy. To determine the pressure profile, we employ the following function.

$$\frac{dP}{d\psi} \propto (1 - \psi)^{\alpha_p}, \quad (1)$$

where $\tilde{\psi} = (\psi - \psi_{axi})/(\psi_{bun} - \psi_{axi})$ is the normalized poloidal flux to $0 < \tilde{\psi} < 1$. In the typical high β_p plasma of E15014, α_p of 5.0 well expresses the measured pressure profile.

Since the q profile is not measured directly in JT-60U, we assume the flat q -profile and adjust to the estimated ℓ_i and q_s . Here, we employ the following function which

well expresses the flat profile with the high value of ℓ_i .

$$\langle J_{\parallel} \cdot B \rangle \propto \{ (1 - \tilde{\psi}^{\alpha_1})^{\alpha_2} \} \{ 1 + \alpha_3 \exp(-\frac{\psi}{\alpha_4})^2 \}. \quad (2)$$

In the following calculation, we use α_1 of 2.5, α_2 of 5.0, α_3 of -0.05 and α_4 of 0.01, corresponding to E15014 with $\ell_i=1.5$ and $q_0=1.2$. The resultant q and P profiles are shown in Fig. 1. The generated equilibria are checked for the ideal infinite- n ballooning code by the BETA code[4] and for the kink and infernal modes by the ERATO-J code[5].

The results of the analyses of the infinite- n ballooning mode and low- n modes are shown in Fig. 2 and Fig. 3, respectively. As shown in Fig. 2, the ballooning mode is locally unstable at the region of the large pressure gradient in the plasma with $q_0=1.2$. Since q_0 was not measured, we investigate the dependence of q_0 using the σ -scaling techniques. In this scaling, q scales approximately q/σ and the β_p and the shear is almost remained fixed. When q_0 rises above 1.3, the ballooning mode becomes stabilized in whole plasma region. Figure 3 shows the growth rate of the low n kink modes with various toroidal mode numbers as a function of q_0 . Almost region from $q_0=1.0$ to 2.0 is unstable for low- n modes. The number of the most unstable mode is changed by q_0 . These modes are called the infernal mode, in which the displacement is spatially localized in the resonance surface. In the measured fluctuation from ECE and FIR, the dominant mode is $m/n = 3/2$ or $4/3$ on the collapse[1]. Thus, the most plausible candidate for the β_p collapse is the infernal mode due to the large pressure gradient on the low shear region.

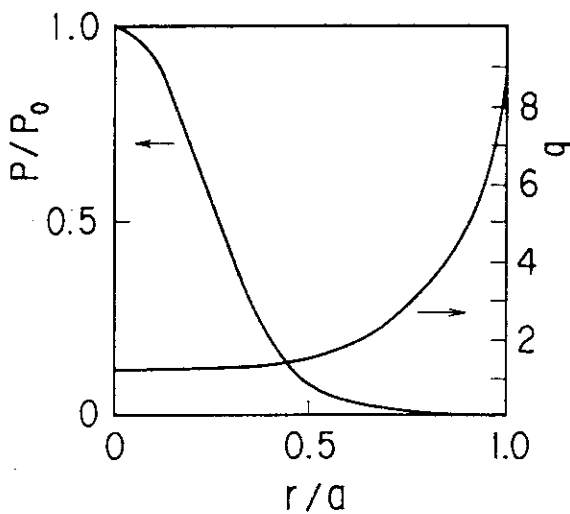


Fig. 1 Estimated P and q profiles of the typical high β_p discharge with the collapse of E15014.

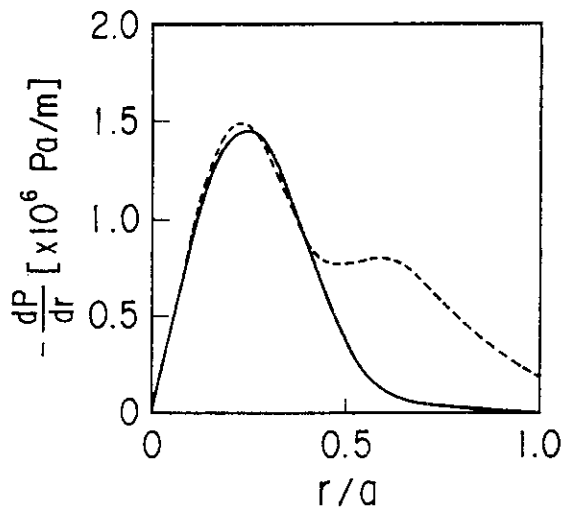


Fig. 2 Marginal pressure gradient (broken line) and pressure gradient of the equilibrium (solid line) as a function of the minor radius for the plasma in Fig. 1.

3. Stabilization of the Infernal Mode

Because the infernal mode is induced as a result of the large pressure gradient in the low shear region, we try to decrease the pressure gradient and increase the shear fixing the other parameter, artificially. Here, we focused on the plasma with $q_0=1.4$ which is unstable for $m/n = 3/2$. First we investigate the effect of the pressure gradient. Figure 5 plots the growth rate as a function of n , treating n as a continuous real variable. Fig. 5(a) shows the nature of the infernal mode which has the alternating stable and unstable band in n . As the pressure gradient decreases from $\alpha_p=5$ to $\alpha_p=3$, as shown in Fig. 4, the growth rate of the infernal mode decreased and stabilized in Fig. 5.(c). The ballooning mode is also stable in all plasma of Fig. 5.

Next, to stabilize the infernal mode, we try to increase the shear near the plasma center fixing the values of q_0 and q_s , as shown in Fig. 6. As the shear increases, the ballooning mode becomes unstable in the plasma with $q_0 < 2$ due to the decrease of the local shear. The oscillatory nature of the growth rate due to the infernal mode becomes weak, but the value of the growth rate increases and the mode structure is changed from the infernal mode to the kink-ballooning mode where various poloidal modes are induced and the displacement is broad in its radial extent. This is because the decrease of the shear in the outer region ($r/a > 0.5$). Consequently, the increase of the shear near the plasma axis destabilizes both the ballooning mode and the infernal mode.

4. Conclusion

The most plausible candidate of the β_p collapse in JT-60U is the infernal mode. The decrease of the pressure gradient can easily stabilize both the ballooning mode and the infernal mode. But, the increase of the shear near the plasma center destabilizes both of the ballooning and kink modes, because the shear near the plasma surface decreases. In this study the scanning of q are carried out fixing q_0 . If q_0 decreases fixing q_s , the shear increases in the whole region of the plasma and the low- n mode may be stabilized when $q_0 > 1$. Thus, the further investigation is necessary for the optimization of q -profile.

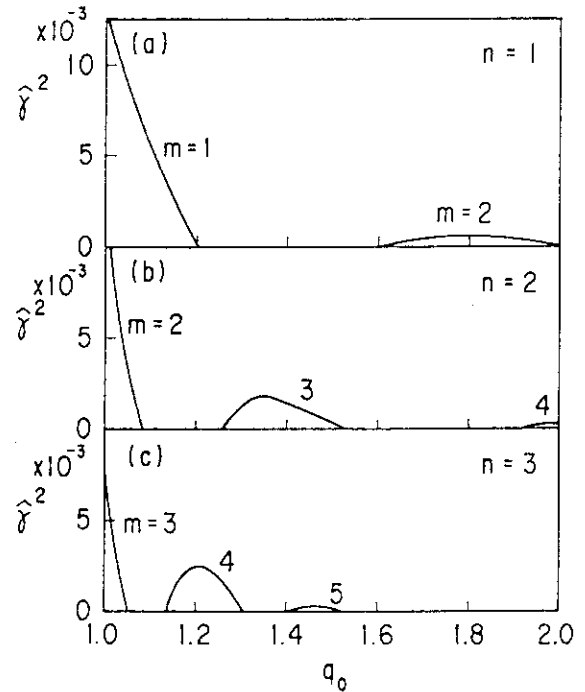


Fig. 3 Growth rate of the infernal modes with various toroidal mode numbers ($=1,2,3$) as a function of q_0 .

REFERENCES

- [1] ISHIDA, S., et al., (in this paper, section 2.5).
- [2] ISHIDA, S., et al., Phys. Rev. Lett. **68** (1992) 1531.
- [3] OZEKI, T., et al., submitted for Nucl. Fusion.
- [4] AZUMI, M., et al., in Inter. Conf. on Plasma Phys. Vol.9f, Part I, (1985) 375.
- [5] TOKUDA, S., et al.: JAERI-M 9899 (1982).

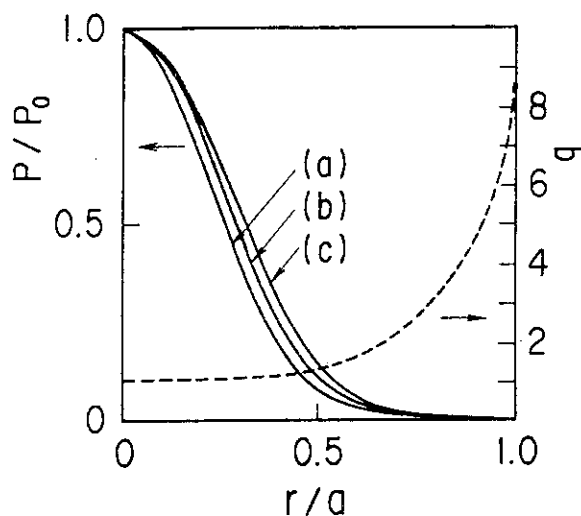


Fig. 4 Pressure profiles (solid line) used in scanning of the pressure gradient for the plasma with $q_0=1.4$.

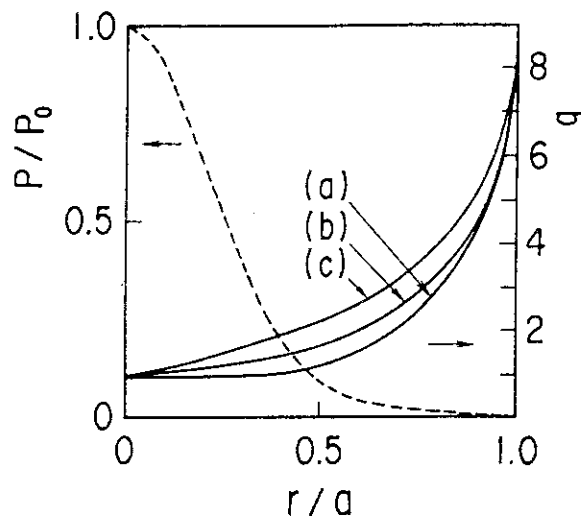


Fig. 6 Safety factor profiles (solid line) used in scanning of the shear for the plasma with $q_0=1.4$.

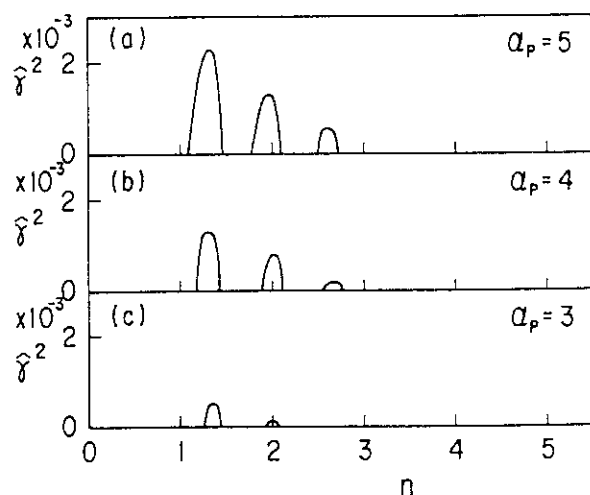


Fig. 5 Growth rate as a function of the toroidal mode number for the plasmas in Fig. 4.

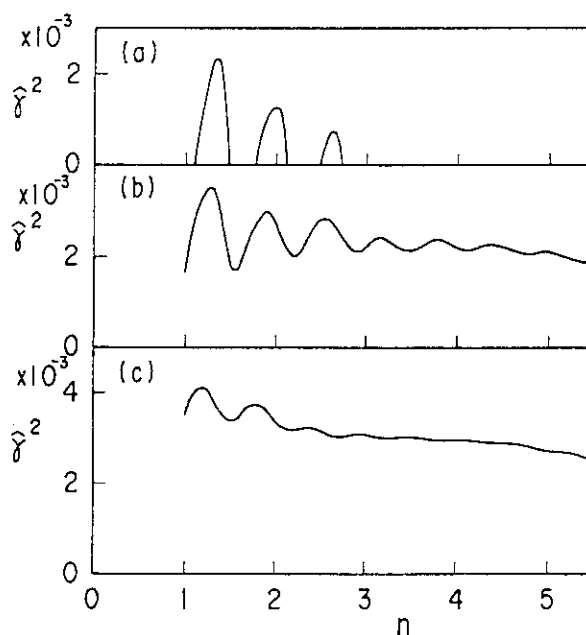


Fig. 7 Growth rate as a function of the toroidal mode number for the plasmas in Fig. 6.

8.4 Magnetic Fluctuation in High β_p Plasma

Y. Neyatani, S. Ishida, Y. Kamada and T. Ozeki

1. Introduction

With increasing plasma performance, many kinds of instabilities have been observed to restrict the plasma parameters. In the high poloidal beta region, ballooning type instabilities have restricted the poloidal beta in the form of a rapid β_p collapse at relatively low plasma currents (up to 1MA) in some tokamaks [1,2,3]. In this paper, the characteristics of fluctuations in high poloidal beta discharges with larger plasma currents ($1.1\text{MA} < I_p < 1.9\text{MA}$) are reviewed

2. Characteristics of Magnetic Fluctuations

The high beta experiments were performed in the range of relatively large plasma current (1.1 to 1.9 MA) at $B_T=4.4\text{T}$. The internal inductance (l_i) was kept low ($l_i < 1.2$) to avoid of sawteeth. The magnetic fluctuations can be separated into three groups in the space of β_p and q_{eff} Figure 1 shows the range of the fluctuation in $q_{\text{eff}}-\beta_p$ diagram. The open and close circles show the data of $n=1$ and $n=2$ modes start. In high q ($q_{\text{eff}} > 7$) region, a rapid β_p collapse ($\sim 100\mu\text{s}$) was observed. An $n=2$ mode appeared at several tens milli seconds before the β_p collapse. At

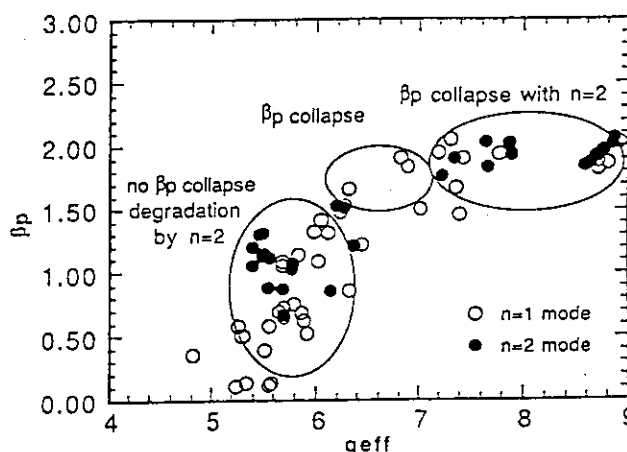


Fig.1 q_{eff} v.s. β_p diagram at the start of $n=1$ or $n=2$ modes in high β_p discharges in JT-60U.

lower q_{eff} ($6 < q_{\text{eff}} < 7$), no $n=2$ mode was observed, but a rapid β_p collapse still occurred. The poloidal beta just before the β_p collapse decreased with decreasing q_{eff} . With $q_{\text{eff}} < 6$, no β_p collapse was observed. In this region, the $n=2$ mode may be limiting the central ion temperature ($T_i(0)$). After $T_i(0)$ decayed, the DD neutron yield and stored energy saturated.

In the high q region, three types of modes were observed around the β_p collapse (Fig.2). First, an $n=2$ mode is seen before the beta collapse and disappears after the β_p collapse. This mode has a small amplitude of 0.3 Gauss on the outer midplane and a high frequency of 21 kHz. The same frequency is observed in the electron temperature fluctuation measured at $r/a \sim 0.5$ by the polychromator (Fig.3). The growth time of this mode is typically of the order of 10ms. The fluctuation amplitudes at the inner and outer midplane are almost the same in spite of more than 2 times different distance from $r/a=0.5$ surface (Fig.4). It implies a strong in-out asymmetry. Hence, the $n=2$ mode is consistent with a pressure driven resistive instability, as is

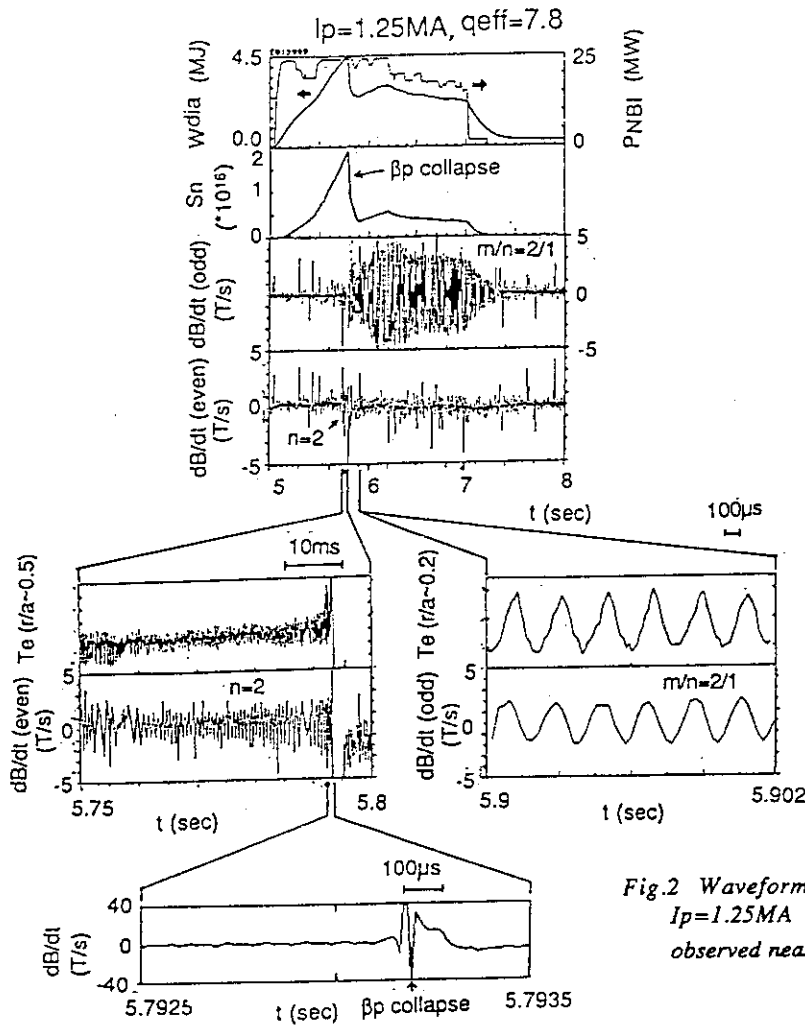


Fig.2 Waveform for the high β_p discharge with $I_p=1.25\text{MA}$, $q_{\text{eff}}=7.8$. Three types of modes are observed near the β_p collapse.

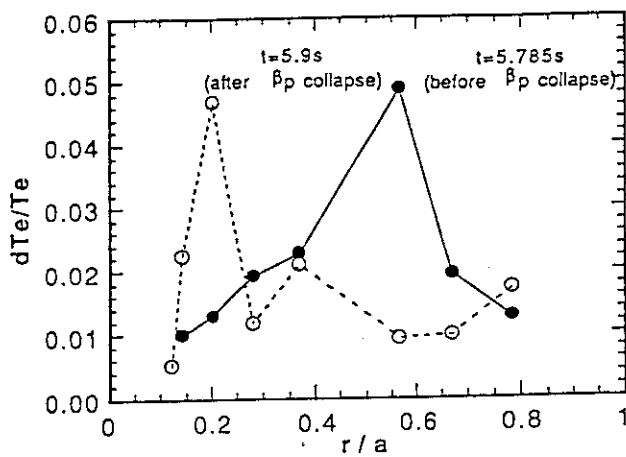


Fig.3 Electron temperature fluctuation as a function of the normalized minor radius before and after β_p collapse.

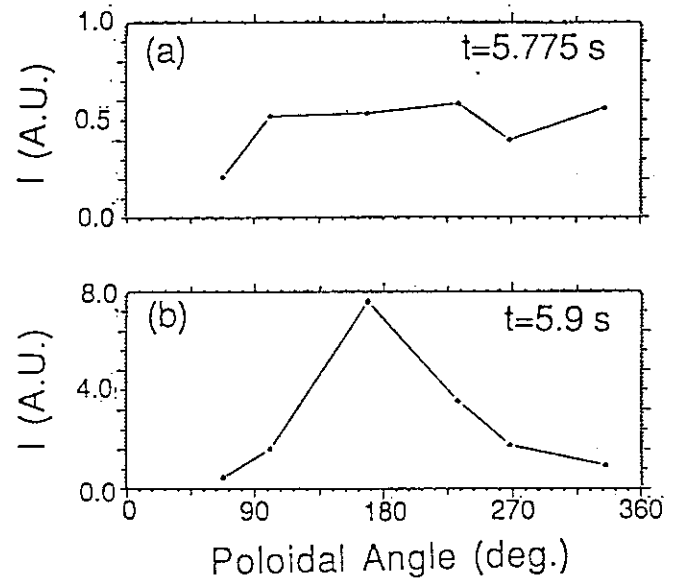


Fig.4 Poloidal distribution of the mode (a) before and (b) after β_p collapse.

also concluded for DIII-D [2]. Just before the βp collapse ($\sim 100 \mu s$), a second type of mode grows with the short growth time of the order of $10 \mu s$. The ideal low n kink-ballooning mode can be unstable in this region [4] and is the most likely candidate for explaining this activity. After the βp collapse, a large amplitude $m/n=2/1$ mode (18 gauss on the inner midplane) grows. The mode rational surface changes to $r/a \sim 0.2$ ($q=2$ surface), which supposed by a current and pressure profile before βp collapse (Fig.3). The toroidal velocity corresponding to the mode frequency of 3 to 4 kHz has the same value and time dependence as the ion toroidal rotational velocity at $r/a \sim 0.2$ (Fig.5). Since the amplitude has no in-out asymmetry, and the Te fluctuation at $r/a \sim 0.35$ is out of phase with that at $r/a \sim 0.2$, this mode could be caused by a tearing instability.

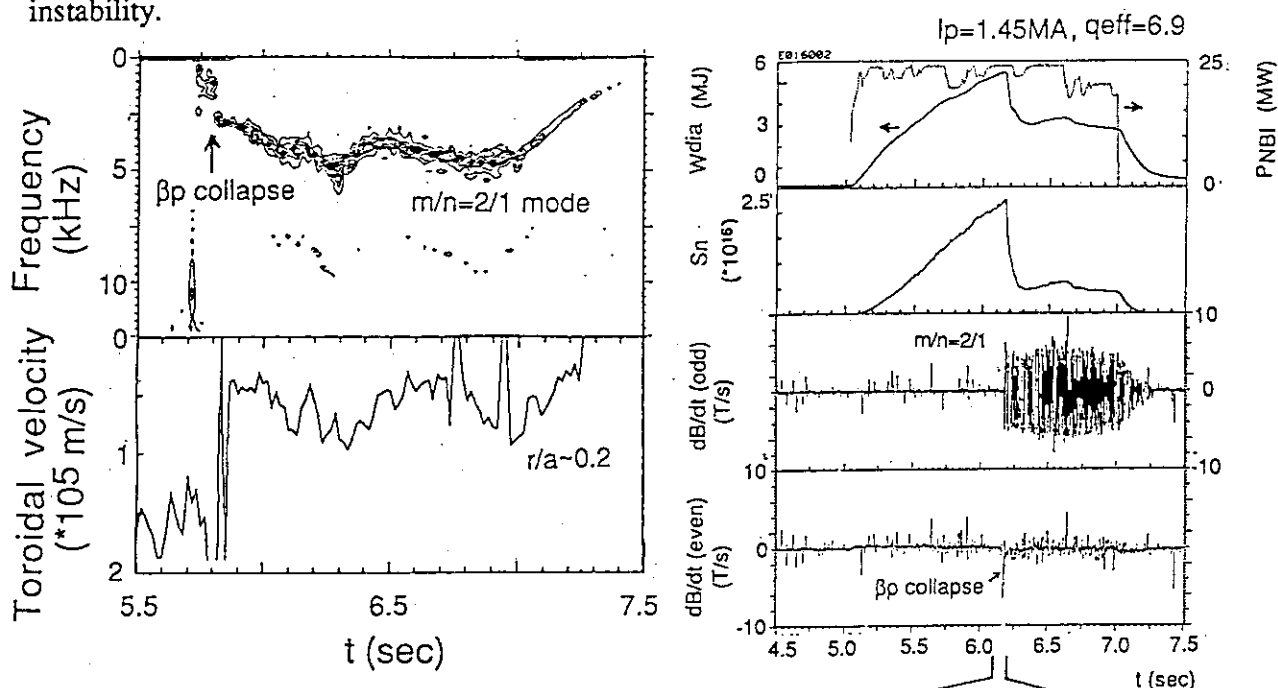


Fig.6 Waveform for the high βp discharge with $I_p=1.45MA$, $q_{eff}=6.9$.

In the range of $6 < q_{eff} < 7$, no $n=2$ mode was observed before the βp collapse. The βp collapse still occurred due to an ideal ballooning type mode (Fig.6). After the βp collapse, the same mode as described above appeared. This mode continued until the neutral beams were turned off.

For $q_{eff} < 6$, no βp collapse was observed. $T_i(0)$ decreased after the $n=2$ mode grew. After that, the DD neutron yield and poloidal beta saturated (Fig.7). Hence, the $n=2$ mode may limit the poloidal beta in this region. This mode also has strong in-out asymmetries, so it may arise from a pressure driven type instability.

Fig.5 Time evolution of the mode frequency and the toroidal velocity at $r/a \sim 0.2$ after βp collapse.

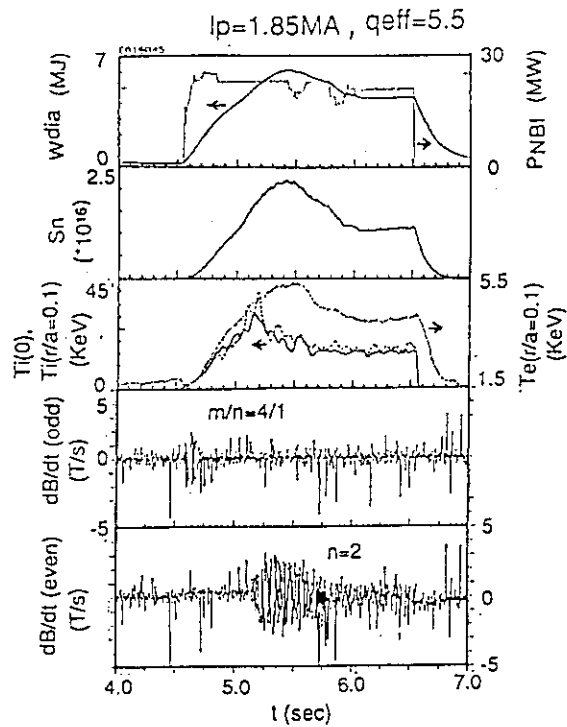


Fig.7 Waveform for the high β_p discharge with $I_p=1.85\text{MA}$, $q_{\text{eff}}=5.5$.

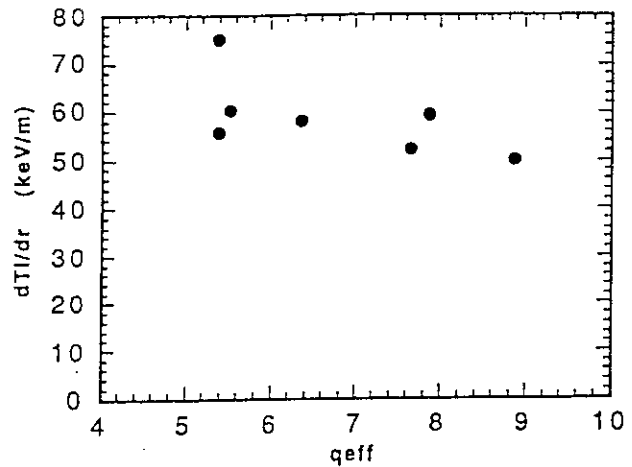


Fig.8 q_{eff} versus ion temperature gradient just before $n=2$ mode grow.

Figure 8 shows the ion temperature gradient (dT_i/dr) at the mode rational surface versus q_{eff} for the $n=2$ mode. The $n=2$ mode would appear to be unstable when dT_i/dr exceeds a threshold. The data of density profile was not obtained, however, it may be one of the evidence that the $n=2$ mode attributes pressure gradient.

3. Summary

Various kinds of instabilities have been observed in JT60U discharges at high β_p . In the $q_{\text{eff}} > 6$ region, the poloidal beta is limited by a β_p collapse associated with the ideal low n kink-ballooning mode. When $q_{\text{eff}} < 6$, an $n=2$ pressure driven resistive mode, correlated with β_p saturation, decreases $T_i(0)$ which limits the DD neutron and the β_p . In this region, the heating power would not be enough to reach the ideal ballooning limit.

References

- [1] ISHIDA S. et al. : in Plasma Physics and Controlled Nuclear Fusion Research 1990 (Proc. 13th Int. Conf. Washington D.C., 1990), Vol.1, IAEA, Vienna (1991) 195.
- [2] STRAIT E.J. et al. : in Plasma Physics and Controlled Nuclear Fusion Research 1988 (Proc. 12th Int. Conf. Nice, 1988), Vol.1, IAEA, Vienna (1989) 83.
- [3] STRACHAN D. et al. : Phys. Rev. Lett. 68(1987) 1004.
- [4] ISHIDA S. et al. : in Plasma Physics and Controlled Nuclear Fusion Research 1992 (Proc. 14th Int. Conf. Wurzburg, 1992), IAEA-CN-56/A-3-5

8.5 Characteristics of Sawteeth

Y.Kamada

1. Introduction

The sawtooth activity releases energy and particles from the plasma center and, then, limits the fusion reaction rate. However this activity may be useful for the helium ash exhaust from the center. Therefore the purpose of the sawtooth study is to clarify the sawtooth characteristics for a precise control (not suppression) of this activity in the fusion plasma core. This section gives the basic database for the study on 'sawtooth effects on confinement (Secs. 1.9 - 1.11)' and for the achievement of high performance in H-mode (Secs. 1.3, 1.4) and in high- β_p mode (Secs. 2.1, 2.2). The summary of the sawtooth study was also reported in refs.[1,2].

2. Sawtoothing and Sawtooth-free Regions on the q_{eff} - I_i Plane

As presented in Sec.8.1, discharges can be clearly categorized by q_{eff} and I_i in the low β region (note $q_{95} \sim 0.8q_{eff}$ in JT-60U). In Fig.1, the characteristic MHD regions are categorized where open and closed circles correspond to sawtoothing discharges and sawtooth free discharges, respectively. The dotted line indicates the boundary of I_i below which sawtooth-free discharges appear. In the sawtoothing region, we can observe the boundary of I_i corresponding to the quasi stationary state given by the dashed line. In usual experimental conditions except active current drive experiments, if I_p is kept constant stably, the value of I_i increases asymptotically toward this boundary and does not increase beyond this line (see Fig.2). In JT-60U, the boundaries of quasi-stationary state (dashed line) and disappearance of sawtooth (dotted line) are empirically given by

$$I_i = 1.4 + 0.005q_{eff} - 0.9\exp[-0.6(q_{eff} - 1.5)] \quad (1)$$

and

$$I_i = 1.22 + 0.006q_{eff} - 1.0\exp[-0.6(q_{eff} - 1.5)], \quad (2)$$

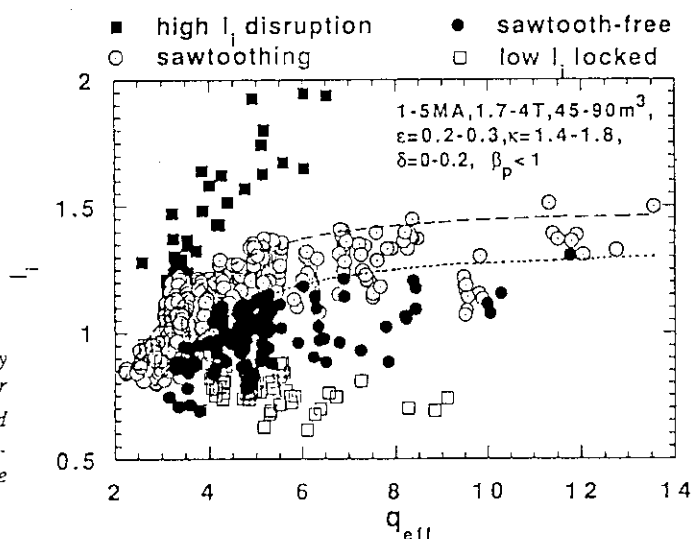


Fig.1: Discharge regions characterized by MHD activities on the q_{eff} - I_i plane for $\beta_p < 1$ deuterium discharges. Dashed and dotted curves correspond to the quasi-stationary current distribution and the sawtooth boundary, respectively.

respectively. In the experiments of high- β_p mode, the necessary condition to achieve the high fusion product is to avoid the sawtooth activity from the target OH plasma before NB injection, for which the l_i -value of the target plasma should be lower than the l_i -boundary given by eq.(2).

3. Sawtooth Inversion Radius

This section treats sawtooth inversion radius r_{inv} and mixing radius r_{mix} . We do not treat the compound type sawteeth [3] or non reconnecting type sawteeth [4]. To express the sawtooth inversion radius, we use $(r_{inv}/a)_{sx}$ evaluated by the line-integrated soft X ray emission (SX) profiles measured with a 64 channel PIN diode array with the typical spatial resolution of 3cm and the time resolution of 40 μ s. Since the SX signal is line integrated, $(r_{inv}/a)_{sx}$ is smaller than the real inversion radius. Based on a calculation to estimate the effect of line integration, $(r_{inv}/a)_{sx}$ is about 80% of the real inversion radius for usual L-mode discharges. The more detailed discussion about the effect of line integration on the evaluation of r_{inv} is given in ref.[5]. In turn, the value of r_{mix} determined by the line integrated SX signal is almost the same as the real mixing radius.

Figure 2 shows time evolution of l_i and $(r_{inv}/a)_{sx}$ during the flat top of I_p for a OH plasma at $q_{eff}=5.1$. Internal inductance l_i increases asymptotically toward the final value of 1.35 which corresponds to the l_i value in the quasi stationary state given by the dashed line in Fig.1. The sawtooth activity starts from $t=5.9$ s when the value of l_i exceeds the threshold value given by the dotted line in Fig.1, then $(r_{inv}/a)_{sx}$ also increases asymptotically toward the final value of 0.23 which is on the dotted line shown later in Fig.3. From these traces, it can be expected that $(r_{inv}/a)_{sx}$ is correlated with l_i (see Fig.5). In Fig.2, rapid change in $(r_{inv}/a)_{sx}$ is observed in the very transient phase just after the start of sawteeth (between two dashed lines) when l_i is just around the threshold value for appearance of sawteeth. In this portion, change in $(r_{inv}/a)_{sx}$

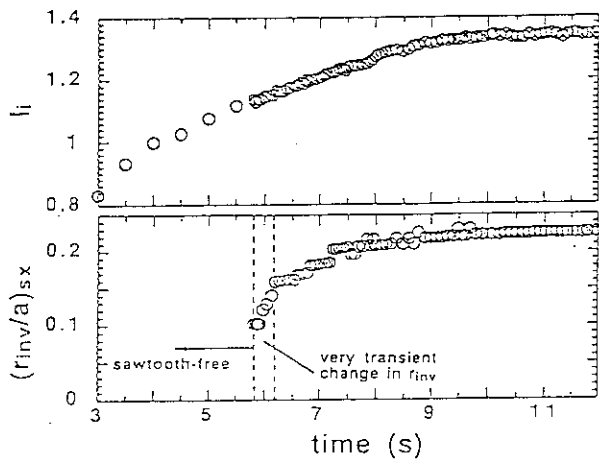


Fig.2: Time evolution of l_i and $(r_{inv}/a)_{sx}$ during the flat top of plasma current at $q_{eff}=5.1$.

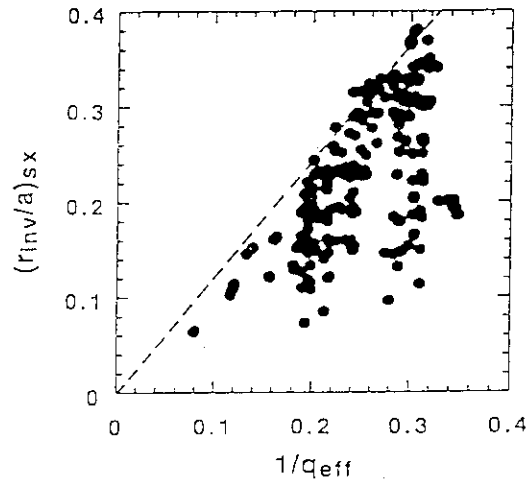


Fig.3: Normalized inversion radius $(r_{inv}/a)_{sx}$ vs. $1/q_{eff}$ for $I_p=1$ -SMA, $B_t=1.7$ -4T, $\beta_p < 1$ and $\beta_N < 1.5$. The dotted line indicates $(r_{inv}/a)_{sx}=1.2/q_{eff}$.

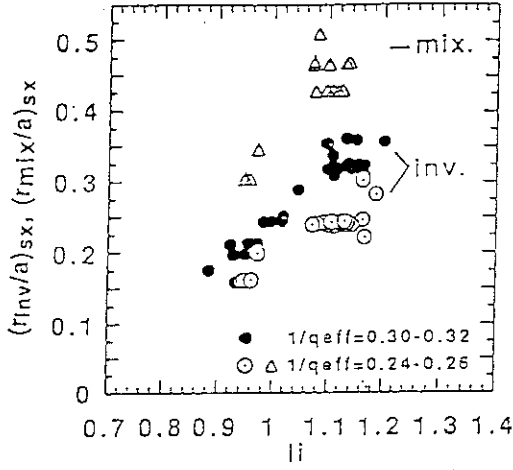


Fig.4: Normalized inversion radius $(r_{inv}/a)_{sx}$ and normalized mixing radius $(r_{mix}/a)_{sx}$ vs. l_i for fixed q_{eff} values.

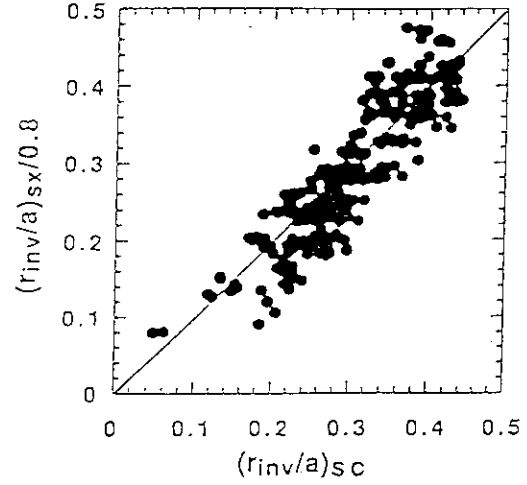


Fig.5: Comparison between the measured values of $(r_{inv}/a)_{sx}/0.8$ and $(r_{inv}/a)_{sc}$ given by eq.(5).

cannot be expressed by change in l_i . We do not treat the data in this very transient phase in the following discussions. Concerning the l_i -boundary for the appearance of sawteeth, the scatter of l_i values for a given q_{eff} is about $\Delta l_i \sim 0.1$ in our data set. These results mean the limit of applicability of the internal inductance as the measure of the central current density profile. Figure 3 shows $(r_{inv}/a)_{sx}$ versus $1/q_{eff}$ which covers wide ranges of plasma parameters: $I_p=1-5\text{MA}$, $B_t=1.7-4\text{T}$, $\beta_p < 1$ and $\beta_N < 1.5$. The maximum value of $(r_{inv}/a)_{sx}$ is almost proportional to $1/q_{eff}$ as given by the dotted line. This proportionality has been reported from many tokamaks [5-7]. Here, the important observation is that the dotted line almost corresponds to the dashed line in Fig.1, which means that $(r_{inv}/a)_{sx}$ is proportional to $1/q_{eff}$ in the steady state. This clear proportionality of maximum $(r_{inv}/a)_{sx}$ to $1/q_{eff}$ suggests that there exists a strong restriction of current density distribution in the tokamak system. In the low q region where the sawtooth mixing region is large, sawtooth activity itself may be the reason of this restriction. In Fig.3, there are many data points below the dotted line. These sawteeth correspond to data where the current profile has not been fully penetrated as shown in Fig.2. In Fig.4, $(r_{inv}/a)_{sx}$ and $(r_{mix}/a)_{sx}$ is plotted against l_i for fixed q_{eff} -values. It is observed that $(r_{inv}/a)_{sx}$ and $(r_{mix}/a)_{sx}$ increase with increasing l_i for a given q_{eff} . It should be noticed that the saturated r_{mix} reaches about half the minor radius at $q_{eff}=4$ ($1/q_{eff}=0.24-0.26$).

To describe r_{inv}/a , we made an empirical scaling based on the above results, which consists of a term proportional to $1/q_{eff}$, an additional term for the l_i -dependence and a correction coefficient for the effect of line integration as given by

$$(r_{inv}/a)_{sc} = (r_{inv}/a)_{sx}/0.8 = 3.5(1/q_{eff})(l_i^{0.6} - 0.5 - 0.18(q_{eff}-2)^{1/3}). \quad (3)$$

The results of the fit to the data in Fig.4 is plotted in Fig.5. Equation (3) satisfies that $(r_{inv}/a)_{sx}/0.8$ is almost proportional to $1/q_{eff}$ in the steady state given by eq.(1). Equation (3) also expresses that r_{inv}/a becomes zero at a certain positive value of l_i . However, from eq.(3), the value of l_i at $(r_{inv}/a)_{sc}=0$ does not satisfy eq.(2). This is because $(r_{inv}/a)_{sx}$ decreases rapidly

with decreasing l_i around the l_i -boundary for the appearance of sawteeth (between two dashed lines in Fig.2) and $(r_{inv}/a)_{sx}$ cannot be expressed by l_i . The scatter of data in Fig.5 may be caused by that the l_i value does not completely reflect the information of the inner current density profile. From the above results, in the quasi steady state,

$$(r_{inv}/a) = (r_{inv}/a)_{sx} / 0.8 = 1.5/q_{eff} \quad (=1.2/q_{95}) \quad (4)$$

This result is also supported by the ECE measurements (Sec.1.17)

4. Sawtooth Period

Figure 6 shows the observed sawtooth period τ_{sw} against $W_{dia}/\bar{n}_e V_p$ which is nearly proportional to the volume averaged electron temperature $\langle T_e \rangle$ for the data with $I_p=2-3\text{MA}$, $B_t=3.5-4\text{T}$, $V_p=70-76\text{m}^3$ and $Z_{eff}=2-3$. The line averaged electron density \bar{n}_e is measured by a FIR interferometer having a line of sight slightly off axis ($\sim 1/3a$). The different symbols correspond to different q_{eff} . The dependence of the sawtooth period increases with $(W_{dia}/\bar{n}_e V_p)$ and seems to be $\tau_{sw} \sim (W_{dia}/\bar{n}_e V_p)^{3/2}$ (solid line). This dependence is almost the same as that obtained in ref.[8] and as predicted theoretically [9] which suggests that the sawtooth period is explained by the resistive diffusion time of the current profile.

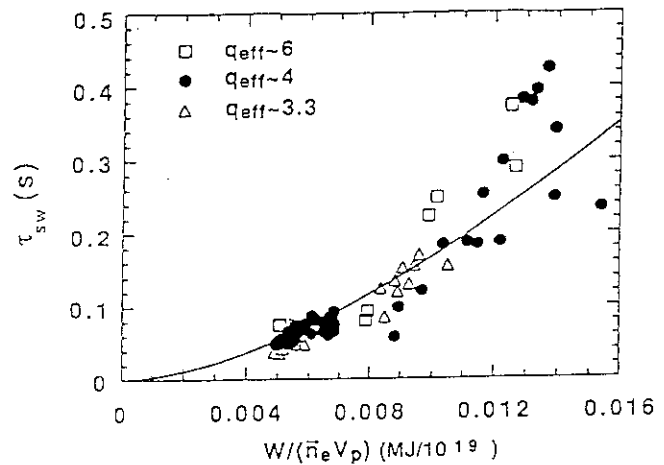


Fig.6: τ_{sw} and $W(\text{MJ})/\bar{n}_e(10^{19}\text{m}^{-3})V_p(\text{m}^3)$ for $q_{eff} \sim 3.3, 4$ and 6 . ($I_p=2-3\text{MA}$, $B_t=3.5-4\text{T}$, $V=70-76\text{m}^3$ and $Z_{eff}=2-3$). $W/\bar{n}_e V_p$ is nearly proportional to $\langle T_e \rangle$.

REFERENCES

- [1] KAMADA Y., et al., in Plasma Phys. Cont. Nucl. Fusion Research (Proc.14th Int. Conf., Wurzburg, 1992) IAEA-CN-56/A-7-13.
- [2] KAMADA Y., et al., 'Effects of the safety factor and the internal inductance on MHD activities and energy confinement in JT-60U' to appear in Nucl. Fusion.
- [3] PFEIFFER, W., Nucl. Fusion **25** (1985) 673.
- [4] KAMADA, Y., OZEKI, T., AZUMI, M., Phys. Fluids B **4** (1992) 124.
- [5] SNIDER, R.T., Nucl. Fusion **30** (1990) 2400
- [6] SNIPES, J.A., GENTLE, K.W., Nucl. Fusion **26** (1986) 1507.
- [7] KAMADA, Y., et al., in Plasma Phys. Con. Nucl. Fusion Research (Proc.13th Int. Conf., Washington, 1990) Vol.I, IAEA, Vienna, (1991) p291; KAMADA, Y., et al., Nucl. Fusion **31** (1991) 23.
- [8] KAMADA, Y., et al., 'Sawtooth Frequency Studies in DIII-D Tokamak' GA-A20611, General Atomics 1992.
- [9] PARK, W., MONTICELLO, D.A., Nucl. Fusion **30** (1990) 2413.
- [10] KADOMTSEV, B.B., Sov. J. Plasma Phys. **1** (1975) 389.

9. Diagnostics

9.1 Absolute Sensitivity Calibration of VUV Spectrometers

T. Sugie, H. Kubo, S. Numazawa and A. Sakasai

Spectroscopic measurements of divertor plasmas are useful to make clear the characteristics and the mechanism of the remote radiative cooling. We have a grazing incidence and a normal incidence spectrometer looking at the divertor region [1]. Here, we describe the method and the results of the absolute sensitivity-calibrations of these spectrometers.

1. Grazing Incidence Spectrometer

We have measured spectral lines radiated from the divertor plasmas with a module-type flat-field grazing incidence spectrometer [2] in the wavelength range 300 Å to 1250 Å. The spectral lines are dispersed with a holographic grating (300 l/mm) and measured with a multichannel detector.

The absolute sensitivity of the spectrometer had been calibrated with a storage ring [3]. After that, the detector was broken before the measurements of divertor plasmas. We exchanged the detector for a same type one and assumed that the relative sensitivity did not change after the exchange. The absolute value was determined by the branching ratio method at two wavelength points with a calibrated visible spectrometer looking at the same area [1] as the grazing incidence spectrometer. We measured two line pairs of CIII (574 Å and 5696 Å) and DI (1025 Å and 6561 Å).

The calibration result is shown in Fig. 1. The reciprocals (photon flux / detector response) of the sensitivity are plotted as a function of wavelength. Here, the relative values shown by the dotted line were converted into the absolute ones using the result of the branching ratio method at 574 Å and 1025 Å.

2. Normal Incidence Spectrometer

We have also measured spectral lines radiated from the divertor plasmas with a module-type normal incidence spectrometer in the wavelength range 970 Å to 1560 Å.

We calibrated the absolute sensitivity of this spectrometer with an argon mini-arc light source [4] which spectral radiance was calibrated in the wavelength range 1235 Å to 3335 Å by National Institute of Standards and Technology in US. Figure 2 shows an experimental arrangement for the sensitivity calibration. The argon mini-arc was connected with a vacuum vessel at position 1. The light radiated from the arc emerged through a MgF₂ window, and

was focused on the entrance slit of the spectrometer with a concave mirror (mirror 1: $f = 400$ mm, Al coated with MgF_2). The distances between the arc and the mirror 1, and the mirror 1 and the entrance slit were 600 mm and 1200 mm, respectively. Since the spectral radiance of the arc had been calibrated in a central region (~ 0.3 mm ϕ) of the arc chamber, we limited the viewing area to 0.05 mm by 0.3 mm in the central region of the arc by setting the width and the height of the entrance slit at 0.1 mm and 0.6 mm. Moreover, we attached a 6.3 mm-diameter aperture to the mirror 1 so that the influence of astigmatism was less than 0.1 mm at the arc chamber.

The intensity $I(\lambda)$ of the light incident to the spectrometer through the entrance slit is

$$I(\lambda) = R(\lambda) \cdot L(\lambda) \cdot A \cdot \Omega, \quad (1)$$

where $R(\lambda)$ is the reflectivity of mirror 1, $L(\lambda)$ is the spectral radiance of the arc with the MgF_2 window, A is the viewing area of the light source and Ω is the solid angle determined by the aperture. The signal voltage $V(\lambda)$ of a channel corresponding to a wavelength λ is written by the sensitivity $K(\lambda)$, the wavelength width $\Delta\lambda$ of the detector channel and $I(\lambda)$ as follows.

$$V(\lambda) = K(\lambda) \cdot I(\lambda) \cdot \Delta\lambda \quad (2)$$

Next, we moved the arc from position 1 to 2 and mounted another mirror (mirror 2: plane mirror, Al coated with MgF_2) as shown in Fig. 2. We got the reflectivity of the mirror 2, comparing the signals with those of the previous arrangement. Here, we assumed the reflectivity $R(\lambda)$ of the mirror 1 was same as that of the mirror 2.

From the equation (2), we derived the sensitivity $K(\lambda)$ in the wavelength range 1235 Å to 1550 Å. In consideration of the viewing area, the solid angle and other condition of the spectrometer installed in JT-60U, we finally derived the sensitivity. Figure 3 shows the reciprocals (photon flux / detector response) of the sensitivity as a function of wavelength. In the wavelength range shorter than 1235 Å, we estimated the sensitivity by comparing the signals with those of the calibrated grazing incidence spectrometer mentioned in the previous section.

References

- [1] KUBO, H., et al., Section 4.9 in this review.
- [2] NAGATA, H., et al., Nucl. Instr. Meth. Phys. Res. A **294** (1990) 292.
- [3] KUBO, H., et al., Rev. Sci. Instrum. **59** (1988) 1515.
- [4] JULES, Z., et al., J. Res. Natl. Bur. Stand. (U.S.) **93** (1988) 21.

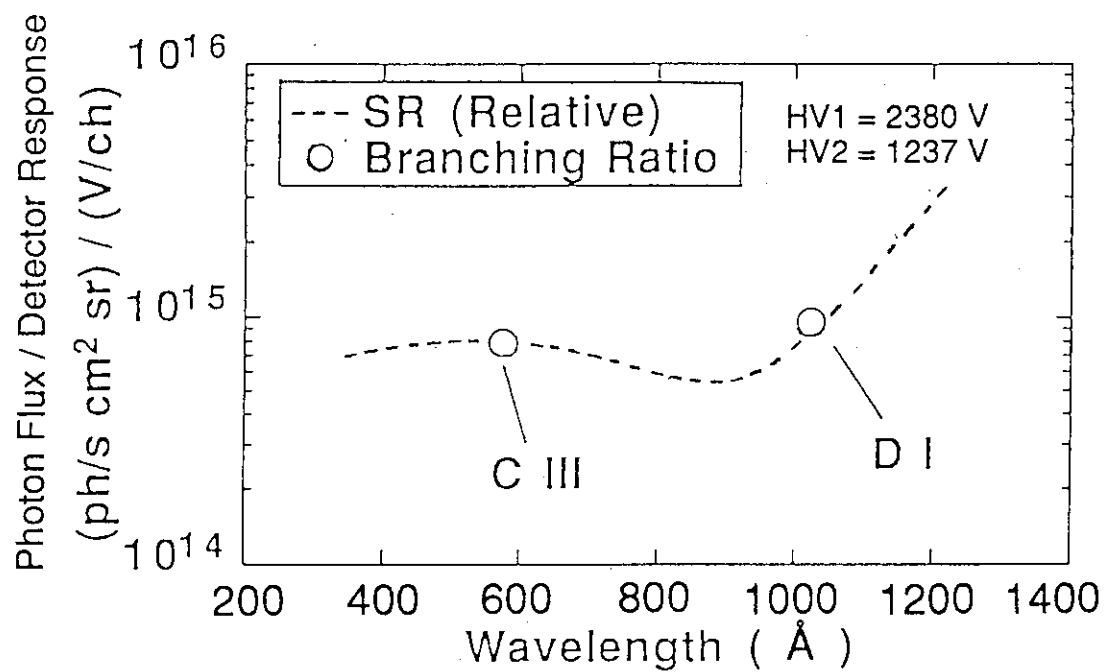


Fig.1 Reciprocal sensitivity (photon flux / detector response) of the grazing incidence spectrometer as a function of wavelength.

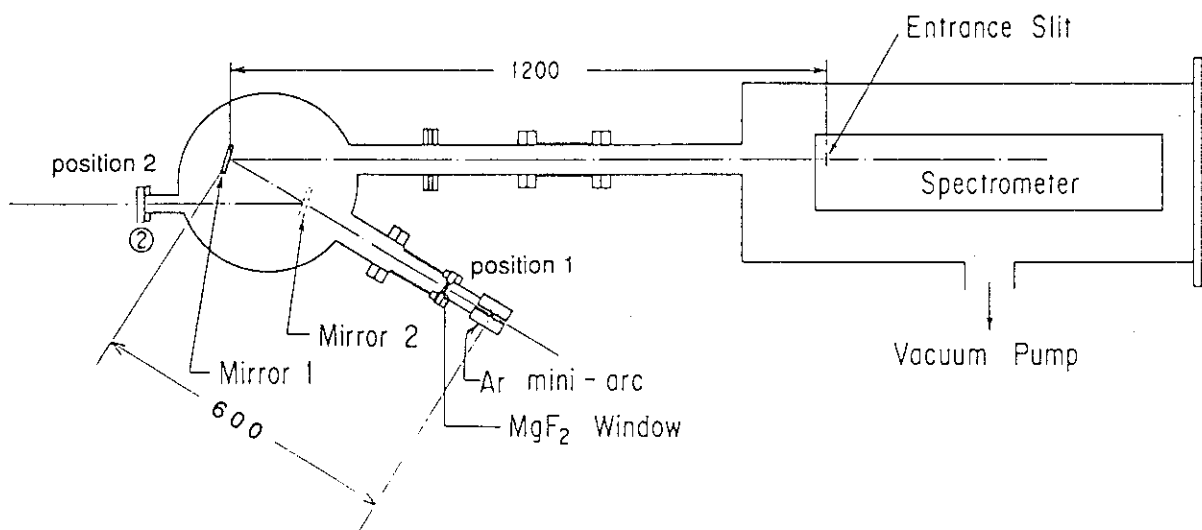


Fig.2 Experimental arrangement for the sensitivity calibration of the normal incidence spectrometer.

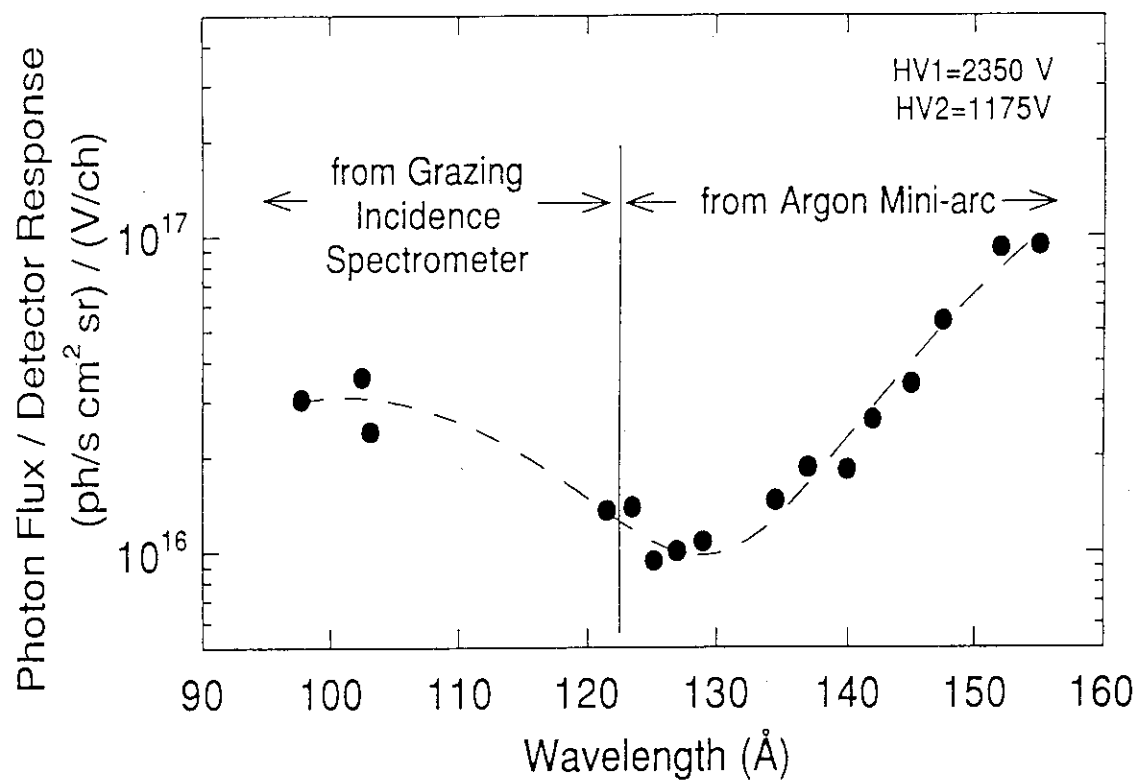


Fig.3 Reciprocal sensitivity (photon flux / detector response) of the normal incidence spectrometer as a function of wavelength.

9.2 First Operation Result of CO₂ Laser Interferometer

Y. Kawano, T. Hatae, A. Nagashima, T. Fukuda and T. Matoba

1. Introduction

A CO₂ laser interferometer has been developed on the JT-60U tokamak. This section describes an outline of the interferometer and the first operation result obtained from August to October 1992.

The main purpose of the interferometer is to measure line electron density at the center of JT-60U. Since the CO₂ laser ($\lambda = 10.6 \mu\text{m}$) has a short wavelength compared with the CH₃OH laser ($\lambda = 119 \mu\text{m}$) of the present interferometer system, the CO₂ laser interferometer improves operation limits such as the beam refraction due to a graded density profile in a tokamak plasma.

The interferometer is useful for the high beta poloidal (β_p) experiment on JT-60U since it is able to observe just the plasma center region where is interested in. Also it is expected to be useful for the pellet injected plasma which has a large density gradient.

2. Outline of Interferometer

The CO₂ laser interferometer has three major features summarized as follows [1]:

(1) From a viewpoint of advantages of a long path length in a plasma and a setting of a reflection mirror at the outside of the vacuum vessel, a toroidally tangential line of sight was selected for the plasma center measurement. Figure 1 shows a CO₂ laser path in the vacuum vessel. The laser beam is launched into the vacuum vessel through a ZnSe window at an equatorial port and it is reflected by a corner cube reflector (CCR) set at another port. Figure 1 (b) shows cross sectional view in the case of a high β_p plasma configuration on JT-60U. The laser beam is passing through the vicinity of the magnetic axis of the plasma.

(2) An IR-HeNe laser ($\lambda = 3.39 \mu\text{m}$) interferometer is introduced to compensate the mechanical mirror vibration. In comparison with the visible HeNe laser ($\lambda = 0.633 \mu\text{m}$), the IR-HeNe laser is expected to have a better transmission coefficient of a damaged surface of the vacuum window and a measurable vibration speed of mirrors. Figure 2 shows a schematic layout of optics on a vibration isolation bench (3 m x 1.5 m size). The CO₂ laser interferometer and the IR-HeNe laser interferometer are arranged so that both laser beams are coaxially propagated to the plasma.

(3) Beams of the CO₂, the IR-HeNe and the visible HeNe lasers propagate one way path length of about 50 m in a similar Gaussian form using a same relay optics (See Fig.3. Note there are two telescopes). Though each laser beam has each propagation mode due to a different beam divergence and diameter at the origin, this similar form propagation is simply achieved by the mode matching technique in a common path [1].

3. Operation Results

A typical interferometer data for the NB heated plasma is shown in Fig.4. Figure 4 (a) and (b) are fringe shift data of the CO₂ and the IR-HeNe laser interferometers, respectively. Vibrations with a frequency of about 10 Hz and an amplitude of 0.05 mm ~ 0.1 mm are observed in both fringe data. This is caused by the motion of mirrors near the vacuum vessel. The drift like change of fringe data seen in Fig.4 (a) and (b) is supposed to be caused by a mechanical displacement of mirror mount structures due to poloidal magnetic fields.

Figure 4 (c) shows the line integrated electron density for one way path length of 6 m in the plasma, which is calculated from Fig.4 (a) and (b), where the fringe shift due to the mirror motion is compensated. A peak value is about $2 \times 10^{20} \text{ m}^{-2}$ at $t = 6.5 \text{ sec}$, which corresponds to two fringes of the CO₂ laser interferometer. An oscillation with a frequency of about 200 Hz and an amplitude of $2 \sim 3 \times 10^{19} \text{ m}^{-2}$ is superimposed on the density trace. In this case, a density resolution is determined by the amplitude mentioned above and it is about ten times larger than the ideal value of $3.1 \times 10^{18} \text{ m}^{-2}$ [1]. An origin of this oscillation is not clear yet, but there are some candidates such as an electrical induced noise from a power supply of the CO₂ laser and a fluctuation of frequencies of the CO₂ laser and/or IR-HeNe laser.

One of the data obtained in the high β_p experiment (SN16040, $I_p = 1.9 \text{ MA}$, $B_t = 4.0 \text{ T}$, $W_{\text{dia}} = 6.1 \text{ MJ}$ and $S_n = 2.6 \times 10^{16} \text{ neutron/sec}$ at $t = 5.44 \text{ sec}$) is shown in Fig.5. Because the tuning of the whole interferometer system was not finished yet at the time of this experiment in August, the obtained line density data has large fluctuations and it is not obtained before $t = 2.5 \text{ sec}$ (a change of a line density before and after the NB injection can be known). The bottom column of Fig.5 (a) is the line density by the CH₃OH laser interferometer at the vertical U1 chord (see Fig.1 (b)). An electron density profile of the high β_p plasma is evaluated as shown in Fig.5 (b) by using of two interferometer data. Here the electron density profile is assumed to have a parabolic function such as $n_e(r) = n_e(0) \{1 - (r/a)^2\}^M + n_e(a)$. And a line electron density at an ohmic heating phase in the CO₂ laser interferometer is estimated by data of the CH₃OH laser interferometer. Though the error is large, the center electron density ; $n_e(0)$ is about $5.5 \times 10^{19} \text{ m}^{-3}$ seen in Fig. 5 (b).

4. Discussion and Summary

A CO₂ laser interferometer on the JT-60U tokamak was successfully developed . A line electron density at a center of a high β_p plasma on JT-60U was measured for the first time and the electron density profile was evaluated. On the other hand, several problems are remained. Two of them are discussed in following:

(1) In the case of high plasma current experiments ($I_p > 2 \text{ MA}$), the displacement of mirror mount structures become large, a fringe counting error is often occurred because the laser beam axis is out of an initial alignment. To eliminate this problem, the material of mount

structures was replaced from stainless steel to fiber-reinforced plastics (FRP). The FRP has a low electric conductivity and little of the eddy current, it is hard to be affected by any magnetic field. The new structures will be used from February in 1993.

(2) At the operation of the interferometer, a difference of the path length between a probing laser beam and a reference laser beam was about 100 m in this period. In such a large difference, a fluctuation and a drift of the laser frequency makes certain fringe shifts which can not be eliminated. An optical delay line is conventionally used in order to solve this problem. It is inserted into the reference laser path so as to match both path lengths, and no frequency fluctuation can generate the fringe data error. A delay line for the CO₂ laser interferometer is planned to be installed in 1993.

References

- [1] Kawano, Y., Nagashima, A., et al., Rev. Sci. Instrum. **63** (1992) 4971.

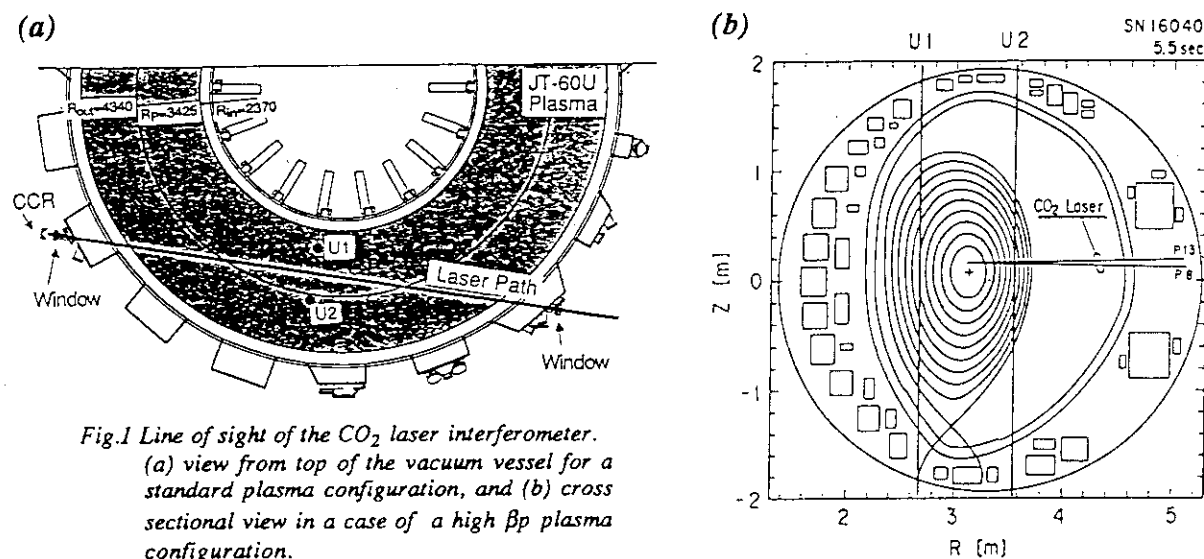


Fig.1 Line of sight of the CO₂ laser interferometer. (a) view from top of the vacuum vessel for a standard plasma configuration, and (b) cross sectional view in a case of a high β_p plasma configuration.

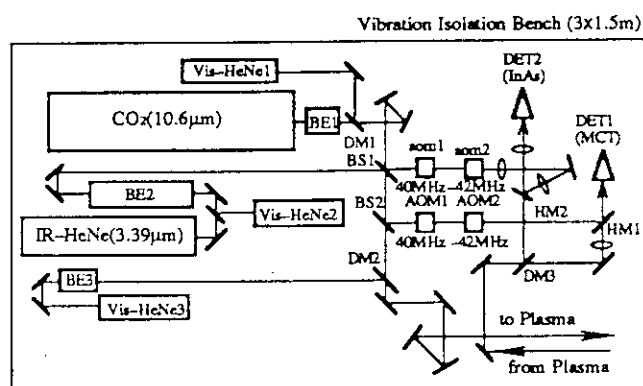


Fig.2 Optical arrangement on the bench.

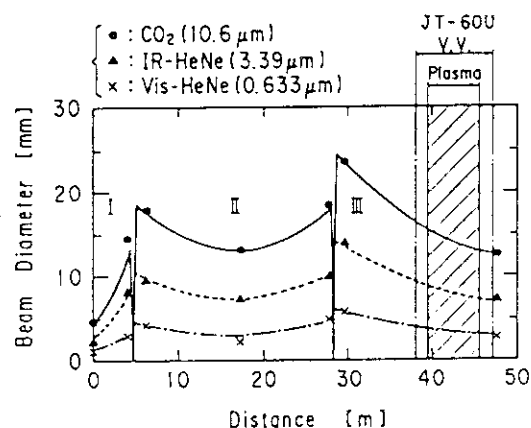


Fig.3 Beam Diameters of three different color lasers propagating in a similar form with the common path mode matching. All lines are designed and symbols are measured diameters, respectively.

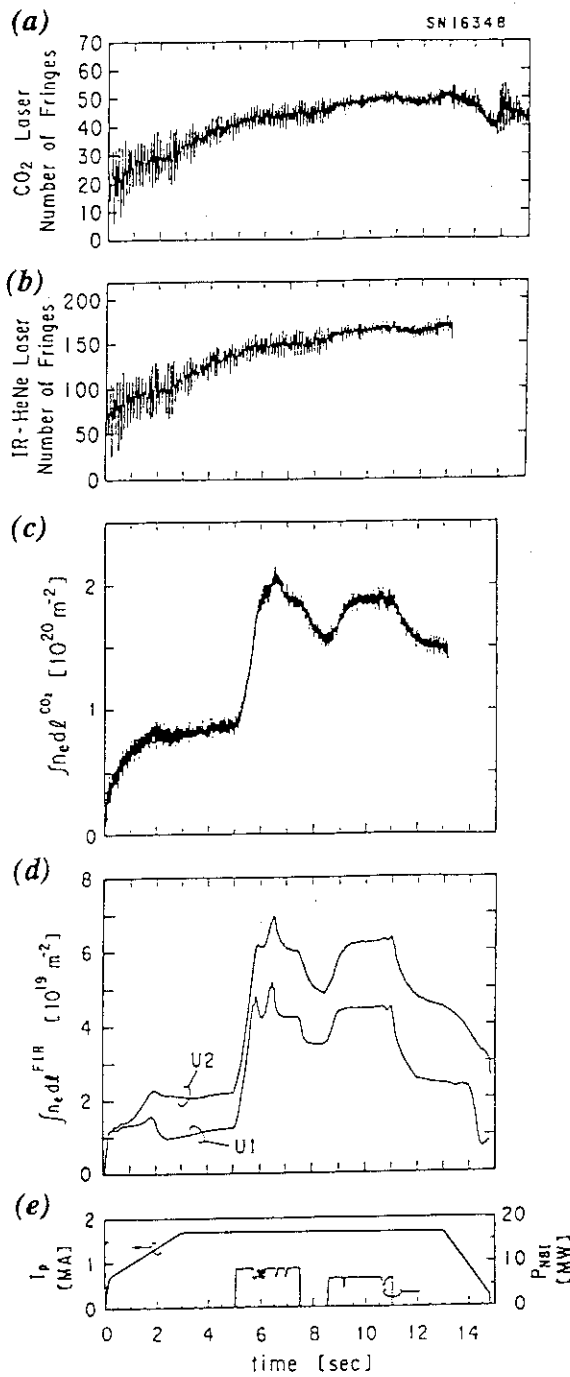


Fig.4 Typical measured signals, fringe shift data of interferometers of (a) CO₂ laser and (b) IR-HeNe laser. (c) is the line integrated electron density calculated from (a) and (b). (d) is the line integrated electron density from CH₃OH laser interferometer. And (e) shows plasma current and NB heating power.

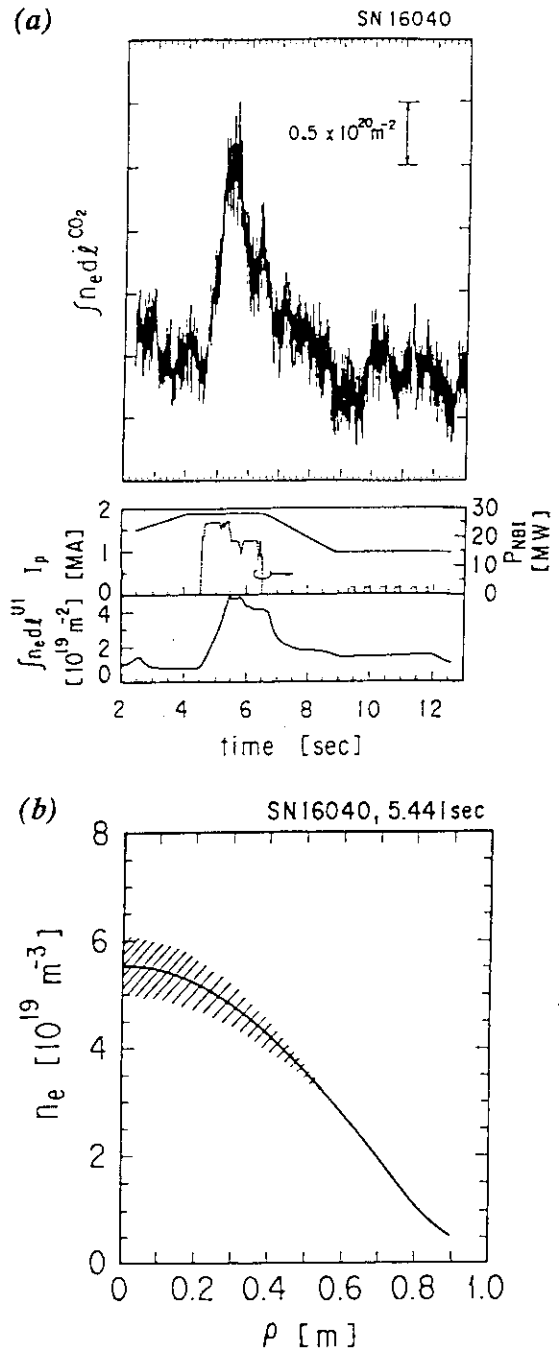


Fig.5 Example of data in a high β_p experiment.

(a) Line integrated electron densities of the CO₂ (top) and the CH₃OH (bottom) laser interferometers, (b) electron density profile evaluated from two interferometer data.

9.3 Motional Stark Effect Polarimeter

H. Kubo, T. Fujita, N. Isei, T. Sugie, S. Numazawa, and H. Takeuchi

1. Introduction

The motional electric field $\mathbf{E} = \mathbf{V}_{\text{beam}} \times \mathbf{B}$, where \mathbf{V}_{beam} is the velocity of the neutral beam and \mathbf{B} is the tokamak magnetic field, produces a strong Stark effect in spectral lines emitted by hydrogenic neutral beams. The pitch angle of the magnetic field is deduced from a measurement of the polarization direction of the Stark components. [1 - 2]. A motional Stark effect polarimeter in JT-60U is discussed in this paper.

2. Apparatus

Schematic layout of the polarimeter on JT-60U is shown in Fig. 1. The polarimeter viewed one of the deuterium neutral beams that was used for heating the plasma. The neutral beam was named #4 beam and it was almost on the cross section where the polarimeter was located. The beam energy was generally 90 keV in 1992. The beam width was about 40 cm. The polarimeter was installed just outside of toroidal coils in order to reduce the Faraday rotation effect which was induced by the magnetic field in the optics. It was possible to change the sight line of the polarimeter by rotating a mirror.

The measurement technique was the same as in PBX [1]. A schematic diagram of the system is shown in Fig. 2. Doppler-shifted $D\alpha$ lines emitted from the neutral beam were transmitted through windows. The polarimeter observed the light reflected with Al + SiO₂ mirrors. The first lens of the polarimeter was 5 cm diameter. The light was transmitted through two photoelastic modulators (PEM) with the frequencies of 42 and 47 kHz, which acted as waveplates with retardation oscillating between approximately $-\lambda/2$ and $+\lambda/2$, where λ was the wavelength. The light was focused through a polarizing beam splitter onto 20 optical fibers. The core of a fiber was 0.2 mm diameter and the fibers was 1.5 mm diameter as a whole. The image size in the plasma was about 9 cm. The numerical aperture of the fiber was 0.20. The fiber-optic bundle was about 250 m in length. The optic material of the windows, polarimeter, and optical fiber was fused silica to minimize the radiation darkening. The ends of the fibers were arrayed on the entrance slit of a 0.25-m Czerny-Turner monochromator. The detector was a photomultiplier with the quantum efficiency of $\sim 5\%$ for $D\alpha$ line. The photomultiplier output was split into two lock-in amplifiers for demodulation at the two reference frequencies from the PEMs. The angle of the polarization was calculated from the lock-in amplifier outputs.

3. Results and Discussion

Fig. 3 shows a spectrum observed with a multichannel spectrometer in stead of the monochromator shown in Fig. 1. The spectrum was obtained in a discharge with the toroidal field of 4 T and the neutral beam energy of 90 keV. The sight line and the neutral

beam crossed each other at $R = 3.75$ m. The sight line is indicated as a solid line in Fig. 1. It was expected that $D\alpha$ and C II lines were emitted from plasmas without the neutral beam injection (Fig. 3 (a)). During the neutral beam injection, $D\alpha$ emission from the neutral beam was observed as unresolved lines around the C II lines (Fig. 3 (b)). The Stark pattern was expected to be complex as shown in Fig. 3 (c), because there were two neutral beams and three ion sources for each beam. Fig. 3 (d) shows a spectrum expected on the assumption that the wavelength resolution of the spectrometer was 2 \AA . Because the Stark pattern was complex, it was difficult to identify the Stark components in detail. Moreover, the signal was so small that the identification was difficult. Although the identification of the spectrum is important to measure the polarization angle efficiently, it is possible to measure the polarization angle without the detailed identification. Comparison between the polarization angle measured experimentally and that calculated with a magnetic equilibrium code [3] is shown in Fig. 4. In the calculation, $q(0)$ was assumed to be unity. The measured polarization angle agreed with the calculated angles within $\sim 3^\circ$. The scattering of the data could be attributed to the statistical error in the measurement. The experimental data were obtained with the averaging time longer than 1 s. Much larger signal is needed for current profile measurements.

The polarimeter was originally designed to measure the polarization angle with the statistical uncertainty of $\sim 0.2^\circ$ and the time resolution of ~ 50 ms. The measured signal was 3 orders of magnitude smaller than the expected one. Coating on the window surface was one of the reason for the discrepancy between the observation and the expectation. Transmittance of the window decreased down to 13 % of the original transmittance after the experimental campaign in 1992. The other reason was that setting of the monochromator, detector, and lock-in amplifiers was not optimized. Further examination and optimization of the system have been needed. Experience in the examination and the optimization will come in useful for designing the next step system: a multichannel polarimeter.

References

- [1] LEVINTON, F. M., et al., Phys. Rev. Lett. **63** (1989) 2060.
- [2] WROBLEWSKI, D., LAO, L., L., Rev. Sci. Instrum. **63** (1992) 5140.
- [3] TSUJI, S., et al., Rep. JAERI-M, 92-073, Japan Atomic Energy Research Institute, Ibaraki-ken (1992) 108.

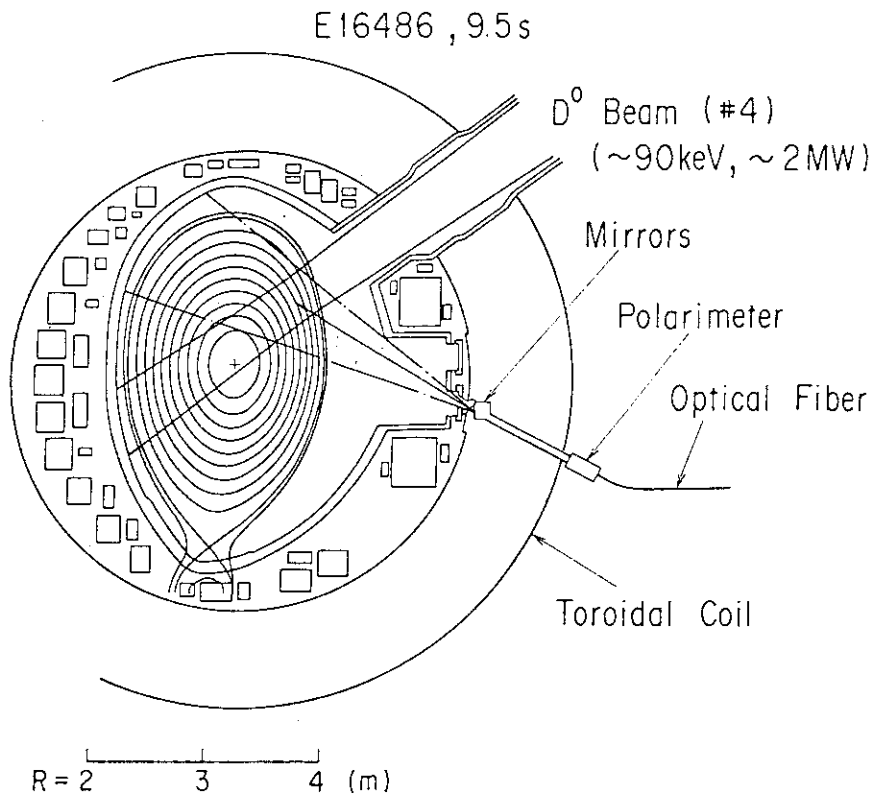


Fig. 1. Schematic layout of the motional Stark effect polarimeter on JT-60U.

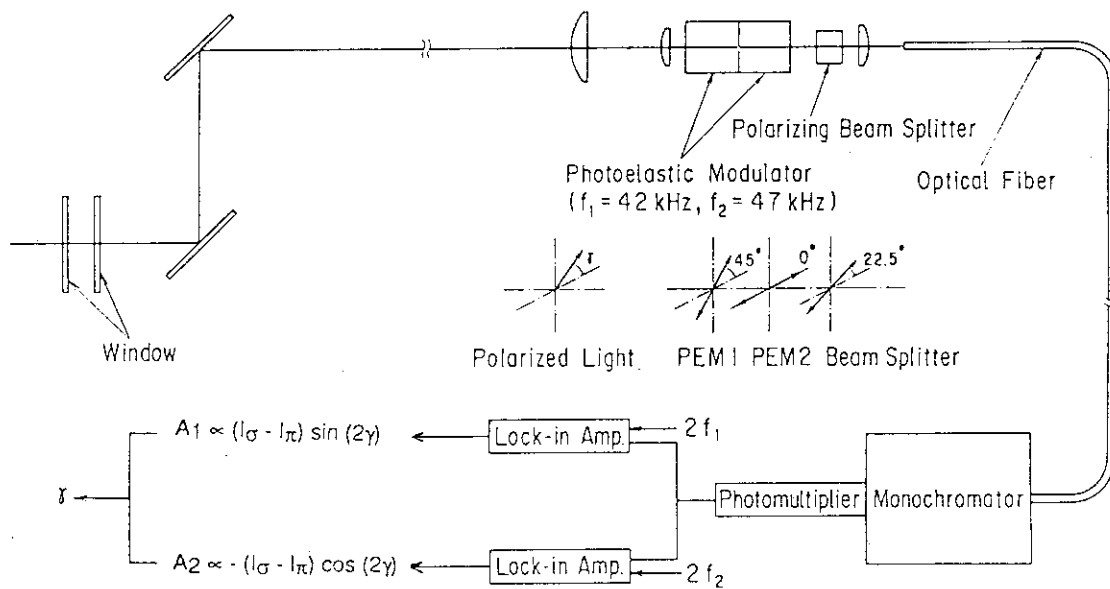


Fig. 2. Schematic diagram of the polarimeter system.

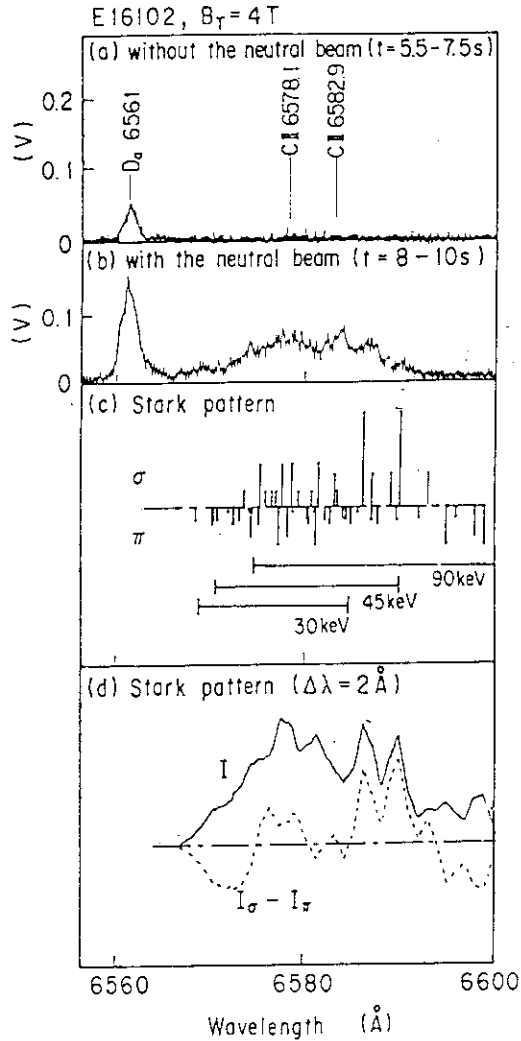


Fig. 3. Spectra of $D\alpha$ lines observed (a) without the neutral beam injection and (b) with the neutral beam injection. The spectra were obtained by averaging the emission over 2 sec. (c) Theoretical diagram of the Stark pattern. The length of a line is proportional to its intensity. The intensities are plotted upward for σ -components, and downward for π -components. (d) The spectrum on the assumption that the wavelength resolution of the spectrometer is 2 Å. The solid line indicates the sum of the intensities of the two components, and the broken line indicates the difference of the intensities. The beam power produced from D^+ (90 keV), D_2^+ (45 keV), and D_3^+ (30 keV) ion sources were assumed to be 80, 13, and 7 % of the total beam power at the observed position, respectively. The emission was integrated over all the observation direction.

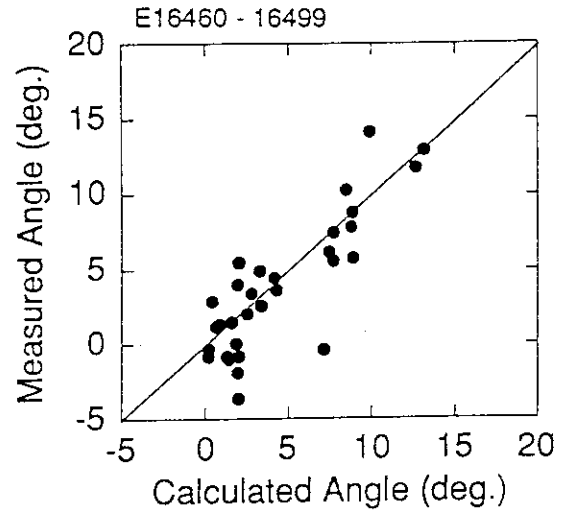


Fig. 4. Comparison between the polarization angle measured experimentally and that calculated with a magnetic equilibrium code. The data were obtained at $R = 2.75$ m in discharges with $I_p = 1.1 - 2.5$ MA, $B_T = 2.4 - 4$ T, and $q_{eff} = 4.2 - 9.1$.

9.4 Development of Fourier Transform Spectrometer System

M. Sato, N. Isei and S. Ishida

1. Introduction

The electron temperature in tokamaks has been measured using the electron cyclotron emission (ECE)[1,2]. The electron temperature from ECE in JT-60U plasma has been measured by a Fourier transform spectrometer system (FTS)[3]. In order to obtain the electron temperature with good accuracy, calibrations of sensitivity and frequency are needed. An absolute sensitivity calibration is made every winter. A relative sensitivity calibration is made normally bi-weekly.

2. Calibration of FTS

2.1 Sensitivity Calibration

The schematic diagram of absolute and relative calibration is shown in Fig.1. For the absolute calibration of FTS, the bellows between the vacuum vessel and window is removed and a mirror is located at the position of the bellows[3]. The calibration source is Eccosorb used at liquid nitrogen temperature and at room temperature. The absolute calibration may be made any time there is a break of vacuum of the vessel. This timing is normally November and December in JT-60U. In order to get sensitivity with good accuracy, relative calibrations in diagnostic room were made more frequently.

The sensitivity was found to be reduced by about 35% in summer 1992. The time history of the sensitivity at 220GHz is shown in Fig.2. Candidates for the cause of the change are as follows: 1) Change of absorption of vapor in the waveguide. 2) Change of the temperature of InSb element. 3) Change in transmission of the window. 4) A looseness of InSb element.

Summers are very humid in Japan. According to our estimation, the decrease of the sensitivity due to this change of humidity is about 7%. The 35% decrease of the sensitivity is therefore not explained by absorption. The temperature of the 4K stage, where the element is set, has been measured. The change of the temperature was about 0.1K, which does not explain the 35% decrease of the sensitivity either. The transmittance of the window, which was also used in JT-60 and was found to be visibly opaque, was measured. It was found to be the same as that of a new window. The opacity is therefore not the cause. The setting of the element was checked, and

was found to be tight, so this was not the cause. The cause has not yet been found. In any case FTS data have been corrected by the following method.

Two different correction methods for FTS data have been made. One method is based on comparison between FTS data and the grating polychromator system(GPS)[4] data assuming the sensitivity of GPS is unchanged. Another method is that the FTS data are normalized by the comparison between measured resistive loop voltage and calculated neoclassical voltage using FTS data. The difference between the two methods is about 1%.

2.1 Frequency Calibration

In ECE measurements, there is correspondence between the frequency of ECE and the position of the electron temperature. It is important for the determination of the position to calibrate the frequency of the FTS. The frequency of the FTS system is calibrated using a monochromatic millimeter source[5]. The results are shown in Fig.3. The agreement between the injected and the measured frequency is good. The frequency difference corresponds to 8% of the frequency resolution.

3. Typical Electron Temperature Profiles

The electron temperature profile is obtained from the second harmonic X mode ECE in JT-60U. The position of the electron temperature profile has been obtained with the internal fields correction[3]. Typical electron temperature profiles in the hot ion H-mode[6] and ICRF heated plasma[7] are shown in Fig.4. The peaking factors are 1.5 and 2.7, respectively.

4. Development of the Calibration Method

The absolute calibration in winter 1991 was not enough for the measurement in low toroidal field discharges. Most of the noise originated from the refrigerator used for cooling the InSb element. The refrigerator was replaced by a cryostat in November 1992. A new pre-amplifier introduced in November 1992 is the same type as the pre-amplifier for the GPS[4]. The relative sensitivity in the cases using the cryostat and new pre-amplifier and using the refrigerator is shown in Fig.5. The signal/noise ratio using the cryostat and new pre-amplifier is better than that using the refrigerator. The absolute sensitivity in the cases using the cryostat and new pre-amplifier and using the refrigerator is shown in Fig.6.

Reference

- [1]A. E.Costley et al, Phys. Rev. Lett. 33(1974) 758
- [2]M. Sato et al, Jpn J. Appl. Phys. 19 (1980) 577
- [3]M. Sato et al, JAERI-M 92-073 p342
- [4]S. Ishida et al, this issue 9.5

[5]SATO, M., et al: Proc. Int. Conf. on IR&MM waves, Takarazuka, 1984, pp

[6]KIKUCHI., M., et al., this issue 1.3

[7]KIMURA., H., et al., this issue 6.1

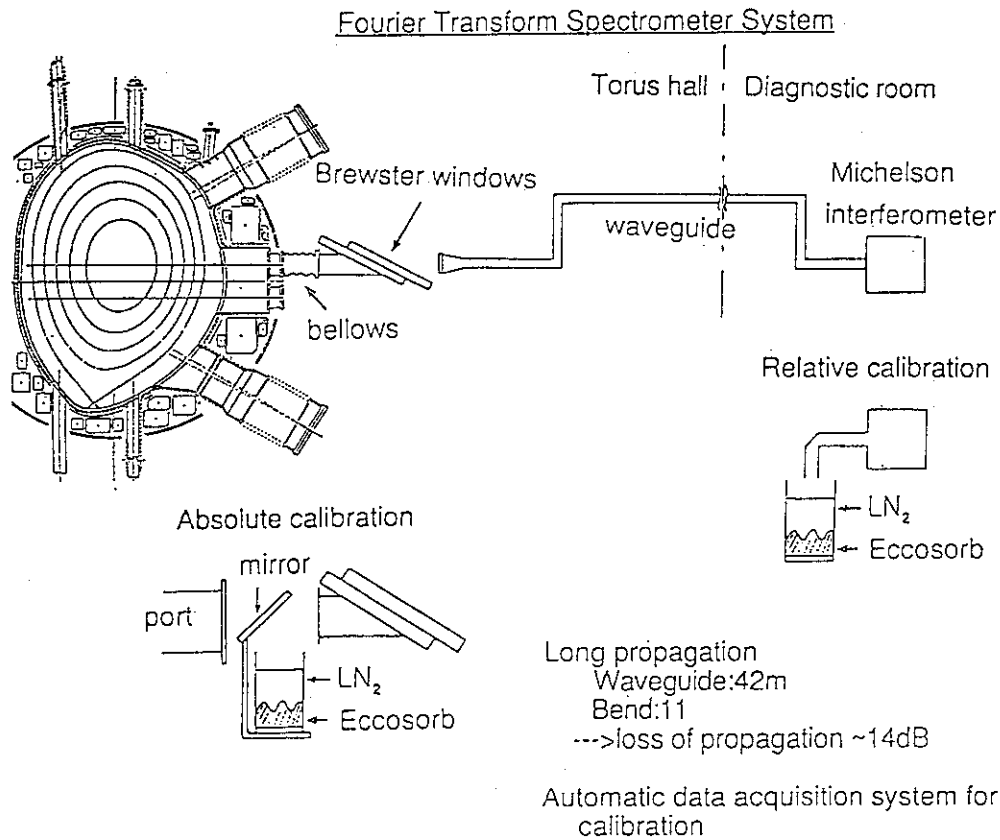


Fig.1. Schematic diagram of the calibration .

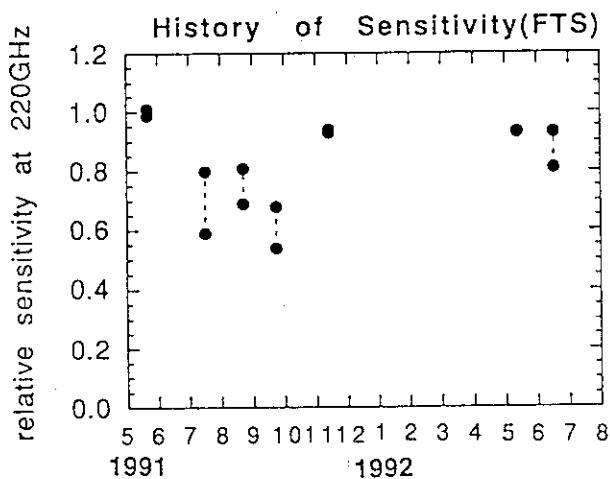


Fig.2. Time history of the sensitivity of FTS at 220GHz.

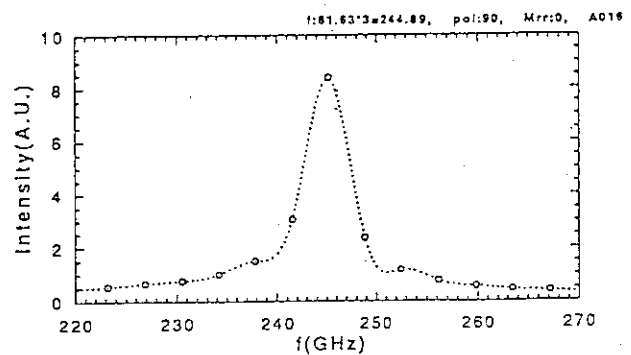
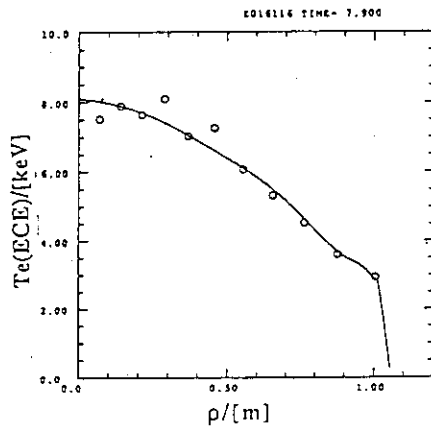


Fig.3. Frequency calibration results.
Frequency of the injected wave is 244.89GHz.

(a) hot ion H-mode plasma



(b) ICRF heated plasma

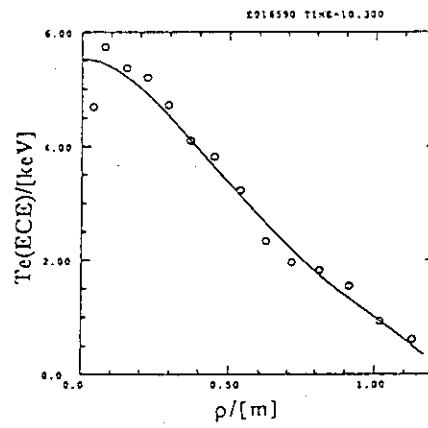


Fig.4. Typical electron temperature profiles. (a) hot ion H-mode plasma and (b) ICRF heated plasma.

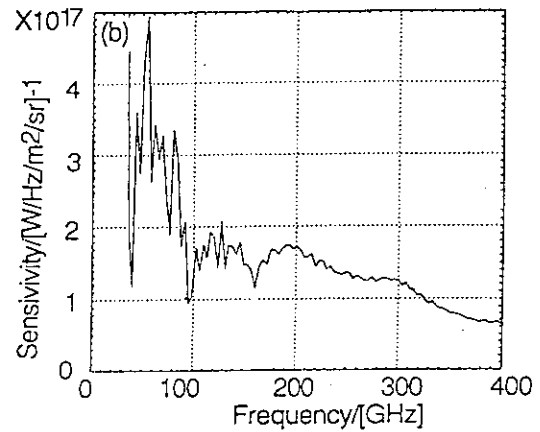
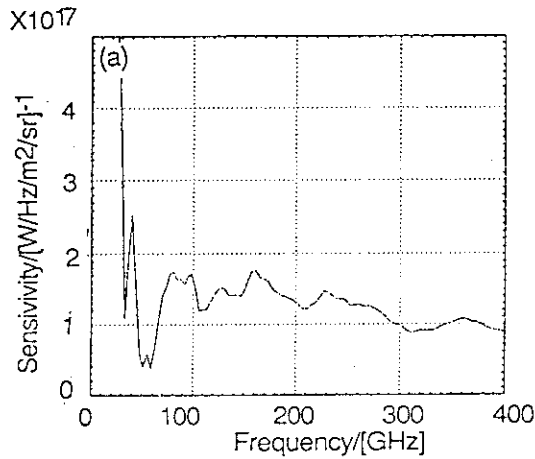


Fig.5. Relative sensitivity in the cases (a) using the cryostat with new pre-amplifier and (b) using the refrigerator.

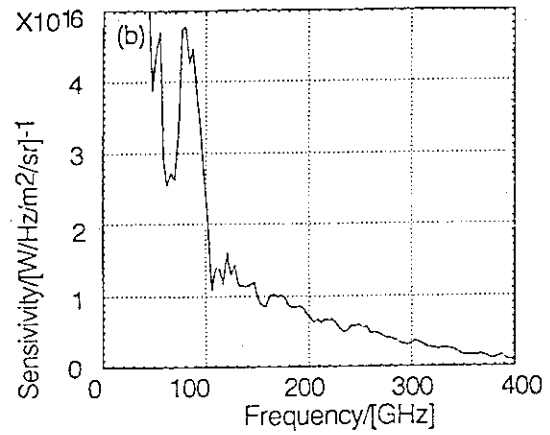
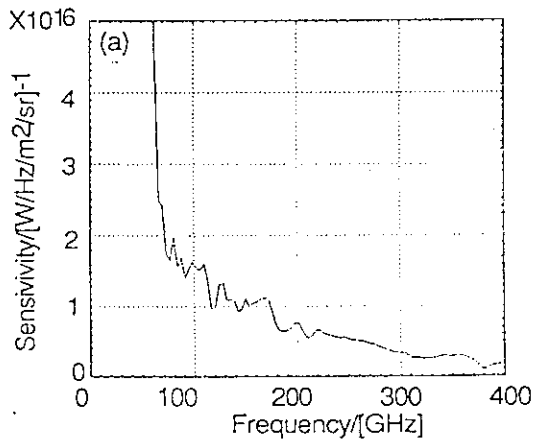


Fig.6 Absolute sensitivity in the cases (a) using the cryostat with new pre-amplifier and (b) using the refrigerator.

9.5 Low-Noise Preamplifier System for the 20-Channel Grating Polychromator and Application to ECE Image Reconstruction

S. Ishida, M. Sato, N. Isei, N. Iwama and M. Teranishi

1. Prologue

A 20-channel grating polychromator diagnostic system (GPS) for electron cyclotron emission (ECE) measurements was originally built for JT-60 in 1989 [1]. As an engineering distinction of the GPS, a cryogenic refrigerator was adopted for cooling the 20-channel indium antimonide (InSb) detectors around 4.3 K near the liquid helium temperature. The use of the refrigerator allows the apparatus to operate continuously under the maintenance work and the helium consumption very much reduced than generally required for a conventional liquid helium cryostat. However, a variety of noises such as pump noises and electrical noises arising from the use of the refrigerator, degrading noise immunity for the ECE measurement. To improve the noise immunity, a new preamplifier system has been developed by the use of low-noise differential preamplifiers during the shutdown period in 1991-1992 for the modification from JT-60 to JT-60U, and was installed in 1992 for the GPS in JT-60U. Operational capability of the present GPS was recently reported in Ref. of [2]. In this paper, noise problems arising from the use of the refrigerator and the development of the new preamplifier system are described. The improvement of the noise immunity in the GPS allows us to study the image reconstruction of ECE signals as discussed later.

2. Cryogenic Refrigerator

The 4 K refrigerator used here is a type of 4 K Gifford-McMahon (GM) /Joule-Thomson (JT) cryocooler which has been developed by Daikin Industries, LTD [3]. The refrigeration capacity rating is 2.5 W at 4.3 K with input power of 5.1 kW for 50 Hz power source. The vibration characteristics at the 4 K stage were measured by the laser Doppler vibrometer. The displacement amplitude of the 4 K stage vibration, caused by pressure change and displacer reciprocating motion (2 Hz) in the expander, was measured to be $\sim 6\text{--}11\text{ }\mu\text{m}$ for X, Y and Z directions. Reliability for the long term operation was quite well; the maintenance interval of the refrigerator is mainly determined by that of the expander which needs the maintenance after 10,000 hours of operation.

In spite of the above advantages of the cryogenic refrigerator, it has not been generally utilized for ECE measurements in fusion research, perhaps because noise problems are believed to be serious. In JT-60, noises arising from the use of the refrigerator were distinguished in the initial operation of the GPS as follows; 1) "2 Hz" noise and drift noise due to temperature fluctuations at the detector (pump noise), 2) Microphonic noise ($\sim 100\text{ kHz}$) due to the fast mechanical vibration of the detector, 3) Electrical pickup noises ($>10\text{ kHz}$) through transmission lines of signals, and 4) 50 Hz noise: picked up probably through electrostatic coupling between the detector and the 4 K stage. Especially, the 2 Hz noise was a dominant component of the

noises. As the non-differential preamplifier system initially installed was tuned supposing the detectors cooled in a conventional cryostat, so simple modification of the preamplifier system would not be workable for the GPS. Thus, we have newly developed the following preamplifier system to eliminate or reduce these noises.

3. Low Noise Preamplifier System

The new preamplifier system has a function of extracting the 2 Hz noise from the signal. A block diagram of the preamplifier system is shown in Fig.1. The 2 Hz noise signals are measured at two or three 'reference' channels, selected from the 20 channels, with closed exit apertures and are distributed to other channels for extraction. While the temperature fluctuations with 2 Hz are roughly same for all the detectors due to high heat conductivity of the 4 K stage, the regulation function for amplitude and phase of the measured 2 Hz noise is equipped with the cancel circuit in the preamplifier system for each channel to minimize the 2 Hz noise level for each signal. The cancelation of the 2 Hz noise was also effective to suppress the drift noise.

By using FET-input differential amplifiers, the developed preamplifier system realized a very-low input-voltage-noise level of $\sim 1.2 \text{ nV/Hz}^{1/2}$ with input short (almost constant for a wide band of 80-200 kHz) and a high common mode rejection rate above 60 dB (measured at 1 Hz-10 kHz). Note that the input current noise level was negligibly small. In order to suppress the pickup noise in the transmission lines, double shielding BNC cables were used for the transmission lines with a length of $\sim 8 \text{ m}$ from the preamplifier system to the 20-channel isolation amplifier system installed in an EMI (Electro Magnetic Isolation) locker.

Total input voltage noise level is measured to be $\sim 3 \text{ nV/Hz}^{1/2}$ at the output of the isolation amplifier system, in which the thermal noise from bias resistance at room temperature and the detector noise are estimated to be $\sim 2.5 \text{ nV/Hz}^{1/2}$ and $\sim 1 \text{ nV/Hz}^{1/2}$, respectively. If the bias resistance was cooled around $\sim 4 \text{ K}$, the total input noise level would be reduced, in principle, down to $\sim 2 \text{ nV/Hz}^{1/2}$. A root-mean-square value of the input voltage noise level, measured at input to A/D convertor, is $V_{\text{rms}} \sim 1 \text{ } \mu\text{V}$ for a band width of 100 Hz-100 kHz. In a typical case of Ch.12, the measured responsivity is $\sim 8 \times 10^{-8} \text{ V/eV}$ from cross-calibration with a Michelson interferometer in the case of $B_t \sim 4 \text{ T}$, so that the noise equivalent temperature can be estimated to be $T_e^{\text{rms}} \sim 13 \text{ eV}$ for $f_c = 100 \text{ kHz}$ and $T_e^{\text{rms}} \sim 4 \text{ eV}$ for $f_c = 10 \text{ kHz}$. While the preamplifier system has a high frequency response up to $\sim 300 \text{ kHz}$, electrical low-pass filters with a cut-off frequency (f_c) of 10 kHz or 100 kHz were normally applied to reduce high frequency noises. The ECE signals were recorded with a digitizing time of $20 \text{ } \mu\text{s}$ over a discharge period of 15 s.

4. Image Reconstruction

Typical ECE signals with precursor oscillations before a sawtooth collapse during neutral beam heating are shown in Fig.2(a). As the ECE signals were not calibrated, the relative shape of the T_e profile within the mixing region was inferred assuming that the T_e profile is fairly flattened in that region just after the sawtooth collapse. Based on the normalized T_e profile, the ECE reconstruction technique was applied. A typical spatial resolution is 3.4 cm at the center of the vacuum vessel and a poloidal resolution determined by the antenna pattern is $\sim 16 \text{ deg.}$ at $q=1$ surface for the present discharge with $I_p = 4 \text{ MA}$ and $B_t \sim 4 \text{ T}$.

With the 20-channel polychromator output, the spatial distribution of electron temperature in the poloidal plane is mapped as follows. The mean radii ρ of the magnetic surfaces from which the multi-channel ECE signals are originated are determined from the MHD equilibrium calculation. We use the 8 channels as indicated in Fig.2(a) corresponding to the low field side of the magnetic axis near the midplane. Assuming the rigid poloidal rotation of the plasma around the magnetic axis, the time sequences acquired over one rotation period with the sampling interval of 20 μ s are located in the two-dimensional ρ space. Locating positions are as shown in Fig.2(b). The periods and directions of the rotation are assumed to be equal and anti-clockwise, respectively, on all the magnetic surfaces in neglecting the differences not so as Δt . The origin ($\rho=0$) is given a time-averaged value of the innermost channel signal (Ch.12) during one rotation period. Based on the ECE signal values so-located, interpolations are made linearly to obtain values at additional points many enough. Figure 2(c) shows the interpolation procedure for determining the value z at point P from the values at the neighboring 4 points of P_a , P_b , P_c and P_d . The whole region in Fig.2(b) is partitioned to 100×100 square pixels, and the interpolation is made at each pixel center within the circle of the outermost Ch.20. The centers of the outside pixels are practically given the minimum value of ECE signals. Here, the contour is plotted every one 16th of the difference of the maximum and minimum values.

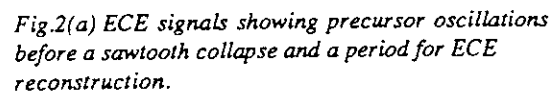
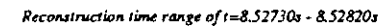
A reconstructed image of the ECE signals for an oscillation from 8.5273 s to 8.5282 s in Fig.2(a) is shown in Fig.2(d), in which a fine structure in the $q=1$ surface is visually manifested to consist of a hot spot, an $m=1$ island and a cold region. The lower temperature region like a groove between the island and the hot spot indicates a cold region corresponding to the dips in the ECE signals in Fig.2(a) (see Ch. 17 and Ch.18).

5. Conclusion

The low-noise preamplifier system has been developed in JT-60U for the GPS operating with the cryogenic refrigerator. The installation of the preamplifier system in the GPS lead to sufficient improvement of the noise immunity for the ECE measurements in JT-60U, as the noises arising from the use of the refrigerator were significantly reduced. ECE reconstruction techniques were applied to the ECE signals with sawtooth precursor oscillations, representing a fine structure composing of an $m=1$ island and a hot spot parted by a narrow cold region.

References

- [1] ISHIDA, S., NAGASHIMA, A., SATO, M., ISEI, N., and MATOBA, T., Rev. Sci. Instrum. 61(1990)2834.
- [2] ISHIDA, S., ISEI, N., and SATO, M., Operation of a 20-channel grating polychromator diagnostic system and its application to sawtooth observations, Rep. JAERI-M 92-111, Japan Atomic Energy Research Institute (1992).
- [3] KONG, Y.M., SAKITANI, K., TONEYA, S., and MIURA, K., Development of 4 K GM/JT cryocooler, in Proceedings of the Twelfth International Cryogenic Engineering Conference, Southampton, UK, 1988, p.582.



A contour plot showing the difference in electron density, ρ , between two time steps: $E14766\ t=8.52730s - 8.52820s$. The plot is a square with axes ranging from -0.6 to 0.6 m. The contours represent the density difference, with a central peak (positive difference) and surrounding regions of decreasing density. Two specific points are marked with dots and labeled: 'Island' at approximately (-0.4, -0.05) and 'Cold region' at approximately (-0.3, -0.05). The 'Cold region' label is positioned below the 'Island' label.

Fig.2(d) Reconstructed image of the ECE signals.

10. Heating and Current Drive Machine Status

10.1 Port Aging and Capability of High Energy and Power in NB System

Masaaki Kuriyama and JT-60 NBI group

1. Port Aging

Since beam drift ducts both the quasi-perpendicular and the tangential beamlines were newly fabricated with the JT-60U vacuum vessel, the duct conditioning to decrease a re-ionization loss of neutral beam was required by injecting short pulse beams under a stray magnetic field from JT-60U in advance of deuterium beam injected plasma heating.

In the case of perpendicular beamline, a integrated beam pulse length for the duct conditioning was in need of almost 50sec to be a re-ionization loss of below 10% as shown in Fig.1, which is more than three times compared with the former JT-60 duct with hydrogen beam. The reasons why the conditioning needs a long time in finishing are that the duct cross-section is smaller size than the former and the deuterium gas conductance is lower the hydrogen. But in the second duct conditioning that was done in February, 1992, just after two months vacuum break, the required integrated beam pulse length decreased to less than one third, about 15sec as shown in Fig. 2. It implies that once the port aging has finished, the aging effect maintains even in a few months of vacuum break. The duct conditioning time, furthermore, seems to be able to shorten by a helium glow discharge cleaning because the re-ionization loss in the duct decrease just after a few hours discharge cleaning in the tokamak vacuum vessel, as shown in Fig. 3.

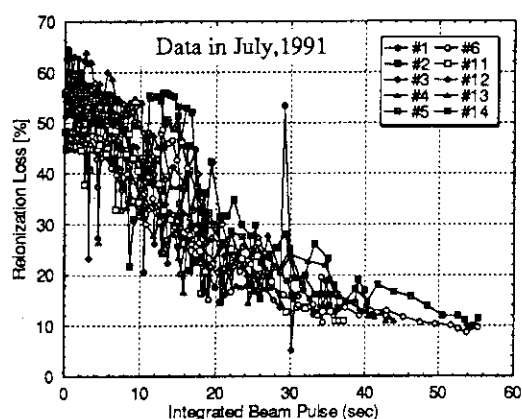


Fig. 1 Port aging in July of 1991 with newly fabricated perpendicular NBI port

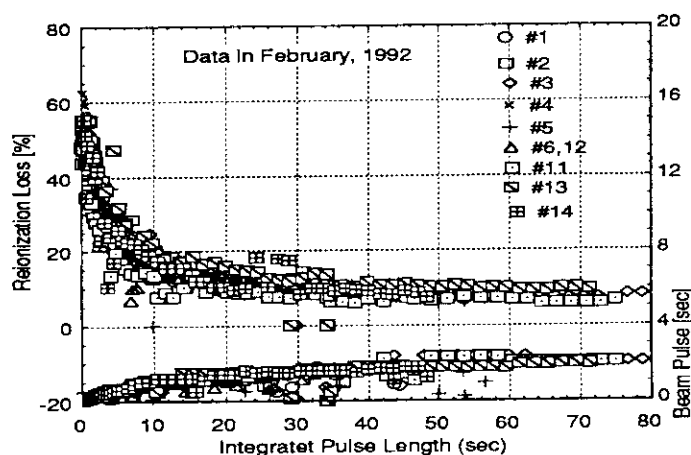


Fig. 2 Port aging in February of 1992 after two months of atmosphere

In the tangential beamline, the integrated beam pulse length for the first duct conditioning was required about 150sec, as shown in Fig. 4, which was almost three times compared with the perpendicular one. It seems to be due to following two reasons. The first reason is for use the duct in common with both upper and lower beamlines in the tangential as compared with one duct with one beamline in the perpendicular. Though the decreasing rate of the re-ionization loss with only one beamline was almost the same with that of the perpendicular, a simultaneous injection with two beamlines cause almost three times larger re-ionization loss because of higher beam power density. The second is for use of graphite armor tiles against the re-ionized beam in the tangential beamline duct as compared with the use of

use of molybdenum tiles in the perpendicular one. The graphite absorbs a large quantity of gases which are hard to detached by the beam impingement. The re-ionization loss increased remarkably with the alteration of the JT-60U plasma parameters such as plasma current and toroidal field, since the impingement position of the re-ionized beam moves with the change of those plasma parameters. The helium glow discharge cleaning seems to be effective also in the tangential beam duct conditioning same as the perpendicular one because the duct (Co-injection line) close to the glow discharge grid in the JT-60U vacuum vessel is shorter conditioning time compared to the other side duct (Counter-injection line) which is positioned at a distance from the anode. The glow discharge cleaning effect will be confirmed in the beginning of 1993 operation with setting directly the newly fabricated glow discharge anode in the tangential NBI ports.

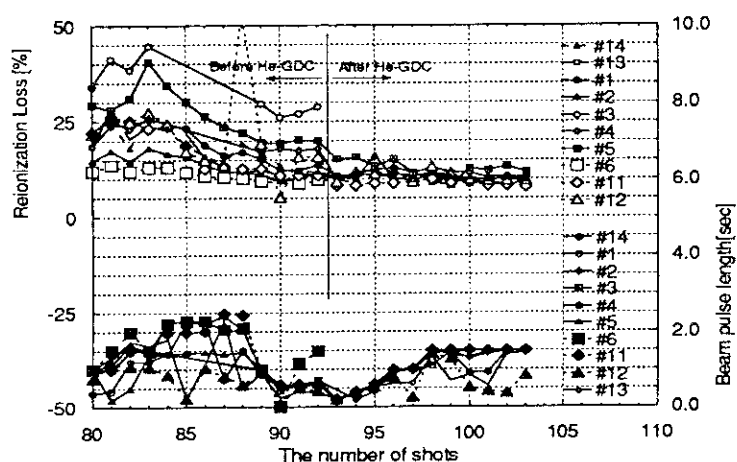


Fig. 3 The He glow discharge cleaning effect on the reionization loss. The reionization loss in No.93 shot decreases rapidly just after a few hours He GDC in the vacuum vessel.

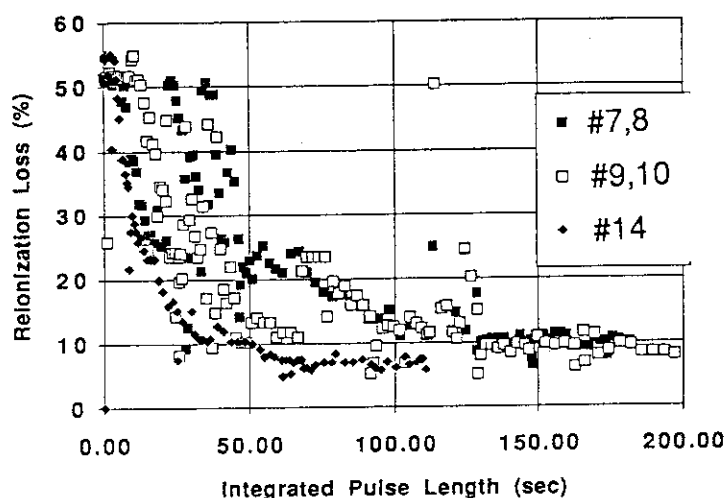


Fig. 4 Comparison of newly fabricated tangential NBI port aging with perpendicular one (#7,8 and #9,10; tangential, #14; perpendicular)

2. Capability of Higher Energy and Higher Power Beam

The ion source accelerator has been modified parts of grid gap spacings and ceramic accelerator column for the purpose of higher energy beam operation up to 120keV. The grid spacing were widened from 4mm/5mm to 4.5mm/10mm, for gap between plasma and gradient grids/gap between gradient and suppression ones. The ceramic insulator column between gradient and suppression grids, which is required more severe voltage holding up to 100kV, altered the surface shape of the column to reduce the concentration of the electric field along the outside of the column.

The operations using the modified accelerator started in spring of 1991 with hydrogen beam. On a few months operations, the beam acceleration voltage rose with ease relatively until around 90kV without the serious voltage breakdown at the accelerator. In July of 1991, the beam species was changed from hydrogen to deuterium. After a several months operation with deuterium, however, the acceleration voltage did not only upward tendency, but rather deterioration. We were identified the cause for the deterioration as the discharge traces on the outside surface of the ceramic insulator column between plasma and gradient grid flanges, which insulator has a voltage holding of about 60kV. Those traces, which causes the discharge easily even in the lower voltage on the outside surface, grow out of numerous surface breakdowns when the voltage applies more than 60kV. This excess voltage, that is correspond to all of the beam acceleration voltage, seems to be applied to the insulator when the gradient grid, which is applied an intermediate voltage of the acceleration, becomes almost the ground by a internal breakdown between the gradient and suppression grids. As the traces are growing up, the voltage holding becomes to be more deteriorated.

The countermeasures against the deterioration of the voltage holding in the accelerator are : one is a cleaning on the insulator surface by a diamond emery paper, other is to set a sphere gap between plasma and gradient grid flanges to make the discharge at the gap before the breakdown on the insulator. The former was getting better the voltage holding just after the cleaning, but the holding deteriorated again after a several days operation by re-creating the discharge traces on the insulator. The later seems to be an effective measure. The spheres, 20mm in diameter, are made of brass. The relation of the sphere gap length and the breakdown voltage was measured by using an accelerator model, and the result is shown in Fig. 5. On the basis of the figure, at first, the gap length of the real accelerator was set at 14mm to be discharged at 40kV, since the maximum voltage between plasma and gradient grids is 30kV in the beam operation. But in case of the gap length of 14mm, the voltage holding in the accelerator has hardly recovered. After that, trying to make the most suitable space of the gap, the optimum was identified as to be 22mm. The operation toward a full performance up to 120keV will start in January of 1993.

Concerning the injection power with deuterium beams, the relation of the neutral beam

power and beam energy has been acquired in the range of up to 105keV as shown in Fig. 6. The acquired neutral power per injector, in maximum so far, is 2.8MW at the beam energy of 100keV. In the beam injected heating experiments in 1992, however, the beam energy could scarcely be risen more than 95keV for the long pulse beam over one second by the ion source breakdown. With the countermeasure against the ion source breakdown as mentioned above, the beam energy will be able to rise over 100keV and the injection power will enhance up to around 3MW per injector in the beam injected plasma heating.

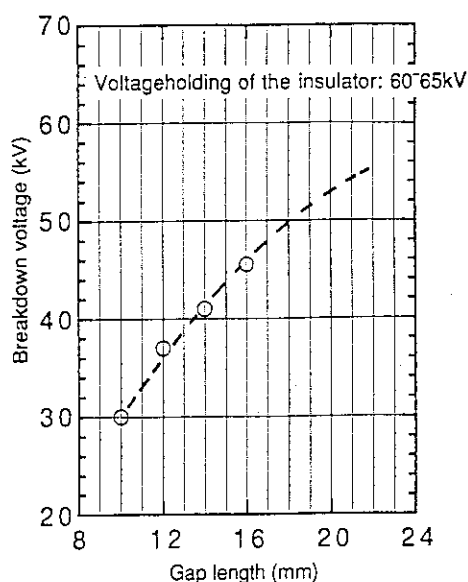


Fig. 5 Measured voltage holding of sphere gap with the accelerator model

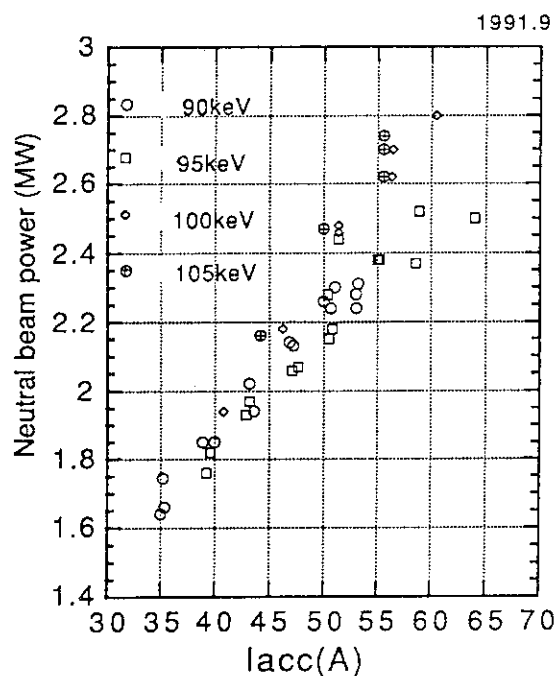


Fig. 6 Neutral beam power per injector in JT-60NBI

10.2 Power Injection Capability and Impedance Matching of ICRF Antennas

S. Moriyama, T. Fujii, M. Saigusa, H. Kimura, K. Annoh,
K. Yokokura, K. Igarashi, M. Terakado, T. Yamamoto

1. Introduction

The modified ICRF heating system for JT-60 Upgrade has started its operation in January of 1992. Though the generator output power of 6 MW and frequency range of 108 ~ 132 MHz are the same as in JT-60, the number of antennas is increased from one to two. Design and size of the antenna, an impedance matching system, transmission lines and a measurement/control system are improved [1]. Performances of the new system such as processes of impedance matching and antenna conditioning are presented.

2. Antenna Conditioning

Figure 1 shows the evolution of the coupled ICRF power to the plasma. The peak voltage on the transmission line between the stub tuner and the antenna is plotted as well. The voltage is only 29 kV for 3.6 MW because of the fairly high coupling resistance of the antenna as shown in [2]. When antenna conditioning will proceed, the peak voltage of 45 kV, which was achieved with the smaller JT-60 antenna, will enable coupled power of 8.7 MW with only two antennas. About 70 shots including impedance matching shots in total for only about 10 days were needed to get 3.6 MW. The number of the shots does not include conditioning shots in vacuum. We repeat conditioning pulses of 200 - 500 kW and 10 - 100 ms width without plasma before experiments and between the plasma shots.

After achievement of 3.6 MW, a gradient of the P_{IC} vs. serial shot number is increasing as the results of antenna conditioning as shown in Fig. 1, so that 3 MW can be coupled after several shots. However experiment time for ICRH are not enough to get higher power so far.

3. Impedance Measurement

The complex antenna input impedance is calculated with forward and reflected power and phase measurements shot by shot. Adequate positions of the stub tuner and the phase shifter for the input impedance are calculated as well. The measured antenna input impedance for shots with the same settings of the stub and the phase shifter are plotted in Fig. 2. The data for two current straps of the antennas among eight are shown on an impedance plane. The calculated power reflection coefficient on the transmission line between stub and amplifier for the stub and the phase shifter positions is also shown as contour lines as a function of the antenna input

impedance. The reflection coefficients are kept below several percent in these shots though antenna-plasma distances are scattered by ~ 0.01 m. Numbers in open circles indicate measured reflection coefficients. This plot shows that the stub and phase shifter positions can be calculated with accuracy which is based on precise calibration on power, phase measurement and electrical length between the antenna and the stub.

4. Frequency Feed-back Control

Frequency feed-back control (FFC) [1] is used to keep precise matching against change of the antenna input impedance due to plasma parameter change during a shot and/or to compensate inadequate stub or phase shifter setting. Figure 3 shows an example for the latter case. In a), trips by the protection circuit occur because reflection coefficient is higher than the threshold, without FFC. In b), the FFC keeps low reflection during the pulse. Frequency shift is about -100 kHz in this case. In c), the reflection is kept low with small frequency shift because the length of the phase shifter is adjusted. Some trippings at low power level in this shot are probably caused by multipactoring discharge or arcing in the antenna.

Scenario for automatic impedance matching is as follows. Length of the stub tuner is scanned (5 cm/sec) during the pulse and is stopped automatically at the adequate length. Then FFC works to keep reflection coefficient less than several percent during the pulse. The FFC is useful for vacuum load as well because the step size of the frequency search can be selected.

5. Coupling to H-mode Plasma

It is not easy to couple ICRF power continuously in L-H transition because change of the density profile with the transition influences coupling resistance or impedance of the antenna, though we have only 5 shots to couple ICRF power to H-mode plasma. Figure 4 shows power trips in H-mode by protection circuit for high reflection coefficient. The coupling resistance, the voltage on the transmission line and the reflection coefficient shown in the figure are for a line which has the highest voltage among eight. In this case, reflection coefficient as in steady state is much lower than threshold of the protection circuit even in the period of H-mode. It shows the change of the antenna impedance is smaller than the range covered by frequency feedback control. In other hand, voltage on the transmission line is increased with decrease of the coupling resistance, and probably arcing occurs because it reaches the voltage limit of the antenna at that time. It seems that something makes the limit lower than usual. Usually we cannot see increment of the reflection coefficient in trips by arcing, because response time of the protection circuit ($< 100 \mu\text{s}$) is much shorter than data sampling time (~ 5 ms).

Though the reduction of the coupling resistance with L-H transition is relatively low (~ 10 %) because of low peak of n_{\parallel} spectrum of the antenna.[2]

6. Summary and Future Plan

The modified ICRF heating system for JT-60 Upgrade has started its operation in January of 1992. RF power up to 3.6 MW for 1.4 sec at 116 MHz has been coupled to the plasma in ~70 shots in total of only about 10 days. Relatively high coupling resistance [2] enables low peak voltage on the transmission line between the stub and the antenna. For example, it is 29 kV for the power of 3.6 MW. When antenna conditioning will proceed, the peak voltage of 45 kV, which was achieved with smaller JT-60 antenna, will enable coupled power of 8.7 MW with only two antennas.

The stub and phase shifter positions can be calculated with accuracy which is based on precise calibration on power, phase measurement and electrical length between the antenna and the stub. The Frequency feed-back control is useful to keep good matching during shot and/or to compensate inadequate stub or phase shifter setting.

The amplifier output power will be increased to 8 MW shortly, by means of selecting higher screen grid voltage and fine tuning of the final stage amplifiers. Moreover, we have a plan to increase output power to 9.5 MW by means of replacing tetrodes of the final stage amplifiers [3].

References

- [1] FUJII, T., et al., Upgrade of JT-60 ICRF heating system, (Proc. 16th SOFT, London 1990), Vol. 2, Fusion Technology (1990) 1171.
- [2] SAIGUSA, M., et al., Sec. 10.3 in this Review.
- [3] MORIYAMA, S., et al., Test results of X2242 and X2274 high power tetrodes with the JT-60 ICRF amplifier in a frequency range of 110-130 MHz, Fusion Engrg. Des. 19 (1992) 41.

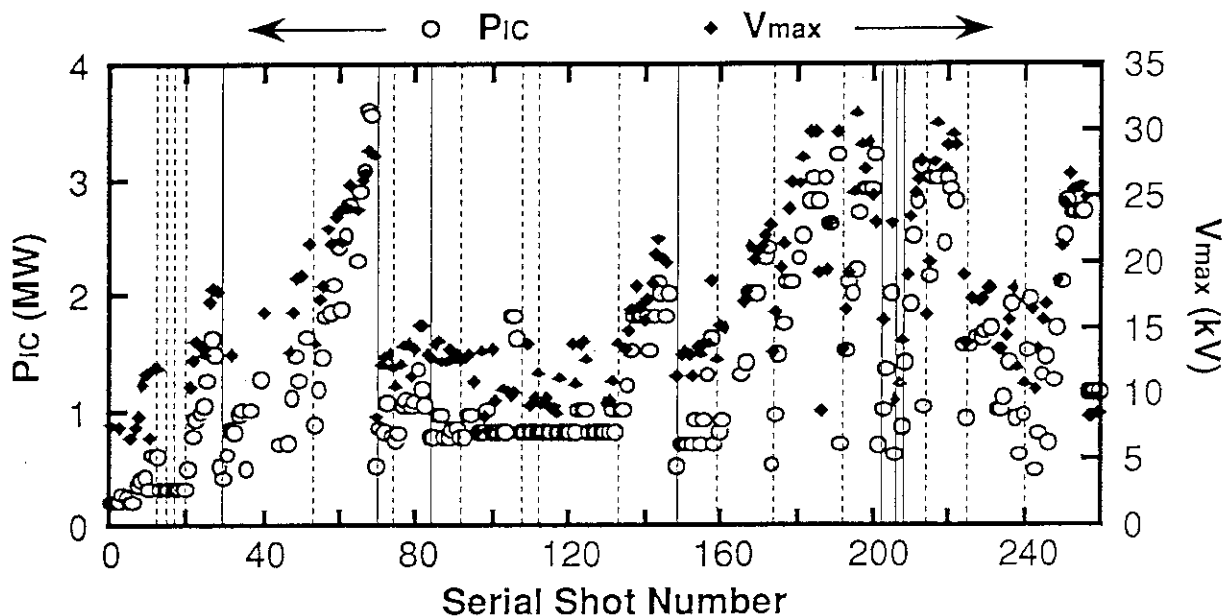


Fig. 1 Evolution of the coupled ICRF power to the plasma. RF power up to 3.6 MW for 1.4 sec at 116 MHz has been coupled to the plasma in ~70 shots in total of only about 10 days. Dotted and solid line show the end of a day and the end of a week respectively.

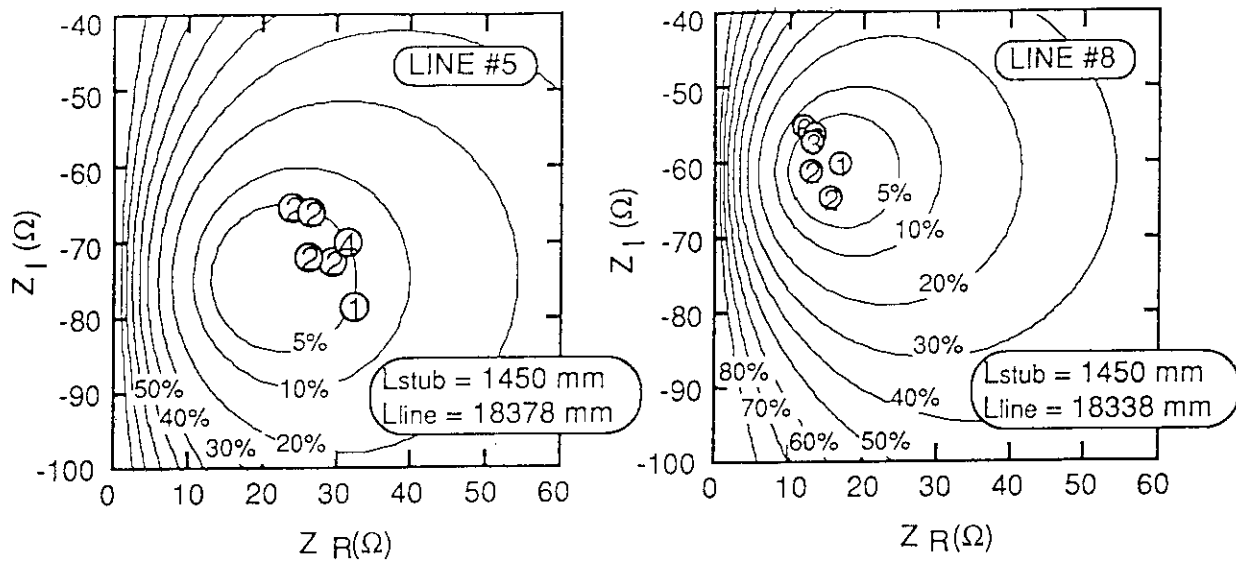


Fig. 2 Measured antenna input impedance for shots with the same settings of the stub and the phase shifter. Two figures are for two lines (current straps) among eight. Numbers in open circles indicate measured reflection coefficients.

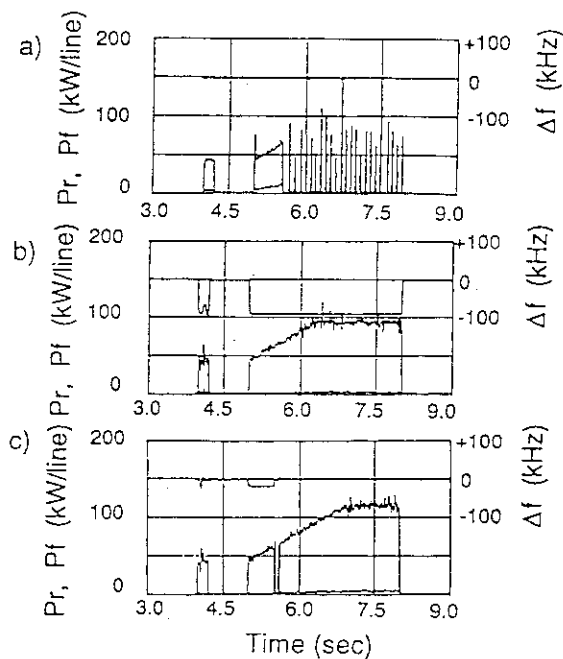


Fig. 3 Frequency feed-back control (FFC) compensate inadequate phase shifter setting. (a) Trippings by high reflection coefficient without FFC. (b) No trippings with FFC. (c) Phase shifter position has been adjusted by the length corresponding to the frequency shift.

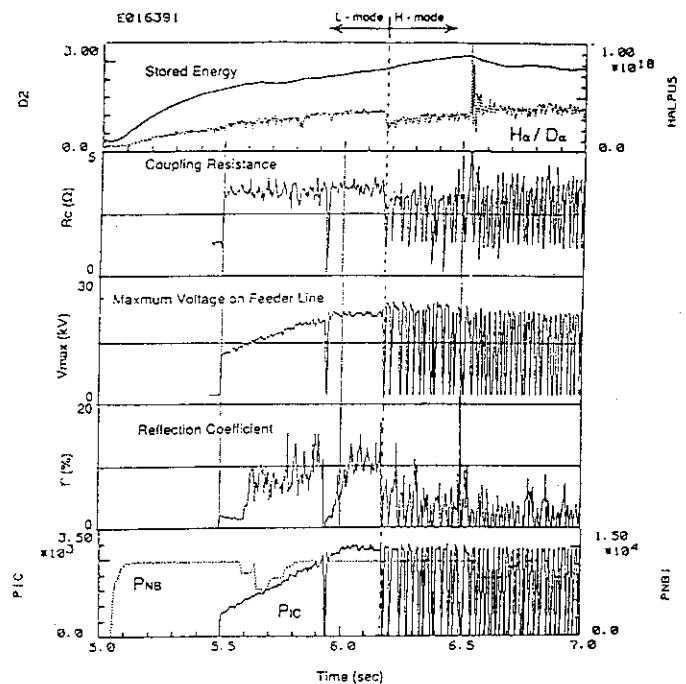


Fig. 4

Power trips in H-mode. The coupling resistance, the voltage on the transmission line and the reflection coefficient are for a line which has the highest voltage among eight. Probably trips occur by arcing in the antenna or transmission line. Coupling resistance of the antenna decreases by 10 % with L-H transition and voltage reaches limit where arcing can be started. The voltage limit (25 kV) is lower than achieved voltage in antenna conditioning (~30 kV). Reflection coefficient does not increase as in steady state because antenna impedance is not remarkably changed in this case.

10.3 Antenna Coupling and radiation Loss During ICRF Power Injection

M.Saigusa, S.Moriyama, T.Fujii, H.Kimura, K.Yokokura, M.Terakado,
K. Igarashi, N.Hosogane, T.Sugie, H.Kubo, T. Yamamoto

1. Introduction

The investigation of coupling properties of ICRF antenna is important for designing a good coupling antenna in real fusion reactor. The heat load of the first wall from the main plasma needs the long distance (15 cm in ITER) between the first wall and the plasma separatrix [1]. The design of JT-60U ICRF antenna was optimized for high loading resistance of out-of-phase, [2] because the distance between separatrix and first wall for a realistic configuration was predicted to be much longer than 5cm, and the heating effects for out-of-phase was higher than that for in-phase in JT-60.

The increase of radiation loss and impurity generation during ICRF pulse has been investigated in many tokamaks for the improvement of heating efficiency. For suppressing the impurity generation from Faraday shield by RF sheath, Beryllium Faraday shield is adopted for JET ICRF antenna, on the other hand, the JT-60U Faraday shield is made of the carbon coated copper plated Inconel 625. However, the proof of the other mechanism for impurity generation is observed in JT-60U.

2. Coupling Properties of ICRF Antenna

The loading resistance (R_c) is defined by $R_c = 2P \cdot (Z_0/V_{\max})^2$ on each element, where P , V_{\max} and Z_0 (50 Ω at JT-60U) are a through power into a stub tuner, the maximum voltage and the characteristic impedance of transmission line connected to the antenna, respectively. The demanded loading resistance for 9 MW heating by two launcher is over 2 ohm, on the assumption that the stand-off voltage is over 50 kV along the transmission line. The actual loading resistance of ICRF antenna is sufficiently high for any toroidal phasing in JT-60U. This result indicates that our design is successful for high power heating experiments with wide gap between separatrix and first wall.

The dependence of the averaged loading resistance of antenna on the averaged electron density is shown in Fig.1. The open circle, open square and open triangle show the experimental data of loading resistance for $(\pi, 0)$, $(0, 0)$ and $(\pi/2, 0)$ phasing, respectively. The solid line is the loading resistance for $(\pi, 0)$ phasing by coupling code assuming that the

separatrix electron density is one tenth of central electron density, and the electron density increase in the distance of 21 cm to the central electron density. The loading resistance for any phasing is over 4Ω in the wide averaged electron density range from 3×10^{18} to $4.5 \times 10^{19} \text{ m}^{-3}$. The loading resistance increase with the averaged electron density in the range below $5 \times 10^{18} \text{ m}^{-3}$ due to the access of cut-off surface to antenna, where the cut-off density of $N_{//}=3$ spectrum, which is the peak of coupled $N_{//}$ spectrum for $(\pi, 0)$ phasing, is about $1.5 \times 10^{18} \text{ m}^{-3}$ at the axial toroidal magnetic field of 4T. On the other hand, the loading resistance decreases gradually with increasing the electron density in the range above $5 \times 10^{18} \text{ m}^{-3}$ due to the steep gradient of wave impedance caused by the steep electron density gradient in front of the antenna.

Figure 2 shows the loading resistance versus the distance between separatrix and first wall for $(\pi, 0)$ phasing. The solid and dashed lines show the calculated loading resistances for $(\pi, 0)$ phasing of JT-60U and JT-60 with the same plasma parameters, respectively. The loading resistance is over 4 ohms at the separatrix-wall distance of about 10 cm in JT-60U. However, the ICRH experiments could not be performed such a large gap in JT-60 because of poor coupling. Therefore, such big improvement of coupling properties from JT-60 to JT-60U is explained as the wider and longer current strap and the longer interval of the toroidal adjacent straps.

The dependence of loading resistance on the toroidal phase difference is shown in Fig.3. The closed circles show the averaged loading resistance of P-12 launcher on each phasing. The open and closed triangles indicate the averaged loading resistances of right two current straps (No.5 and No.6) and the left two (No.7 and No.8) current straps, respectively. The solid, dashed and dotted lines show the fitted lines for each data by the cubic spline functions. The averaged loading resistance decreases with increasing the toroidal phase difference from 0 to 180 degrees as observed in JT-60. However, It is strange that the left side averaged loading resistance is minimum at the phase difference of 180 degrees, because that the minimum coupling is usually around 90 degree phasing in JT-60. The phase difference of minimum coupling is shifted to higher direction due to the dependence of total loading resistance on the phase difference. Therefore, the very steep gradient of loading resistance on the toroidal phasing may shift the phase difference of minimum loading point to 180 degrees.

3. Radiation Loss and Impurity during ICRH

Figure 4(a) and 4(b) show the dependence of the ratio of incremental radiation loss from main plasma and the spectral intensity of Ni+24 on the incidental ICRF power for on-axis-heating and off-axis-heating, respectively. The ratio of the incremental radiation loss to net ICRF power ($\Delta P_{r \text{ main}}/P_{\text{IC}}$) was almost 30 percents in JT-60 limiter discharge with carbon wall and carbon guard-limiter [3]. On the other hand, ($\Delta P_{r \text{ main}}/P_{\text{IC}}$) decreases with increasing ICRF power in the range below 1.5 MW and saturates about 10 percents in the range above 1.5

MW with the on-axis-heating in JT-60U. The reason of high $\Delta P_{r \text{ main}}/P_{IC}$ in low RF power is thought as the multipactoring discharge or the weak single path absorption without high energy ion tail, because the multipactoring discharge has been observed below the same power threshold and a Fokker-Planck code predicts the weak single path absorption in low RF power level. The dependence of incremental spectral intensity of Ni+24 on ICRF power is similar to that of $\Delta P_{r \text{ main}}/P_{IC}$. The $\Delta P_{r \text{ main}}/P_{IC}$ in the off-axis heating regime is 10-40 percents, and the power dependence of $\Delta P_{r \text{ main}}/P_{IC}$ and the incremental spectral intensity of Ni+24 is not clear. Therefore, the impurity generation is caused by the some mechanism concerned with the cavity resonance in vacuum vessel due to the weak single path absorption. The increase of spectral intensity of Ni+24 and Fe+22 could be observed during ICRF pulse. The Nickel ion is which may be generated from Faraday shield made of carbon coated copper plated Inconel 625, because the surface of several Faraday shield elements are damaged.

4. Summary

The loading resistance for any phasing is sufficiently high i.e., about 5 ohm at the distance between separatrix and wall of about 10 cm in the wide electron density range from 3×10^{18} to $4.5 \times 10^{19} \text{ m}^{-3}$. Especially, the loading resistance for (0,0) phasing is over 18 ohm.

The $\Delta P_{r \text{ main}}/P_{IC}$ decreases with RF power for on-axis-heating and saturates about 10 % above RF power of 1.5 MW. The $\Delta P_{r \text{ main}}/P_{IC}$ does not depend on the RF power for off-axis-heating regime. The increase of spectral intensity of Ni+24 during ICRH is observed, which may be generated from Faraday shield made of Inconel 625.

References

- [1] PARAIL, V., FUJISAWA, N., HOPMAN, H., KIMURA, H., LINDQUIST, W., NEVINS, W., REBUFFI, L., SIRONI, M., SWAIN, D., WEGROWE, J.G., "ITER Current Drive and Heating System", ITER Documentation Series, No.32, (1991).
- [2] SAIGUSA, M., FUJII, T., KIMURA, H., MORIYAMA, S., ANNOH, K., "ELECTRICAL DESIGN AND TEST OF ICRF ANTENNA FOR JT-60U", Fusion Engineering and Design, to be published (1993).
- [3] SAIGUSA, M., MORIYAMA, S., FUJII, T., KIMURA, H. and YAMAMOTO, T., "Antenna Coupling Properties and Radiation Loss During ICRF Heating in JT-60U", Radio Frequency Heating and Current Drive of Fusion Devices, Europhysics Top. Conf. Brussels, (1992) 45.

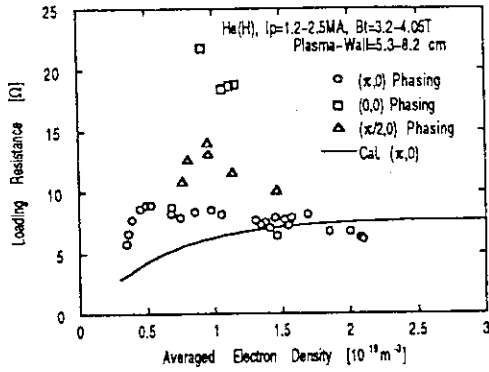


Fig.1 The dependence of the averaged loading resistance of antenna on the averaged electron density.

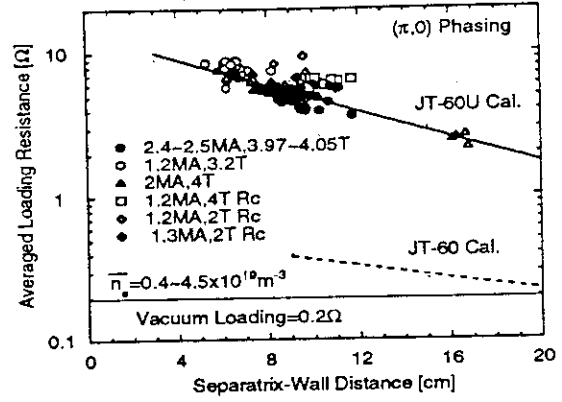


Fig.2 The loading resistance versus the distance between separatrix and first wall for $(\pi,0)$ phasing.

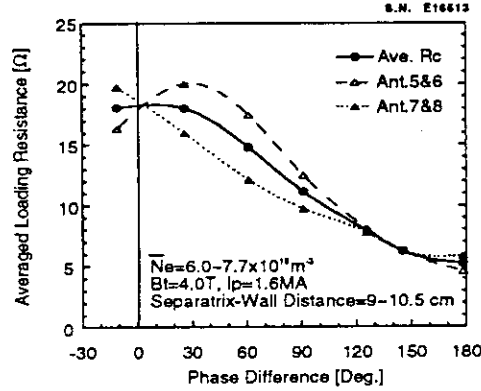


Fig.3 The dependence of loading resistance on the toroidal phase difference.

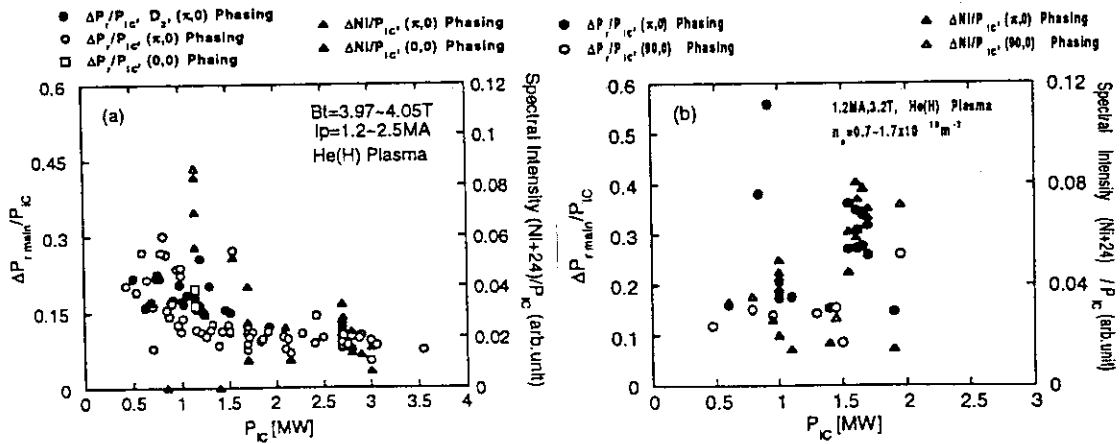


Fig.4 The dependence of the ratio of incremental radiation loss and the flux intensity of Ni+24 on the incidental ICRF power for (a) on-axis-heating, and (b) off-axis-heating, respectively

Acknowledgements

The authors wish to acknowledge the dedicated efforts of the members of Japan Atomic Energy Research Institute in the support of the JT-60U experiments reported here. They also wish to express their gratitude for domestic and international collaborations for the JT-60U program. The contributions of collaborators from many institution and universities have been critical to the success of these experiments.